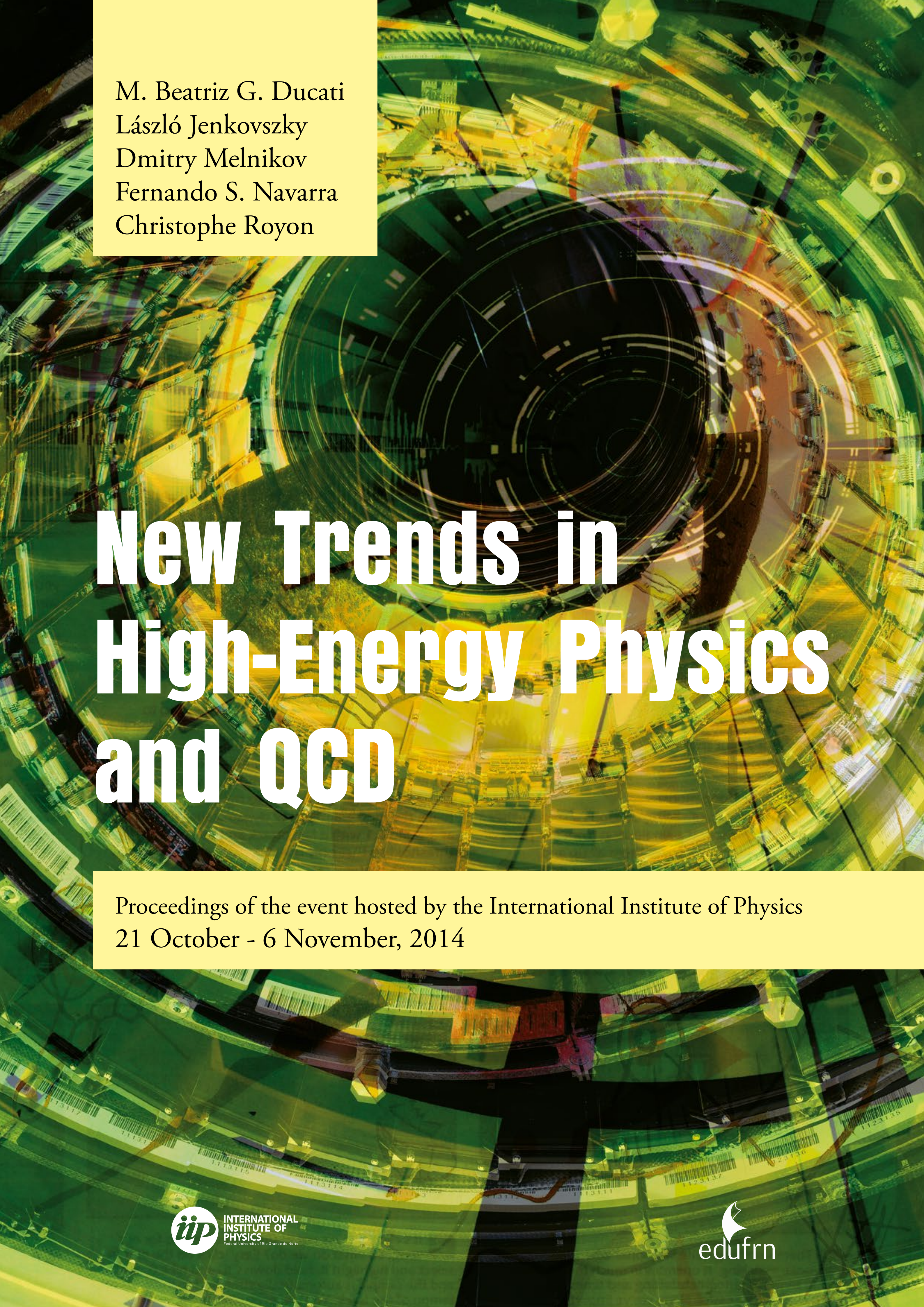

M. Beatriz G. Ducati
László Jenkovszky
Dmitry Melnikov
Fernando S. Navarra
Christophe Royon

New Trends in High-Energy Physics and QCD

Proceedings of the event hosted by the International Institute of Physics
21 October - 6 November, 2014

INTERNATIONAL INSTITUTE OF PHYSICS
Federal University of Rio Grande do Norte

edufrn

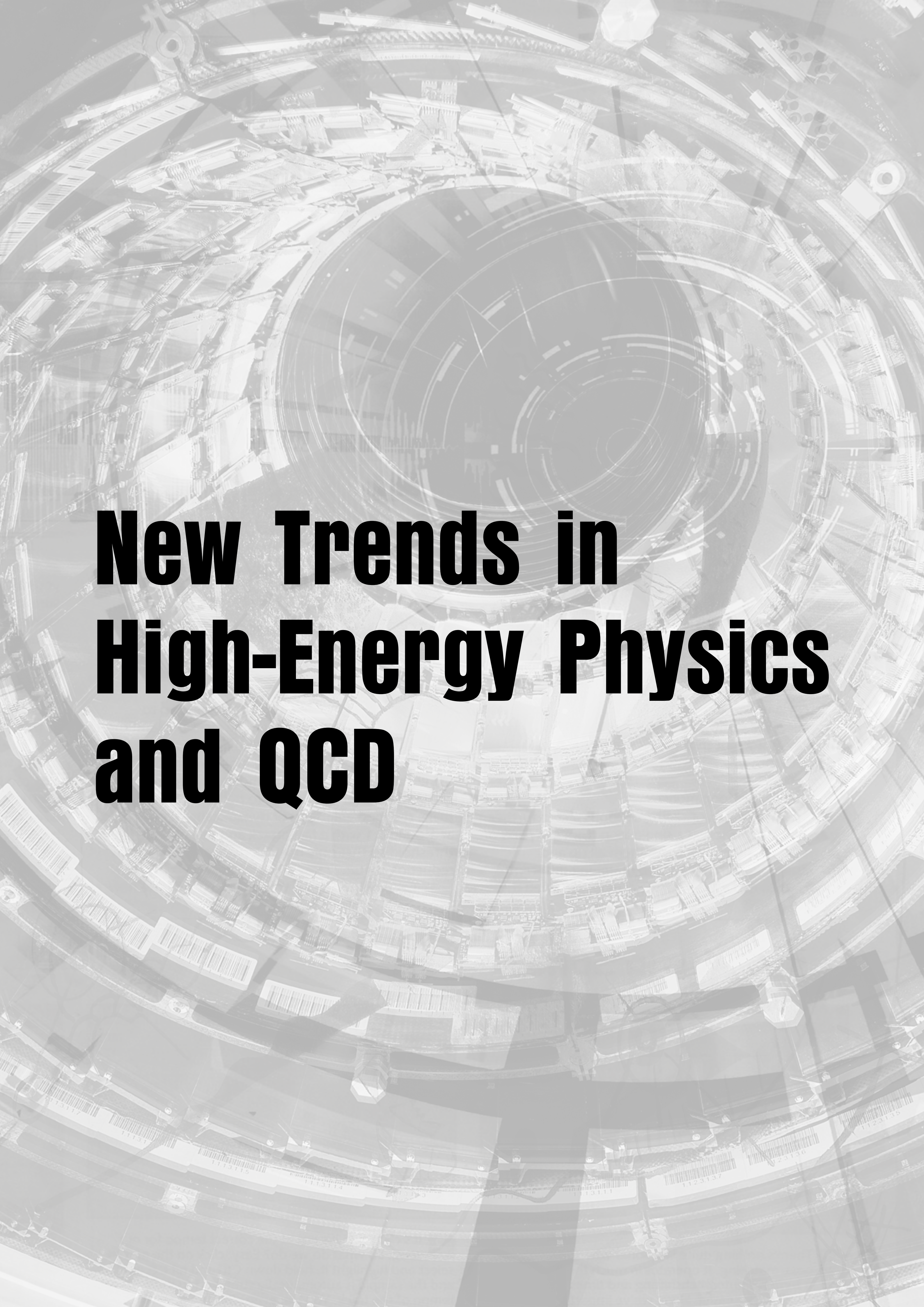

New Trends in High-Energy Physics and QCD

M. Beatriz G. Ducati
László Jenkovszky
Dmitry Melnikov
Fernando S. Navarra
Christophe Royon

New Trends in High-Energy Physics and QCD

Proceedings of the event hosted by the International Institute of Physics
21 October - 6 November, 2014

edufrn

Catalogação da Publicação na Fonte. UFRN / SISBI / Biblioteca Setorial
Especializada do Centro de Ciências Exatas e da Terra – CCET.

New trends in high energy physics and QCD (2014 : Natal, RN).
New trends in high energy physics and QCD: proceedings of the event hosted by the International Institute of Physics 21 October – 6 November, 2014 / edited by M. Beatriz G. Ducati … [et. al]. – Natal: International Institute of Physics, 2016.
xii, 259 p. : il.

Inclui bibliografia.
ISBN: 978-85-425-0697-6

1. Física - Congresso. 2. High energy physics – Congresso. 3. Cromodinâmica quântica (QCD) - Congresso. 4. Física do LHC - Congresso. 5. Física de partículas elementares - Congresso. I. Ducati, M. Beatriz G. II. Universidade Federal do Rio Grande do Norte. III. Instituto Internacional de Física. IV. Titulo.

RN/UF/BSE-CCET CDU 53

Published by:
International Institute of Physics
Federal University of Rio Grande do Norte
http://www.iip.ufrn.br

Credits:
Graphic project: Waldelino Duarte
Cover design: Juliano Lima Barreto
Poster design: Rhonise Pereira Martins
LATEX editor: Dmitry Melnikov
using LATEX's 'iipproc' class by D. Melnikov

Printed in Natal by Unigráfica - Gráfica e Editora Ltda.

Preface

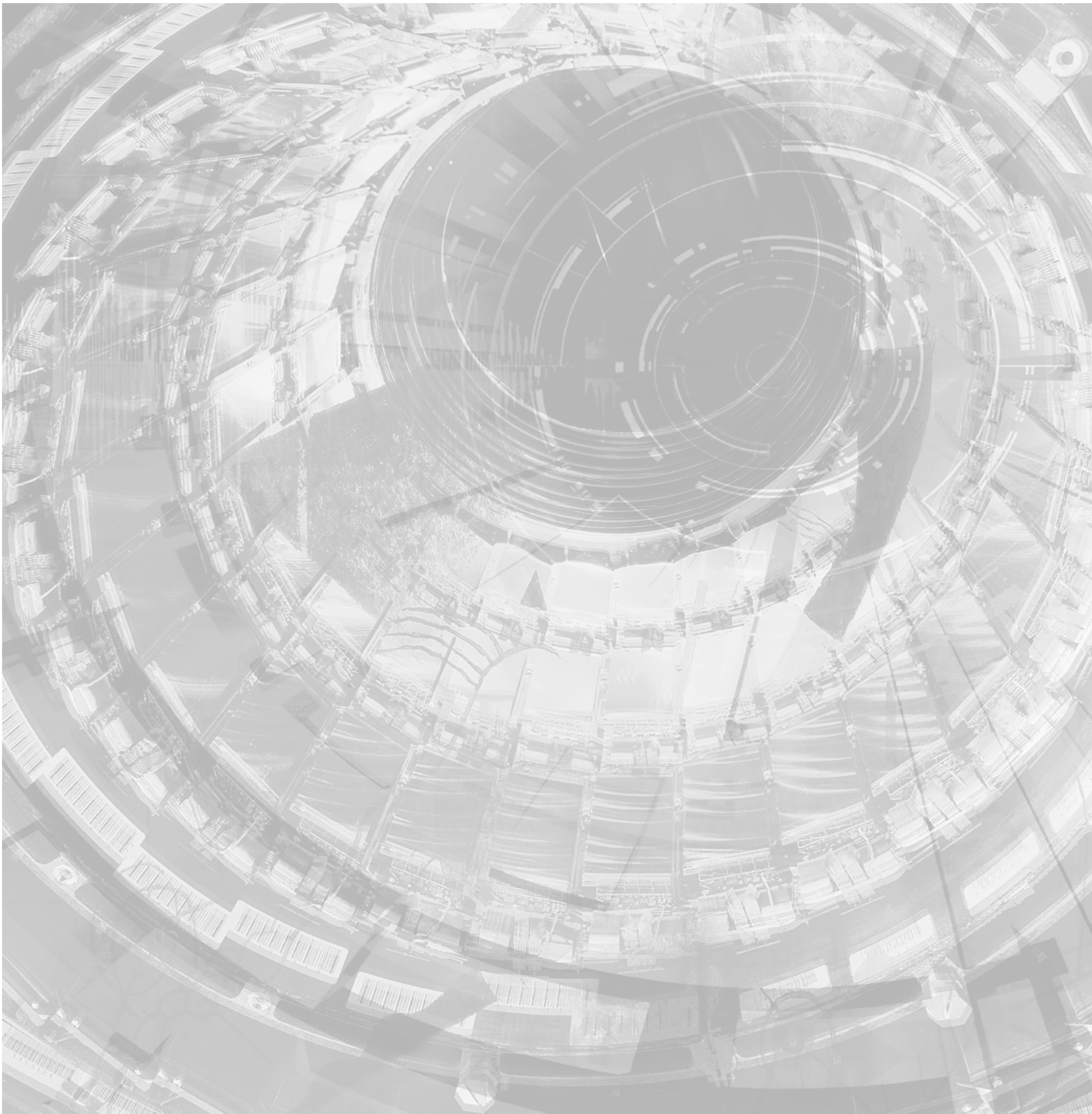

From the editors

M. Beatriz G. Ducati [a] , László Jenkovszky [b] , Dmitry Melnikov [c] , Fernando S. Navarra [d] ,
Christophe Royon [e]

[a]High Energy Physics Phenomenology Group, GFPAE IF-UFRGS, Porto Alegre, Brazil

[b]Bogolyubov Institute for Theoretical Physics, Kiev, Ukraine

[c]The International Institute of Physics, UFRN, Natal, Brazil

[d]The Institute of Physics, University of Sao Paulo, Sao Paulo, Brazil

[e]The University of Kansas, Lawrence, USA

The school and workshop "New Trends in High Energy Physics and QCD" focused on Physics at LHC, took place in Natal, Brazil, between October 21 and November 6, 2014. The event was organized by the International Institute of Physics (IIP) of the Federal University of Rio Grande do Norte (UFRN). The first part of the event, the school, aimed at reviewing the recent developments in all major areas of high energy physics, both theoretical and experimental. The two weeks of school were quite dense and contained 26 lecture series, from two to four lectures, by different physicists, on topics ranging from the recent LHC data analyses on QCD, new phenomena, Higgs physics, etc, and overview of future collider experiments to modern theoretical topics in cosmology and string theory. The full list of lectures and titles is shown in the table below. The last four days of the event were organized in form of a workshop, where 25 talks have been given by 20 physicists. More than 75 participants from 37 institutions from Brazil and abroad (from 15 countries) have attended the event. We are in particular happy to have been able to attract a large number of graduate students from and outside Brazil to participate in this event.

Figure 1: Official photo of the event "New Trends in High Energy Physics and QCD".

Modern high energy physics is represented by many active and quite independent directions in both theory and experiment. Those directions reflect the fundamental challenges that still remain in the theory of elementary particles, as they attempt to resolve them. Indeed, on one hand we do have the Standard Model, which up to now has been a perfect theory of particles as far as the direct experiments, such as colliders are considered. Standard Model predictions have been tested to an impressive accuracy by LHC, Fermilab, LEP and previous generations of collider experiments. However, many less direct experiments, as well as theoretical speculations indicate that this is not yet the whole story. During the school, many aspects related to standard model have been presented and discussed going from perturbative QCD, BFKL formalism, diffractive studies to the physics of the top quark and the Higgs boson. A few lectures were also dedicated to experimental techniques (such as recent developments of jet reconstruction and advanced techniques in Higgs analyses) and new detector developments. The experimental search for physics beyond standard model was also deeply discussed during the school.

One of the most important issue is the challenge brought to us by astronomical observations. They tell us that out there, in the sky, and also around us, there ought to be an enormous amount of known matter and energy that do not fit in Standard Model. Dark Matter consists roughly a quarter of the Unverse's matter density, five times more than ordinary matter, and all evidence signal that it cannot be made of Standard Model particles. Many experimental searches of the Dark Matter particles including Pierre Auger, LHC, etc have not yet reveal any reliable traces of them. This overwhelming topic was also presented and discussed during the school.

One of the most important conceptual challenge to Standard Model is the question of naturalness: matching the theoretical parameters of the model with experimental observations requires extreme fine-tuning which is not natural. Other aspects also include the number of independent parameters (19) and unification of interactions. Among various attempts to solve the naturalness problem, in either some particular aspect of it, or altogether, the one that deserves a special mention is supersymmetry. By expanding the spectrum of particles and imposing a large degree of symmetry on their interactions, SUSY offers a patch that is able in principle to cure many of the Model's problems. Yet it naturally offers candidates for the Dark Matter particles. For this and its beautiful mathematical properties SUSY has derserved a lot of attention from high energy physicists. The big hopes of the community of the SUSY discovery at the LHC have not been realized upon the first phase. The big question now is whether it will be discovered it in the second phase. Both theoretical aspects of SUSY and additional extension of the Standard Model (string or brane theories) as well as the experimental searches were presented during the school.

To make the event more interactive, the students were invited to present the topic of their PhD in a short 30-minute talk. Presenting research results in a consise and clear manner is a necessary skill that every scientist should aim for, and we are glad that we could provide a suitable environment for those young scientists to present their work and studies in the presence of their fellow colleagues as well as senior experts in high energy physics. A four-day miniworkshop, following the school allowed the students to participate in a real scientific meeting in particle physics, where they could apply the knowledge and experience acquired during the school.

We believe that nearly three weeks of the event were very productive for the participants. We hope that its program helped younger ones to expand their horizons in modern particle physics and to stimulate their interest in pursuing a career in fundamental research. Last but not least, we are happy for the opportunity to host this school in Latin America, and in particular, in the Northeast of Brazil.

On behalf of the participants and the organizers we would like to thank the supporting organizations, including the IIP and the UFRN, as well as Brazilian agencies supporting fundamental research: the Coordination for the Improvement of Higher Education Personnel (CAPES) of the Ministry of Education and the National Council for Scientific and Technological Development (CNPq) of the former Ministry of Science, Technology and Innovation. We would also like to thank the local organizing committee and support staff, including Stivny Batista, Waldelino Duarte, Luana Fernandes, Juliano Lima, Rodrigo Lopes, Bruno Pacheco, Sylvio Quezado, Rodrigo Soares, Cyro Souza and especially Juan Cabral and Bia Pessoa, for the help and efforts to make the event smooth and enjoyable.

The volume is separated in two parts. The first one contains the notes of a part of the lectures delivered at the two-week school. The second part is a collection of short contributions from the talk given at the workshop of last week of the event. We close the welcome word with the full list of contributions to the school (Table 1) and to the workshop (Table 2).

Speaker	**Parts**	**Title**
Marc Besançon	1-4	*Phenomenology and experimental aspects of SUSY and searches for extra dimensions at the LHC*
Grigorios Chachamis	1-4	*BFKL phenomenology*
Emmanuel de Oliveira	1-4	*QCD, partons and all that*
Albert de Roeck	1-3	*Introduction to LHC and QCD/SM measurements and search for SUSY/dark matter*
Beatriz Ducati	1-2	*From DGLAP to non linear evolution equations*
Victor Fadin	1-3	*Impact factors for reggeon gluon transitions*
Brian Foster	1-3	*Future accelerators*
Rikkert Frederix	1-3	*Top physics*
Vitor de Souza	1-3	*Astroparticle Physics*
Victor Gonçalves	1-2	*Photon - Hadron Interactions at LHC*
Dmitry Gorbunov	1-3	*Cosmology*
Edmond Iancu	1-4	*QCD for heavy ion collisions: from color glass condensate to quark gluon plasma*
László Jenkovszky	1-2	*Diffraction in lepton- and hadron-induced reactions*
Bruno Lenzi	1-4	*Higgs physics and experimental results*
Magno Machado	1-2	*Phenomenology of hard diffraction at high energy*
Dmitry Melnikov	1-2	*Holography and hadron physics*
Fernando Navarra	1-2	*New exotic hadrons: production and decay in heavy ion collisions*
Jorge Noronha	1-3	*AdS/CFT and applications to particle physics*
Eduardo Pontón	1-3	*BSM and extra-dimensions*
Risto Orava	1-2	*Basic introduction to diffractive scattering*
Murilo Rangel	1-2	*Jet physics at the LHC (experimental aspects)*
Christophe Royon	1-2	*Diffraction and photon-induced processes at the LHC*
Gary Shiu	1-3	*Introduction to string theory*
Andrei Slavnov	1-3	*Gauge fields with spontanously broken symmetry*
Gregory Soyez	1-3	*Jet physics at the LHC*

Table 1: List of titles of the school lectures

Speaker	**Title**
Gilson Batista	*Quarks in the nuclear medium*
Massimo Bianchi	*More on soft theorems: trees, loops and strings*
João de Melo	*Spin-1 Light-Front Prescriptions whitout Zero Modes*
Mateus da Rocha	*Energy-dependent form factors and the total cross section at LHC*
Victor Fadin	*Introduction to the BFKL equation*
Daniel Fagundes	*Minijets and cosmic ray particle production at very high energy*
Márcio Ferreira	*Inverse magnetic catalysis in the Polyakov–Nambu–Jona-Lasinio models*
Sylvain Fichet	*Light-by-light scattering at the LHC from new physics*
Dmitri Gitman	*Coherent and semi-classical states of a free particle*
Dmitri Gitman	*Supercritical nuclei revisited*
Victor Gonçalves	*Heavy quark production in cosmic ray interactions*
Dmitry Gorbunov	*Baryonic dark matter and the LHC*
Andrei Grabovsky	*Higher Fock states in CGC*
László Jenkovszky	*Vector meson production at HERA and at the LHC*
Eloi le Quilleuc	*Measuring the top-quark coupling at the LHC in the ttH channel*
Magno Machado	*Exclusive photoproduction of charmonium and bottomonium states in pp, pA and AA collisions at the LHC*
Uri Maor	*Diffraction as a fundamental ingredient in soft scattering*
Cristiano Mariotto	*Double J/Psi production in diffractive processes at the LHC*
Eduardo Miranda	*Elastic and inelastic diffraction at the LHC*
Gilberto Ramalho	*A covariant model for the nucleon spin structure*
Christophe Royon	*Search for BFKL resummation effects at hadronic colliders*
Matthias Saimpert	*Anomalous quartic neutral gauge couplings at the LHC*
Werner Sauter	*Production of particles at large momentum transfer*
Simão Silva	*Search for a Torsion Field in pp+e-+X collisions at =8 TeV with the ATLAS/LHC*
Anatoly Shabad	*Point charge as a soliton in truncated QCD*

Table 2: List of titles of the workshop talks

Contents

Lecture Notes

Grigorios Chachamis

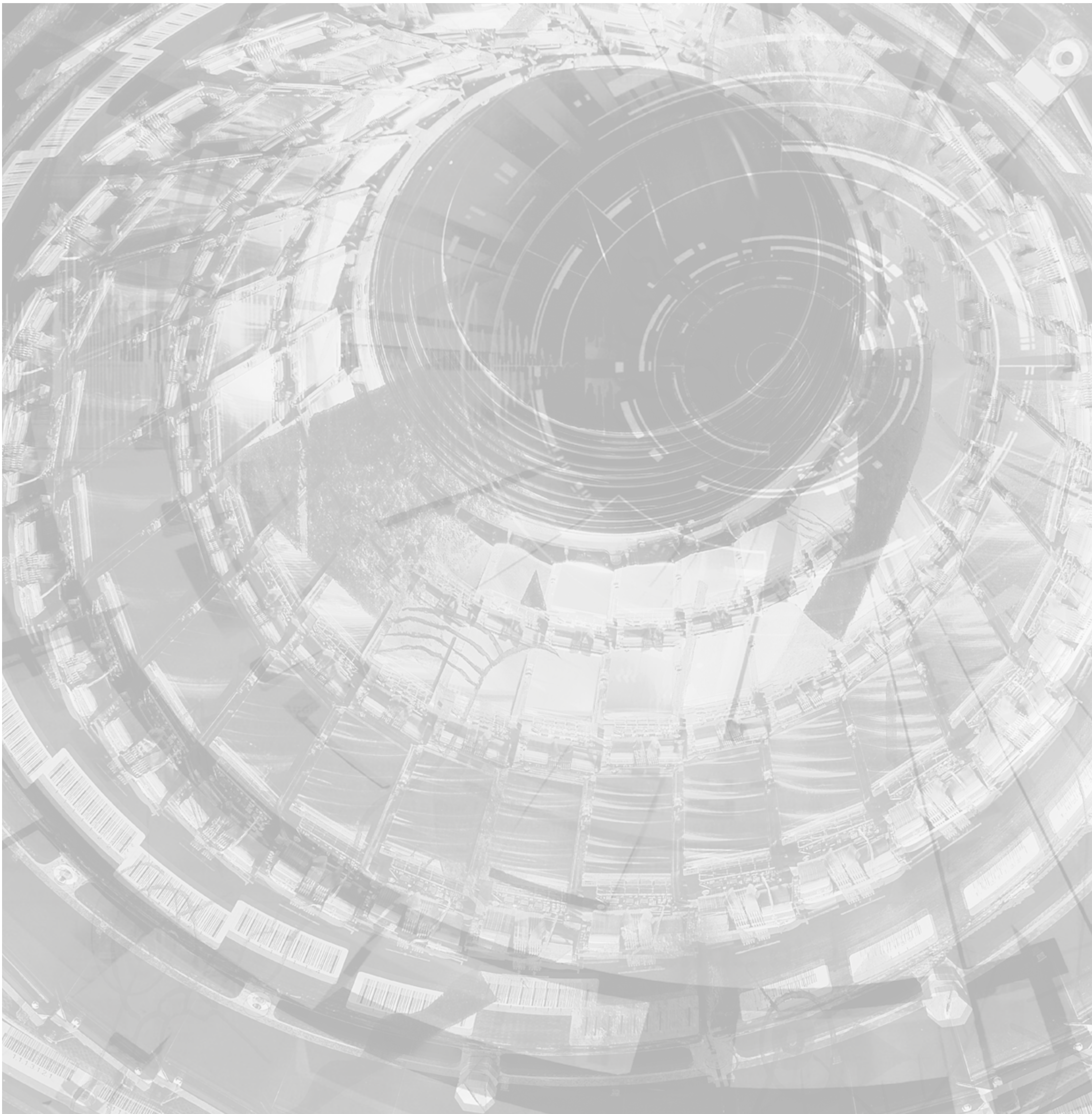

BFKL phenomenology

Grigorios Chachamis [f]

[f]Instituto de Física Teórica UAM/CSIC & Universidad Autónoma de Madrid, Madrid, Spain

Abstract

We discuss some of the topics covered in a series of lectures under the same title that was given at the Summer School on High Energy Physics at the LHC: New trends in HEP in Natal, Brazil. In particular, after some general thoughts on phenomenology we present a pedagogical introduction to the BFKL formalism and we discuss recent BFKL phenomenological studies for LHC observables.

1 Introduction

Phenomenology in its broader meaning, one would argue, has generally been instrumental in advancing the progress of human thought. Despite the fact that the etymology of the term, from the Greek words *phainómenon* and *lógos*, implies that phenomenology is the study of 'that which is observed', one has to stress that there is not a unique definition for phenomenology, or more accurately, that the definition varies a lot depending on the context (philosophy, psychology, science) and different people from different origins may associate different notions with the term.

If we restrict ourselves in seeking a definition for phenomenology within the grounds of modern physics, the following directive provides a possible candidate:"Observe 'that which appears', a collection of phenomena that share a unifying principle, and try to find patterns to describe it. The patterns might or might not be of fundamental nature or they might be up to a certain extend". More specifically, for high energy physics, a possibly satisfactory statement could be the following: "Use assumed fundamental laws to produce theoretical estimates for physical observables and then compare against experimental data to validate or falsify the assumed laws".

In the past decades, high energy physics was mostly studied in colliders and the vast majority of experimentally measured quantities were observables stemming from the collision of particles. If the Standard Model (SM) enjoys such a wide acceptance as the correct theory for the description of the Strong and the Electroweak (EW) interactions, it has to do with a titanic effort from the experimental side (HERA, LEP, Tevatron, LHC) and an equally important effort from the theory community to provide theoretical estimates for a large amount of processes. The comparison between theory and experiment results in favor of the SM and so far no clear signal for new physics has emerged in any of the collision experiments. It will be very interesting to see whether the second run of the LHC could change this picture.

Apart from the (generally rare) times that an experimental situation is a standalone manifestation of a new phenomenon, it is usually after copious and demanding studies from both theoretical and experimental sides that one can speak about agreement or disagreement of the predictions with the data. Focusing hereafter on the theory side, we could argue that SM phenomenology actually means computing estimates for observables by employing perturbation theory since the SM Lagrangian cannot be solved exactly. We know that perturbation theory is only an approximation and cannot be applied without the presence of a small expansion parameter. The usual small parameter is the EW coupling in calculations in the EW sector of the SM and the strong coupling α_s in QCD. Moreover, in hadronic colliders, practically no physical observable lives solely in a region of the phase space[1] where non-perturbative input is unnecessary. This becomes evident for LHC observables if we think that the

[1]The term "phase space" here is to be understood as a very wide notion: all possible configurations of initial conditions connected to all possible configurations of final states consist the phase space of observables.

colliding particles are protons, objects of a non-perturbative nature due to their size and structure. Various factorization theorems and schemes are employed to put some order to that picture. The main idea behind factorization is that one separate the hard (perturbative) from the soft (non-perturbative) physics such that in order to have a theoretical estimate for an observable one needs to calculate the contribution from hard physics to that process and convolute it with a parametrization of the soft physics involved that takes into account all available data. The parametrization is based on the fact that soft physics can be in general process independent, e.g. the proton PDF's describe the probability to find a certain parton in the proton disregarding of the process in which the proton is involved.

The main bulk of phenomenological studies in the past decades is based on the so-called 'fixed order' calculations in which one considers only the first few terms of the perturbative expansion for a (hard) process and computes these terms fully. The perturbative expansion is realized via Feynman calculus and each term is graphically represented by Feynman diagrams. Assuming only the first term results to leading order (LO) calculations, assuming the first and second term results to next-to-leading (NLO) calculations, assuming the first three terms leads to next-to-next-to leading (NNLO) calculations and so forth. Most of the LHC processes require theoretical prediction at least to NLO and some of them to NNLO accuracy for a definite answer after comparing against experimental data. The complexity increases enormously as one goes from one order to the next and also as the number of external particles that participate in the process increases. Fixed order calculations justify fully their reputation of being 'precision physics' calculations since the only uncertainty that remains at the end is the uncertainty from omitting the higher term contributions and this can be well estimated in most cases[2].

In many cases, especially in hadron collider processes, not only a fixed order calculation is too complicated to be done beyond LO (e.g. multi-jet production) but also we have the presence of a large scale (usually the logarithm of a kinematical invariant or a mass) that persistently appears in every order combined with the small expansion parameter in a certain way and potentially could break down the convergence of the perturbative expansion. In such cases, we need a resummation scheme to sum all the large contributions from all terms (to order infinity). The result of the resummation can either be combined with a fixed order calculation or, if it encodes truly the most important contributions of each term in the expansion, it can be used alone as the theoretical estimate for a hard process. We should stress that any resummation approach is to be understood in the context of perturbation theory and also that each term of the perturbative expansion is represented by (effective) Feynman diagrams.

One of the most important resummation programs appears in the context of high energy scattering. If in a process the center-of-mass energy, $\sqrt{s}$, is really large then the product $(\alpha_s \ln s)$ can easily be of order unity. If in addition s is much larger than any other scale present, then in principle any term $\sim (\alpha_s \ln s)^n$, where n is arbitrarily high, would give the main contribution of the n-th term of the expansion and this term cannot be omitted. Instead, one has to resum all these important contributions up to $n \to \infty$. This is done within the Balitsky-Fadin-Kuraev-Lipatov (BFKL) formalism at leading logarithmic (LA) [1–4] and at next-to-leading logarithmic (NLA) accuracy [5, 6]. For the latter, also terms that behave like $\alpha_s(\alpha_s \ln s)^n$ are resummed. One sees thus, that resummation programs can also be regarded as a new perturbative expansion: the first term contains all the leading logarithmic terms to all orders (LO approximation), the second term the sub-leading logarithms (NLO corrections) and so on.

In the next section we will sketch a derivation of the BFKL equation that resume all large logarithms in s after introducing some important notions that are ubiquitous in the BFKL framework and of which the origin or the relevance are not obvious to the non-expert. In Section 3 we will discuss recent phenomenological studies for BFKL related observables and in Section 4 we will conclude with a general discussion.

[2]There is also uncertainty from the non-perturbative input (e.g. PDF's) but this is not directly connected to the fixed order calculation of the hard part of a process, or at least this is what factorization dictates.

2 The BFKL equation and the Pomeron

In this section, using a diagrammatic approach, our aim is to see

- How logarithms in s make their appearance in high energy scattering
- That these logarithms appear in all orders of the perturbative expansion
- How to resum these logarithms.

Setting our goals as listed above accounts as a minimal but hopefully an honest try to gain a first insight in BFKL physics. Following this course of reasoning though, will actually permit us to see a lot more, albeit on a very pedagogical level only. The ambitious reader who wants a deeper insight should consult more complete presentations of the topic, for example the works in Refs. [7–12] and the original publications which arguably hide a richness of thought that cannot be covered in any review article.

Nevertheless, even in this minimalistic setting of goals as presented above and while we are chasing $(\alpha_s \ln s)^n$-like terms in Feynman diagrams we will still be able to see

- How we separate virtual from real corrections and treat them in a separate manner and why this is of great importance.
- What the reggeization of the gluon is and pinpoint its origin.
- The different role of longitudinal and transverse degrees of freedom
- The "derivation" of the BFKL equation and its solution for the forward case.
- What the Pomeron is and whether we can describe it in a simple manner.

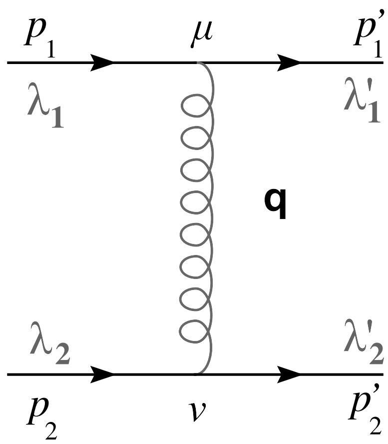

Figure 2: qq-scattering at LO order.

Let us start by considering qq-scattering at lowest order (Born level) as depicted in Fig. 2. Our discussion will be based a lot on the way the topic is presented in [7,8]. Since we are concerned with high energy scattering, we will work in the high energy limit which is defined by the condition

$$s \gg |t|,\, u \simeq -s\,. \tag{1}$$

The two quarks are interacting via a gluon exchange in the t-channel. We can write the momentum of the gluon in Sudakov parametrisation:

$$q \,=\, \rho\, p_1 \,+\, \sigma\, p_2 \,+\, q_\perp\,, \tag{2}$$

where p_1 and p_2 are the momenta of the incoming quarks and $q_\perp = (0, \mathbf{q}_\perp, 0)$ is a four-vector with non-zero entries for only the transverse part of the gluon momentum. To denote two-dimensional transverse vectors we use boldface characters hereafter. To keep contact with the physical picture of a collision in an experiment, any transverse momentum in the following should be understood as the projection of the total momentum on the transverse to the beam axis plane. Our kinematical invariants then expressed in Sudakov variables read: $s = 2p_1p_2$ and $t = q^2 = \rho\,\sigma s - \mathbf{q}^2$. We should keep in mind that for perturbation theory to apply, we need the presence of a hard scale Q that will ensure the smallness of the strong coupling $\alpha_s(Q)$. We assume that such a scale exists but we leave it unidentified for the moment. Moreover, all factors in the formulae to follow that are irrelevant to the kinematics (such as color factors) will be suppressed.

For the upper vertex in Fig. 2 we have:

$$-\,ig_s\bar{u}(p_1+q)\gamma_\mu u(p_1)\,. \tag{3}$$

Because of Eq. 1, $q \ll p_1$ and the above formula can be approximated by

$$-\,ig_s\bar{u}(p_1)\gamma_\mu u(p_1) \simeq -2ig_s p_1^\mu\,. \tag{4}$$

Following the same reasoning for the lower vertex, the amplitude for the process at hand at LO reads

$$A^{(0)}(s,t) = 8\pi a_s\;\mathcal{CF}_1\frac{s}{q^2} = 8\pi a_s\;\mathcal{CF}_1\frac{s}{t}\,. \tag{5}$$

where $\mathcal{CF}_1$ denotes a color factor. We see that there are no logarithms in s in Eq. 5 as was easy to guess beforehand. We would like now to move to the next order and consider diagrams that stem from the tree diagram after attaching another gluon. This new gluon can either be virtual, in which case we will have one-loop diagrams (virtual radiative corrections), or it can be real which would mean that it could in principle be detected in the final state (real corrections). Instead of considering both real and virtual corrections simultaneously at NLO, we will follow a different course. We will consider first only the virtual correction, first at NLO, then at NLLO and see where this approach can take us.

It turns out that one-loop diagrams with self-energy and vertex corrections are sub-leading in $\ln s$ and do not need to be computed. Only box diagrams are contributing and the ones that give the relevant $\ln s$ term are shown in Fig. 3.

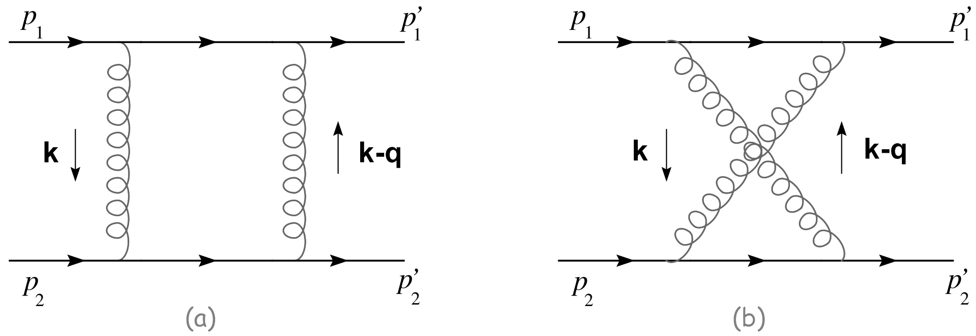

Figure 3: qq-scattering, one-loop corrections.

Let us focus on the Fig. 3(a) diagram. We can calculate its imaginary part using the Cutkosky rules (see Fig 4) and then obtain the full amplitude by dispersion relations. Denoting the NLO amplitude by $A^{(1)}(s,t)$ we have:

$$ImA^{(1)}(s,t) = \frac{1}{2}\int d\mathrm{PS}^{(2)}A^{(0)}(s,k^2)A^{(0)\dagger}(s,(k-q)^2)\,, \tag{6}$$

where $A^{(0)}(s,k^2)$ and $A^{(0)\dagger}(s,(k-q)^2)$ are the tree amplitudes in Fig. 4 with the quark lines being on shell at the cut points and $A^{(0)\dagger}$ denoting the hermitian conjugate of $A^{(0)}$. The two-body phase space

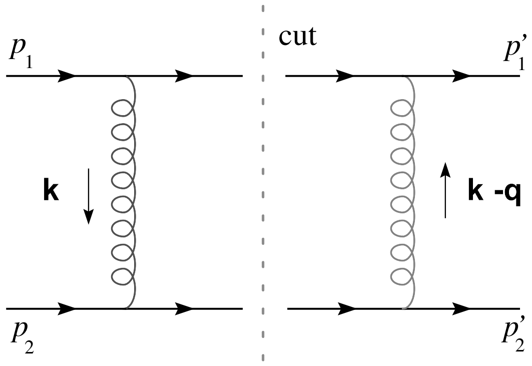

Figure 4: qq-scattering, one-loop cut amplitude.

$\int d\mathrm{PS}^{(2)}$ is given by

$$\int d\mathrm{PS}^{(2)} = \int \frac{d^4k}{(2\pi)^2}\delta((p_1-k)^2)\delta((p_2+k)^2)\,. \tag{7}$$

Again, by introducing Sudakov variables ρ, σ we can express k and d^4k as

$$k = \rho\, p_1 + \sigma\, p_2 + k_\perp,\quad d^4k = \frac{s}{2}d\rho d\sigma d^2\mathbf{k}\,. \tag{8}$$

so that we finally obtain for the two-body phase space:

$$\int d\mathrm{PS}^{(2)} = \frac{1}{8\pi^2 s}\int d^2\mathbf{k}\,. \tag{9}$$

The two tree level amplitudes in Eq. 6 read

$$A^{(0)}(s,k^2) \ = \ -8\pi a_s \mathcal{CF}_2\frac{s}{\mathbf{k}^2} \tag{10}$$

and

$$A^{(0)\dagger}(s,(k-q)^2) \ = \ -8\pi a_s \mathcal{CF}_3\frac{s}{(\mathbf{k}-\mathbf{q})^2}, \tag{11}$$

where $\mathcal{CF}_2$ and $\mathcal{CF}_3$ are color factors. The imaginary part of $A^{(0)}(s,t)$, with the help of Eq. 9, becomes:

$$\mathrm{Im}A^{(1)}(s,t) \ = \ 4\alpha_s^2\, s\,\mathcal{CF}_4\int\frac{d^2\mathbf{k}}{\mathbf{k}^2(\mathbf{k}-\mathbf{q})^2} \tag{12}$$

and by dispersion relations we can reconstruct the full amplitude which reads:

$$A^{(1)}(s,t) \ = \ -4\frac{\alpha_s^2}{\pi}\,\mathcal{CF}_4\ln(\frac{s}{t})\, s\int\frac{d^2\mathbf{k}}{\mathbf{k}^2(\mathbf{k}-\mathbf{q})^2}\,. \tag{13}$$

We remind the reader that we are tracing leading logarithms in s, and since $s/t<0$ we can write for a generic amplitude $\mathcal{A}\sim\mathcal{B}\ln\frac{s}{t}$ after making the decomposition into real and imaginary parts:

$$\mathcal{A} = \mathrm{Re}\mathcal{A} + i\ \mathrm{Im}\mathcal{A} \sim \mathcal{B}\ln\frac{s}{t} = \mathcal{B}\ln\frac{s}{|t|} - i\pi\mathcal{B} \tag{14}$$

which simply means $\mathrm{Re}\mathcal{A} \ = \ -\frac{1}{\pi}\,Im\mathcal{A}\ \ln\frac{s}{|t|}$. Thus, after defining

$$\epsilon(t) = \frac{N_c\alpha_s}{4\pi^2}\int -\mathbf{q}^2\,\frac{d^2\mathbf{k}}{\mathbf{k}^2(\mathbf{k}-\mathbf{q})^2}\,, \tag{15}$$

where the function $\epsilon(t)$ is called gluon Regge trajectory, we rewrite Eq. 13 as

$$A^{(1)}(s,t) \;=\; -\frac{16\pi\alpha_s}{N_c}\,\mathcal{CF}_4\frac{s}{t}\,\ln(\frac{s}{t})\,\epsilon(t)\,, \tag{16}$$

whereas for the Fig. 3(b) diagram in the crossed channel it will be:

$$A^{(1)}_{\rm cross}(s,t) \;=\; -\frac{16\pi\alpha_s}{N_c}\,\mathcal{CF}_5\frac{u}{t}\,\ln(\frac{u}{t})\,\epsilon(t)\,. \tag{17}$$

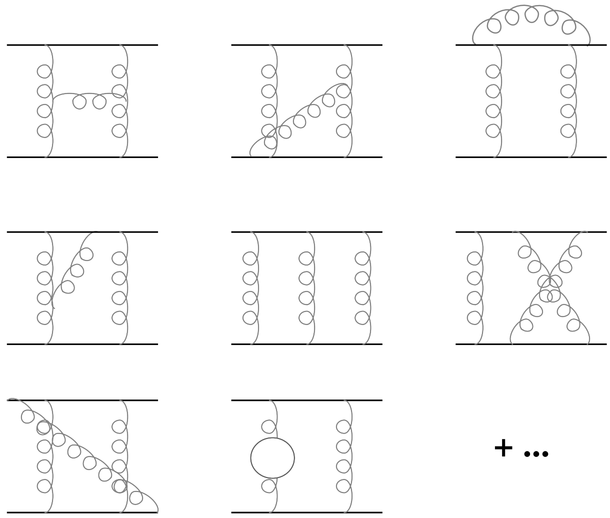

Figure 5: qq-scattering, two-loop diagrams.

By adding the last two relations and keeping in mind that $u \simeq -s$ we obtain the one-loop amplitude. Considering colour octet exchange[3], we can express the one-loop amplitude in terms of the tree level one, specifically:

$$A^{(1)}_8(s,t) = 8\pi a_s\mathcal{CF}_1\;\frac{s}{t}\;\ln(\frac{s}{|t|})\,\epsilon(t)\;=\;A^{(0)}\;\ln(\frac{s}{|t|})\,\epsilon(t)\,. \tag{18}$$

One order higher in the perturbative expansion, to $\mathcal{O}(\alpha_s^3)$, we have to consider many Feynman diagrams like the ones in Fig. 5 but fortunately not all of them are accompanied by leading logarithms. The ones we need to compute are box diagrams, in particular the two-loop box diagrams in Fig. 6. Using the Cutkosky rules again, we can express the two-loop diagrams into one-loop and tree contributions that are known from the analysis so far. Indeed in Fig 6, after multiplying the amplitudes in the left hand side of the cut line with the hermitian conjugates of the ones in the right hand side, summing over helicities and integrating over the phase space we reach the very interesting result:

$$A^{(2)}_8(s,t) =\; A^{(0)}(s,t)\,\frac{1}{2}\ln^2(\frac{s}{|t|})\,\epsilon^2(t)\,, \tag{19}$$

where the two-loop amplitude is expressed in terms of the LO one. The expressions for $A^{(2)}_8(s,t)$ and $A^{(1)}_8(s,t)$ tell us that the partial result for the amplitude up to order $\mathcal{O}(\alpha_s^3)$ is

$$A^{\rm partial}_8(s,t) =\; A^{(0)}(s,t)\;\left(1+\ln(\frac{s}{|t|})\,\epsilon(t)+\frac{1}{2}\ln^2(\frac{s}{|t|})\,\epsilon^2(t)\right)\,. \tag{20}$$

[3]We have hidden any color dependence of the amplitudes in the color factors $\mathcal{CF}_i$, any reader interested in color decomposition should consult Ref. [9] in particular Section 9.4.3.

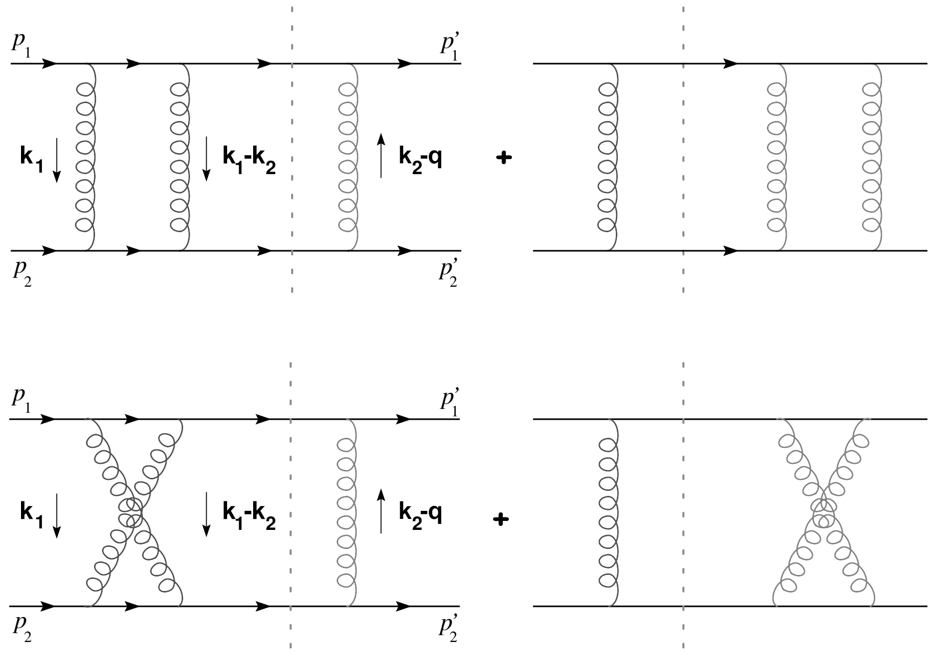

Figure 6: qq-scattering, two-loop box virtual corrections.

suggesting that the all-orders virtual amplitude might be of the form

$$A_8(s,t) = A^{(0)}(s,t)\left(1+\ln(\frac{s}{|t|})\,\epsilon(t)+\frac{1}{2}\ln^2(\frac{s}{|t|})\,\epsilon^2(t)+...\right), \tag{21}$$

namely, a product of the tree level amplitude and something that looks very much like a series expansion. From that point on, it only takes a small logical step to postulate that

$$A_8(s,t) = A^{(0)}(s,t)\left(\frac{s}{|t|}\right)^{\epsilon(t)}. \tag{22}$$

It is impressive to know that the ansatz in Eq. 22 is proven to be true by the so-called bootstrap equation.

At this point, we have partially achieved one of our primary goals, we have seen how logarithms in s appear in virtual diagrams in different orders of the perturbative expansion and we have managed to resum them in a closed form to all orders. The final result can be written in a factorized form involving two terms, the Born amplitude and the expression $\left(\frac{s}{|t|}\right)^{\epsilon(t)}$ which accounts for the resummation of the large energy logarithms. We can actually obtain Eq. 22 by going back to Fig. 2 and calculating the tree level amplitude using for the t-channel gluon a modified propagator which would read:

$$D_{\mu\nu}(s,q^2) = -i\frac{g_{\mu\nu}}{q^2}\left(\frac{s}{\mathbf{k}^2}\right)^{\epsilon(q^2)}. \tag{23}$$

Eq. 23 states that in the high energy limit, in order to take into account all the important contributions from virtual diagrams to all orders it suffices to calculate the tree level amplitude using a modified propagator for the t-channel gluon. The importance of this striking result cannot be overestimated. The gluon with the modified propagator is called a reggeized gluon or Reggeon and it hints that the relevant degrees of freedom in high energy scattering might not be just quarks and gluons.

Let us now focus on the real corrections and in particular the real gluon emission diagrams in Fig. 7 which are the first real emission corrections to the Born amplitude. Formally these are $\mathcal{O}(\alpha_s^3)$ corrections.

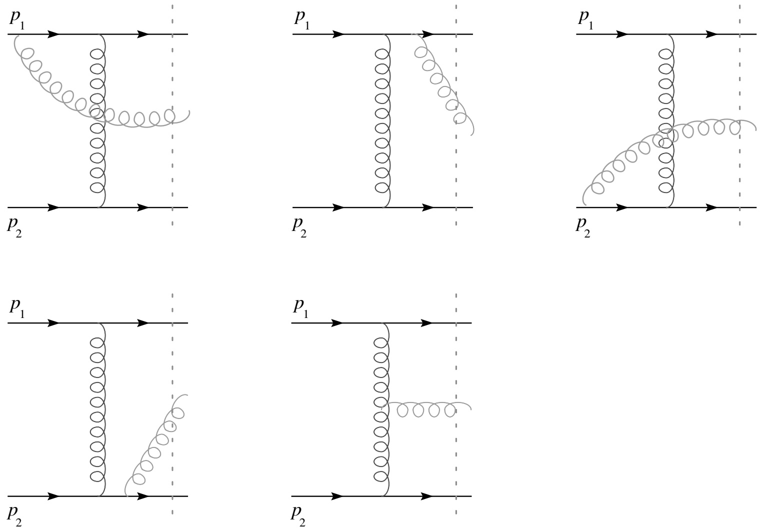

Figure 7: qq-scattering, one real gluon emission.

It turns out that instead of computing the amplitudes of all these diagrams it suffices to substitute their contribution by the diagram in Fig. 8 where the blob stands for the Lipatov effective vertex which is gauge invariant and has a tensorial structure. The Lipatov effective vertex is an elegant way to sum over the contributions from the graphs in Fig. 7. Using once more Sudakov decomposition,

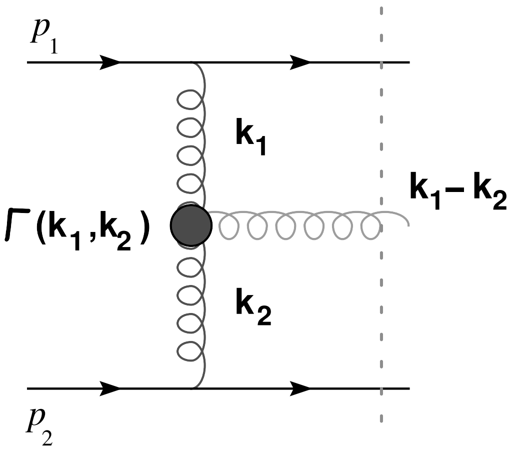

Figure 8: Lipatov effective vertex.

the momenta of the two t-channel gluons in Fig. 8 read

$$\begin{aligned} k_1 &= \rho_1 p_1 + \sigma_1 p_2 + k_{1\perp} \\ k_2 &= \rho_2 p_1 + \sigma_2 p_2 + k_{2\perp}\,, \end{aligned} \tag{24}$$

and the relevant kinematical limit is given by the following conditions:

$$\begin{aligned} 1 &>> \rho_1 &>> \rho_2 \\ 1 &>> |\sigma_2| &>> |\sigma_1| \end{aligned} \tag{25}$$

Using the Cutkosky rules once more, we contract the tree level amplitude from the diagram in Fig. 8 with its hermitian conjugate and we integrate over the three-body phase space which in our Sudakov parametrization reads

$$\begin{aligned}\int d\mathrm{PS}^{(3)} &= \frac{s^2}{4(2\pi)^5}\int d\rho_1 d\rho_2 d\sigma_1 d\sigma_2 d^2\mathbf{k}_1 d^2\mathbf{k}_2\\ &\delta(-\sigma_1(1-\rho_1)s-\mathbf{k}_1^2)\;\delta(\rho_2(1+\sigma_2)s-\mathbf{k}_2^2)\\ &\quad\delta((\rho_1-\rho_2)(\sigma_1-\sigma_2)s-(\mathbf{k}_1-\mathbf{k}_2)^2)\,.\end{aligned}\tag{26}$$

Because of Eq. 25 we may use the following approximations:

$$\begin{aligned}1-\rho_1 &\simeq 1,\\ 1+\sigma_2 &\simeq 1,\\ \rho_1-\rho_2 &\simeq \rho_1,\;\;\sigma_1-\sigma_2\simeq-\sigma_2\,,\end{aligned}\tag{27}$$

so that Eq. 26 now reads

$$\begin{aligned}\int d\mathrm{PS}^{(3)} &= \frac{s^2}{4(2\pi)^5}\int d\rho_1 d\rho_2 d\sigma_1 d\sigma_2 d^2\mathbf{k}_1 d^2\mathbf{k}_2\\ \delta(-\sigma_1 s-\mathbf{k}_1^2)\;&\delta(\rho_2 s-\mathbf{k}_2^2)\;\delta(-\rho_1\sigma_2 s-(\mathbf{k}_1-\mathbf{k}_2)^2)\,.\end{aligned}\tag{28}$$

It is from the rightmost delta function in (Eq. 28) that the $\ln s$ behavior of the real corrections arises. Indeed, after carrying out the integration over σ_2, an $(1/\rho_1)$ factor will be generated in the integrand:

$$\int d\mathrm{PS}^{(3)} = \frac{1}{4(2\pi)^5 s}\int_{\mathbf{k}_2^2/s}^{1}\frac{d\rho_1}{\rho_1}\int d^2\mathbf{k}_1 d^2\mathbf{k}_2 \tag{29}$$

and finally performing the ρ_1 integration yields a factor

$$\ln\left(\frac{s}{\mathbf{k}_2^2}\right) = \ln\left(\frac{s}{s_0}\right)\,, \tag{30}$$

where s_0 is a typical momentum, a typical normalisation scale.

To consider one order higher corrections, we need to consider two real gluon emissions. The diagrammatic depiction would be the one in Fig 8 but now with two Lipatov effective vertices and three gluon propagators in the t-channel. We would need to integrate over the four-body phase space in order to get the leading logarithms in s. It is straightforward to generalise this procedure for three, four and finally an arbitrary number of real gluon emissions. We would like at this point to find a way to combine the real with the virtual corrections and most importantly, to find a way to account for the real emission corrections to all orders in an closed form expression.

Let us recapitulate here what insight we have gained and assess where where stand with regard to our initial aims. In the discussion about the virtual corrections, we have introduced the notion of gluon reggeization: a t-channel gluon with a modified propagator defined as in Eq. 23 takes into account the leading logarithmic contributions from virtual diagrams to all orders. This is the closest one can have for a recipe: to account for virtual corrections, substitute the t-channel gluon by a Reggeon. On the other hand, the idea of combining the various one real emission diagrams into a single diagram where we consider one gluon emission in the s-channel that connects to the t-channel gluon by means of a Lipatov effective vertex allows for the iteration of this prescription to cover an arbitrary high n-gluon emissions. All these lead very naturally to what we call ladder diagrams, an example is depicted in Fig. 9. This is the general picture of a BFKL ladder in the colour singlet exchange, and a graphical depiction of what we call the perturbative Pomeron. Let us have a closer view at the diagram in Fig 9. It consists of n rungs (real emitted gluons) connected to the t-channel reggeized gluons (zig-zag lines) via Lipatov effective vertices. The vertical gluons are subdivided into $n+1$ reggeized propagators. The imaginary part of the amplitude, $\mathrm{Im}\mathcal{A}(s,t)$ for such a process will be given by contracting the two tree level amplitudes to the left and right hand side of the cut and after integrating over the $n+2$-body phase space. The generalisation of the condition in Eq. 1, leads to the kinematical configuration called multi-Regge kinematics (MRK):

$$\begin{aligned}
\mathbf{k}_1^2 \simeq \mathbf{k}_2^2 \simeq ... \mathbf{k}_i^2 \simeq \mathbf{k}_{i+1}^2 ... \simeq \mathbf{k}_n^2 \simeq \mathbf{k}_{n+1}^2 \gg \mathbf{q}^2 \simeq s_0, \\
1 \gg \rho_1 \gg \rho_2 \gg ... \rho_i \gg \rho_{i+1} \gg \rho_{n+1} \gg \frac{s_0}{s}, \\
1 \gg |\sigma_{n+1}| \gg |\sigma_n| \gg ... \gg |\sigma_2| \gg |\sigma_1| \gg \frac{s_0}{s}\,.
\end{aligned} \tag{31}$$

The integration over the phase space is nested and the way to turn the multi-nested integral into a

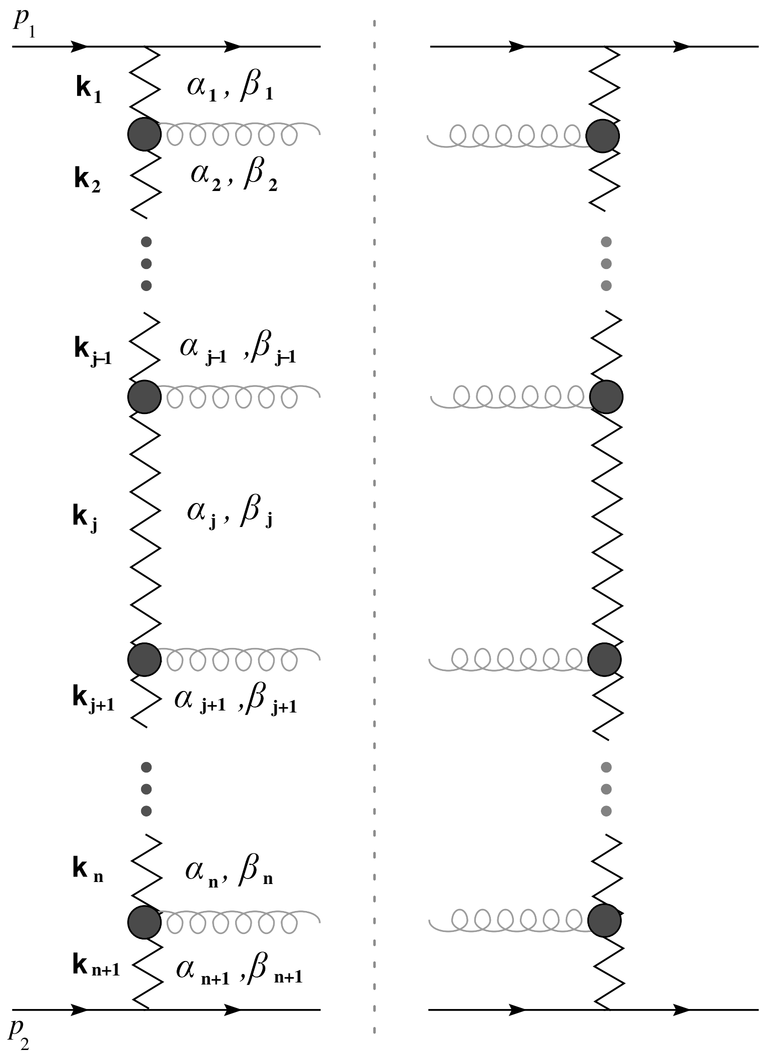

Figure 9: A typical gluonic ladder diagram.

product of integrals is by working in the complex angular momentum space ω by taking the Mellin transform of $\mathrm{Im}\mathcal{A}(s,t)$:

$$f(\omega,t) = \int_1^\infty d\left(\frac{s}{s_0}\right)\left(\frac{s}{s_0}\right)^{-\omega-1}\frac{\mathrm{Im}\mathcal{A}(s,t)}{s}\,. \tag{32}$$

Starting from $f(\omega,t)$, we can further define a function $f_\omega(\mathbf{k}_a,\mathbf{k}_b,t)$ which as its arguments indicate, is the Mellin transform of the amplitude with the integrations over the transverse momenta $\mathbf{k}_a$ and $\mathbf{k}_b$ still to be performed, where $\mathbf{k}_a$ and $\mathbf{k}_b$ are the topmost and bottommost reggeized gluon propagators in the ladder. This is called BFKL Green's function. Since $t \simeq -\mathbf{q}^2$, we will prefer the notation $f_\omega(\mathbf{k}_a, \mathbf{k}_b, \mathbf{q}^2)$ in the following, in which the propagators $\mathbf{k}_a$ and $(q-\mathbf{k}_b)^2$ are contained and with $\mathbf{q}^2$ denoting the momentum transfer in the t-channel. One could then take $n=1$ in the ladder diagram in Fig. 9 and calculate the corresponding $f_\omega^{(1)}(\mathbf{k}_a, \mathbf{k}_b, \mathbf{q}^2)$ function and then set $n=2$ and calculate the $f_\omega^{(2)}(\mathbf{k}_a, \mathbf{k}_b, \mathbf{q})$ and after iterating this procedure up to an arbitrary $n \to \infty$ and summing up all contributions, one would compute $f_\omega(\mathbf{k}_a, \mathbf{k}_b, \mathbf{q}^2)$. Easy to describe but impossible to do. Instead, there is an elegant way through. After taking the Mellin transform in Eq. 32 and writing the generic expression for $f_\omega(\mathbf{k}_a, \mathbf{k}_b, \mathbf{q}^2)$ with the phase space integration still to be done, one realizes[4] that there exists an integral equation which governs the behavior of f_ω:

$$
\begin{aligned}
\omega f_\omega(\mathbf{k}_a, \mathbf{k}_b, \mathbf{q}) &= \delta^2(\mathbf{k}_a - \mathbf{k}_b) \\
&+ \frac{\bar{\alpha_s}}{2\pi} \int d^2\mathbf{l} \Big\{ \frac{-\mathbf{q}^2}{(\mathbf{l}-\mathbf{q})^2 \mathbf{k}_a^2} f_\omega(\mathbf{l}, \mathbf{k}_b, \mathbf{q}) \\
&+ \frac{1}{(\mathbf{l}-\mathbf{k}_a)^2} \left(f_\omega(\mathbf{l}, \mathbf{k}_b, \mathbf{q}^2) - \frac{\mathbf{k}_a^2 f_\omega(\mathbf{k}_a, \mathbf{k}_b, \mathbf{q})}{\mathbf{l}^2 + (\mathbf{k}_a - \mathbf{l})^2} \right) \\
&+ \frac{1}{(\mathbf{l}-\mathbf{k}_a)^2} \Big(\frac{(\mathbf{k}_a - \mathbf{q})^2 \mathbf{l}^2 f_\omega(\mathbf{l}, \mathbf{k}_b, \mathbf{q}^2)}{(\mathbf{l}-\mathbf{q})^2 \mathbf{k}_a^2} \\
&- \frac{(\mathbf{k}_a - \mathbf{q})^2 f_\omega(\mathbf{k}_a, \mathbf{k}_b, \mathbf{q}^2)}{(\mathbf{l}-\mathbf{q})^2 (\mathbf{k}_a - \mathbf{l})^2} \Big) \Big\} ,
\end{aligned}
\tag{33}
$$

with $\bar{\alpha_s} = N_c \alpha_s / \pi$. This is the BFKL equation. In the case of zero momentum transfer, $\mathbf{q^2} = 0$, Eq. 33 becomes:

$$
\begin{aligned}
\omega f_\omega(\mathbf{k}_a, \mathbf{k}_b) &= \delta^2(\mathbf{k}_a - \mathbf{k}_b) \\
&+ \frac{\bar{\alpha_s}}{2\pi} \int \frac{d^2\mathbf{l}}{(\mathbf{l}-\mathbf{k}_a)^2} \left(f_\omega(\mathbf{l}, \mathbf{k}_b) - \frac{\mathbf{k}_a^2 f_\omega(\mathbf{k}_a, \mathbf{k}_b)}{\mathbf{l}^2 + (\mathbf{k}_a - \mathbf{l})^2} \right) .
\end{aligned}
\tag{34}
$$

The impossible task of summing an infinite number of integrals, each one with a $(i+1)$-body phase space if its previous has an i-body phase space turns into finding a way to solve Eq. 33. We can rewrite the BFKL equation in a more symbolic form as

$$
\omega f_\omega(\mathbf{k}_a, \mathbf{k}_b) = \delta^2(\mathbf{k}_a - \mathbf{k}_b) + \int d^2\mathbf{l}\, \mathcal{K}(\mathbf{k}_a, \mathbf{l})\, f_\omega(\mathbf{l}, \mathbf{k}_b) \,,
\tag{35}
$$

where $\mathcal{K}(\mathbf{k}_a, \mathbf{l})$ is the BFKL kernel:

$$
\mathcal{K}(\mathbf{k}_a, \mathbf{l}) \;=\; \underbrace{2\epsilon(-\mathbf{k}^2)\, \delta^2(\mathbf{k}_a - \mathbf{l})}_{\mathcal{K}_{virt}} + \underbrace{\frac{N_c \alpha_s}{\pi^2} \frac{1}{(\mathbf{k}_a - \mathbf{k}_b)^2}}_{\mathcal{K}_{real}} .
\tag{36}
$$

$\mathcal{K}_{\text{virt}}$ and $\mathcal{K}_{\text{real}}$ are the parts of the kernel that correspond to the virtual and real corrections respectively.

Solving the BFKL equation will provide us with the BFKL gluon Green's function from which we can reconstruct the imaginary part of the amplitude for qq-scattering in two steps. Firstly, we will need to take the inverse Mellin transform and go back to s space:

$$
f(s, \mathbf{k}_a, \mathbf{k}_b, \mathbf{q}) \;=\; \frac{1}{2\pi i} \int_{c-i\infty}^{c+i\infty} d\omega \left(\frac{s}{s_0} \right)^{\omega} f_\omega(\mathbf{k}_a, \mathbf{k}_b, \mathbf{q})
\tag{37}
$$

[4] To demonstrate that, one needs to go through the calculation which is beyond our scope here. The reader is encouraged to try it out with the help of the references cited in the beginning of the section in order to see how magic works.

and subsequently to perform the integrations over the $\mathbf{k}_a$ and $\mathbf{k}_b$ momenta of the reggeized gluons:

$$\mathcal{A}_{\text{singlet}}(s,t) = i(8\pi\alpha_s)^2\, s\, \frac{N_c^2-1}{4N_c^2} \int \frac{d^2\mathbf{k}_a}{(2\pi)^2}\frac{d^2\mathbf{k}_b}{(2\pi)^2}\frac{f(s,\mathbf{k}_a,\mathbf{k}_b,\mathbf{q})}{\mathbf{k}_b^2(\mathbf{k}_a-\mathbf{q})^2}\,, \tag{38}$$

where we kept the color factor for qq-scattering explicit.

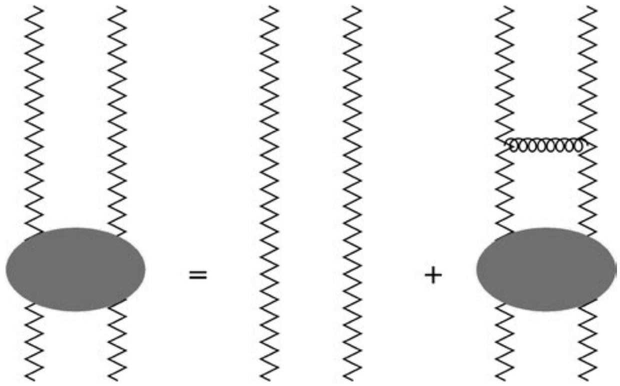

Figure 10: Graphical depiction of the BFKL equation.

The amplitude in Eq. 38 is the amplitude for scattering via a perturbative Pomeron exchange. If nature were to follow the BFKL dynamics, or more precisely, in the kinematical limit where BFKL dynamics is dominant and describes fully the perturbative QCD picture, the interaction between two quarks would be the outcome of summing all possible ladder diagrams with n-rungs, $n \to \infty$, and this would be the equivalent of saying that the two quarks exchange a Pomeron. This is obviously not a definition of the Pomeron but describes a good deal of how to perceive it in an intuitive manner.

The BFKL kernel in Eq. 36 is infrared finite, $\mathcal{K}_{\text{real}}$ and $\mathcal{K}_{\text{virt}}$ are both singular but their divergencies cancel one against the other. The amplitude though is still infrared divergent due to the gluon propagators $\frac{1}{\mathbf{k}_b^2}$ and $\frac{1}{(\mathbf{k}_a-\mathbf{q})^2}$. In practice, the quarks (or scattering gluons for that matter) are not on mass-shell as we assumed here in sketching the derivation of BFKL equation. In physical processes, as for example in hadron hadron collisions at the LHC, the Pomeron couples to partons inside a hadron which are off shell. To take into account the structure of the hadrons we need the introduction of a quantity Φ which serves as the coupling of the Pomeron to the hadron and which is called impact factor. Then a hadronic elastic amplitude between hadrons A and B (Fig. 11) will be written as

$$\mathcal{A}(s,t) \;=\; i\,s\,\mathcal{C} \int \frac{d^2\mathbf{k}_a}{(2\pi)^2}\frac{d^2\mathbf{k}_b}{(2\pi)^2}\,\Phi_A(\mathbf{k}_a,\mathbf{q})\,\frac{f(s,\mathbf{k}_a,\mathbf{k}_b,\mathbf{q})}{\mathbf{k}_b^2(\mathbf{k}_a-\mathbf{q})^2}\Phi_B(\mathbf{k}_b,\mathbf{q})\,, \tag{39}$$

where $\mathcal{C}$ accounts for the colour factor[5] of the process and the quantities Φ_A and Φ_B are the hadron impact factors for the hadrons A and B. Whenever we have scattering of particles via Pomeron exchange, we also have to consider impact factors for each of these particles. In general, impact factors are process dependent object and mostly of non perturbative nature and thus non-calculable and subjects to modelling. Still, there has been quite significant effort by the community to calculate perturbative impact factors to NLO [13–34]. Nevertheless, all impact factors have to share a very important universal behavior, i.e. they become zero in the limits

$$\Phi(\mathbf{k},\mathbf{q})\Big|_{\mathbf{k}\to 0}^{\mathbf{k}-\mathbf{q}\to 0} \;\to 0\,. \tag{40}$$

and they regulate thus the infrared divergencies of Eq. 39 which exactly appear in these limits.

We can rewrite Eq. 35 as

$$\omega F \;=\; 1\!\!I + \mathcal{K} \,\otimes\, F, \tag{41}$$

[5]For example, $\mathcal{C} = (N_c^2-1)/4N_c^2$ for qq-scattering

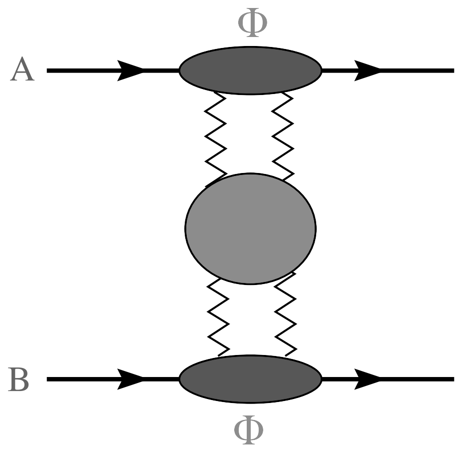

Figure 11: High energy hadron-hadron scattering. The interaction factorizes into the process independent part which is the BFKL gluon Green's function (green blob) and the its effective couplings to the scattering projectiles, the impact factors (brown blobs).

with $\mathcal{K}$ being the BFKL kernel as in Eq. 36, and attempt to diagonalise the BFKL equation by finding the eigenfunctions ϕ_a of the kernel $\mathcal{K}$

$$\mathcal{K} \otimes \phi_a = \omega_a \phi_a \,. \tag{42}$$

If θ is the azimuthal polar coordinate of the momenta, then the eigenfunctions can be expressed as:

$$\phi_{n\nu}(|\boldsymbol{k}|, \theta) = \frac{1}{\pi\sqrt{2}} (\boldsymbol{k}^2)^{-\frac{1}{2}+i\nu} \, e^{in\theta} \,. \tag{43}$$

The high energy behavior of the total cross section is determined when we consider the angular averaged kernel (averaged over the azimuthal angle between $\boldsymbol{k}_a$ and $\boldsymbol{k}_b$) and then $(\boldsymbol{k}^2)^{\gamma-1}$ can be used as eigenfunctions such that:

$$\int d^2k \, \mathcal{K}(\boldsymbol{k}_a, \boldsymbol{k})(\boldsymbol{k}^2)^{\gamma-1} = \frac{N_c \alpha_s}{\pi} \, \chi_0(\gamma)(\boldsymbol{k}_a^2)^{\gamma-1} \tag{44}$$

with eigenvalues

$$\omega_n(\gamma) = \frac{\alpha_s N_c}{\pi} \left(2\psi(1) - \psi(\gamma + \frac{n}{2}) - \psi(1 - \gamma + \frac{n}{2}) \right), \quad \psi(\gamma) = \Gamma'(\gamma)/\Gamma(\gamma)$$

and $\gamma = 1/2 + i\nu$. The set of eigenfunctions, where the real ν ranges between $-\infty$ and ∞ is complete. The solution can therefore be expressed using the expansion on the eigenfunctions and reads

$$f(\mathbf{k}_a, \mathbf{k}_b, Y) = \frac{1}{\pi \mathbf{k}_a \mathbf{k}_b} \sum_{n=-\infty}^{\infty} \int \frac{d\omega}{2\pi i} e^{\omega Y} \int \frac{d\gamma}{2\pi i} \left(\frac{\mathbf{k}_a^2}{\mathbf{k}_b^2} \right)^{\gamma - \frac{1}{2}} \frac{e^{in\theta}}{\omega - \omega_n(\alpha_s, \gamma)}, \tag{45}$$

where $Y = \ln\left(\frac{s}{s_0}\right)$ is the rapidity interval between $\mathbf{k}_a$ and $\mathbf{k}_b$. Eq. 45 makes apparent the distinct power-like growth with energy prediction within the BFKL dynamics that characterises the behavior of the cross sections at large energies. The relevant term here is $e^{\omega Y}$.

So far, we have encountered a number of important features of the BFKL resummation program all seen at leading logarithmic accuracy. At next-to-leading logarithmic approximation (NLLA), it turns out that the reggeization of the gluon still holds which is a key point. It means that one can use the leading order form of BFKL equation changing only the kernels and the eigenvalues [5]. We will not discuss in any detail the NLO BFKL equation here. We will only sketch the origin of the terms $\alpha_s(\alpha_s \ln s)^n$ and we will mention a couple of important points for BFKL phenomenology.

The NLO[6] corrections stem from two different kinematical configurations. In MRK, the next-to-leading order corrections for the gluon Regge trajectory as well as the virtual corrections to the Reggeon-Reggeon-g vertex have to be included. The reggeized gluon trajectory has to be calculated at two-loop approximation, $\epsilon^{(2)}$ [35], whereas, the real part of the kernel, $\mathcal{K}_{\rm real}$ gets contributions from one-loop level gluon production [36].

One can also obtain a term of the type $\alpha_s(\alpha_s \ln s)^n$ starting from an amplitude at LLA and after losing a relative $\ln s$ term. We saw that the key feature that generates these logarithmic terms is the strong ordering in rapidity. Thus, if we allow for a state in which two of the emitted particles are close in rapidity, we are in the Quasi-Multi-Regge-kinematics (QMRK) where Eq. 31 still holds with the exception of a pair of particles. The pair can be a pair of gluons or a $q\bar{q}$ pair [37, 38] (Fig. 12).

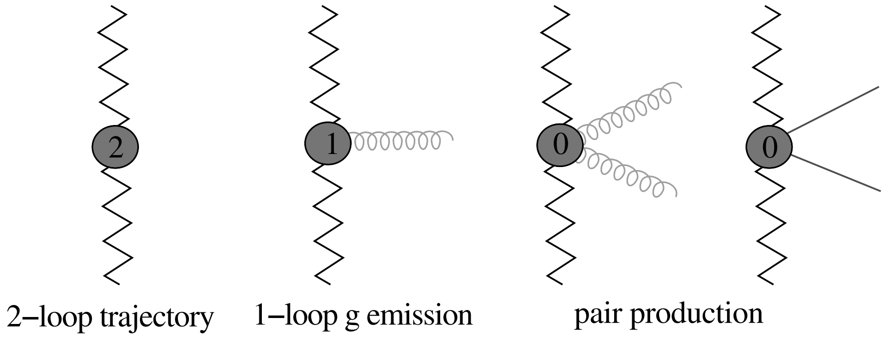

Figure 12: Contributions to the NLL approximation.

The project of computing the next-to-leading corrections was an impressive feat that took almost ten years to finish [5, 6]. When it was completed, in the late nineties, it came as a surprise that the corrections compared to LLA were very large questioning the convergence itself of the perturbative expansion in terms of $(\alpha_s \ln s)$. The problem has its origin to the fact that since we impose no restrictions on the values of the transverse momenta for the emissions, there can be final configurations in which the transverse momenta of the emitted particles are strongly ordered. This leads to large logarithms of transverse momenta (collinear logarithms) that make the expansion in $(\alpha_s \ln s)$ terms unstable. To eliminate these unphysical logarithms one can perform a complete collinear resummation of these large logarithms which stabilizes the convergence of the expansion [39].

3 BFKL phenomenology at the LHC

In the past thirty years, a number of probes of BFKL physics have been proposed for different collider environments. Actually, BFKL phenomenology had its first major flourish in the nineties, especially after HERA at DESY started producing data for the proton structure function F_2 that were showing a power-like rise with decreasing x, the Bjorken scaling variable. Since the early HERA days, much of the progress seen on more formal theoretical issues regarding the BFKL formalism was driven from a need to compare against experimental measurements. Nevertheless, the absence of a clear signal that would only be described by BFKL physics and by nothing else was a drawback. Despite the big progress in the field, most of the studies we still have are beyond LO but only a few calculations provide full NLO accuracy estimates within the BFKL framework.

Nowadays, the general consensus is that one should apply the BFKL formalism to processes that have two hard scales at the two ends of the BFKL ladder that are of the same magnitude. Otherwise, if there is strong ordering in the transverse momentum of the two scales, DGLAP [40–42] logarithms appear and BFKL is not any more the only relevant framework. A very strict list of probes would

[6]As mentioned in the introduction, in the field, there is an interchangeability between the terms 'NLL' and 'NLO'. We will follow the practise here with the assurance that by now the context makes clear what one really means.

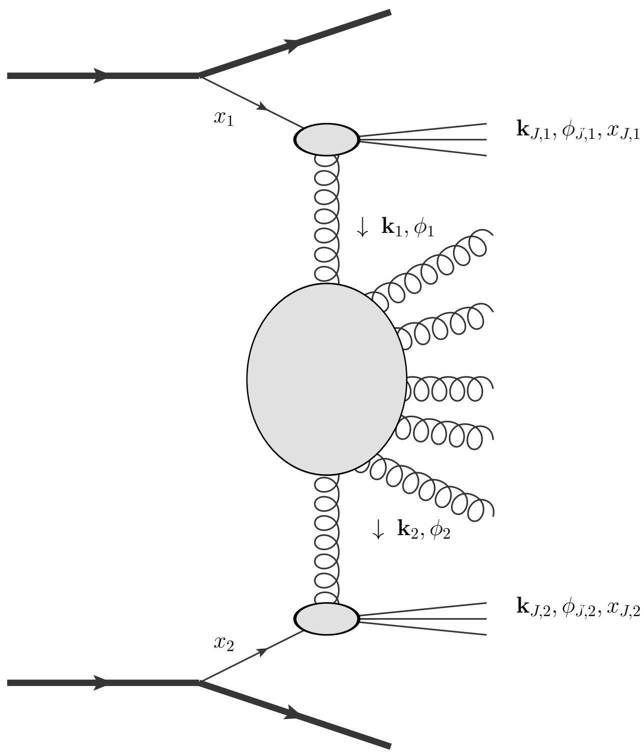

Figure 13: The kinematics of Mueller-Navelet jets. Figure taken from Ref [44].

include the processes $\gamma^*\gamma^* \to$ hadrons in a e^+e^- collider, forwards jets in Deep Inelastic Scattering (DIS) at HERA, Mueller-Navelet jets and Mueller-Tang jets at hadron colliders (Tevatron, LHC). We do not include in the list the F_2 behavior in DIS which is also driven by non-perturbative physics. From the list of probes above, Mueller-Navelet jets [43] is the observable that has received most of the theoretical attention in recent years as the process can be studied experimentally at the LHC. In the following, we will focus on recent Mueller-Navelet studies and we will also review the comparison with experimental data.

The initial idea behind considering the Mueller-Navelet jets cross section as a probe for BFKL physics is the following: in a hadron collider, let us assume that two partons interact (one from each hadron) such that in the final state we find a forward and backward jet of similar and sizeable p_T. Then these can be the hard scales attached to the two ends of a BFKL ladder and any collinear (DGLAP) logarithms are suppressed in the evolution from one jet to the other. The main contribution to this process on the partonic level then would come from the BFKL logarithms given that the two jets are well separated in rapidity. The process is depicted in Fig. 13.

One would think that already at Tevatron, the aim would be to see in the data the power-like growth with energy of the cross section characteristic for BFKL dynamics. The problem with that though is that this growth is drown due to the rapidly falling PDFs in forward-backward dijet production with large rapidity separation. For that reason, the main observable to be studied is the decorrelation in azimuthal angle between the two tagged jets as a function of the rapidity separation.

At tree level (Fig. 14), the produced jets have to be back-to-back due to energy-momentum conservation: the partonic cross section is a $2 \to 2$ process. As the partonic centre-of-mass energy increases though, the tree level approximation is not a good approximation at all. One is bound to consider extra real radiation in the final state which breaks the back-to-back configuration of the two outmost jets. The larger the available energy, the larger is the phase space and more emissions need to be considered in order to describe more accurately what really happens in the collider and the more azimuthally decorrelated is the system of the forward-backward jets. To measure the correlation, one

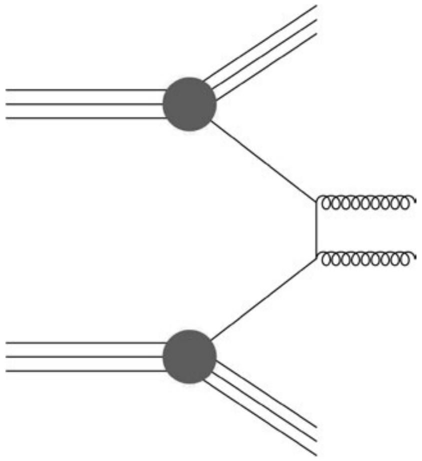

Figure 14: Diagrammatic tree level approximation for Mueller-Navelet jets.

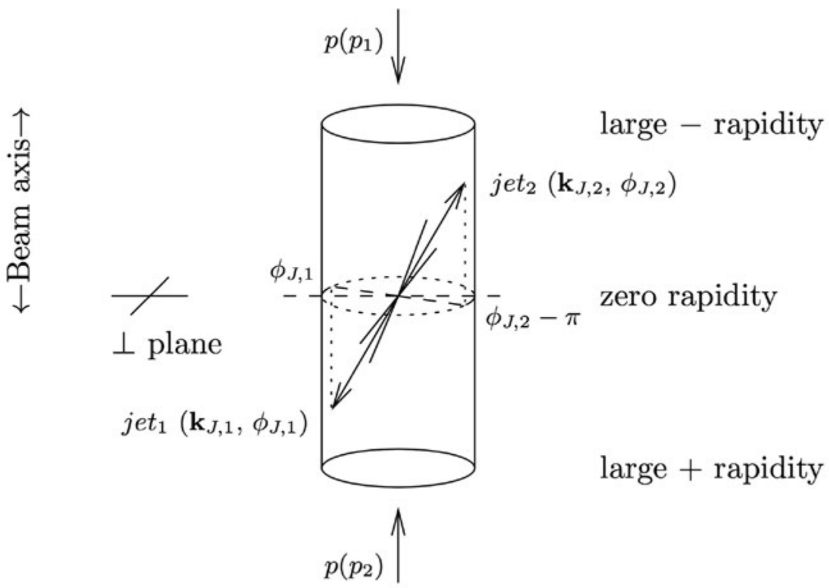

Figure 15: Tree level approximation for Mueller-Navelet jets in a collision setup. Figure taken from Ref [45].

projects the momenta of the two jets on the transverse plane and calculates the average $cos(\Delta\phi)$, where $\Delta\phi$ is defined as the difference of the angles of the two jets minus π, $\Delta\phi = \phi_{J,1} - \phi_{J,2} - \pi$. One can go further along these lines and compute the following moments: $C_n = \langle cos(n\Delta\phi)\rangle$, where n can be 1,2 or 3. In an effort to minimise further any contamination from collinear logarithm, the ratios

$$\frac{C_n}{C_m} = \frac{\langle cos(n\Delta\phi)\rangle}{\langle cos(m\Delta\phi)\rangle} \tag{46}$$

have been proposed as better observables to probe BFKL dynamics in Ref. [46].

At the moment, we have two groups with full NLO BFKL predictions for Mueller-Navelet jet observables at LHC energies. Both groups are using an analytic approach (as opposed to Monte Carlo studies) [44, 47, 48]. In their studies, they compare and find good agreement with the average cosine ratios. This agreement was summarized in the results of CMS on multijet correlations [49] where Figs. 16 and 17 are taken from. The success of BFKL physics to describe the data for the average cosine ratios and the not so good performance of the standard collinear tools is a very promising starting point while waiting for relevant results from the second run of the LHC.

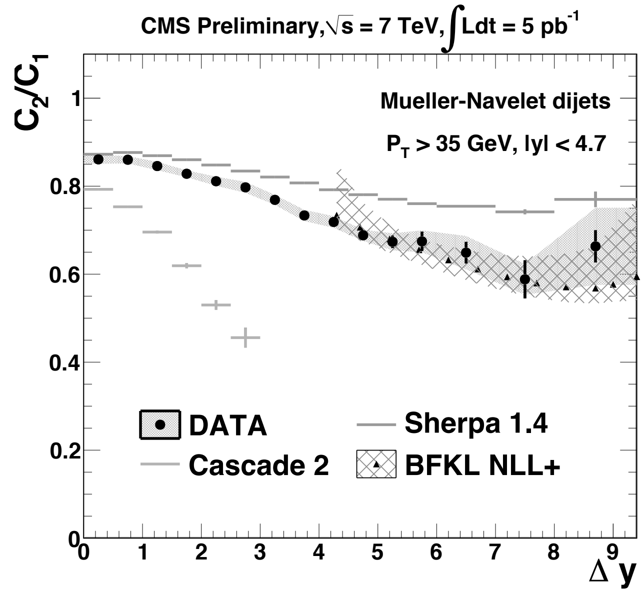

Figure 16: Ratio C_2/C_1 as a function of Δy compared to various theory predictions. Figure taken from Ref [49].

Recently, new observables sensitive to BFKL dynamics were proposed in the context of multijet production at the LHC [50]. The idea is to study events with two tagged forward-backward jets, separated by a large rapidity span, and also tag on a third jet produced in the central region of rapidity, allowing for inclusive radiation in the remaining areas of the detectors. A kinematical configuration can be seen in Fig 18. The proposed distributions have a very different behavior to the ones characteristic of the Mueller-Navelet case. These new distributions are defined using the projections on the two relative azimuthal angles formed by each of the forward jets with the central jet, $\Delta\phi_1 = \phi_1 - \phi_c - \pi$ and $\Delta\phi_1 = \phi_c - \phi_2 - \pi$. The experimentally relevant observable is the mean value in the selected events of the two cosines of the azimuthal angle differences, i.e. $\langle cos(M\Delta\phi_1)cos(N\Delta\phi_2)\rangle$. To eliminate again any collinear logarithm contamination, one can form ratios and finally the observables are defined as:

$$\mathcal{R}^{M,N}_{P,Q} = \frac{\langle cos(M\Delta\phi_1)cos(N\Delta\phi_2)\rangle}{\langle cos(P\Delta\phi_1)cos(Q\Delta\phi_2)\rangle}, \tag{47}$$

where M, N, P and Q can be equal to 1 or 2.

In Fig. 19 one sees plotted the ratio R^{12}_{22} after setting the momentum of the forward jet to $k_A = 40$ GeV, the momentum of the backward jet to $k_B = 50$ GeV and their rapidities to $Y_A = 10$ and $Y_B = 0$ respectively. For the transverse momentum of the central jet three values $k_J = 30, 45, 70$ GeV were chosen and the rapidity of the central jet y_J varies between the two rapidities of the forward-backward jets. The claim is that these ratio distributions as defined in Eq. 47 are probing the fine structure of the QCD radiation in the high energy limit and one should expect the LHC data to agree with the theoretical BFKL estimates especially in the regions where y_J is closer to $(Y_A - Y_B)/2$. Apart from the analytic approach followed in Ref. [50], it would be very interesting to see BFKL theoretical estimates with Monte Carlo techniques [51–54] for these proposed ratio observables.

4 Discussion

The LHC has opened up a new era in particle physics. So far, there is no clear signal for new physics and the SM seems to secure even more its position as the best and only theory we have to describe the fundamental interactions (Gravity excluded). Despite that though, there is an awful lot we do not

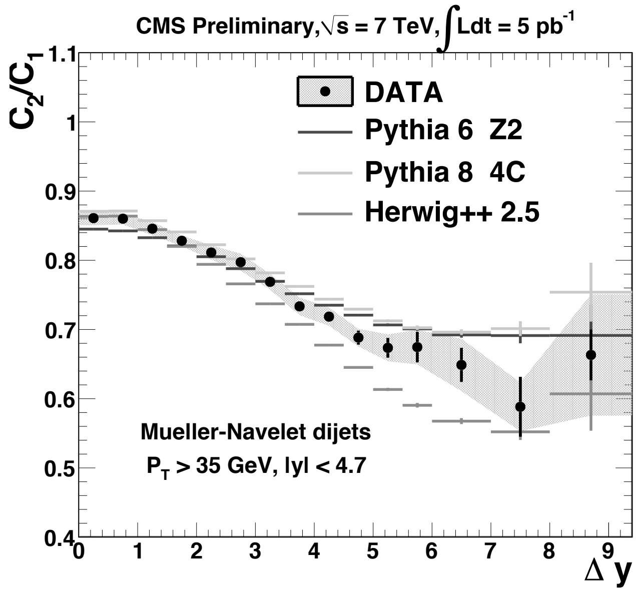

Figure 17: Ratio C_2/C_1 as a function of Δy compared to various theory predictions. Figure taken from Ref [49].

know about the SM. If we exclude lattice works, the only way we have at our disposal to do calculations is perturbation theory. And clearly, knowing the first two-three terms of an expansion to a function does not give a full insight to the function itself and its special properties. It only allows to learn about the behavior of the function in the small region where the expansion makes sense. It remains to be seen whether the LHC era will be an exciting time of new physics but even if not, it should be the era in which we learn and understand more about the SM, especially more so if it surfaces at the end of the day as the only fundamental theory available to describe consistently experimental data.

To that end, the role of phenomenology is crucial. We do not calculate theoretical estimates and then compare to data sets in order to fill out a checklist of processes. We do confront our theory using the experiment because we want to understand better our theory. We want to see whether different approaches within the same fundamental model can reveal properties that were previously masked. Phenomenology in modern particle physics, apart from carrying the responsibility of validating or falsifying a theory, it should also shed light to corners of a valid theory that are not in plain view.

BFKL physics is connected to some very important and still open issues within QCD and beyond. Factorization theorems, the transition from the perturbative to the non-perturbative regime, the correct degrees of freedom in high energies, the connection of QCD to the old Regge theory are few examples. BFKL phenomenology should try to give answers to all these important questions. Before that though, it needs to answer the most pressing question: which is the rough collision energy threshold after which BFKL dynamics becomes –for the relevant kinematical configurations–, if not dominant, at least the main player. Does the LHC reach beyond that threshold? In that respect, to find the window of applicability for this formalism, more work is needed in identifying observables where the BFKL approach is distinct. We should define more exclusive experimental quantities such that BFKL fits the measured data and all other possible approaches fail if we are already beyond the threshold at the LHC. It remains to be seen whether the second run of the LHC will be the time of great progress for BFKL phenomenology.

Acknowledgements

The author would like to thank the organisers and in particular C. Royon for the invitation, all the help and the warm hospitality.

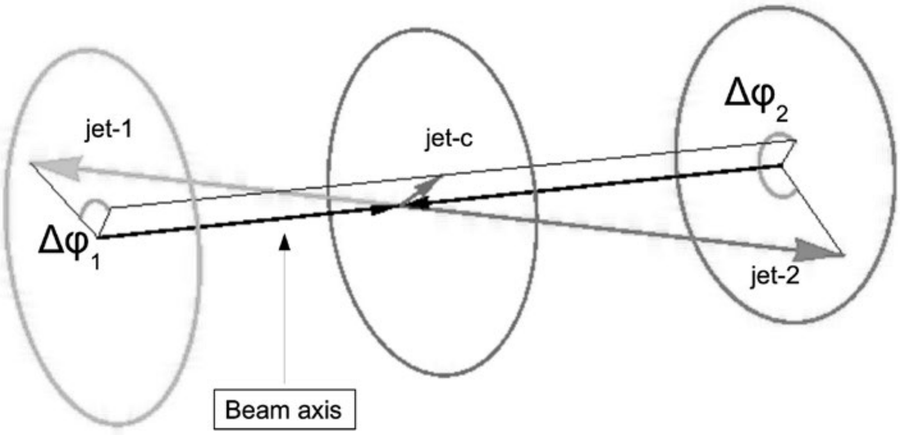

Figure 18: Kinematics of a 3-jet event.

References

1. L. N. Lipatov, Sov. J. Nucl. Phys. **23**, 338 (1976) [Yad. Fiz. **23**, 642 (1976)].
2. V. S. Fadin, E. A. Kuraev and L. N. Lipatov, Phys. Lett. B **60**, 50 (1975).
3. E. A. Kuraev, L. N. Lipatov and V. S. Fadin, Sov. Phys. JETP **44**, 443 (1976) [Zh. Eksp. Teor. Fiz. **71**, 840 (1976)].
4. I. I. Balitsky and L. N. Lipatov, Sov. J. Nucl. Phys. **28**, 822 (1978) [Yad. Fiz. **28**, 1597 (1978)].
5. V. S. Fadin and L. N. Lipatov, Phys. Lett. B **429**, 127 (1998) [hep-ph/9802290 [hep-ph]].
6. M. Ciafaloni and G. Camici, Phys. Lett. B **430**, 349 (1998) [hep-ph/9803389 [hep-ph]].
7. V. Barone and E. Predazzi, *High-Energy Particle Difraction*, Springer (2002).
8. J. R. Forshaw and D. A. Ross, Cambridge Lect. Notes Phys. **9**, 1 (1997).
9. B. L. Ioffe, V. S. Fadin and L. N. Lipatov, *Quantum Chromodynamics. Perturbative and Nonperturbative Aspects*, Cambridge Monogr. Part. Phys. Nucl. Phys. and Cosmology **30** (2014).
10. V. Del Duca, hep-ph/9503226 [hep-ph].
11. G. P. Salam, Acta Phys. Polon. B **30**, 3679 (1999) [hep-ph/9910492 [hep-ph]].
12. V. S. Fadin, hep-ph/9807528 [hep-ph].
13. V. S. Fadin, R. Fiore, M. I. Kotsky and A. Papa, Phys. Rev. D **61**, 094006 (2000) [hep-ph/9908265 [hep-ph]].
14. M. Ciafaloni and G. Rodrigo, JHEP **0005**, 042 (2000) [hep-ph/0004033 [hep-ph]].
15. V. S. Fadin, R. Fiore, M. I. Kotsky and A. Papa, Phys. Rev. D **61**, 094005 (2000) [hep-ph/9908264 [hep-ph]].
16. D. Y. Ivanov, M. I. Kotsky and A. Papa, Eur. Phys. J. C **38**, 195 (2004) [hep-ph/0405297 [hep-ph]].
17. D. Y. Ivanov, M. I. Kotsky and A. Papa, Nucl. Phys. Proc. Suppl. **146**, 117 (2005).
18. J. Bartels, D. Colferai and G. P. Vacca, Eur. Phys. J. C **29**, 235 (2003) [hep-ph/0206290 [hep-ph]].
19. J. Bartels, D. Colferai and G. P. Vacca, Eur. Phys. J. C **24**, 83 (2002) [hep-ph/0112283 [hep-ph]].
20. F. Caporale, D. Y. Ivanov, B. Murdaca, A. Papa and A. Perri, JHEP **1202**, 101 (2012) [arXiv:1112.3752 [hep-ph]].
21. D. Y. Ivanov and A. Papa, JHEP **1205**, 086 (2012) [arXiv:1202.1082 [hep-ph]].
22. D. Y. Ivanov and A. Papa, JHEP **1207**, 045 (2012) [arXiv:1205.6068 [hep-ph]].
23. G. Chachamis, M. Hentschinski, J. D. Madrigal Martinez and A. Sabio Vera, Phys. Rev. D **87**(7), 076009 (2013) [arXiv:1212.4992 [hep-ph]].
24. G. Chachamis, M. Hentschinski, J. D. Madrigal Martinez and A. Sabio Vera, Phys. Part. Nucl.

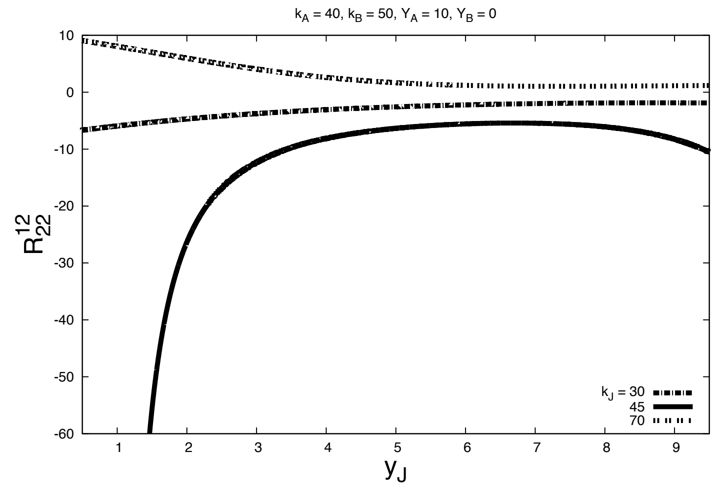

Figure 19: A study of the ratio R^{12}_{22} as defined in Eq. 47 for fixed values of the p_T of the two forward jets and three values of the p_T of the tagged central jet, as a function of the rapidity of the central jet y_J.

45(4), 788 (2014) [arXiv:1211.2050 [hep-ph]].
25. J. Bartels, D. Colferai, S. Gieseke and A. Kyrieleis, Phys. Rev. D **66**, 094017 (2002) [hep-ph/0208130 [hep-ph]].
26. J. Bartels and A. Kyrieleis, Phys. Rev. D **70**, 114003 (2004) [hep-ph/0407051 [hep-ph]].
27. J. Bartels, S. Gieseke and A. Kyrieleis, Phys. Rev. D **65**, 014006 (2002) [hep-ph/0107152 [hep-ph]].
28. J. Bartels, S. Gieseke and C. F. Qiao, Phys. Rev. D **63**, 056014 (2001) [Phys. Rev. D **65**, 079902 (2002)] [hep-ph/0009102 [hep-ph]].
29. G. Chachamis and J. Bartels, PoS DIFF **2006**, 026 (2006).
30. I. Balitsky and G. A. Chirilli, Phys. Rev. D **87**(1), 014013 (2013) [arXiv:1207.3844 [hep-ph]].
31. I. Balitsky and G. A. Chirilli, Phys. Rev. D **83**, 031502 (2011) [arXiv:1009.4729 [hep-ph]].
32. G. Chachamis, M. Deak and G. Rodrigo, PoS EPS-HEP **2013**, 092 (2013) [arXiv:1310.7763 [hep-ph]].
33. G. Chachamis, M. Deak and G. Rodrigo, PoS DIS **2014**, 085 (2014).
34. G. Chachamis, M. Deak and G. Rodrigo, JHEP **1312**, 066 (2013) [arXiv:1310.6611 [hep-ph]].
35. V. S. Fadin, JETP Lett. **61**, 346 (1995) [Pisma Zh. Eksp. Teor. Fiz. **61**, 342 (1995)]; V. S. Fadin, R. Fiore and A. Quartarolo, Phys. Rev. D **53**, 2729 (1996) [hep-ph/9506432 [hep-ph]]; V. S. Fadin, M. I. Kotsky, Phys. Atom. Nucl. **59**, 1035 (1996) [Yad. Fiz. **59**(6), 1080 (1996)]; V. S. Fadin, M. I. Kotsky and R. Fiore, Phys. Lett. B **359**, 181 (1995).
36. V. S. Fadin and L. N. Lipatov, Nucl. Phys. B **406**, 259 (1993); V. S. Fadin, R. Fiore and A. Quartarolo, Phys. Rev. D **50**, 5893 (1994) [hep-th/9405127 [hep-th]].
37. V. S. Fadin, M. I. Kotsky and L. N. Lipatov, Phys. Lett. B **415**, 97 (1997).
38. S. Catani, M. Ciafaloni and F. Hautmann, Phys. Lett. B **242**, 97 (1990); S. Catani, M. Ciafaloni and F. Hautmann, Nucl. Phys. B **366**, 135 (1991); G. Camici and M. Ciafaloni, Phys. Lett. B **386**, 341 (1996) [hep-ph/9606427 [hep-ph]]; V. S. Fadin, R. Fiore, A. Flachi and M. I. Kotsky, Phys. Lett. B **422**, 287 (1998) [hep-ph/9711427 [hep-ph]].
39. M. Ciafaloni, D. Colferai and G. P. Salam, Phys. Rev. D **60**, 114036 (1999) [hep-ph/9905566 [hep-ph]].
40. Y. L. Dokshitzer, Sov. Phys. JETP **46**, 641 (1977) [Zh. Eksp. Teor. Fiz. **73**, 1216 (1977)].

41. V. N. Gribov and L. N. Lipatov, Sov. J. Nucl. Phys. **15**, 438 (1972) [Yad. Fiz. **15**, 781 (1972)].
42. G. Altarelli and G. Parisi, Nucl. Phys. B **126**, 298 (1977).
43. A. H. Mueller and H. Navelet, Nucl. Phys. B **282**, 727 (1987).
44. B. Ducloue, L. Szymanowski and S. Wallon, JHEP **1305**, 096 (2013) [arXiv:1302.7012 [hep-ph]].
45. D. Colferai, F. Schwennsen, L. Szymanowski and S. Wallon, JHEP **1012**, 026 (2010) [arXiv:1002.1365 [hep-ph]].
46. A. Sabio Vera and F. Schwennsen, Nucl. Phys. B **776**, 170 (2007) [hep-ph/0702158 [hep-ph]].
47. B. Ducloue, L. Szymanowski and S. Wallon, Phys. Rev. Lett. **112**, 082003 (2014) [arXiv:1309.3229 [hep-ph]].
48. F. Caporale, D. Y. Ivanov, B. Murdaca and A. Papa, Eur. Phys. J. C **74**, 3084 (2014) [arXiv:1407.8431 [hep-ph]].
49. G. Safronov [CMS Collaboration], AIP Conf. Proc. **1654**, 040003 (2015) [arXiv:1501.02332 [hep-ex]].
50. F. Caporale, G. Chachamis, B. Murdaca and A. Sabio Vera, arXiv:1508.07711 [hep-ph].
51. G. Chachamis, M. Deak, A. Sabio Vera and P. Stephens, Nucl. Phys. B **849**, 28 (2011) [arXiv:1102.1890 [hep-ph]].
52. G. Chachamis and A. Sabio Vera, Phys. Lett. B **709**, 301 (2012) [arXiv:1112.4162 [hep-th]].
53. G. Chachamis and A. Sabio Vera, Phys. Lett. B **717**, 458 (2012) [arXiv:1206.3140 [hep-th]].
54. G. Chachamis, A. Sabio Vera and C. Salas, Phys. Rev. D **87**(1), 016007 (2013) [arXiv:1211.6332 [hep-ph]].

Roberto Fiore
László Jenkovszky
Risto Orava

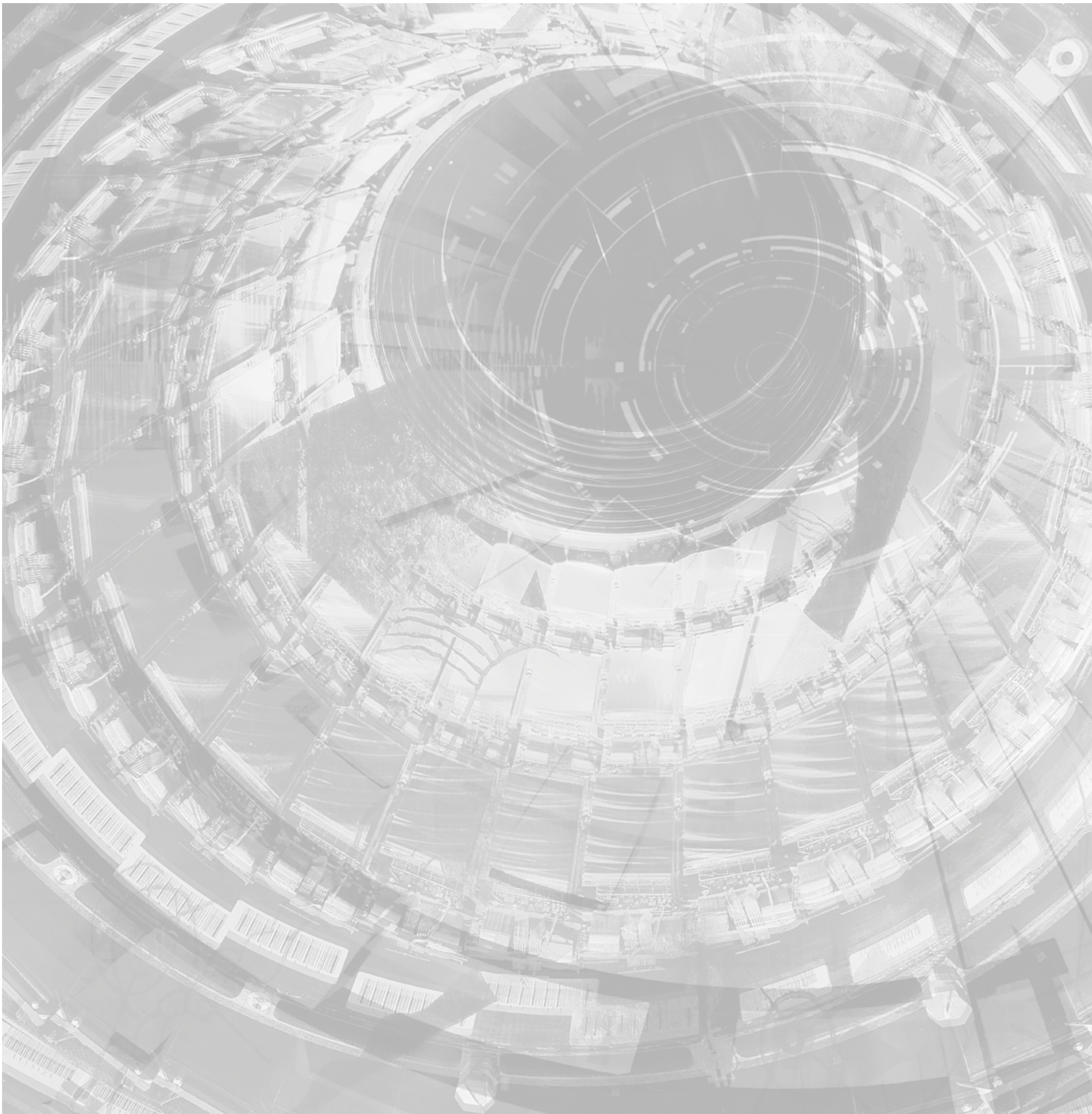

Elastic and inelastic diffraction at the LHC

Roberto Fiore [g], László Jenkovszky [b7], Risto Orava [h]

[g]Universitá della Calabria, Consenza, Italy

[b]Bogolyubov Institute for Theoretical Physics, Kiev, Ukraine

[h]Helsinki University, Helsinki, Finland

Abstract

For the first time, at the LHC forward physics is dominated by Pomeron exchange in the t channel, enabling full use of Regge factorization. Elastic scattering and diffraction dissociation are related by using this property of the theory. The possibility of an Odderon exchange is scrutinized. The dynamics of the dip-bump structure in elastic scattering is modelled. In diffracion dissociation the role of low missing mass resonances is estimated. Fits to the LHC data at 7 TeV are presented.

1 Introduction. Regge factorization

With the advent of the LHC, elastic and inelastic scattering entered a new area, where diffraction can be seen uncontaminated by non-diffractive events. In terms of the Regge-pole theory this means, that the scattering amplitude is completely determined by a Pomeron exchange, and, in a simple-pole approximation, Regge factorization is of practical use! Let us remind that the Pomeron is not necessarily a simple pole: perturbative QCD suggests that the Pomeron is made of an infinite number of poles (useless in practice), and the unitarity condition requires corrections to the simple pole, whose calculation is far from unique. Instead a simple Pomeron pole approximation is efficient in describing a variety of diffraction phenomena.

The elastic scattering amplitude is simply

$$A(s,t)=\xi(t)\beta(t)^2(s/s_0)^{\alpha_P(t)-1}+A_R(s,t), \tag{48}$$

where $\xi(t)$ is the signature factor, and $\alpha(t)$ is the (linear) Pomeron trajectory. The signature factor can be written as $\xi(t)=e^{-i\pi/2}$. The residue is chosen to be a simple exponential, $\beta(t)=e^{b_P t}$. "Minus one" in the propagator term $(s/s_0)^{\alpha_P(t)-1}$ of (48) correspond for normalization $\sigma_T(s)=ImA(s,t=0)$. The scale parameter s_0 is not fixed by the Regge-pole theory: it can be fitted do the data or fixed to a "plausible" value of a hadronic mass, or to the inverse "string tension" (inverse of the Pomeron slope), $s_0=1/\alpha'$. The second term in Eq. (48), corresponding to sub-leading Reggeons, has the same functional form as the first one (that of the Pomeron), just the values of the parameters differ.

Fig. 20 shows the simplest configurations of Regge-pole diagrams for elastic, single- and double diffraction dissociation, as well as central diffraction dissociation (CD). In this lecture we consider only SD and DD.

Factorization of the Regge residue $\beta(t)$ and the "propagator" $(s/s_0)^{\alpha_P(t)-1}$ is a basic property of the theory. At the LHC for the first time we have the opportunity of testing Regge-factorization directly, since the scattering amplitude here is dominated by a simple Pomeron-pole exchange, identical in elastic and inelastic diffraction. Simple factorization relations between elastic ($\frac{d\sigma_{el}}{dt}$), single ($\frac{d\sigma_{el}}{dt}$) and double ($\frac{d^3\sigma_{DD}}{dtdM_1^2dM_2^2}$) DD are known from the literature Really, by writing the scattering amplitude as

[7]Corresponding author. See Table 1 for the complete list of lectures given at the school.

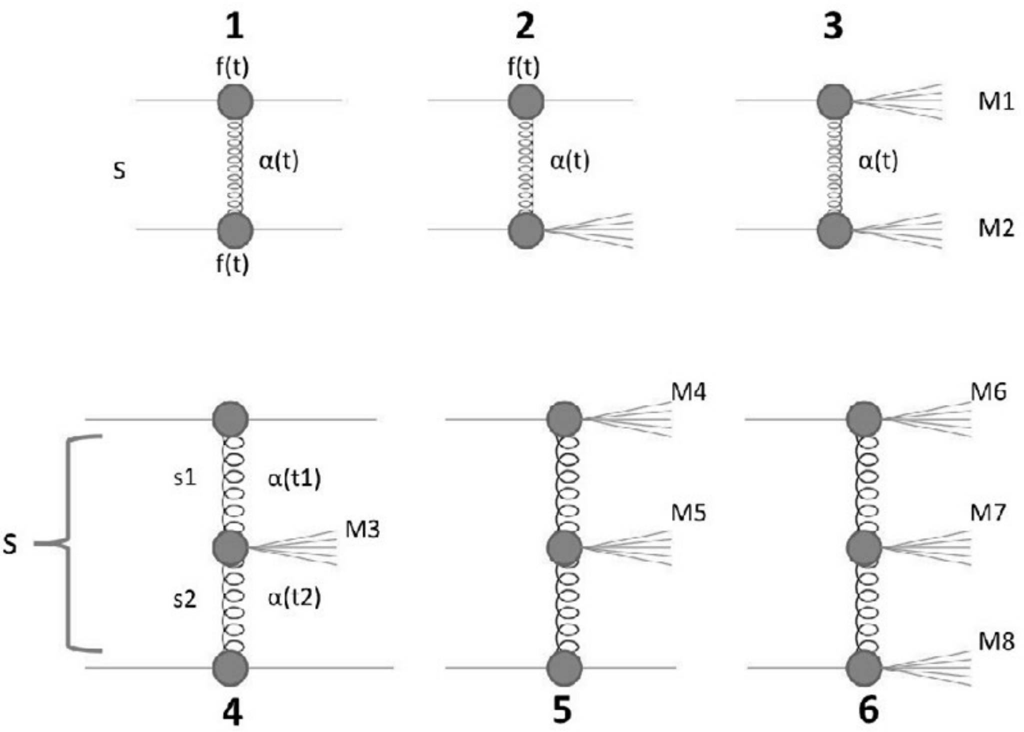

Figure 20: Diagrams for elastic scattering and diffraction dissociation (single, double and central).

product of the vertices, elastic f and inelastic F, multiplied by the (universal) propagator (Pomeron exchange), $f^2s^\alpha \quad fFs^\alpha, \quad F^2s^\alpha$ for elastic scattering, SD and DD, respectively, one gets

$$\frac{d^3\sigma_{DD}}{dtdM_1^2dM_2^2} = \frac{d^2\sigma_{SD1}}{dtdM_1^2}\frac{d^2\sigma_{SD2}}{dtdM_2^2}/\frac{d\sigma_{el}}{dt}. \tag{49}$$

Assuming e^{Bt} as a $t-$dependence for both SD and elastic scattering, integration over t yields:

$$\frac{d^3\sigma_{DD}}{dM_1^2dM_2^2} = k\frac{d^2\sigma_{SD1}}{dM_1^2}\frac{d^2\sigma_{SD2}}{dM_2^2}/\sigma_{el}. \tag{50}$$

where $k = r^2/(2r-1), \quad r = B_{SD}/B_{el}$.

For pp interactions at the ISR, $r = 2/3$ and hence $k = 4/3$. Taking the value $r = 2/3$, consistent with the experimental results at Fermilab and ISR, one obtains $\sigma_{DD} = \frac{4\sigma_{SD}}{3\sigma_{el}},$. Notice that for $r = 1/2, \quad k \to \infty$. Thus k is very sensitive to the ratio r, which shows that direct measurements of the slopes at the LHC are important. Interestingly, relation (50) can be used in different ways, e.g. to cross check any among the four inputs.

To summarize this discussion, we emphasize the important role of the ratio between the inelastic and elastic slope, which at the LHC is close to its critical value $B_{SD}/B_{el} = 0.5$ (it cannot go below!), which means a very sensitive correlation between these two quantities. The right balance may require a correlated study of the two by keeping the ratio above 0.5. This constrain may guide future experiments on elastic and inelastic diffraction.

2 Elastic scattering

The experimental data on proton-proton elastic and inelastic scattering emerging from the measurements at the LHC, call for an efficient model to fit the data and identify their diffractive (Pomeron) component. To this end, there is a need for a reasonably simple and feasible model of the scattering amplitude, yet satisfying the basic theoretical requirements such as analyticity, crossing and unitarity. In our opinion, the expected (dip-bump) structure in the differential cross section is most critical in discriminating models of high-energy diffraction, although other observables, such as the rate of the increase of the total cross sections, the ratio of the elastic to total cross section, detail concerning the shape of the elastic cross section, such as its "break" at small $|t|$ and flattening at large $|t|$ are important as well.

We show that, while the contribution from secondary reggeons is negligible at the LHC, the inclusion of the Odderon is mandatory, even for the description of pp scattering alone. To make our analyzis complete, we include in our fits $\bar{p}p$ data as well.

Simplicity and efficiency are the main reasons why the model of Donnachie and Landshoff (DL) is so popular and useful. A supercritical Pomeron term, appended with non-leading (secondary) Reggeon contributions, with linear Regge trajectories describes elastic scattering data in a wide range of energies at small $-t$. Due to this simplicity it can be used also as a part of more complicated inelastic reactions, whenever Regge-factorization holds.

Any extension of this model should include:

- The dip-bump structure typical to high-energy diffractive processes;
- Non-linear Regge trajectories;
- Possible Odderon (odd-C asymptotic Regge exchange),and be
- Compatible with $s-$ and $t-$ channel unitarity;

The first attempt to describe high-energy diffraction, in particular the appearance of the characteristic dip-bump structure in the differential cross sections, was made by Chou and Yang: the distribution of matter in the nuclei was assumed to follow that of the electric charge (form factors). The original "geometrical" Chou and Young model qualitatively reproduces the t dependence of the differential cross sections in elastic scattering, however it does not contain any energy dependence, subsequently introduced by means of Regge-pole models.

A particularly efficient parametrization of dip was suggested by Phillips and Barger, right after its first observation at the ISR. Their formula reads

$$\frac{d\sigma}{dt} = |\sqrt{A}\exp(Bt/2) + \sqrt{C}\exp(Dt/2 + i\phi)|^2, \tag{51}$$

where $A,\ B,\ C,\ D$ and ϕ are determined independently at each energy.

We suggest a simple model that can be used as a handle in studying diffraction at the LHC. It combines the simplicity of the above models approach, and goes beyond their limitations. Being flexible, it can be modified according to the experimental needs or theoretical prejudice of its user and can be considered as the "minimal model" of high-energy scattering while its flexibility gives room for various generalizations/modifications or further developments (e.g. unitarization, inclusion of spin degrees of freedom etc.).

Consider the spinless case of the invariant high-energy scattering amplitude, $A\,(s,t)$, where s and t are the usual Mandelstam variables. The basic assumptions of the model are:

$\alpha(0)\backslash C$	+	-
>1	P	O
<1	f	ω

Table 3: Relative contribution of various reggeons to the scattering amplitude.

1. The scattering amplitude is a sum of four terms, two the asymptotic (Pomeron (P) and Odderon (O)) and two non-asymptotic ones or secondary Regge pole contributions.

Viewed vertically, P and f (second column) have positive C-parity, thus entering in the scattering amplitude with the same sign in pp and $\bar{p}p$ scattering, while the Odderon and ω (third column) have negative C-parity, thus entering pp and $\bar{p}p$ scattering with opposite signs, as shown below:

$$A\left(s,t\right)_{pp}^{\bar{p}p} = A_P\left(s,t\right) + A_f\left(s,t\right) \pm \left[A_\omega\left(s,t\right) + A_O\left(s,t\right)\right], \tag{52}$$

where the symbols $P,\ f,\ O,\ \omega$ stand for the relevant Regge-pole amplitudes and the super(sub)script, evidently, indicate $\bar{p}p(pp)$ scattering with the relevant choice of the signs in the sum (52). This sum can be extended by adding more Reggeons, whose role may become increasingly important towards lower energies; their contribution can be effectively absorbed by f and ω.

2. We treat the Odderon, the C-odd counterpart of the Pomeron on equal footing, differing by its $C-$ parity and the values of its parameters (to be fitted to the data). We examined also a fit to pp scattering alone, without any Odderon contribution. The (negative) result is presented in Sec. 4 of Ref. [1].

3. The main subject of our study is the Pomeron, and it is a double pole (DP), lying on a nonlinear trajectory, whose intercept is slightly above one. This choice is motivated by the unique properties of the DP: it produces logarithmically rising total cross sections at unit Pomeron intercept. By letting $\alpha_P\left(0\right) > 1$, we allow for a faster rise of the total cross section [8] Due to its geometric form (see below) the DP reproduces itself against unitarity (eikonal) corrections. As a consequence, these corrections are small, and one can use the model at the "Born level" without complicated (and ambiguous) unitarity (rescattering) corrections. DP combines the properties of Regge poles and of the geometric approach, initiated by Chou and Yang.

4. Regge trajectories are non-linear complex functions. In a limited range and with limited precision, they can be approximated by linear trajectories (which is a common practice, reasonable when non-linear effects can be neglected). This nonlinearity is manifest e.g. as the "break" i.e. a change the slope $\Delta B \approx 2$ GeV^2 around $t \approx -0.1$ GeV^2 and at large $|t|$, beyond the second maximum, $|t| > 2$ GeV^2, where the cross section flattens and the trajectories are expected to slowdown logarithmically.

A simple mechanism of the diffractive dip-bump structure combining geometrical features and Regge behavior was suggested by L. Jenkovszky and A. Wall. In their model the dip is generated by the Pomeron contribution. The relevant Pomeron is a double pole arises from the interference between this dipole with a simple one, it is accompanied by. The dip-bump in the model shows correct dynamics, that is it develops from a shoulder, progressively deepening in the ISR energy region. As energy increases further, the dip is filled by the Odderon contribution. At low energies the contribution from non-leading, "secondary" Reggeons is also present.

Physically, the components of the Pomeron have the following interpretation: the first term in Eq. (57) is a Gaussian in the impact parameter representation, while the second term contains absorption corrections generating the dip.

The dipole Pomeron produces logarithmically rising total cross sections and nearly constant ratio of σ_{el}/σ_{tot} at unit Pomeron intercept, $\alpha_P\left(0\right) = 1$. While a mild, logarithmic increase of σ_{tot} does not contradict the data, the rise of the ratio σ_{el}/σ_{tot} beyond the SPS energies requires a supercritical DP intercept, $\alpha_P\left(0\right) = 1 + \delta$, where δ is a small parameter $\alpha_P(0) \approx 0.05$. Thus DP is about "twice softer" then that of Donnachie-Landshoff, in which $\alpha_P(0) \approx 0.08$.

In spite of a great varieties of models for high-energy diffraction (for a recent review see [2]), only a few of them attempted to attack the complicated and delicate mechanism of the diffraction structure. In the 80-ies and early 90-ies, DP was fitted to the ISR, SPS and Tevatron data. Now we find it appropriate to revise the state of the art in this field, to update the earlier fits, analyze the ongoing

[8]A supercritical Pomeron trajectory, $\alpha_P(0) > 1$ in the DP is required by the observed rise of the ratio σ_{el}/σ_{tot}, or, equivalently, departure form geometrical scaling, although the intercept is about half compared to that in the DL model since the double pole (or dipole) itself drives the rise in energy.

measurements at the LHC and/or make further predictions. We revise the existing estimates of the Pomeron contribution to the cross sections as a functions of s and t and argue that while the contribution from non-leading trajectories in the nearly forward region is negligible (smaller than the experimental uncertainties), the Odderon may be important, especially in the non-forward direction.

2.1 A simple Regge-pole model

We use the normalization:

$$\frac{d\sigma}{dt} = \frac{\pi}{s^2}|A(s,t)|^2 \quad \text{and} \quad \sigma_{tot} = \frac{4\pi}{s}\Im m A(s,t)\Big|_{t=0} . \tag{53}$$

Neglecting spin dependence, the invariant proton(antiproton)-proton elastic scattering amplitude is that of Eq. (52). The secondary Reggeons are parametrized in a standard way [3,4], with linear Regge trajectories and exponential residua, where R denotes f or ω - the principal non-leading contributions to pp or $\bar{p}p$ scattering:

$$A_R(s,t) = a_R e^{-i\pi\alpha_R(t)/2} e^{b_R t}\Big(s/s_0\Big)^{\alpha_R(t)}, \tag{54}$$

with $\alpha_f(t) = 0.70 + 0.84t$ and $\alpha_\omega(t) = 0.43 + 0.93t$; the values of other parameters of the Reggeons are quoted in Tables 5, 6, 7.

As argued, the Pomeron is a dipole in the $j-$plane

$$A_P(s,t) = \frac{d}{d\alpha_P}\Big[e^{-i\pi\alpha_P/2} G(\alpha_P)\Big(s/s_0\Big)^{\alpha_P}\Big] = \tag{55}$$

$$e^{-i\pi\alpha_P(t)/2}\Big(s/s_0\Big)^{\alpha_P(t)}\Big[G'(\alpha_P) + \Big(L - i\pi/2\Big)G(\alpha_P)\Big].$$

Since the first term in squared brackets determines the shape of the cone, one fixes

$$G'(\alpha_P) = -a_P e^{b_P[\alpha_P - 1]}, \tag{56}$$

where $G(\alpha_P)$ is recovered by integration, and, as a consequence, the Pomeron amplitude Eq. (55) can be rewritten in the following "geometrical" form

$$A_P(s,t) = i\frac{a_P}{b_P}\frac{s}{s_0}[r_1^2(s)e^{r_1^2(s)[\alpha_P - 1]} - \varepsilon_P r_2^2(s)e^{r_2^2(s)[\alpha_P - 1]}], \tag{57}$$

where $r_1^2(s) = b_P + L - i\pi/2$, $r_2^2(s) = L - i\pi/2$, $L \equiv \ln(s/s_0)$.

The main features of the nonlinear trajectories are: 1) presence of a threshold singularity required by $t-$channel unitarity and responsible for the change of the slope in the exponential cone (the so-called "break") near $t = -0.1$ GeV^2, and 2) logarithmic asymptotic behavior providing for a power fall-off of the cross sections in the "hard" region. The combination of theses properties is however not unique.

We examine representative examples of the Pomeron trajectories, namely: 1) Linear Eq. (TR.1); 2) With a square-root threshold, Eq. (TR.2), required by $t-$channel unitarity and accounting for the small-t "break", as well as the possible "Orear", $e^{\sqrt{-t}}$ behavior in the second cone; and 3) A logarithmic one, Eq. (TR.3) anticipating possible "hard effects" at large $|t|$ (in fact, our fits (see below) do not show the expected large-t logarithmic regime in the transition region $|t| < 8$ GeV^2.

$$\alpha_P \equiv \alpha_P(t) = 1 + \delta_P + \alpha_{1P}t, \tag{TR.1}$$

$$\alpha_P \equiv \alpha_P(t) = 1 + \delta_P + \alpha_{1P}t - \alpha_{2P}\left(\sqrt{4\alpha_{3P}^2 - t} - 2\alpha_{3P}\right), \tag{TR.2}$$

$$\alpha_P \equiv \alpha_P(t) = 1 + \delta_P - \alpha_{1P}\ln(1 - \alpha_{2P}t). \tag{TR.3}$$

An important property of the DP Eq. (57) is the presence of absorptions, quantified by the value of the parameter ε_P in Eq. (57); this property, together with the non-linear nature of the trajectories, justifies the neglect of the rescattering corrections.

The unknown Odderon contribution is assumed to be of the same form as that of the Pomeron, Eqs. (55), (57), apart from different values of adjustable parameters (labeled by the subscript "O"). Also, only one trajectory of type (TR.1) is considered for the Odderon.

$$A_O(s,t) = \frac{a_O}{b_O}\frac{s}{s_0}[r_{1O}^2(s)\mathrm{e}^{r_{1O}^2(s)[\alpha_O-1]}], \tag{58}$$

The adjustable parameters are: δ_P, α_{iP}, a_P, b_P, ε_P for the Pomeron and δ_O, α_{iO}, a_O, b_O for the Odderon. The results of the fitting procedure is presented below.

2.2 Fitting to the data

The model contains from 14 to 16 parameters (depending on the choice of the trajectories) to be fitted to 1024 data points simultaneously in s and t. By a straightforward minimization one has little chances to find the solution, because of possible correlations between different contribution and the parameters, including the $P-f$ and $O-\omega$ mixing and the unbalanced role of different contributions/data points. Although we apply the best global fit (minimal χ^2) as a formal criterion for the valid description, we are primarily interested in the dip region, critical for the identification of the Pomeron and the Odderon. As mentioned in the Introduction, we perform also a fit to pp data alone, see Subsection 4.1, to see whether the observed dynamics of dip can be reproduced by the Pomeron alone. The contribution to the global χ^2 from tiny effects, such as the small-$|t|$ "break" in the first (and second) cone, possible oscillations in the slope of the cone(s) etc. should not corrupt the study of the dynamics in the dip-bump region.

To avoid false χ^2 minima, we proceed step-by-step. We start with a fit to the to the forward data: the total cross section and the ratio $\rho = \Re eA(s,t=0)/\Im mA(s,t=0)$ with the Pomeron contribution alone, by assuming that the contribution from the Odderon is small and no absorption in the Pomeron amplitude, $\varepsilon_P = 0$. The forward data are sensitive only to the parameters like a_P, δ_p, therefore we fit them at first. Using obtained values of the parameters as an initial point we proceed with the fitting of the pp and $\bar{p}p$ differential cross sections data in the first cone $|t| < 0.5$ GeV^2, thus applying further constraints on previously mentioned parameters, b_P and α_{iP}. These fits give satisfactory description ($\chi^2/NDF \approx 1.5$) of the total cross sections, ratios of real to imaginary part of the forward amplitude and of the first cone in both pp and $\bar{p}p$ cases for each energy. To describe the second cone and the dip-bump structure, we fit the ε_P and the Pomeron's trajectory parameters: α_{iP}. Next we assume that a shelf, which is clearly seen in $p\bar{p}$ data at 546 and 630 GeV, is generated by the Odderon. Since there is no information about Odderon's structure we fit all its parameters simultaneously, but fixing the Pomeron. After these steps to polish out the minimum we release all parameters of the primary reggeons and add the secondary regeons for the final fit.

To find the best set of parameters we minimize a combined $\chi^2 = \chi^2_{tot} + \chi^2_\rho + \chi^2_{pp} + \chi^2_{p\bar{p}}$ using the MINUIT code. The obtained minimal value of χ^2 for the model with trajectory (TR.1) corresponds to $\chi^2/NDF = 3$. Details of the fit results for different trajectories are summarized in Tables (5,6,7).

Finally we note that the best fit to the data does not necessarily implies the best physical model. For example, the inclusion of spin may affect any seemingly perfect fit to the data. In our opinion, such a minimization procedure improves our understanding of the physical meaning of each term introduced phenomenologically in the amplitude.

To check the role of the Odderon, we first fit only pp scattering without any Odderon (that is supposed to fill the dip in $\bar{p}p$). The best fit is shown in Figs 21 (a,b), demonstrating that, while the Pomeron appended with sub-leading reggeons reproduces the dip for several energies, namely 45, 53, 62 GeV, it fails otherwise (we remind that the deepening of dip is not monotonic: after the minimum at $\sqrt{s} \approx 35$ GeV the trend gets reversed). The presence of the Odderon seems inevitable. Henceforth we use the complete amplitude Eq. (52), including the Odderon.

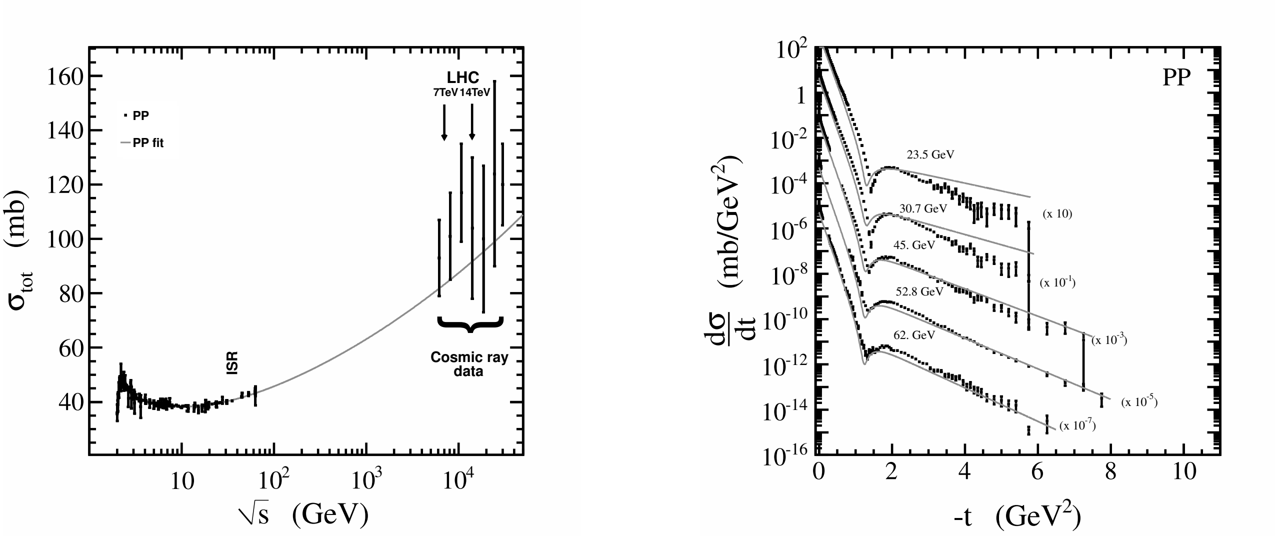

(a) (b)

Figure 21: (a) Total pp cross section calculated in the model, Eqs. (2-8, TR.1), without the Odderon term and fitted to the data in the range $\sqrt{s} = 5$ — 30 TeV; (b) Differential pp cross sections calculated in model, Eqs. (2-8, TR.1), without the Odderon term and fitted to the data in the range $-t = 0.1$ — 8 GeV^2

.

2.3 Elastic cross sections and the diffraction minimum at the LHC

Figure 22 (a) shows the pp and $\bar{p}p$ total elastic scattering cross section calculated in model with the parameters presented in Table 5. On this plot the yellow band represents statistical uncertainties on the calculated values of the total cross section. Figure 22 (b) shows the ratio of the real to imaginary part of the forward amplitude. The model with a linear trajectory sufficiently well describes the forward quantities in a wide range of collision energies for pp and $\bar{p}p$. Different choices of the Pomeron trajectory give similar description of the data. The values of parameters fitted with different trajectory forms are summarized in Tables 5,6,7. Figures 23 (a,b) show the fitted $\bar{p}p$ and pp differential elastic scattering cross sections. The model reasonably describe both reactions with slight excess around the dip region at $\sqrt{s}$ =23 GeV for pp scattering and small deviations for $|t| > 1$ GeV^2 in $\bar{p}p$. In Figure 24 predictions for three different center of mass energies are shown. The yellow area exhibits the statistical uncertainty on the calculations, described earlier. Calculations are characterized by an approximately exponential fall-off in range $0 < |t| < 8$ GeV^2, with the slope change around $-t \approx 0.6$ GeV^2. The dip moved towards lower momentum transfer and became almost filled by the Odderon contribution. Predictions on elastic scattering at the LHC are summarized in the Table 4.

2.4 Inelastic cross section $\sigma_{in}(s)$ and the ratio σ_{el}/σ_{tot}

We calculate $\sigma_{el}(s)$ by integration

$$\sigma_{el} = \int_{t_{min}}^{t_{max}} (d\sigma/dt\, dt), \tag{59}$$

where formally $t_{min} = -s/2$ and $t_{max} = t_{threshold}$. Since the integral is saturated basically by the first cone, we use $t_{max} = 0$ and $t_{min} = -25$ GeV^2 ($t_{min} = -3$ GeV^2 would do as well.) Next we calculate $\sigma_{in}(s) = \sigma_{tot} - \sigma_{el}$ The calculated ratios $\sigma_{el}(s)/\sigma_{tot}(s)$ and $\sigma_{in}(s)/\sigma_{tot}(s)$ are shown in Figure 25 (a). Figure 25 (b) shows pp inelastic cross section. On that figure recent measurements by ATLAS and CMS are also shown. The model is found to be in a good agreement with $\bar{p}p$ and low energy pp data as well as with the the newest measurements at 7 TeV (not fitted).

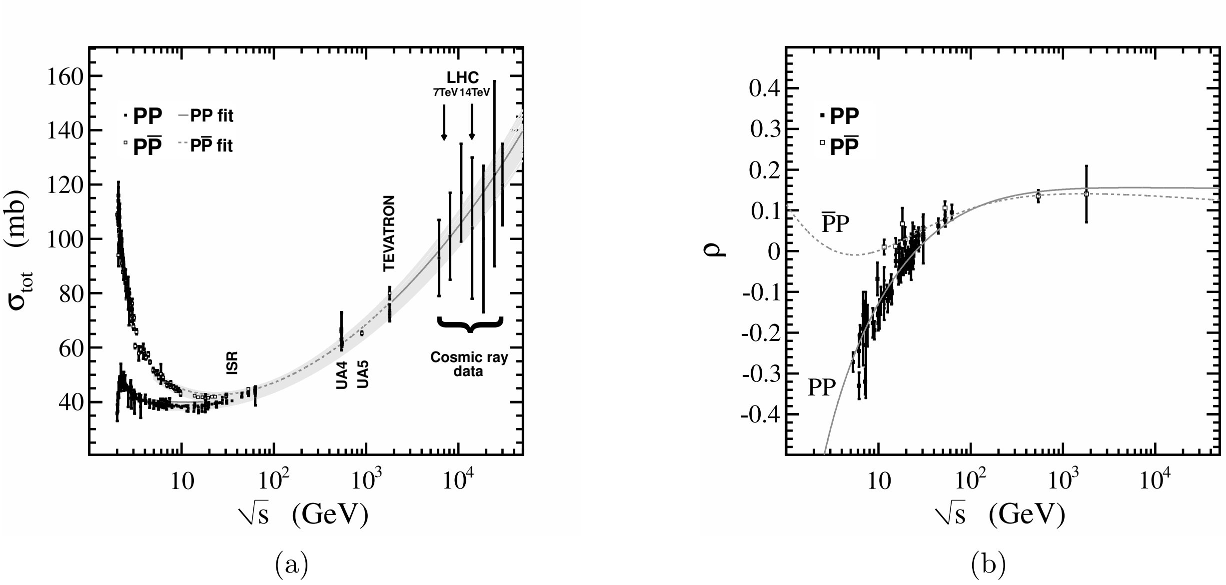

Figure 22: (a) Total pp and $\bar{p}p$ cross sections calculated in the model, Eqs. (2-8, TR.1), and fitted to the data in the range $\sqrt{s} = 5$ — 30 TeV and 5 GeV — 1.8 TeV, respectively. (b) Ratio of the real to imaginary part of the forward amplitude for pp and $\bar{p}p$, calculated in model and fitted to the data. The curves correspond to calculations with the parameters shown in Table (5).

2.5 Local Nuclear Slope

Having fitted the parameters to the data on differential and total cross sections as well as on the ratio ρ, we proceed to calculate the local slope

$$B(s,t) = \frac{d}{dt}\left(\ln\frac{d\sigma(s,t)}{dt}\right). \tag{60}$$

It is a sensitive tool to investigate the fine structure of the cone.

The purpose of the present calculations of $B(s,t)$ is to reproduce and predict the behavior of the slope (usually not fitted) at different energies, including those of the LHC. We have calculated the local nuclear slope $B(s,t)$ within the present model using the parameters from Table 5, and compared it with the "experimental" local nuclear slope, obtained by the "overlapping bins" procedure. To calculate $B(s,t)$, we use the approximate formula

$$B(s,t) = \frac{\frac{1}{2\Delta t}\left(\frac{d\sigma}{dt}(s,t+\Delta t) - \frac{d\sigma}{dt}(s,t-\Delta t)\right)}{\frac{d\sigma}{dt}(s,t)}. \tag{61}$$

The results of the calculations are shown in Fig. 26. One can see that $B(s,t)$ agrees with the experimental data for 63 GeV pp and 1800 GeV $\bar{p}p$. With increasing energy, the curvature decreases and changes the sign when the energy exceeds ~ 2 TeV.

2.6 Pomeron dominance at the LHC

A basic problem in studying the Pomeron is its identification i.e. its discrimination from other contributions. We try to answer the important question: where (in s and in t) and to what extent are the elastic data from the LHC dominated by the Pomeron contribution? The answer to this question is of practical importance since, by Regge-factorization, it can be used in other diffractive processes, such as diffraction dissociation. It is also of conceptual interest in our definition and understanding of the phenomenon of high-energy diffraction.

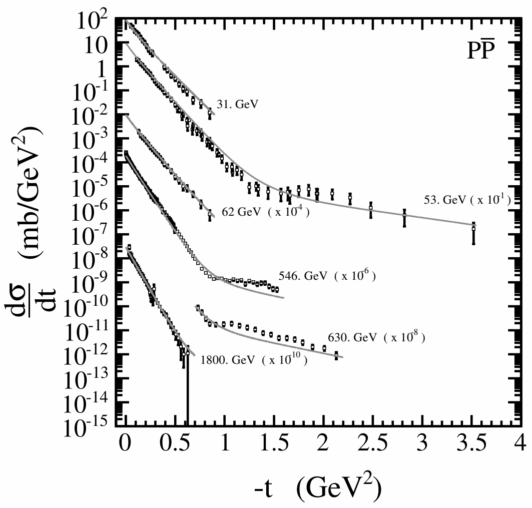

(a)

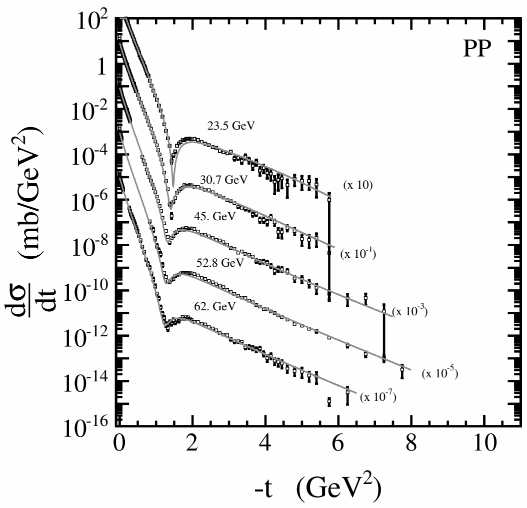

(b)

Figure 23: (a) $\bar{p}p$ differential cross sections calculated in model, Eqs. (2-8, TR.1), and fitted to the data, and fitted to the data in the range $-t = 0.1$ — 8 GeV^2. (b) pp differential cross sections calculated in the model and fitted to the data. The curves present calculations with the parameters shown in Table (5).

First we show the energy variation of the relative importance of the Pomeron with respect to contributions from the secondary trajectories and the Odderon. In the case of the pp total cross-section, we calculated the ratio:

$$R(s,t=0) = \frac{\Im m\,(A(s,t) - A_P(s,t))}{\Im m\,A(s,t)}, \tag{62}$$

where the total scattering amplitude A includes the Pomeron contribution A_P plus the contribution from the secondary Reggeons and the Odderon. The results are shown in Fig. 27 (a).

We conclude that starting from the Tevatron energy region, the relative contribution of the non-Pomeron terms to the total cross-section becomes smaller than the experimental uncertainty and hence at higher energies they may be completely neglected, irrespective of the model used. Such a discrimination (between Pomeron and non-Pomeron contributions) is more problematic in the non-forward direction, where the real and imaginary parts of various components of the scattering amplitude behave in a different way and the phase can not be controlled experimentally. Similarly, we calculate the ratio for non-forward scattering ($t \neq 1$):

$$R(s,t) = \frac{|(A(s,t) - A_P(s,t)|^2}{|A(s,t)|^2}. \tag{63}$$

Thus, we have calculated this ratio for pp scattering at LHC energies within the framework of the model. The results are shown in Fig. 27 (b), where $R(s,t)$ is plotted versus $|t|$ <1 GeV^2 at the energy equal to 14 TeV. The common feature of these results is that the Reggeons and the Odderon contributions increase in the vicinity of the dip (shoulder in the case of pp scattering).

Further studies of the small-t curvature (the "break" or fine structure of the Pomeron), with the Coulombic term added will reproduce (and predict) the behavior of elastic cross sections in the Coulomb interference region, while the intermediate- and large-t behavior can be accounted for by using a Pomeron trajectory with a logarithmic asymptotics.

We conclude that:

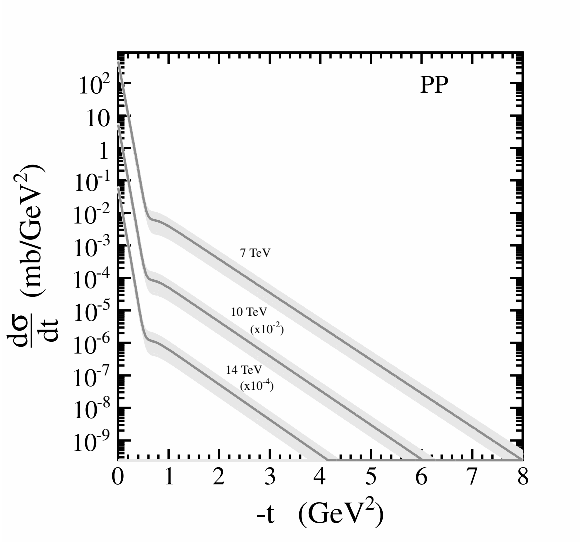

Figure 24: Predictions for the *pp* differential cross section calculated in model, Eqs. (2-8, TR.1) for three different LHC energies. Curves present calculations with the parameters shown in Table (5). The width of the yellow band corresponds to the uncertainty in the cross sections, estimated as described in Sec. 3.

1. A single shallow dip (in fact, a break) is expected in the elastic differential cross section at the LHC, followed by a smooth behavior in t.
2. The Odderon is indispensable in the description of elastic scattering. Its relative contribution, small in the forward direction, increases away from $t = 0$, becoming particularly important in the dip-bump region.
3. The contribution from the non-leading (secondary) Regge trajectories can be neglected in the kinematic region of the LHC measurements. Their relative contribution as a function of s and t has been quantified in Sec. 2.6 Figs. 27.
4. To summarize, our predictions for the LHC are:

	σ_{tot} (mb)	σ_{el} (mb)	σ_{inel} (mb)	$\frac{\sigma_{el}}{\sigma_{tot}}$	ρ
7 TeV	98 ± 1	26	72	0.27	0.16
14 TeV	111 ± 2	32	79	0.29	0.16

	$B\,(t = 0.1)$ GeV^{-2}	$B\,(t = 0.3)$ GeV^{-2}	$-t_{min}$ GeV^2
7 TeV	19.2	19.6	0.65
14 TeV	20.4	20.9	0.60

Table 4: Predictions for total elastic, inelastic *pp* cross sections, local slope and the position of the diffractive minimum calculated in model with the parameters presented in Table (5).

3 Odderon at the LHC

The nature of the Odderon - an asymptotic odd-C Regge pole exchange, counterpart of the Pomeron - for a long time remains a subject of debate. Although there is little doubt about its existence, we still lack direct evidence of the Odderon. Various reactions supposedly dominated by Odderon

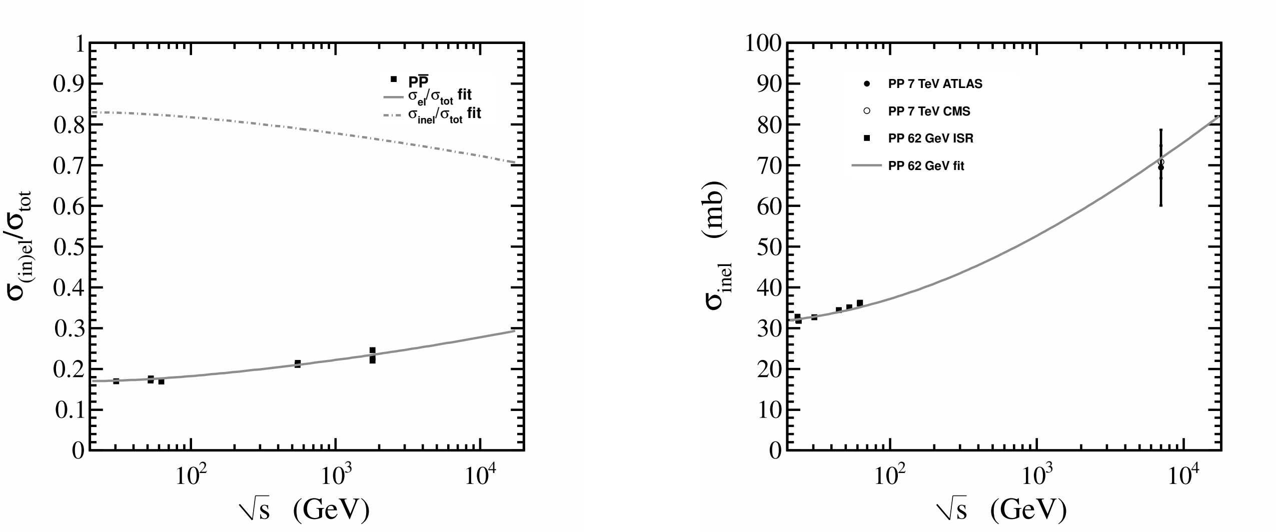

(a) (b)

Figure 25: (a) The ratios $\frac{\sigma_{el}}{\sigma_{tot}}$ and $\frac{\sigma_{inel}}{\sigma_{tot}}$ calculated in model using the trajectory (TR.1). (b) Predictions for the pp inelastic cross section calculated in model, Eq. (53). The curves correspond to the calculations with the parameters quoted in Table (5).

Pomeron		Odderon		Reggeons	
a_P	262	a_O	0.088	$-a_f$	12.6
b_P [GeV^{-2}]	8.4	b_O [GeV^{-2}]	14.2	b_f [GeV^{-2}]	4.4
δ_P	0.05	δ_O	0.17	$-$	$-$
α_{1P}	0.44	α_{1O}	0.043	a_ω	8.2
ε_P	0.015	ε_O	0.	b_ω [GeV^{-2}]	23.8
s_P [GeV^2]	100	s_O [GeV^2]	100	s_0 [GeV^2]	1
	$\sigma_{tot}, \sigma_\rho, \frac{d\sigma_{pp}}{dt}, \frac{d\sigma_{p\bar{p}}}{dt}$				
χ^2/NDF	3.2				

Table 5: Fitted parameters of the model with trajectory TR.1.

exchanges, called "Odderon filters", may offer only indirect evidence either because of low statistics or contamination by competing exchanges.

In quantum chromodynamics the Odderon corresponds to the exchange of an odd number of gluons. Relevant calculations were done in a number of papers.

The only direct way to see the Odderon is by comparing particle and antiparticle scattering at high enough energies. The high-energy proton-proton and proton-antiproton elastic scattering amplitude is a difference or sum of even- and odd $C-$parity contributions, $A_{pp}^{\bar{p}p}(s,t) =$ "*Even*" $\pm$ "*Odd*", where, essentially, the even part consists of the Pomeron and f Reggeon, while the odd part contains the Odderon and the ω Reggeon. It is clear from the above formula that the odd component of the amplitude can be extracted from the difference of the proton-antiproton and proton-proton scattering amplitudes, and, since at high enough energies the contributions from secondary Regge trajectories die out, this difference offers a direct way of extracting the Odderon contribution. Unfortunatelly, pp and $\bar{p}p$ elasctic scatterings were typically measured at different $\sqrt{s}$, with the exception of the ISR energies of 31, 53, 62 GeV, see Fig. 28.

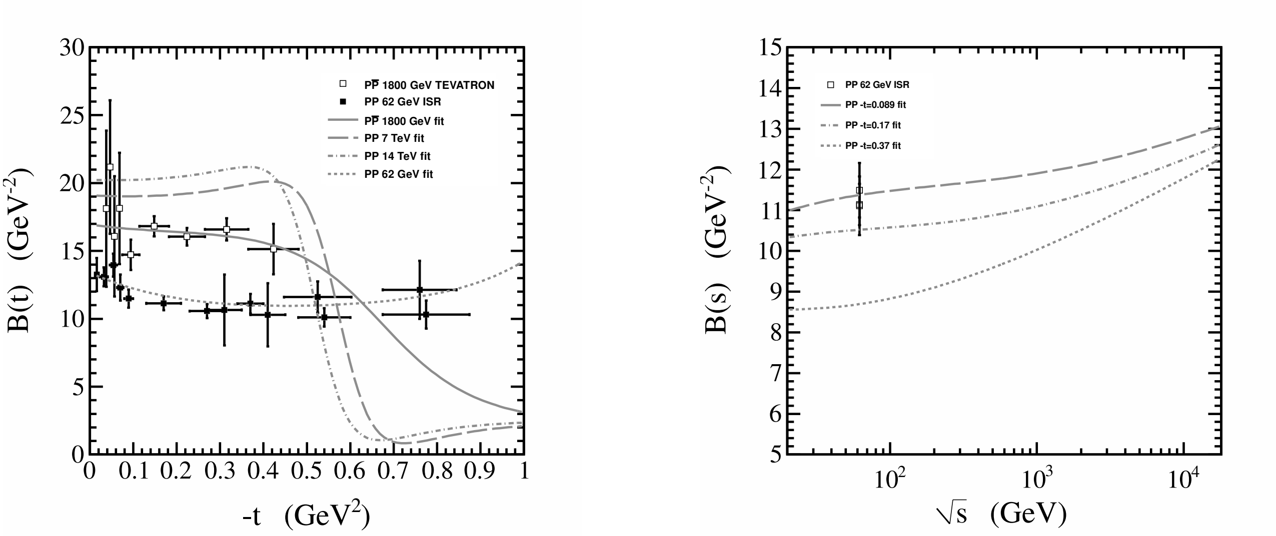

Figure 26: pp and $p\bar{p}$ slope $B(s,t)$ calculated from the model, Eq. (55).

Pomeron		Odderon		Reggeons	
a_P	253	a_O	0.11	$-a_f$	12.4
b_P [GeV^{-2}]	8.4	b_O [GeV^{-2}]	14	b_f [GeV^{-2}]	4.0
δ_P	0.05	δ_O	0.16	–	–
α_{1P}	0.41	α_{1O}	0.046	a_ω	8.0
α_{2P} [GeV^{-1}]	3.34	α_{2O} [GeV^{-2}]	–	b_ω [GeV^{-2}]	15.4
α_{3P} [GeV^2]	0.14	–	–	–	–
ε_P	0.017	ε_O	–	–	–
s_P [GeV^2]	100	s_O [GeV^2]	100	s_0 [GeV^2]	1
	$\sigma_{tot}, \sigma_\rho, \frac{d\sigma_{pp}}{dt}, \frac{d\sigma_{p\bar{p}}}{dt}$				
χ^2/NDF	3.1				

Table 6: Fitted parameters of the model with trajectory TR.2.

At present, the only way to extract the Odderon from the difference of the $\bar{p}p$ and pp scattering amplitudes is by means of a reliable interpolation of both amplitudes (or cross sections) over the missing energy regions. While the energy dependence of the forward amplitude (or total cross sections) is controlled by the Regge-pole theory, its t dependence, especially in the dip-bump region, to large extent is model-dependent and unpredictable.

A simple, general and reliable parametrization of the complicated diffraction structure in high at high energies at any fixed energy is a sum of two exponentials in t related by a complex phase $e^{i\phi}$. Using this generic expression Phillips and Barger (PB) (for brevity we shall referred to as the PB ansatz) obtained good fits to the proton-proton differential cross sections, including the dip-bump region at several CERN ISR fixed energies. Let us remind what is the PB ansatz:

$$\mathcal{A}(s,t) = i[\sqrt{A}\exp(Bt/2) + \exp(i\phi(s))\sqrt{C}\exp(Dt/2)], \tag{64}$$

where s and t are the standard Mandelstam variables; $A,\ B,\ C,\ D$ and ϕ were fitted to each energy independently, i.e. energy dependence in the PB ansatz enters parametrically.

As mentioned, in addition to elastic pp scattering, the PB ansatz describes also $p\bar{p}$ data, with a different set of the parameters (see below), thus opening the way to be used as a tool in extracting

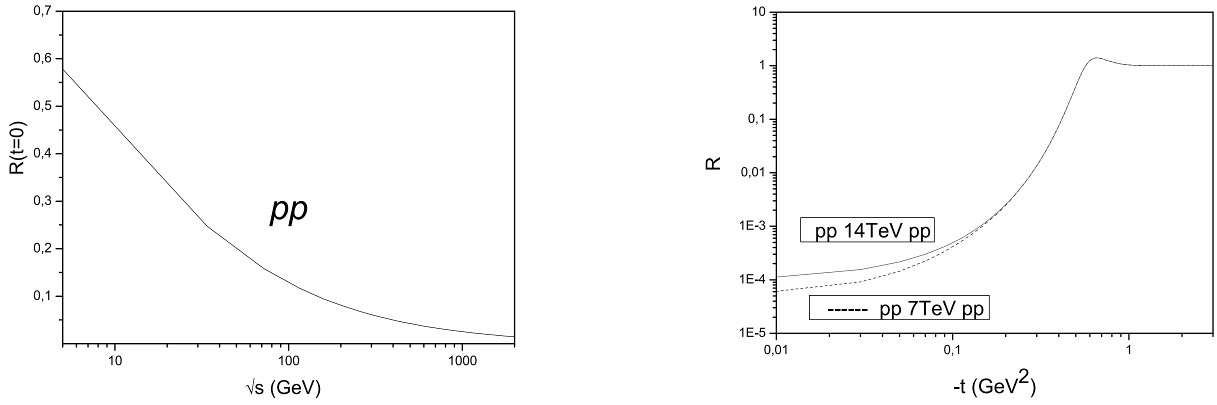

(a) (b)

Figure 27: (a) Relative importance of the non-leading (non-Pomeron) contributions R(s,t=0) to the pp total cross-sections versus energy. (b) Relative importance of non-leading (non-Pomeron) contribution R(s,t) to the pp differential cross-sections calculated versus t.

Pomeron		Odderon		Reggeons	
a_P	258	a_O	0.0386	$-a_f$	12.4
b_P [GeV^{-2}]	8.6	b_O [GeV^{-2}]	20.8	b_f [GeV^{-2}]	4.3
δ_P	0.05	δ_O	0.16	–	–
α_{1P}	$1.33 \cdot 10^4$	α_{1O}	$8.86 \cdot 10^3$	a_ω	8.1
α_{2P} [GeV^{-2}]	$3.2 \cdot 10^{-5}$	α_{2O} [GeV^{-2}]	$3.66 \cdot 10^{-6}$	b_ω [GeV^{-2}]	282.3
ε_P	0.02	ε_O	0.47	–	–
s_P [GeV^2]	100	s_O [GeV^2]	100	s_0 [GeV^2]	1
	$\sigma_{tot}, \sigma_\rho, \frac{d\sigma_{pp}}{dt}, \frac{d\sigma_{p\bar{p}}}{dt}$				
χ^2/NDF	3.08				

Table 7: Fitted parameters of the model with trajectory TR.3.

the Odderon from the difference of the two. However, in its original form, the PB ansatz does not describe the $\sqrt{s}$ dependence of the model parameters.

In this section we try to remedy this limitation, by combining the appealingly simple and efficient form of its t dependence with energy dependence inspired to the Regge-pole model.

We address the following issues: 1) smooth interpolation between the values of the parameters fitted at fixed energy values; 2) Extracting the Odderon contribution from the difference of the $\bar{p}p$ and pp cross sections.

3.1 Generalized PB model

Here we use the norm where

$$\sigma_{tot} = 4\pi \Im A(t=0) = 4\pi[\sqrt{A} + \sqrt{C}\cos\phi] \tag{65}$$

and

$$\frac{d\sigma}{dt} = \pi|\mathcal{A}(t)|^2 = \pi[Ae^{Bt} + Ce^{Dt} + 2\sqrt{A}\sqrt{C}e^{(B+D)t/2}\cos\phi]. \tag{66}$$

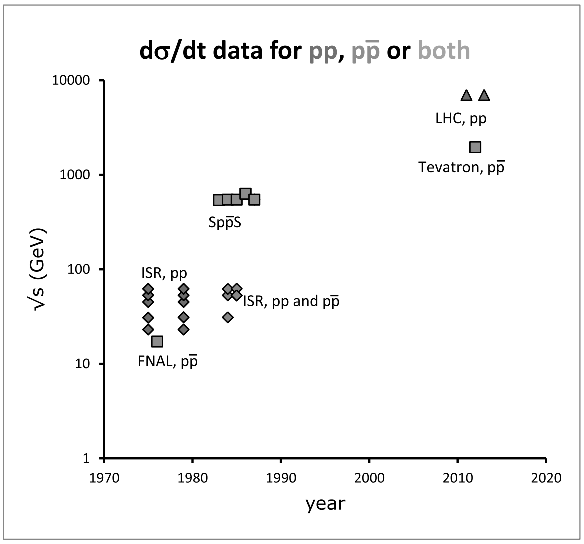

Figure 28: Timeline of proton and antiproton elastic scattering measurements. New accelerators are run first at the maximum available energies, however, at the start of the S$p\bar{p}$S accelerator, the pp and the $p\bar{p}$ elastic scattering data were measured at the same $\sqrt{s} = 31$, 53 and 62 GeV.

Following the Regge-pole theory, we make the following assignment

$$\sqrt{A} \to \sqrt{A(s)} = a_1 s^{-\epsilon_{a_1}} + a_2 s^{\epsilon_{a_2}}, \quad \sqrt{C} \to \sqrt{C(s)} = c s^{\epsilon_c} \tag{67}$$

inspired by the Donnachie and Landshoff model of cross sections (see Eq. (65)) with effective falling (sub-leading Reggeons) and rising (Pomeron) components. It follows from our fits that the falling (sub-leading Reggeon) components in $\sqrt{C}$ is small, hence it is neglected.

The slopes B and D in the Regge-pole theory are unambiguously logarithmic in s, providing shrinkage of the cone:

$$B \to B(s) = b_0 + b_1 \ln(s/s_0), \quad D \to D(s) = d_0 + d_1 \ln(s/s_0). \tag{68}$$

In the above formulae a normalization factor $s_0 = 1$ GeV^2 is implied.

The phase ϕ is the weakest point of this "toy" model or generalized PB model. In Regge theory, it should depend on t rather than on s. Fortunately, at high $\sqrt{s}$ the dependence of Φ on energy is weak (see the fits below). However, this is not the case as the energy decreases. The best we can do, is to fit the data with

$$cos(\phi(s)) = k_0 + k_1 s^{-\epsilon_{cos}}. \tag{69}$$

The "low"-energy behaviour is a week point in any case. Apart from the varying phase, we must account in some way for the sub-leading (f and ω) Reggeon contributions. This is done partly by the inclusion in $\sqrt{A(s)}$ of a decreasing term (absent in $\sqrt{C}$). A complete treatment of these terms with proper $t-$dependent signatures will require a radical revision of the model, and we hope to come back to this issue in the future.

Now we proceed with this simple approach that has a chance to be viable at high energies, where the Pomeron and Odderon dominate and the above complications may be insignificant.

To understand better the existence of any connection between ansatz (64) and the Regge-pole model, we plot the values of the parameters $A,\ B,\ C,\ D$ and ϕ against s and fit their "experimental" values to Regge-like formulas.

This can be done in two complementary way: A successive"two-step" fit. First gain the values of the parameters $A,\ B,\ C,\ D,\ \phi$ from the fits to the pp and $\bar{p}p$ data, then fit their Regge forms (see below) to the obtained "experimental" values of $A,\ B,\ C,\ D,\ \phi$. Alternatively, one may determine the parameters of Eqs.(67,68) from a single simultaneous fit to all available data. We chose the first option (5 parameters) since otherwise there were too many (at least, 12) free parameters. Thus, we proceed with a two-step fit, by which the final values are determined from a fit to the "experimental" values of $A,\ B, C, D$ and ϕ.

We fitted separately pp and $p\bar{p}$ in two variables, s and t, by using pp and $p\bar{p}$ data on total and differential cross sections ranging from the ISR to the LHC for pp and from S$p\bar{p}$S to the Tevatron for $\bar{p}p$.

Here the following remarks are in order:

1) It is clear from Eqs. (67) and (68) that, while the parameters A and C are particularly sensitive to the data on total cross sections, B and D are correlated mainly with the differential cross sections (the slopes!).

2) Although we are interested mainly in the high-energy behaviour (the Odderon!), low energies effects cannot be fully neglected. They are taken into account approximately by including in A and C sub-leading terms of the type s^{ϵ}, $\epsilon \approx 0.5$.

3) Having fitted $A,\ B,\ C,\ D$ and ϕ, we perform a cross-check by calculating the resulting total cross sections.

4) At high energies, the proton-proton and antiproton-proton total cross sectoins are supposed to converge. (We consider only this simple option, although we are aware of alternatives.) Since the existing data are not yet in this asymptotic domain, we introduce an extra constraint.

5) The most delicate issue is the phase, that in Regge phenomenology are expected to be t – rather than s – dependent. Our fits show considerable energy dependence of the phase at low energies but week dependence at high energies, where we are particularly interested in looking for the Odderon signal. Postponing the introduction of a true Regge-pole motivated, a t-dependent phase to a further study here we assume a simple parametrization $\cos\phi = k_0 + k_1 s^{\epsilon_\phi}$, fitting to the $\sqrt{s}$ dependence to the values of $\cos\phi$ directly extracted from data.

3.2 Fitting the parameters to the data

We calculate the s dependence of the parameters using a fitting strategy consisting of three consecutive steps described in detail below. In doing so, the following criteria are applied:

- best χ^2 for each fit;
- the $-t$ range was set within $0.35 - 2.5$ GeV^2;
- for each fixed energy the model was fitted simultaneously to $d\sigma/dt$ and σ_{tot} (focussing on the dip region);
- from the resulting fits σ_{tot} was reconstructed in the whole available energy range;

Fig. 1 shows a fit to the data on the pp and $\bar{p}p$ differential cross sections. The parameters $A,\ B,\ C,\ D$ and ϕ were fitted to each energy separately. Given the simplicity of the model, the fits look reasonable.

Fig. 2 shows the fitted values of the parameters $A,\ B,\ C,\ D$ and ϕ both for pp and $\bar{p}p$ scattering to be used as "experimental" data in the second stage of our fitting procedure, in which the explicit expressions (67), (68) and (69) are inserted. The fitted values of the parameters and relevant χ^2/NDF values are quoted in Tables 1 and 2.

3.3 Fitting the parameters $a_i,\ b_i, ...$ entering Eqs. (67), (68) and (69) to the "data" $A,\ B,\ C,\ D,\ cos(\phi)...$, quoted in Tables 8 and 9.

The resulting values of the parameters after the second stage of fitting are:

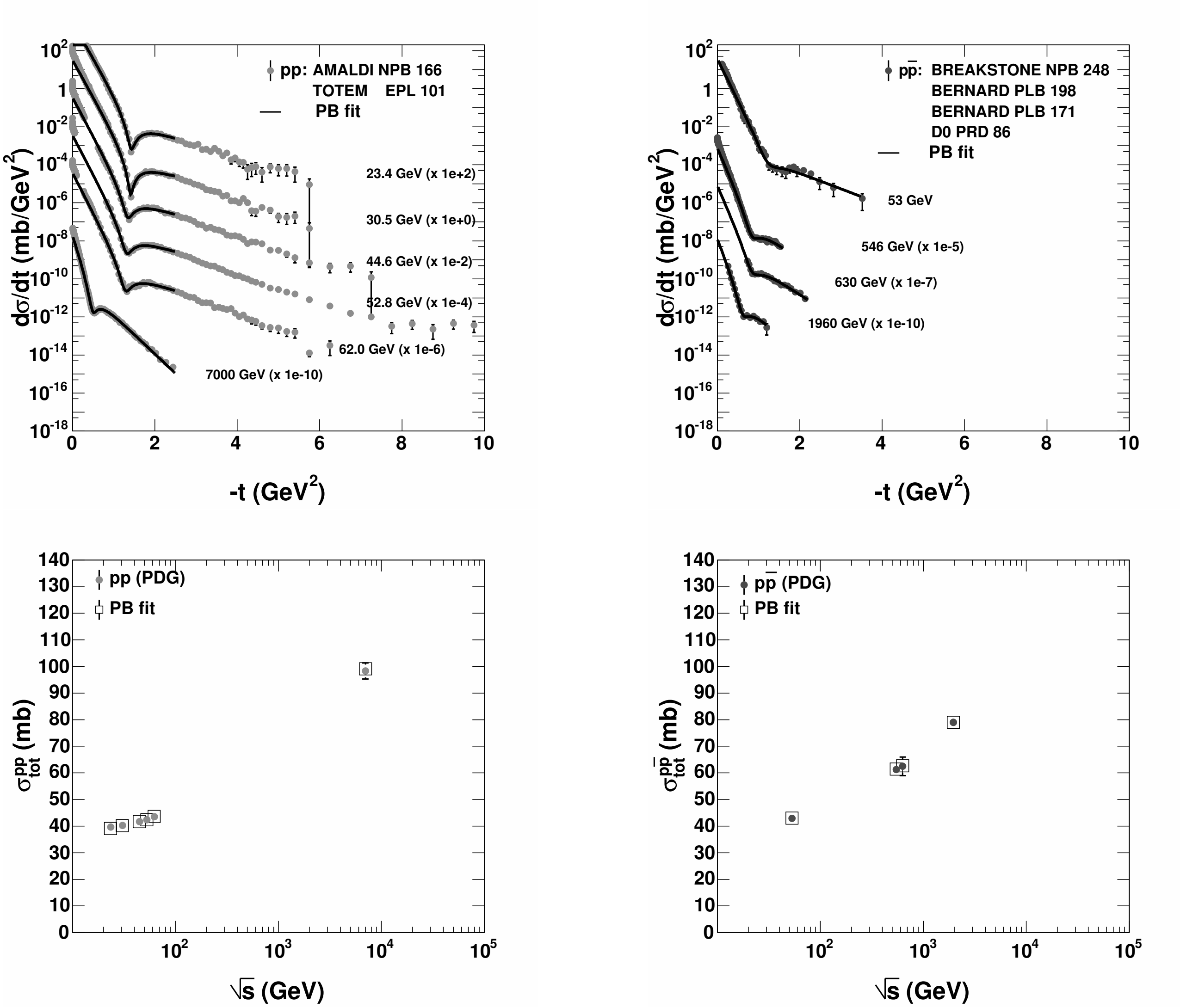

Figure 29: The PB model fitted to the pp and $\bar{p}p$ data at discrete energy values

.

$$\begin{aligned}
\sqrt{A_{pp}(s)} &= 1.31s^{0.106} + 3.90s^{-0.298}, \\
\sqrt{C_{pp}(s)} &= 0.00117s^{0.358}, \\
B_{pp}(s) &= 5.13 + 0.555 \ln s, \\
D_{pp}(s) &= -0.838 + 0.312 \ln s. \\
cos(\phi_{pp}(s)) &= -0.928 - 0.863s^{-0.429}.
\end{aligned} \tag{70}$$

$$\begin{aligned}
\sqrt{A_{p\bar{p}}(s)} &= 1.31s^{0.106} + 4.28s^{-0.298}, \\
\sqrt{C_{p\bar{p}}(s)} &= 0.00177s^{0.358}, \\
B_{p\bar{p}}(s) &= 7.87 + 0.274 \ln s, \\
D_{p\bar{p}}(s) &= -0.552 + 0.312 \ln s, \\
cos(\phi_{p\bar{p}}(s)) &= -0.928 + 4.37s^{-0.328}.
\end{aligned}$$

Energy (GeV)	$\sqrt{A}$	B	$\sqrt{C}$	D	$cos(\phi)$	χ^2/NDF
23.4	3.13± 0.6%	8.66± 0.4%	0.019± 8.3%	1.54± 5.1%	-0.97± 0.3%	1.6
30.5	3.21± 0.2%	8.95± 0.3%	0.014± 7.4%	1.28± 5.6%	-0.98± 0.2%	1.1
44.6	3.33± 0.7%	9.32± 0.5%	0.017± 8.0%	1.45± 5.3%	-0.93± 0.8%	1.7
52.8	3.38± 0.3%	9.44± 0.6%	0.017± 7.6%	1.43± 5.0%	-0.92± 0.9%	1.1
62.0	3.49± 0.5%	9.66± 0.6%	0.018± 9.9%	1.53± 6.3%	-0.92± 1.6%	1.5
7000.0	8.51± 1.6%	15.05± 0.8%	0.670± 2.3%	4.71± 0.8%	-0.93± 0.3%	1.4

Table 8: Values of the parameters from a fit to the pp data at various $\sqrt{s}$. The quoted errors correspond to the relative errors, as given by CERN MINUIT fitting package (status= converged, error matrix accurate).

Energy (GeV)	$\sqrt{A}$	B	$\sqrt{C}$	D	$cos(\phi)$	χ^2/NDF
63	3.43± 1.1%	10.07± 1.3%	0.022±30.8%	1.90±14.8%	-0.60±22.7%	0.7
546	5.06± 1.2%	11.25± 1.3%	0.204±21.0%	3.55± 8.6%	-0.86± 2.7%	0.6
630	5.13± 3.9%	11.26± 3.7%	0.176±26.6%	3.23± 9.6%	-0.81± 7.9%	0.5
1960	6.85± 3.7%	12.46± 3.3%	0.629±41.6%	4.69±15.4%	-0.90± 3.6%	0.4

Table 9: Values of the parameters fitted to $p\bar{p}$ data

The lowest right icon in Fig. 2 is a "cross-check", showing the pp and $\bar{p}p$ total cross-sections calculated from Eq. (65) with the explicit values of the parameters defined by (67), (68) and (69). The $\bar{p}p$ total cross-section turns down at highest energies, deflecting dramatically from that of pp. The reason for that non-physical effect is the scarcity of $p\bar{p}$ data, leaving too much freedom in the high-energy extrapolation of the cross section, where one expects asymptotic equality $\sigma_t^{pbarp} = \sigma_t^{pp}$ for $s \to \infty$. This deficiency should and can be cured by imposing an additional constraint on the model. This will be done in the next Subsection, by fixing (tuning) the parameter ϵ_{a_2} ((the leading powers in s of $\sqrt{A}$) to be the same in pp and $\bar{p}p$ scattering.

The above, unbiased fit does not satisfy automatically the required asymptotic constraint $\sigma_t^{pp} = \sigma_t^{\bar{p}p}$, since the available freedom (especially due to the lack of simultaneous pp and $p\bar{p}$ elastic scattering data at $sqrts = 540$, 630, 1800 and 7000 GeV) leave much freedom for the extrapolation to energies beyond the existing accelerators. To remedy this problem, we have tuned the parameters to meet the above constraint in the currently available energy range. Below are the results of the "tuned" fit satisfying the asymptotic condition $\sigma_t^{pp} = \sigma_t^{\bar{p}p}$in the $\sqrt{s} \le 14$ TeV energy range.

The refitted $s-$dependent values of the parameters for pp and $p\bar{p}$ scatterings are:

$$\begin{aligned}
\sqrt{A_{pp}(s)} &= 1.41s^{0.0966} + 2.78s^{-0.267}, \qquad (71)\\
\sqrt{C_{pp}(s)} &= 0.00223s^{0.308},\\
B_{pp}(s) &= 4.86 + 0.586\ln s,\\
D_{pp}(s) &= -0.189 + 0.250\ln s.\\
cos(\phi_{pp}(s)) &= -0.928 - 0.838s^{-0.425}.
\end{aligned}$$

$$
\begin{aligned}
\sqrt{A_{p\bar{p}}(s)} &= 1.41s^{0.0996} + 4.00s^{-0.267}, \\
\sqrt{C_{p\bar{p}}(s)} &= 0.00588s^{0.264}, \\
B_{p\bar{p}}(s) &= 6.55 + 0.398\ln s, \\
D_{p\bar{p}}(s) &= 2.351 + 0.068\ln s, \\
cos(\phi_{p\bar{p}}(s)) &= -0.908 + 4.376s^{-0.328}.
\end{aligned}
$$

3.4 Extracting the Odderon from the differencee of $\bar{p}p$ and pp data

The existence of a parametrization for both pp and $\bar{p}p$ scattering offers the possibility to extract the odd-C contribution, by using the formula

$$\mathcal{A}_{pp}^{\bar{p}p} = \mathcal{A}_{even} \pm \mathcal{A}_{odd}, \tag{72}$$

where $\mathcal{A}_{even}$ and $\mathcal{A}_{odd}$ are respectively the C-even and C-odd components of the scattering amplitude. While the $C-$ odd component contains the Pomeron and the f trajectory (both known), the C even part is made of the poorly known Odderon and the familiar ω trajectory. At the LHC energies, the contribution from secondary trajectories, *e.g.* f and ω, is negligible, therefore, by taking the difference between the known (fitted) $p\bar{p}$ and pp amplitudes one gets a pure odd-C contribution, that, in the LHC energy range, is the Odderon. From the explicit expressions for pp and $\bar{p}p$ amplitudes (cross sections) we calculate the Odderon amplitude (or its contribution to the cross section) by taking the difference $\mathcal{A}^{\bar{p}p} - \mathcal{A}^{pp} = \mathcal{A}_{Odd}$. The result (the energy dependence for several fixed values of t and t dependence for several fixed values of s) is shown in Fig. 4

The extracted model parameters are used then to evaluate the even and odd contributions to the forward scattering amplitude. In Fig. 5 we show the Pomeron and the Odderon contributions as the sum or the difference of the differential cross section of $p\bar{p}$ and pp elastic scattering. We see that, as expected, the Pomeron dominates at large colliding energies, while the Odderon contribution is small and at $t = 0$ even changes sign. A particularly interesting feature is shown on the lower right panel of Fig. 5, where the Odderon/Pomeron ratio is shown at different values of t at various $\sqrt{s}$. Apparently, at $\sqrt{s} \approx 100$ GeV, the Odderon/Pomeron ratio becomes t-independent and the t-dependent curves pass through the same point of about 0.03 .

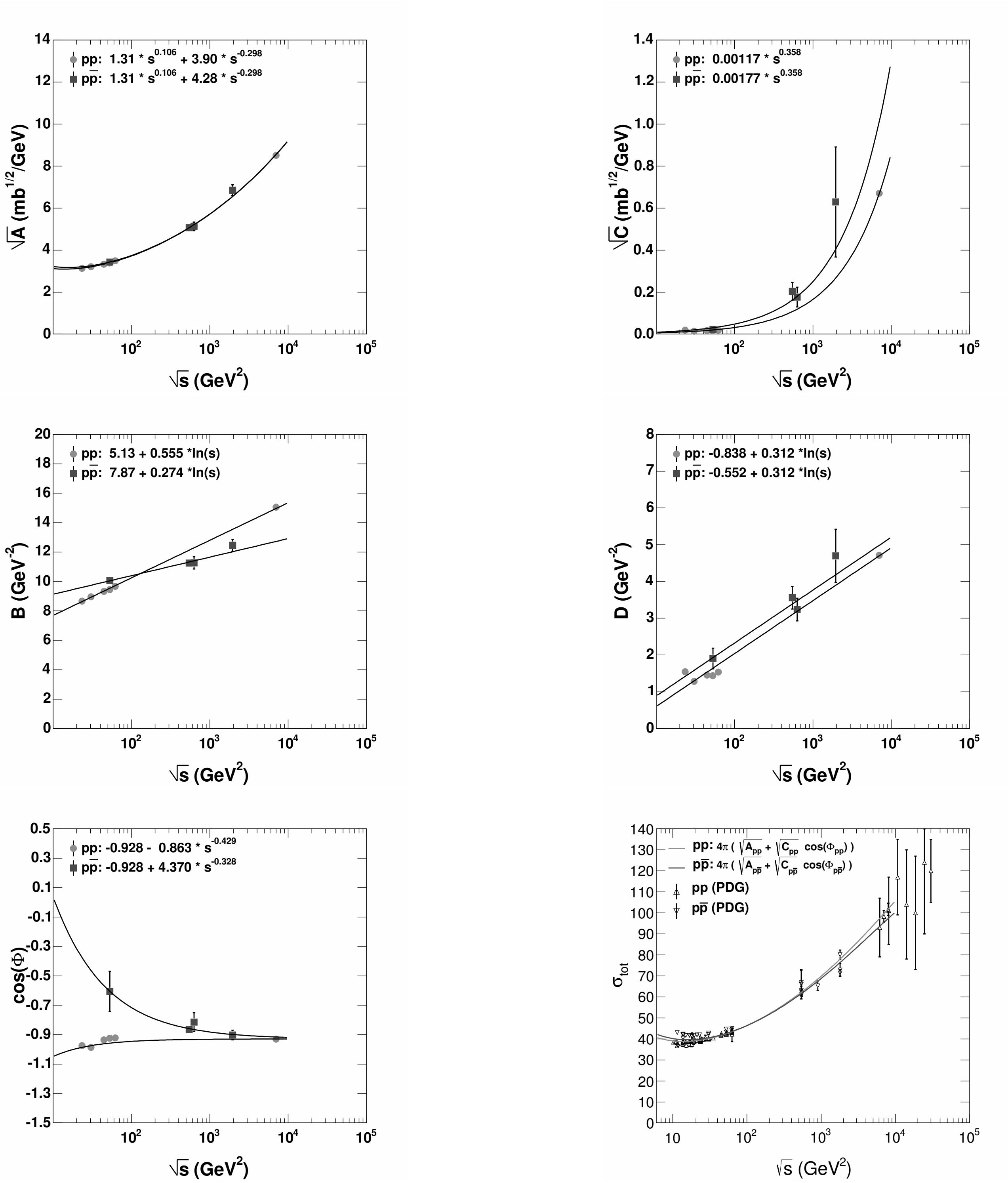

Figure 30: Energy-dependent values of the parameters extracted form a fit to pp and $p\bar{p}$ data. The data on σ_{tot} are from the Particle Data Group database

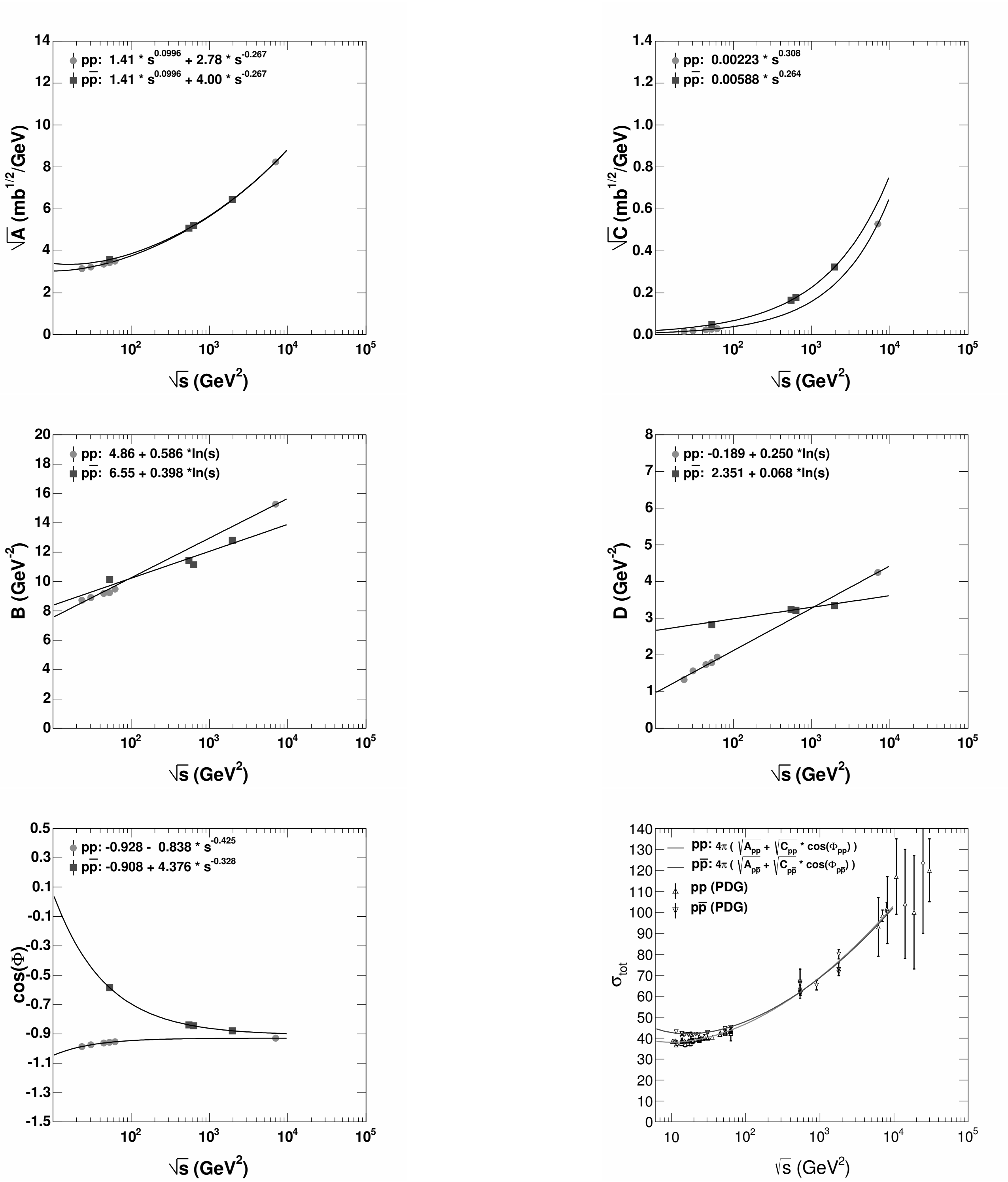

Figure 31: Energy-dependent values of the parameters from a fit to pp and $p\bar{p}$ data, constraint by $\sigma_t^{p\bar{p}} = \sigma_t^{pp}$ as $\sqrt{s} \to \infty$. The lowest right icon shows a cross-check for the (asymptotically converting) total cross sections.

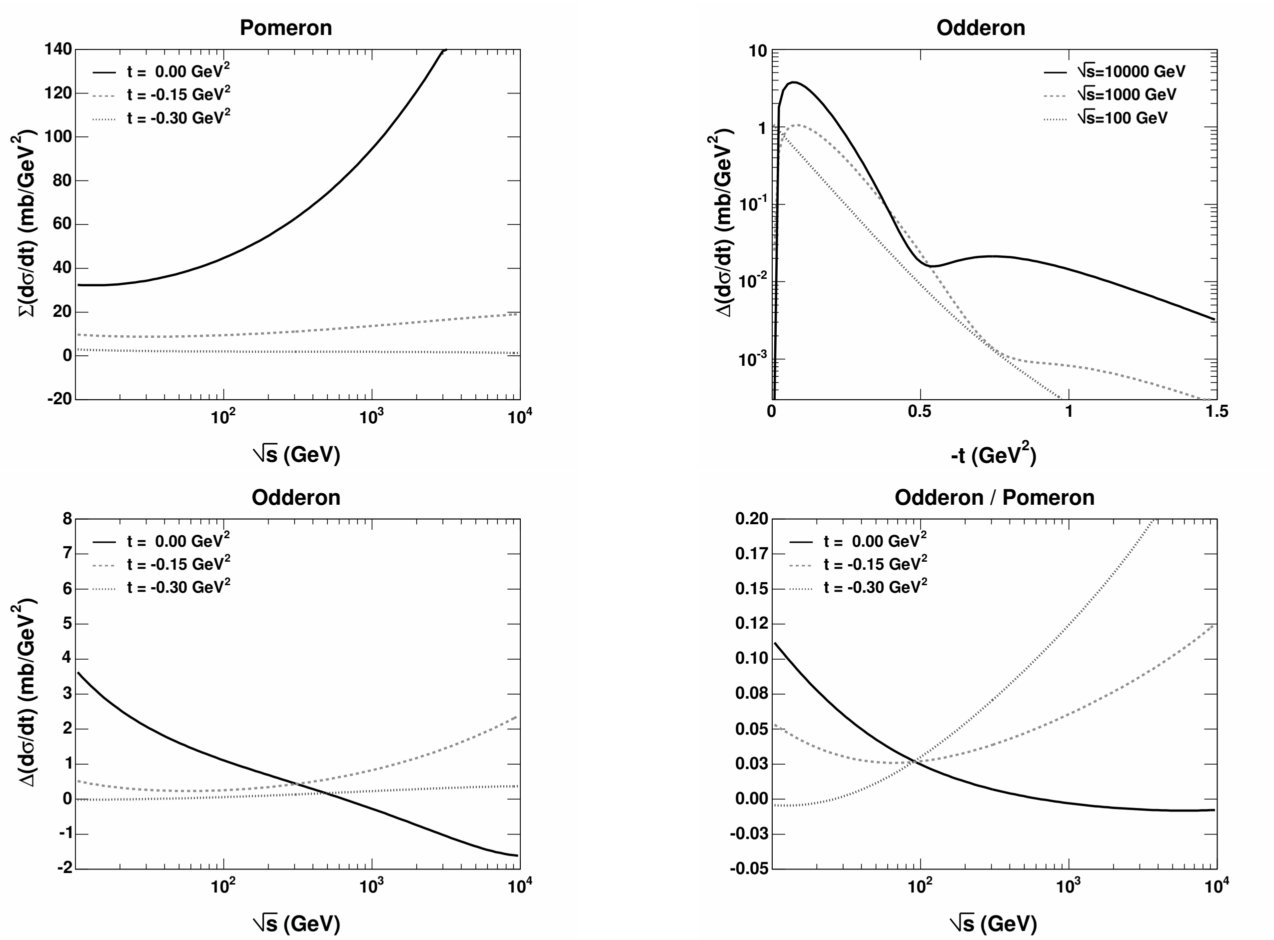

Figure 32: Odd- (”Odderon”) and even (”Pomeron”) parts of the $d\sigma/dt$ cross sections calculated from the difference $|\mathcal{A}|^2_{\bar{p}p} - |\mathcal{A}|^2_{pp} = \Delta_{Odd}$ and from the sum $|\mathcal{A}|^2_{\bar{p}p} + |\mathcal{A}|^2_{pp} = \Sigma_{Pom}$ fitted to the data.

- We strongly recommend to run the LHC accelerator the injection energy $\sqrt{s} = 900$ GeV and at the Tevatron energy of 1.8-1.96 TeV, so that the missing energy range of pp elastic scattering be covered and elastic pp scattering data be measured in the region where already elastic $p\bar{p}$ scattering is measured. It would be also desireable to measure elastic pp scattering at the $\sqrt{s} = 500$ GeV region, which corresponds to the upper energy range of the RHIC accelerator. Such data may significantly improve the possibility to determine the Odderon contribution to elastic scattering. Using the presently available data, the indefinite rise of the $C(s)$, multiplied by a negative ”signature factor” $\cos\phi$, prevents the use of the generalized PB model beyond the LHC energy region of 14-15 TeV;

- For the sake of simplicity, we ignore the low-t non-exponential behaviour (sharpening) of the differential cross section. This simplification has dramatic impact on the low $-t$ behaviour of the Odderon contribution because of the large errors due to the cancellation of the Pomeron contribution.

- The s, rather than t-dependent) signature factor (phase) is in agreement with the data, but it is in contrast to expectations based on Regge phenomenology;

- oversimplified treatment of the low-energy (”secondary Reggeons”) contributions (Odderon/Pomeron here imply, generally, odd- and even exchanges);

- absence for the moment of any physical interpretation in terms of Reggeon exchanges of the components in the PB ansatz.

Given these limitations/simplifications, our approach can be considered as semi-quantitative, showing however some new aspects of the enigmatic Odderon.

4 Diffraction dissociation

Measurements of single (**SD**), double(**DD**) and central(**CD**) diffraction dissociation is among the priorities of the LHC research program.

In the past, intensive studies of high-energy diffraction dissociation were performed at the Fermilab, on fixed deuteron target, and at the ISR. Fig. 35 shows representative curves of low-mass SD as measured at the Fermilab. One can see the rich resonance structure there, typical for low missing masses, often ignored by extrapolating whole region by a simple $1/M^2$ dependence. When extrapolating (in energy), one should however bear in mind that, in the ISR region, secondary Reggeon contributions are still important (their relative contribution depends on momenta transfer considered), amounting to nearly 50% in the forward direction. At the LHC, however, their contribution in the nearly forward direction in negligible, i.e. less than the relevant error bars in the measured total cross section.

In most of the papers on the subject SD is calculated from the triple Regge limit of an inclusive reaction, as shown in Fig. 33.

In that limit, the double diffraction cross section can be written as

$$\frac{d^2\sigma}{dtdM_x^2}=\frac{G_{13,2}^{PP,P(t)}}{16\pi^2 s_0^2}\left(\frac{s}{s_0}\right)^{2\alpha_P(t)-2}\left(\frac{M^2}{s_0}\right)^{\alpha_P(0)-\alpha_P(t)}.$$

This approach has two shortcomings. The first one is that it leaves outside the small-M^2 resonance region. The second one is connected with the fact that whatever the Pomeron, the (partial) SD cross section overshoots the total one, thus obviously conflicting with unitarity. Various ways of resolving this deficiency are known from the literature, including the vanishing (decoupling) of the triple Pomeron coupling, but none of them can be considered completely satisfactory.

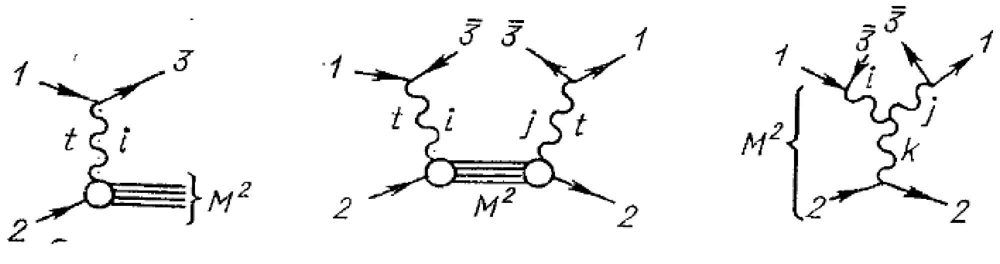

Figure 33: From SD to the triple Regge limit.

We instead follow the idea according to which the Reggeon (here, the Pomeron) is similar to the photon and that the Reggeon-nucleon interaction is similar to deep-inelastic photon-nucleon scattering (DIS), with the replacement $-Q^2 = q^2 \to t$ and $s = W^2 \to M_x^2$. There is an obvious difference between the two: while the C parity of the photon is negative, it is positive for the Pomeron. We believe that while the dynamics is essentially invariant under the change of C, the difference between the two being accounted for by the proper choice of the parameters. Furthermore, while Jaroszewicz and Landshoff, in their Pomeron-nucleon DIS structure function (SF) (or Pp total cross section) use the Regge asymptotic limit, we include also the low missing mass, resonance behavior. As is known, gauge invariance requires the DIS SF to vanish as Q^2 (here, t) $\to 0$. This property is built in the SF, and it has important consequences for the behavior of the resulting cross sections at low t.

It is evident that Regge factorization is essential in both approaches (triple Regge and the present one). It is feasible when Regge singularities are isolated poles. While the pre-LHC data require the inclusion of secondary Reggeons, at the LHC we are in the fortunate situation of a single Pomeron exchange (Pomeron dominance) in the t channel in single and double diffraction (not necessarily so in central diffraction, to be treated elsewhere). Secondary Regge pole exchanges will appear however, in our dual-Regge treatment of Pp scattering (see below), not to be confused with the the t channel of pp. This new situation makes diffraction at the LHC unique in the sense that for the first time Regge-factorization is directly applicable. We make full use of it.

4.1 Measurements prior to the LHC: CERN ISR and SPS, Fermilab. Generalities

Diffraction dissociation was predicted by theory and was intensively studied prior to the LHC on fixed targets (deuteron jets) at the Fermilab by a very successful Soviet-US collaboration and subsequently at the ISR, SPS and RHIC colliders. Below we briefly summarize the results and conclusions of those studies, mainly of single SD.

1. First measurements concerned low missing masses near the threshold region. Resonance peaks e.g. in the reaction $pp \to X$, depending on the relevant value of the momentum transfer t, were observed beyond the threshold. The origin and properties of theses peaks, still subject of debates, were revealed. The main deficiency of the missing mass method is the lack of any information on the decay properties of the produced particles. The missing information was obtained in bubble chamber experiments and in spark chambers, used also in exclusive channels at the ISR Collider.

Apart from low missing masses, SD was found to persist also to high missing masses. Diffraction (coherence) imposes, however, an upper limit on the highest missing masses M_x, roughly as $\xi = M_X^2/s < 0.05$.

Beyond the resonance region, the smooth M_x dependence of the cross section is approximated by $\frac{d\sigma}{dtdM^2} \sim M^n,\ n \approx -2$. The value of n is related to the intercept of the trajectories exchanged in the proton-Reggeon scattering, as will be shown in Sec. 4.3

2. As expected, SD and DD are peaked in the forward direction, and the slope of the exponential peak of SD was found to be around $8 \div 12$ GeV^{-2}, varying with $s,\ t$ and M^2. Near the threshold, the slope is much (about twice) larger than that in elastic scattering, however near $M_x \sim 1.6$ GeV it is already half of that of elastic pp. The correlation between the slope parameter and the mass of the excited state is a common feature of SD.

A diffraction minimum around $t \approx 1$ GeV^2, similar to that in elastic hadron scattering, is expected also in SD (and DD). There are indications of such a structure in $pp \to p(n\pi^+)$ at rather small $|t|$, around $|t| \sim 0.2 \div 0.3$ GeV^2 at $\sqrt{s} = 53$ GeV, however its origin, fate and affinity to the dip-bump structure in elastic scattering is still a matter of debate.

Diffraction is limited both in the missing mass (coherence), $\xi < 0.05$ and in t (”soft” collisions). There is a transition region in t from ”soft” to ”hard” collisions, with a possible dip-bump structure between the two. To be sure, in our analysis we leave outside these interesting but controversial points, concentrating on the ”first” cone with clear exponential behavior.

Before the advent of the LHC, single diffraction dissociation was intensively studied in many different experiments: low energy ISR and SPS CERN experiments, low energy Fermilab (fixed deuteron target) experiments and high energy UA4, UA5, E710 and CDF experiments. All they cover the range $14 < \sqrt{s} < 1800$ GeV, $|t| < 2$ GeV^2, and missing masses range from the threshold up to $\xi < 0.15$. Here $\xi = \frac{M^2}{s}$. The diffraction region is limited up to $\xi < 0.15$. At $\xi \sim 0.15$ non-diffraction contribution become sizeable to diffractive one, and differential cross section become growing with ξ. The main results of these measurements and of their theoretical interpretation can be summarized as follows

1. **Energy dependence.** At energies below 30 GeV the integrated SD cross section rises with s according to the standard prescription of the the Regge-pole theory, however it slows down beyond. This effect was expected due to the familiar problem related to the violation of unitarity, namely that at high energies, implying the triple Pomeron limit, the DD cross section overshoot the total cross section, $\sigma_{SD} > \sigma_t(s)$. Various means were suggested to remedy this deficiency, including decoupling (vanishing) of the triple Pomeron vertex. K. Goulianos instead renormalizes the standard Pomeron

flux to meet the data. Such a "renormalization" produces a break near $\sqrt{s}$ slowing down the rise of $\sigma_{SD}(s)$ in accord with the CDF data from the Tevatron, as shown in Fig. 34.

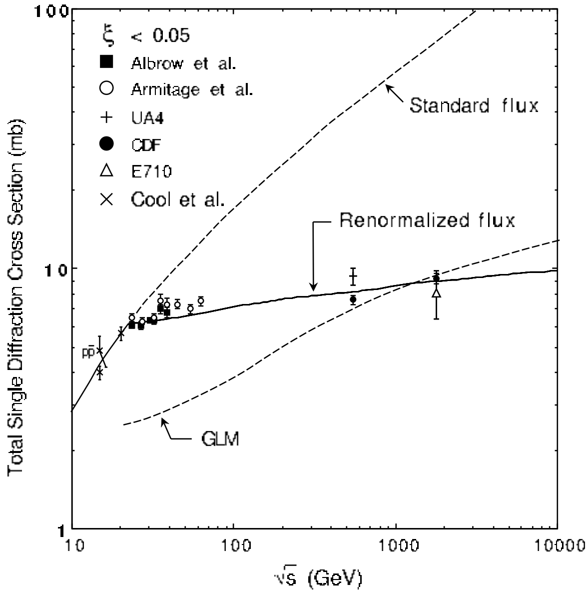

Figure 34: Renormalization by Dino Goulianos

.

An alternative approach to resolve this crises (violation of unitarity) is possible within the dipole Pomeron approach.

2. $t-$ **dependence.** SD cross section and the slope $B(s,t,M^2)$ were measured in the range $0.01 < |t| < 2$. The diffraction cone in SD essentially is exponential in t; a dip, similar to that in elastic scattering, is likely to appear (somewhere near $t \sim 1$ GeV^2).

3. M^2 **dependence.** Probably, this is the most delicate issue in the present studies (and diffraction in general). At the ISR, Fermilab and Tevatron, SD was measured in a wide span of the missing mass, starting from the inelastic threshold $M_{th}^2 = (m_p + m_\pi)^2$ up to $\xi < 0.05$ (or even to $\xi < 0.15$ and higher), Fig. 35(b).

As shown in Figs. 35, there is a rich resonance structure in the small M^2 region. In most of the papers on the subject, this resonance structure is ignored and replaced by a smooth function $\sim M^{-2}$. Moreover, this simple power-like behavior is extended to the largest available missing masses. In Secs. 4.2 and 4.9 we question this point on the following reasons: a) The low-M^2, resonances introduce strong irregularities in the behavior of the resulting cross sections. LHC measurements, are able to probe low-M^2 region, and will be sensitive to these structures. b) The large-M behavior of the amplitude (cross sections) is another delicate point. Essentially, it is determined by the proton-Pomeron (pP) total cross section, proportional to the pP structure function, discussed in details in Sec. 4.2. By duality, the averaged contribution from resonances sums up to produce high missing mass Regge behavior $(M^2)^{-n}$, where n is related to the intercept of the exchanged Reggeon and may be close (but not necessarily equal) to the above-mentioned empirical value ~ 1.

4.2 Model for single and double diffraction dissociation

The model relies on the following premises:

1. **Regge factorization** is feasible since, as stressed repeatedly, at the LHC energies in the region of $|t| < 1$ GeV^2, which is typical for diffraction, the contribution from secondary Reggeons is negligible, and, for a single Pomeron term, factorization (49) is exact. Due to factorization, the relevant expressions for the cross sections (elastic, SD, DD) have simple forms (78), (79), (80). Such relations are known from literature.

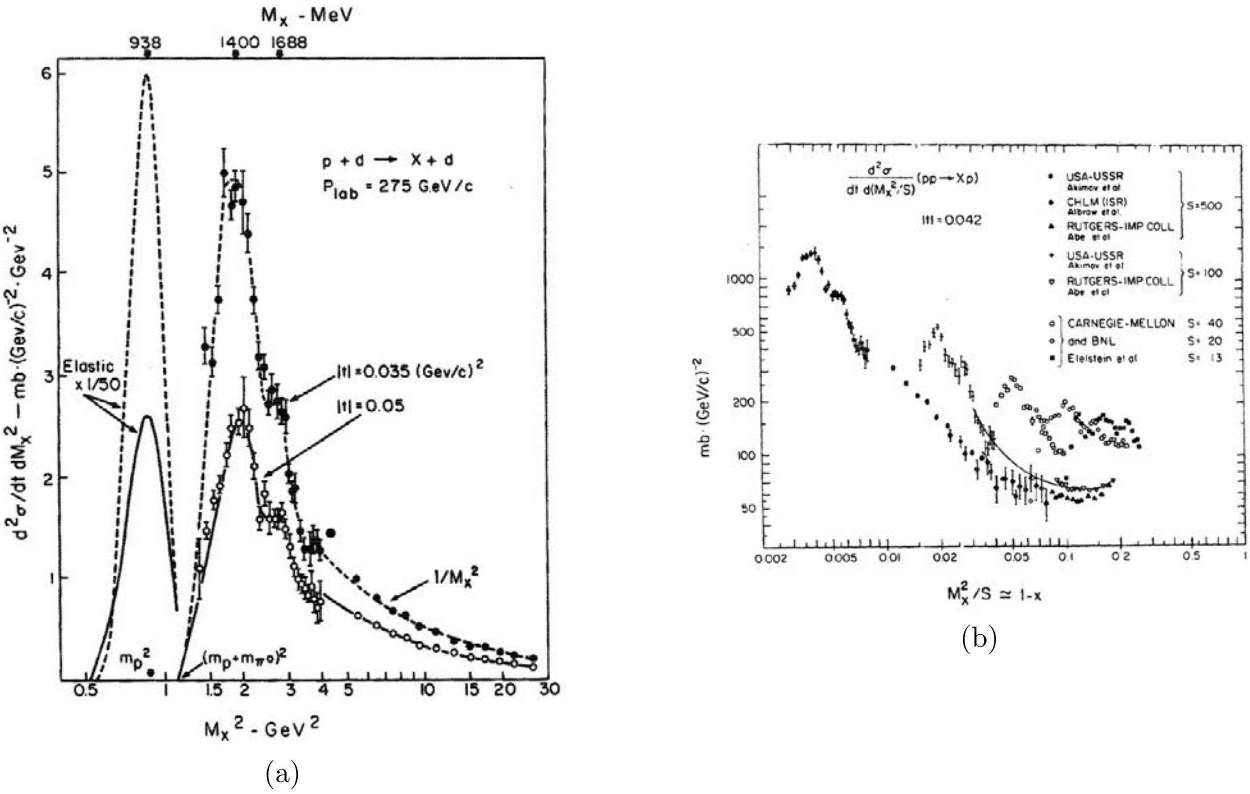

Figure 35: Compilation of low-mass SD data form Fermilab experiments.

2. **The inelastic pPX vertex** receives special care. Following Refs. we consider this vertex as a deeply inelastic process, similar to $\gamma p \to X$ in lepton-hadron DIS, e.g et HERA or JLab. The virtual photon of DIS here is replaced by the (virtual) Pomeron with an obvious change of Q^2, typical of DIS, to $-t$ in the present $pP \to X$ sub-processes of Fig. 36 the total c.m. energy here being M. There is one important difference the two, namely the quantum numbers of the Pomeron and the photon (positive and negative C parities, respectively). However, this is not essentially since the dynamics is the same and the the produced states in the pP system will be those of the relevant nucleon trajectory with the right quantum numbers (see below). Contrary to Jaroszewicz and Landshoff who use the Regge asymptotic (in the missing mass) form of the Pp structure function and, consequently the triple Pomeron limit, leaving outside the low-M resonance structure, we concentrate on the low-M resonance region with and use a "Reggeized Breit-Wigner" formula for the structure function elaborated in Ref. (see also earlier citations therein). By duality, the relevant sum of the two parts (low- and high missing masses) should be equivalent.

Having justified and accepted the factorized form of the scattering amplitude, the main object of our study is now the inelastic proton-Pomeron vertex or transition amplitude. It can be treated as the proton structure function (SF), probed by the Pomeron, and proportional to the Pomeron-proton total cross section, $\sigma_T^{Pp}(M_x^2,t)$, with the norm $\sigma_T^{Pp}(M_x^2,t) = \mathcal{I}mA(M^2,t)$, in analogy with the proton SF probed by a photon (in ep scattering e.g. at HERA or JLab).

$$\nu W_2(M_x^2,t) = F_2(x,t) = \frac{4(-t)(1-x)^2}{\alpha(M_x^2-m_p^2)(1+4m_p^2x^2/(-t))^{3/2}}\mathcal{I}mA(M^2,t),$$

where α is the fine structure constant, $\nu = \frac{M_x^2-m_p^2-t}{2m_p}$, and $x = \frac{-t}{2m_p\nu}$ is the Bjorken variable.

The only difference is that the Pomeron's (positive) C parity is opposite to that of the photon. This difference is evident in the values of the parameters but is unlikely to affect the functional form of the SF itself, for which we choose its high-M_x^2 (low Bjorken x) behavior. Notice that the the total energy in this subprocess, the analogy of $s = W^2$ in DIS, here is M_x^2 and t here replaces $q^2 = -Q^2$ of DIS. Notice that gauge invariance requires that the SF vanishes towards $Q^2 \to 0$ (here, t), resulting in the dramatic vanishing of the SD and DD differential cross section towards $t = 0$. How fast does the SF (and relevant cross sections) recover from $t = 0$ a priori is not known.

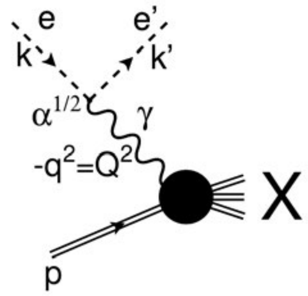

Figure 36: Virtual photon + proton $\to M_x^2$ transition.

Furthermore, according to the ideas of two-component duality, the cross sections of any process, including that of $pP \to X$, is a sum of a non-diffraction component, in which resonances sum up in high-energy (here: mass M^2 plays the role of energy s) Regge exchanges and the smooth background (below the resonances), dual to the Pomeron exchange. The dual properties of diffraction dissociation can be quantified also by finite mass sum rules. In short: the high-mass behavior of the $pP \to X$ cross section is a sum of a decreasing term going like $\sim \frac{1}{M^m}, m \approx 2$ and a "Pomeron exchange" increasing slowly with mass. All this has little affect on the low-mass behavior at the LHC, however normalization implies calculation of cross sections integrated over all physical values of M^2, i.e. until $M^2 < 0.05s$.

3. **The background** is a delicate issue. In the reactions (SD, DD) under consideration there are two sources of the background. The first is that related to the t channel exchange in Fig 35(b) and it can be accounted for by rescaling the parameter s_0 in the denominator of the Pomeron propagator. In any case, at high energies, those of the LHC, this background is included automatically in the Pomeron. The second component of background comes from the subprocesses $pP \to X$. Its high-mass behavior is not known experimentally and it can be only conjecture on the bases of the known energy dependence of the typical meson-baryon processes appended by the ideas of duality. The conclusion is that the Pp total cross section at high energies (here: missing masses M) has two components: a decreasing one, dual to direct-channel resonances and going as $\sigma_{tot}^{Pp} \sim \sum_R (s')^{\alpha_R(0)-1} = \sum_R \left(M^2\right)^{\alpha_R(0)-1}$, where R are non-leading Reggeons, and a slowly rising Pomeron term producing $\sim M^{2 \cdot 0.08}$.

4.3 Duality

Any meson-baryon total cross section (or scattering amplitude) is a sum of two contributions: diffractive and non-diffractive. By the concept of two-component duality, the diffractive component, the smooth background at low energies (here: missing masses) is dual to a Pomeron t-channel exchange at high energies, while the non-diffractive component contains direct channel resonances, dual to high-energy $t-$ channel (sub-leading) Reggeon exchanges, as shown in Fig. 37.

According to our present knowledge about two-body hadronic reactions, two distinct classes of reaction mechanisms exist.

The first one includes the formation of resonances in the $s-$channel and the exchange of particles, resonances, or Regge trajectories in the $t-$channel. The low-energy resonance behavior and the high-energy Regge asymptotics are related by duality, which at Born level, or, alternatively, for tree diagrams, mathematically can be formalized in the Veneziano model, which is a combination of Euler Beta-functions.

The second class of mechanisms does not exhibit resonances at low energies and its high-energy behavior is governed by the exchange of a vacuum Regge trajectory, the Pomeron, with an intercept

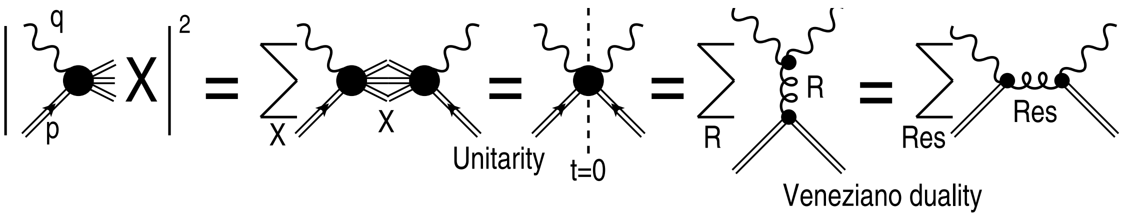

Figure 37: Connection, through unitarity (generalized optical theorem) and Veneziano-duality, between the inelastic form factor and sum of direct-channel resonances.

equal to or slightly greater than one. Harari and Rosner hypothesized that the low-energy non-resonating background is dual to the high-energy Pomeron exchange, or diffraction. In other words, the low energy background should extrapolate to high-energy diffraction in the same way as the sum of narrow resonances sum up to produce Regge behaviour. However, contrary to the case of narrow resonances, the Veneziano amplitude, by construction, cannot be applied to (infinitely) broad resonances. This becomes possible in a generalization of narrow resonance dual models called dual amplitudes with Mandelstam analyticity (DAMA), allowing for (infinitely) broad resonances, or the background.

In the resonance region, roughly $1 < M < 4$ GeV, the non-diffractive component of the amplitude is adequately described by a "reggeized Breit-Wigner" term Eq. (73), following from the low-energy decomposition of a dual amplitude, with a direct-channel meson-baryon (Pomeron-proton, in our case) trajectory (see Fig. 7 in Ref. [8]), with relevant nucleon resonances lying on it, appended by a Roper resonance (see Eq. (77)).

$\mathcal{I}mA(a+b\to c+d) =$	R	Pomeron
$s-$channel	$\sum A_{Res}$	Non-resonant background
$t-$channel	$\sum A_{Regge}$	Pomeron $(I=S=B=0;\ C=+1)$
High energy dependence	$s^{\alpha-1},\ \alpha<1$	$s^{\alpha-1},\ \alpha\geq 1$

Table 10: Two-component duality

By duality, a proper sum of direct channel resonances produces smooth Regge behavior, and, to avoid "double counting", one should not add the two. Actually, this is true only for an infinite number of resonance poles. For technical reasons, we include only a finite number of resonance poles, moreover, apart from the "regular" contribution of the nucleon resonances, lying on the N^* trajectory, the Roper resonance is also included (see Sec. 4.5). The spectroscopic status of this resonance is disputable. It has no place on the known baryonic trajectories, but its hight exceeds that of the neighboring, next most important $N^*(1680)$. In view of the "truncated" series of resonance poles, we do not expect that it will reproduce correctly the high-energy Regge behavior, therefore we add it to the total cross section in the form of an "effective" Regge pole contribution.

The second, diffractive component, is essentially the contribution from a Pomeron pole exchange $\sigma_T^{Pp} \sim (M^2)^{\alpha(0)-1}$, with $\alpha(0) \approx 1.08$, and, as shown by Donnachie and Landshoff, this term also can give some contribution to the low-energy (here, missing mass) flat background.

To summarize this discussion, Regge-pole exchanges take place at two distinct parts of the diagrams shown in Fig. 20: in the t channel, where, at the LHC, only the Pomeron contributes, and in the inelastic form factor, sub-diagram shown in Fig. 36, where, depending of the value of the missing mass, both the Pomeron and Reggeons are equally important. At low missing masses, the direct-channel proton trajectory N^*, dominates, replaced by an effective Reggeon exchange at high masses, appended by a Pomeron. The Roper resonance (with its controversial status) in the direct channel stay apart. Although we concentrate on the low missing mass region, the behavior of the cross sections at high masses are important in the calculation of the cross sections integrated in M^2. We remind that we impose a limit on diffraction events to be about $\xi < 0.05$ or $M < 200$ GeV (as is used in some experiments).

4.4 Resonances in the Pp system; the N^* trajectory

The Pp total cross section at low missing masses is dominated by nucleon resonances. In the dual-Regge approach [7], the relevant cross section is a "Breit-Wigner" sum Eq. (73), in which the direct-channel trajectory is that of N^*.

$$\sigma_T^{Pp}(M_x^2, t) = \mathcal{I}m\, A(M_x^2, t) = \mathcal{I}m \left(\sum_{n=0,1,\ldots} \frac{af(t)^{2(n+1)}}{2n + 0.5 - \alpha_{N^*}(M_x^2)} \right) . \tag{73}$$

The Pomeron-proton channel, $Pp \to M_X^2$ couples to the proton trajectory, with the $I(J^P)$ resonances: $1/2(5/2^+)$, F_{15}, $m = 1680$ MeV, $\Gamma = 130$ MeV; $1/2(9/2^+)$, H_{19}, $m = 2200$ MeV, $\Gamma = 400$ MeV; and $1/2(13/2^+)$, $K_{1,13}$, $m = 2700$ MeV, $\Gamma = 350$ MeV. The status of the first two is firmly established, while the third one, $N^*(2700)$, is less certain, with its width varying between 350 ± 50 and 900 ± 150 MeV . Still, with the stable proton included, we have a fairly rich trajectory, $\alpha(M^2)$, whose real part is shown in Fig. 7 of Ref. [8].

Despite the seemingly linear form of the trajectory, it is not that: the trajectory must contain an imaginary part corresponding to the finite widths of the resonances on it. The non-trivial problem of combining the nearly linear and real function with its imaginary part was solved by means of dispersion relations.

We use the explicit form of the trajectory derived in Ref. [9], ensuring correct behaviour of both its real and imaginary parts. The imaginary part of the trajectory can be written in the following way:

$$\mathcal{I}m\, \alpha(s) = s^{\delta} \sum_n c_n \left(\frac{s - s_n}{s} \right)^{\lambda_n} \cdot \theta(s - s_n)\,, \tag{74}$$

where $\lambda_n = \mathcal{R}e\ \alpha(s_n)$. Eq. (74) has the correct threshold behaviour, while analyticity requires that $\delta < 1$. The boundedness of $\alpha(s)$ for $s \to \infty$ follows from the condition that the amplitude, in the Regge form, should have no essential singularity at infinity in the cut plane.

The real part of the proton trajectory is given by

$$\mathcal{R}e\, \alpha(s) = \alpha(0) + \frac{s}{\pi} \sum_n c_n \mathcal{A}_n(s)\ , \tag{75}$$

where

$$\mathcal{A}_n(s) = \frac{\Gamma(1-\delta)\Gamma(\lambda_n + 1)}{\Gamma(\lambda_n - \delta + 2) s_n^{1-\delta}} {}_2F_1 \left(1, 1-\delta; \lambda_n - \delta + 2; \frac{s}{s_n} \right) \theta(s_n - s) +$$
$$\left\{ \pi s^{\delta - 1} \left(\frac{s - s_n}{s} \right)^{\lambda_n} \cot[\pi(1-\delta)] - \right.$$
$$\left. \frac{\Gamma(-\delta)\Gamma(\lambda_n + 1) s_n^{\delta}}{s\Gamma(\lambda_n - \delta + 1)} {}_2F_1 \left(\delta - \lambda_n, 1; \delta + 1; \frac{s_n}{s} \right) \right\} \theta(s - s_n)\ .$$

The proton trajectory, called N^+ also trajectory , contains the baryons N(939) $\frac{1}{2}^+$, N(1680) $\frac{5}{2}^+$, N(2220) $\frac{9}{2}^+$ and N(2700) $\frac{13}{2}^+$. In the fit, the input data are the masses and widths of the resonances.

The quantities to be determined are the parameters c_n, δ and the thresholds s_n. We set $n = 1, 2, x$ and $s_1 = (m_\pi + m_N)^2 = 1.16$ GeV^2, $s_2 = 2.44$ GeV^2 and $s_x = 11.7$ GeV^2.

Other parameters of the trajectory, obtained in the fit, are summarized below: $\alpha(0) = -0.41$, $\delta = -0.46 \pm 0.07$, $c_1 = 0.51 \pm 0.08$, $c_2 = 4.0 \pm 0.8$ and $c_x = (4.6 \pm 1.7) \cdot 10^3$. Taking the central values of these parameters we obtain the following values for the λ's: $\lambda_1 = 0.846$, $\lambda_2 = 2.082$, $\lambda_x = 11.177$.

The elastic contribution, is separated from SD and DD by a gap extending from the proton mass m_p to the first threshold, at $m_p + m_\pi$, and it should be treated separately.

Thus, we obtain:

$$\mathcal{I}m\, A(M_X^2, t) = a \sum_{n=1,3} [f(t)]^{2(n+1)} \frac{\mathcal{I}m\, \alpha(M_X^2)}{(2n + 0.5 - Re\, \alpha(M_X^2))^2 + (\mathcal{I}m\, \alpha(M_X^2))^2} . \tag{76}$$

4.5 The Roper resonance

Apart from the well established protonic trajectory with a sequence of four particles, there is a prominent single resonance $I = 1/2, \quad J = 1/2^+$ with mass 1440 MeV, known as the Roper resonance. It is wide, the width being nearly one fourth of its mass, its spectroscopic status being disputable. There is no room for the Roper resonance on the proton trajectory of Sec. 4.4, although it could still be a member of protons daughter trajectory. Waiting for a future better understanding of Roper's status, here we present the contribution to SD cross section of a single Roper resonance, calculated from a simple Breit-Wigner formula:

$$\mathcal{I}mA_{Roper}(M_x^2, t) = b \frac{f^2(t) M_{Roper} \Gamma_{Roper}/2}{(M_x^2 - M_{Roper}^2)^2 + (\Gamma_{Roper}/2)^2}, \tag{77}$$

where $M_{Roper} = 1440$ MeV, $\Gamma_{Roper} = 325$ MeV, and c is another normalization parameter.

4.6 Compilation of the basic formulae

This subsection contains a compilation of the main formulae used in the calculations and fits to the data.

The elastic cross section is:

$$\frac{d\sigma_{el}}{dt} = A_{el} {F_p}^4(t) \left(\frac{s}{s_0} \right)^{2(\alpha(t)-1)} . \tag{78}$$

The single diffraction (SD) dissociation cross section is:

$$2 \cdot \frac{d^2\sigma_{SD}}{dt dM_x^2} = {F_p}^2(t) {F_{inel}}^2(t, M_x^2) \left(\frac{s}{M_x^2} \right)^{2(\alpha(t)-1)} . \tag{79}$$

Double diffraction (DD) dissociation cross section:

$$\frac{d^3\sigma_{DD}}{dt dM_1^2 dM_2^2} = N_{DD} {F_{inel}}^2(t, M_1^2) {F_{inel}}^2(t, M_2^2) \left(\frac{s s_0}{M_1^2 M_2^2} \right)^{2(\alpha(t)-1)} . \tag{80}$$

with the norm $N_{DD} = \frac{1}{4A_{el}}$, with the inelastic vertex:

$$ {F_{inel}}^2(t, M_x^2) = A_{res} \frac{1}{M_x^4} \sigma_T^{Pp}(M_i^2, t) + C_{bg} \sigma_{Bg}, \tag{81}$$

where the Pomeron-proton total cross section is the sum N^* resonances (Eq. (76)) and the Roper resonance (Eq. (77)), with a relevant norm factor R (we remove the t dependent $f_{res}(t)$ out of the sum):

$$\sigma_T^{Pp}(M_x^2,t) = R\frac{[f_{res}(t)]^2 \cdot M_{Roper}\left(\frac{\Gamma_{Roper}}{2}\right)}{\left(M_x^2 - M_{Roper}^2\right)^2 + \left(\frac{\Gamma_{Roper}}{2}\right)^2} + [f_{res}(t)]^4 \sum_{n=1,3} \frac{\mathcal{I}m\,\alpha(M_x^2)}{(2n+0.5-\mathcal{R}e\,\alpha(M_x^2))^2 + (\mathcal{I}m\,\alpha(M_x^2))^2}, \tag{82}$$

and the background corresponding to non-resonance contributions:

$$\sigma_{Bg} = \frac{f_{bg}(t)}{\frac{1}{(M_x^2-(m_p+m_\pi)^2)^\varsigma} + (M_x^2)^\eta}, \tag{83}$$

NB: *In Eq. (83) M_x, m_p and m_p are in $[GeV]$.*

The Pomeron trajectory is:

$$\alpha(t) = 1.075 + 0.34t,$$

and the $t-$dependente elastic and inelastic form factors are:

$$F_p(t) = e^{b_{el}t}, \qquad f_{res}(t) = e^{b_{res}t}, \qquad f_{bg}(t) = e^{b_{bg}t}.$$

The slope of the cone is defined as:

$$B = \frac{d}{dt}\ln\frac{d\sigma}{dt}, \tag{84}$$

where $\frac{d\sigma}{dt}$ stands for $\frac{d\sigma_{el}}{dt}$, $\frac{d\sigma_{SD}}{dt}$, or $\frac{d\sigma_{DD}}{dt}$, defined by Eq. (78), (79) and (80), respectively.

The local slope B_M at fixed M_x^2 is defined in the same way:

$$B_M = \frac{d}{dt}\ln\frac{d^2\sigma}{dtdM_x^2} \tag{85}$$

NB: $\frac{d\sigma}{dt}$ *in Eq. (84) is in units of* $[mb{\cdot}GeV^{-2}]$, *and* $\frac{d^2\sigma}{dtdM_x^2}$ *in Eq. (85) in units of* $[mb{\cdot}GeV^{-4}]$.

The integrated cross sections are calculated as:

$$\frac{d\sigma_{SD}}{dt} = \int_{M_1^2}^{M_2^2} \frac{d^2\sigma_{SD}}{dtdM_x^2}dM_x^2 \tag{86}$$

for the case of SD and:

$$\frac{d\sigma_{DD}}{dt} = \int\int_{f(M_{x_1}^2,M_{x_2}^2)} \frac{d^3\sigma_{SD}}{dtdM_{x_1}^2dM_{x_2}^2}dM_{x_1}^2dM_{x_2}^2 \tag{87}$$

for the case of DD.

We also calculate the fully integrated cross sections:

$$\sigma_{SD} = \int_0^1 dt \int_{M_{th}^2}^{0.05s} dM_x^2\frac{d^2\sigma_{SD}}{dtdM_x^2}, \tag{88}$$

$$\sigma_{DD} = \int_0^1 dt \int\int_{\Delta\eta>3} dM_{x_1}^2dM_{x_2}^2\frac{d^3\sigma_{DD}}{dtdM_{x_1}^2dM_{x_2}^2} \tag{89}$$

and

$$\frac{d^2\sigma_{DD}}{dM_{x_1}^2dM_{x_2}^2} = \int_0^1 \frac{d^3\sigma_{DD}}{dtdM_{x_1}^2dM_{x_2}^2}dt. \tag{90}$$

4.7 Fitting procedure

The model contains 12 parameters, a large part of which is fixed either by their standard values (e.g. those of Regge trajectories, except for the Pomeron slope, whose slope exceeds the "standard" value to meet the SD data) or are set close to previous fits.

- In our strategy we first adjust the model to the "standard candles" of **elastic** pp **scattering** at high energies (starting form 500 GeV). We considered only the data corresponding to the first cone, described by a linear exponential, implying also a linear Pomeron trajectory.

  The elastic data and Regge theory fix the parameters $s_0, \alpha(0)$, α', A_{el}, b_{el}. The relevant curves, the data and values of the fitted parameters are shown in Fig. 9(a) of Ref. [8], and in Tables 12 and 11.

  The data at larger $|t|$, with the dip-bump structure and subsequent flattening of the cross section, both in elastic scattering and in SD may indicate the onset of new physics and the transition to hard scattering, implying a non-exponential residue and/or a non-linear Pomeron trajectory, that goes beyond the present study.

  NB: *The parameter s_0 is strongly correlated with the slope parameters b_{el}, b_{res} and $b_b g$.*

- **Single diffraction dissociation (SD)** is an important pillar in our fitting procedure. The following parameters were fitted to SD data: A_{res}, C_{bg}, R, b_{res}, b_{bg}, ς, η. As input data we used: a)double differential cross sections $\frac{d^2\sigma_{SD}}{dtdM^2}$ versus M_x^2 at $|t| = 0.05$ GeV^2 (see Fig. 38(a)) and b) at at $|t| = 0.5$ GeV^2 (see Fig. 38(b)); c)single differential cross sections $\frac{d\sigma_{SD}}{dt}$ vs. t (see Fig. 10(b) of Ref. [8]); d) fully integrated cross sections versus energy $\sqrt{s}$ (see Fig. 10(a) of Ref. [8]).

  At low t (below 0.5 GeV^2), the $t-$ dependence of SD cross section are well described by an exponential fit, see Figs. 10(b) of Ref. [8] and Fig. 38(b)), but beyond this region the cross sections start flattening due to transition effects towards hard physics.

  Low-energy data $\sqrt{s} < 100$ GeV (see Figs. 10(a) of Ref. [8], Fig. 39) require the inclusion of non-leading Reggeons, so they are outside our single Pomeron exchange in the t channel.

- **Double diffraction dissociation (DD) cross sections** follow, up to some fine-tuning of the parameters, from our fits to SD and factorization relation.

Integration in M_1^2 and M_2^2 comprises the range $\Delta\eta > 3$, where $\Delta\eta = \ln\left(\frac{ss_0}{M_1^2 M_2^2}\right)$.

The χ^2 values are quoted at relevant figures. The values of the fitted parameters are presented in Table 13 and our prediction are summarized in Table VI of Ref. [8].

	Data [GeV^{-2}]
B_{el}(7 TeV)	19.9 ± 0.3
B_{el}(1.8 TeV)	17.0 ± 0.5 17.9 ± 2.5 16.99
B_{el}(546 GeV)	15.35 15.0

Table 11: Forward slope of elastic pp scattering, see Fig. 9(b) of Ref. [8]

	Data [mb]	Calcuation [mb]
σ_{el}(7 TeV)	25.4 ± 1.1	24.5
σ_{el}(1.8 TeV)	16.6 ± 1.6	17.99
σ_{el}(546 GeV)	13.6	13.8

Table 12: pp elastic cross section, Eq. (78), calculated with the parameters quoted in Tab. 13.

$A_{el}[mb]$	33.579
$b_{el}[\mathrm{GeV}^{-2}]$	1.937
$A_{res}[mb{\cdot}\mathrm{GeV}^4]$	2.21
$C_{bg}[mb]$	2.07
R	0.45
$b_{res}[\mathrm{GeV}^{-2}]$	−0.507
$b_{bg}[\mathrm{GeV}^{-2}]$	−1.013

s_0	1
ς	0.8
η	1
$\alpha(t) = \alpha(0) + \alpha' t$	
$\alpha(0)$	1.075
$\alpha'[\mathrm{GeV}^{-2}]$	0.34

Table 13: Fitted parameters, see Eqs. (78), (79), (80).

4.8 pp elastic

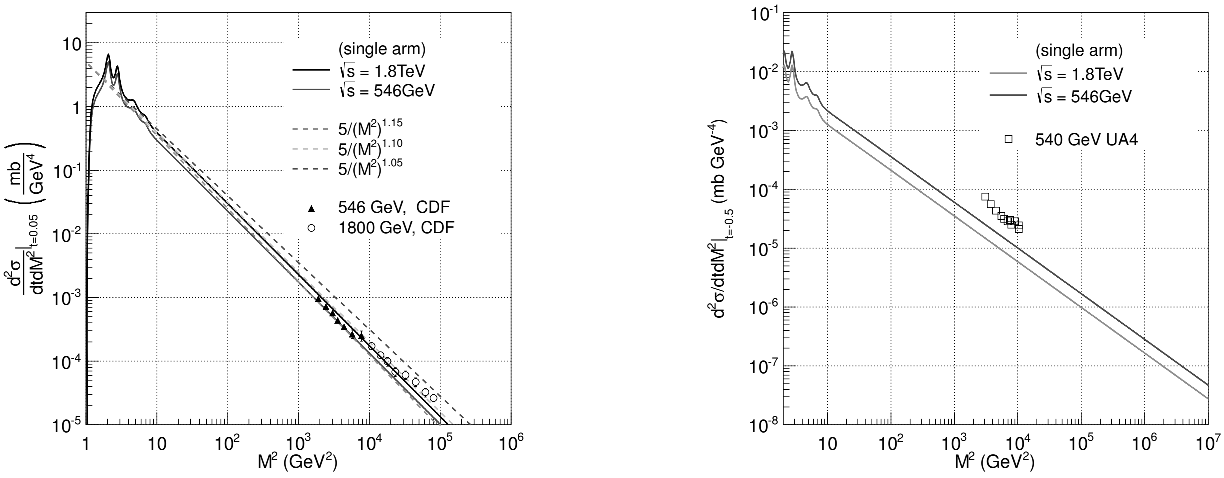

(a) (b)

Figure 38: Double differential cross sections for SD at $t = -0.05$ (a) and $t = -0.5$ (b) calculated from Eq. (79); χ^2/n= 1.2, n= 8 for 1800 GeV^2 and χ^2/n= 4.6, n= 8 for 546 GeV^2 (only Fig. (a));

4.9 Summary

Below we summary the main results :

- At the LHC, in the diffraction cone region ($t < 1$ GeV^2) proton-proton scattering is dominated (over 95%) by Pomeron exchange. This enables full use of factorized Regge-pole models. Contributions from non-leading (secondary) trajectories can (and should be) included in the extension of the model to low energies, e.g. below those of the SPS.

- Unlike to the most of the approaches which use the triple Regge limit for construction of inclusive diffraction, our approaches based on the assumed similarity between the Pomeron-proton and virtual photon-proton scattering. The proton structure function (SF) probed by the Pomeron is the central object of our studies. This SF, similar to the DIS SF, is exhibits direct-channel (i.e. missing mass, M) resonances transformed in resonances in single- double- and central diffraction dissociation. The high-M behaviour of the SF (or Pomeron-proton cross section) is Regge-behaved and contains two components: one decreasing roughly like M^{-m}, $m \approx 2$ due to

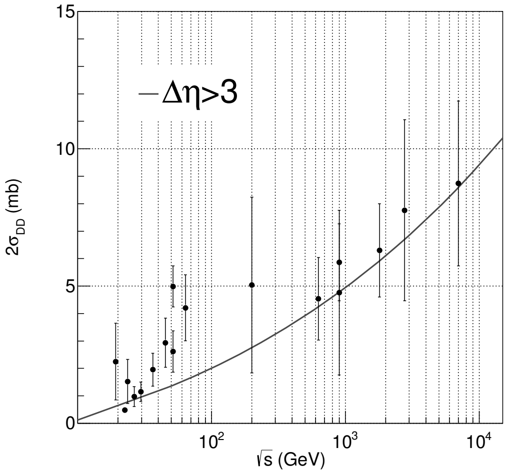

Figure 39: Double diffraction dissociation cross section vs. energy $\sqrt{s}$ calculated from Eq. (80)
.

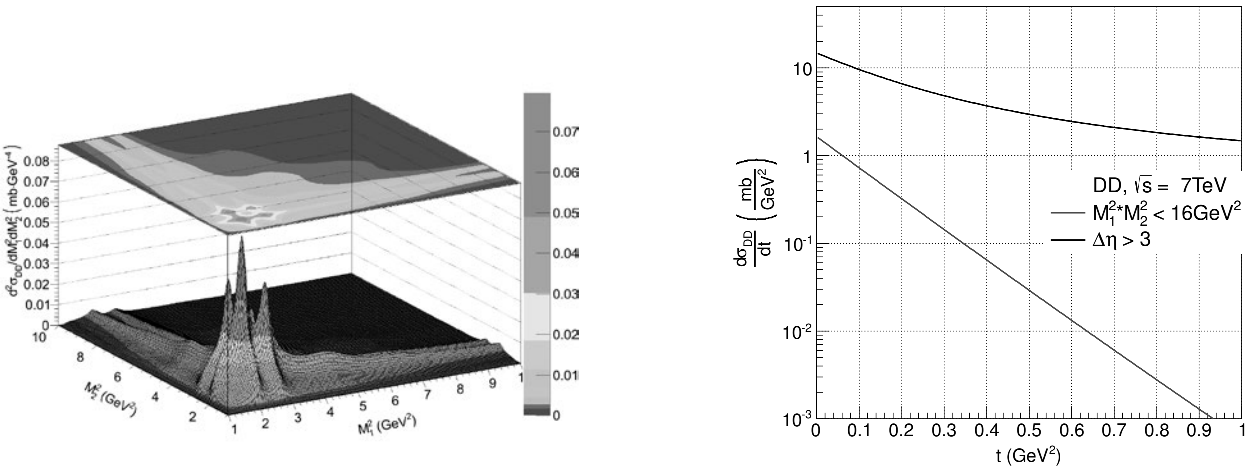

Figure 40: Double differential DD cross section as a function of M_1^2 and M_2^2 integrated over t; see Eq. (80).

the exchange of a secondary Reggeon (not to be confused with the Pomeron exchange in the t channel!). The latter dominates the large-M part of the cross sections. Its possible manifestation may be seen in the data see Fig. 15(b) of Ref. [8]. On the other hand, the large-M region is the border of diffraction, $\xi > 0.05$.

- An important and intriguing prediction of the present model is the possible turn-down of the cross sections towards $t = 0$. The forward direction cannot be reached kinematically in SD or DD, moreover even the non-zero but small $|t|$ events are difficult to be reached, especially that they are masked by electromagnetic interactions (although weaker than in elastic scattering. Further studies, both theoretical and experimental, of this intriguing phenomena are of great importance.

Predicted values for integrated, within various limits of t and/or M^2, cross sections can be also

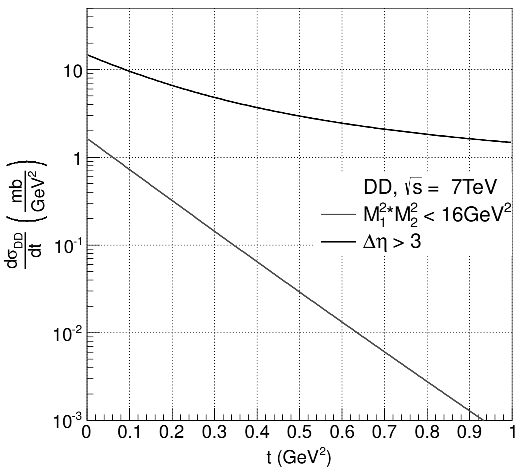

(a)

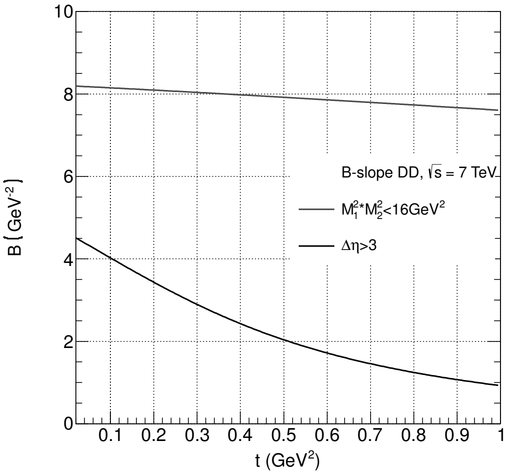

(b)

Figure 41: (a) Single differential cross section $\frac{d\sigma_{DD}}{dt}$ as a function of t integrated over the region of resonances $\left(M_1^2 M_2^2 < 16 \text{ GeV}^2\right)$ and over the whole region of diffraction ($\Delta\eta > 3$), see Eq. (80). (b) The slope $B = \frac{d}{dt} \ln\left(\frac{d\sigma_{DD}}{dt}\right)$ is calculated from Eq. (80).

found in that section. The quality of the fit is quantified by the relevant χ^2 values.

- The model has an important and interesting prediction, following from the gauge invariance of the structure functions (Pp production amplitudes), namely that the cross sections turn down at very small values of $|t|$, probably accessible in the nearly forward direction of future measurements. This result was anticipated in Ref. [7].

- Our approach in this paper is inclusive, ignoring e.g. the angular distribution of the produced particles from decaying resonances. All resonances, except Roper, lie on the N^* trajectory. Any complete study of the final states should included also spin degrees of freedom, ignored in the present model.

- For simplicity we used linear Regge trajectories and exponential residue functions, thus limiting the applicability of our model to low and intermediate values of $|t|$. Its extension to larger $|t|$ is straightforward and promising. It may reveal new phenomena, such as the the possible dip-bump structure is SD and DD as well as the transition to hard scattering at large momenta transfers, although it should be remembered that diffraction (coherence) is limited (independently) both by t and ξ.

Comment on the Bibliography:

The results presented in these Lectures are based on the following papers: a) [1,5,6] (elastic scattering), b) [7] (diffraction dissociation), and c) [2,10] (review).

Acknowledgement

L.J. is grateful to IIP, Natal, the Organizers of this School for their hospitality and support.

References

1. L. L. Jenkovszky, A. I. Lengyel and D. I. Lontkovskyi, Int. J. Mod. Phys. A **26**, 4755 (2011) [arXiv:1105.1202 [hep-ph]].
2. L. L. Jenkovszky, Fortsch. Phys. **34**, 791 (1986); L. L. Jenkovszky, Riv. Nuovo Cim. **10**(12), 1 (1987); L. L. Jenkovszky, Phys. Part. Nucl. **34**, 619 (2003) [Fiz. Elem. Chast. Atom. Yadra **34**, 1196 (2003)].
3. J. Kontros, K. Kontros and A. Lengyel, hep-ph/0104133 [hep-ph].
4. J. Kontros, K. Kontros and A. Lengyel, hep-ph/0006141 [hep-ph].
5. G. Cohen-Tannoudji, V. V. Ilyin and L. L. Jenkovszky, Lett. Nuovo Cim. **5**(2), 957 (1972) [Lett. Nuovo Cim. **5**, 957 (1972)].
6. L. L. Jenkovszky and D. Lontkovskiy, *Lessons from the first measurements of elastic pp scattering at the LHC*, in *New Trends in High-Energy Physics*, edited by P. N. Bogolubov and L. L. Jenkovszky, 305, Kiev (2011) [http://crimea.bitp.kiev.ua/crimea2011/]; L. L. Jenkovszky and D. Lontkovskiy, Rencontres du Vietnam, 14th Workshop on EDS 2011, edited by M. A. Rotondo and Chung I-Tan.
7. L. L. Jenkovszky, O. E. Kuprash, J. W. Lamsa, V. K. Magas and R. Orava, Phys. Rev. **D83**, 056014 (2011) [arXiv:1011.0664 [hep-ph]].
8. L. Jenkovszky, O. Kuprash, R. Orava and A. Salii, Phys. Atom. Nucl. **77**(12), 1463 (2014) [Odessa Astron. Pub. **25**, 102 (2012) 102][arXiv:1211.5841 [hep-ph]].
9. R. Fiore, L. L. Jenkovszky, F. Paccanoni and A. Prokudin, Phys. Rev. D **70**, 054003 (2004) [hep-ph/0404021 [hep-ph]].
10. A. N. Vall, L. L. Jenkovszky and B. V. Struminsky, Fiz. Elem. Chast. Atom. Yadra **19** (1988) 180.

Magno Machado

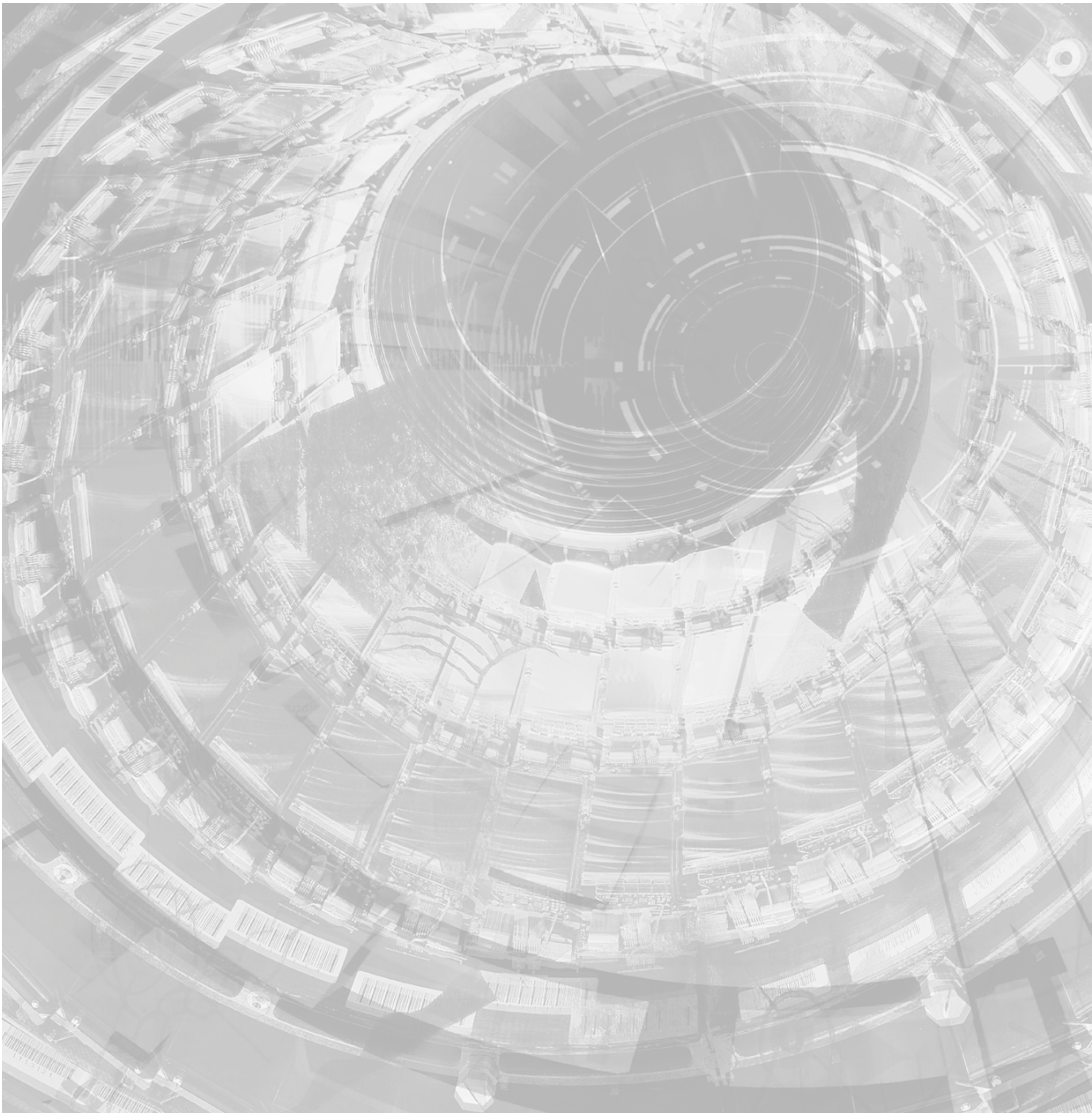

Phenomenology of hard diffraction at high energies

Magno V. T. Machado [a]

[a]High Energy Physics Phenomenology Group, GFPAE IF-UFRGS, Porto Alegre, Brazil

Abstract

In this contribution we give a brief review on the application of perturbative QCD to the hard diffractive processes. Such reactions involving a hard scale can be understood in terms of quarks and gluons degrees of freedom and have become an useful tool for investigating the low-x structure of the proton and the behavior of QCD in the high-density regime. We start using the information from the ep collisions at HERA concerned to the inclusive diffraction to introduce the concept of diffractive parton distributions. Their interpretation in the resolved pomeron model is addressed and we discuss the limits of diffractive hard-scattering factorization for hadron-hadron collisions. Some examples of phenomenology for the diffractive production of W/Z, heavy $Q\bar{Q}$ and quarkonium in hadron-hadron reactions are presented. We also discuss the exclusive diffractive processes in ep interactions. They are in general driven by the gluon content of proton which is strongly subject to parton saturation effects in the very high energy limit. These saturation effects are well described within the color dipole formalism. We present some examples of corresponding phenomenology as the elastic vector meson production and the DVCS relying on the color dipole approach.

1 Introduction

Diffractive scattering envolves a large area of study in particle physics and gives rise to a wide range of theoretical approaches. Several aspects of diffraction in electron-proton collisions can be successfully described in QCD if a hard scale (large photon vituality, heavy quark/quarkonia masses, large transverse momentum of particles) is present. An important ingredient is the use of factorization theorems, which render parts of the dynamics accessible to calculation in perturbation theory. Namely, hard physics is associated with the well established parton picture and perturbative QCD. The remaining non-perturbative quantities, as the diffractive PDFs can be extracted from measurements and contain specific information about small-x partons in the proton that can only be obtained in diffractive processes. In first part of this contribution we will review the main features of diffractive deep inelastic scattering, where there are abundant and precise data which allow to explore the transition from hard to soft physics. On the other hand, for the hard diffractive hadron-hadron collisions the situation is more evolved since factorization is broken by rescattering between spectator partons which are related with multiple scattering effects. We will give some examples of phenomenology using the resolved pomeron model and simplified absorption corrections (the gap survival probability) for the diffractive production of heavy electroweak bosons, heavy quarks and quarkonia production in $p\bar{p}$ and pp collisions of collider energies. We quote the review papers [1–3] and textbooks [4–6] to the reader interested in a deeper analysis of the soft/hard diffraction phenomena in hadron-hadron and lepton-hadron collisions.

In the second part of this contribution, we discuss the diffractive exclusive processes in ep collisions. We analyse the combination of data on inclusive and diffractive ep scattering and their connection to the test the onset of parton saturation at HERA. In particular, the diffractive vector meson production and deeply virtual Compton scattering (DVCS) have been extensively studied at HERA and provide a valuable probe of the QCD dynamics at high energies. In a general way, these processes are driven by the gluon content of target (proton or nuclei) which is strongly subject to parton saturation effects as well as considerable nuclear shadowing corrections when one considers scattering on nuclei. The cross sections for exclusive processes in DIS are proportional to the square of scattering amplitude, which turn it strongly sensitive to the underlying QCD dynamics. They have been successfully described using color dipole approach and phenomenological model inspired in general aspects of parton saturation physics. We give some examples of the corresponding phenomenology using those approaches. We quote the review papers [7–11] and textbook [12] for a pedagogical treatment of these topics.

2 Regge phenomenology for hadron interactions

In hadron-hadron scattering an important fraction of the total cross section is due to diffractive reactions. Examples of them are elastic scattering (where both projectiles emerge intact in the final state), the single or double diffractive dissociation (where one or both of hadrons are scattered into a low-mass state). A general feature of such diffractive processes is the two groups of final-state particles being well separated in phase space and in particular have a large gap in rapidity (LRG) between them. Therefore, classical definition of diffraction in hadron-hadron or (virtual) photon-hadron scattering is the quasi elastic scattering of one hadron combined with the dissociation of the second hadron or photon.

Diffractive hadron-hadron scattering can be described within Regge theory [13], which it was developed in the 1960s and predates the theory of the strong interactions, QCD. In this framework, the exchange of particles in the t-channel is summed coherently to give the exchange of so-called *regge trajectories.* At sufficient high energies, diffraction is characterized by the exchange of a specific trajectory, the *Pomeron*, which has the quantum numbers of the vacuum. Afterwards, it was found that QCD perturbation theory in the high-energy limit can be organized following the general concepts of Regge theory, referred to as BFKL formalism [14].

In Regge theory the basic idea is that sequences of hadrons of mass m_i and spin j_i lie on Regge trajectories $\alpha(t)$ such that $\alpha(m_i^2) = j_i$. The corresponding Regge phenomenology is able to successfully describe all kinds of *soft* high energy hadronic scattering data: differential, elastic and total cross section measurements. The high energy behaviour of a hadron scattering amplitude at small angles ($t \to 0$) has the form

$$A(s,t) \;\sim\; \sum_R \beta(t)\, s^{\alpha_R(t)} \tag{91}$$

Here, s is the square of the centre-of-mass energy and t is the square of the four-momentum transfer. The observed hadrons were found to lie on trajectories $\alpha_R(t)$ which are approximately linear in t. The leading such trajectories are the ρ, a_2, ω and f trajectories which are all approximately degenerate with [15]

$$\alpha_R(t) \;\simeq\; 0.5 \,+\, 0.9t. \tag{92}$$

From experimental point of view, the total cross sections are observed to increase slowly with energy at high energies. Thus, one needs a higher lying trajectory as we can see using the optical theorem. This theorem expresses the total cross section for the process $AB \to X$ in terms of the imaginary part of the forward elastic scattering amplitude ($AB \to AB$):

$$\sigma(AB \to X) \;=\; \frac{1}{s}\mathrm{Im}A(s,0) \;=\; \sum_R \beta_R\, s^{\alpha_R(0)-1}. \tag{93}$$

To account for the $s \to \infty$ dependence of the total cross sections a Pomeron trajectory is invoked with intercept $\alpha_{I\!P}(0) \sim 1.08$. This Regge Pomeron is often called the *soft Pomeron.* The total, elastic and differential hadronic cross section data are found to be well described in the small-t limit by taking a universal pole form for the Pomeron

$$\alpha_{I\!P}(t) \;\simeq\; 1.08 \,+\, 0.25t, \tag{94}$$

plus the other sub-leading trajectories as in Eq. (92) [15]. As a remark, the Pomeron should be regarded as an effective trajectory, since the corresponding power behaviour on energy of the total cross sections will ultimately violate the Froissart bound.

The effort in understanding diffraction in QCD has reached significant progress from studies of diffractive events [16] at the ep collider HERA ($E_{e^\pm} \simeq 27.5$ GeV and $E_p \simeq 920$ GeV). The virtual photons/gauge bosons produced in these interactions can provide a hard scale where perturbative QCD methods can be applied. Several aspects of diffracion are well understood in QCD when a hard scale is present and then the dynamics can be formulated in the language of quarks and gluons. The possibility at HERA to scan a very large interval of photon virtualities allows to investigate what happens towards the non-perturbative region. This brings information on the soft diffractive processes as well.

In order to apply the Regge phenomenology to inclusive deep-inelastic scattering (DIS) and especially to its diffractive component one makes use of the generalized optical theorem (Mueller's theorem [17]). The optical theorems express the total cross sections in terms of the imaginary parts of the 2-body (or 3-body) forward elastic scattering amplitudes, or to be precise the discontinuities of the amplitudes across the cuts along the W^2 (or M^2) axes. In the case of the inclusive DIS the optical theorem gives

$$F_2 \propto \sum_i \beta_i (W^2)^{\alpha_i(0)-1} \quad \propto \quad \sum_i \beta_i x^{1-\alpha_i(0)} \tag{95}$$

for small x, see (99). In the naive parton model the valence and sea quark contributions to F_2 are associated with meson and Pomeron exchange respectively, and so using (100) we have $xq_V \propto x^{1-\alpha_R(0)} \propto x^{0.5}$, $xq_S \propto x^{1-\alpha_{I\!P}(0)} \propto x^{-0.08}$ for small-x values.

For diffractive DIS, $\gamma^* p \to Xp$, one applies Mueller's optical theorem [17]. In the limit of large s/M^2, the cross section is given by the discontinuity across the M^2 cut of the (three-body) $\gamma^* p\bar{p}$ elastic amplitude, where a sum over the exchange Reggeons is implied. The Regge prediction depends on whether M^2 is large or small. For small M^2 the quark box gives the main contribution to photon-Pomeron scattering. Assuming $C = 1$ vector current coupling of the Pomeron to quarks Ref. [18], the resulting contribution to diffraction is found to be

$$F_2^D \sim \beta(1-\beta). \tag{96}$$

On the other hand, for large M^2 one has the double Regge limit ($s/M^2 \to \infty$ and $M^2 \to \infty$) and the diffractive structure function is described by a sum of triple Regge diagrams

$$F_2^D \sim \sum_{i,j,k} \beta_{ijk} \left(\frac{s}{M^2}\right)^{\alpha_j(t)+\alpha_k(t)} (M^2)^{\alpha_i(0)}. \tag{97}$$

The leading behaviour, which is given by the triple Pomeron contribution, is

$$F_2^D \sim (M^2)^{\alpha_{I\!P}(0)-2\alpha_{I\!P}(t)} \sim 1/M^2. \tag{98}$$

In next section, we address the extraction of diffractive structure function at HERA and its interpretation in the Regge phenomenology and the corresponding factorization formalism for the diffractive DIS processes.

3 Difractive DIS and diffractive parton distributions

Let us consider the inclusive DIS, $ep \to eX$, where X represents all the fragments of the proton which has been broken up by the high energy electron. The basic subprocess $\gamma^* p \to X$, which can be expressed in terms of two functions F_2 and F_L which characterize the structure of the proton. These proton structure functions depend on two invariant variables, the *virtuality* of the photon $Q^2 \equiv -q^2$ and the Bjorken x-variable

$$x \;\equiv\; \frac{Q^2}{2p.q} \;=\; \frac{Q^2}{Q^2+W^2}, \tag{99}$$

where p and q are the four-momenta of the proton and virtual photon, respectively. The quantity W is the total $\gamma^* p$ centre-of-mass energy. In the parton model, x is the fraction of the proton's momentum carried by the quark struck by the virtual photon. In this simple quark model $F_L = 0$ and

$$F_2 \;=\; F_T \;=\; \sum_q e_q^2\, xq(x) \tag{100}$$

is independent of Q^2. The sum is over the flavours of quarks, with electric charge e_q (in units of e) and distributions $q(x)$. $F_{T,L}$ are the proton structure functions for DIS by transversely, longitudinally polarised photons. In the parton-QCD model (including the QCD radiation from the valence quarks and gluon radiation) the parton distributions $q(x) = q(x, Q^2)$ acquire dependence on the hard scale associated to the process. They are now evoluted by evolution equations on the virtuality Q^2 (the DGLAP equations [19]).

The general form of the DIS cross section, up to target mass corrections, is

$$\frac{d^2\sigma(ep\to eX)}{dxdQ^2} \;=\; \frac{2\pi\alpha^2}{xQ^4}\,\left\{\left[1+(1-y)^2\right]F_2(x,Q^2) \;-\; y^2 F_L(x,Q^2)\right\} \tag{101}$$

where α is the electromagnetic coupling. The third variable y is needed to fully characterize the DIS process, $ep \to eX$, namely $y = Q^2/xs$ where $\sqrt{s}$ is the total centre-of-mass energy of the electron-proton collision.

Now, in a typical diffractive event at HERA the collision of the virtual photon with the proton produces a hadronic final state X with the photon quantum numbers and invariant mass M_X. A large gap in rapidity is present between X and the final-state proton, which emerges with its momentum barely changed. Diffractive DIS thus combines features of hard and soft scattering. The kinematics of $\gamma^* p \to Xp$ can be described by the invariants $Q^2 = -q^2$ and $t = (p-p')^2$, and by the scaling variables $x_{\mathbb{P}}$ and β given by

$$x_{\mathbb{P}} = \frac{(p-p')\cdot q}{P\cdot q} = \frac{Q^2+M_X^2-t}{W^2+Q^2-M_p^2}, \qquad \beta = \frac{Q^2}{2(p-p')\cdot q} = \frac{Q^2}{Q^2+M_X^2-t}, \tag{102}$$

where $W^2 = (p+q)^2$. The variable $x_{\mathbb{P}}$ is the fractional momentum loss of the incident proton. The quantity β has the form of a Bjorken variable defined with respect to the momentum $p-p'$ lost by the initial proton instead of the initial proton momentum p. The usual Bjorken variable $x = Q^2/(2p\cdot q)$ is related to β and $x_{\mathbb{P}}$ as $\beta x_{\mathbb{P}} = x$.

The cross section for $ep \to eXp$ in the one-photon exchange approximation can be written in terms of diffractive structure functions $F_2^{D(4)}$ and $F_L^{D(4)}$ as

$$\frac{d\sigma^4(ep\to eXp)}{d\beta\, dQ^2\, dx_{\mathbb{P}}\, dt} = \frac{4\pi\alpha^2}{\beta Q^4}\left[\left(1-y+\frac{y^2}{2}\right)F_2^{D(4)}(\beta,Q^2,x_{\mathbb{P}},t) - \frac{y^2}{2}F_L^{D(4)}(\beta,Q^2,x_{\mathbb{P}},t)\right], \tag{103}$$

in analogy with the way $d\sigma(ep\to eX)/(dx\, dQ^2)$ is related to the structure functions F_2 and F_L for inclusive DIS, $ep \to eX$. Here $y = (p\cdot q)/(p\cdot k)$ is the fraction of energy lost by the incident lepton in the proton rest frame. The structure function $F_L^{D(4)}$ corresponds to longitudinal polarization of the virtual photon; its contribution to the cross section is small in a wide range of the experimentally accessible kinematic region (in particular at low y). The structure function $F_2^{D(3)}$ is obtained from $F_2^{D(4)}$ by integrating over t:

$$F_2^{D(3)}(\beta,Q^2,x_{\mathbb{P}}) = \int dt\, F_2^{D(4)}(\beta,Q^2,x_{\mathbb{P}},t). \tag{104}$$

In a parton model picture, inclusive diffraction $\gamma^* p \to Xp$ proceeds by the virtual photon scattering on a quark, in analogy to inclusive scattering. In this picture, β is the momentum fraction of the struck quark with respect to the exchanged momentum $p - p'$. The diffractive structure function describes the proton structure in these specific processes with a fast proton in the final state. F_2^D may also be viewed as describing the structure of whatever is exchanged in the t-channel in diffraction. In the Regge language this is the exchange of a Pomeron if multiple regge exchange can be neglected. However, the Pomeron in QCD (for instance, the two-gluon exhange model) cannot be interpreted as a particle on which the virtual photon scatters. Using the QCD factorization theorem for inclusive diffraction, $\gamma^* p \to Xp$, the diffractive structure function, in the limit of large Q^2 at fixed β, $x_{I\!P}$ and t, can be written as [20–22]

$$F_2^{D(4)}(x, Q^2, x_{I\!P}, t) \,=\, \sum_a \int_0^{x_{I\!P}} d\xi\; \mathcal{F}^D_{a/p}(\xi, \mu^2, x_{I\!P}, t)\; \mathcal{C}_a(x/\xi, Q^2/\mu^2)\,, \tag{105}$$

with $a = q, g$ denoting a quark or gluon distribution in the proton, respectively. In the infinite momentum frame the diffractive parton distributions describe the probability to find a parton with the fraction ξ of the proton momentum, provided the proton stays intact and loses only a small fraction $x_{I\!P}$ of its original momentum. $\mathcal{C}_a$ are the coefficient functions describing hard scattering of the virtual photon on a parton a. They are identical to the coefficient functions known from inclusive DIS,

$$\mathcal{C}_a(x/\xi, Q^2/\mu^2) \,=\, e_a^2\, \delta(1 - x/\xi) \,+\, \mathcal{O}(\alpha_s)\,. \tag{106}$$

Formula in Eq. (105) is the analogue of the inclusive leading twist description for inclusive DIS. The scale μ^2 is the factorization/renormalization scale and we notice that since the l.h.s of Eq. (105) does not depend on this scale ($dF_2^{D(4)}/d\mu^2 = 0$), one finds the renormalization group equations for the diffractive parton distribution

$$\mu^2 \frac{d}{d\mu^2}\, \mathcal{F}^D_{a/p}(\xi, \mu^2, x_{I\!P}, t) \,=\, \sum_b \int_\xi^{x_{I\!P}} \frac{dz}{z}\, P_{a/b}(\xi/z, \alpha_s(\mu^2))\; \mathcal{F}^D_{b/p}(z, \mu^2, x_{I\!P}, t)\,, \tag{107}$$

where $P_{a/b}$ are the standard Altarelli-Parisi splitting functions in leading (LO) or next-to-leading (NLO) logarithmic approximation. Since the scale μ is arbitrary, we can choose $\mu = Q \gg \Lambda_{QCD}$. If we refer the longitudinal momenta of the partons to $x_{I\!P} p$ instead of the proton total momentum p, the structure functions and parton distributions become functions of $\beta = x/x_{I\!P}$ or $\beta' = \xi/x_{I\!P}$. Using this notation, one rewrites Eqs. (105) and (107) in the following way:

$$F_2^{D(4)}(\beta, Q^2, x_{I\!P}, t) \,=\, \sum_a \int_0^1 d\beta'\; x_{I\!P} \mathcal{F}^D_{a/p}(\beta', \mu^2, x_{I\!P}, t)\; \mathcal{C}_a(\beta/\beta', Q^2/\mu^2) \tag{108}$$

and

$$\mu^2 \frac{d}{d\mu^2}\, \mathcal{F}^D_{a/p}(\beta, \mu^2, x_{I\!P}, t) \,=\, \sum_b \int_\beta^1 \frac{dz}{z}\, P_{a/b}(\beta/z, \alpha_s(\mu^2))\; \mathcal{F}^D_{b/p}(z, \mu^2, x_{I\!P}, t)\,. \tag{109}$$

Thus, we obtain a description similar to inclusive DIS but modified by the additional variables $x_{I\!P}$ and t. Moreover, the Bjorken variable x is replaced by its diffractive analogue β. Notice that $x_{I\!P}$ and t play the role of parameters of the evolution equations and does not affect the evolution. According to the factorization theorem the evolution equations (109) are applicable to all orders in perturbation theory. In LO approximation for the coefficient functions (106), one finds for the diffractive structure function (summing over the quark flavours)

$$F_2^{D(4)}(\beta, Q^2, x_{I\!P}, t) \,=\, \sum_{a=q,\bar{q}} e_a^2\; \beta\; x_{I\!P} \mathcal{F}^D_{a/p}(\beta, Q^2, x_{I\!P}, t)\,, \tag{110}$$

where the sum over the quark flavours is performed.

The collinear factorization formula (108) holds to all orders in α_s for diffractive DIS [22]. However, this is no longer true in hadron–hadron hard diffractive scattering [2,23], where collinear factorization fails due to final state soft interactions. Thus, unlike inclusive scattering, the diffractive parton distributions are no universal quantities. The can safely be used, however, to describe hard diffractive processes involving leptons.

Using a Regge language, in the resolved pomeron model (Ingelman-Schlein model [24]) diffraction is described with the help of the concept of pomeron exchange. It is assumed that the pomeron has a hard structure and in DIS diffraction this structure would be resolved by the virtual photon. Thus, the resolved pomeron model is based on the assumption of *Regge factorization.* In this picture the diffractive structure function takes a factorized form $F_2^{D(4)} = f_{\mathbb{P}}\, F_2^{\mathbb{P}}$, where $f_{\mathbb{P}}$ is the *Pomeron flux* describing the emission of the Pomeron from the proton and its subsequent propagation, and where $F_2^{\mathbb{P}}$ is the *pomeron structure function.* Phenomenologically, such a factorizing ansatz works not too badly and is often used. In the context of the diffractive parton distributions it means that the following factorization holds [25,26]

$$x_{I\!P}\mathcal{F}^D_{a/p}(\beta,Q^2,x_{I\!P},t) \;=\; f(x_{I\!P},t)\; f_{a/I\!P}(\beta,Q^2)\,, \tag{111}$$

where the pomeron flux $f(x_{I\!P},t)$ is given by

$$f(x_{I\!P},t) \;=\; \frac{F^2(t)}{8\pi^2}\, x_{I\!P}^{1-2\alpha_{I\!P}(t)}\,. \tag{112}$$

Thus, the variables $(x_{I\!P},t)$, related to the loosely scattered proton, are factorized from the variables characterizing the diffractive system (β,Q^2). $F(t)$ is the Dirac electromagnetic form factor [18], $\alpha_{I\!P}(t) = 1.1 + 0.25\ \mathrm{GeV}^{-2}\cdot t$ is the soft pomeron trajectory [15] and the normalization of $f(x_{I\!P},t)$ follows the convention of [18]. The function $f_{a/I\!P}(\beta,Q^2)$ in Eq. (111) describes the hard structure in DIS diffraction, and is interpreted as the pomeron parton distribution. Now, the diffractive structure function (110) becomes

$$F_2^{D(4)}(\beta,Q^2,x_{I\!P},t) \;=\; f(x_{I\!P},t)\sum_{a=q,\bar{q}} e_a^2\,\beta\, f_{a/I\!P}(\beta,Q^2)\,, \tag{113}$$

where the summation over quarks and antiquarks is performed. The Q^2-evolution of $f_{a/I\!P}(\beta,Q^2)$ is given by the DGLAP equations (109). The t-dependence in the pomeron parton distributions is neglected. The pomeron parton distributions are determined as the parton distributions of real hadrons. Some functional form with several parameters is assumed at an initial scale and then the parameters are found from a fit to data [27–30] using the DGLAP evolution equations.

Despite the success for describing diffractive DIS and related processes in *ep* collisions the diffractive hard-scattering factorization does not apply to hadron-hadron collisions [21,22]. The discrepancy is quite large as the fraction of diffractive dijet events at CDF is a factor 3 to 10 smaller than would be expected on the basis of the HERA data [31]. The same type of discrepancy is consistently observed in all hard diffractive processes in $p\bar{p}$ events, see e.g. [32]. In general, while at HERA hard diffraction contributes a fraction of order 10% to the total cross section, it contributes only about 1% at the Tevatron. Attempts to establish corresponding factorization theorems fail because of interactions between spectator partons of the colliding hadrons. The contribution of these interactions to the cross section does not decrease with the hard scale. Since they are not associated with the hard-scattering subprocess, we no longer have factorization into a parton-level cross section and the parton densities of one of the colliding hadrons. These interactions are generally soft, and we have at present to rely on phenomenological models to quantify their effects [33]. The yield of diffractive events in hadron-hadron collisions is lowered precisely because of these soft interactions between spectator partons. They can produce additional final-state particles which fill the would-be rapidity gap. This is the season for the often terminology *rapidity gap survival.* When such additional particles are produced, a very fast proton can no longer appear in the final state because of energy conservation. Diffractive factorization breaking is thus intimately related to multiple scattering in hadron-hadron collisions.

In next section, we give some examples of phenomenology of hard diffraction in hadron-hadron collisions using the resolved pomeron model supplemented by *rapidity gap survival* corrections for some representative processes as heavy electroweak boson, heavy quarks and quarkonia production in Tevatron and LHC energies.

4 Some examples of phenomenology in proton-proton collisions

One of the main baseline process in hard diffraction is the production of heavy gauge bosons. In what follows we summarize the results obtained in [34], where the diffractive W and Z production are computed for the Tevatron energy and estimates are provided for the CERN LHC experiment. For the hard diffractive processes we will consider the resolved-pomeron picture [24] where the Pomeron structure is probed as discussed in previous section. The generic cross section for a process in which partons of two hadrons, A and B, interact to produce a massive electroweak boson, $A+B \to W^{\pm}+X$, reads as

$$\frac{d\sigma}{dx_a\, dx_b} = \sum_{a,b} f_{a/A}(x_a, \mu^2)\, f_{b/B}(x_b, \mu^2)\, \frac{d\hat{\sigma}(ab \to W(Z)\, X)}{d\hat{t}}\,, \tag{114}$$

where $x_i f_{i/h}(x_i, \mu^2)$ is the distribution function of a parton of flavour $i = a, b$ in the hadron $h = A, B$. The quantity $d\hat{\sigma}/d\hat{t}$ gives the elementary hard cross section of the corresponding subprocess and $\mu^2 = M_W^2$ is the hard scale in the QCD evolution. In the expression for diffractive processes, one assumes that one of the hadrons, say hadron A, emits a Pomeron whose partons interact with partons of the hadron B. Thus the parton distribution $x_a f_{a/A}(x_a, \mu^2)$ in Eq. (114) is replaced by the convolution between a distribution of partons in the Pomeron, $\beta f_{a/\mathbb{P}}(\beta, \mu^2)$, and the "emission rate" of Pomerons by the hadron, $f_{\mathbb{P}/h}(x_{\mathbb{P}}, t)$. The last quantity, $f_{\mathbb{P}/h}(x_{\mathbb{P}}, t)$, is the Pomeron flux factor and its explicit formulation is described in terms of Regge theory. Therefore, we can rewrite the parton distribution as

$$x_a f_{a/A}(x_a,\, \mu^2) \;=\; \int dx_{\mathbb{P}}\;\, \bar{f}(x_{\mathbb{P}})\, \frac{x_a}{x_{\mathbb{P}}}\, f_{a/\mathbb{P}}(\frac{x_a}{x_{\mathbb{P}}}, \mu^2). \tag{115}$$

where we have defined the quantity $\bar{f}(x_{\mathbb{P}}) \equiv \int_{-\infty}^{0} dt\;\, f_{\mathbb{P}/\mathtt{A}}(x_{\mathbb{P}}, t)$.

Concerning the $W^{\pm}$ diffractive production, one considers the reaction $p+\bar{p}(p) \to p+\, W(\to e\,\nu)+\, X$, assuming that a Pomeron emitted by a proton in the positive z direction interacts with a $\bar{p}$ (or a p) producing $W^{\pm}$ that subsequently decays into $e^{\pm}\;\nu$. By using the same concept of the convoluted structure function, the diffractive cross section for the inclusive lepton production becomes

$$\begin{aligned} \frac{d\sigma^{\rm SD}_{\rm lepton}}{d\eta_e} \;&=\; \sum_{a,b} \int \frac{dx_{\mathbb{P}}}{x_{\mathbb{P}}}\, \bar{f}(x_{\mathbb{P}}) \int dE_T\;\, f_{a/\mathbb{P}}(x_a,\, \mu^2)\, f_{b/\bar{p}(p)}(x_b,\, \mu^2) \\ & \left[\frac{V_{ab}^2\; G_F^2}{6\; s\; \Gamma_W}\right]\; \frac{\hat{t}^2}{\sqrt{A^2-1}} \end{aligned} \tag{116}$$

where

$$x_a = \frac{M_W\; e^{\eta_e}}{(\sqrt{s}\;\, x_{\mathbb{P}})}\;\, \left[A \pm \sqrt{(A^2-1)}\right],\;\; x_b = \frac{M_W\; e^{-\eta_e}}{\sqrt{s}}\;\, \left[A \mp \sqrt{(A^2-1)}\right], \tag{117}$$

with $A = M_W/2E_T$, E_T being the lepton transverse energy, G_F is the Fermi constant and the hard scale $\mu^2 = M_W^2$. The quantity V_{ab} is the Cabibbo-Kobayashi-Maskawa matrix element and $\hat{t} = -E_T\; M_W\; \left[A + \sqrt{(A^2-1)}\right]$. The upper signs in Eqs. (117) refer to W^+ production (that is, e^+

detection). The corresponding cross section for W^- is obtained by using the lower signs and $\hat{t} \leftrightarrow \hat{u}$. The detection of this reaction is triggered by the leptons (e^+ for W^+ and e^- for W^-) that appears boosted towards negative rapidity η in coincidence with a rapidity gap in the right hemisphere.

Since the same concept, the cross section for the diffractive hadroproduction oh the boson Z is given by

$$\sigma_Z = \sum_{a,b} \int \frac{dx_{I\!P}}{x_{I\!P}} \int \frac{dx_b}{x_b} \int \frac{dx_a}{x_a} \bar{f}(x_{I\!P}) f_{a/I\!P}(x_a, \mu^2) f_{b/\bar{p}(p)}(x_b, \mu^2) \times \left[\frac{2\pi C^Z_{a,b} G_F M_Z^2}{3\sqrt{2}s} \right] \frac{d\hat{\sigma}(ab \to ZX)}{d\hat{t}}, \tag{118}$$

where

$$C^Z_{q\bar{q}} = \frac{1}{2} - 2|e_q||sin^2\theta_W + 4|e_q|^2 sin^4\theta_W \tag{119}$$

with θ_W being the Weinberg angle. The definitions for $x_{a,b}$ are similar as for the W case and now $\mu^2 = M_Z^2$. $\theta_C = 0.2269$ is the Cabibbo angle and the other values of the electroweak parameters are taken from the Particle Data Group [35].

As we discussed in previous section, the factorization does not necessarily hold for diffractive production processes. The suppression of the single-Pomeron Born cross section due to the multi-Pomeron contributions depends, in general, on the particular hard process. We will consider this suppression through a gap survival probability factor, $S^2_{\rm gap}$, using two theoretical estimates for this factor: (a) model of [36] (labeled KMR), which considers a two-channel eikonal model. The survival probability is computed for single, central and double diffractive processes at several energies. We will consider the results for single diffractive processes, where $S^2_{\rm gap}(KMR) = 0.15$ for $\sqrt{s} = 1.8$ TeV (Tevatron) and $S^2_{\rm gap}(KMR) = 0.09$ for $\sqrt{s} = 14$ TeV (LHC). (b) The second theoretical estimate is from [37] (labeled GLM), which considers a single channel eikonal approach, where $S^2_{\rm gap}(GLM) = 0.126$ for $\sqrt{s} = 1.8$ TeV (Tevatron) and $S^2_{\rm gap}(GLM) = 0.081$ for $\sqrt{s} = 14$ TeV (LHC).

$\sqrt{s}$	Rapidity	Data (%)	Estimate (%)
1.8 TeV	$\lvert\eta_e\rvert < 1.1$	1.15 ± 0.55 [38]	0.715 ± 0.045
1.8 TeV	$\lvert\eta_e\rvert < 1.1$	1.08 ± 0.25 [39]	0.715 ± 0.045
1.8 TeV	$1.5 < \lvert\eta_e\rvert < 2.5$	0.64 ± 0.24 [39]	1.700 ± 0.875
1.8 TeV	Total $W \to e\nu$	0.89 ± 0.25 [39]	0.735 ± 0.055
14 TeV	$\lvert\eta_e\rvert < 2$	—	0.311 ± 0.016

Table 14: Data versus model predictions for diffractive $W^\pm$ hadroproduction (cuts $E_{T_{\rm min}} = 20$ GeV and $x_{I\!P} < 0.1$).

Let us present some results for hard diffractive production of W and Z based on the present discussion. They are compared with experimental data from [38, 39] in Table I, where estimates for the LHC are also presented. In the numerical calculations, we have used the new H1 parameterizations for the diffractive pdf's [30] As the larger uncertainty comes from the gap survival factor, the error in the predictions correspond to the theoretical band for $S^2_{\rm gap}$. In the theoretical expressions of previous section one computes only the interaction of pomerons (emmitted by protons) with antiprotons (protons in LHC case), that means events with rapidity gaps on the side from which antiprotons come from. Disregarding the gap factor, the diffractive production rate is approximately 7 % (using the cut $|\eta| < 1$) being very large compared to the Tevatron data. When considering the gap survival probability correction, the values are in better agreement with data. When considering central W boson fraction, $-1.1 < \eta_e < 1.1$ (cuts of CDF and D0 [38, 39]), we obtain a diffractive rate of 0.67 %

using the KMR estimate for $S^2_{\rm gap}$, whereas it reaches 0.76% for the GLM estimate. The average rate considering the theoretical band for the gap factor is then $R_W = 0.715 \pm 0.045$ %. Considering the forward W fraction, $1.5 < |\eta_e| < 2.5$ (D0 cut), one obtains $R_W = 0.83$ % for KMR and $R_W = 2.58$ % for GLM, with an averaged value of $R_W = 1.7 \pm 0.875$ %. In this case, our estimate is larger than the central experimental value $R_W^{\rm D0} = 0.64$ %. For the total $W \to e\nu$ we have $R_W = 0.68$ % for KMR and $R_W = 0.79$ % for GLM and the mean value $R_W = 0.735 \pm 0.055$ %, which is in agreement with data and consistent with a large forward contribution. Finally, we estimate the diffractive ratio for LHC energy, $\sqrt{s} = 14$ TeV. In this case we extrapolate the pdf's in proton and diffractive pdf's in Pomeron to that kinematical region. This procedure introduces somewhat additional uncertainties in the theoretical predictions. We take the conservative cuts $|\eta_e| < 2$, $E_{T_{\rm min}} = 20$ GeV for the detected lepton and $x_{\mathbb{P}} < 0.1$. We find $R_W = 0.327$ % for KMR gap survival probability factor and $R_W = 0.295$ % for GLM, with a mean value of $R_W^{\rm LHC} = 0.0311 \pm 0.016$ %. The CMS Collaboration already has a signal for single diffractive boson production [40] at 7 TeV, where the diffractive ratio was determined to be 0.73 ± 0.34 [40].

We now refer to recent works on this topic. For instance, in Ref. [41] the analysis of diffractive electroweak vector boson production was done and the author show that the single diffractive W production asymmetry in rapidity is a good observable at the LHC to test the concept of the flavour symmetric pomeron parton distributions. Along these studies, in Ref. [42] has been shown taht double diffractive electroweak boson production is an ideal probe of QCD based mechanisms of diffraction. Namely, assuming the resolved pomeron model with flavour symmetric pdfs, the W production asymmetry in rapidity equals zero at LHC. On the other hand, in the soft color interaction (SCI) model [43] that asymmetry is non-zero and it is similar to the asymmetry in the inclusive case. A discrepancy also occurs for the ratio W/Z, which is independent of rapidity in the resolved pomeron model and rapidity-dependent in SCI models. Finally, the diffractive production has been addressed also within the color dipole approach [44], where the introduction of higher twist contributions and breakdown of diffractive factorization are naturally embeded.

The next example refers to the heavy quark production in single and double diffractive dissociation in hadron colliders. In what follows we summarize the results found in Refs. [45–47]. Let us present the main formulas for the inclusive diffractive cross sections for the production of heavy quarks in proton-proton collisions at high energies. In the inclusive case, the process is described for partons of two protons, interacting to produce a heavy quark pair, $p + p \to Q\bar{Q} + X$, with center of mass energy $\sqrt{s}$. At LHC energies, the gluon fusion channel dominates over the $q\bar{q}$ annihilation process and qg scattering. The NLO cross section is obtained by convoluting the partonic cross section with the parton distribution function (PDF), $g(x, \mu_F)$, in the proton, where μ_F is the factorization scale. At any order, the partonic cross section may be expressed in terms of dimensionless scaling functions $f_{ij}^{k,l}$ that depend only on the variable ρ [48],

$$\hat{\sigma}_{ij}(\hat{s}, m_Q^2, \mu_F^2, \mu_R^2) = \frac{\alpha_s^2(\mu_R)}{m_Q^2} \sum_{k=0}^{\infty} [4\pi\alpha_s(\mu_R)]^k \sum_{l=0}^{a} f_{ij}^{(k,l)}(\rho) \ln^l \left(\frac{\mu_F^2}{m_Q^2} \right) , \tag{120}$$

where $\rho = \frac{\hat{s}}{4m_Q^2 - s_0}$, $i, j = q, \bar{q}, g$, specifying the types of the annihilating partons, $\hat{s}$ is the partonic center of mass, m_Q is the heavy quark mass, μ_R is the renormalization scale ($s_0 = 1$ GeV^2). It is calculated as an expansion in powers of α_s with $k = 0$ corresponding to the Born cross section at order $\mathcal{O}(\alpha_s^2)$. The first correction, $k = 1$, corresponds to the NLO cross section at $\mathcal{O}(\alpha_s^3)$. To calculate the f_{ij} in perturbation theory, both renormalisation and factorisation scale of mass singularities must be performed. The subtractions required are done at the mass scale μ. The running of the coupling constant α_s is determined by the renormalization group. The total hadronic cross section for the heavy quark production is obtained by convoluting the total partonic cross section with the parton distribution functions of the initial hadrons [49]

$$\sigma_{pp}(s, m_Q^2) \;=\; \sum_{i,j} \int_\tau^1 dx_1 \int_{\frac{\tau}{x_1}}^1 dx_2 f_i^p(x_1, \mu_F^2) f_j^p(x_2, \mu_F^2) \hat{\sigma}_{ij}(\hat{s}, m_Q^2, \mu_F^2, \mu_R^2),$$

with the sum i, j over all massless partons. Here, $x_{1,2}$ are the hadron momentum fractions carried by the interacting partons, $f^p_{i(j)}$ is the parton distribution functions, evaluated at the factorization scale and assumed to be equal to the renormalization scale in our calculations. Here, the cross sections were calculated with the following mass and scale parameters: $\mu_c = 2m_c$, $m_c = 1.5$ GeV, $\mu_b = m_b = 4.5$ GeV, based on the current phenomenology for heavy quark hadroproduction [50].

For diffractive processes, we rely on the resolved pomeron model where the Pomeron structure (quark and gluon content) is probed. In the case of single diffraction, a Pomeron is emitted by one of the colliding hadrons. That hadron is detected, at least in principle, in the final state and the remaining hadron scatters off the emitted Pomeron. A typical single diffractive reaction is given by $p + p \to p + Q\bar{Q} + X$, with the cross section assumed to factorise into the total Pomeron–hadron cross section and the Pomeron flux factor [24], $f_{\mathbb{P}/i}(x_{\mathbb{P}}^{(i)}, |t_i|)$. As usual, the Pomeron kinematical variable $x_{\mathbb{P}}$ is defined as $x_{\mathbb{P}}^{(i)} = s_{\mathbb{P}}^{(j)}/s_{ij}$, where $\sqrt{s_{\mathbb{P}}^{(j)}}$ is the center-of-mass energy in the Pomeron–hadron j system and $\sqrt{s_{ij}} = \sqrt{s}$ the center-of-mass energy in the hadron i–hadron j system. The momentum transfer in the hadron i vertex is denoted by t_i. A similar approach can also be applied to double Pomeron exchange (DPE) process, where both colliding hadrons can in principle be detected in the final state. Thus, a typical reaction would be $p+p \to p+Q\bar{Q}+X+p$, and DPE events are characterized by two quasi–elastic hadrons with rapidity gaps between them and the central heavy flavor products. The inclusive DPE cross section may then be written as,

$$\frac{d\sigma(pp \to pp + Q\bar{Q} + X)}{dx_{\mathbb{P}}^{(1)} dx_{\mathbb{P}}^{(2)} d|t_1| d|t_2|} \;=\; f_{\mathbb{P}/p}(x_{\mathbb{P}}^{(1)}, |t_1|)\, f_{\mathbb{P}/p}(x_{\mathbb{P}}^{(2)}, |t_2|) \sum_{i,j=q,g} \sigma\left(\mathbb{P} + \mathbb{P} \to Q\bar{Q} + X\right), \tag{121}$$

where the Pomeron-Pomeron cross section is given by,

$$\sigma\left(\mathbb{P} + \mathbb{P} \to Q\bar{Q} + X\right) \;=\; \int\!\!\int dx_1\, dx_2\, \hat{\sigma}_{ij}(\hat{s}, m_Q^2, \mu^2) f_{i/\mathbb{P}}\left(\beta_1, \mu^2\right) f_{j/\mathbb{P}}\left(\beta_2, \mu^2\right), \tag{122}$$

where $f_{i/\mathbb{P}}\left(\beta, \mu^2\right)$ are the diffractive parton (quark, gluon) distribution functions (DPDFs) evaluated for parton momentum fraction $\beta_a = x_a/x_{\mathbb{P}}^a$ $(a = 1, 2)$ and evolution scale μ^2.

We further correct Eq. (121) by considering the suppression of the hard diffractive cross section by multiple-Pomeron scattering effects. As a baseline value, we follow Ref. [36]. For the present purpose, we consider $S^2_{\mathrm{gap}} = 0.032\,(0.031)$ at $\sqrt{s} = 5.5\,(6.3)$ TeV in nucleon-nucleon collisions, which is obtained using a parametric interpolation formula for the KMR survival probability factor [36] in the form $S^2_{\mathrm{gap}} = a/[b + \ln(\sqrt{s/s_0})]$ with $a = 0.126$, $b = -4.688$ and $s_0 = 1$ GeV^2. This formula interpolates between survival probabilities for central diffraction (CD) in proton-proton collisions of 4.5 % at Tevatron and 2.6 % at the LHC. In addition, in order to analyze the model dependence of the cross section, we consider another approach to inclusive diffractive production of heavy quarks. In order to do so, the Bialas-Landshoff (BL) approach [51, 52] for the process $p + p \to p + Q\bar{Q} + p$ is taken into account. The calculation that follows concerns central inclusive process, where the QCD radiation accompanying the produced object is allowed. Thus, we did not include a Sudakov survival factor $T(\kappa, \mu)$ [53] which is needed for exclusive central processes. The cross-section is given by [54]:

$$\sigma_{\mathbb{P}\mathbb{P}}(\mathrm{BL}) = \frac{1}{2s\,(2\pi)^8} \int \overline{|M_{fi}|^2}\, \left[F\left(t_1\right) F\left(t_2\right)\right]^2 dPH, \tag{123}$$

where $F(t)$ is the nucleon form-factor approximated by $F(t) = \exp(bt)$, with slope parameter $b = 2$ GeV^{-2}. The differential phase-space factor is denoted by dPH. Following [54], the use of Sudakov parameterization for momenta is given by

$$\begin{aligned} Q &= \frac{x}{s}p_1 + \frac{y}{s}p_2 + v, \qquad k_1 = x_1 p_1 + \frac{y_1}{s}p_2 + v_1, \\ k_2 &= \frac{x_2}{s}p_1 + y_2 p_2 + v_2, \qquad r_2 = x_Q p_1 + y_Q p_2 + v_Q, \end{aligned}$$

where v, v_1, v_2, v_Q are two-dimensional four-vectors describing the transverse components of the momenta. The momenta for the incoming (outgoing) protons are p_1, p_2 (k_1, k_2) and the momentum for the produced quark (antiquark) is r_2 (r_1), whereas the momentum for one of the exchanged gluons is Q. The square of the invariant matrix element averaged over initial spins and summed over final spins is given by [54],

$$\overline{|M_{fi}|^2} = \frac{x_1 y_2 H}{(s x_Q y_Q)^2 (\delta_1\delta_2)^{1+2\epsilon}\, \delta_1^{2\alpha' t_1} \delta_2^{2\alpha' t_2}} \left(1 - \frac{4\, m_Q^2}{s\delta_1\delta_2}\right) \exp\left[2\beta\,(t_1+t_2)\right]. \tag{124}$$

In the expression above, $\delta_1 = 1 - x_1$, $\delta_2 = 1 - y_2$, $t_1 = -\vec{v}_1^{\,2}$ and $t_2 = -\vec{v}_2^{\,2}$. The factor $\exp\left[2\beta\,(t_1+t_2)\right]$ takes into account the effect of the momentum transfer dependence of the non-perturbative gluon propagator with $\beta = 1$ GeV^{-2}. The overall normalization can be expressed as,

$$H = S^2_{\rm gap} \times 2s \left[\frac{4\pi m_Q\,(G^2 D_0)^3 \mu^4}{9\,(2\pi)^2}\right]^2 \left(\frac{\alpha_s}{\alpha_0}\right)^2, \tag{125}$$

where α_s is the perturbative coupling constant (it depends on the hard scale) and α_0 (supposed to be independent of the hard scale) is the unknown nonperturbative coupling constant. In the numerical calculation, we use the parameters [54] $\epsilon = 0.08$, $\alpha' = 0.25$ GeV^{-2}, $\mu = 1.1$ GeV and $G^2 D_0 = 30$ GeV$^{-1}\mu^{-1}$. The Regge Pomeron trajectory is then $\alpha_{\mathbb{P}}(t) = 1 + \epsilon + \alpha' t$. It is taken $k_{\rm min} = 0$ for the minimum value for the transverse momentum of the quark. For the strong coupling constant, we use $\alpha_s = 0.2\,(0.17)$ for charm (bottom). An indirect determination of the unknown parameter α_0 has been found in Ref. [55] using experimental data for central inclusive dijet production cross section at Tevatron. Namely, it has been found the constraint $S^2_{\rm gap}\,(\sqrt{s} = 2\,{\rm TeV})/\alpha_0^2 = 0.6$, where $S^2_{\rm gap}$ is the gap survival probability factor (absorption factor). Considering the KMR [36] value $S^2_{\rm gap} = 0.045$ for CD processes at Tevatron energy, one obtains $\alpha_0^2 = 0.075$.

$Q\bar{Q}$	$\sigma_{\rm inc}$ [μb]	$\sigma_{\rm DPE}$ [μb]	$R_{\rm DPE}$ [%]
$c\bar{c}$	7811	13.6–0.53	0.17–7×10^{-3}
$b\bar{b}$	393	0.053–0.027	0.01–0.007

Table 15: The inclusive and DPE (corrected by absorption effects) cross sections in *pp* collisions at the LHC (14 TeV). For the inclusive diffractive cross section the first value corresponds to the resolved pomeron mode and the second one BL model. The corresponding diffractive ratios, $R_{\rm DPE}$, are also presented.

The calculations for the inclusive and diffractive cross sections as well as the diffractive ratios to heavy quark production in proton-proton collisions are showed at Tab. (15). For the inclusive diffractive cross section the first value corresponds to the partonic picture of Pomeron, Eq. (121), and the second one to the BL approach, Eq. (123). We assume the value $S^2_{\rm gap} = 0.026$ for the absorption corrections at energy of 14 TeV. The partonic PDFs and scales are mentioned in previous section. For the diffractive gluon PDF, we take the experimental (H1 collaboration) FIT A [30]. The main theoretical uncertainty in the diffractive ratio is the survival probability factor, whereas uncertainties associated to factorization/renormalization scale, parton PDFs and quark mass are minimized taking a ratio. The present results are consistent with a previous estimate performed in Ref. [47], where a value $S^2_{\rm gap} = 0.04$ was considered and cross sections were computed at LO accuracy.

The single diffraction case can be also addresses, where the reaction is given by $p+p \to p+Q\bar{Q}+X$. The single diffractive cross section may then be written as [47]

$$\frac{d\sigma^{\rm SD}\left(pp \to p + Q\bar{Q} + X\right)}{dx_{I\!P}^{(a)}\,d|t_a|} \;=\; f_{I\!P/a}(x_{I\!P}^{(a)}, |t_a|)\sigma\left(I\!P + p \to Q\bar{Q} + X\right), \tag{126}$$

where $x_{I\!P}$ is the Pomeron kinematical variable, defined as $x^a_{I\!P} = s^{(b)}_{I\!P}/s_{ab}$, where $\sqrt{s^b_{I\!P}}$ is the center-of-mass energy in the Pomeron-hadron b system and $\sqrt{s}_{ab} = \sqrt{s}$ is the center-of-mass energy in the hadron$_a$-hadron$_b$ system, with t_a denoting the momentum transfer in the hadron a vertex. In terms of pomeron pdfs and pomeron flux, the expression for the single diffractive cross section for $Q\bar{Q}$ production is written as [47]

$$\sigma^{\rm SD}_{ab}(s, m^2_Q) = \sum_{i,j=q\bar{q},g} \int_\rho^1 dx_1 \int_{\rho/x_1}^1 dx_2 \int_{x_1}^{x_{I\!P}^{\max}} \frac{dx^{(1)}_{I\!P}}{x^{(1)}_{I\!P}}$$
$$\times \quad \bar{f}_{I\!P/a}\left(x^{(1)}_{I\!P}\right) f_{i/I\!P}\left(\frac{x_1}{x^{(1)}_{I\!P}}, \mu^2\right) f_{j/b}(x_2, \mu^2)\, \hat{\sigma}_{ij}(\hat{s}, m^2_Q, \mu^2)\, (1 \rightleftharpoons 2).$$

The calculations for the inclusive and diffractive cross sections, as well the diffractive ratios to heavy quark production in proton-proton collisions are showed at Tab. (16). We take the value $S^2_{\rm gap} = 0.06$ for the absorption corrections in hadronic collisions at the LHC. The partons PDF and scales are mentioned in previous section. For the diffractive gluon PDF, we take the experimental FIT A (the fully integrated cross section is insensitive to a different choice, i.e. FIT B). The main theoretical uncertainty in the diffractive ratio is the survival probability factor, whereas uncertainties associated to factorization/renormalization scale, parton PDFs and quark mass are minimized taking a ratio.

Heavy Quark	$\sigma_{\rm inc}$ [μb]	$\sigma_{\rm SD}$ [μb]	$R_{\rm SD}$
$c\bar{c}$	7811	178	2.3 %
$b\bar{b}$	393	7	1.7 %

Table 16: The inclusive and single diffractive (corrected by absorption effects) cross sections in *pp* collisions at the LHC (14 TeV). The corresponding diffractive ratios, $R_{\rm SD}$, are also presented.

As a last example, we consider the diffractive quarkonium production at the LHC. We use the Color Evaporation Model (CEM) [56] for the production model. The main reasons for this choice are its simplicity and fast phenomenological implementation, which are the base for its relative success in describing high energy data. In this model, the cross section for a process in which partons of two hadrons, h_1 and h_2, interact to produce a heavy quarkonium state, $h_1 + h_2 \to H(nJ^{\rm CP}) + X$, is given by the cross section of open heavy-quark pair production that is summed over all spin and color states. All information on the non-perturbative transition of the $Q\bar{Q}$ pair to the heavy quarkonium H of quantum numbers $J^{\rm PC}$ is contained in the factor $F_{nJ^{\rm PC}}$ that *a priori* depends on all quantum numbers [56],

$$\sigma(h_1\, h_2 \to H[nJ^{\rm CP}]\, X) = F_{nJ^{\rm PC}}\, \bar{\sigma}(h_1\, h_2 \to Q\bar{Q}\, X)\,, \tag{127}$$

where $\bar{\sigma}(Q\bar{Q})$ is the total hidden cross section of open heavy-quark production calculated by integrating over the $Q\bar{Q}$ pair mass from $2m_Q$ to $2m_O$, with m_O is the mass of the associated open meson. The hidden cross section can be obtained from the usual expression for the total cross section to NLO as mentioned before. Here, we assume that the factorization scale, μ_F, and the renormalization scale, μ_R, are equal, $\mu = \mu_F = \mu_R$. We also take $\mu = 2m_Q$, using the quark masses $m_c = 1.2$ GeV and $m_b = 4.75$ GeV. These parameters provide an adequate description of open heavy-flavour production [57]. The invariant mass is integrated over $4m_c^2 \leq \hat{s} \leq 4m_D^2$ in the charmonium case and $4m_b^2 \leq \hat{s} \leq 4m_B^2$ for Υ production. The factors $F_{nJ^{\rm PC}}$ are experimentally determined [58] to be $F_{11--} \approx 2.5 \times 10^{-2}$ for J/Ψ and $F_{11--} \approx 4.6 \times 10^{-2}$ for Υ. These coefficients are obtained with NLO cross sections for heavy quark production [58].

In the resolved pomeron model, the diffractive process $p + p \to pp + H[nJ^{\rm CP}] + X$, may then be written as

$$\frac{d\sigma^{\rm SD}\left(p_i + p_j \to p_i + H[nJ^{\rm CP}] + X\right)}{dx_{I\!P}^{(i)} d|t_i|} = F_{nJ^{\rm PC}} f_{I\!P/p_i}(x_{I\!P}^{(i)}, |t_i|)\, \bar{\sigma}\left(I\!P + p_j \to Q\bar{Q} + X\right), \tag{128}$$

where the Pomeron kinematical variable $x_{I\!P}$ is defined as $x_{I\!P}^{(i)} = s_{I\!P}^{(j)}/s_{ij}$, where $\sqrt{s_{I\!P}^{(j)}}$ is the center-of-mass energy in the Pomeron–hadron j system and $\sqrt{s_{ij}} = \sqrt{s}$ the center-of-mass energy in the hadron i–hadron j system. The momentum transfer in the hadron i vertex is denoted by t_i. A similar factorization can also be applied to central diffraction, where both colliding hadrons can in principle be detected in the final state. The central quarkonium production, $p_1 + p_2 \to p_1 + H[nJ^{\rm CP}] + p_2$, is characterized by two quasi–elastic hadrons with rapidity gaps between them and the central heavy quarkonium products. The double pomeron exchange cross section may then be written as,

$$\begin{aligned}\frac{d\sigma^{\rm DPE}\left(p_i + p_j \to p_i + H[nJ^{\rm CP}] + p_j\right)}{dx_{I\!P}^{(i)} dx_{I\!P}^{(j)} d|t_i| d|t_j|} &= F_{nJ^{\rm PC}} \times \\ f_{I\!P/i}(x_{I\!P}^{(i)}, |t_i|)\, f_{I\!P/j}(x_{I\!P}^{(j)}, |t_j|)\, \bar{\sigma}\left(I\!P + I\!P \to Q\bar{Q} + X\right).\end{aligned}$$

Here, we assume that one of the hadrons, say proton p_1, emits a Pomeron whose partons interact with partons of the proton p_2. Using the same notation as for the diffractive heavy quark production, the hidden heavy flavour cross section can be obtained from Pomeron-hadron cross sections for single and central diffraction processes,

$$\begin{aligned}\frac{d\sigma\left(I\!P + h \to Q\bar{Q} + X\right)}{dx_1\, dx_2} &= \sum_{i,j=q\bar{q},g} \frac{f_{i/I\!P}\left(x_1/x_{I\!P}^{(1)};\, \mu_F^2\right)}{x_{I\!P}^{(1)}} \\ \times \quad & f_{j/h_2}(x_2, \mu_F^2)\, \hat{\sigma}_{ij}(\hat{s}, m_Q^2, \mu_F^2, \mu_R^2) + (1 \rightleftharpoons 2),\end{aligned} \tag{129}$$

and

$$\begin{aligned}\frac{d\sigma\left(I\!P + I\!P \to Q\bar{Q} + X\right)}{dx_1\, dx_2} &= \sum_{i,j=q\bar{q},g} \frac{f_{i/I\!P}\left(x_1/x_{I\!P}^{(1)};\, \mu_F^2\right)}{x_{I\!P}^{(1)}} \\ \times \frac{f_{j/I\!P}\left(x_2/x_{I\!P}^{(2)};\, \mu_F^2\right)}{x_{I\!P}^{(2)}} & \hat{\sigma}_{ij}(\hat{s}, m_Q^2, \mu_F^2, \mu_R^2).\end{aligned}$$

We will consider the theoretical estimates for $S^2_{\rm gap}$ from Ref. [36], which considers a two-channel eikonal model and rescattering effects. Thus, we have $S^2_{\rm gap}(SD) = 0.15$, [0.09] and $S^2_{\rm gap}(DPE) = 0.08$, [0.04] for $\sqrt{s} = 1.8$ TeV (Tevatron) [$\sqrt{s} = 14$ TeV (LHC)].

$\sqrt{s}$	Quarkonium	$R_{\rm SD}$ (%)	$R_{\rm DPE}$ (%)
2.0 TeV	J/Ψ	0.93	0.2
14 TeV	J/Ψ	0.50	0.15
2.0 TeV	$(\Upsilon + \Upsilon' + \Upsilon'')$	0.78	0.06
14 TeV	$(\Upsilon + \Upsilon' + \Upsilon'')$	0.39	0.03

Table 17: Model predictions for single and DPE diffractive quarkonium production [58] in Tevatron and the LHC (14 TeV).

5 Exclusive diffractive processes in ep collisions

Let us now consider the case of diffractive processes where a photon dissociates into a single particle. Due to the vacuum quantum numbers carried by the pomeron this particle can in particular be a vector meson having the same photon quantum numbers. In addition, we can have also a deeply virtual Compton scattering (DVCS), $\gamma^* p \to \gamma p$. It is known from HERA data that the energy dependence of these processes becomes steep in the presence of a hard scale, which can be either the photon virtuality Q^2 or the mass of the meson in the case of J/Ψ or Υ production [11]. This is similar to the energy dependence of the $\gamma^* p$ total cross section, which changes from flat to steep when going from real photons to Q^2 of a few GeV^2. In pQCD diffraction proceeds by two-gluon exchange and the transition from a virtual photon to a real photon or to a $q\bar{q}$-pair subsequently hadronizing into a meson is a short-distance process involving these gluons, provided that either Q^2 or the quark mass is large. Within certain approximations, the DVCS and vector meson cross sections are proportional to the square of the gluon distribution in the proton, evaluated at a scale of order $Q^2 + M_V^2$ and at a momentum fraction $x_{I\!P} = (Q^2 + M_V^2)/(W^2 + Q^2)$, where the vector meson mass M_V now takes the role of M_X in inclusive diffraction [59]. In analogy to the case of the total $\gamma^* p$ cross section, the energy dependence of the cross sections thus reflects the x and scale dependence of the gluon density in the proton, which grows with decreasing x with a slope becoming steeper as the scale increases.

The inclusive DIS cross section is related to the imaginary part of the forward virtual Compton amplitude. Therefore, the usual gluon distribution gives the probability to find one gluon in the proton. On the other hand, the corresponding graphs for DVCS and exclusive meson production represent the amplitudes of exclusive processes, which are proportional to the probability amplitude for first extracting a gluon from the initial proton and then returning it to form the proton in the final state. Making use of high energy theorems, at large Q^2 the short-distance factorization holds, in analogy to the case of inclusive DIS. QCD factorization theorems [60] state that in the limit of large Q^2 the Compton amplitude factorizes into a hard-scattering subprocess and a hadronic matrix element describing the emission and reabsorption of a parton by the proton target. The analogous result for exclusive meson production involves in addition the $q\bar{q}$ distribution amplitude of the meson, the so-called meson wave function, which is a non-perturbative input. In this collinear factorization approach, the hadronic matrix elements for exclusive processes are not the usual PDFs as the proton has not the same momentum in the initial and final state. Consequently, they are more general functions named generalized PDFs taking into account the momentum difference between the initial and final state proton.

In last decades, a different type of factorization has been very fruitful in phenomenology. It is the high-energy or k_t factorization approach, which is based on the BFKL formalism. Now, the gluon distribution appearing in the factorization formulae depends explicitly on the transverse momentum k_t of the emitted gluon. In collinear factorization, this k_t is integrated over in the parton distributions and set to zero when calculating the hard-scattering process. Similarly, the meson wave functions appearing in k_t factorization explicitly depend on the relative transverse momentum between the q and $\bar{q}$ in the meson, whereas this is integrated over in the quark-antiquark distribution amplitudes of the collinear approach. The two formalisms implement different ways of separating different parts of the dynamics in a scattering process. The building blocks in a short-distance factorization formula correspond to either small or large particle virtuality, whereas the separation criterion in high-energy factorization is the particle rapidity.

The different building blocks in the graphs for Compton scattering and meson production can be rearranged in a such way that it admits a very intuitive interpretation in a reference frame where the photon carries large momentum. In the typical proton rest frame the initial photon splits into a quark-antiquark pair, which scatters on the proton and finally forms a photon or meson again. In addition, one can perform a Fourier transformation and trade the relative transverse momentum between quark and antiquark for their transverse distance r, which is conserved in the scattering on the target. The quark-antiquark pair acts as a color dipole, and its scattering on the proton is described by a *dipole cross section*, $\sigma_{q\bar{q}}$ depending on r and on $x_{I\!P}$ (or on x in the case of inclusive DIS). The wave functions of the photon and the meson depend on r after Fourier transformation, and at small r the photon wave function is perturbatively calculable. Typical values of r in a scattering process are determined by the inverse of the hard momentum scale, i.e. $r \sim (Q^2 + M_V^2)^{-1/2}$. An important result of high-energy factorization is the relation

$$\sigma_{q\bar{q}}(r,x) = \frac{\pi^2}{3}\,\alpha_S(A/r)\,r^2 xg(x,A/r), \tag{130}$$

at small r, where we have replaced the generalized gluon distribution by the usual one in the spirit of the leading $\log x$ approximation. A more precise version of the relation (130) involves the k_t dependent gluon distribution. The dipole cross section vanishes at $r = 0$ in accordance with the phenomenon of *color transparency*, where a hadron becomes more and more transparent for a color dipole of decreasing size.

5.1 The parton saturation phenomenom and saturation models

Diffraction involves scattering on small-x gluons in the proton. Taking the density in the transverse plane of gluons with longitudinal momentum fraction x that are resolved in a process with hard scale Q^2 one can think of $1/Q$ as the *transverse size* of these gluons as seen by the probe. The number density of gluons at given x increases with increasing Q^2, as described by DGLAP evolution. According to the BFKL evolution equation it also increases at given Q^2 when x becomes smaller, so that the gluons become more and more densely packed. At some point, they will start to overlap and thus reinteract and screen each other. One then enters a regime where the density of partons saturates and where the linear DGLAP and BFKL evolution equations cease to be valid. If Q^2 is large enough to have a small coupling α_s, we have a theory of this non-linear regime called *Color Glass Condensate* (CGC) [7, 8]. To quantify the onset of non-linear effects, one introduces a saturation scale Q_s^2 depending on x, such that for $Q^2 < Q_s^2(x)$ these effects become important. For smaller values of x, the parton density in the target proton is higher, and saturation sets in at larger values of Q^2.

The color dipole picture is well suited for the theoretical description of saturation effects. When such effects are important, the relation (130) between dipole cross section and gluon distribution ceases to be valid; in fact the gluon distribution itself is then no longer an adequate quantity to describe the dynamics of a scattering process. In a certain approximation, the evolution of the dipole cross section with x is described by the Balitsky-Kovchegov equation [61], which supplements the BFKL equation with a non-linear term taming the growth of the dipole cross section with decreasing x. Essential features of the saturation phenomenon are captured in a phenomenological model for the dipole cross section, originally proposed by Golec-Biernat and Wüsthoff, see [62, 63]. In this model, the dipole size r now plays the role of $1/Q$. At small r the cross section rises following the relation $\sigma_{q\bar{q}}(r,x) \propto r^2 xg(x)$. At some value $R_s(x)$ of r, the dipole cross section is so large that this relation ceases to be valid, and $\sigma_{q\bar{q}}$ starts to deviate from the quadratic behavior in r. As r continues to increase, $\sigma_{q\bar{q}}$ eventually saturates at a value typical of a meson-proton cross section. In terms of the saturation scale introduced above, $R_s(x) = 1/Q_s(x)$. For smaller values of x, the initial growth of $\sigma_{q\bar{q}}$

with r is stronger because the gluon distribution is larger. The target is thus more opaque and as a consequence saturation sets in at lower r.

An important feature found both in this phenomenological model [64] and in the solutions of the Balitsky-Kovchegov equation [65] is that the total γ^*p cross section only depends on Q^2 and x_B through a single variable $\tau = Q^2/Q_s^2(x)$. This property, referred to as *geometric scaling*, is well satisfied by the data at small x_B and is an important piece of evidence that saturation effects are visible in these data. Phenomenological estimates find Q_s^2 of the order 1 GeV^2 for x around 10^{-3} to 10^{-4}. The dipole formulation is suitable to describe not only exclusive processes and inclusive DIS, but also inclusive diffraction $\gamma^*p \to Xp$. For a diffractive final state $X = q\bar{q}$ at parton level, the theory description is very similar to the one for deeply virtual Compton scattering, with the wave function for the final state photon replaced by plane waves for the produced $q\bar{q}$ pair. The inclusion of the case $X = q\bar{q}g$ requires further approximations [62] but is phenomenologically indispensable for moderate to small β. In next section, we give some examples where one uses the phenomenological models including saturation physics to compute the exclusive production of particles (vector mesons or real photons at the final state) and compare them to the available high precision HERA data.

6 Examples of phenomenology in photon-proton interactions

Let us consider photon-hadron scattering in the color dipole frame, in which most of the energy is carried by the hadron, while the photon has just enough energy to dissociate into a quark-antiquark pair before the scattering. In this representation the probing projectile fluctuates into a quark-antiquark pair (a dipole) with transverse separation $\boldsymbol{r}$ long after the interaction, which then scatters off the hadron [66]. In the dipole picture the amplitude for production of an exclusive final state E, such as a vector meson ($E = V$) or a real photon in DVCS ($E = \gamma$) is given by (See e.g. Refs. [66–68])

$$\mathcal{A}_{T,L}^{\gamma^*p\to Ep}\,(x, Q^2, \Delta) = \int dz\, d^2\boldsymbol{r}\, (\Psi^{E*}\Psi)_{T,L}\, \mathcal{A}_{q\bar{q}}(x, \boldsymbol{r}, \Delta)\,, \tag{131}$$

where $(\Psi^{E*}\Psi)_{T,L}$ denotes the overlap of the photon and exclusive final state wave functions. The variable z $(1-z)$ is the longitudinal momentum fractions of the quark (antiquark), Δ denotes the transverse momentum lost by the outgoing proton ($t = -\Delta^2$) and x is the Bjorken variable. For DVCS, the amplitude involves a sum over quark flavors. Moreover, $\mathcal{A}_{q\bar{q}}$ is the elementary elastic amplitude for the scattering of a dipole of size $\boldsymbol{r}$ on the target. It is directly related to $\mathcal{N}(x, \boldsymbol{r}, \boldsymbol{b})$ and consequently to the QCD dynamics (see below). One has that [68]

$$\mathcal{A}_{q\bar{q}}(x, \boldsymbol{r}, \Delta) \;\;=\;\; i \int d^2\boldsymbol{b}\, e^{-i\boldsymbol{b}.\boldsymbol{\Delta}}\, 2\mathcal{N}(x, \boldsymbol{r}, \boldsymbol{b})\;, \tag{132}$$

where $\boldsymbol{b}$ is the transverse distance from the center of the target to one of the $q\bar{q}$ pair of the dipole. Consequently, one can express the amplitude for the exclusive production of a final state E as follows

$$\mathcal{A}_{T,L}^{\gamma^*p\to Ep}(x, Q^2, \Delta) \;\;=\;\; i \int dz\, d^2\boldsymbol{r}\, d^2\boldsymbol{b} e^{-i[\boldsymbol{b}-(1-z)\boldsymbol{r}].\boldsymbol{\Delta}} (\Psi_E^*\Psi)_T\, 2\mathcal{N}(x, \boldsymbol{r}, \boldsymbol{b}), \tag{133}$$

where the factor $[i(1-z)\boldsymbol{r}].\boldsymbol{\Delta}$ in the exponential arises when one takes into account non-forward corrections to the wave functions [68]. Finally, the differential cross section for exclusive production is given by

$$\frac{d\sigma_{T,L}}{dt}(\gamma^*p \to Ep) = \frac{1}{16\pi} |\mathcal{A}_{T,L}^{\gamma^*p\to Ep}(x, Q^2, \Delta)|^2\, (1+\beta^2)\,, \tag{134}$$

where β is the ratio of real to imaginary parts of the scattering amplitude. For the case of heavy mesons, skewness corrections are quite important and they are also taken into account. (For details, see Refs. [67, 68]).

The photon wavefunctions appearing in Eq. (133) are well known in literature [66]. For the meson wavefunction, we have considered the Gauss-LC model which is a simplification of the DGKP wavefunctions (for a review on the meson wavefunctions see Ref. [11]). The motivation for this choice is its simplicity and the fact that the results are not sensitive to a different model. In photoproduction, this leads only to an uncertainty of a few percents in overall normalization. We consider the quark masses $m_{u,d,s} = 0.14$ GeV, $m_c = 1.4$ GeV and $m_b = 4.5$ GeV. The parameters for the meson wavefunction can be found in Ref. [67]. In the DVCS case, as one has a real photon at the initial state, only the transversely polarized overlap function contributes to the cross section. Summed over the quark helicities, for a given quark flavor f it is given by,

$$(\Psi_\gamma^*\Psi)_T^f = \frac{N_c\,\alpha_{\rm em}e_f^2}{2\pi^2}\left\{\left[z^2+\bar{z}^2\right]\varepsilon_1 K_1(\varepsilon_1 r)\varepsilon_2 K_1(\varepsilon_2 r) + m_f^2 K_0(\varepsilon_1 r)K_0(\varepsilon_2 r)\right\}, \tag{135}$$

where we have defined the quantities $\varepsilon_{1,2}^2 = z\bar{z}\,Q_{1,2}^2 + m_f^2$ and $\bar{z} = (1-z)$. Accordingly, the photon virtualities are $Q_1^2 = Q^2$ (incoming virtual photon) and $Q_2^2 = 0$ (outgoing real photon).

The scattering amplitude $\mathcal{N}(x, \boldsymbol{r}, \boldsymbol{b})$ contains all information about the target and the strong interaction physics. In the Color Glass Condensate (CGC) formalism [7, 8], it encodes all the information about the non-linear and quantum effects in the hadron wave function. It can be obtained by solving an appropriate evolution equation in the rapidity $y \equiv \ln(1/x)$, which in its simplest form is the Balitsky-Kovchegov equation. In leading order (LO), and in the translational invariance approximation—in which the scattering amplitude does not depend on the collision impact parameter $\boldsymbol{b}$—it reads

$$\frac{\partial\mathcal{N}(r,Y)}{\partial Y} = \int \mathrm{d}\boldsymbol{r_1}\, K^{\rm LO}(\boldsymbol{r},\boldsymbol{r_1},\boldsymbol{r_2})[\mathcal{N}(r_1,Y)+\mathcal{N}(r_2,Y)-\mathcal{N}(r,Y)-\mathcal{N}(r_1,Y)\mathcal{N}(r_2,Y)], \tag{136}$$

where $\mathcal{N}(r, Y)$ is the scattering amplitude for a dipole (a quark-antiquark pair) off a target, with transverse size $r \equiv |\boldsymbol{r}|$, $Y \equiv \ln(x_0/x)$ (x_0 is the value of x where the evolution starts), and $\boldsymbol{r_2} = \boldsymbol{r} - \boldsymbol{r_1}$. $K^{\rm LO}$ is the evolution kernel, given by

$$K^{\rm LO}(\boldsymbol{r},\boldsymbol{r_1},\boldsymbol{r_2}) = \frac{N_c\alpha_s}{2\pi^2}\frac{r^2}{r_1^2 r_2^2}, \tag{137}$$

where α_s is the (fixed) strong coupling constant. This equation is a generalization of the linear BFKL equation (which corresponds of the first three terms), with the inclusion of the (non-linear) quadratic term, which damps the indefinite growth of the amplitude with energy predicted by BFKL evolution. It has been shown [69] to be in the same universality class of the Fisher-Kolmogorov-Pertovsky-Piscounov (FKPP) equation [70] and, as a consequence, it admits the so-called traveling wave solutions. This means that, at asymptotic rapidities, the scattering amplitude is a wavefront which travels to larger values of r as Y increases, keeping its shape unchanged. Thus, in such asymptotic regime, instead of depending separately on r and Y, the amplitude depends on the combined variable $rQ_s(Y)$, where $Q_s(Y)$ is the saturation scale. This property of the solution of BK equation is a natural explanation to the *geometric scaling*, a phenomenological feature observed at the DESY *ep* collider HERA, in the measurements of inclusive and exclusive processes [64, 71–73]. Although having its properties been intensely studied and understood, both numerically and analytically, the LO BK equation presents some difficulties when applied to study DIS small-x data. In particular, some studies concerning this equation [74–78] have shown that the resulting saturation scale grows much faster with increasing energy ($Q_s^2 \sim x^{-\lambda}$, with $\lambda \simeq 4.88N_c\alpha_s/\pi \approx 0.5$ for $\alpha_s = 0.2$) than that extracted from phenomenology ($\lambda \sim 0.2 - 0.3$). This difficulty could be solved by considering smaller values of the strong coupling constant α_s, but this procedure would lead to physically unrealistic values. One can conclude that

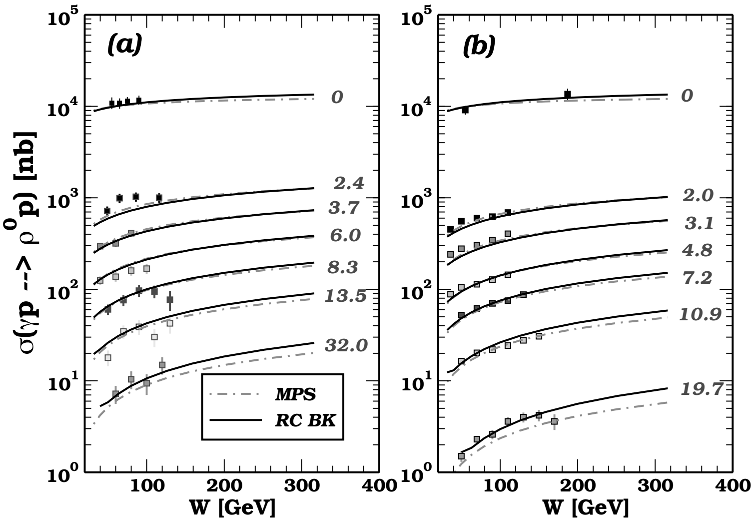

Figure 42: Energy dependence of the γp cross section for ρ^0 production for different photon virtualities. Data from (a) ZEUS and (b) H1 collaborations [94, 95].

higher order corrections to LO BK equation should be taken into account to make it able to describe the available small-x data.

The calculation of the running coupling corrections to BK evolution kernel was explicitly performed in [79, 80], where the authors included $\alpha_s N_f$ corrections to the kernel to all orders. The improved BK equation is given in terms of a running coupling and a subtraction term, with the latter accounting for conformal, non running coupling contributions. In the prescription proposed by Balitsky in [80] to single out the ultra-violet divergent contributions from the finite ones that originate after the resummation of quark loops, the contribution of the subtraction term is mmized at large energies. In [82] this contribution was disregarded, and the improved BK equation was numerically solved replacing the leading order kernel in Eq. (136) by the modified kernel which includes the running coupling corrections and is given by [80]

$$K^{\rm Bal}(\boldsymbol{r},\boldsymbol{r_1},\boldsymbol{r_2}) = \frac{N_c \alpha_s(r^2)}{2\pi^2}\left[\frac{r^2}{r_1^2 r_2^2} + \frac{1}{r_1^2}\left(\frac{\alpha_s(r_1^2)}{\alpha_s(r_2^2)} - 1\right) + \frac{1}{r_2^2}\left(\frac{\alpha_s(r_2^2)}{\alpha_s(r_1^2)} - 1\right)\right]. \tag{138}$$

From a recent numerical study of the improved BK equation [83], it has been confirmed that the running coupling corrections lead to a considerable increase in the anomalous dimension and to a slow-down of the evolution speed, which implies, for example, a slower growth of the saturation scale with energy, in contrast with the faster growth predicted by the LO BK equation. Moreover, as shown in [82, 84, 85] the improved BK equation has been shown to be really successful when applied to the description of the *ep* HERA data for the inclusive and diffractive proton structure function, as well as for the forward hadron spectra in *pp* and *dA* collisions. It is important to emphasize that the impact parameter dependence was not taken into account in Ref. [82], the normalization of the dipole cross section was fitted to data and two distinct initial conditions, inspired in the Golec Biernat-Wusthoff (GBW) [86] and McLerran-Venugopalan (MV) [87] models, were considered. The predictions resulted to be almost independent of the initial conditions and, besides, it was observed that it is impossible to describe the experimental data using only the linear limit of the BK equation, which is equivalent to Balitsky-Fadin-Kuraev-Lipatov (BFKL) equation [88]. In next section we will compare the results of the RC BK approach to the experimental data on exclusive processes at DESY-HERA and present our predictions for the kinematical range of a future electron - proton collider [89].

In what follows we calculate the exclusive observables using as input in our calculations the solution of the RC BK evolution equation. The results has been published in Ref. [90]. In numerical calculations we have considered the GBW initial condition for the evolution (we quote Ref. [82] for details) and it

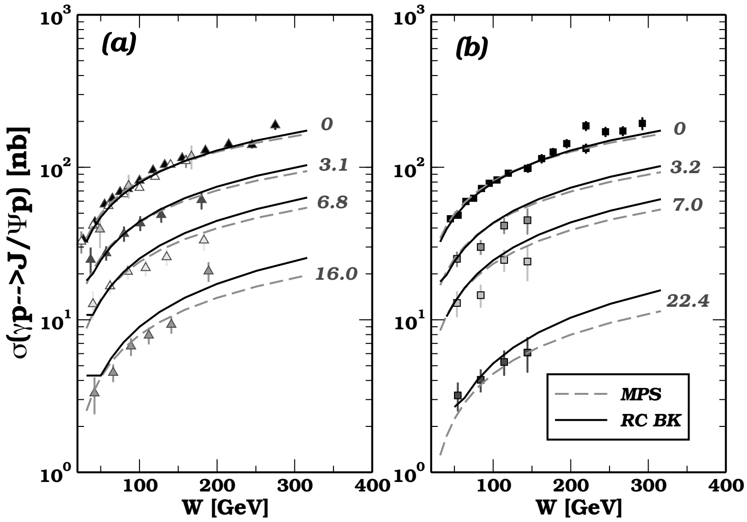

Figure 43: Energy dependence of the γp cross section for J/Ψ production for different photon virtualities. Data from (a) ZEUS and (b) H1 collaborations [96, 97].

was verified the MV initial condition gives cross section with overall normalization $10 - 15\,\%$ smaller and unchanged energy dependence. Furthermore, we compare the RC BK predictions with those from the non-forward saturation model of Ref. [91] (hereafter MPS model), which captures the main features of the dependence on energy, virtual photon virtuality and momentum transfer t. In the MPS model, the elementary elastic amplitude for dipole interaction is given by,

$$\mathcal{A}_{q\bar{q}}(x, r, \Delta) = 2\pi R_p^2\, e^{-B|t|} \mathcal{N}\left(rQ_{\rm sat}(x, |t|), x\right), \tag{139}$$

with the asymptotic behaviors $Q^2_{\rm sat}(x,\Delta) \sim \max(Q_0^2, \Delta^2)\, \exp[-\lambda \ln(x)]$. Specifically, the t dependence of the saturation scale is parametrised as

$$Q^2_{\rm sat}\,(x, |t|) = Q_0^2(1 + c|t|)\, \left(\frac{1}{x}\right)^{\lambda}, \tag{140}$$

in order to interpolate smoothly between the small and intermediate transfer regions. For the parameter B we use the value $B = 3.754$ GeV^{-2} [91]. Finally, the scaling function $\mathcal{N}$ is obtained from the forward saturation model [92].

Here, in order to take into account the skewedness correction, in the limit that $x' \ll x \ll 1$, the elastic differential cross section should be multiplied by a factor R_g^2, given by [93]

$$\begin{aligned} R_g(\lambda_e) &= \frac{2^{2\lambda_e+3}}{\sqrt{\pi}} \frac{\Gamma(\lambda_e + 5/2)}{\Gamma(\lambda_e + 4)}, \\ \text{with} \quad \lambda_e &\equiv \frac{\partial \ln\left[\mathcal{A}(x, Q^2, \Delta)\right]}{\partial \ln(1/x)}, \end{aligned} \tag{141}$$

which gives an important contribution mostly at large virtualities. In addition, we will take into account the correction for real part of the amplitude, using dispersion relations $Re\mathcal{A}/Im\mathcal{A} = \tan(\pi\lambda_e/2)$. In the MPS model, the skewedness correction is absorbed in the model parameters and only real part of amplitude will be considered.

Let us start to compare the RC BK predictions to the available HERA data for exclusive vector meson (ρ, J/Ψ and Υ) photo and electroproduction. In Fig. 42 we present the predictions of the RC BK and MPS models for the diffractive ρ^0 vector meson production and compare it with the current experimental data from ZEUS (left panel) and H1 (right panel) Collaborations [94, 95]. These

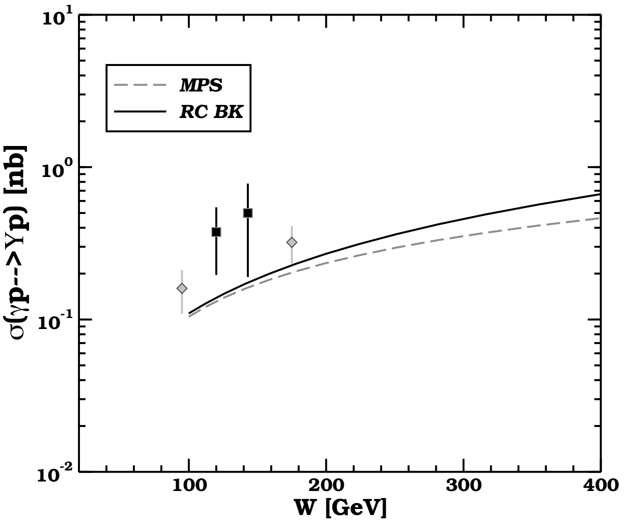

Figure 44: Energy dependence of the γp cross section for Υ photoproduction. Data from ZEUS and H1 collaborations [97, 98].

measurements are interesting as they cover momenta scale that are in the transition region between perturbative and nonperturbative physics, where saturation effects is expected to play an very important role. As the numerical RC BK solution there exists only for forward dipole-target amplitude we need an approximation to compute the non-forward amplitude. Here, we assume the usual exponential ansatz for the t-dependence which implies that the total cross-section is given by

$$\sigma_{tot}(\gamma^* p \to Vp) = \frac{1}{B_V} \left[\left.\frac{d\sigma_T}{dt}\right|_{t=0} + \left.\frac{d\sigma_L}{dt}\right|_{t=0} \right] . \tag{142}$$

Notice that values of the slope parameter B_V are not very accurately measured. We use the parametrisation

$$B_V\,(Q^2) = 0.60 \left[\frac{14}{(Q^2 + M_V^2)^{0.26}} + 1 \right] \tag{143}$$

obtained from a fit to experimental data referred in Ref. [90]. The uncertainty in this approximation can be larger than 20–30 % depending on the Q^2 value. It is verified that the effective power λ_e is similar for both RC BK (solid line curves) and MPS (long dashed curves) predictions, with the deviation starting only at the higher Q^2 values where the predictions differ by a factor 1.5. This can be a result of the similar small-x behaviour for both models, where the effective power ranges from the soft Pomeron intercept $\lambda_e(Q^2 = 0) \approx \alpha_{\mathbb{P}}(0) = 1.08$ up to a hard QCD intercept $\lambda_e(Q^2) \simeq cN_c\alpha_s/\pi \approx 0.3$ for large Q^2. The data description is fairly good, with the main theoretical uncertainty associated to the choice of the light cone wavefunction (about a 15 % error). It was verified that the contribution of real part of amplitude and skewedness are very small for ρ production.

In Fig. 43 we present the predictions of the RC BK model for the diffractive J/Ψ production and compare with the ZEUS (left panel) and H1 (right panel) data [94, 95]. It is verified that the effective power λ_e is similar for both RC BK and MPS only in the photoproduction case. The situation changes when the photon virtuality increases. The effective power for RC BK (solid line curves) is enhanced in Q^2 in comparison with the non-forward saturation model (long dashed curves). The data description is reasonable since it is a parameter-free calculation and the uncertainties are similar as for ρ production. For J/Ψ production, the contribution of real part of amplitude increase by 10 % the overall normalization, while the skewedness have a 20 % effect. In the MPS model, as discussed before, the off-forward effects are absorbed in the parameters of model. The RC BK and MPS predictions differ by a factor 1.4 for large energies. For sake of completeness, in Fig. 44 the results for Υ photoproduction is presented. The RC BK and MPS predictions are similar in the HERA energy range and differ by a factor 1.5 for large energies. It is known so far that the dipole approach underestimates the experimental data for Υ. However, the deviation concerns only to overall normalization, whereas the energy dependence is fairly described. The referred enhancement in the effective power λ_e is already evident in Υ photoproduction as the meson mass, $m_V = 9.46$ GeV, is a scale hard enough for deviations to be present. Skewedness is huge in the Υ case, giving a factor $R_g^2 \approx 1.3$ in photoproduction. For this reason, we have included this effect in both models. However, this is not enough to bring the theoretical results closer to experimental measurements.

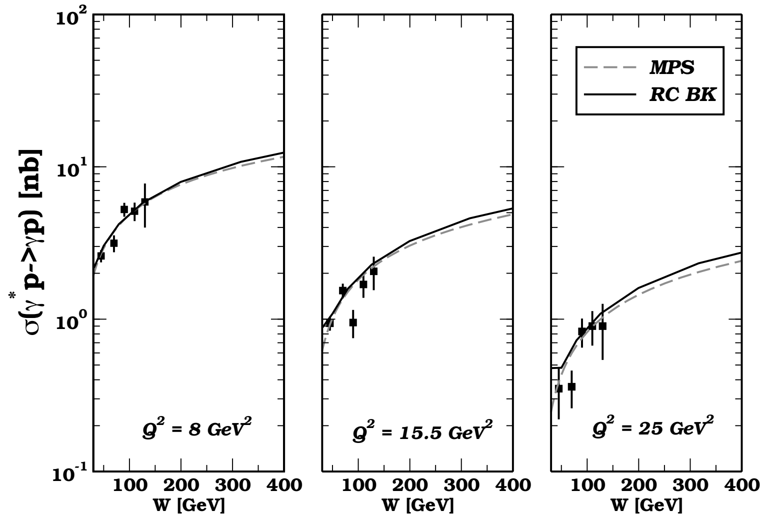

Figure 45: Energy dependence of the DVCS cross section for different photon virtualities. Data from H1 collaboration [99].

Finally, we analyse the DVCS cross section and compare it to the recent H1 data [99]. The cross sections are presented as a function of W, for different values of Q^2, in Fig. 45. Here, the approximations concerning the final state particle are not present and the cross section suffers of less uncertainties. For the slope value, we take the experimental parametrization [99], $B\,(Q^2) = a[1 - b\log(Q^2/Q_0^2)]$, with $a = 6.98 \pm 0.54$ GeV^2, $b = 0.12 \pm 0.03$ and $Q_0^2 = 2$ GeV^2. The situation for DVCS is similar as for vector meson photoproduction, where the effective power λ_e is similar for both RC BK and MPS for small virtualities and starts to change as Q^2 grows. Skewedness is increasingly important for DVCS at high Q^2 and it was introduced for RC BK model. For the MPS model this effect is absorbed in the its parameters as noticed before. The RC BK and MPS predictions are similar for the HERA energy range, describing the current data, and differ by a factor 1.2 for large energies.

Acknowledgments

It is a pleasure to thank the organizers and all participants for the fruitful atmosphere in the school and workshop.

References

1. A. Hebecker, Phys. Rept. **331**, 1 (2000) [hep-ph/9905226].
2. M. Wusthoff and A. D. Martin, J. Phys. G **25**, R309 (1999) [hep-ph/9909362].
3. M. G. Albrow, T. D. Coughlin and J. R. Forshaw, Prog. Part. Nucl. Phys. **65**, 149 (2010) [arXiv:1006.1289 [hep-ph]].
4. J. R. Forshaw and D. A. Ross, Cambridge Lect. Notes Phys. **9**, 1 (1997).

5. V. Barone and E. Predazzi, *High-Energy Particle Difraction*, Springer (2002).
6. S. Donnachie, G. Dosch, P. Landshoff, O. Nachtmann, *Pomeron Physics and QCD*, Cambridge University Press (2005).
7. F. Gelis, E. Iancu, J. Jalilian-Marian and R. Venugopalan, Ann. Rev. Nucl. Part. Sci. **60**, 463 (2010) [arXiv:1002.0333 [hep-ph]].
8. F. Gelis, T. Lappi and R. Venugopalan, Int. J. Mod. Phys. E **16**, 2595 (2007) [arXiv:0708.0047 [hep-ph]].
9. B. Z. Kopeliovich and A. H. Rezaeian, Int. J. Mod. Phys. E **18**, 1629 (2009) [arXiv:0811.2024 [hep-ph]].
10. B. Z. Kopeliovich, I. K. Potashnikova and I. Schmidt, Braz. J. Phys. **37**, 473 (2007) 473 [hep-ph/0604097 [hep-ph]].
11. I. P. Ivanov, N. N. Nikolaev and A. A. Savin, Phys. Part. Nucl. **37**, 1 (2006) [hep-ph/0501034 [hep-ph]].
12. Y.V. Kovchegov, E. Levin, Cambridge Monogr. Part. Phys. Nucl. Phys. and Cosmology **33** (2012).
13. P. D. B. Collins, *An Introduction to Regge Theory and High-Energy Physics*, Cambridge University Press, Cambridge (1977).
14. E. A. Kuraev, L. N. Lipatov and V. S. Fadin, Sov. Phys. JETP **44**, 443 (1976) [Zh. Eksp. Teor. Fiz. **71**, 840 (1976)]; I. I. Balitsky and L. N. Lipatov, Sov. J. Nucl. Phys. **28**, 822 (1978) [Yad. Fiz. **28**, 1597 (1978)].
15. A. Donnachie and P. V. Landshoff, Nucl. Phys. B **231**, 189 (1984).
16. M. Derrick *et al.* [ZEUS Collaboration], Phys. Lett. B **315**, 481 (1993); M. Derrick *et al.* [ZEUS Collaboration], Phys. Lett. B **332**, 228 (1994); M. Derrick *et al.* [ZEUS Collaboration], Z. Phys. C **68**, 569 (1995) [hep-ex/9505010 [hep-ex]]; J. Breitweg *et al.* [ZEUS Collaboration], Eur. Phys. J. C **1**, 81 (1998) [hep-ex/9709021 [hep-ex]]; J. Breitweg *et al.* [ZEUS Collaboration], Eur. Phys. J. C **6**, 43 (1999) [hep-ex/9807010 [hep-ex]]; T. Ahmed *et al.* [H1 Collaboration], Nucl. Phys. B **429**, 477 (1994); T. Ahmed *et al.* [H1 Collaboration], Phys. Lett. B **348**, 681 (1995) [hep-ex/9503005 [hep-ex]]; S. Aid *et al.* [H1 Collaboration], Nucl. Phys. B **472**, 3 (1996) [hep-ex/9603005 [hep-ex]]; S. Aid *et al.* [H1 Collaboration], Z. Phys. C **69**, 27 (1995) [hep-ex/9509001 [hep-ex]]; C. Adloff *et al.* [H1 Collaboration], Z. Phys. C **75**, 607 (1997) [hep-ex/9705014 [hep-ex]]; C. Adloff *et al.* [H1 Collaboration], Z. Phys. C **76**, 613 (1997) [hep-ex/9708016 [hep-ex]].
17. A. H. Mueller, Phys. Rev. D **2**, 2963 (1970).
18. A. Donnachie and P. V. Landshoff, Phys. Lett. B **191**, 309 (1987) [Erratum: Phys. Lett. B **198**, 590 (1987)].
19. Y. L. Dokshitzer, Sov. Phys. JETP **46**, 641 (1977) [Zh. Eksp. Teor. Fiz. **73**, 1216 (1977)]; V. N. Gribov and L. N. Lipatov, Sov. J. Nucl. Phys. **15**, 438 (1972) [Yad. Fiz. **15**, 781 (1972)]; V. N. Gribov and L. N. Lipatov, Sov. J. Nucl. Phys. **15**, 675 (1972) [Yad. Fiz. **15**, 1218 (1972)]; G. Altarelli and G. Parisi, Nucl. Phys. B **126**, 298 (1977).
20. L. Trentadue and G. Veneziano, Phys. Lett. B **323**, 201 (1994).
21. A. Berera and D. E. Soper, Phys. Rev. D **53**, 6162 (1996) [hep-ph/9509239 [hep-ph]].
22. J. C. Collins, Phys. Rev. D **57**, 3051 (1998) [Erratum: Phys. Rev. D **61**, 019902 (2000)] [hep-ph/9709499 [hep-ph]].
23. J. C. Collins, L. Frankfurt and M. Strikman, Phys. Lett. B **307**, 161 (1993) [hep-ph/9212212 [hep-ph]].
24. G. Ingelman and P. E. Schlein, Phys. Lett. B **152**, 256 (1985).
25. A. Berera and D. E. Soper, Phys. Rev. D **50**, 4328 (1994) 4328 [hep-ph/9403276 [hep-ph]].
26. Z. Kunszt and W. J. Stirling, in Proceedings of DIS **1996**, 240 (1996) [hep-ph/9609245 [hep-ph]].
27. C. Royon, L. Schoeffel, J. Bartels, H. Jung and R. B. Peschanski, Phys. Rev. D **63**, 074004 (2001) [hep-ph/0010015 [hep-ph]]
28. C. Adloff *et al.* [H1 Collaboration], Z. Phys. C **76**, 613 (1997) [hep-ex/9708016 [hep-ex]].
29. J. Breitweg *et al.* [ZEUS Collaboration], Eur. Phys. J. C **6**, 43 (1999) [hep-ex/9807010 [hep-ex]].

30. A. Aktas *et al.* [H1 Collaboration], Eur. Phys. J. C **48**, 749 (2006) [hep-ex/0606003 [hep-ex]].
31. T. Affolder *et al.* [CDF Collaboration], Phys. Rev. Lett. **84**, 5043 (2000).
32. L. Alvero, J. C. Collins, J. Terron and J. J. Whitmore, Phys. Rev. D **59**, 074022 (1999) [hep-ph/9805268 [hep-ph]].
33. E. Gotsman, E. Levin, U. Maor, E. Naftali and A. Prygarin, hep-ph/0511060 [hep-ph].
34. M. B. Gay Ducati, M. M. Machado and M. V. T. Machado, Phys. Rev. D **75**, 114013 (2007) [hep-ph/0703315 [hep-ph]].
35. W. M. Yao *et al.* [Particle Data Group], J. Phys. G **33**, 1 (2006).
36. A. B. Kaidalov, V. A. Khoze, A. D. Martin and M. G. Ryskin, Eur. Phys. J. C **21**, 521 (2001) [hep-ph/0105145[hep-ph]].
37. E. Gotsman, E. Levin and U. Maor, Phys. Rev. D **60**, 094011 (1999) [hep-ph/9902294 [hep-ph]].
38. F. Abe *et al.* [CDF Collaboration], Phys. Rev. Lett. **78**, 2698 (1997) [hep-ex/9703010].
39. V. M. Abazov *et al.* [D0 Collaboration], Phys. Lett. B **574**, 169 (2003) [hep-ex/0308032].
40. J. Eugster, thesis at ETH Zürich (2012) [Diss. ETH **20683**] .
41. K. Golec-Biernat and A. Luszczak, Phys. Rev. D **81** 014009 (2010) [arXiv:0911.2789 [hep-ph]].
42. K. Golec-Biernat, C. Royon, L. Schoeffel and R. Staszewski, Phys. Rev. D **84**, 114006 (2011) [arXiv:1110.1825 [hep-ph]].
43. G. Ingelman, R. Pasechnik, J. Rathsman and D. Werder, Phys. Rev. D **87**(9), 094017 (2013) [arXiv:1210.5976 [hep-ph]].
44. R. Pasechnik, B. Kopeliovich and I. Potashnikova, Phys. Rev. D **86**, 114039 (2012) [arXiv:1204.6477 [hep-ph]].
45. M. B. Gay Ducati, M. M. Machado and M. V. T. Machado, Phys. Rev. D **81**, 054034 (2010) [arXiv:1002.4043 [hep-ph]].
46. M. B. Gay Ducati, M. M. Machado and G. G. Silveira, Phys. Rev. D **83**, 074005 (2011) [arXiv:1101.5602 [hep-ph]].
47. M. V. T. Machado, Phys. Rev. D **76**, 054006 (2007) [arXiv:0705.1005 [hep-ph]].
48. M. L. Mangano, P. Nason and G. Ridolfi, Nucl. Phys. B **373**, 295 (1992).
49. P. Nason, S. Dawson and R. K. Ellis, Nucl. Phys. B **303**, 607 (1988).
50. R. Vogt, J. Phys. G **31**, S773 (2005).
51. P. V. Landshoff and O. Nachtmann, Z. Phys. C **35**, 405 (1987).
52. A. Bialas and P. V. Landshoff, Phys. Lett. B **256**, 540 (1991).
53. V. A. Khoze, A. D. Martin and M. G. Ryskin, Eur. Phys. J. C **23**, 311 (2002) [hep-ph/0111078 [hep-ph]].
54. A. Bialas and W. Szeremeta, Phys. Lett. B **296**, 191 (1992).
55. A. Bzdak, Phys. Lett. B **615**, 240 (2005) [hep-ph/0504086 [hep-ph]].
56. J. F. Amundson, O. J. P. Eboli, E. M. Gregores and F. Halzen, Phys. Lett. B **390**, 323 (1997) [hep-ph/9605295 [hep-ph]]; C. Brenner Mariotto, M. B. Gay Ducati and G. Ingelman, Eur. Phys. J. C **23**, 527 (2002) [hep-ph/0111379 [hep-ph]].
57. M. L. Mangano, P. Nason and G. Ridolfi, Nucl. Phys. B **373**, 295 (1992); A. Petrelli, M. Cacciari, M. Greco, F. Maltoni and M. L. Mangano, Nucl. Phys. B **514**, 245 (1998) [hep-ph/9707223 [hep-ph]]; S. Frixione, M. L. Mangano, P. Nason and G. Ridolfi, Adv. Ser. Direct. High Energy Phys. **15**, 609 (1998) [hep-ph/9702287 [hep-ph]].
58. M. V. T. Machado, Eur. Phys. J. C **54**, 443 (2008) [arXiv:0708.2133 [hep-ph]].
59. M. G. Ryskin, Z. Phys. C **57**, 89 (1993).
60. J. C. Collins, L. Frankfurt and M. Strikman, Phys. Rev. D **56**, 2982 (1997) [hep-ph/9611433 [hep-ph]]. J. C. Collins and A. Freund, Phys. Rev. D **59**, 074009 (1999) [hep-ph/9801262 [hep-ph]].
61. I. Balitsky, Nucl. Phys. B **463**, 99 (1996) [hep-ph/9509348 [hep-ph]]; Y. V. Kovchegov, Phys. Rev. D **61**, 074018 (2000) [hep-ph/9905214 [hep-ph]].
62. K. J. Golec-Biernat and M. Wusthoff, Phys. Rev. D **60**, 114023 (1999) [hep-ph/9903358 [hep-ph]].
63. K. J. Golec-Biernat, Acta Phys. Polon. B **33**, 2771 (2002) [hep-ph/0207188 [hep-ph]].

64. A. M. Stasto, K. J. Golec-Biernat and J. Kwiecinski, Phys. Rev. Lett. **86**, 596 (2001) [hep-ph/0007192 [hep-ph]].
65. K. J. Golec-Biernat, L. Motyka and A. M. Stasto, Phys. Rev. D **65**, 074037 (2002) [hep-ph/0110325 [hep-ph]]; M. Lublinsky, Eur. Phys. J. C **21**, 513 (2001) [hep-ph/0106112 [hep-ph]]; S. Munier and R. B. Peschanski, Phys. Rev. Lett. **91**, 232001 (2003) [hep-ph/0309177 [hep-ph]].
66. N. N. Nikolaev and B. G. Zakharov, Phys. Lett. B **332**, 184 (1994) [hep-ph/9403243 [hep-ph]]; N. N. Nikolaev and B. G. Zakharov, Z. Phys. C **64**, 631 (1994) [hep-ph/9306230 [hep-ph]].
67. V. P. Goncalves and M. V. T. Machado, Eur. Phys. J. C **38**, 319 (2004) [hep-ph/0404145 [hep-ph]].
68. J. Bartels, K. J. Golec-Biernat and K. Peters, Acta Phys. Polon. B **34**, 3051 (2003) [hep-ph/0301192 [hep-ph]].
69. S. Munier and R. B. Peschanski, Phys. Rev. Lett. **91**, 232001 (2003) [hep-ph/0309177 [hep-ph]]; S. Munier and R. B. Peschanski, Phys. Rev. D **69**, 034008 (2004) [hep-ph/0310357 [hep-ph]]; S. Munier and R. B. Peschanski, Phys. Rev. D **70**, 077503 (2004) [hep-ph/0401215 [hep-ph]].
70. R. A. Fisher, Ann. Eugenics **7**(4), 355 (1937); A. Kolmogorov, I. Petrovsky and N. Piscounov, Moscow Univ. Bull. Math. **A1**, 1 (1937).
71. C. Marquet and L. Schoeffel, Phys. Lett. B **639**, 471 (2006) [hep-ph/0606079 [hep-ph]].
72. V. P. Goncalves and M. V. T. Machado, Phys. Rev. Lett. **91**, 202002 (2003) [hep-ph/0307090 [hep-ph]].
73. V. P. Goncalves and M. V. T. Machado, JHEP **0704**, 028 (2007) [hep-ph/0607125 [hep-ph]].
74. E. Iancu, K. Itakura and L. McLerran, Nucl. Phys. A **708**, 327 (2002) [hep-ph/0203137 [hep-ph]].
75. A. H. Mueller and D. N. Triantafyllopoulos, Nucl. Phys. B **640**, 331 (2002) [hep-ph/0205167 [hep-ph]].
76. N. Armesto and M. A. Braun, Eur. Phys. J. C **20**, 517 (2001) [hep-ph/0104038 [hep-ph]].
77. M. A. Braun, Phys. Lett. B **576**, 115 (2003) [hep-ph/0308320 [hep-ph]].
78. J. L. Albacete, N. Armesto, J. G. Milhano, C. A. Salgado and U. A. Wiedemann, Phys. Rev. D **71**, 014003 (2005) [hep-ph/0408216 [hep-ph]].
79. Y. V. Kovchegov and H. Weigert, Nucl. Phys. A **784**, 188 (2007) [hep-ph/0609090 [hep-ph]]; Y. V. Kovchegov and H. Weigert, Nucl. Phys. A **789**, 260 (2007) [hep-ph/0612071 [hep-ph]]; Y. V. Kovchegov, J. Kuokkanen, K. Rummukainen and H. Weigert, Nucl. Phys. A **823**, 47 (2009) [arXiv:0812.3238 [hep-ph]].
80. I. Balitsky, Phys. Rev. D **75**, 014001 (2007) [hep-ph/0609105 [hep-ph]];
81. I. Balitsky and G. A. Chirilli, Phys. Rev. D **77**, 014019 (2008) [arXiv:0710.4330 [hep-ph]].
82. J. L. Albacete, N. Armesto, J. G. Milhano and C. A. Salgado, Phys. Rev. D **80**, 034031 (2009) [arXiv:0902.1112 [hep-ph]].
83. J. L. Albacete and Y. V. Kovchegov, Phys. Rev. D **75**, 125021 (2007) [arXiv:0704.0612 [hep-ph]].
84. M. A. Betemps, V. P. Goncalves and J. T. de Santana Amaral, Eur. Phys. J. C **66**, 137 (2010) [arXiv:0907.3416 [hep-ph]].
85. J. L. Albacete and C. Marquet, Phys. Lett. B **687**, 174 (2010) [arXiv:1001.1378 [hep-ph]].
86. K. J. Golec-Biernat and M. Wusthoff, Phys. Rev. D **59** 014017 (1998) [hep-ph/9807513 [hep-ph]] ibid. K. J. Golec-Biernat and M. Wusthoff, Phys. Rev. D **60**, 114023 (1999) [hep-ph/9903358 [hep-ph]].
87. L. D. McLerran and R. Venugopalan, Phys. Rev. D **49**, 2233 (1994) [hep-ph/9309289 [hep-ph]].
88. L. N. Lipatov, Sov. J. Nucl. Phys. **23**, 338 (1976) [Yad. Fiz. **23**, 642 (1976)]; E. A. Kuraev, L. N. Lipatov and V. S. Fadin, Sov. Phys. JETP **45**, 199 (1977) [Zh. Eksp. Teor. Fiz. **72**, 377 (1977)]; I. I. Balitsky and L. N. Lipatov, Sov. J. Nucl. Phys. **28**, 822 (1978) [Yad. Fiz. **28**, 1597 (1978)].
89. J. B. Dainton, M. Klein, P. Newman, E. Perez and F. Willeke, JINST **1**, P10001 (2006) [hep-ex/0603016 [hep-ex]].
90. V. P. Goncalves, M. V. T. Machado and A. R. Meneses, Eur. Phys. J. C **68**, 133 (2010) [arXiv:1003.0828 [hep-ph]].

91. C. Marquet, R. B. Peschanski and G. Soyez, Phys. Rev. D **76**, 034011 (2007) [hep-ph/0702171 [hep-ph]].
92. E. Iancu, K. Itakura and S. Munier, Phys. Lett. B **590**, 199 (2004) [hep-ph/0310338 [hep-ph]].
93. A. G. Shuvaev, K. J. Golec-Biernat, A. D. Martin and M. G. Ryskin, Phys. Rev. D **60**, 014015 (1999) [hep-ph/9902410 [hep-ph]].
94. C. Adloff *et al.* [H1 Collaboration], Eur. Phys. J. C **13**, 371 (2000) [hep-ex/9902019 [hep-ex]].
95. S. Chekanov *et al.* [ZEUS Collaboration], PMC Phys. A **1**, 6 (2007) [arXiv:0708.1478 [hep-ex]].
96. S. Chekanov *et al.* [ZEUS Collaboration], Eur. Phys. J. C **24**, 345 (2002) [hep-ex/0201043 [hep-ex]].
97. C. Adloff *et al.* [H1 Collaboration], Phys. Lett. B **483**, 23 (2000) [hep-ex/0003020 [hep-ex]].
98. J. Breitweg *et al.* [ZEUS Collaboration], Phys. Lett. B **437**, 432 (1998) [hep-ex/9807020 [hep-ex]]; S. Chekanov *et al.* [ZEUS Collaboration], Phys. Lett. B **680**, 4 (2009) [arXiv:0903.4205 [hep-ex]].
99. F. D. Aaron *et al.* [H1 Collaboration], Phys. Lett. B **659**, 796 (2008) [arXiv:0709.4114 [hep-ex]].

Christophe Royon

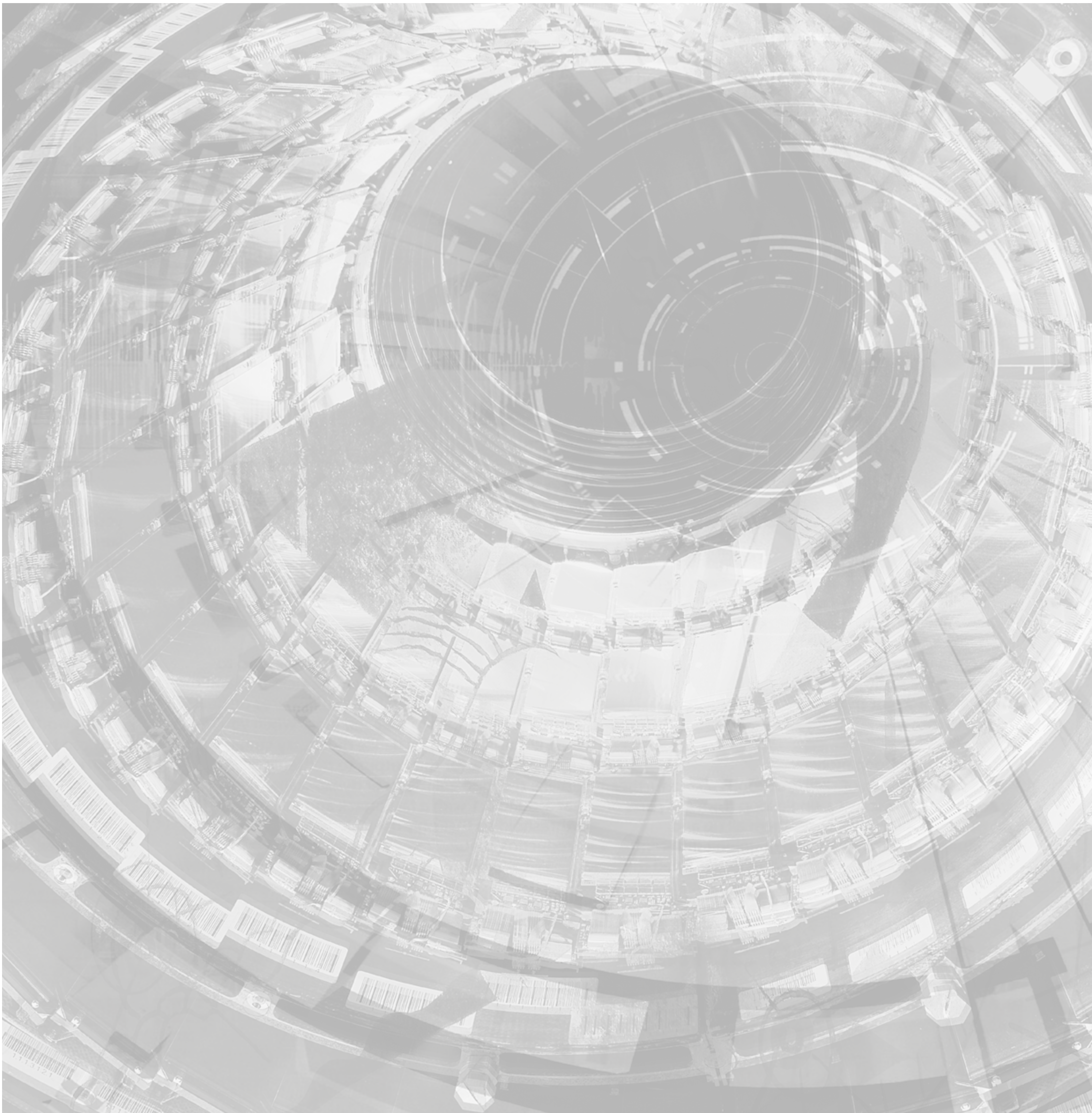

Diffractive and photon exchange processes at the LHC[9]

Christophe Royon [e, i, j]

[e]The University of Kansas, Lawrence, USA

[i]Institute of Physics, Academy of Science of the Czech Republic, Prague, Czech Republic

[j]Institute of Nuclear Physics, Polish Academy of Sciences, Krakow, Poland

Abstract

In these lectures, we give a brief description of diffractive and photon exchange physics at the LHC.

1 Experimental definition of diffraction

In this section, we discuss the different experimental ways to define diffraction. As an example, we describe the methods used by the H1 and ZEUS experiments at HERA, DESY, Hamburg in Germany since it is simpler for an *ep* collider.

1.1 The rapidity gap method

HERA is a collider where electrons of 27.6 GeV collide with protons of 920 GeV. A typical event as shown in the upper plot of Fig. 1 is $ep \rightarrow eX$ where electron and jets are produced in the final state. We notice that the electron is scattered in the H1 backward detector[10] (in green) whereas some hadronic activity is present in the forward region of the detector (in the LAr calorimeter and in the forward muon detectors). The proton is thus completely destroyed and the interaction leads to jets and proton remnants directly observable in the detector. The fact that much energy is observed in the forward region is due to colour exchange between the scattered jet and the proton remnants. In about 10% of the events, the situation is completely different. Such events appear like the one shown in the bottom plot of Fig. 46. The electron is still present in the backward detector, there is still some hadronic activity (jets) in the LAr calorimeter, but no energy above noise level is deposited in the forward part of the LAr calorimeter or in the forward muon detectors. In other words, there is no color exchange between the proton and the produced jets. As an example, this can be explained if the proton stays intact after the interaction.

This experimental observation leads to the first definition of diffraction: request a rapidity gap (in other words a domain in the forward detectors where no energy is deposited above noise level) in the forward region. For example, the H1 collaboration requests no energy deposition in the rapidity region $3.3 < \eta < 7.5$ where η is the pseudorapidity. Let us note that this approach does not insure that the proton stays intact after the interaction, but it represents a limit on the mass of the produced object $M_Y < 1.6$ GeV. Within this limit, the proton could be dissociated. The adavantage of the rapidity gap method is that it is quite easy to implement and it has a large acceptance in the diffractive kinematical plane.

[9]Presented at the School "New trends in HEP and QCD", October 21 - November 6 2014, Natal, Brazil.

[10]At HERA, the backward (resp. forward) directions are defined as the direction of the outgoing electron (resp. proton).

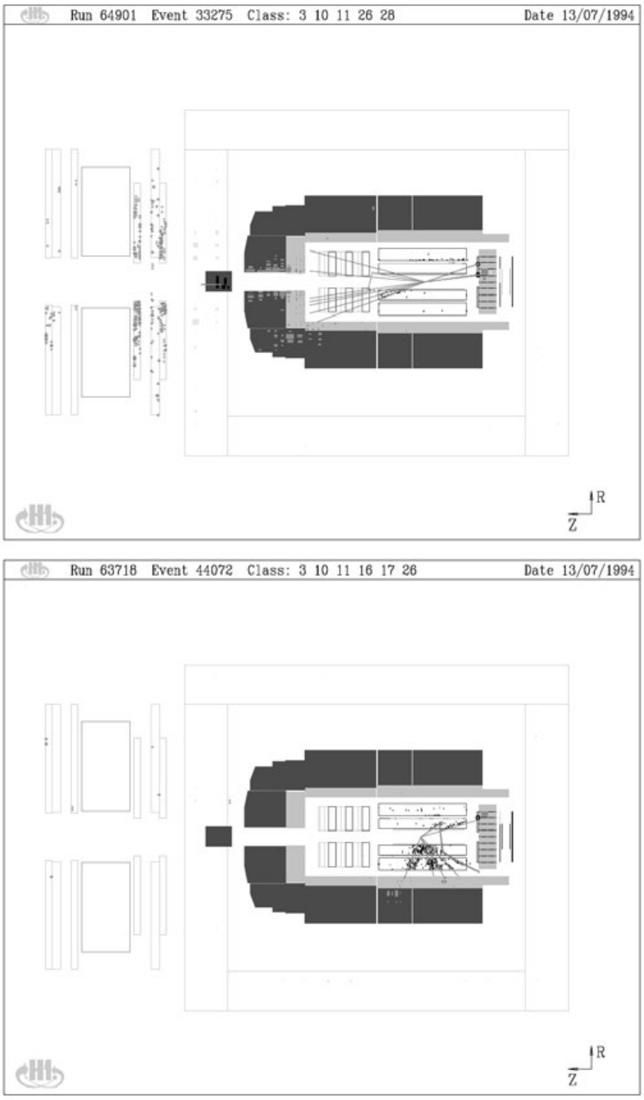

Figure 46: "Usual" and diffractive events in the H1 experiment.

1.2 Proton tagging

The second experimental method to detect diffractive events is also natural: the idea is to detect directly the intact proton in the final state. The proton loses a small fraction of its energy and is thus scattered at very small angle with respect to the beam direction. Some special detectors called roman pots can be used to detect the protons close to the beam. The basic idea is simple: the roman pot detectors are located far away from the interaction point and can move close to the beam, when the beam is stable, to detect protons scattered at vary small angles. The inconvenience is that the kinematical reach of those detectors is much smaller than with the rapidity gap method. On the other hand, the advantage is that it gives a clear signal of diffraction since it measures the diffracted proton directly.

A scheme of a roman pot detector as it is used by the H1 or ZEUS experiment is shown in Fig. 47. The beam is the horizontal line at the upper part of the figure. The detector is located in the pot itself and can move closer to the beam when the beam is stable enough (during the injection period, the detectors are protected in the home position). Step motors allow to move the detectors with high precision. A precise knowledge of the detector position is necessary to reconstruct the transverse momentum of the scattered proton and thus the diffractive kinematical variables. The detectors are placed in a secondary vaccuum with respect to the beam one.

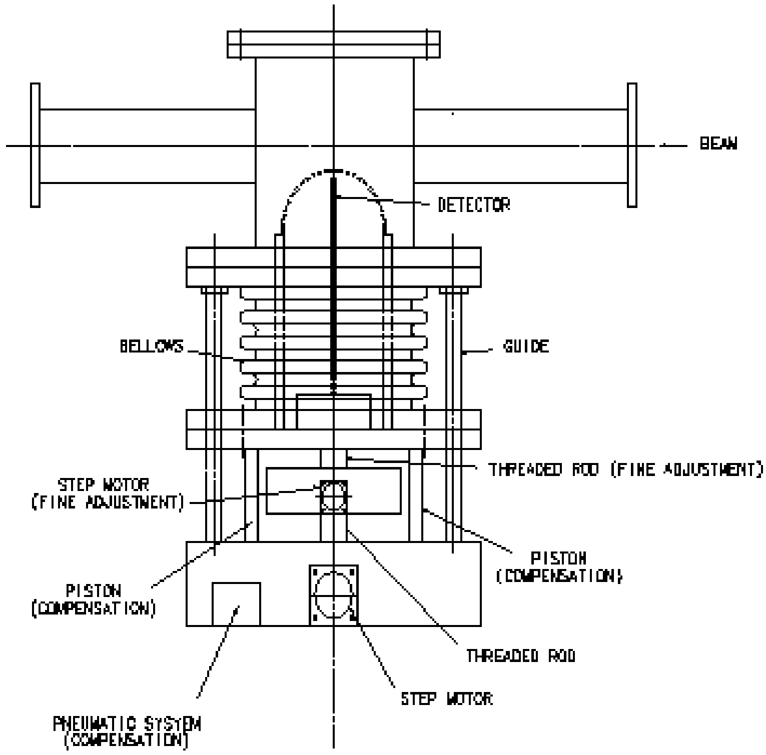

Figure 47: Scheme of a roman pot detector.

1.3 Diffractive kinematical variables

After having described the different experimental definitions of diffraction at HERA, we will give the new kinematical variables used to characterise diffraction. A typical diffractive event is shown in Fig. 48 where $ep \rightarrow epX$ is depicted. In addition to the usual deep inelastic variables, Q^2 the transfered energy squared at the electron vertex, x the fraction of the proton momentum carried by the struck quark, $W^2 = Q^2(1/x - 1)$ the total energy in the final state, new diffractive variables are defined: x_P (called ξ at the Tevatron and the LHC) is the momentum fraction of the proton carried by the colourless object called the pomeron, and β the momentum fraction of the pomeron carried by the interacting parton inside the pomeron if we assume the pomeron to be made of quarks and gluons:

$$x_P = \xi = \frac{Q^2 + M_X^2}{Q^2 + W^2} \tag{144}$$

$$\beta = \frac{Q^2}{Q^2 + M_X^2} = \frac{x}{x_P}. \tag{145}$$

2 Diffractive structure function measurement at HERA

2.1 Diffractive factorisation

In the following diffractive structure function analysis, we distinguish two kinds of factorisation at HERA. The first factorisation is the QCD hard scattering collinear factorisation at fixed x_P and t (see left plot of Fig. 49) [1], namely

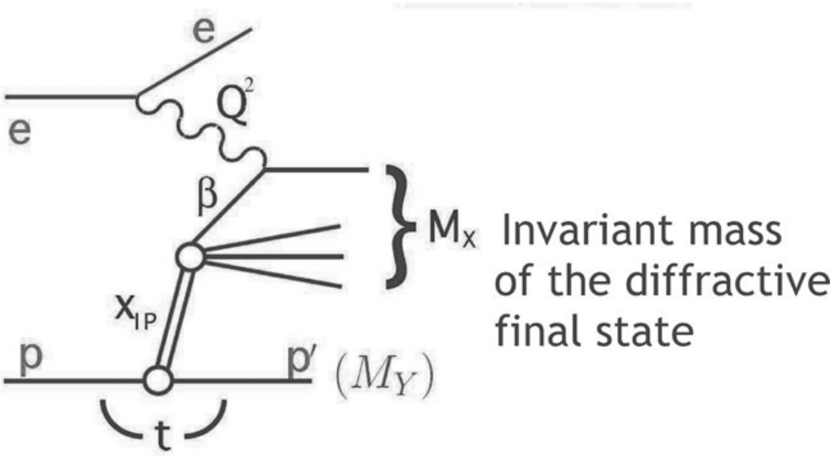

Figure 48: Scheme of a diffractive event at HERA.

$$d\sigma(ep \to eXY) = f_D(x, Q^2, x_P, t) \times d\hat{\sigma}(x, Q^2) \tag{146}$$

where we can factorise the flux f_D from the cross section $\hat{\sigma}$. This factorisation was proven recently, and separates the γq coupling to the interaction with the colourless object.

The Regge factorisation at the proton vertex allows to factorise the (x_P, t) and (β, Q^2) dependence, or in other words the hard interaction from the pomeron coupling to the proton (see right plot of Fig. 49).

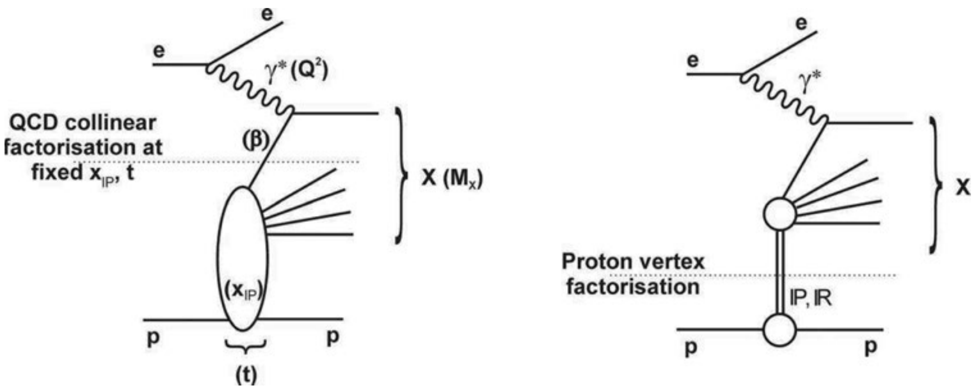

Figure 49: Diffractive factorisation.

2.2 Measurement of the diffractive proton structure function

The different measurements are performed using the three different methods to define diffractive events described in the first section. As an example, the H1 collaboration measures the diffractive cross section σ^D using the rapidity gap method:

$$\frac{d^3\sigma^D}{dx_P dQ^2 d\beta} = \frac{2\pi\alpha_{em}^2}{\beta Q^4}\left(1 - y + \frac{y^2}{2}\right)\sigma_r^D(x_P, Q^2, \beta) \tag{147}$$

where σ_r^D is the reduced diffractive cross section. The measurement [2] is presented in Fig. 50. We notice that the measurement has been performed with high precision over a wide kinematical domain:

$0.01 < \beta < 0.9$, $3.5 < Q^2 < 1600$ GeV^2, $10^{-4} < x_P < 5.10^{-2}$. The data are compared to the result of a QCD fit which we will discuss in the following.

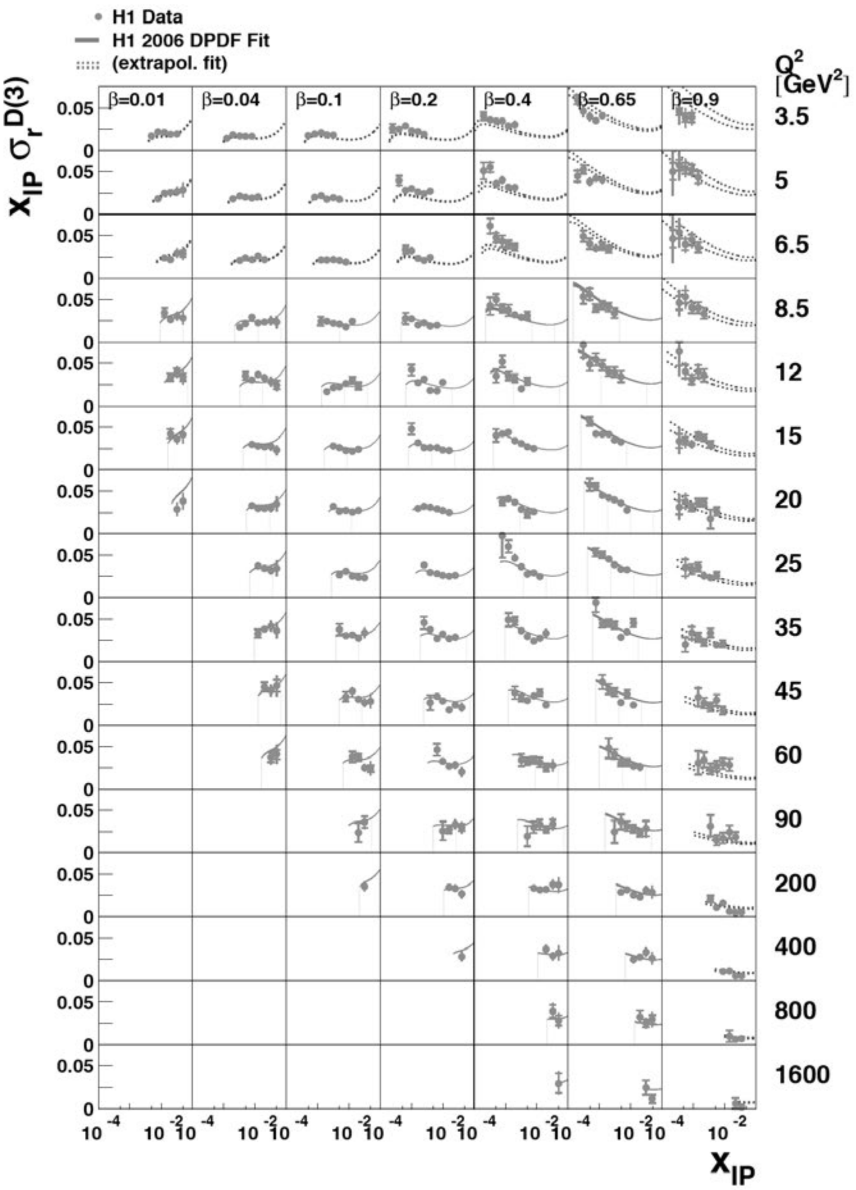

Figure 50: Measurement of the diffractive structure function by the H1 collaboration.

The rapidity gap data are also compared with the data obtained either using the M_X method or the one using proton tagging in roman pot detectors. Since they do not correspond exactly to the same definition of diffraction, a correction factor of 0.85 must be applied to the ZEUS M_X method to be compared to the rapidity gap one (this factor is due to the fact that the two methods correspond to two different regions in M_Y, namely $M_Y < 1.6$ GeV for H1 and $M_Y < 2.3$ GeV for ZEUS). It is also possible to measure directly in the H1 experiment the ratio of the diffractive structure function measurements between the rapidity gap and the proton tagging methods as illustrated in Fig. 51. Unfortunately, the measurement using the proton tagging method is performed only in a restricted kinematical domain. No kinematical dependence has been found within uncertainties for this ratio inside this kinematical domain (see Fig. 51 for the β and Q^2 dependence, and Ref. [3] for the x_P

dependence as well). Note that the ratio could still be depending on β and Q^2 outside the limited domain of measurement.

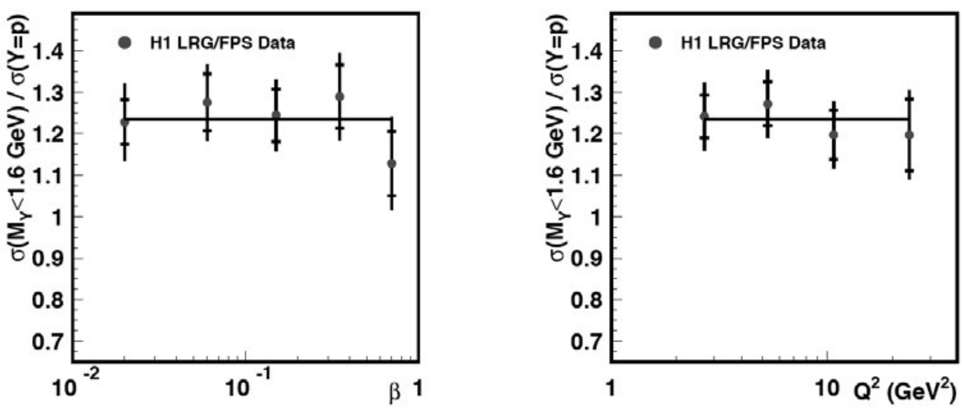

Figure 51: Measurement of the ratio of the diffractive structure function between the rapidity gap and the proton tagging methods (H1 experiment).

2.3 QCD analysis of the diffractive structure function measurement

As we mentionned already, according to Regge theory, we can factorise the (x_P, t) dependence from the (β, Q^2) one. The first diffractive structure function measurement from the H1 collaboartion [4] showed that this assumption was not true. The natural solution as observed in soft physics was that two different trajectories, namely pomeron and secondary reggeon, were needed to describe the measurement, which lead to a good description of the data. The diffractive structure function then reads:

$$F_2^D \sim f_p(x_P)(F_2^D)_{Pom}(\beta, Q^2) + f_r(x_P)(F_2^D)_{Reg}(\beta, Q^2) \tag{148}$$

where f_p and f_r are the pomeron and reggeon fluxes, and $(F_2^D)_{Pom}$ and $(F_2^D)_{Reg}$ the pomeron and reggeon structure functions. The flux parametrisation is predicted by Regge theory:

$$f(x_P, t) = \frac{e^{B_P t}}{x_P^{2\alpha_P(t)-1}} \tag{149}$$

with the following pomeron trajectory

$$\alpha_P(t) = \alpha_P(0) + \alpha'_P t. \tag{150}$$

The t dependence has been obtained using the proton tagging method, and the following values have been found: $\alpha'_P = 0.06^{+0.19}_{-0.06}$ GeV^{-2}, $B_P = 5.5^{+0.7}_{-2.0}$ GeV^{-2} (H1). Similarly, the values of $\alpha_P(0)$ have been measured using either the rapidity gap for H1 or the M_X method for ZEUS in the QCD fit described in the next paragraph [2, 5]. The Reggeon parameters have been found to be $\alpha'_R = 0.3$ GeV^{-2}, $B_R = 1.6$ GeV^{-2} (H1). The value of $\alpha_R(0)$ has been determined from rapidity gap data and found to be equal to 0.5. Since the reggeon is expected to have a similar $q\bar{q}$ structure as the pion and the data are poorly sensitive to the structure function of the secondary reggeon, it was assumed to be similar to the pion structure with a free normalisation.

The next step is to perform Dokshitzer Gribov Lipatov Altarelli Parisi (DGLAP) [6] fits to the pomeron structure function. If we assume that the pomeron is made of quarks and gluons, it is natural to check whether the DGLAP evolution equations are able to describe the Q^2 evolution of these parton densities. As necessary for DGLAP fits, a form for the input distributions is assumed at a given Q_0^2 and is evolved using the DGLAP evolution equations to a different Q^2, and fitted to the diffractive structure function data at this Q^2 value. The form of the distribution at Q_0^2 has been chosen to be:

$$\beta q = A_q \beta^{B_q} (1-\beta)^{C_q} \tag{151}$$
$$\beta G = A_g (1-\beta)^{C_g}, \tag{152}$$

leading to three (resp. two) parameters for the quark (resp. gluon) densities. At low β, the evolution is driven by $g \to q\bar{q}$ while $q \to qg$ becomes more important at high β. All diffractive data with $Q^2 > 8.5$ GeV^2 and $\beta < 0.8$ have been used in the fit [2,5] (the high β points being excluded to avoid the low mass region where the vector meson resonances appear). This leads to a good description of all diffractive data included in the fit.

The DGLAP QCD fit allows to get the parton distributions in the pomeron as a direct output of the fit, and is displayed in Fig. 52 as a blue shaded area as a function of β. We first note that the gluon density is much higher than the quark one, showing that the pomeron is gluon dominated. We also note that the gluon density at high β is poorly constrained which is shown by the larger shaded area.

Another fit was also performed by the H1 collaboration imposing $C_g = 0$. While the fit quality is similar, the gluon at high β is quite different, and is displayed as a black line in Fig. 52 (z is the equivalent of β for quarks). This shows further that the gluon is very poorly constrained at high β and some other data sets such as jet cross section measurements are needed to constrain it further.

3 Diffraction at the LHC

The LHC is a *pp* collider located close to Geneva, at CERN, Switzerland. It is presently the collider with the highest center-of-mass energy of about 13 TeV.

3.1 Diffractive kinematical variables

The difference between diffraction at HERA and at the Tevatron is that diffraction can occur not only on either p side as at HERA, but also on both sides. The former case is called single diffraction whereas the other one double pomeron exchange. In the same way as we defined the kinematical variables x_P and β at HERA, we define $\xi_{1,2}(=x_P$ at HERA) as the proton fractional momentum loss (or as the p momentum fraction carried by the pomeron), and $\beta_{1,2}$, the fraction of the pomeron momentum carried by the interacting parton. The produced diffractive mass is equal to $M^2 = s\xi_1$ for single diffractive events and to $M^2 = s\xi_1\xi_2$ for double pomeron exchange. The size of the rapidity gap is of the order of $\Delta\eta \sim \log 1/\xi_{1,2}$.

The rapidity gap method can be only used at low luminosity at the LHC. At high instantaneous luminosity, many interactions (called pile up) occur within the same bunch crossing. The pile up interactions will fill in the rapidity gap devoid of any energy, making difficult to use the rapidity gap method. It is thus preferable to tag directly the protons at the LHC.

3.2 Diffraction at the LHC

In this short report we discuss some potential measurements that can be accomplished in forward physics at the LHC. We distinguish between the low luminosity (no pile up), medium luminosity

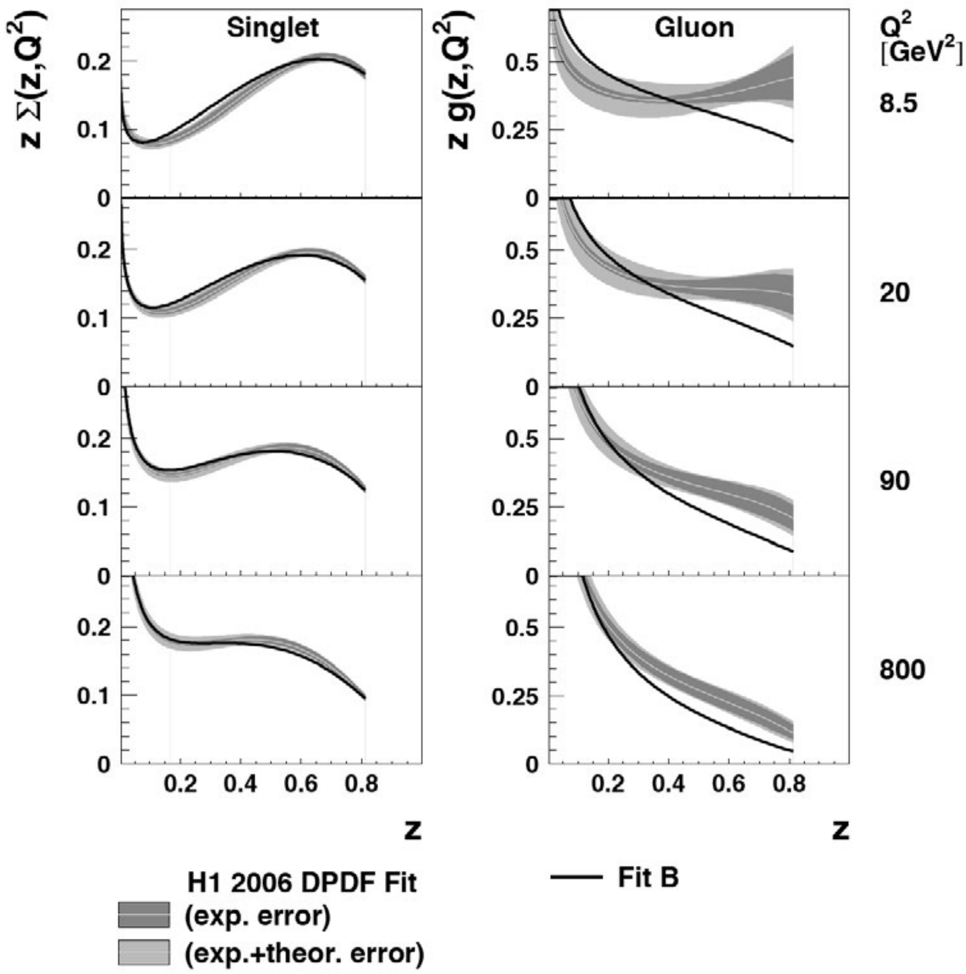

Figure 52: Extraction of the parton densities in the pomeron using a DGLAP NLO fit (H1 collaboration).

(moderate pile up) and high luminosity (high pile up) environments. Forward physics is fundamental at the LHC since it adresses the QCD dynamics at the interface between hard and soft physics. For instance, the soft total *pp* cross section probes long transverse distances, and the BFKL pomeron is valid at short distances. Most of the energy in a standard *pp* collision goes in the forward direction and not in the central one, and it is important to tune the MC expectations for a good understanding of the event topology. In addition, diffraction and especially photon exchange processes allow performing searches beyond the standard model. Further more, diffractive events are important to tune MC and understand underlying events and soft QCD. Almost all Monte Carlo are designed for hard processes and new physics, and they have difficulties with incorporating diffraction and need improvement. Diffractive measurements are fundamental to achieve this goal. More details about the different measurements can be found in [7].

3.3 LHC running conditions and forward detectors

Forward detectors

At the LHC, the different detectors are sensitive to different programs of forward physics. The LHCf detector [8] measures the multiplicities and energy flow in the very forward direction at very low luminosity. The selection of diffractive events in LHCb [9] and Alice [10] is performed by using the so-called rapidity gap method and will benefit from new scintillators that cover the forward region as was installed previously in CMS. The present coverage of the CMS and ATLAS forward detectors will be complemented by the AFP and CMS-TOTEM/CT-PPS projects to add additional proton detectors at about 220 meters from the interaction point [11, 12].

Running at low and high β^* using the CMS-TOTEM, CT-PPS and ATLAS-AFP detectors allows accessing different kinematical domains for diffraction. In Fig. 53 are dispalyed the acceptances in proton relative energy loss ξ versus the proton transverse momentum p_T for two values of β^* (0.65 m, the nominal collision optics, and 90 m) for vertical (ALFA) or horizontal (AFP) roman pot detector configurations located about 220 m from the ATLAS interaction point. We notice that one can access low and high mass diffraction (low and high ξ) at high β^* in ALFA and only low mass diffraction (up to $\xi \sim$0.15) at low β^* using AFP. Both measurements will be thus interesting in order to cover easily low and high mass diffraction. The kinematical coverage is similar for the vertical (CMS-TOTEM) and the horizontal pots (CT-PPS) of CMS and TOTEM.

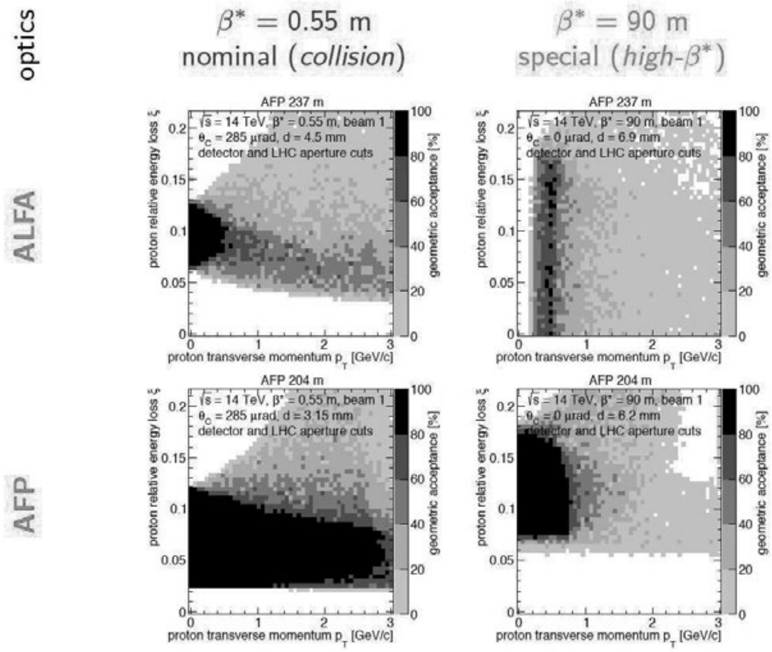

Figure 53: Acceptance ξ versus t at low and high β^* for vertical (ALFA) and horizontal (AFP) roman pots at 220 m.

Different luminosity conditions

As we mentioned in the last section, we distinguish between the low, medium and high luminosity runs.

The low luminosity runs (without pile up) allow performing multiplicity and energy flow measurements useful to tune MC as well as to measure the total and soft diffractive cross sections in the ATLAS/ALFA and TOTEM experiments. Additional measurements such as single diffraction, low mass resonances and glueballs typically require a few days of data taking (0.1 to 1. pb^{-1}).

Medium luminosity runs are specific for the different LHC experiments. LHCb accumulate typically a few fb^{-1} at low pile up during their nominal data taking while the CMS-TOTEM and ATLAS (ALFA and AFP) can accumulate low pile up data in low and high β^* special runs at low luminosity at the LHC. It is then typically possible to accumulate 1 to 10 pb^{-1} at high β^* with a pile up $\mu \sim 1$ with a few days of data taking and 10 to 100 pb^{-1} at low β^* with one to two weeks of data taking at $\mu \sim 2$ to 5.

High pile up data taking means taking all the luminosity delivered typically to ATLAS and CMS with a pile up μ between 20 and 100. It is also possible to collect data at a lower pile up $\mu \sim 25$ by restricting to end of store data taking (up to 40% of the total luminosity can be collected in this way). or to data originating from the tails of the vertex distribution.

3.4 Low luminosity measurements

In addition to measurements of the total and soft diffraction cross sections performed at high β^* in dedicated runs, data taken without pile up are specially interesting to measure multiplicities and energy flow especially useful to tune MC benefitting from the different coverage in rapidity of the different LHC experiments. There is also a special interested especially driven by the cosmic ray community to measure the multiplicities in proton-oxygen runs at the LHC since models make different predictions in those conditions even if they lead to similar predictions in proton proton interactions at 14 TeV. This will allow making precise predictions on proton oxygen events for cosmic ray physics.

Another example of fundamental measurements to be performed at very low luminosity is the measurement of the size of the forward gap in diffractive events when the protons are tagged in AFP or in TOTEM. The differences between the models are much larger when the protons are tagged [13], and this will allow further tuning of the models as shown in Fig. 54.

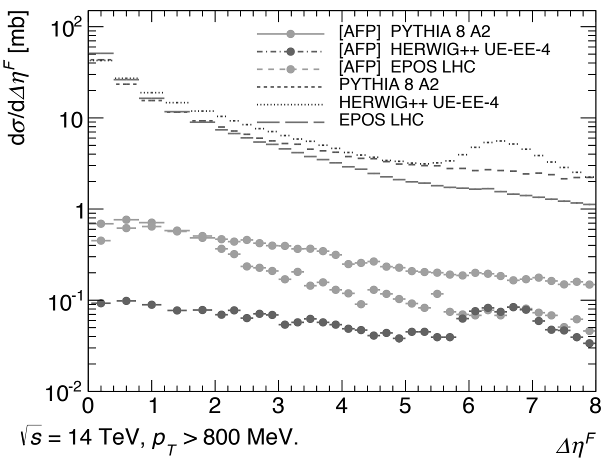

Figure 54: Size of rapidity in diffractive events for different MC models when protons are tagged in AFP or not.

3.5 Medium luminosity measurements

Inclusive diffractive measurements

Medium luminosity measurements with the rapidity gap method used in Alice (two new scintillator hodoscopes covering $-7.0 < \eta < -4.9$ and $4.8 < \eta < 6.3$ are being installed in Alice in order to improve the forward coverage) or with proton tagging in AFP and CMS-TOTEM allow constraining further the pomeron structure using γ+jet and dijet events [14]. The aim is to answer mainly the following questions that are fundamental from the QCD point of view:

- Is it the same object (the same pomeron) which explains diffraction in *pp* (LHC) and *ep* (HERA)? Are the measurements compatible between the different accelerators?
- If yes, what are the further constraints of the pomeron structure in terms of quarks and gluons?
- What is the value of the survival probability? It is important to measure it since it is difficult to compute it theoretically being sensitive to non-perturbative physics

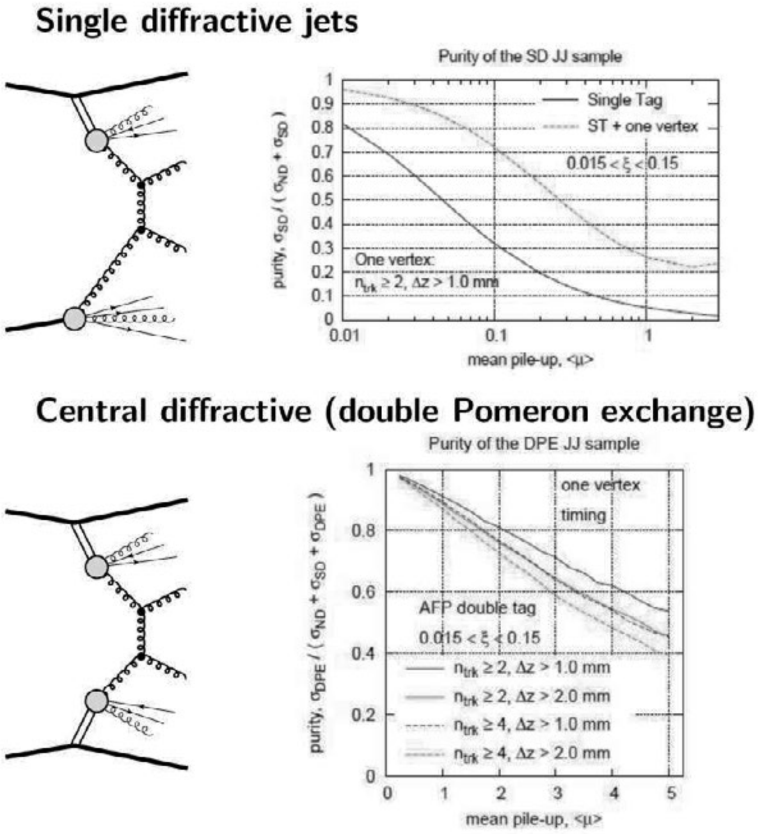

Figure 55: Feasibility studies of measuring jet production cross section in single diffractive and double pomeron exchange events.

Feasibility studies have been performed in ATLAS (and measurements started in CMS-TOTEM at 8 TeV) concerning the possibility to measure jet production cross sections in single diffractive and double pomeron exchange events at low β^*. The results are shown in Fig. 55 where the sample purity is shown as a function of pile up (the main background being due to non diffractive events superimposed by protons originating from soft diffractive events). In order to obtain a quite pure sample with a purity larger than 70%, low pile up runs ($\mu \sim$0.1) are needed for single diffractive jet measurements whereas moderate pile up ($\mu \sim 2-3$) is needed for double pomeron exchange jet measurements together with the request of the presence of a single reconstructed vertex. Typically, a few days of data taking will be enough to perform these measurements useful to constrain further the pomeron structure. It is also worth noticing that these measurements are also possible at higher values of β^*.

The CMS-TOTEM collaboration also studied many additional processes to be measured at high β^* [12]. For instance, 10 pb^{-1} of data are enough to obtain 3080 $\pm$ 90 single diffractive J/Ψ by tagging two muons of opposite charges with $3.05 < M_{\mu\mu} < 3.15$ GeV, 340$\pm$10 and 30$\pm$1 single diffractive W and Z by requesting a leading lepton with p_T >20 GeV.

Last but not least, the medium luminosity runs will allow probing the BFKL evolution using the jet gap jet events in diffraction [14].

Exclusive diffraction

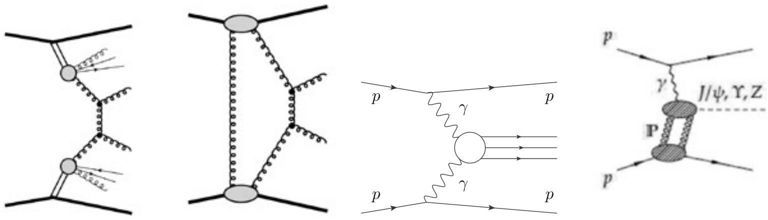

Figure 56: Exclusive diffractive and photon exchange processes. The left diagram shows the double pomeron exchange event for reference, the second one the QCD exclusive production, the third one the production of a system X via photon exchanges, and the last one the exclusive photo-production events.

The advantage of the exclusive diffractive and photon exchange processes illustrated in Fig. 56 is that all particles can be measured in the final state. Both protons can be measured in AFP or CMS-TOTEM and the produced particles (jets, vector mesons, Z boson....) in ATLAS or CMS, and there is no energy losses such as in the pomeron remnants as shown in Fig. 56, left diagram. It is thus possible to reconstruct the properties of the object produced exclusively (via photon and gluon exchanges) from the tagged proton since the system is completely constrained. It is worth mentioning that it is also possible to constrain the background by asking the matching between the information of the two protons and the produced object, and thus, central exclusive production is a potential channel for beyond standard modelphysics at high masses.

Exclusive vector mesons can be measured for instance in the LHCb experiment which recently measured for the first time the diffractive production of charmonium [15]. The Herschel scintillators are now being installed in LHCb to enhance the coverage at high rapidities in order to get a better control of non-exclusive background. Such channels are also sensitive to new physics: if a medium mass resonance due to a glueball or a tetraquark state exists, it could lead to a bump in the invariant mass distribution of the charmonium states.

The CMS-Totem experiment also performed extensive studies of possible measurements of exclusive states at high β^*. It is worth mentioning that the search for glueball states and the probe of the low x gluon density down to $x \sim 10^{-4}$ will be possible. With 1 pb^{-1}, it will be possible to confirm or not the existence of the unobserved possible $f_0(1710)$ and $f_0(1500)$ decay modes and with 5 to 10 pb^{-1}, the unambiguous spin determination and the precise measurement of cross-section times branching ratio. In addition, the measurement of the cross section times branching ratio for the three $\chi_{C,0,1,2}$ states, will be performed allowing a comparison with the results to the LHCb measurement [16] and the exclusive QCD calculations [17]

In addition, it is possible to measure the exclusive dijet production at the LHC with about 40 fb^{-1} and a pile up of 40 as was shown by the ATLAS and CT-PPS collaborations. Despite the high level of pile up background, it is possible to obtain a pure enough of exclusive jets that can further constrin the models of exclusive diffractive production.

4 Soft diffraction and measurement of the total cross section in ATLAS and TOTEM

4.1 The TOTEM experiment and the measurement of the total cross section

In this section, we will only give a short summary of the measurement of the total cross section by the TOTEM collaboration. For more details, see the proceedings written by U. Maor at this workshop [18].In Fig. 57, we display the different beam conditions (different values of β^*) that can be used to perform the total cross section as a function of t on the widest possible kinematical range. It is foreseen to perform the measurement at a β^* ∼1000 m in the next years at a center-of-mass energy of 13 TeV. The present result on the total, elastic and inelastic cross sections originating from TOTEM and ATLAS-ALFA experiments is given in Fig. 58 [19]. given in Fig. 58.

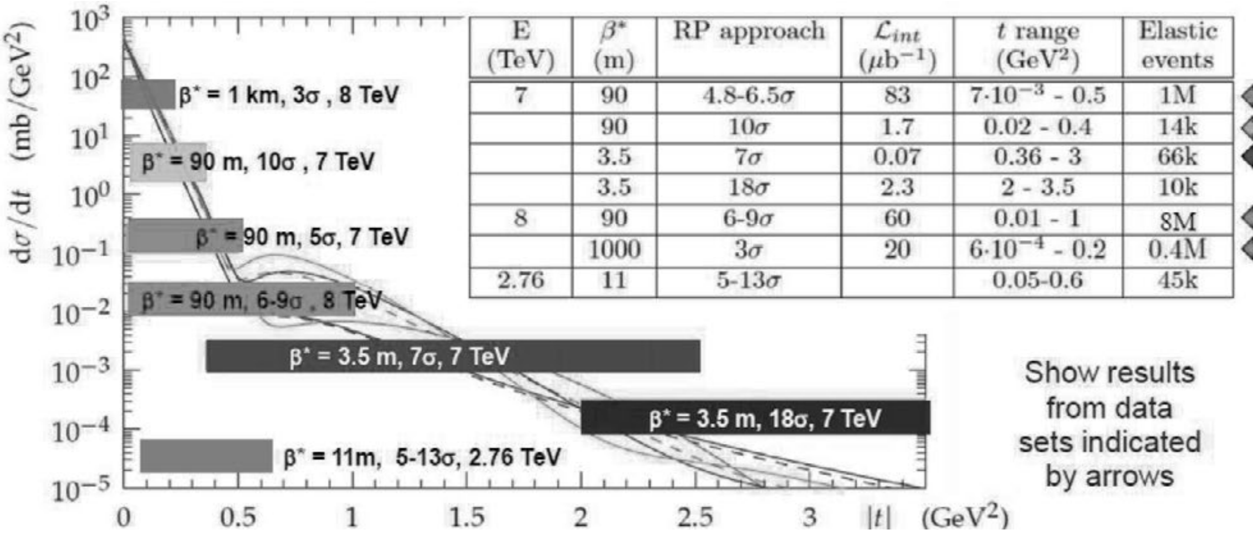

E (TeV)	β^* (m)	RP approach	$\mathcal{L}_{int}$ (μb^{-1})	t range (GeV^2)	Elastic events
7	90	4.8-6.5σ	83	$7 \cdot 10^{-3}$ - 0.5	1M
	90	10σ	1.7	0.02 - 0.4	14k
	3.5	7σ	0.07	0.36 - 3	66k
	3.5	18σ	2.3	2 - 3.5	10k
8	90	6-9σ	60	0.01 - 1	8M
	1000	3σ	20	$6 \cdot 10^{-4}$ - 0.2	0.4M
2.76	11	5-13σ		0.05-0.6	45k

Figure 57: Different beam conditions needed to measure the total cross section on a wide kinematical range in $|t|$.

4.2 Prospects in ATLAS/ALFA

The main motivation for installing the ALFA detectors is the total cross section measurement. The idea is to measure the elastic cross section in the Coulomb and interference region (see Fig. 2), which can be used to provide an absolute measurement of the luminosity. The elastic cross section is the sum of the coulombian, nuclear and interference terms

$$\frac{dN}{dt} = L\left(\frac{4\pi\alpha^2 G^4(t)}{|t|^2} - \frac{\alpha\rho\sigma_{tot}G^2(t)e^{-B|t|/2}}{|t|} + \frac{\sigma_{tot}^2(1+\rho)^2 e^{-B|t|}}{16\pi}\right). \tag{153}$$

The luminosity L, the total cross section, and the B and ρ parameters appearing in the elastic cross section formula are determined by fitting the dN/dt spectrum in the interference and nuclear regions. The measurement requires the possibility to detect the protons in the final state down to $t \sim 3.7\ 10^{-4}$ GeV^2 which means a proton angle down to 3 μrad, which requires special high β^* runs at low luminosity. The total uncertainties on the elastic cross section measurement are expected to be less than 3% (beam properties: 1.2%, detector properties: 1.4%, background substraction: 1.1% and a 1.8% statistical error for 100 hours of measurement at low luminosity).

The ALFA detector also allows to measure soft single diffractive events in dedicated runs where ALFA will be used to measure elastic events. It is possible to measure forward protons in the region:

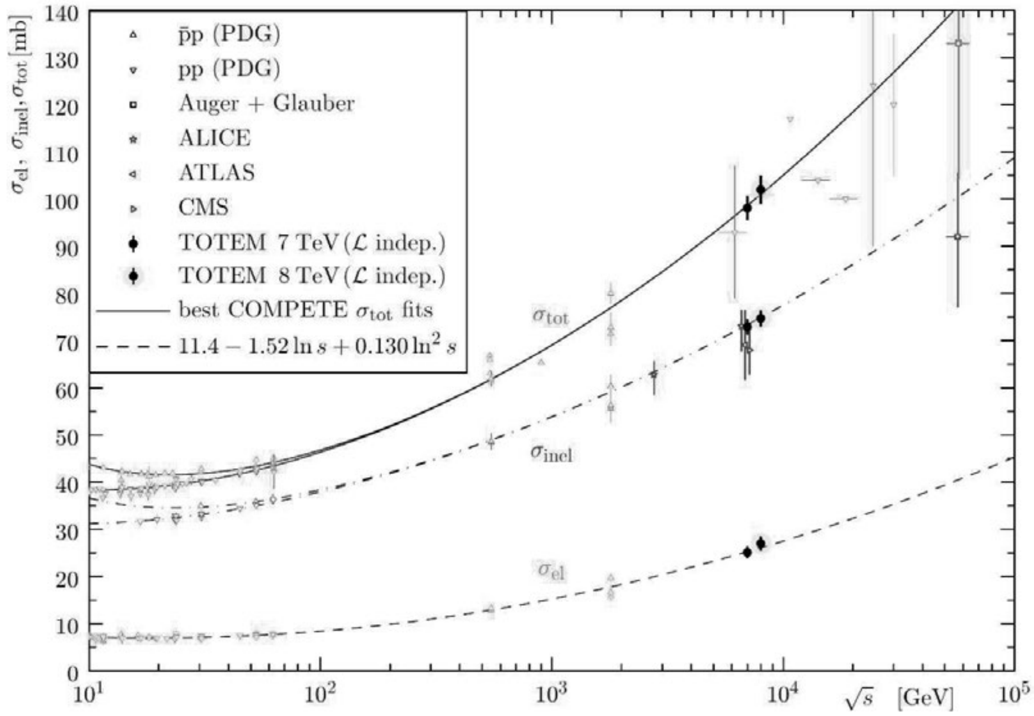

Figure 58: Measurement of the total, inelastic, and elastic cross sections by the TOTEM and ATLAS-ALFA collaborations.

$6.3 < E_{proton} < 7$ TeV, and single diffractive measurements are possible for $\xi < 0.01$ and non-diffractive proton measurements for $0.01 < \xi < 0.1$. 1.5 million events are expected in 100 hours at 10^{27} cm^{-2}s^{-1}.

5 Photon induced processes at the LHC and anomalous coupling studies

In this section, we discuss some potential measurements to be performed using proton tagging detectors at the LHC based on γ-induced processes. The main motivation is to explore rare events, searching for beyond standard model physics such as quartic anomalous couplings between photons and W/Z bosons and photons. We assume in the following intact protons to be tagged in dedicated detectors located at about 210 m for ATLAS (220 m for CMS).

In the first part of this section, we discuss the SM production of W and γ pairs at the LHC via photon exchanges. In the second, third and fourth sections, we discuss the sensitivities of these processes to trilinear and quartic gauge anomalous couplings.

5.1 Standard Model exclusive $\gamma\gamma$, WW and ZZ production

Standard Model exclusive $\gamma\gamma$ production at the LHC: Photon and gluon induced processes

In Fig. 60 and 61, we show the leading processes leading to two photons and two intact protons in the final state as an example. The first diagram (Fig. 60) corresponds to exclusive QCD diphoton production via gluon exchanges (the second gluon ensures that the exchange is colorless leading to intact protons in the final state) and the second one (Fig. 61) via photon exchanges, It is worth noticing that quark, lepton and W loops need to be considered in order to get the correct SM cross section for diphoton production as shown in Fig 62. The QCD induced processes from the Khoze Martin Ryskin model are dominant at low masses whereas the photon induced ones (QED processes) dominate at

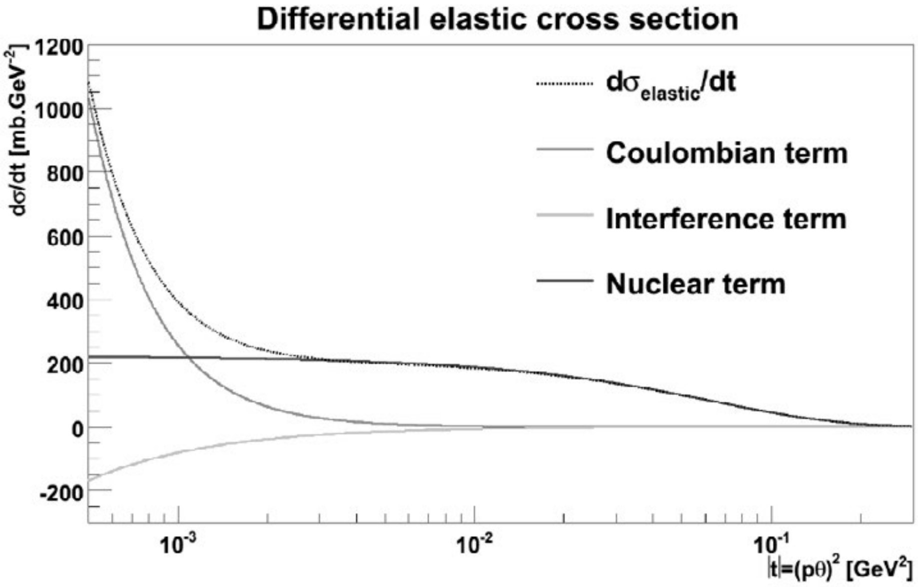

Figure 59: Coulombian, nuclear and interference terms in the elastic cross section.

higher diphoton masses [17]. It is very important to notice that the W loop contribution dominates at high diphoton masses [20–22] whereas this contribution is omitted in most studies. This is the first time that we put all terms inside a MC generator, FPMC [23].

Standard Model WW and ZZ production

In the Standard Model (SM) of particle physics, the couplings of fermions and gauge bosons are constrained by the gauge symmetries of the Lagrangian. The measurement of W and Z boson pair productions via the exchange of two photons allows to provide directly stringent tests of one of the most important and least understood mechanism in particle physics, namely the electroweak symmetry breaking.

The process that we study is the W pair production induced by the exchange of two photons [24]. It is a pure QED process in which the decay products of the W bosons are measured in the central detector and the scattered protons leave intact in the beam pipe at very small angles and are detected in AFP or CT-PPS. All these processes as well as theb different diffractive backgrounds were inplemented in the FPMC Monte Carlo [23].

After simple cuts to select exclusive W pairs decaying into leptons, such as a cut on the proton momentum loss of the proton ($0.0015 < \xi < 0.15$) — we assume the protons to be tagged in AFP or CT-PPS at 210 and 420 m — on the transverse momentum of the leading and second leading leptons at 25 and 10 GeV respectively, on $\not{E}_T > 20$ GeV, $\Delta\phi > 2.7$ between leading leptons, and $160 < W < 500$ GeV, the diffractive mass reconstructed using the forward detectors, the background is found to be less than 1.7 event for 30 fb^{-1} for a SM signal of 51 events [24].

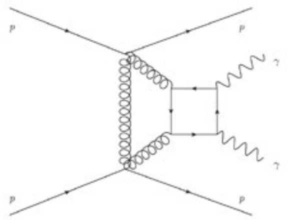

Figure 60: Diphoton QCD exclusive production.

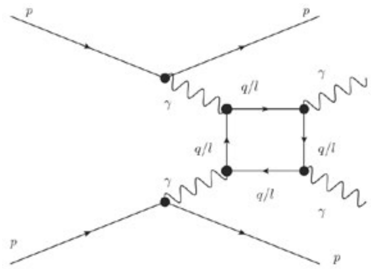

Figure 61: Diphoton production via photon exchanges.

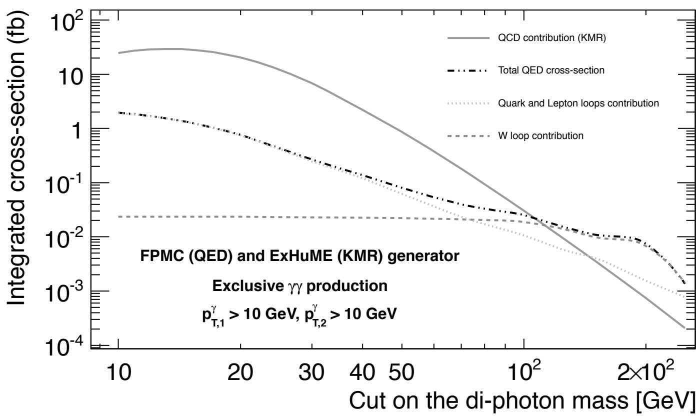

Figure 62: Diphoton production cross section as a function of the diphoton mass requesting two intact protons in the final state and the photons to have a transverse momentum larger than 10 GeV. The QCD exclusive processes (Khoze Martin Ryskin) in full line dominate at low masses while QED diphoton production dominates at higher masses (dashed lines). The QED production corresponds to diphoton production via lepton/fermion loops (dotted line) and W boson loops (dashed-dotted line).

5.2 Triple anomalous gauge couplings

In Ref. [25], we also studied the sensitivity to triple gauge anomalous couplings at the LHC. The Lagrangian including anomalous triple gauge couplings λ^γ and $\Delta\kappa^\gamma$ is the following

$$\begin{aligned}\mathcal{L} \sim\ & (W^\dagger_{\mu\nu} W^\mu A^\nu - W_{\mu\nu} W^{\dagger\mu} A^\nu) \\ & + (1+\Delta\kappa^\gamma) W^\dagger_\mu W_\nu A^{\mu\nu} + \frac{\lambda^\gamma}{M_W^2} W^\dagger_{\rho\mu} W^\mu{}_\nu A^{\nu\rho}). \end{aligned} \tag{154}$$

The strategy is the same as for the SM coupling studies: we first implement this lagrangian in FPMC [23] and we select the signal events when the Z and W bosons decay into leptons. The difference is that the signal appears at high mass for λ^γ and $\Delta\kappa^\gamma$ only modifies the normalization and the low mass events have to be retained. The sensitivity on triple gauge anomalous couplings is a gain of about a factor 3 with respect to the LEP limits, which represents one of the best reaches before the LHC.

5.3 Quartic WW and ZZ anomalous couplings

The parameterization of the quartic couplings based on [26] is adopted. The cuts to select quartic anomalous gauge coupling WW events are similar as the ones we mentioned in the previous section, namely $0.0015 < \xi < 0.15$ for the tagged protons corresponding to the AFP or CT-PPS detector

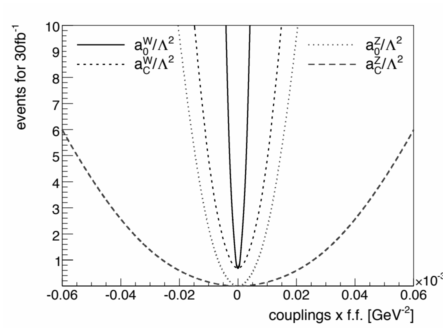

Figure 63: Number of events for signal due to different values of anomalous couplings after all cuts (see text) for a luminosity of 30 fb^{-1}.

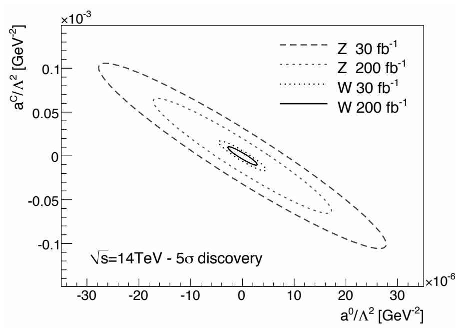

Figure 64: 5σ discovery contours for all the WW and ZZ quartic couplings at $\sqrt{s} = 14$ TeV for a luminosity of 30 fb^{-1} and 200 fb^{-1}.

at 210 and 420 m, $\not{E}_T > 20$ GeV, $\Delta\phi < 3.13$ between the two leptons. In addition, a cut on the p_T of the leading lepton $p_T > 160$ GeV and on the diffractive mass $W > 800$ GeV are requested since anomalous coupling events appear at high mass. After these requirements, we expect about 0.7 background events for an expected signal of 17 events if the anomalous coupling is about four orders of magnitude lower than the present LEP limit [27] ($|a_0^W/\Lambda^2| = 5.4\ 10^{-6}$) or two orders of magnitude lower with respect to the D0 and CDF limits [28] for a luminosity of 30 fb^{-1}. The strategy to select anomalous coupling ZZ events is analogous and the presence of three leptons or two like sign leptons are requested. Table 1 gives the reach on anomalous couplings at the LHC for luminosities of 30 and 200 fb^{-1} compared to the present OPAL limits from the LEP accelerator [27]. More recent limits were published recently by the D0 and CMS collaborations [28] on a_0^W and a_C^W, and they are respectively 1.5 10^{-4} and 5 10^{-4} from CMS with a form factor of 500 GeV,

Figs. 63 and 64 show respectively the number of expected events for signal as a function of the anomalous coupling value and the 5σ discovery contours for all WW and ZZ anomalous couplings for 30 and 200 fb^{-1}. It is possible to reach the values expected in extra dimension models. The tagging of the protons using the ATLAS Forward Physics detectors is the only method at present to test so small values of quartic anomalous couplings.

Couplings	OPAL limits [GeV^{-2}]	Sensitivity @ $\mathcal{L} = 30$ (200) fb^{-1}	
		5σ	95% CL
a_0^W/Λ^2	[-0.020, 0.020]	5.4 10^{-6} (2.7 10^{-6})	2.6 10^{-6} (1.4 10^{-6})
a_C^W/Λ^2	[-0.052, 0.037]	2.0 10^{-5} (9.6 10^{-6})	9.4 10^{-6} (5.2 10^{-6})
a_0^Z/Λ^2	[-0.007, 0.023]	1.4 10^{-5} (5.5 10^{-6})	6.4 10^{-6} (2.5 10^{-6})
a_C^Z/Λ^2	[-0.029, 0.029]	5.2 10^{-5} (2.0 10^{-5})	2.4 10^{-5} (9.2 10^{-6})

Table 18: Reach on anomalous couplings obtained in γ induced processes after tagging the protons in AFP or CT-PPS compared to the present OPAL limits. The 5σ discovery and 95% C.L. limits are given for a luminosity of 30 and 200 fb^{-1} [24]

The search for quartic anomalous couplings between γ and W bosons was performed again after a full simulation of the ATLAS detector including pile up [29] assuming the protons to be tagged in AFP or CT-PPS at 210 m only. Integrated luminosities of 40 and 300 fb^{-1} with, respectively, 23 or 46 average pile-up events per beam crossing have been considered. In order to reduce the background, each W is assumed to decay leptonically (note that the semi-leptonic case in under study). The full list of background processes used for the ATLAS measurement of Standard Model WW cross-section was simulated, namely $t\bar{t}$, WW, WZ, ZZ, W+jets, Drell-Yan and single top events. In addition, the additional diffractive backgrounds mentioned in the previous paragraph were also simulated, The requirement of the presence of at least one proton on each side of AFP or CT-PPS within a time window of 10 ps allows us to reduce the background by a factor of about 200 (50) for $\mu = 23$ (46). The p_T of the leading lepton originating from the leptonic decay of the W bosons is required to be $p_T >$ 150 GeV, and that of the next-to-leading lepton $p_T > 20$ GeV. Additional requirement of the dilepton mass to be above 300 GeV allows us to remove most of the diboson events. Since only leptonic decays of the W bosons are considered, we require in addition less than 3 tracks associated to the primary vertex, which allows us to reject a large fraction of the non-diffractive backgrounds (e.g. $t\bar{t}$, diboson productions, W+jet, etc.) since they show much higher track multiplicities. Remaining Drell-Yan and QED backgrounds are suppressed by requiring the difference in azimuthal angle between the two leptons $\Delta\phi < 3.1$. After these requirements, a similar sensitivity with respect to fast simulation without pile-up was obtained.

5.4 Quartic photon anomalous couplings

Theoretical motivations

In this section, four-photon (4γ) interactions through diphoton production via photon fusion with intact outgoing protons are considered. In the assumption of a new physics mass scale Λ heavier than experimentally accessible energy E, all new physics manifestations can be described using an effective Lagrangian valid for $\Lambda \gg E$. Among these operators, the pure photon dimension-eight operators

$$\mathcal{L}_{4\gamma} = \zeta_1^\gamma F_{\mu\nu}F^{\mu\nu}F_{\rho\sigma}F^{\rho\sigma} + \zeta_2^\gamma F_{\mu\nu}F^{\nu\rho}F_{\rho\lambda}F^{\lambda\mu} \tag{155}$$

can induce the $\gamma\gamma\gamma\gamma$ process, highly suppressed in the SM [20, 30]. We discuss here possible new physics contributions to $\zeta_{1,2}^\gamma$ that can be probed and discovered at the LHC using the forward proton detectors.

Loops of heavy charged particles contribute to the 4γ couplings [20, 30] as $\zeta_i^\gamma = \alpha_{\rm em}^2 Q^4\, m^{-4}\, N\, c_{i,s}$, where $c_{1,s}$ is related to the spin of the heavy particle of mass m running in the loop and Q its electric charge. The factor N counts all additional multiplicities such as color or flavor. These couplings scale as $\sim Q^4$ and are enhanced in presence of particles with large charges. For example, certain light composite fermions, characteristic of composite Higgs models, have typically electric charges of several units. For a 500 Gev vector (fermion) resonance with $Q = 3$ (4), large couplings ζ_i^γ of the order of $10^{-13} - 10^{-14}$ Gev^{-4} can be reached.

Beyond perturbative contributions to ζ_i^γ from charged particles, non-renormalizable interactions of neutral particles are also present in common extensions of the SM. Such theories can contain scalar, pseudo-scalar and spin-2 resonances that couple to the photon and generate the 4γ couplings by tree-level exchange as $\zeta_i^\gamma = (f_s\, m)^{-2}\, d_{i,s}$, where $d_{1,s}$ is related to the spin of the particle. Strongly-coupled conformal extensions of the SM contain a scalar particle ($s = 0^+$), the dilaton. Even a 2 TeV dilaton can produce a sizable effective photon interaction, $\zeta_1^\gamma \sim 10^{-13}$ GeV^{-4}. These features are reproduced at large number of colors by the gauge-gravity correspondence in a warped extra dimension. Warped-extra dimensions also feature Kaluza-Klein (KK) gravitons [31], that can induce anomalous couplings [30]

$$\zeta_i^\gamma = \frac{\kappa^2}{8\tilde{k}^4}\, d_{i,2}\,, \tag{156}$$

where $\tilde{k}$ is the IR scale that determines the first KK graviton mass and κ is a parameter that can be taken $\mathcal{O}(1)$. For $\kappa \sim 1$, and $m_2 \lesssim 6$ TeV, the photon vertex can easily exceed $\zeta_2^\gamma \sim 10^{-14}$ GeV^{-4}.

Experimental sensitivity to quartic four photon couplings

As we mentionned already, the $\gamma\gamma\gamma\gamma$ process (Fig. 61) can be probed via the detection of two intact protons in the forward proton detectors and two energetic photons in the corresponding electromagnetic calorimeters [20]. The SM cross section of diphoton production with intact protons is dominated by the QED process at high diphoton mass — and not by gluon exchanges — and is thus very well known.

As mentioned in Ref. [32], the photon identification efficiency is expected to be around 75% for $p_T > 100$ GeV, with jet rejection factors exceeding 4000 even at high pile-up (>100). In addition, about 1% of the electrons are mis-identified as photons. These numbers are used in the phenomenological study presented below.

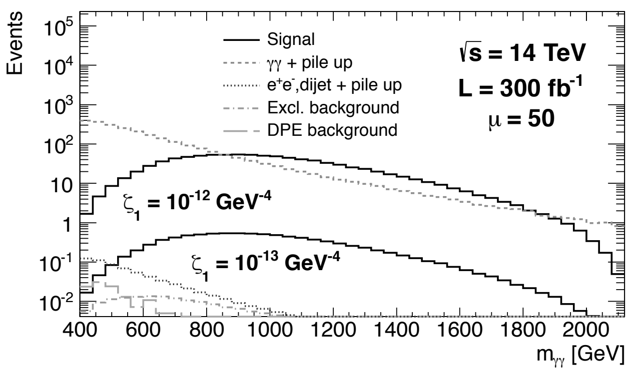

Figure 65: Diphoton invariant mass distribution for the signal ($\zeta_1 = 10^{-12},\ 10^{-13}$ Gev^{-4}, see Eq. 155) and for the backgrounds (dominated by $\gamma\gamma$ with protons from pile-up), requesting two protons in the forward detectors and two photons of $p_T > 50$ GeV with at least one converted photon in the central detector, for a luminosity of 300 fb^{-1} and an average pile-up of $\mu = 50$.

Cut / Process	Signal (full)	Signal with (without) f.f (EFT)	Excl.	DPE	DY, di-jet + pile up	$\gamma\gamma$ + pile up
$[0.015 < \xi_{1,2} < 0.15$, $p_{\mathrm{T}1,(2)} > 200, (100)$ GeV]	130.8	36.9 (373.9)	0.25	0.2	1.6	2968
$m_{\gamma\gamma} > 600$ GeV	128.3	34.9 (371.6)	0.20	0	0.2	1023
$[p_{\mathrm{T}2}/p_{\mathrm{T}1} > 0.95$, $\lvert\Delta\phi\rvert > \pi - 0.01]$	128.3	34.9 (371.4)	0.19	0	0	80.2
$\sqrt{\xi_1\xi_2 s} = m_{\gamma\gamma} \pm 3\%$	122.0	32.9 (350.2)	0.18	0	0	2.8
$\lvert y_{\gamma\gamma} - y_{pp}\rvert < 0.03$	119.1	31.8 (338.5)	0.18	0	0	0

Table 19: Number of signal events for $S = 1$, $Q_{\mathrm{eff}} = 4$, $m = 340$ GeV and background events after various selections for an integrated luminosity of 300 fb^{-1} and $\mu = 50$ at $\sqrt{s} = 14$ TeV. Values obtained using the corresponding EFT couplings with and without form factors are also displayed. At least one converted photon is required. Excl. stands for exclusive backgrounds and DPE for double pomeron exchange backgrounds (see text).

As for the previous studies, the anomalous $\gamma\gamma\gamma\gamma$ process has been implemented in the Forward

Physics Monte Carlo (FPMC) generator [23]. The FPMC generator was also used to simulate the background processes giving rise to two intact protons accompanied by two photons, electrons or jets that can mimic the photon signal. Those include exclusive SM production of $\gamma\gamma\gamma\gamma$ via lepton and quark boxes and $\gamma\gamma \to e^+e^-$. The central exclusive production of $\gamma\gamma$ via two-gluon exchange, not present in FPMC, was simulated using ExHuME [33]. This series of backgrounds is called "Exclusive" in Table 19 and Figs. 65, 66. FPMC was also used to produce $\gamma\gamma$, Higgs to $\gamma\gamma$ and dijet productions via double pomeron exchange (called DPE background in Table 19 and Fig. 65). Such backgrounds tend to be softer than the signal and can be suppressed with requirements on the transverse momenta of the photons and the diphoton invariant mass. In addition, the final-state photons of the signal are typically back-to-back and have about the same transverse momenta. Requiring a large azimuthal angle $|\Delta\phi| > \pi - 0.01$ between the two photons and a ratio $p_{T,2}/p_{T,1} > 0.95$ greatly reduces the contribution of non-exclusive processes.

Additional background processes include the quark and gluon-initiated production of two photons, two jets and Drell-Yan processes leading to two electrons. The two intact protons arise from pile-up interactions (these backgrounds are called $\gamma\gamma$ + pile-up and e^+e^-, dijet + pile-up in Table 19).These events were produced using HERWIG [34] and PYTHIA [35]. The pile-up background is further suppressed by requiring the proton missing invariant mass to match the diphoton invariant mass within the expected resolution and the diphoton system rapidity and the rapidity of the two protons to be similar.

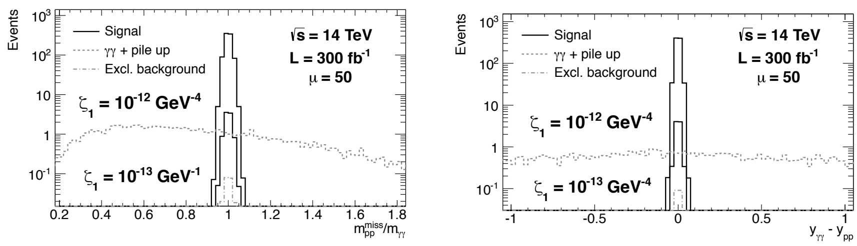

Figure 66: Diphoton to missing proton mass ratio (left) and rapidity difference (right) distributions for signal considering two different coupling values (10^{-12} and 10^{-13} GeV^{-4}, see Eq. 155) and for backgrounds after requirements on photon p_T, diphoton invariant mass, p_T ratio between the two photons and on the angle between the two photons. At least one converted photon is required. The integrated luminosity is 300 fb^{-1} and the average pile-up is $\mu = 50$.

The number of expected signal and background events passing respective selections is shown in Table 19 for an integrated luminosity of 300 fb^{-1} for a center-of-mass energy of 14 TeV [20]. Exploiting the full event kinematics with the forward proton detectors allows to completely suppress the background with a signal selection efficiency after the acceptance cuts exceeding 70%. Tagging the protons is absolutely needed to suppress the $\gamma\gamma$ + pile-up events. Further background reduction is even possible by requiring the photons and the protons to originate from the same vertex that provides an additional rejection factor of 40 for 50 pile-up interactions, showing the large margin on the background suppression. A similar study at a higher pile-up of 200 was performed and led to a very small background. The sensitivities on photon quartic anomalous couplings are given in Table 20. The sensitivity extends up to $7 \cdot 10^{-15}$ GeV^{-4} allowing us to probe further the models of new physics described above.

If discovered at the LHC, $\gamma\gamma\gamma\gamma$ quartic anomalous couplings would be a major discovery related to the existence of extra dimensions in the universe asa an example. In addition, it might be inveestigated if there could be a link with some experiments in atomic physics. As an example, the Aspect photon correlation experiments [36] might be interpreted via the existence of extra dimensions. Photons could communicate through extra dimensions and the deterministic interpretation of Einstein for these experiments might be true if such anomalous couplings exist. From the point of view of atomic

Luminosity	300 fb^{-1}	300 fb^{-1}	300 fb^{-1}	300 fb^{-1}	3000 fb^{-1}
pile up (μ)	50	50	50	50	200
coupling (GeV^{-4})	$\geq$ 1 conv. γ 5 σ	$\geq$ 1 conv. γ 95% CL	all γ 5 σ	all γ 95% CL	all γ 95% CL
ζ_1 f.f.	$8 \cdot 10^{-14}$	$5 \cdot 10^{-14}$	$4.5 \cdot 10^{-14}$	$3 \cdot 10^{-14}$	$2.5 \cdot 10^{-14}$
ζ_1 no f.f.	$2.5 \cdot 10^{-14}$	$1.5 \cdot 10^{-14}$	$1.5 \cdot 10^{-14}$	$9 \cdot 10^{-15}$	$7 \cdot 10^{-15}$
ζ_2 f.f.	$2 \cdot 10^{-13}$	$1 \cdot 10^{-13}$	$9 \cdot 10^{-14}$	$6 \cdot 10^{-14}$	$4.5 \cdot 10^{-14}$
ζ_2 no f.f.	$5 \cdot 10^{-14}$	$4 \cdot 10^{-14}$	$3 \cdot 10^{-14}$	$2 \cdot 10^{-14}$	$1.5 \cdot 10^{-14}$

Table 20: $5\,\sigma$ discovery and 95% CL exclusion limits on ζ_1 and ζ_2 couplings in GeV^{-4} (see Eq. 155) with and without form factor (f.f.), requesting at least one converted photon ($\geq$ 1 conv. γ) or not (all γ). All sensitivities are given for 300 fb^{-1} and $\mu = 50$ pile up events (medium luminosity LHC) except for the numbers of the last column which are given for 3000 fb^{-1} and $\mu = 200$ pile up events (high luminosity LHC).

physics, the results of the Aspect experiments would depend on the distance of the two photon sources. Further more, it is clear that extra dimensions might be relevant also for the fast expansion of the universe within inflation models.

5.5 Conclusion

In this section, we detailled the interest of tagging the intact protons to study in detail WW, ZZ and $\gamma\gamma$ productions via photon exchanges. Uprecedented sensitivities can be achieved at the LHC in the CMS-TOTEM and ATLAS experiments on quartic anomalous couplings, especially on $\gamma\gamma\gamma\gamma$ couplings, that will lead to one of the best sensitivity on extra dimensions at the LHC.

6 The installation of forward proton detectors in CMS and ATLAS

6.1 The AFP and CT-PPS projects

Several improvements are made to the ATLAS and CMS detectors to exploit the new energy regime of 13 TeV at the LHC; this section describes the project to install the ATLAS Forward Proton (AFP) detector at 206 and 214 meters on both sides of the ATLAS experiment [29] (see Fig. 67) and the similar project by the TOTEM and CMS collaborations, the so called CT-PPS, to be installed on both sides of the CMS detector. In this article, we will concentrate on the main characteristics of the AFP and CT-PPS detectors, while their physics reach was described in the previous section [20, 24, 25].

Each arm of the AFP detector will consist of two sections: AFP1 at 206 meters, and AFP2, at 220 meters. In AFP1, a tracking station composed by 6 layers of Silicon detectors will be deployed. The second section, AFP2, will contain a second identical tracking station and a timing detector. In addition, a similar structure could be installed at about 420 m from the ATLAS interaction point. The aim of the combined two arms of this setup is to tag the protons emerging intact from the pp interactions, allowing ATLAS to exploit the program of diffractive and photon induced processes described in the previous sections. Likewise, the CT-PPS of CMS will also use the same combination of tracking and timing detectors, with the far station using specially designed cylindrical roman pots to house the timing detectors.

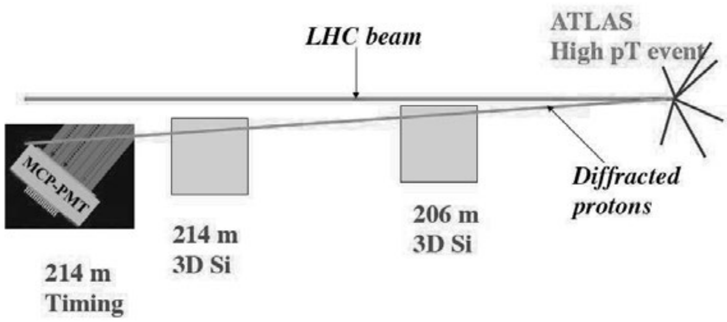

Figure 67: Scheme of the AFP proton detector in ATLAS. The same detector is implemented on the other side of ATLAS.

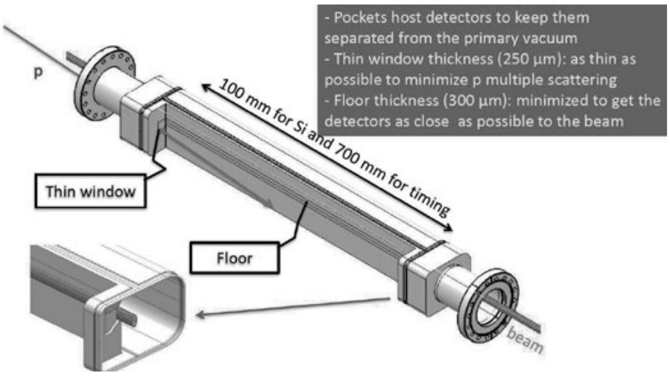

Figure 68: Scheme of the movable beam pipe.

6.2 Movable beam pipes and roman pots

In order to house the detectors needed by the AFP and CT-PPS projects, two different types of modification of the beam-pipe are currently considered: (i) roman pots and (ii) movable beam pipes). Roman pots have been used already in many experiments at the SPS, HERA, Tevatron and LHC colliders (in the TOTEM and ATLAS-ALFA experiments). The roman pots, in their basic design, are pockets where the detectors can be hosted. These pockets are pushed inside the beam pipe to a position closer to the beam line once stable beam has been declared (a typical motion is of the order of a few cm). To minimize multiple scattering, protons will enter the roman pots via a thin window located at the bottom of the pot, on the side facing the beams. Different types of roman pots can host the tracking and timing detectors: tracking detectors need less space than timing detectors, and therefore can be housed in smaller roman pots.

Conversely, in the movable beam pipe design, no pocket is pushed closer to the beam, but the whole beam pipe moves closer to the beam. The idea of movable Hamburg beam pipes is quite simple [37]: a section of the LHC beam pipe is replaced by a larger one, specially designed to have a cutout to host the detectors. When allowed by beam conditions, using specially designed bellows that allow for transverse motions, this part of the beam pipe is moved, by about 2.5 cm, so that the detectors located at its edge (called pocket) are brought closer to the beam. In its design, the most challenging aspect is the minimization of the thickness of the portions called floor and window (see Fig. 68). This is necessary as the floor might be rather long, of the order of 10-40 centimeters in the direction parallel to the motion of the particles: minimizing its depth of the floor ensures that the detectors can be brought as close to the beam as possible allowing detecting protons scattered at very small angles. Two configurations exist for the movable beam pipes: the first one at 206 m from the ATLAS interaction point hosts a Si detector (floor length of about 100 mm) and the second one (floor length of about 400 mm) the timing and the Si detectors.

The AFP and CT-PPS detectors will use Roman Pots in their starting configuration. In the meantime, the development of the Hamburg beam pipe is carried on together by both collaborations. However, it is clear that movable beam pipes are needed at 420 m, if later upgrades include installation of forward detectors at that location. At 420 m, not enough space is available and new specially designed cryostats have been developed to host these movable beam pipes in the cold region. The usage of roman pots at 420 m would require a costly cryogenic bypass to be installed to isolate the part of the beam pipe where roman pots would be installed.

6.3 3D Silicon detectors

The purpose of the tracker system is to measure points along the trajectory of beam protons that are deflected at small angles as a result of collisions. The tracker, when combined with the LHC dipole and quadrupole magnets, forms a powerful momentum spectrometer. Silicon tracker stations will be installed in Hamburg beam pipes or roman pots at ± 206 and ± 214 m from the ATLAS interaction point (and also at 420 m later if these additional detectors are appoved).

The key requirements for the silicon tracking system at 220 m are:

- Spatial resolution of $\sim$ 10 (30) μm per detector station in x (y)
- Angular resolution for a pair of detectors of a few μrad
- High efficiency over the area of 20 mm × 20 mm corresponding to the distribution of diffracted protons
- Minimal dead space at the edge of the sensors towards the beam line, allowing measuring the scattered protons at low angles
- Sufficient radiation hardness in order to sustain the radiation at high luminosity
- Capable of robust and reliable operation at high LHC luminosity

The basic building unit of the AFP detection system is a module consisting of an assembly of a sensor array, on-sensor read-out chip(s), electrical services, data acquisition and detector control system. The module will be mounted on the mechanical support with embedded cooling and other necessary services. The sensors are double sided 3D 50×250 micron pixel detectors with slim-edge dicing built by FBK and CNM companies. The sensor efficiency has been measured to be close to 100% over the full size in beam tests. A possible upgrade of this device will be to use 3D edgeless Silicon detectors built in a collaboration between SLAC, Manchester, Oslo, Bergen...

A new front-end chip FE-I4 has been developed for the Si detector by the Insertable B Layer (IBL) collaboration in ATLAS [38]. The FE-I4 integrated circuit contains readout circuitry for 26 880 hybrid pixels arranged in 80 columns on 250 μm pitch by 336 rows on 50 μm pitch, and covers an area of about 19 mm × 20 mm. It is designed in a 130 nm feature size bulk CMOS process. Sensors must be DC coupled to FE-I4 with negative charge collection. The FE-I4 is very well suited to the AFP requirements: the granularity of cells provides a sufficient spatial resolution, the chip is radiation hard enough up to a dose of 3 MGy, and the size of the chip is sufficiently large that one module can be served by just one chip.

The dimensions of the individual cells in the FE-I4 chip are 50 μm × 250 μm in the x and y directions, respectively. Therefore to achieve the required position resolution in the x-direction of $\sim$ 10 μm, six layers with sensors are required (this gives $50/\sqrt{12}/\sqrt{5} \sim 7$ μm in x and roughly 5 times worse in y). Offsetting planes alternately to the left and right by one half pixel will give a further reduction in resolution of at least 30%. The AFP sensors are expected to be exposed to a dose of 30 kGy per year at the full LHC luminosity of $10^{34}\mathrm{cm}^{-2}\mathrm{s}^{-1}$.

The baseline CT-PPS tracking system is also based on 3D pixel sensors, produced either by FBK (Trento, Italy) or CNM (Barcelona, Spain), which provide the best performance in terms of active region and radiation hardness.

The chosen configuration for the tracking system consists of two detector stations in each arm. Each station will contain one stack of silicon tracking detectors. Each stack will consist of six planes, where each plane conatains a 1.6×2.4 cm^2 pixel sensor read out by six PSI46dig readout chips ROCs [39]. Each ROC reads 52×80 pixels with dimensions 150×100 μm^2. The design of the front-end electronics and of the DAQ is based on that developed for the Phse I upgrade of the CMS silicon pixel detectors [40].

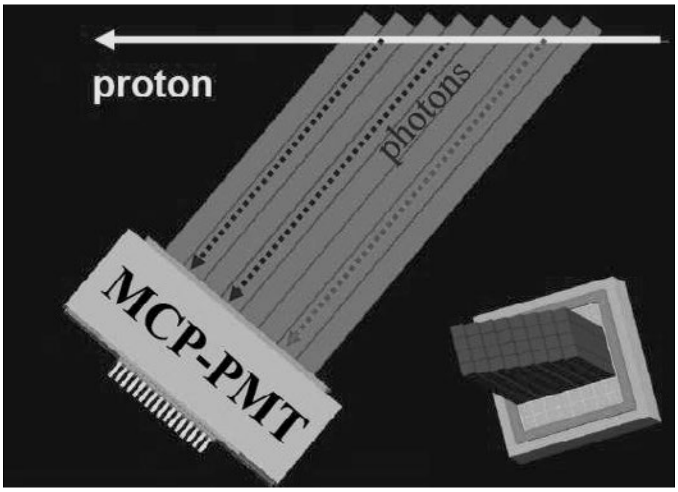

Figure 69: A schematic diagram of the QUARTIC fast timing detector.

6.4 Timing detectors

Requirements and present achievement

A fast timing system that can precisely measure the time difference between the two outgoing scattered protons is a key component of the AFP and CT-PPS detectors. The time difference is equivalent to a constraint on the event vertex, thus the AFP and CT-PPS timing detectors can be used to reject overlapping background events by establishing that the two scattered protons did not originate from the same vertex that triggered the central ATLAS or CMS detectors. The final timing system should have the following characteristics [41]:

- 10 ps or better resolution (which leads to a factor 40 rejection on pile up background)
- Efficiency close to 100% over the full detector coverage
- High rate capability (there is a bunch crossing every 25 ns at the nominal LHC)
- Enough segmentation for multi-proton timing
- High level trigger capability

Fig. 69 shows a schematic overview of the first proposed timing system in AFP, consisting of a quartz-based Cerenkov detector coupled to a microchannel plate photomultiplier tube (MCP-PMT), followed by the electronic elements that amplify, measure, and record the time of the event along with a stabilized reference clock signal. The QUARTIC detector consists of an array of 8×4 fused silica bars ranging in length from about 8 to 12 cm and oriented at the average Cerenkov angle. A proton that is sufficiently deflected from the beam axis will pass through a row of eight bars emitting

Cerenkov photons providing an overall time resolution that is approximately $\sqrt{8}$ times smaller than the single bar resolution of about 30 ps, thus approaching the 10 ps resolution goal. Prototype tests have generally been performed on one row (8 channels) of 5 mm × 5 mm pixels, while the initial detector is foreseen to have four rows to obtain full acceptance out to 20 mm from the beam. The beam tests lead to a time resolution per bar of the order of 34 ps. The upgraded design of the timing detector has equal rate pixels, and we plan to reduce the width of detector bins close to the beam, where the proton density is highest.

The CT-PPS also has a detector based on Cerenkov technology as the baseline proposal. It has chosen a Cherenkov L-bar Quartic design (Quartz Timing Cherenkov) with 5 × 4 equal to twenty 3 × 3 mm^2 independent channels. They are read-out by SiPM photodetectors, relatively far from the beam, in a region where the neutron flux is $\sim$2 10^{12} neq/cm^2 per 100 fb^{-1}. SiPM devices that tolerate this radiation level are available, and already in use in the CMS detector [42]. The SiPMs will probably require replacement after 100 fb^{-1}, which is feasible given the small number of devides involved. Two such Quartic detectors fit inside a cylindrical roman pot, providing a combined resolution of the order of 20 ps.

Future developments

At higher luminosity of the LHC (phase I starting in 2019), higher pixelisation of the timing detector will be required in order to fight against high pile up environment. For this sake, a R&D phase to develop timing detector developments based on Silicon sensors [11], and diamonds [43] has started. This new R&D aims at installing a prototype of such detector at the LHC in the TOTEM experiment as soon as they are available. In parallel to this sensor R&D, a new timing readout chip has been developed in Orsay/Saclay. It uses waveform sampling to reach the best possible timing resolution and it is described in detail in the next section.

The CT-PPS project has now been endorsed by the CMS and TOTEM collaboration at least for the first phase at low luminosity. If everythings works as expected, and the beam induced background (not easily simulated) is not found to be an issue at 14 TeV, the project will be naturally approved to work at higher luminosity. The AFP project is almost at the same stage, pending the approval at low luminosities until enough resources are found within and outside the ATLAS collaboration.

6.5 Timing detector optimisation for pile up rejection

In this section, we discuss possible optimisation of the timing detector in terms of spacial resolution in order to reject pile up background.

Proton detection in the forward region

The main source of background in the timing detectors is due to pile up events. Intact protons may obviously originate from the diffractive and photon-exchange events but also from additional soft interactions (pile up). For instance a non-diffractive WW event can be superimposed with two single diffractive soft events with intact porons and it is important to be able to distinguish this background from the event where both protons originate from the WW vertex. In order to suppress this background, it is useful to measure precisely the proton time-of-flights in order to know if the protons originate from the main event hard vertex or not.

Two parameters to build a detector are important to reject pile up:

- the precision of the proton time-of-flight, which is the timing detector resolution. Typically a measurement of 10 ps gives a precision of 2.1 mm on the vertex position
- the pixelisation of the timing detector: at highest luminosity, the number of intact protons per bunch crossing is high and in order to compute the time-of-flight of each proton it is needed

to have enough pixelisation or space resolution so that each proton can be detected in different cells of the timing detector. If two protons with different time-of-flight fall in the same cell, the information is lost.

Pixelisation of the timing detector

In order to study the required pixelisation of the timing detector, we simulated 10 million minimum bias events (non diffractive, single diffractive and double diffractive events) using the PYTHIA generator. The protons were transported through the LHC magnets up to the proton detectors. Events are characterised as no tagged (NT), single tagged (ST) and double tagged (DT) depending on the number of protons in the forward proton detector acceptance. For one minimim bias event, we get a probability of 97% NT, p =1.6% ST, and q =0.01% DT. The multinomial distribution was adopted to simulate pile up since we assume that the different interactions are independant [44]. For a given number of pile up proton N, the probability to have N_L (N_R) protons tagged in the left (right) side only, N_B protons on both sides and N_N protons not tagged reads:

$$P(N_B, N_L, N_R, N_N) = \frac{N!}{N_B! N_L! N_R! N_N!} p^{N_L} q^{N_B} p^{N_R} (1-2p-q)^{N_N} \tag{157}$$

and the probability of no proton tagged, of at least one proton tagged on the left side, and of at least one proton tagged on both sides reads

$$\begin{aligned} P_{no\ hit} &= P(0,0,0,N) = (1-2p-q)^N && (158)\\ P_{hit\ left} &= \sum_{N_L=1}^{N} P(0,N_L,0,N-N_L) = (1-p-q)^N - (1-2p-q)^N && (159)\\ P_{double\ hit} &= 1 - P_{no\ hit} - 2P_{hit\ left} = 1 + (1-2p-q)^N - 2(1-p-q)^N && (160) \end{aligned}$$

μ	P_N	$P_{S,left}$	$P_{S,right}$	P_D
0	0.97	0.016	0.016	9.9e-05
50	0.189	–	0.248	0.316
100	0.036	–	0.155	0.655
300	0.	–	0.007	0.986

Figure 70: No tag, single tag on the left or right side (same by definition) and double tagged probablity.

The hit probabilities can then be calculated for various pile up values (see Fig. 70). For a pile up μ =50 (100) for instance, the probability of no tag is 19% (3.6%). Let us note that this simplified approach does not work at very high pile up (300 for instance) since we neglected the cases when two or more protons from pile up events can hit one side of the detector at the same time. In order to illustrate this, the percentage of events corresponding to 0, 1, 2, 3... protons on one side for μ =50, 100 and 300 is given in Fig. 71. This leads to larger inefficiencies that can be taken account in a more refined approach or by a full pile up simulation, which was performed for the $\gamma\gamma\gamma\gamma$ quartic anomalous coupling study. The detector needed to detect intact protons has a coverage of about 2 cm$\times$2 cm and is located 15σ from the beam. The inefficiency of such a detector assuming 20$\times$8 pixels is given in Fig. 72. The numbers displayed in the table correspond to the probability of getting one proton or more in a given pixel for μ =100 or a 20$\times$8 pixellised detector. The upper limit on the inefficiencies if the order of 8% for the pixels closest to the bins, but is found negligible for pixels further away which measure higher mass diffractive objects. For comparison, the inefficiences for μ =50 is about half, and vertical bar detectors lead to larger inefficiencies between 10 and 20% on a large part of the detector (a 7 bar detector with 2 mm width for the first bar and 3.25 mm for other bars, leads to inefficiences betweem 8% and 19% for the first 6 bars). It is also worth mentioning that this study only includes physics backgrounds and not beam-induced backgrounds which are not in the simulation. Recent results from TOTEM show that the beam-induced backgrounds have the tendency to be high and located in the pixels closest to the beam [45], and this is why a full pixelised detector is preferable to bars.

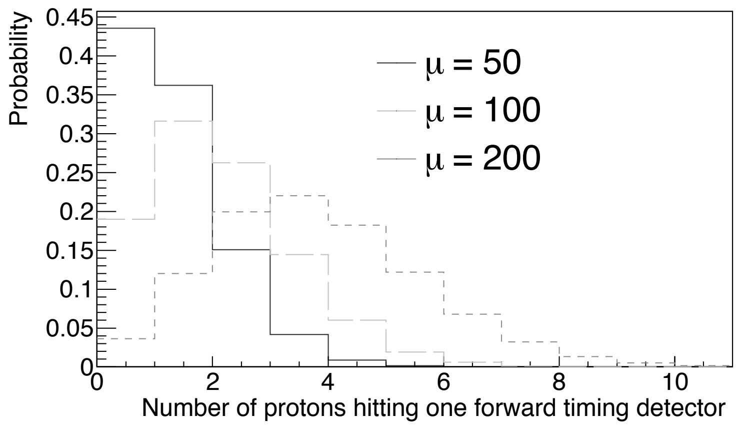

Figure 71: Probability of getting 0, 1, 2, 3... intact protons on one side of the detector for 3 different values of μ.

Inefficiencies - 20x8 pixel design - μ = 100										
Row/Column	1	2	3	4	5	6	7	8	9	10
8	0.	0.	0.	0.	0.	0.	0.	0.	0.	0.
7	0.	0.	0.	0.	0.	0.	0.	0.	0.	0.
6	0.038	0.002	0.	0.	0.	0.	0.	0.	0.	0.
5	0.067	0.077	0.051	0.006	0.001	0.001	0.001	0.001	0.001	0.
4	0.001	0.001	0.015	0.049	0.042	0.024	0.012	0.006	0.004	0.003
3	0.	0.	0.	0.001	0.007	0.019	0.022	0.018	0.013	0.008
2	0.	0.	0.	0.	0.	0.002	0.006	0.010	0.012	0.011
1	0.	0.	0.	0.	0.	0.	0.001	0.003	0.005	0.007
Row/Column	11	12	13	14	15	16	17	18	19	20
8	0.	0.	0.	0.	0.	0.	0.	0.	0.	0.
7	0.	0.	0.	0.	0.	0.	0.	0.	0.	0.
6	0.	0.	0.	0.	0.	0.	0.	0.	0.	0.
5	0.001	0.001	0.001	0.001	0.001	0.	0.	0.	0.	0.
4	0.002	0.002	0.001	0.001	0.001	0.001	0.001	0.001	0.001	0.
3	0.006	0.004	0.003	0.003	0.002	0.002	0.001	0.001	0.001	0.
2	0.010	0.008	0.006	0.004	0.004	0.003	0.003	0.002	0.002	0.
1	0.008	0.008	0.007	0.006	0.005	0.004	0.004	0.003	0.003	0.

Figure 72: Probability of more than 1 proton to fall in a given pixel of the timing detector.

7 The SAMPIC chip

7.1 Introduction: Timing measurements in particle physics and in medical imaging

In order to measure rare events at the LHC, the luminosity (or in other words the number of interactions per second) has to be as large as possible. In order to achieve this goal, the number of interactions per bunch crossing can be very large, up to 40-70 during the LHC running of 2015-2017 as an example. Timing measurements are crucial at the LHC in order to determine if the intact protons originate from the main hard interaction or from secondary ones (pile up). Measuring the proton time-of-flight with a typical precision of 10 ps allows constraining the protons to originate from the main interaction point of the event (hard interaction) with a precision of about 2.1 mm. For a pile up of 40 (which means about 40 interactions occuring in the same bunch crossing at the LHC), such a precision on time-of-flight measurements leads to a reduction in background of a factor of about 40 [44].

Timing measurements have also many applications in drone technology and in medical imaging as an example. The "holy grail" of medical imaging would be a PET detector with a 10 ps timing precision. With such an apparatus, image reconstruction is no longer necessary (the analysis can be performed online) since many fake coincidences can be suppressed, only attenuation corrections are needed, and real time image formation can be performed.

In order to achieve a 10 ps precision, many steps are needed going from the detector to the electronics and the readout software. In this article, we will concentrate on the achievement concerning the picosecond timing electronics that is currently being done in IRFU/SEDI Saclay and in LAL-Orsay [46, 47].

7.2 SAMPIC: SAMpler for PICosecond time pick-off

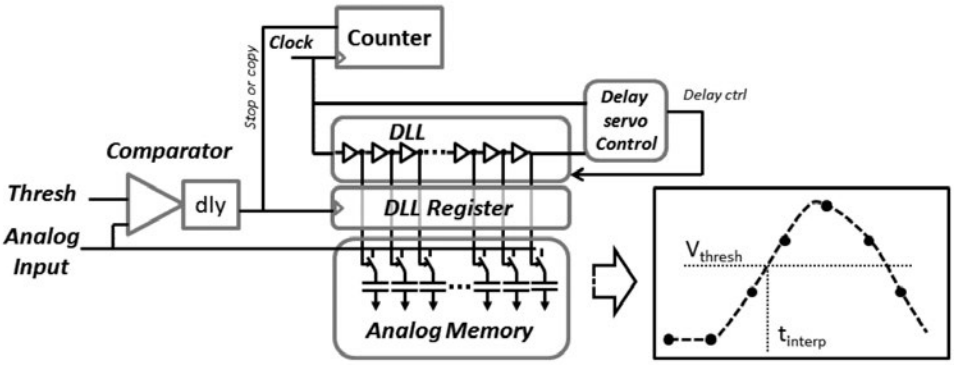

Figure 73: Scheme of the SAMPIC chip.

Figure 74: Picture of the SAMPIC chip and its acquisition board.

Before SAMPIC, the most performant Time to Digit Converters (TDCs) used digital counters and Delay Line Loops (DLLs). The timing resolution is limited by the DLL step and with most advanced Application Specific Integrated Circuit (ASICs), one gets a resolution of about 20 ps (new developments at CERN target 5 ps). The inconvenient is that a TDC needs a digital input signal: the analog input signal has to be transformed into a digital one with a discriminator which means that the timing resolution will be given by the quadratic sum of the discriminator and the TDC timing resolutions, thus leading to worse timing resolutions.

A new approach had to be developed using the principle of a wafeform based TDC. The idea is to acquire the full waveform shape of a detector signal in an ASIC dedicated to picosecond timing measurements. The input signal range has to be between 0.1 and 1. V with a fast rising time up to 1.ns in order to get the best possible performance of SAMPIC. The present version of the chip holds 16 channels (50 Ω terminated) with independent dead time. The possible trigger modes are either self triggered or triggered externally. Each channel includes an analog memory (64 cells) and recording is triggered by a discriminator. A Gray counter associated to DLLs allows assigning a time to the different samples and an ADC provides the conversion into a digital signal.

Three timing measurements with different precision are performed in SAMPIC. The time stamp Gray counter has a 6 ns step (it samples the reference clock), the DLL 150 ps (it defines a region of interest) and the waveform shape a few ps RMS after interpolation between the acquired points (they are acquired on a 64 step analog memory).

As we already mentioned, SAMPIC acquires the full waveform shape of a detector signal. The discriminator is used only for triggering, not for timing, and thus there is no jitter originating from the discriminator. All the information concerning the signal is kept in SAMPIC, and it is possible to use offline signal processing algorithms in order to improve the timing resolution. It can also be used to obtain other signal characteristics such as the deposited charge. In the present version, SAMPIC suffers an important dead time per channel due to the ADC conversion of about 1 μs. It will be reduced by about one order a magnitude in the next version of SAMPIC, using in particular the so called "ping-pong" method and analog buffering. Two SAMPIC chips can be hosted in a mezzanine board developed in LAL, Orsay, leading to a 32-channel system. The input into SAMPIC is sent via MCX connectors. SAMPIC can be read out using an USB-Ethernet-Optic fiber readout is also provided. A 5 V voltage power supply is the only element needed to run the mezzanine board and the readout software runs on Windows or Linux. A scheme of SAMPIC is given in Fig. 74 and a picture of SAMPIC together with its acquisition board in Fig. 72.

SAMPIC is quite cheap (about 10 Euros per channel) with respect to a few 1000s Euros for previous technology, which means that it can be used in large scale detectors such as PET for medical applications.

As a reference, a table giving the parameters of the SAMPIC chip is given in Fig. 75.

7.3 SAMPIC performance

Electronics tests

In this section, we describe the SAMPIC performance obtained from pure electronics tests. The maximum signal size is about 1.V, and after corrections, the average noise is quite low, of about 1 mV RMS (the noisiest cells being 1.5 mV RMS), which means a dynamic 10 bits RMS.

The SAMPIC cross talk was measured by sending a signal of 800 mV with a 300 ps rise time on one channel and reading out the neighbouring channels. The cross talk was found to be less than 1%. The quality of sampling was tested using a sinus wave signal, and the signal was perfectly reproduced without corrections at a sampling frequency of 10 Gigasamples per second. The sampling speed in SAMPIC is possible between 3 and 8.2 Gigasamples per second on 16 channels (up to 10 Gigasamples per second for 8 channels).

The timing resolution was studied by using two different channels of SAMPIC. The same signal was sent on both channels, one being delayed compared to the other one using a delay box or longer cables. The pulse had an amplitude of about 1.2 V, and we used the 6.4 Gigasamples per second

		Unit
Technology	AMS CMOS 0.18µm	
Number of channels	16	
Power consumption	180 (1.8V supply)	mW
Discriminator noise	2	mV rms
SCA depth	64	Cells
Sampling Speed	<3-8.4 (10.2 for 8 channels only)	GSPS
Bandwidth	1.6	GHz
Range (Unipolar)	1	V
ADC resolution	8 to 11 (trade-off time/resolution)	bit
SCA noise	<1.3	mV rms
Dynamic range	9.6	Bit rms
Conversion time	0.2-1.6 (8bit-11bit)	µs
Readout time (can be probably be /2)	25 + 6.2/sample	ns
Time precision before correction	15	ps rms
Time precision after timing INL correction	< 5	ps rms

Figure 75: Parameters of the SAMPIC chip.

configuration. The RMS of the time difference between the two signals as a function of delay is given in Fig. 76 using two different offline algorithms to reconstruct the time difference (CDF as constant fraction discriminator and CC as cross correlation using a linear or a spline interpolation between the different points measured by SAMPIC). The time resolution is quite flat as a function of the delay between the two signals and is about 5 ps, leading to a time resolution per channel of about 4 ps.

A similar study of the timing resolution versus the signal amplitude is shown in Fig. 77. The signal has to be above 450 mV in order to obtain the best timing resolution possible of about 4 ps.

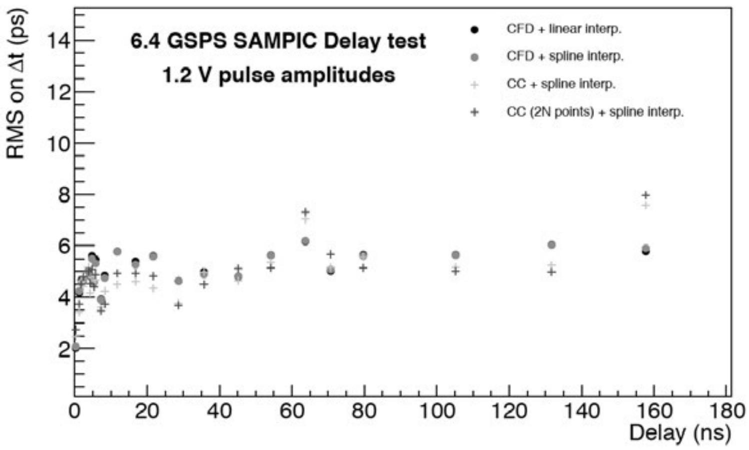

Figure 76: RMS on the time difference between two signals, one being delayed with respect to the other using two offline algorithms (Constant Fraction Discriminator (CFD) and cross correlation (CC)) using a linear or a spline interpolation.

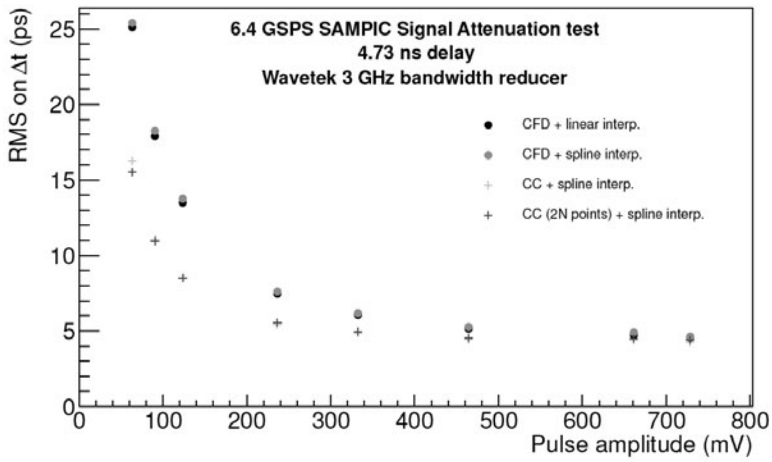

Figure 77: RMS on the time difference between two signals as a function of the signal amplitude using two offline algorithms (Constant Fraction Discriminator (CFD) and cross correlation (CC)) using a linear or a spline interpolation.

Timing resolution using detectors

The second series of tests was performed by plugging SAMPIC into a real detector. We used a laser signal splitted in two, and going through two fast Si detectors [11]. The time difference between the two channels was measured using SAMPIC. The result is shown in Fig. 78 using the offline cross correlation algorithm. The time resolution is about 30 ps. It is of course dominated by the fast Si detectors, the resolution of SAMPIC being of the order of 4 ps. Additional studies are being performed in beam tests using diamond detectors leading to a time resolution of 80 to 90 ps [48].

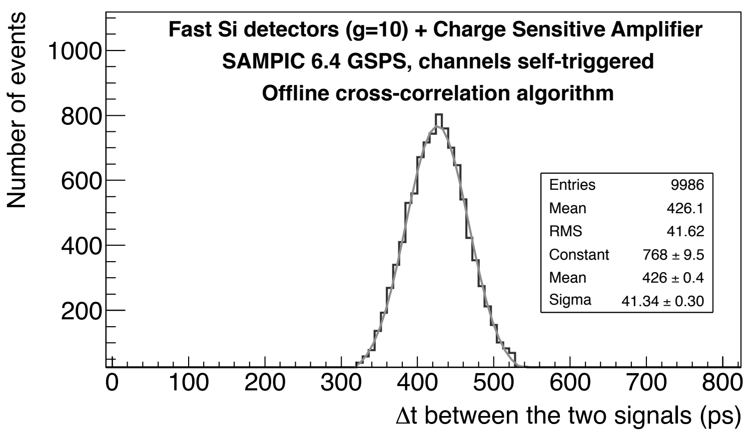

Figure 78: Time difference between two SAMPIC channels reading out Si detectors, a laser signal splitted in two going through the two Si detectors.

7.4 Conclusion

A self triggered timing chip demonstrator has been designed and characterised with 1.6 GHz bandwidth, up to 10 Gigasamples per second, low noise and of the order of 4 ps timing resolution. The chip is now ready and can be used for tests. Tests already started within the AFP, CT-PPS and CMS/TOTEM projects using quartz, diamond and Si detectors. Work is still going on in order to improve the chip concerning the DAQ system optimisation (firmware and software) and the improvement of the dead time using the "ping-pong" method. SAMPIC can now be used in many applications for tests in addition to particle physics for instance in medical imaging, drones, in detectors including many channels due to the low cost per channel.

8 Conclusion

In these lectures, we described some topics related to diffraction at the LHC going from soft diffraction to hard inclusive, exclusive diffraction and to photon-exchange processes. We finished by describing the experimental setup that is being built by the CMS, TOTEM and ATLAS collaborations.

Acknowledgments

The write up of these lectures was based on many publications and proceedings with my collaborators and I would like to thank D. Breton, V. de Caqueray, N. Cartiglia, E. Chapon, E. Delagnes, S. Fichet, G. von Gersdorff, H. Grabas, Y. Hatta, O. Kepka, J. Maalmi, C. Marquet, N. Minafra, R. Peschanski, M. Saimpert, L. Schoeffel, G. Soyez, R. Staszewski, M. Trzebinski, D. Werder...

References

1. J. C. Collins, Phys. Rev. D **57**, 3051 (1998) [Erratum: Phys. Rev. D **61**, 019902 (2000)] [hep-ph/9709499 [hep-ph]].
2. A. Aktas *et al.* [H1 Collaboration], Eur. Phys. J. C **48**, 715 (2006) [hep-ex/0606004 [hep-ex]].
3. A. Aktas *et al.* [H1 Collaboration], Eur. Phys. J. C **48**, 749 (2006) [hep-ex/0606003 [hep-ex]].
4. C. Adloff *et al.* [H1 Collaboration], Z. Phys. C **76**, 613 (1997) [hep-ex/9708016 [hep-ex]].
5. C. Royon, L. Schoeffel, S. Sapeta, R. B. Peschanski and E. Sauvan, Nucl. Phys. B **781**, 1 (2007) [hep-ph/0609291 [hep-ph]]; C. Royon, L. Schoeffel, R. B. Peschanski and E. Sauvan, Nucl. Phys. B **746**, 15 (2006) [hep-ph/0602228 [hep-ph]].
6. G. Altarelli and G. Parisi, Nucl. Phys. B **126**, 298 (1977); V. N. Gribov and L. N. Lipatov, Sov. J. Nucl. Phys. **15**, 438 (1972) [Yad. Fiz. **15**, 781 (1972)]; V. N. Gribov and L. N. Lipatov, Sov. J. Nucl. Phys. **15**, 675 (1972) [Yad. Fiz. **15**, 1218 (1972)]; Y. L. Dokshitzer, Sov. Phys. JETP **46**, 641 (1977) [Zh. Eksp. Teor. Fiz. **73**, 1216 (1977)].
7. *Report from the LHC Forward Physics Working Group*, edited by N. Cartiglia and C. Royon (2015).
8. http://hep.fi.infn.it/LHCf [LHCf Collaboration].
9. http://lhcb.web.cern.ch/lhcb/Physics-Results/LHCb-Physics-Results [LHCb Collaboration].
10. https://twiki.cern.ch/twiki/bin/view/ALICEpublic /ALICEPublicResults [ALICE Collaboration].
11. C. Royon and N. Cartiglia, Int. J. Mod. Phys. A **29**, 1446017 (2014); N. Cartiglia, in Proceedings of the workshop on timing detectors, Clermont-Ferrand (2014).
12. ATLAS Collaboration, report CERN-LHCC-2011-012; TOTEM Collaboration, report CERN-LHCC-2014-020; CMS and TOTEM Collaborations, report CERN-LHCC-2014-021.
13. T. Martin, in CERN yellow report on LHC Forward Physics, to be published.
14. C. Royon, these proceedings.
15. R. Aaij *et al.* [LHCb Collaboration], J. Phys. G **41**(11), 115002 (2014) [arXiv:1407.5973 [hep-ex]].
16. https://twiki.cern.ch/twiki/bin/view/LHCb/PrelimExclDiMu [LHCb Collaboration].
17. V. A. Khoze, A. D. Martin and M. G. Ryskin, Eur. Phys. J. C **23**, 311 (2002) [hep-ph/0111078 [hep-ph]].
18. U. Maor, these proceedings.

19. http://totem-experiment.web.cern.ch/totem-experiment [TOTEM Collaboration]; http://atlas.cern [ATLAS Collaboration].
20. S. Fichet, G. von Gersdorff, O. Kepka, B. Lenzi, C. Royon and M. Saimpert, Phys. Rev. D **89**, 114004 (2014) [arXiv:1312.5153 [hep-ph]]; S. Fichet, G. von Gersdorff, B. Lenzi, C. Royon and M. Saimpert, JHEP **1502**, 165 (2015) [arXiv:1411.6629 [hep-ph]].
21. E. Chapon, C. Royon and O. Kepka, Phys. Rev. D **81**, 074003 (2010) [arXiv:0912.5161 [hep-ph]]; O. Kepka and C. Royon, Phys. Rev. D **78**, 073005 (2008) [arXiv:0808.0322 [hep-ph]].
22. D. d'Enterria and G. G. da Silveira, Phys. Rev. Lett. **111**, 080405 (2013) [Erratum: Phys. Rev. Lett. **116**(12), 129901 (2016)][arXiv:1305.7142 [hep-ph]]; H. Sun, Eur. Phys. J. C **74**(8), 2977 (2014) [arXiv:1406.3897 [hep-ph]].
23. M. Boonekamp, A. Dechambre, V. Juranek, O. Kepka, M. Rangel, C. Royon and R. Staszewski, arXiv:1102.2531 [hep-ph]; M. Boonekamp, V. Juranek, O. Kepka and C. Royon, in "*Proceedings of the workshop: HERA and the LHC workshop series on the implications of HERA for LHC physics,*" arXiv:0903.3861 [hep-ph].
24. E. Chapon, C. Royon and O. Kepka, Phys. Rev. D **81**, 074003 (2010) [arXiv:0912.5161 [hep-ph]]; J. de Favereau de Jeneret *et al.*, arXiv:0908.2020 [hep-ph].
25. O. Kepka and C. Royon, Phys. Rev. D **78**, 073005 (2008) [arXiv:0808.0322 [hep-ph]].
26. G. Belanger and F. Boudjema, Phys. Lett. B **288**, 201 (1992).
27. G. Abbiendi *et al.* [OPAL Collaboration], Phys. Rev. D **70**, 032005 (2004) [hep-ex/0402021 [hep-ex]].
28. S. Chatrchyan *et al.* [CMS Collaboration], JHEP **1307**, 116 (2013) [arXiv:1305.5596 [hep-ex]]; V. M. Abazov *et al.* [D0 Collaboration], Phys. Rev. D **88**, 012005 (2013) [arXiv:1305.1258 [hep-ex]].
29. ATLAS Collaboration, report CERN-LHCC-2011-012; M. G. Albrow [CMS and TOTEM Collaborations], PoS DIS **2015** (2015) 064.
30. S. Fichet and G. von Gersdorff, JHEP **1403**, 102 (2014) [arXiv:1311.6815 [hep-ph]]; R. S. Gupta, Phys. Rev. D **85**, 014006 (2012) [arXiv:1111.3354 [hep-ph]].
31. L. Randall and R. Sundrum, Phys. Rev. Lett. **83**, 3370 (1999) [hep-ph/9905221 [hep-ph]].
32. ATL-PHYS-PUB-2013-009, ATLAS Collaboration; G. Aad *et al.* [ATLAS Collaboration], JINST **3**, S08003 (2008).
33. J. Monk and A. Pilkington, Comput. Phys. Commun. **175**, 232 (2006) [hep-ph/0502077 [hep-ph]]; V. A. Khoze, A. D. Martin and M. G. Ryskin, Eur. Phys. J. C **55**, 363 (2008) [arXiv:0802.0177 [hep-ph]].
34. G. Corcella, I. G. Knowles, G. Marchesini, S. Moretti, K. Odagiri, P. Richardson, M. H. Seymour and B. R. Webber, hep-ph/0210213 [hep-ph].
35. T. Sjostrand, S. Mrenna and P. Z. Skands, Comput. Phys. Commun. **178**, 852 (2008) [arXiv:0710.3820 [hep-ph]].
36. A. Aspect, P. Grangier and G. Roger, Phys. Rev. Lett. **49**, 91 (1982); A. Aspect, J. Dalibard and G. Roger, Phys. Rev. Lett. **49**, 1804 (1982).
37. K. Piotrzkowski, U. Schneekloth, in Proc. of the ZEUS Collaboration meeting, DESY, Hamburg (1994).
38. ATLAS IBL Collaboration, report CERN-LHCC-2010-013 [ATLAS-TDR-019 5/09/2010].
39. H. C. Kästli, Nucl. Instrum. Meth. A **731**, 88 (2013).
40. CMS Collaboration, report CERN-LHCC-2012-016; CMS Collaboration, report CMS-TDR-11.
41. A. Brandt, in Microchannel Plate PMT Lifetime and Performance, DIRC2011: Workshop on Fast Cerenkov detectors, Giessen (2011).
42. CMS Collaboration, report CERN-LHCC-2012-015; CMS Collaboration, report CMS-TDR-010.
43. G. Chiodini, in Proceedings of the workshop on timing detectors, Clermont-Ferrand (2014).
44. C. Royon, M. Saimpert, O. Kepka, R. Žlebčík, Acta Phys. Polon. B, Proceedings supplement, **7**(4), 735 (2014).

45. M. Beretti, talk given at *LHC Working Group on Forward Physics and Diffraction*, Trento (2014).
46. E. Delagnes, H. Grabas, D. Breton, J. Maalmi, P. Rusquart, Acta Phys. Polon. B, Proceedings supplement, **7**(4), 685 (2014).
47. D. Breton, E. Delagnes, J. Maalmi, P. Rusquart, Acta Phys. Polon. B, Proceedings supplement, **7**(4), 685 (2014).
48. Beam tests performed at CERN/DESY [TOTEM Collaboration], private communication.

Gary Shiu

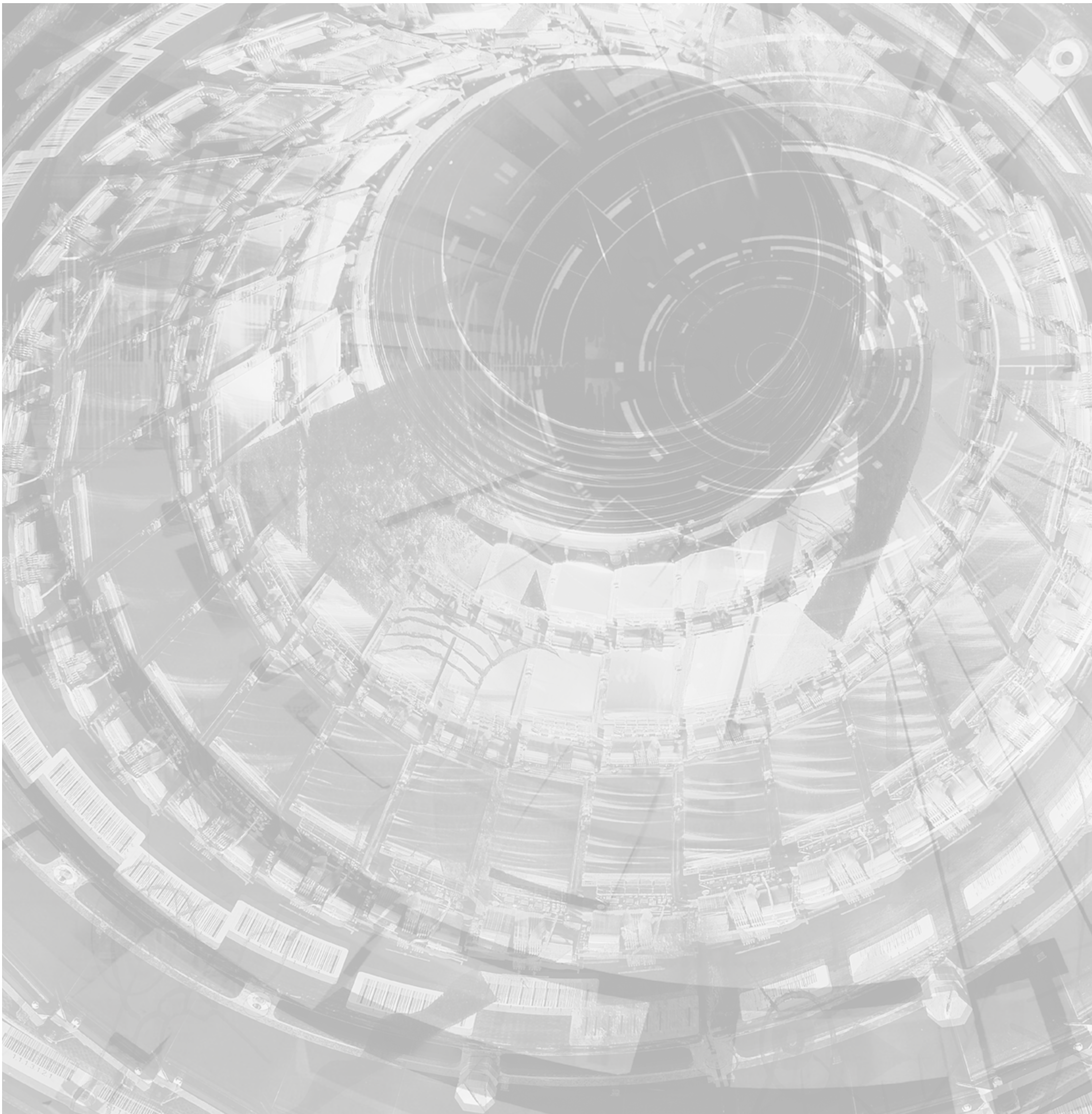

String Theory and Particle Physics Model Building

Gary Shiu [k]

[k]Department of Physics, University of Wisconsin, Madison, USA

Abstract

These lectures are devoted to introducing some basic notions of string theory, with an emphasis on their applications to particle physics model building. I will discuss different ways of building four-dimensional string vacua with $\mathcal{N} \leq 1$ supersymmetry, and various attempts to construct realistic models. Focussing on D-brane models, I will describe how several beyond the Standard Model ideas such as supersymmetry, extra dimensions (large or warped), and technicolor-like theories can arise in string theory.

1 Introduction

String theory is by far our best developed quantum theory of gravity. As such, it provides a consistent framework to address questions about early universe cosmology and black hole physics. As other lecturers in this school have discussed, the holographic principle provides a powerful tool to study strongly coupled gauge theories akin to QCD. But does string theory have anything to say about physics beyond the Standard Model (BSM) that we hope to unveil from the LHC?

Many of us have our own favorite scenario (or scenarios) of BSM physics. Only experiment can tell, and it may well be something that nobody has thought about. However, it is fair to say that the main contenders of BSM physics are:

- Supersymmetry
- Extra Dimensions
- Strong dynamics (technicolor)

Let's see how string theory score on this front. Supersymmetry was discovered to some extent first in the context of string theory, as a way to introduce fermions and to remove the unwanted tachyons (see, e.g., recent textbooks [1–5]). The idea of extra dimensions dated back to Kaluza and Klein so string theory cannot claim credit for their discovery. However, theories with extra dimensions are not renormalizable. To make sense of these theories, we need to complete them in the UV. String theory provides such a UV completion. In fact, string theory *requires* extra dimensions. Moreover, as we will see in these lectures, there are stringy constraints on extra dimensional physics that are not apparent from a low-energy bottom-up approach. So, one might hope that string theory can shed light on what kinds of extra dimensional scenarios are more likely to be realized in nature. Finally, technicolor [6, 7], just like extra dimensions, was introduced without any input from string theory. Nevertheless, one of the earlier proponents of this idea is a string theorist! More importantly, the advent of the AdS/CFT correspondence [8–11] provides a dual gravity description of such theories, and have offered insights into technicolor model building. In contrast to what we might have thought, string theory has a lot to say about BSM physics. More generally, the driving force behind the studies of physics beyond the Standard Model is arguably the hierarchy problem which is intrinsically about the existence of a high cutoff scale. String theory is one of the best motivated theories at work at such high energies. At any rate, string theory has shown to be a rather rich scenario generator. While we are still in the dark waiting for the dawn, string theory ideas such as branes and different extra dimensional scenarios may shed light on what to anticipate at the LHC.

Therefore, my lectures will be centering around string constructions with a view towards these BSM ideas. I will first introduce the five different superstring theories which are formulated in 10 dimensions and discuss their low energy effective theories upon compactication. As you will see, D-brane models allow for the possibility of a much lower fundamental scale and so are of interests to the LHC. I then discuss different ways in which chirality can arise in D-brane models, and apply these results to building "semi-realistic" models. Finally, I will discuss how warped models can be constructed from string theory. These models are string theory realizations of the Randall-Sundrum scenario [12, 13]. They can also be thought of as the gravity duals of technicolor theories.

My lectures are drawn heavily from my review articles [14, 15] and several excellent lectures notes on the subject [16, 17]. I refer the readers to the review and these lecture notes for details that I have omitted and for references therein. Due to severe page limitations, the list of references in this set of lecture notes will be kept to a minimal. I apologize to those whose important work has not been properly cited. Fortunately, the referencing in the aforementioned articles is rather exhaustive and so the readers should be able to start from the references given there and follow the trails.

2 String Theory Scenarios

2.1 The Pre D-brane Era

First, let us go back in time to the mid 1980s (when many of the students in the school were still babies!) and assess the state of string phenomenology. It was known that there are five consistent string theories, all formulated in ten dimensions: Type I theory with gauge symmetry $SO(32)$ (open and closed strings), Type IIA and IIB closed strings, and two closed heterotic strings with gauge symmetries $E_8 \times E_8$ and $SO(32)$ respectively. The massless spectrum of these five string theories are shown in the table. The yet unknown extension of string theory, M-theory, adds a further theory

Theory	Strings	Supercharges	Bosonic Spectrum
Heterotic $E_8 \times E_8$	Closed Oriented	16	$g_{\mu\nu}$, $B_{\mu\nu}$, ϕ $A_\mu^{i\bar{j}}$ in adjoint rep.
Heterotic $SO(32)$	Closed Oriented	16	$g_{\mu\nu}$, $B_{\mu\nu}$, ϕ $A_\mu^{i\bar{j}}$ in adjoint rep.
Type I $SO(32)$	Open Closed Unoriented	16	NS-NS: $g_{\mu\nu}$, ϕ R-R: C_2 Open: $A_\mu^{i\bar{j}}$ in adjoint rep.
Type IIA	Closed Oriented	32	NS-NS: $g_{\mu\nu}$, $B_{\mu\nu}$, ϕ R-R: C_1, C_3
Type IIB	Closed Oriented	32	NS-NS: $g_{\mu\nu}$, $B_{\mu\nu}$, ϕ R-R: C_0, C_2, C_4

Table 21: The massless bosonic spectrum for the five consistent string theories in 10-dimensions. In Type I and II theories, the spectrum is splitted into an NS-NS sector corresponding to states built out of two worldsheet bosonic states in the NS-R formulation of the theories and a R-R sector corresponding to those constructed from two worldsheet fermionic states. The number of supersymmetries is related to the number of supercharges. 16 supercharges correspond to $\mathcal{N} = 1$ supersymmetry in 10 dimensions, leading to $\mathcal{N} = 4$ supersymmetry in 4D upon dimensional reduction on a torus, whereas 32 supercharges correspond to $\mathcal{N} = 2$ and $\mathcal{N} = 8$ in 10D and 4D respectively.

to these five, which has the massless spectrum of 11-dimensional supergravity g_{MN}, C_{MNP} (plus the fermionic partners). One can appreciate the difficulty in constructing a realistic string model by comparing the spectrum in this table to that of the Standard Model.

A few observations are in order:

- Among the five string theories, three of them (Type I and the two heterotic strings) already contain gauge bosons in ten dimensions. They seem more promising as a starting point to construct the Standard Model and chiral fermions upon dimensional reduction.
- For this reason, Type II theories look much less interesting. There was even a no-go theorem which forbids them to produce the Standard Model at low energies [18]. We will revisit this no-go theorem again after we discuss D-branes.
- The heterotic $E_8 \times E_8$ attracted much of the attention because it seems the most promising for phenomenology: upon compactification to 4D, it can give rise to chiral $\mathcal{N} = 1$ supersymmetric models with familiar gauge and matter content. The observable sector comes from the first E_8 which contains the Standard Model gauge symmetry

$$E_8 \supset SU(3) \times SU(2) \times U(1) \tag{161}$$

  and several families of mater fields. The second E_8 gives rise to a hidden sector, which fits perfectly with attempts of supersymmetric model building prior to string theory. A hidden sector was often proposed to break supersymmetry at an intermediate scale $\sim 10^{12}$ GeV and gravity plays the role of messenger of supersymmetry breaking to the observable sector, which feels the breaking of supersymmetry just above the electroweak scale $\sim 10^3$ GeV.
- Type I and the $SO(32)$ heterotic string can in principle also lead to realistic gauge and matter content at low energies. However, the connection to GUT model building and the hidden sector paradigm is less direct.

Therefore, in the mid 1980s, the standard paradigm of string phenomenology was the $E_8 \times E_8$ heterotic string. A great deal of effort was dedicated to constructing and studying different compactifications that lead to realistic models. The properties of the compact 6D manifold determine the low-energy physics. Hence, Calabi-Yau manifolds (or its singular limits known as orbifolds) are often chosen because they preserve $\mathcal{N} = 1$ supersymmetry in 4D, as well as permitting the existence of chiral fermions. In the simplest case (known as the standard embedding), the observable E_8 symmetry group is broken to E_6 which was a natural grand unified group, with the hidden E_8 unbroken. Also, the number of chiral families is given by the topological Euler number of the manifold. This deep connection between geometry with physics results in a great flourish of activities in string model building.

Energy Scales in Heterotic String Theories

Instead of discussing details of these heterotic string constructions, let us take a first look at a more basic property, namely, the fundamental energy scale. In heterotic string theory, both gravity and gauge fields come from the same source which are closed strings. So, both kinds of fields propagate in the full 10 spacetime dimensions. In 10D, the low energy effective action takes the form:

$$S_{10d} = M_s^8 \int d^{10}x \sqrt{-g} e^{-2\phi} \left(\mathcal{R} + \frac{1}{4} M_s^{-2} F_{MN}^2 + \dots \right) \tag{162}$$

where $M_s = 1/\sqrt{\alpha'}$ is the string scale and ϕ is the dilaton field. We have suppressed the fermionic part of the effective action. Upon compactification to 4D, each of the two terms above will receive a volume factor coming from the integration of the 6 extra dimensions (assuming a factorized geometry $\mathcal{M}_{10} = \mathcal{M}_4 \times \mathcal{M}_6$). Comparing with the 4D effective action for gravity and Yang-Mills gauge fields:

$$S_{4d}^{eff} = \int d^4x \sqrt{-g} \left(M_P^2 \mathcal{R}_4 + \frac{1}{4g_{YM}^2} F_{\mu\nu}^2 + \dots \right) \tag{163}$$

we obtain the expression for the gravitational and gauge couplings:

$$M_P^2 = \frac{1}{g_s^2} M_s^8 V_6, \qquad g_{YM}^{-2} = \frac{1}{g_s^2} M_s^6 V_6 \tag{164}$$

where V_6 is the overall volume of the extra dimensions and $g_s =< e^{\phi} >$. (Precise numerical factors can be found in Polchinski's textbook [2]). Taking the ratio of these expressions, the volume and the dilaton factors cancel and we obtain:

$$M_P^2 \simeq g_{YM}^{-2} M_s^2 \tag{165}$$

Therefore for $\alpha_{YM} \equiv g_{YM}^2/(4\pi)$ not too different from 1/25 (as expected from low energies), we have the fundamental scale M_s to be not far from the Planck scale $M_P \sim 10^{19}$ GeV, i.e.,

$$M_s \simeq g_{YM} M_P \sim (10^{17} - 10^{18}) GeV \tag{166}$$

Note that:

- M_s is very high, which makes the heterotic scenario very hard to test directly.
- In addition, the compactification scale $M_c \equiv V_6^{-1/6}$ cannot be too small, because M_c is the scale of KK modes of the Standard Model gauge bosons and matter.
- To trust the low energy supergravity approximation, $M_c < M_s$, this gives $g_{YM} < g_s$ and so we are in the perturbative limit.
- Since the relevant energy scales (M_c and M_s) are much bigger than M_{EW}, we need to protect Standard Model physics from large radiative corrections. Usually, supersymmetry is invoked to do the job.
- Although our present discussion assumes V_6 and g_s are parameters dialable at will, they are actually vevs of scalar fields known as moduli. These moduli parametrizes the size and shape of the extra dimensions and are stabilized by a potential. Moduli stabilization is a subject on its own and we will discuss some recent ideas in the last lecture.

2.2 The Post D-brane Era

String phenomenology has taken a drastic turn in the mid 1990s. The discovery of string dualities suggested that the five consistent string theories together with 11D SUGRA are different manifestations of the same underlying M-theory. It has also become clear that higher dimensional surfaces known as D-branes play a key role in string theory and its applications to phenomenology, giving support to the "brane world" idea.

The techniques of constructing realistic models have been very much increased. We can now start from any of the 6 descriptions of M-theory and obtain models with features of the Standard Model.

1. *11D SUGRA:* Just as the requirement of $\mathcal{N} = 1$ supersymmetry in 4D singles out Calabi-Yau compactifications of string theory, G_2 manifolds provide a geometric construction if we start from 11D. These G_2 manifolds are much less understood but it has been shown that it is not possible to obtain chiral fermions except for singular points. General and elegant results exist for these constructions but no explicit compact models have been constructed in this way so far (except in the weak coupling limit when such compactifications reduce to known string theory constructions).

   A simpler way to obtain $\mathcal{N} = 1$ models from 11D SUGRA is in fact closely related to the heterotic string theory we just discussed. In the strong coupling limit, an extra dimension opens up. In the Horava-Witten construction, the 11-th dimension is an interval (an S_1/Z_2 orbifold).

One can think of the two E_8 as living at the endpoints of the interval which are 10D surfaces. Further compactification on Calabi-Yau manifolds give rise to interesting chiral models. Some explicit models have been constructed although their phenomenological properties are difficult to extract given the mathematical complexity and the fact that we do not actually know what is the full completion of 11D SURGRA. Still interesting results continued to be obtained in this direction. Incidentally, an additional dimension accessible only to gravity and not to gauge and matter fields helps solve the discrepancy between the unification scale and the Planck scale.

2. *Type I, IIA, IIB Strings:* The main new ingredient in these models is the existence of D-branes, which are surfaces on which open strings can end. D-branes can carry gauge and matter fields within their worldvolume. They come in various dimensions: a D_p brane has 1 time and p space dimensions. The subject of these lectures is to introduce model building techniques with D-branes. Details will be discussed further as we go along, but as a preview, let us mention that to get chiral models, the branes have to placed at singular points of a manifold, or to intersect at non-trivial angles and chiral matter lives only at the intersection, or to turn on world-volume flux.

   Further generalizations of these D-brane constructions include the so called F-theory (proposed by Vafa). In Type IIB string theory, the two scalar fields of the 10D theory, the dilaton and axion are combined into one complex field $S = a + i\phi$, which realizes the S-duality symmetry $SL(2, \mathbf{Z})$:
$$S \to \frac{aS+b}{cS+d} \qquad a, b, c, d \in \mathbf{Z} \text{ with } ad - bc = 1 \tag{167}$$
   which is similar to how the modular parameter of a torus transforms. Therefore, one can "geometrize" this varying axio-dilaton background as compactification on a 4 complex dimensional Calabi-Yau manifold which is locally a product of this torus with a six-dimensional (non Calabi-Yau) base B_3 under which the Type II theory is compactified. The four-fold is then said to be an elliptically fibered Calabi-Yau[11]. These compactifications naturally incorporate D7-branes, which are given by points in the base[12] where the elliptic fibration degenerates.

Let us take stock of these new insights we gain in the post D-brane era. The common feature in these new constructions is the fact that our world can be a brane – either a D-brane or the end-of-the-world brane in the Horava-Witten construction, or possibiliy a surface at the singularity of a G_2 or elliptically fibered Calabi-Yau four-fold in M and F-theory respectively. The brane world scenario has been a subject of intense investigations during the past 10 years and new mechanisms have been proposed to solve longstanding problems with the Standard Model, such as the hierarchy problem, gauge coupling unification, neutrino masses, the strong CP problem etc, without necessarily referring to string theory. Some of these topics will be discussed in Bodgan Dobrescu's lectures. Here we will concentrate only on string theoretical realizations.

One of the interesting properties of this scenario is that it allows for a fundamental scale of nature to be much lower than the Planck scale and therefore closer to the energies accessible to experiments. We wil discuss explicit realizations of this scenario in the next lecture.

D-brane Scenarios

Before we discuss the construction of D-brane models, let us revisit the relation between the gravitational and gauge couplings with the fundamental scale.

If the Standard Model is localized on the worldvolume of D_p branes, the low energy effective action

[11] In particular, B_3 itself can be thought of as a local product of K_3 and P_1.

[12] More precisely, points in P_1.

in 4D takes the form:

$$S_{4d} = \int d^4x\sqrt{-g}\left(M_s^8 V_6 e^{-2\phi}\mathcal{R}_4 + \frac{1}{4}M_s^{p-3}V_{p-3}e^{-\phi}F_{\mu\nu}^2 + \dots\right) \tag{168}$$

There are two crucial differences in comparison to the heterotic case. First, the power of the dilaton is different for the gravity and the gauge kinetic terms. Second, the total volume V_6 enters on the gravity part but only the volume of the $p-3$ cycle (i.e., $p-3$ dimensional subspace) of the internal manifold V_{p-3} that the p-branes wrap around appears in the gauge part of the action. In particular for a $D3$-brane, there is no volume factor contribution to the gauge coupling. The gravitational and gauge couplings are then related to the fundamental string scale as follows:

$$M_P^2 = \frac{M_s^8}{(2\pi)^7}\frac{V_6}{g_s^2}\ , \qquad \alpha_{YM}^{-1} = 4\pi\frac{M_s^{p-3}V_{p-3}}{g_s} \tag{169}$$

where we have restored factors of 2 and π. We can easily see that if the Standard Model fits inside a D3-brane, for instance, we may have M_s substantially smaller than M_P as long as the volume of the extra dimensions are large enough, without affecting the gauge couplings. More generally, the above relations illustrate the "brane world" effect where the dimensions transverse to the branes (which are not necessarily D3-branes) if large can lower the fundamental string scale. In the heterotic case, setting the volume very large would make the gauge couplings extremely small, which is unrealistic.

The different power of the dilaton in the gravity and gauge kinetic terms also give rise to added flexibilities. Even if the Standard Model is within a set of D9-branes which fill all space, for sufficiently weak string coupling, the string scale can be significantly lower than the Planck scale because of the difference in dilaton factor. However, this dilaton factor can only help us in getting a few orders of magnitude suppression (say $M_s = M_{GUT}$ rather than $M_s = M_{EW}$) since otherwise the gauge couplings will be too weak.

The possibility of having large dimensions add a "geometrical" view of the hierarchy problem, though we still need to explain why the size of the dimensions are stabilized to a large value. Several scenarios have been proposed depending on the value of the fundamental scale. The main scenarios at present are:

1. $M_s \sim M_P$. This is analogous to the heterotic scenario and similar comments apply.

2. $M_s \sim M_{GUT} \sim 10^{16}$ GeV. This corresponds to a compactification scale $r \equiv V_6^{1/6} \sim 10^{-30}$cm or equivalently $M_c \sim 10^{14}$ GeV. This is analogous to the Horava-Witten construction and allow the possibility of the unification of gauge *and* gravitational couplings (if the Standard Model is realized on the same set of branes).

3. $M_s \sim M_I \sim 10^{10-12}$ GeV $\sim \sqrt{M_{EW}M_P}$. If the Standard Model is realized on a set of D3-branes, this corresponds to a compactification scale $r \sim 10^{-23}$ cm. This proposal was based on the special role played by the intermediate scale M_I in different issues beyond the Standard Model. Examples include the scale of SUSY breaking in graviy mediated SUSY breaking scenario and the scale of the axion field introduced to solve the strong CP problem. This then allows one to identify the string scale with the SUSY breaking scale and opens up the possibility for non-SUSY string models to be relevant at low energies, solving the hierarchy problem. A simple example is to have a set of $\overline{D3}$ branes breaking the supersymmetry preserved by the background geometry and the SUSY breaking effects are transmitted to the observable sector by Planck suppressed interactions.

4. $M_s \sim M_{EW} \sim$ TeV. This is the string theory realization [19] of the large extra dimensions scenario a la ADD [20–22]. We will discuss concrete models in the next lecture. If only two of the extra dimensions are large, the corresponding compactification scale is about a mm, which is the extreme case of the "brane world" scenario. However, the hierarchy problem is not totaly solved. We still need to explain why the compactification size is so large.

Thus, D-branes offer many more scenarios with $M_{EW} < M_s < M_P$ in contrast to the heterotic string where the fundamental string scale is fixed by the low energy couplings. Which of these scenarios is actually realized depends on how the moduli (size and shape of the extra dimensions) are stabilized.

Without going into details of the construction, a few observations can already be made:

- Gauge unification is not necessarily realized in D-brane models. The tree-level gauge coupling depends on the volume of the cycles the branes wrap around and can be different for different gauge factors of the Standard Model.

- We may or may not consider SUSY in the D-brane constructions because the fundamental string scale can be much lower than the Planck scale. However, stable D-brane configurations realizing non-supersymmetric models are harder to construct since they usually come with (i) closed string tachyons, and (ii) runaway potentials for moduli (dilaton, volume, etc). So, for the purpose of these lectures, we wil focus on $\mathcal{N} = 1$ supersymmetric examples. In particuar, one of our goals is to construct $\mathcal{N} = 1$ supersymmetric extensions of the Standard Model.

- D-brane models can be easily combined with other ingredients such as sources of moduli stabilization and supersymetry breaking such as background fluxes. These background fluxes are generalizations of the electromagnetic fluxes in string theory, and will be the subject of the last lecture.

- Although we will focus on D-brane models, much of our discussions can be generalized to other brane constructions in M/F theory models.

- D-brane models have been used to motivate many new BSM ideas. Just like the heterotic case, they are also useful in realizing more traditional scenarios such as hidden sector and gravity mediated SUSY breaking, but now in a more geometrical and stringy way.

3 D-branes and Chirality

We now turn to the main point of these lectures, which is the construction of realistic D-brane models. In addition to the $SU(3) \times SU(2) \times U(1)$ gauge structure, an important property of the Standard Model is that it is chiral. Before we can appreciate issue involved in introducing chirality to D-brane models, let us recall a few facts about D-branes:

3.1 D-brane Primer

D-branes are interesting objects for constructing particle physics models because their worldvolumes support non-Abelian gauge fields. What is interesting is that not only are they solutions to the SUGRA equations of motion, they admit a full string description as boundaries on which open strings can end. For the purpose of this lecture, there are several properties of D-branes we need to recall:

- D-branes are dynamical objects – the open strings ending on them describe the collective coordinates of the D-branes. The worldvolume of a D_p brane contains a $U(1)$ gauge field, $9-p$ scalars and the corresponding fermion partners. The scalars correspond to the Goldstone modes of the part of the Poincare symmetry broken by the presence of the brane. The fermions are Goldstinos for supersymmetry. The D-brane breaks half of the supersymmetries. Therefore in flat space, after toroidal compactification, one D-brane carries the spectrum of an $\mathcal{N} = 4$ supersymmetric vector superfield.

- Furthermore, D-branes are BPS objects for which a no force condition applies. One can understand this condition as follows. Both D-branes have the same positve tension and therefore are naturally attracted to each other by gravitational interactions. The exchange of the dilaton field has the same effect of an attraction. However, D-branes are also charged under the antisymmetric Ramond-Ramond fields for which the interaction is repulsive, given both branes have the same charge. It turns out the combined effect of these three interactions cancels exactly if both of them are D-branes. This can be seen explicitly by computing a one-loop open string diagram corresponding to a cylinder (see, e.g., [2]). An anti D-brane carries the opposite RR charge as a D-brane and so there is a net attractive force between them.

- This gives rise to an interesting phenomenon which is essentially (but not quite) the inverse Higgs effects. Open strings with both endpoints on one brane give rise to the $U(1)$ gauge field for that brane. In the presence of a second brane, besides having the second $U(1)$ there are now pairs of strings with endponts on each of the two branes. These correspond to massive states with mass proportional to the separation of the branes. We may identify one string with a particle like W^+ (of the Standard Model) and the string with opposite orientation with W^-. The important point is that when both branes overlap these particles become massless and enhance the $U(1) \times U(1)$ symmetry to the full $U(2)$ symmetry. This is then the way to obtain non-Abelian supersymmetric theories on the branes. The bi-fundamental matter fields are also enhanced to adjoints.

- There are additional properties of D-branes which are useful for model building and we will discuss them along the way. (Other properties are given in the appendix for completeness).

3.2 D-branes and Chirality

However, the D-brane configurations we have considered so far are too simple to incorporate chirality, a key property of the Standard Model. This is because of the large amount of supersymmetry preserved by the D-brane configurations considered. In flat space, a D-brane preserve $\mathcal{N} = 4$ supersymmetry since D3-branes are 1/2 BPS. However, changing the compactification space from a torus to an orbifold or a Calabi-Yau does not improve the situation since this is a local issue at the location of the brane.

To make this point more precise, consider a D3-brane sitting at a point P in the extra dimensional space $\mathcal{M}_6$, with background fluxes. The background fluxes can in principle break the supersymmetry to $\mathcal{N} = 1$ or $\mathcal{N} = 0$ so chirality is possible. However, one can continuously deform $\mathcal{M}_6$ and dilute the fluxes to reach again flat space. Along this deformation, the gauge group does not change, so gauge protected quantities, like the number of chiral families should not change. Therefore, the spectrum in the original configuration is non-chiral. (A more stringy argument goes as follows. At P, we see flat space and constant fluxes. Around P, we start seeing deviations from flat space and non-constant fluxes. From the D3-brane point of view, this comes from closed strings running in loops, etc. So, we have the initial D3-brane theory together with perturbative corrections. If the initial theory is non-chiral, so will be the final theory.)

In general, an open string with both ends on a stack of N D-branes tansforms in the adjoint representation of $U(N)$, hence the theory is non-chiral. Let us consider instead a stack of N_{D3} D3-branes and N_{D7} D7-branes. If we place them on top of each other, we have

$$U(N_{D3}) \times U(N_{D7}) \tag{170}$$

gauge groups and matter in the representations:

$$m(N_{D3}, \overline{N}_{D7}) + m'(\overline{N}_{D3}, N_{D7}) \tag{171}$$

where m, m' are multiplicities. But since we can separate them by a distance ℓ the strings between D3 and D7 will have a minimal mass of ℓ/α'. Hence $m = m'$ and the theory is non-chiral.

How could one obtain chirality? Four dimensional chirality is a violation of four-dimensional parity. In string theory, the chirality in 4D is correlated with the chirality in the 6 extra dimensions. Hence

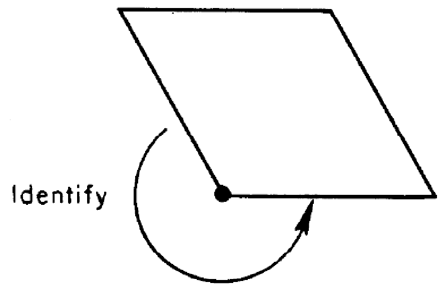

Figure 79: An orbifold identifies points in space under a discrete symmetry

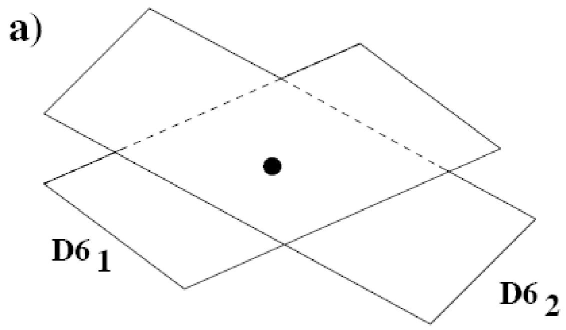

Figure 80: Intersecting branes

to achieve 4D chirality, the D-brane configuration must violate 6D parity. The D-brane configurations we consided so far are too simple to introduce a preferred orientation in 6D.

This observation also suggests how one can construct D-brane configurations which admit 4D chiral fermions. The requirement is that the configuration introduces a preferred orientation in the 6 transverse dimensions. There are several ways to achieve this. These seemingly different strategies are in fact related.

1. **D-branes at singularities:** We can consider placing D-branes in spaces that are not smooth. Chirality can arise if the D-branes are sitting at a singularity. A simple example is to consider a stack of D3-branes sitting at an orbifold singularity. An orbifold is a discrete identification of space and this defines a preferred orientation.

2. **Intersecting branes:** We can also consider pairs of D-branes that cannot be separated from one another. Intersecting D-branes lead to chiral fermions in the sector of open strings stretched between different kinds of D-branes. (Again, the angle between one stack of branes with respect to another defines a preferred orientation).

3. **Magnetized D-branes:** Finally, chirality also arises when we turn on a non-trivial field strength background for the worldvolume $U(1)$ gauge fields. The magnetic fields introduce a preferred orientation in the internal dimensions through the wedge product $F \wedge F \wedge F$ as the volume form.

We will discuss these three methods in this particular order. The main point we will try to make is that these constructions are "modular" in the sense that we can locally obtain the Standard Model witout having to know all the details of the compactification. This is of great importance because we can follow a bottom-up approach instead of looking at random compactifications that could give rise to the Standard Model.

We will present this bottom-up approach for building realistic models. Most of the important details of the model, such as the gauge group, chiraliy, number of chiral families, etc, will depend only on the

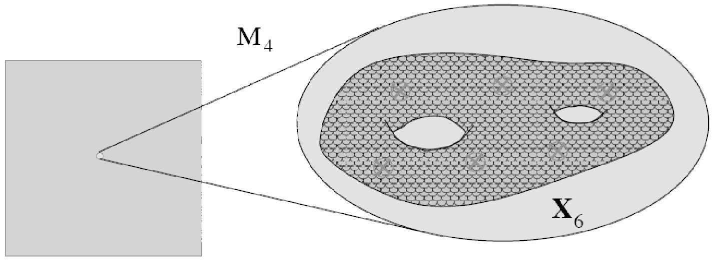

Figure 81: Magnetized D-branes

structure of the singularities that the branes sit at or the way the branes intersect. This can happen in all sorts of spaces and therefore we can keep the main properties whether we are talking about a complicated Calabi-Yau space or a simple toroidal orbifold compactification. This makes the models constructed more robust. This is the main practical advantage of D-brane model building over the heterotic string.

Before we go on, let me point out that these methods of obtaining chirality are in fact related by dualities. The simplest way to see this is to note that turning on a gauge bundle on the worldvolume of D-branes induces lower-dimensional D-brane charges. For example, one can think of a D_p brane with n units of magnetic flux on a torus:

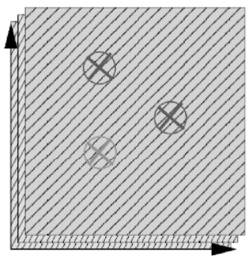

as a bound state of a D_p brane and n D_{p-2} brane. Now there is a remarkable symmetry of string theory known as T-duality:

$$R \to \alpha'/R \tag{172}$$

which maps a universe of enormous universe to a universe which is incredibly small in size. Here $\alpha' = 1/\ell_s$ where ℓ_s is the string length. This symmetry has the effect of exchanging the momentum and winding states. The mass spectrum of string theory is therefore the same under this large $\leftrightarrow$ small radius interchange. However, the dimension of D-branes changes: A D_p brane with its worldvolume extended along the T-dual direction will become a D_{p-1} brane whereas a D_p brane with its worldvolume transverse to the T-dual direction will become a D_{p+1} brane. Now let's T-dualize along one direction:

The D_p and the D_{p-2} branes both turn into a D_{p-1} brane but they orient along different directions. Thus branes with magnetic fluxes become branes at angles. Likewise, we will see later that the D3-branes at singularities which give rise to chiral fermions, known as fractional branes, can be thought of higher dimensional branes wrapping around a collapsed cycle with some gauge bundle on them.

So, why do we discuss these approaches separately if the setups are dual to one another? It turns out that in some situations, one side of the duality is simplier than the other. Furthermore, we will in the last lecture consider D-brane models with fluxes. Under duality, the background flux turns into a non-trivial metric background and the two descriptions are no longer equivalent at least in this simple form. So it is useful to have an intuition about each of these approaches independently.

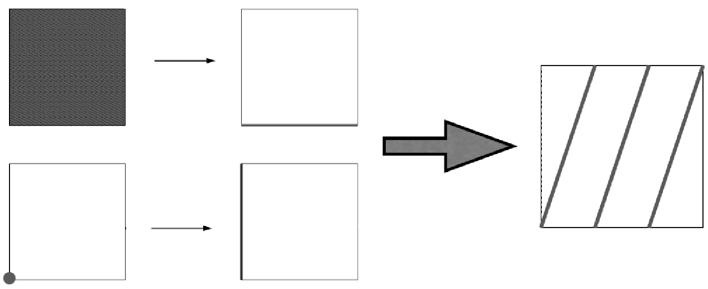

Figure 82: Intersecting branes and magnetized D-branes are related by T-duality

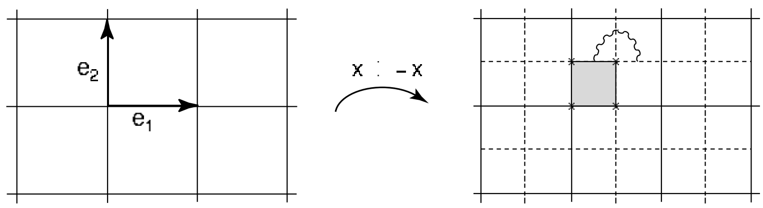

Figure 83: A $T^2/\mathbb{Z}_2$ orbifold

4 D-branes at Singularities

First, let us discuss how one can construct chiral models from D-branes at singularities. We will begin with a quick review of orbifolds.

- A manifold $\mathcal{M}_6$ is by definition locally like $\mathbb{R}^6$, but string theory is defined even on manifolds that are not smooth. The extra dimensions can contain singularities, like orbifold or conifold singularities.
- Orbifolds are spaces that locally look like $\mathbb{R}^6$ or $\mathbb{R}^6/\Gamma$ where Γ is a discrete subgroup of $SO(6)$, the rotation group of the 6 extra dimensional space.
- Although the gravity background is singular, strings are well-behaved at orbifold singularities. This has been shown in the classic papers [23, 24] for closed strings and [25] for open strings.
- What is an orbifold? Consider a simple case $T^2/\mathbb{Z}_2$. The $\mathbb{Z}_2$ orbifold symmetry acts on the two-dimensional torus as follows:

$$\theta : (x_1, x_2) \to (-x_1, -x_2) \tag{173}$$

  There are 4 fixed points: $(0,0), (1/2,0), (0,1/2), (1/2,1/2)$ (if we normalize the radii of T^2 to 1).

  Locally, the singularity looks like a cone and globally the $T^2/\mathbb{Z}_2$ orbifold is a tetrahedral (or ravioli) as show in Figure 84.
- Let's look at a slightly more non-trivial example: $T^2/\mathbb{Z}_3$. The discrete $\mathbb{Z}_3$ orbifold symmetry acts on the complex coordinates $z = x_1 + ix_2$ of the torus as follows:

$$\theta : z \to \alpha z \qquad \text{where} \qquad \alpha = e^{2\pi i/3} \tag{174}$$

  There are three fixed points as shown in the Figure 85.

  Note that vectors undergo a non-trivial rotation when transported along a closed curve around the singularity (local holonomy).

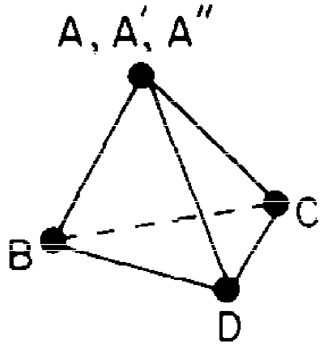

Figure 84: A $T^2/\mathbb{Z}_2$ orbifold is a tetrahedral.

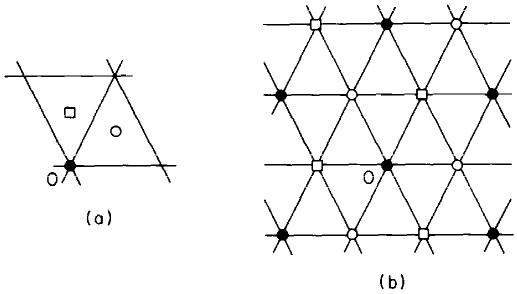

Figure 85: A Z_3 orbifold

- In general, we can consider a local singularity of the form $\mathbb{C}^3/\Gamma$ where $\Gamma = \mathbb{Z}_N$. The discrete symmetry $\mathbb{Z}_N$ acts on the complex coordinates of $\mathbb{C}^3$ as follows:

$$\theta : (z_1, z_2, z_3) \to (\alpha^{\ell_1} z_1, \alpha^{\ell_2} z_2, \alpha^{\ell_3} z_3) \tag{175}$$

  where $\alpha = e^{2\pi i/N}$, $\ell_i \in \mathbb{Z}$ such that $\theta^N = 1$.

- One can check that if θ is a matrix of determinant 1:

$$\theta \in SU(3) \Leftrightarrow \ell_1 \pm \ell_2 \pm \ell_3 = 0 \pmod N \tag{176}$$

  for some choices of sign, then

$$\Gamma \subset SU(3) \subset SO(6)\ , \qquad \text{SUSY is preserved} \tag{177}$$

  If this condition is not satisfied, then we find closed tachyons in the closed string spectrum. For concreteness, we will take the choice of signs, $\ell_1 + \ell_2 + \ell_3 = 0 \pmod N$.

- Furthermore, only if we require:

$$\sum_i \ell_i = \text{even} \tag{178}$$

  do we have fermions in the spectrum. In more technical terms, the orbifold is called a spin manifold.

- The orbifold action has the following effects on closed strings. It projects out states that are not invariant under the twist, reducing the number of states in the spectrum. It also increases the

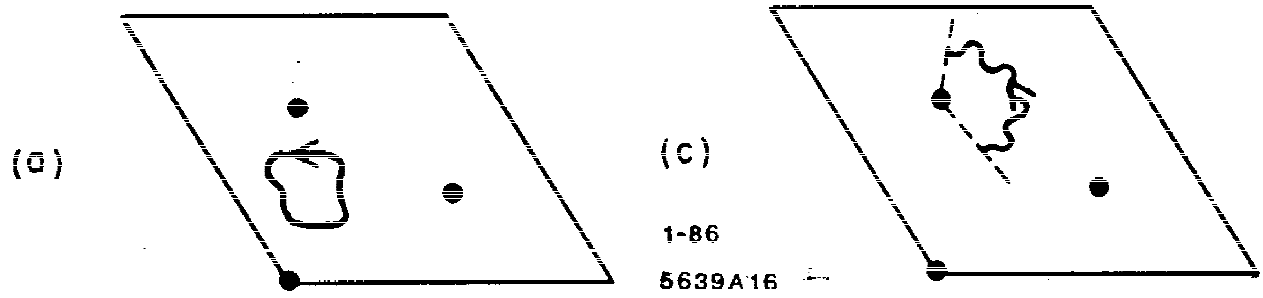

(a) An untwisted sector state

(b) A twisted sector state.

Figure 86: Untwisted & twisted sectors of a $\mathbb{Z}_3$ orbifold (figure from Ref. [26].)

number of states in another way since it now includes the so called "twisted sector". An open string around a fixed point with its two endpoints lying at points which are identified under the orbifold is not included in the spectrum of states in the unorbifolded space but it is a valid closed string in the orbifold. In other words, there are two sectors:

- Untwisted sector: strings closed on $\mathbb{C}^3$
- Twisted sector: strings not closed on $\mathbb{C}^3$ but closed on $\mathbb{C}^3/\Gamma$ (confined to the singularity)

- Closed strings are not charged under the D-brane gauge group and so they will not give us the Standard Model particles. We will not analyze their spectrum. However, the closed string spectrum determines the types and number of moduli fields we have. They will be important later on when we discuss moduli stabilization.

- The open string spectrum is our main concern for particle physics model building. We know how to quantize open strings exactly to all orders in α' in these backgrounds. We will however discuss only the massless spectrum.

- If we are away from the singularity, things work as in flat space. The branes are arranged in a $\mathbb{Z}_N$ invariant fashion. They are identified and the open string spectrum is that of $U(N)$ $\mathcal{N}=4$ SYM (plus α' corrections).

- If the branes sit on the singularity, we have an "orbifolded" gauge theory. The spectrum is given by the open strings that are well defined at the singularity. This means open strings invariant under the action of θ.

- The orbifold twist θ has two actions
  - $\theta \in SO(6)$: R-symmetry group of $D=4$, $\mathcal{N}=4$ SYM.
  - $\theta \in U(N)$: "permutes" the D-brane positions.

  The action of θ on the $U(N)$ gauge degrees of freedom is then given by an $N \times N$ matrix Γ_θ. We will elaborate on this shortly.

4.1 Explicit Examples

We now see explicitly how the spectrum of D-branes at a $\mathbb{Z}_N$ singularity, like the fixed points of orbifolds, become chiral. As discussed before, the spectrum is determined by the local properties so for simplicity, let us consider a D3-brane in flat 10D space with the six extra dimensions modded out by a $\mathbb{Z}_N$ twist θ. (There are too many N in this business! Here, we refer to N for the order of the twist, n for the number of overlapping D-branes, and $\mathcal{N}$ for the number of supersymmetries).

If we have a stack of n D-branes, the original gauge group is $U(n)$. The gauge degrees of freedom are represented by the Chan-Paton matrices λ^i_j, $i,j = 1,\ldots,n$, associated to the endpoints of the open strings and which belongs to the adjoint of $U(n)$. The action of the orbifold twist on the gauge degrees of freedom are given by:

$$\lambda \to \Gamma_\theta \lambda \Gamma_\theta^{-1} \tag{179}$$

where Γ_θ is of order N and can be diagonalized to take the simple form:

$$\Gamma_\theta = \begin{pmatrix} I_{n_0} & & & & & \\ & \alpha I_{n_1} & & & & \\ & & \alpha^2 I_{n_2} & & & \\ & & & . & & \\ & & & & . & \\ & & & & & \alpha^{N-1} I_{n_{N-1}} \end{pmatrix} \tag{180}$$

Here I_{n_k} is the identity matrix in n_k dimensions and the integers n_k satisfy the constraint $\sum_k n_k = n$. (*i.e., n D-branes are split into groups of n_k's*).

Let us now see how the original $\mathcal{N} = 4$ vector multiplet transforms under the action of the twist defined by θ and Γ_θ. We can write the $\mathcal{N} = 4$ multiplet in terms of the $\mathcal{N} = 1$ multiplets:

- Vector Multiplet: $V \equiv (A_\mu, \lambda)$
- Chiral Multiplets: $\Phi_a \equiv (\phi_a, \psi_a)$, $a = 1, 2, 3$ (a labels the 3 complex extra dimensions)

Therefore Φ_a which has an a index feels both the action of θ and Γ_θ where V feels only the action through Γ_θ.

Remember that we have to keep only the states that are invariant under the twist. This means that $V = \Gamma_\theta V \Gamma_\theta^{-1}$. This breaks the gauge group to:

$$U(n) \to U(n_0) \times U(n_1) \times \cdots \times U(n_{N-1}) \tag{181}$$

with the number of factors equal to the order of the twist N. This means that if we want three gauge factors, we should have a $\mathbb{Z}_3$ twist and so on.

The surviving chiral superfields satisfy $\Phi_a = \alpha^{\ell_a} \Gamma_\theta \Phi_a \Gamma_\theta^{-1}$. The first factor being the action of θ. Therefore remembering that λ carries adjoint indices (which are composed of fundamentals and anti-fundamentals) we can easily see that the remaining matter fields transform as:

$$\sum_{a=1}^{3} \sum_{i=0}^{N-1} (\mathbf{n}_i, \overline{\mathbf{n}}_{i+\ell_a}) \tag{182}$$

Here the sum over i is understood to be mod N, and n_i means the fundamental of $U(n_i)$.

This is a typical spectrum in this class of models. The matter fields tend to come in bi-fundamentals of the product of gauge groups. These can be arranged into "quiver" diagrams (see figure). These diagrams are made out of one node per group factor, i.e., the i-th node corresponding to the gauge group $U(n_i)$. There are also arrows joining the nodes. An arrow going from the i-th to the j-node correspond to a chiral field the representation $(n_i, \overline{n}_j)$ (note the orientation). A closed triangle of arrow would indicate the existence of a gauge invariant cubic superpotetial for those fields.

A D3-brane in a quiver node is called a "fractional" D3-brane, and it cannot be taken away from the singularity. This is why two fractional D3-branes in different nodes can host a chiral fermion. Besides putting D-branes at a $\mathbb{C}^2/\mathbb{Z}_N$ singularity, one can also consider other types of singularities such as the conifold.

From the generic chiral spectrum in eqn. (182), we can extract a very simple but powerful conclusion: Only for $\mathbb{Z}_3$ will we get the chiral matter spectrum in three identical copies or families. The reason

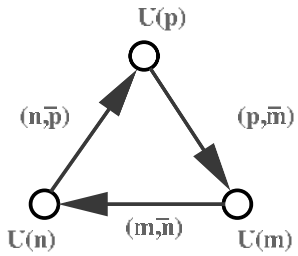

Figure 87: The Z_3 quiver

is that only for that case we have $\ell_1 = \ell_2 = \ell_3 \mod N$, since $\ell_1 = \ell_2 = 1$ and $\ell_3 = -2 = 1 \mod 3$. Other twists given by $(1/N, 1/N, -2/N)$ will give rise to two families. Therefore three is not only the maximum number of families for this class of models but is obtained only for one twist, the $\mathbb{Z}_3$ twist. This is a rather remarkable result.

If we want to have the Standard Model we can consider $n_0 = 3$, $n_1 = 2$, $n_2 = 1$ to get the gauge group $U(3) \times U(2) \times U(1)$. The spectrum will then be:

$$3 \times \left[(\mathbf{3}, \mathbf{2}) + (\mathbf{1}, \mathbf{2}) + (\overline{\mathbf{3}}, \mathbf{1})\right] \tag{183}$$

where we have suppressed the $U(1)$ quantum numbers. This gives the 3 families of left-handed quarks, right-handed up quarks, and leptons, just as in the Standard Model. However, we can easily see that we are missing at least the right-handed down quarks. Actually, the spectrum as it is, is anomalous. What happens from the string theory point of view is that there are uncancelled tadpoles for twisted sector fields. We will take care of this shortly and construct models that are fully consistent, but until then we can explore some general properties of the model as it stands now.

First, there are actually three $U(1)$'s. Only one combination of them is anomaly free and it is defined in general (for any N) by:

$$Q_Y = -\left(\frac{1}{3}Q_3 + \frac{1}{2}Q_2 + \sum_{s=1}^{N-2} Q_i^{(s)}\right) \tag{184}$$

In a general orbifold all other $N-1$ additional $U(1)$ factors are anomalous and therefore massive due to a version of the Green-Schwarz mechanism. The Green-Schwarz mechanism is the cancellation of one-loop diagrams by tree-level diagrams due to the exchange of p-forms. We will discuss the Green-Schwarz mechanism in more detail later. For now, we can quickly check that this $U(1)$ does correspond to the hypercharge, as expected since hypercharge is essentially the only non-anomalous $U(1)$ with the spectrum of the Standard Model. For instance, fields transforming in the $(\mathbf{3}, \mathbf{2})$ representation have Q_Y charge $-\frac{1}{3} + \frac{1}{2} = \frac{1}{6}$ as correspond to left-handed quarks. Fields transforming in the $(\mathbf{3}, \mathbf{1})$ (which necessarily have charge -1 under one of the $Q_1^{(s)}$ generators) have a Q_Y charge $-\frac{1}{3} + 1 = -\frac{2}{3}$, as corresponds to right-handed U quarks, etc.

It is worth noticing that the normalization of this hypercharge $U(1)$ depends on the order of the twist N. In fact, by normalizing $U(n)$ generators such that $\mathrm{Tr}_a^2 = \frac{1}{2}$, the normalization of the Y generator is fixed to be

$$k_1 = 5/3 + 2(N-2) \tag{185}$$

This amounts to a dependence on N in the Weinberg angle, namely

$$\sin^2\theta_W = \frac{g_1^2}{g_1^2 + g_2^2} = \frac{1}{k_1 + 1} = \frac{3}{6N - 4} \tag{186}$$

Thus the weak angle decreases as N increases. Notice that the $SU(5)$ result $3/8$ is only obtained for a $\mathbb{Z}_2$ singularity. However in that case the D3-brane spectrum is necessarily vector-like and hence

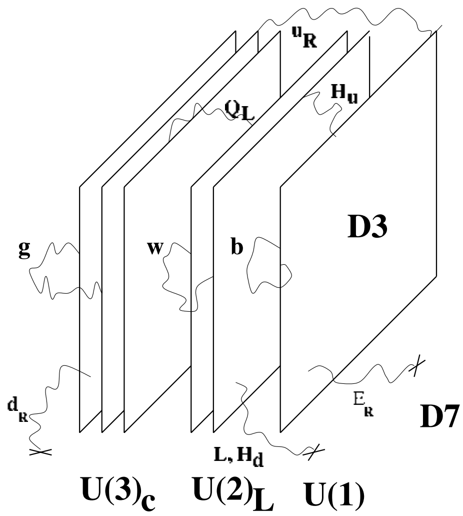

Figure 88: A bottom-up construction of the MSSM

one cannot reproduce the Standard Model spectrum. For the interesting case for us, $N = 3$, we find $\sin^2\theta_W = 3/14$.

Now, back to the uncancelled tadpoles. To cancel these tadpoles at the singlarity it is necessary to have not only the D3-branes but also D7-branes. There are three types of D7-branes that can be introduced depending on which 2 of the 3 complex dimensions they contain. The consistency condition (tadpole cancellation) can be written as

$$\mathrm{Tr}\Gamma_{\theta,7_3} - \mathrm{Tr}\Gamma_{\theta,7_1} - \mathrm{Tr}\Gamma_{\theta,7_2} + 3\mathrm{Tr}\Gamma_{\theta,3} = 0 \tag{187}$$

This condition can be obtained by analyzing one-loop open string diagrams with boundaries on various combinations of D3 and D7-branes. More intuitively, we can understand this condition as equivalent to non-Abelian anomaly cancellation in the effective field theory (since $3-7$ strings introduce chiral matter fields charged under the D3-brane gauge groups). Notice that without the D7-branes we could not have the Standard Model on the D3-brane. Nevertheless, the choice $n_0 = n_1 = n_2 = 3$ gives an anomaly free spectrum even without introducing D7-branes, and so the trinification model with gauge group $U(3)^3$ can be realized.

The D7-branes will have extra gauge groups and matter fields living on the D7-brane which can be obtained in a similar way, with a matrix $\Gamma_{\theta,7_i}$ (with $i = 1, 2, 3$ labeling different D7-branes) acting on the gauge degrees of freedom of the D7-branes. There are also massless matter fields living at the intersection of the D7 and D3-branes, corresponding to open strings with one endpoint on the D3-branes and the other on the D7-branes. This will complete the spectrum of the Standard Model and render the model anomaly free at the singularity. The D7-brane gauge couplings depend on the volumes of the wrapped cycles. If the volumes are large, the D7 gauge groups act essentially as global symmetries. We can picture the Standard Model realized on the D3-D7 system as follows:

As an illustration, a particular example of configuration of D3 and D7 branes and the resulting spectrum is given in the following table:

A similar model can be constructed choosing $n_0 = 3$, $n_1 = 2$, and $n_2 = 2$ with

$$\Gamma_\theta = \mathrm{diag}\left(I_3, \alpha I_2, \alpha^2 I_2\right) \tag{188}$$

giving rise to a left-right symmetric model with gauge group:

$$U(3) \times U(2)_L \times U(2)_R \tag{189}$$

and three families of chiral matter:

$$3 \times \left[(\mathbf{3},\mathbf{2},\mathbf{1}) + (\bar{\mathbf{3}},\mathbf{1},\mathbf{2}) + (\mathbf{1},\mathbf{2},\mathbf{2}) + (\mathbf{1},\mathbf{2},\mathbf{1}) + (\mathbf{1},\mathbf{1},\mathbf{2})\right] \tag{190}$$

Matter fields	Q_3	Q_2	Q_1	$Q_{u_1^r}$	$Q_{u_2^r}$	Y
33 sector						
$3(3,2)$	1	-1	0	0	0	1/6
$3(\bar{3},1)$	-1	0	1	0	0	-2/3
$3(1,2)$	0	1	-1	0	0	1/2
$\mathbf{37}_r$ sector						
$(3,1)$	1	0	0	-1	0	-1/3
$(\bar{3},1;2')$	-1	0	0	0	1	1/3
$(1,2;2')$	0	1	0	0	-1	-1/2
$(1,1;1')$	0	0	-1	1	0	1
$\mathbf{7}_r\mathbf{7}_r$ sector						
$3(1;2)'$	0	0	0	1	-1	0

Table 22: Spectrum of $SU(3) \times SU(2) \times U(1)$ model. We present the quantum numbers under the $U(1)^9$ groups. The first three $U(1)$'s come from the D3-brane sector. The next two come from the D7_r-brane sectors, written as a single column with the understanding that e.g. fields in the $\mathbf{37}_r$ sector are charged under the $U(1)$ in the $\mathbf{7_r 7_r}$ sector.

where we suppressed the $U(1)$ charges above. Again, $B-L$ is the only anomaly free $U(1)$, the other $U(1)$'s acquire a mass by the Green-Schwarz mechanism.

It is important to emphasize that this is not the full story for these models. Remember that we are building them step by step from a bottom-up approach. There are further issues involved in constructing compact models. So far we have concentrated only on a singularity in flat space modded out by the action of $\mathbb{Z}_N$. If we compactify the extra dimensions, the total RR charge of the D7-branes has to cancel, since there is no place for the RR flux to escape in the compact space (think of an analogous problem of an electric charge in electromagnetism). This will force us to add objects with negative RR charges like anti D7-branes or orientifold planes. For stability reasons, the anti D7-branes have to be separated from the D7-branes or else they will annihilate. They can be placed at different orbifold fixed points, for instance. Orientifolds are stringy objects that we will introduce in the next lecture.

An anti D7-brane breaks supersymmetry since it preserves the half of the supersymmetry that the D-brane breaks. Therefore if both are present, the full supersymmetry is broken. If the anti-branes are trapped at different fixed points, then only bulk fields can mediate the breaking of supersymmetry to the observable brane. This is a realization of the gravity mediated SUSY breaking scenario. In order to obtain a realistic spectrum of supersmmetric particles, the scale of SUSY breaking (string scale in this model) is typically the intermediate scale $M_I \sim 10^{11}$ GeV. The LR model mentioned earlier is particularly interesting in this regard since the unification scale is also close to M_I. Therefore, one might realize gauge unification at the string scale and low energy supersymmetry breaking solving the hierarchy problem. (The intermediate scale M_I is also motivated from axion physics).

Finally, let us emphasize again the flexibility of this bottom-up approach in model building. Our discussions can be generalized to F-theory since the D3-brane gauge and matter content depends only on the local geometry. However, F-theory allows for more general D7-brane configurations, e.g., it allows D7-branes carrying both "electric" and "magnetic" charges to coexist in the model (more precisely, they are the so called (p,q) 7-branes). Furthermore, singularities beyond the simplest $\mathbb{Z}_N$ singularities discussed here have been considered in Ref. [27]. These include non-Abelian twists, orientifold singularities, and conifold singularities. For the case of non-Abelian singularities, an interesting

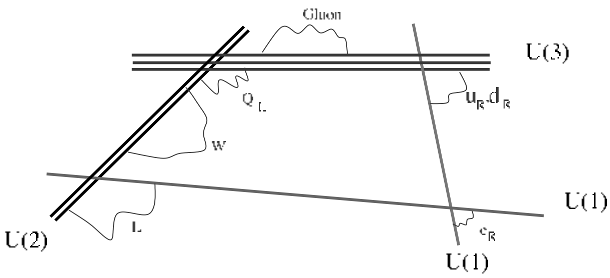

Figure 89: A building block of the Standard Model

model was proposed in [28] (see also [29]). There, a singularity of the type $\mathbb{C}^3/G$ with $G = \Delta_{27}$ was considered. The group $G = \Delta_{27}$ is one of the non-Abelian discrete subgroups of $SU(3)$ and thus preserves SUSY on the D3-brane, like in the $\mathbb{Z}_N$ cases. The Δ_{27} group is actually one of the Δ_{3n^2} series whose action on $\mathbb{C}^3$ is given by:

$$\begin{aligned} e_1 : (z_1, z_2, z_3) &\rightarrow (\omega_n z_1, \omega_n^{-1} z_2, z_3) \\ e_2 : (z_1, z_2, z_3) &\rightarrow (z_1, \omega_n z_2, \omega_n^{-1} z_3) \\ e_3 : (z_1, z_2, z_3) &\rightarrow (z_3, z_1, z_2) \end{aligned} \tag{191}$$

One of the interesting properties of this model is that there is no need to introduce D7-branes to cancel the local tadpoles. The gauge group on the D3-branes is $U(3)^2 \times U(1)^9$ which can further be broken to the Standard Model with three families (due partly to the $\mathbb{Z}_3$ subgroup of Δ_{27}).

5 Intersecting Branes

Another mechanism to obtain $D = 4$ chiral fermions is to consider intersection of branes. Before we discuss all the details and subtleties, let's begin with the overall picture. We know by now that an open string carries indices in the adjoint representation of $U(n)$. The adjoint can be seen as the product of fundamental and anti-fundamental representation, therefore one end of the open string transform as the fundamental and the other as the anti-fundamental. When the two endpoints of the open string lie on the same stack of branes, we have particles like the gauge bosons in the adjoint. But when they lie on different stacks of branes it gives rise to bi-fundamentals. This is what happens at the intersections of two branes. The states corresponding to open strings ending on each of the two branes correspond to bi-fundamentals that can naturally lead to a chiral spectrum.

A way to obtain the Standard Model group and spectrum is to intersect several stacks of branes. One stack of three correspond to the strong interactions, it can intersect with a stack of two D-branes corresponding to $SU(2)_L$. At the intersection, we have then the quark doublets. At a different intersection point the stack of two D-branes will intersect with one brane carrying $U(1)$ and the leptons will be at the intersection and so on. As it turns out, we need to introduce minimally four stacks of branes to fully account for the quantum number of all the Standard Model particles. Pictorially, the building block looks something like this:

The four stacks of branes are named the baryonic branes, the left brane, the right brane, and the leptonic brane for obvious reasons.

If this is all it takes to construct the Standard Model from intersecting branes, this lecture will be very short. As you will see, there are further string theory constraints both in constructing a "local model" and in embedding this setup in a compact setting. The purpose of this lecture is to discuss these subtleties.

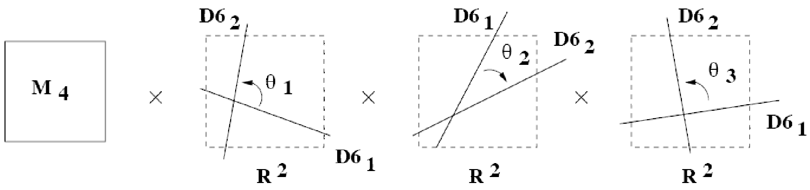

Figure 90: The local geometry of intersecting branes

5.1 Local Geometry and Spectrum

The basic configuration of intersecting D-brane models leading to 4D chiral fermions involve two stacks of D6-branes, each spanning our 4D space and three additional real dimensions.

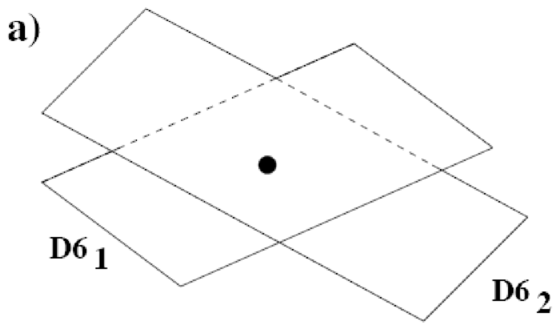

The local geometry is fully specified by the angles of rotations between the branes, which can be depicted as follows:

As we discussed, chiral fermions in bi-fundamental representations are localized at the intersection of the brane worldvolumes, which is our usual 4D space. The appearance of chirality can be understood from the fact that the geometry of the two D-branes introduces a preferred orientation in the 6D space. We can see this by considering the relative rotation of the second D6-brane with respect to the first. This also explains why we consider configuration of D6-branes (and not other types of branes, like D4 and D5, etc). D6-branes are the only type of branes that intersect at a point and so the chiral fermions are confined in our four-dimensional space. They don't intersect at a line or a surface for instance, so one can define an orientation in the full 6D space.

The open string spectrum can also be obtained easily. In fact, one can quantize open strings in this intersecting brane background and obtain the full string spectrum and not only the massless states (see appendix) but we will skip over these details. As far as massless states go, the open strings ending on the same stack of D-branes provide the $U(N)$ gauge bosons, three real adjoint scalars and their superpartners propagating over the 7D worldvolume of the D6-branes. The open strings stretching between different kinds of branes lead to a 4D chiral fermion transforming in the bi-fundamental representation and localized at the intersection. The chirality is encoded in the orientation defined by the intersection.

This last point requires some elaboration. Notice that:

- Two intersecting D6-branes define 3 angles:

$$\vec{\theta}^{ab} = (\theta_1^{ab}, \theta_2^{ab}, \theta_3^{ab}) \tag{192}$$

  This is because each 3-plane has an orientation, which differentiates between a D6-brane and an $\overline{D6}$-brane. Under a π rotation of any of these angles, a D6-brane becomes an $\overline{D6}$-brane:

$$\underset{D6}{(\theta_1^a, \theta_2^a, \theta_3^a)} \to \underset{\overline{D6}}{(\theta_1 + \pi, \theta_2^a, \theta_3^a)} \to \underset{D6}{(\theta_1^a + \pi, \theta_2^a + \pi, \theta_3)} \tag{193}$$

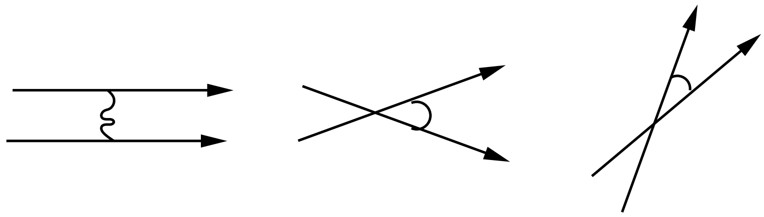

Figure 91: A non-chiral intersection of D-branes

- We can always choose $-\pi \leq \theta_i^{ab} \leq \pi$. Then if $\theta_i^{ab} \neq 0, \pm\pi$,

$$\vec{\theta}^{ab} = -\vec{\theta}^{ba} \tag{194}$$

  and so

$$\epsilon^{ab} \equiv \mathrm{sign}(\theta_1^{ab}\theta_2^{ab}\theta_3^{ab}) = -\epsilon^{ba} \tag{195}$$

  is a well defined quantity.

- If some $\theta_i^{ab} = 0$ or π, then ϵ^{ab} is not well defined, but the system is non-chiral since one can separate the branes, as shown in Figure 91. If they are separated by a length ℓ, the minimal mass is ℓ/α'.

- If all $\theta_i^{ab} \neq 0, \pi$, then the intersection cannot be removed by deforming the D6-branes. Therefore, there could be a chiral fermion at the intersection.

- It was shown by [30] that there is indeed an $D = 4$ chiral fermion, of chirality ϵ^{ab}, at the intersection, as well as some light scalars (also in bi-fundamental representation) whose masses depend on the θ_i^{ab}'s. In string units, their masses are given by

$$\begin{array}{ll} \frac{1}{2\pi}(-\theta_1+\theta_2+\theta_3) & \frac{1}{2\pi}(\theta_1-\theta_2+\theta_3) \\ \frac{1}{2\pi}(\theta_1+\theta_2-\theta_3) & 1-\frac{1}{2\pi}(-\theta_1-\theta_2-\theta_3) \end{array} \tag{196}$$

  where for simplicity of notation, we drop the ab superscript. These light scalars can be massless, massive or tachyonic depending on the angles between the branes. This point will become clear after we analyze the SUSY preserved by the branes (see Section 5.3).

- Notice that:
  - An open string from a to b has quantum number $(N_a, \overline{N}_b)$ and chirality ϵ^{ab}.
  - An open string from b to a has quantum number $(\overline{N}_a, N_b)$ and chirality $-\epsilon^{ab}$.

  They are anti-particles of one another and together gives the two fermionic degrees of freedom corresponding to one chiral Weyl fermion from a 4D spacetime point of view.

5.2 Compactification

Although intersecting D6-branes provide a mechanism to obtain 4D chiral fermions, the gauge bosons can propagate in the entire worldvolume of the D6-branes and so the gauge interactions remain 7D. Likewise, the gravitational interactions remain 10D before compactification. So, let us introduce the intersecting D-branes in a compact setting.

The general kind of configurations we will consider is string theory on a spacetime of the form $M_4 \times X_6$ where X_6 is compact.

The D6-branes are space-filling and wrap 3-cycles of the compact space. The new feature is that two 3-cycles in the compact space intersect several times, leading to replicated families of chiral fermions.

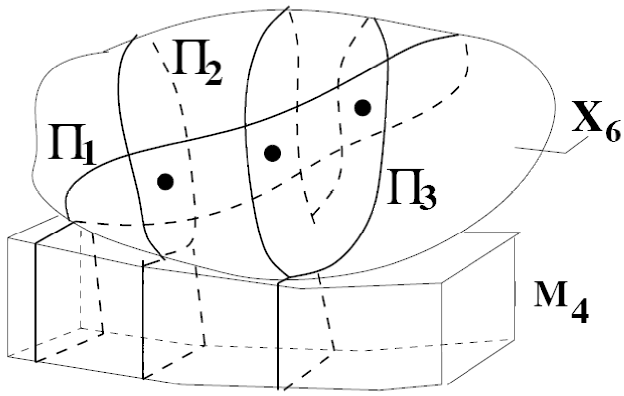

Figure 92: Compactification and intersecting brane models

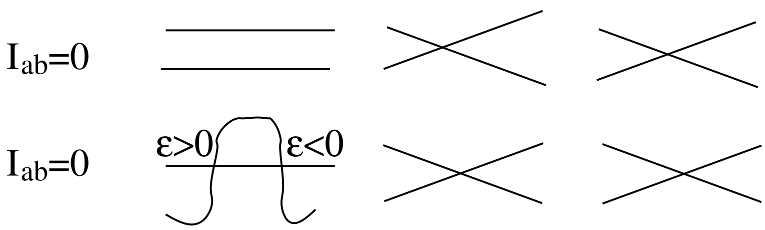

Figure 93: The intersection number is a topological quantity.

- Consider N_a D6-branes on $\mathcal{M}_4 \times \Pi_3^a$ and N_b D6-branes on $\mathcal{M}_4 \times \Pi_3^b$, we have
  - $U(N_a) \times U(N_b)$ gauge group
  - One chiral fermion in $(N_a, \overline{N}_b)$ representation at each intersection

  since we have locally the setup of flat space.

- Now, different intersections may have different ϵ^{ab}'s, so different chiralities. The gauge protected quantity is the net number of chiral fermions (say left-handed):

$$(\#\text{Intersections with } \epsilon^{ab} > 0) - (\#\text{Intersections with } \epsilon^{ab} < 0) \tag{197}$$

- The above is a topological quantity, known as the intersection number of two 3-cycles:

$$I_{ab} = [\Pi_a] \cdot [\Pi_b] \tag{198}$$

- I_{ab} is topological because it does not depend on the specific embedding of Π_a, only on the topology (more precisely, the homology class $[\Pi_a]$). It does not change as we deform the background geometry or the D-branes, as illustrated in Figure 93.

- The spectrum is thus:
  - Gauge Group: $\Pi_a U(N_a)$
  - Left chiral Fermions: $\sum_{a,b} I_{ab}(N_a, \overline{N}_b)$

  where in our convention, $I_{ab} < 0$ means right-handed chiral fermions. The possibility of $I_{ab} \neq 0, 1$ gives rise to an interesting mechanism of family replication.

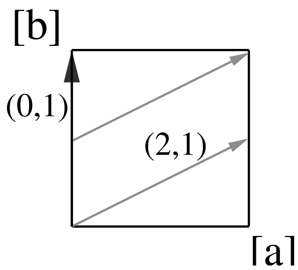

Figure 94: Examples of 1-cycles wrapping T^2.

- How do we compute the intersection number? Given $[\Pi_a]$, consider its Poincare dual defined as follows:

$$\int_{\Pi_a} \omega = \int_{X_6} \omega \wedge \alpha_a \ , \qquad \forall \omega \tag{199}$$

The intersection number is given by

$$I_{ab} = \int_{X_6} \alpha_a \wedge \alpha_b \tag{200}$$

- As an illustration, consider T^2 whose volume form is $dvol_{T^2} = dx \wedge dy$, then

$$[\Pi_a] = n_a[a] + m_a[b] \to \alpha_a = n_a dy - m_a dx \tag{201}$$

The intersection number is

$$I_{ab} = \int_{T^2} (n_a dy - m_a dx) \wedge (n_b dy - m_b dx) = (n_a m_b - n_b m_a) \tag{202}$$

Thus, the cycles shown in Figure 94 have intersection number $[(2,1)] \cdot [(0,1)] = 2$.

- Now, consider a 6D torus which is factorizable, $X_6 = T^2 \times T^2 \times T^2$. We make a further simplification by assuming that the three-cycle are also factorizable, i.e., they can be expressed as products of 1-cycles on each T^2:

$$[\Pi_a] = [(n_a^1, m_a^1)] \otimes [(n_a^2, m_a^2)] \otimes [(n_a^3, m_a^3)] \tag{203}$$

This is not the most general form of 3-cycles[13]. In this case, the intersection number can be generalized from that for T^2 to:

$$I_{ab} = [\Pi_a] \otimes [\Pi_b] = \prod_{i=1}^{3} \left(n_a^i m_b^i - m_a^i n_b^i \right) \tag{204}$$

The intersection number I_{ab} is the intersection number in homology, and can be easly shown using the intersection of the basic homology cycles

$$[a_i] \circ [b_j] = \delta_{ij} \qquad [a_i] \circ [a_i] = [b_i] \circ [b_j] = 0 \tag{205}$$

and linearity and antisymmetry of the intersection pairing.

- Let's consider a few toroidal examples to check this formula and to illustrate the point that chirality arises when the branes cannot be separated from one another. First consider the following system:

[13]In fact, by brane recombination, one can start with two factorizable ones and construct a non-factorizable 3-cycle.

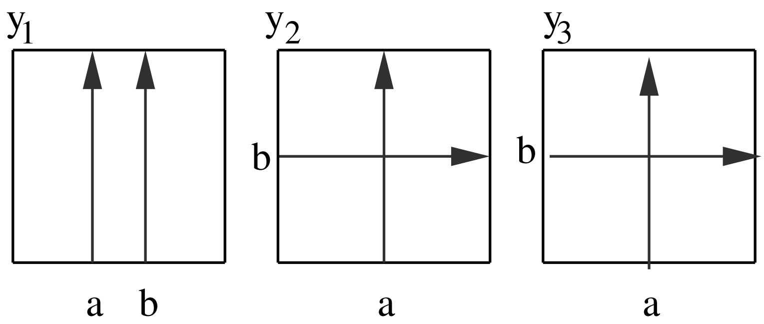

Figure 95: A non-chiral intersection of branes.

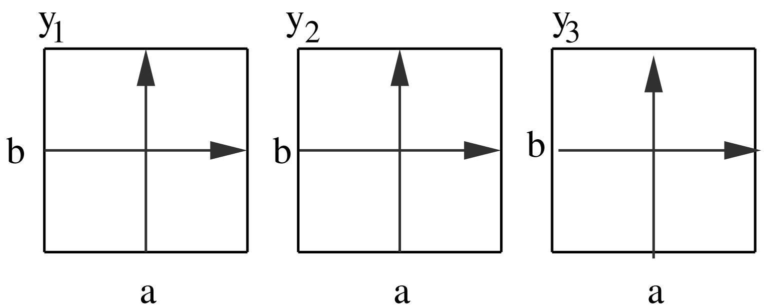

Figure 96: A chiral intersection of branes.

If we T-dualize on along all the y directions, we obtain:

$$D6_a \rightarrow D3 \tag{206}$$
$$D6_b \rightarrow D7 \tag{207}$$

which is the non-chiral system previously considered. This is is consistent with $\theta_i^{ab} = 0$.

- If we consider instead the system:

  T-dualizing along all y directions give:

$$\begin{array}{rcl} D6_a & \rightarrow & D3 \\ D6_b & \rightarrow & D9 \end{array} \tag{208}$$

We see that this is a chiral system (as the intersection number I_{ab} also shows) since we cannot separate a $D3$-brane from a $D9$ (same for $D5$ and $D7$).

- What about the following system?

  T-dializing along the y directions does not turn $D6_b$ into a pure $D9$, but rather a *bound state* of D-branes with different dimensions due to the worldvolume fluxes (see previously discussed T^2

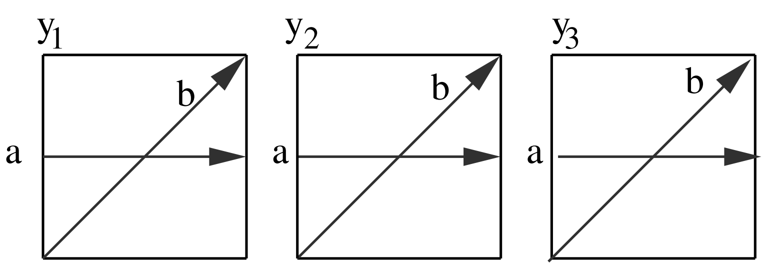

Figure 97: Another example of chiral intersection.

example in Section 3). The intersection number has the interpretation of the index of a Dirac operator:

$$\text{index}_Q D = \int_{X_6} \text{ch}(F_a) \wedge \text{ch}(-F_b) \wedge \hat{A}(R) \tag{209}$$

where $Q = (N_a, \overline{N}_b)$ and ch (F_a) is the Chern character, and $\hat{A}(R)$ is the A-roof genus. We will not need details of this expression. It is given here for completeness.

- Summarizing, compactification has the effect of family replication. The number of chiral families is topological:
  - **Type IIA:** Take two D6-branes, add and subtract intersection points. Number of chiral families is $I_{ab} = \int_{X_6} \alpha_a \wedge \alpha_b$.
  - **Type IIB:** A D_{2p+1}-brane and a $D_{2p'+1}$-brane intersect on submanifold $S_{2m} \subset X_6$. Number of chiral families is $\text{index}_Q D = \int_{S_{2m}} \text{ch}(F_a) \wedge \text{ch}(-F_b) \wedge \hat{A}(R)$.

5.3 Supersymmetry for intersecting branes

Intersecting D6-branes provide a particular setup for the brane world scenario:

- Gravity propagates in 10D
- Gauge bosons propagate in 7D
- Chiral matter propagates in 4D

So, in principle, we can consider both high and low string scale scenarios. In the former case, SUSY at the string scale helps to protect the Higgs mass from large radiative corrections. In the latter, one can consider the possibility of breaking SUSY at the string scale.

Nevertheless, we will focus on $\mathcal{N} = 1$ models whose effective theory is better understood. However, most of our results will be applicable to the $\mathcal{N} = 0$ case. SUSY models have the advantage that they are free of tachyons and the brane configurations are stable.

So, let us analyze the conditions for the D6-brane configuration to preserved SUSY. D-branes preserves 1/2 of the supersymmetries but two D-branes can a priori preserve a different SUSY.

Let R be the $SO(6)$ rotation that takes the first D6-branes into the second. The condition that some supersymmetry is preserved by the combined system is that there exists a 6D spinor which is invariant under R. Such a spinor exists if and only if R belongs to an $SU(3)$ subgroup of $SO(6)$. The reason is that the spinor of $SO(6)$ which transform as a $\mathbf{4}$ decomposes under $SU(3)$ as

$$\mathbf{4} = \mathbf{3} \oplus \mathbf{1} \tag{210}$$

and the singlet is invariant under $SU(3)$ transformation. This condition can be more explicitly stated (locally at the intersection) as

$$\theta_1 + \theta_2 + \theta_3 = 0 \pmod{2\pi} \tag{211}$$

Indeed, one can check that the open string spectrum computed before is Bose-Fermi degenerate in such cases. In the generic case, there is no supersymmetry invariant under the two stacks of branes, and the open string sector at the intersection is non-supersymmetric. The configuration is at least $\mathcal{N} = 1$ supersymmetric if the sum of the angles is zero. $\mathcal{N} = 2$ supersymmetry arises if, in addition, one of the angles also vanishes while $\mathcal{N} = 4$ arises only for parallel stacks, i.e., $\theta_i = 0$.

More generally, for a Calabi-Yau manifold, the three-cycles that the D6-branes can wrap while preserving SUSY are the so-called special Lagrangian (sLag) cycles, which are defined as follows.

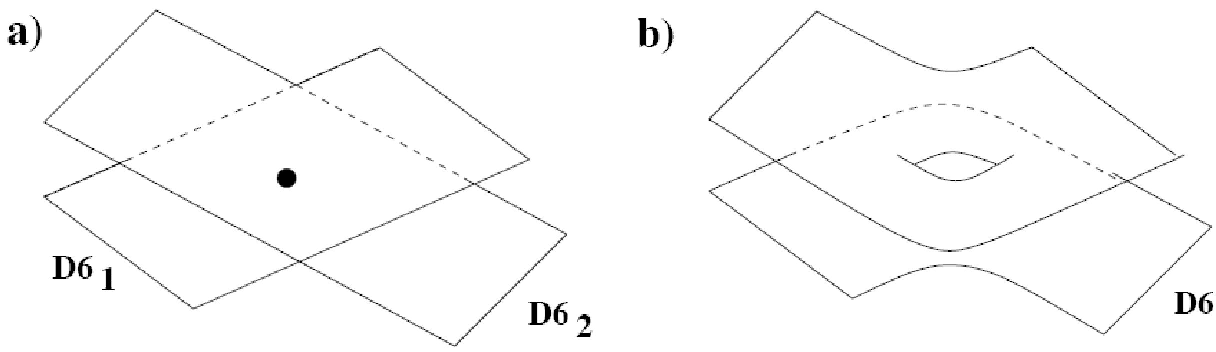

Figure 98: D-brane recombination

On a Calabi-Yau manifold there exist a covariantly constant holomorphic three-form, Ω_3, and a Kähler 2-form J. Locally, the holomorphic 3-form Ω_3 and the Kähler form J can be defined by

$$\Omega_3 = dz_1 \wedge dz_2 \wedge dz_3, \quad J = i \sum_{i=1}^{3} dz_i \wedge d\bar{z}_i. \tag{212}$$

A three-cycle π_a is called Lagrangian if the restriction of the Kähler form on the cycle vanishes

$$J|_{\pi_a} = 0. \tag{213}$$

If the three-cycle in addition is volume minimizing, which can be expressed as the property that the imaginary part of the three-form Ω_3 vanishes when restricted to the cycle,

$$\Im(e^{i\varphi_a}\,\Omega_3)|_{\pi_a} = 0, \tag{214}$$

then the three-cycle is called a sLag cycle. The parameter φ_a is a constant depending only on the homology class of π_a and determines which $\mathcal{N} = 1$ supersymmetry is preserved by the brane. Thus, different branes with different values for φ_a preserve different $\mathcal{N} = 1$ supersymmetries. One can show that (214) implies that the volume of the three-cycle is given by

$$\mathrm{Vol}(\pi_a) = \left| \int_{\pi_a} \Re(e^{i\varphi_a}\,\Omega_3). \right| \tag{215}$$

A shift of $\varphi_a \to \varphi_a + \pi$ corresponds to exchanging a D-brane by its anti-D-brane, where the D-brane really satisfies (215) without taking the absolute value. Therefore a supersymmetric cycle π_a is calibrated with respect to $\Re(e^{i\varphi_a}\Omega_3)$. To obtain a globally $\mathcal{N} = 1$ supersymmetric intersecting D-brane model all D6-branes have to wrap sLag three-cycles which are calibrated with respect to the same three-form.

Exercise: Show that for a torus, the condition that π_a is sLag reduces to the condition Eq. (211) derived before.

As mentioned earlier, the light scalars at the intersection can be massless, massive or tachyonic.

- The massless case corresponds to a situation with some unbroken supersymmetry. The massless scalar is a modulus whose vacuum expectation value parametrizes the possibility of recombining the two intersecting D-branes into a single smooth one.

- The configuration with tachyonic scalars corresponds to situations where this recombination is triggered dynamically, as a result of tachyon condensation at the intersection.

- The configuration where all light scalars have positive squared mass corresponds to a non-supersymmetric configuration, which is nevertheless dynamically stable against recombination. Namely, the recombined 3-cycle has a volume larger than the sum of the volumes of the intersecting 3-cycles.

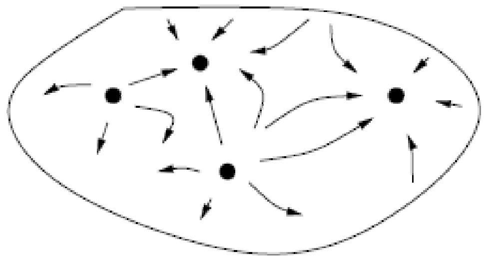

Figure 99: RR charges and Gauss's Law

5.4 RR tadpole Cancellation

However, compactification also leads to new subtleties. This is because D-branes act as a source for RR fields via the disk coupling:

$$\int_{W^{p+1}} C_{p+1} \tag{216}$$

In a compact space, the total RR charge must vanish as required by Gauss's law.

The RR charges are characterized by the 3-cycles on which the branes are wrapped. Hence, the sum of the homological cycles wrapped by all the branes must be topologically trivial.

$$[\pi_{total}] = \sum_a N_a[\pi_a] = 0 \tag{217}$$

Equivalently, one can understand this constraint as the consistency requirement of the equations of motion for the RR fields. Keeping only terms in the spacetime action which depend on the RR 7-form C_7, we have:

$$\begin{aligned} S_{C7} &= \int_{M_4\times X_6} H_8 \wedge *H_8 + \sum_a N_a \int_{M_4\times\pi_a} C_7 \\ &= -\int_{M_4\times X_6} C_7 \times dH_2 + \sum_a N_a \int_{M_4\times X_6} C_7 \wedge \delta(\pi_a) \end{aligned} \tag{218}$$

where H_8 is the 8-form field strength, H_2 its Hodge dual, and $\delta(\pi_a)$ is a bump 3-form localized on the 3-cycle. The equation of motion reads:

$$dH_2 = \sum_a N_a \delta(\pi_a) \tag{219}$$

Integrating this equation gives the tadpole constraint Eq. (217) on the homology classes.

5.5 Anomaly Cancellation

Cancellation of RR tadpoles in the underlying string theory is important because it implies the cancellation of chiral anomalies in the four dimensional effective field theory. These anomalies include the cubic non-Abelian anomalies, and mixed $U(1)$ non-Abelian anomalies, and mixed gravitational anomalies. Let's discuss them one by one.

1. **Cubic non-Abelian anomalies**

   The $SU(N_a)^3$ anomaly is proportional to the number of fundamental minus anti-fundamental representations of $SU(N)$. Since the matter fields transform as bifundamentals, the cubic anomaly it is proportional to the sum of the intersection number times the number of branes:

$$A_a = \sum_b I_{ab} N_b \tag{220}$$

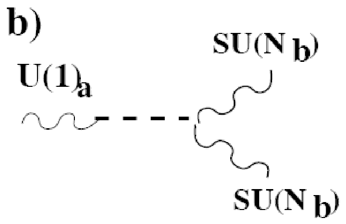

Figure 100: The Green-Schwarz term

It is easy to check that this vanishes due to RR tadpole cancellation. By taking the intersection of the tadpole condition with any 3-cycle, we find

$$0 = [\pi_a] \circ \sum_b N_b[\pi_b] = \sum_b N_b I_{ab} \tag{221}$$

as claimed. Note that the tadpole condition is slightly stronger than the absence of cubic anomalies because it must hold even for $N = 1, 2$ where no cubic anomaly exists. As we will see, this observation will turn out important in phenomenological model building.

2. **Mixed anomalies**

What about mixed $U(1)_a - SU(N_b)^2$ anomalies? The usual field theory triangle diagram gives a non-zero contribution, even after using the RR tadpole conditions:

$$A_{ab} \simeq N_a I_{ab} \tag{222}$$

However, in string theory there is an extra diagram known as the Green-Schwarz diagram, where the $U(1)$ gauge boson mixes with a 2-form which subsequently couples to two gauge bosons of $SU(N)$:

Exercise: Show that the following couplings arising in the KK reduction of the D6-brane worldvolume action

$$N_a \int_{D6_a} C_5 \wedge trF_a, \qquad \int_{D6_b} C_3 \wedge trF_b^2 \tag{223}$$

give rise to the Green-Schwarz term which leads to a cancellation of the residual field theory triangle anomalies.

Solutions: Introducing a basis of 3-cycles $[\Lambda_k]$ and its dual $[\Lambda_{\tilde{\ell}}]$, we can define the KK reduced 4d fields

$$(B_2)_k = \int_{[\Lambda_k]} C_5, \qquad \phi_{\tilde{\ell}} = \int_{[\Lambda_{\tilde{\ell}}]} C_3 = -\delta_{k\tilde{\ell}} *_{4d} (B_2)_k \tag{224}$$

The KK reduced 4d couplings read

$$N_a q_{ak} \int_{4d} (B_2)_k trF_a, \qquad q_{b\tilde{\ell}} \int_{4d} \phi_{\tilde{\ell}} trF_b^2 \tag{225}$$

with $q_{ak} = [\pi_a] \circ [\Lambda_k]$, and similarly for $q_{b\tilde{\ell}}$. The total amplitude is proportional to

$$A_{ab}^{GS} = -N_a \sum_k q_{ak} q_{b\tilde{\ell}} \delta_{k\tilde{\ell}} = \cdots - N_a I_{ab} \tag{226}$$

leading to cancellation between both kinds of contributions.

3. **Mixed gravitational anomalies:** It is left as an exercise to show that for toroidal models, the mixed gravitational anomalies cancel automatically, without the Green-Schwarz contribution. **(Exercise)** This is no longer true for orbifolds/orientifolds.

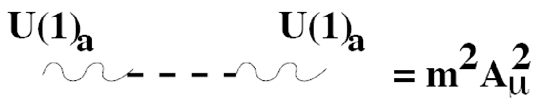

Figure 101: $B \wedge F$ coupling and massive $U(1)$

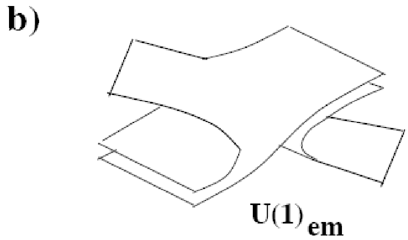

Figure 102: Electroweak symmetry breaking as brane recombination.

An important observation is that any $U(1)$ gauge boson with $B \wedge F$ coupling gets massive, with mass roughly of the order of the string scale.

There can be several of them, and they are not necessarily anomalous. Such $U(1)$'s disappear as gauge symmetries from the low energy effective theory, but remains as global symmetries, unbroken in perturbation theory. In constructing D-brane Standard Model, we need to make sure that the candidate for the hypercharge is not one of these massive $U(1)$.

5.6 Phenomenological features

Before we construct more realistic examples, let us briefly mention some phenomenological features we can extract from the toroidal examples studied so far. These features are natural in the general setup of intersecting brane models and are not restricted only to toroidal models.

- **Proton Stability:** First of all, in these models, the proton is perturbatively stable. This is because the $U(1)$ within the $U(3)$ plays the role of baryon number, and is preserved as a global symmetry, unbroken in perturbation theory though it can be broken by non-perturbative instanton effects. In some cases, the instanton effects breaking the Standard Model baryon number is calculable, e.g., as a Euclidean D2-brane wrapped on 3-cycles.

- **Gauge Unification:** These models do not have a natural gauge coupling unification, even at the string scale. Each gauge factor has a gauge coupling controlled by the volume of the wrapped 3-cycle. Gauge couplings are related to geometric volumes, hence the moduli controlling the sizes of these volumes are constrained by experiments.

- **Electroweak Symmetry Breaking:** These exists a geometric interpretation for the spontaneous electroweak symmetry breaking. In explicit models, the Higgs particle arises from the light scalar at the intersections, whose vev parametrizes the possibility of recombining two intersecting branes into a single smooth one. In this process, the gauge symmetry is reduced, corresponding to a Higgs mechanism in the effective field theory.

- **Yukawa Couplings:** There is a natural exponential hierarchy in the Yukawa couplings. Yukawa couplings among the scalar Higgs and chiral fermions arise at tree level in the string coupling from open string worldsheet instantons, namely from string worldsheet spanning the triangle with vertices at the intersections and sides on the D-branes.

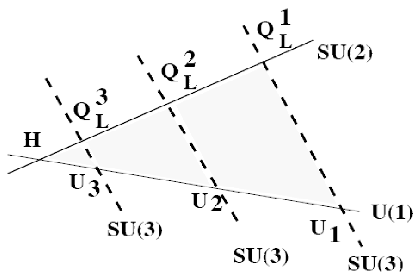

Figure 103: Yukawa couplings arise from worldsheet instantons.

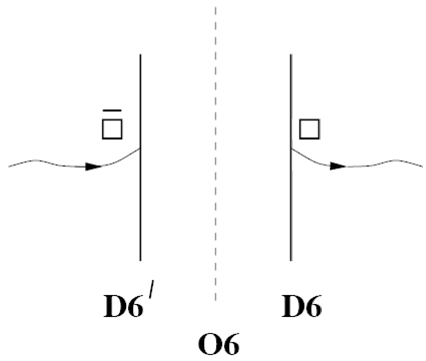

Figure 104: An orientifold 6-plane

Their values are exponentially suppressed by the area of the string worldsheet in string units. Different families are located at different intersections, leading to an exponential hierarchy in the Yukawa couplings between different families.

5.7 Orientifold Models

It turns out what we have introduced so far are not yet sufficient to construct a realistic model. We need an extra element, known as the orientifold planes.

Orientifold is a play of the word orbifold. Unlike an orbifold which acts only on the target space, an orientifold acts as on the worldsheet as well.

An orientifold projection flips the orientation of the worldsheet and reflects the coordinates. The set of points fixed under the orientifold projection is called an orientifold plane.

So, why orientifolds? We have already seen that the total RR charge in a compact space must vanish. So, we need objects with negative charge. In order to preserve SUSY, these objects must also carry negative tension. We will see shortly that an orientifold plane has precisely these properties. Another reason to consider orientifolds is that as it turns out, intersecting D-brane models without orientifold planes are bounded to contain chiral exotics.

5.8 Properties of O6-planes

To see why this is the case, let us first review the properties of orientifold planes. To cancel the RR charges of the D6-branes, we need objects of the same dimensionality and hence O6-planes. Again, to start, consider the simplest case which is Type IIA string theory on 10d flat space and mod it out by the so called orientifold action $\Omega R(-1)^{F_L}$ where Ω is the worldsheet parity symmetry: $(\sigma,\tau) \to (-\sigma,\tau)$ which flips the orientation of the fundamental strings; R is a $\mathbb{Z}_2$ geometric action, acting locally as $(x^5,x^7,x^9) \to (-x^5,-x^7,-x^9)$; finally $(-1)^{F_L}$ is the left-moving worldsheet fermion number, introduced for technical reasons. One can argue for this $(-1)^{F_L}$ factor from T-duality (**Exercise**).

The subspace in spacetime, fixed under the geometric part R of the above action, is known as an

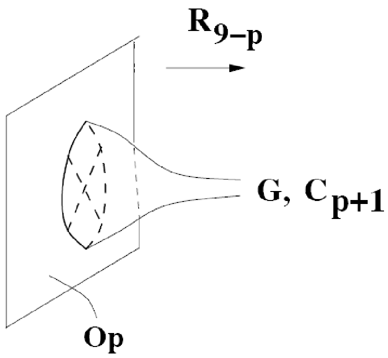

Figure 105: An orientifold plane carries tension and RR-charge.

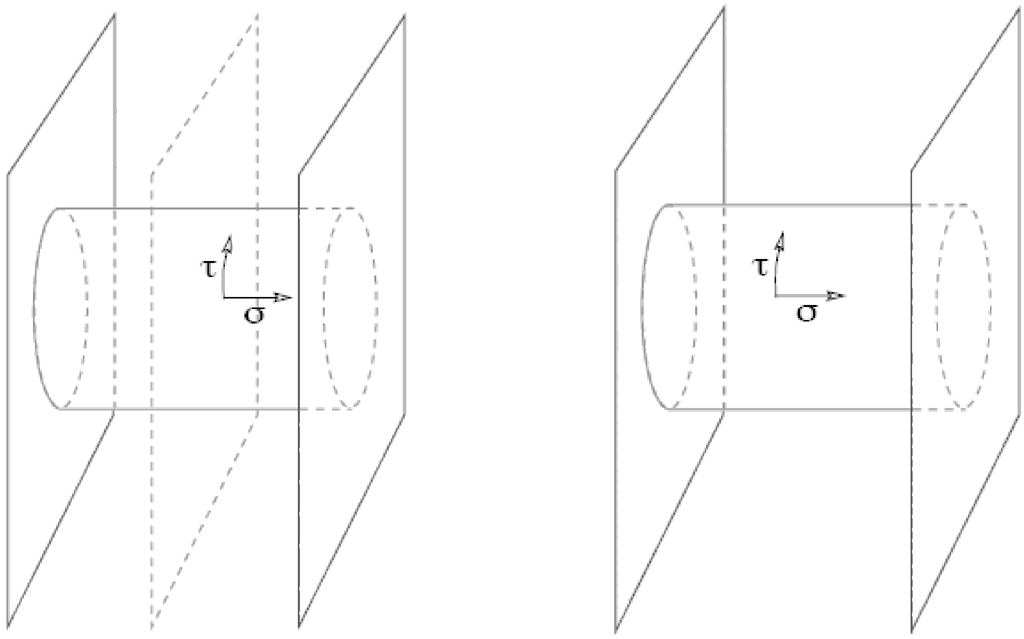

Figure 106: (a) One-loop open string amplitude in the presence of O-planes, (b) without O-planes.

orientifold 6-plane. It is a 7d plane defined by $x^5 = x^7 = x^9 = 0$ and spanned by the remaining 7 coordinates. Physically, it corresponds to *a region of spacetime where the orientation of a string can flip.* The description of string theory in the presence of orientifold planes is modified by the inclusion of unoriented worldsheets, for instance with the topology of the Klein bottle.

Orientifold planes have some features similar to D-branes of the same dimension. For instance, an O_p plane carries tension and are charged under the RR $(p+1)$ form C_{p+1}.

In fact, one can compute its tension and charge by comparing the one-loop open string diagrams with and without the orientifold plane.

One finds that the charge of an O6-plane is -4 if the charge of a D6-brane is normalized to 1. (Actually, there are O6-planes which carry positive RR charges but to avoid confusion, let's ignore this possibility in what follows). Furthermore, O6-planes preserve the same supersymmetry as a D6-brane. This implies that there is a relation between the tension and the charge of an O-plane.

Hence, in a compact space, the cancellation of RR charges implies:

$$\sum_a N_a[\pi_a] + \sum_a N_a[\pi_{a'}] - 4 \times [\pi_{O6}] = 0 \tag{227}$$

where $[\pi_{a'}]$ is the homology class of the 3-cycle wrapped by the image D6-branes. *There are additional* *discrete constraints arising from cancellation of* $\mathbf{Z}_2$ *valued K-theory charges.* We will skip the discussion of such constraints for now and come back to them later when we construct concrete models.

There are however important differences between O-planes and D-branes. The most important one being that an orientifold plane has no worldvolume degrees of freedom since open strings are not stuck on them. So, unlike D-branes, they are not dynamical objects [14].

Although we have been discussing flat space and toroidal models so far, more generally, an O6-plane can be defined by the quotient $\Omega\overline{\sigma}(-1)^{F_L}$ where $\overline{\sigma}$ is an isometric, antiholomorphic involution of X_6, and acts on the Kahler class J and the holomorphic 3-form Ω_3 as:

$$\overline{\sigma}J = -J \qquad \overline{\sigma}\Omega_3 = e^{2\pi i\varphi}\overline{\Omega}_3 \tag{228}$$

with $\varphi \in \mathbb{R}$. For $\varphi = 0$ in local coordinates, this can be thought of as complex conjugation. The orientifold 6-plane is localized at the fixed point of $\overline{\sigma}$ which topologically is a three-cycle.

5.9 Open String Spectrum with O6-planes and D6-branes

To describe orientifold models, it is convenient to go to the covering space, and include the images of D-branes under the orientifold action. The spectrum of open strings in the orientifold construction can be obtained by simply computing the spectrum in the covering space, and then imposing the identification implied by the orientifold action.

First, consider configurations with parallel D6-branes and O6-planes.

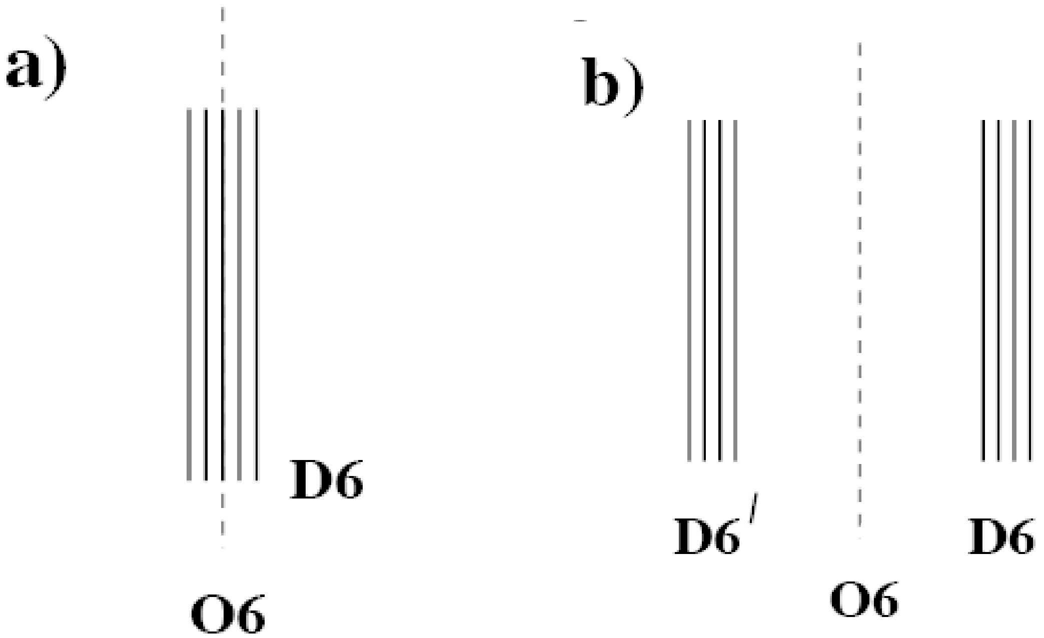

Figure 107: Parallel D6-branes and O6-planes: (a) on top of each other, (b) separated.

- If the D6-branes are on top of the O-plane, the orientifold action identifies the endpoints of the string:

$$|ab> \leftrightarrow \pm|ba> \tag{229}$$

  This identification breaks the $U(N)$ gauge group to SO or Sp depending on some subtle choices of sign.

[14] In F-theory, which can be thought of as Type IIB orientifold compactification with varying dilaton, an orientifold planes can be interpreted as a bound state of mutually non-local 7-branes and so O-planes are dynamical in such a limit.

- If the D6-branes are parallel but separated from the O-plane, the orientifold action maps a stack of D6-branes to its image. The two $U(N)$ factors are identified, only a linear combination survives. This agrees with the intuition that massless modes on D-branes are not sensitive to distant objects, hence the N D6-branes in the quotient do not notice, at the level of the massless spectrum, the distant O6-planes.

  An important observation is that due to the orientation reversal, an open string starting on a stack of D6-branes is mapped to an open string ending on the image stack. This implies that a fundamental representation is mapped to an anti-fundamental representation and vice versa. This fact will be important later on.

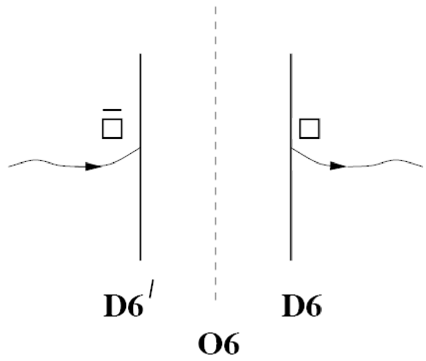

Figure 108: An O-plane reverses the orientation of an open string.

Now, consider situations with intersecting branes (and their images) in the presence of O-planes. There are several cases to consider (illustrated in Figures 109 and 110):

- If two stacks of D6-branes, labeled a and b, are intersecting away fom the O-plane, the orientifold action simply maps these two stacks of branes to their images. After the identification,we are left with a $U(N)\times U(M)$ gauge group and a chiral fermion in the bi-fundamental representation.

- Consider now the intersection of D-branes in the a-stack with the orientifold image of the b-stack, the only difference is that the chiral fermion transform in the fundamental representations of both gauge groups.

- Finally, we can consider a stack of D-branes intersecting with its own image either on top of the O-plane or away from it. The open strings ending on the D6-branes and their images transform in the symmetric or antisymmetric representations of $U(N)$. If the intersection is right on top of the orientifold plane, only the antisymmetric representation survives. If the intersection is away from the O-plane, the orientifold action simply maps these two sets of symmetric plus anti-symmetric representations to each other.

To summarize, this is the chiral spectrum of an orientifold model.

Representation	Multiplicity
$\begin{smallmatrix}\Box\\\Box\end{smallmatrix}_a$	$\frac{1}{2}\left(\pi'_a \circ \pi_a + \pi_{O6} \circ \pi_a\right)$
$\Box\!\Box_a$	$\frac{1}{2}\left(\pi'_a \circ \pi_a - \pi_{O6} \circ \pi_a\right)$
$(\overline{\Box}_a, \Box_b)$	$\pi_a \circ \pi_b$
$(\Box_a, \Box_b)$	$\pi'_a \circ \pi_b$

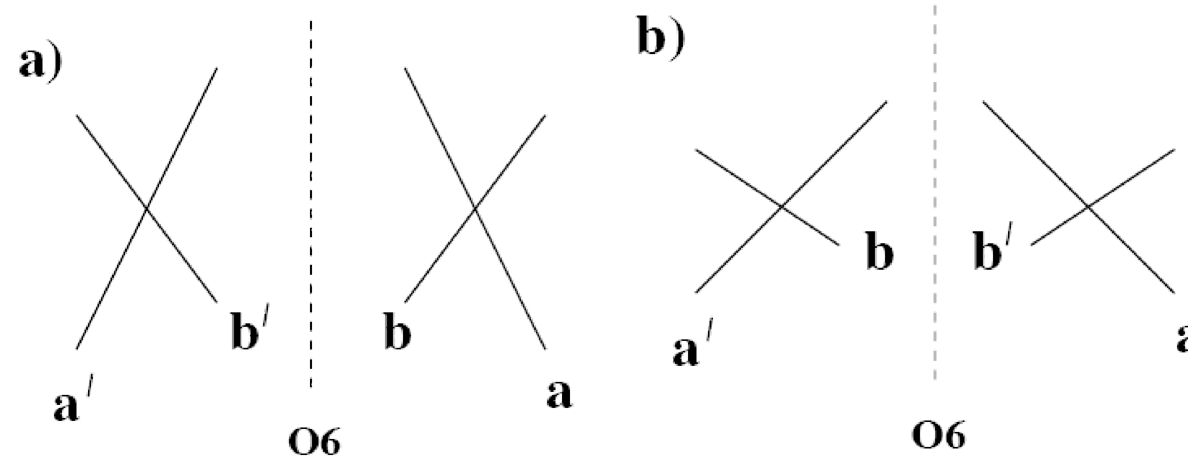

Figure 109: Intersection of different D6-planes in the presence of an O6-plane.

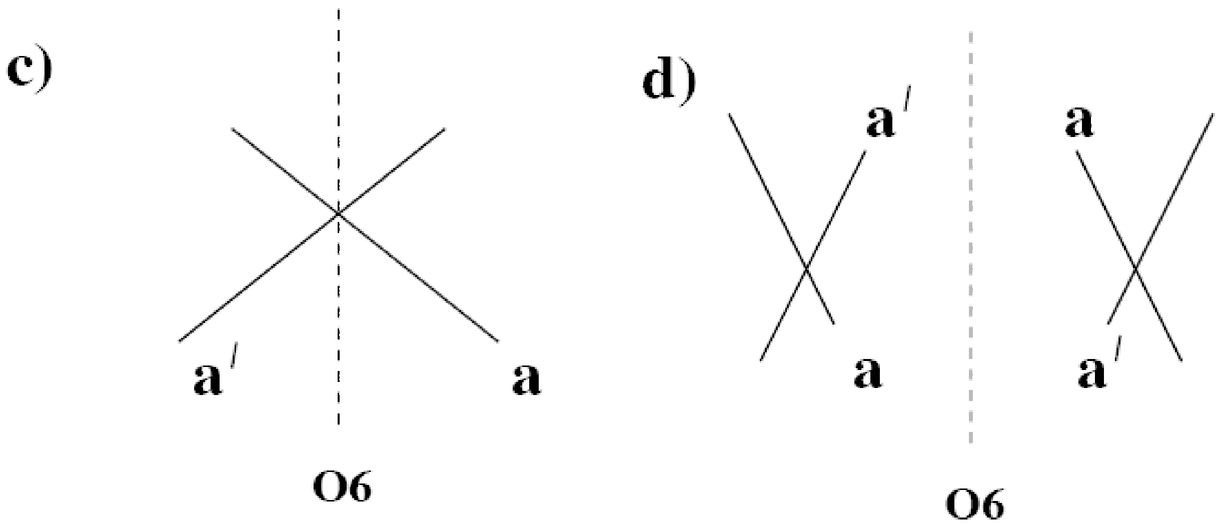

Figure 110: Intersection of a D6-plane and its image in the presence of an O6-plane.

We will see later that the same chiral spectrum applies to more general backgrounds such as orbifolds and even Calabi-Yau manifolds, *provided that we interpret these homology cycles correctly.*

There is one more subtlety, involving orientfold planes, when we compactified the theory. The $\mathbb{Z}_2$ involution $\overline{\sigma}$ may only be a discrete symmetry for certain choices of the moduli. For example, $\overline{\sigma}=$ complex conjugate is a Z_2 involution on a torus only for two choices of complex structure moduli: a rectangular torus or a specifically "tilted" torus:

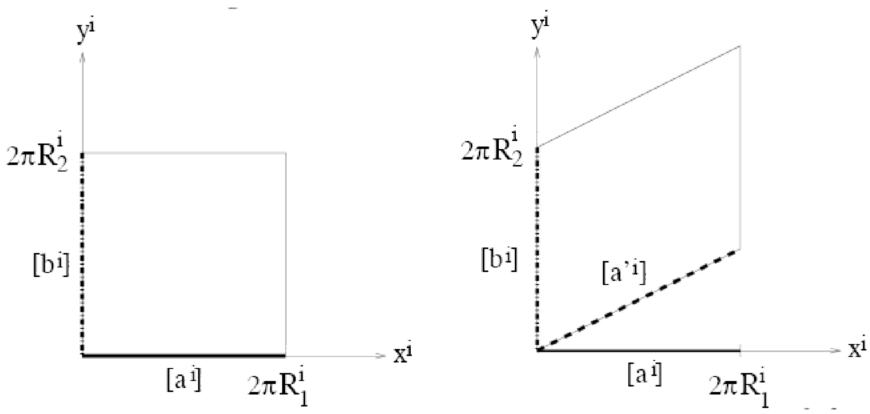

The basic homology cycles of the tilted torus can be expressed in terms of the untilted ones:

$$[a'] = [a] + \frac{1}{2}[b] \qquad [b'] = [b] \tag{230}$$

The orientifold image of a D-brane is again given by the reflection along the O-plane.

5.10 Getting just the Standard Model

In addition to their importance in canceling the D-brane charges, there is in fact a general argument which shows that in the absence of O-planes, D-brane models necessarily contain $SU(2)$ chiral exotics. To see this, first notice that without the O-planes, the electroweak $SU(2)$ must belong to a $U(2)$ factor of the gauge group. An important point emphasized earlier is that the tadpole condition implies that the number of fundamentals and anti-fundamentals must be equal, even for $U(2)$ (where the 2 and the $\overline{2}$ are distinguished by their $U(1)$ charge). Now, since there are 3 families and the left-handed quarks transform as $(3, \overline{2})$, they contribute altogether 9 anti-fundamentals of $SU(2)$. The complete spectrum must necessarily contain 9 fundamentals, three of which may be interpreted as left-handed leptons; the remaining six doublets are however exotic chiral fermions, beyond the spectrum of the SM.

There are two ways to avoid these exotics, both involving orientifolds.

The U(2) case

One possibility is to exploit the fact there are two kinds of bi-fundamental fields in an orientifold model, namely, $(N_a, \overline{N}_b)$ and (N_a, N_b). Consider realizing the three families of left-handed quarks as a combination of $(3, \overline{2}) + 2(3, 2)$. The number of $SU(2)$ doublets needed to cancel the tadpoles is 3 which is precisely number of left-handed leptons.

Exercise: Consider four stacks of branes denoted a, b, c, d (and their images), giving rise to a gauge group $U(3)_a \times U(2)_b \times U(1)_c \times U(1)_d$. If the intersection numbers between the corresponding 3-cycles are given by:

$$\begin{array}{llll} I_{ab} = 1 & I_{ab'} = 2 & I_{ac} = -3 & I_{ac'} = -3 \\ I_{bd} = 0 & I_{bd'} = -3 & I_{cd} = -3 & I_{cd'} = 3 \end{array} \tag{231}$$

Show that the chiral spectrum has the non-Abelian quantum numbers of the Standard Model (plus three right-handed neutrinos). In order to reproduce exactly the Standard Model one also needs to require that the linear combination of $U(1)$'s

$$Q_Y = \frac{1}{6}Q_a - \frac{1}{2}Q_c + \frac{1}{2}Q_d \tag{232}$$

to be massless.

However, several comments are in order. It is important to emphasize that at this level, we have not constructed any explicit model. In particular, we have only presented a set of intersection numbers.

We haven't shown that there exist cycles on which the D-branes wrapped which lead to the given intersection numbers. Moreover, even if we manage to do so, the intersection numbers only define a local model. We still need to introduce additional hidden sector branes to cancel the tadpoles in constructing compact models. On the other hand, the intersection numbers are not restricted to toroidal models. In fact, it was shown that such topological data can indeed arise in more general approach such as Calabi-Yau orientifolds and Gepner constructions.

The USp(2) Case

Another way to avoid the $SU(2)$ exotics is to make use of the fact that $D6$-branes in the presence of orientifold planes can give rise to symplectic groups. For symplectic groups, all representations are real, and RR tadpole conditions do not impose any constraint on the number of doublets. Since $USp(2) \equiv SU(2)$, it is possible to realize the electroweak $SU(2)$ as a symplectic group, and thus circumvent the constraints on the number of doublets.

Again, as an exercise, you can show that the following set of branes with gauge groups $U(3)_a \times USp(2)_b \times U(1)_c \times U(1)_d$ and intersection numbers

$$\begin{array}{cccccc} & & I_{ab}=3 & I_{ab'}=3 & I_{ac}=-3 & I_{ac'}=-3 \\ I_{db}=3 & I_{db'}=3 & I_{dc}=-3 & I_{dc'}=3 & I_{bc}=-1 & I_{bc'}=1 \end{array} \tag{233}$$

give rise to the chiral spectrum of the Standard Model. The $U(1)$ that needs to be massless in order to reproduce the Standard Model hypercharge is

$$Q_Y = \frac{1}{6}Q_a - \frac{1}{2}Q_c - \frac{1}{2}Q_d \tag{234}$$

In fact, explicit models with D6-branes on 3-cycles and these intersection numbers have been constructed. We will discuss some examples later.

5.11 Supersymmetric models

Let us try to embed these D-brane configurations into a supersymmetric setup. We are interested in chiral models, which can arise in theories with $N = 1$ or less supersymmetry. The simplest way of reducing the supersymmetry to $N = 1$ is via orbifolding. For example, the $\mathbb{Z}_2 \times \mathbb{Z}_2$ orbifold whose generators acts on the three complex compactified coordinates as follows:

$$\begin{aligned} \theta : (z_1, z_2, z_3) &\rightarrow (-z_1, -z_2, z_3) \\ \omega : (z_1, z_2, z_3) &\rightarrow (z_1, -z_2, -z_3) \end{aligned} \tag{235}$$

preserves $N = 1$ supersymmetry. Recall the orientifold projection introduced earlier:

$$\Omega R(-1)^{F_L} \tag{236}$$

Orbifolding introduces 3 new types of orientifold planes: $\Omega R\theta(-1)^{F_L}$, $\Omega R\omega(-1)^{F_L}$, and $\Omega R\theta\omega(-1)^{F_L}$. Hence, there are 4 kinds of O-planes, associated to the worldsheet parity couples with four different types of spatial reflection. The O6-planes are invariant under the $\mathbb{Z}_2$ involution, so we can depicted them as follows:

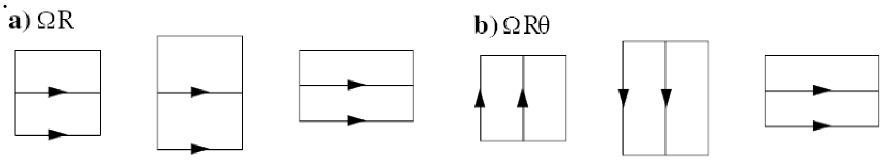

Sector	Matter	$SU(4)\times SU(2)_L \times SU(2)_R$	Q_a	Q_h	Q'
(ab)	F_L	$3(4,2,1)$	1	0	1/3
(ac)	F_R	$3(\bar{4},1,2)$	−1	0	−1/3
(bc)	H	$(1,2,2)$	0	0	0
(bh)		$2(1,2,1)$	0	-1	2
(ch)		$2(1,1,2)$	0	+1	−2

Figure 111: The full spectrum of the model in [31, 32] after D-brane recombination.

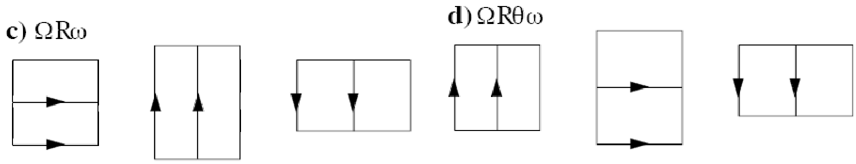

The chiral spectrum can be computed from the general results obtained earlier, except to keep in mind that the homology cycles are defined on the orbifold space instead of the torus.

To provide an illustrative example, consider the following model:

N_α	(n^1_α, m^1_α)	(n^2_α, m^2_α)	(n^3_α, m^3_α)
$N_a = 6$	$(1,0)$	$(3,1)$	$(3,-1)$
$N_b = 2$	$(0,1)$	$(1,0)$	$(0,-1)$
$N_c = 2$	$(0,1)$	$(0,-1)$	$(1,0)$
$N_d = 2$	$(1,0)$	$(3,1)$	$(3,-1)$
$N_{h1} = 2$	$(-2,1)$	$(-3,1)$	$(-4,1)$
$N_{h2} = 2$	$(-2,1)$	$(-4,1)$	$(-3,1)$
40	$(1,0)$	$(1,0)$	$(1,0)$

Up to some redefinition, the subset of branes in blue gives rise to the intersection numbers in the $USp(2)$ case introduced earlier.

The D-brane configurations preserve SUSY if the 3-cycles are sLag. For toroidal orbifolds (see homework), the condition can be simply stated as:

$$\theta_1 + \theta_2 + \theta_3 = 0 \tag{237}$$

or equivalently, in terms of the complex structure moduli $\chi_i = (R_2/R_1)_i$:

$$\sum_i \arctan(\chi_i \frac{m_i}{n_i}) = 0 \tag{238}$$

which admits solutions [15] for χ_i.

The spectrum is fairly complicated, but under D-brane recombination, the chiral spectrum is greatly simplified (see [31, 32]):

Exercise: Show that unlike the toroidal model, the mixed gravitational anomalies in the $\mathbb{Z}_2 \times \mathbb{Z}_2$ orientifold are not canceled, even after the cancellation of RR charges. They are canceled by the Green-Schwarz mechanism.

In the strong coupling limit, these $\mathcal{N} = 1$ supersymmetric intersecting D-brane models are lifted to M theory on singular G_2 manifolds. This is an interesting subject which I have no time to discuss. For a brief discussion, see [14].

[15]This formula is actually only valid for the case $n^i_a \geq 0$. See below for some other important cases.

I hope these examples suffice to illustrate the concepts we have learned. Much of our discussions so far have centered on the open string sector since we are interested in getting the gauge and chiral spectrum of the Standard Model from string theory. The closed string sector is however also relevant for low energy dynamics, and leads to an additional set of important questions. This is the topic to which we now turn.

6 Warped Compactifications

The main such question that we have not yet addressed is the existence of moduli, massless fields with flat potential and hence undetermined vevs. Stabilization of these moduli (namely, providing them with a potential which fixes their vevs and give them masses) is an important question, of immediate relevance to phenomenology and cosmology. A proposal to attack this problem is to consider compactification with fluxes [33–37]. We will begin with a general discussion of flux compactifications and then discuss issues that arise when combining this mechanism of moduli stabilization with D-brane model building. For simplicity and concreteness, we consider Type IIB compactifications with 3-form fluxes. Similar analysis should (and could in principle) be carried out for other setups.

6.1 Flux Compactification

Flux compactification has developed into a very broad subject. Here, we will focus on aspects which are relevant for model building. General discussions can be found in some recent reviews [14, 38, 39]. The basic idea is that in string theory, there are many p-form gauge fields C_p in its massless spectrum. In particular, Type IIB contains NS-NS 0 and 2-forms, and RR 2 and 4 forms and their magnetic dual $8-p$ forms. Analogous to electromagnetism, one can consider solutions with a non-vanishing flux $F_{p+1} = dC_p \neq 0$. Turning on fluxes has the following interesting consequences:

- The kinetic term
$$S_{kin} = \int_{\mathcal{M}} F \wedge *F \tag{239}$$
induces a scalar potential in the 4D effective action, which in general depends on the moduli controlling the size of the cycles Σ the flux is running through, i.e.,
$$\int_{\Sigma} F \neq 0 \tag{240}$$
This leads to *moduli stabilization.* This is analogous to the statement in electromagnetism that the electromagnetic energy $U = \frac{1}{8\pi}\int \left(E^2 + B^2\right)$ which depends on the volume of space.

- The background flux provides a source term to the Einstein equation. Hence its backreaction warps the geometry of space and the metric is no longer Ricci flat.

- Fluxes carry D3-charge through Chern-Simons terms in the 10D action. They can affect the number of D-branes in compact examples.

In more details, consider Type IIB compactification with non-trivial NSNS and RR 3-form fluxes H_3 and F_3. These 3-form fluxes must satisfy the Bianchi identity
$$dF_3 = 0 \qquad dH_3 = 0 \tag{241}$$
and they should be properly quantized, namely, for any 3-cycle $\Sigma \subset X_6$
$$\frac{1}{(2\pi)^2\alpha'}\int_{\Sigma} F_3 \in \mathbb{Z} \qquad \frac{1}{(2\pi)^2\alpha'}\int_{\Sigma} H_3 \in \mathbb{Z} \tag{242}$$

An immediate consequence is that these background fluxes induce an effective D3 charge through the Chern-Simons terms in the Type IIB effective action:

$$\int_{M_4 \times X_6} H_3 \wedge F_3 \wedge C_4 \tag{243}$$

where C_4 is the IIB self-dual 4-form gauge potential. This coupling implies that upon compactification, the flux background contributes to a tadpole for C_4, and hence the 3-form fluxes carry D3-brane charges. With proper normalization factor restored, the flux-induced D3 charge is:

$$N_{flux} = \frac{1}{(4\pi^2\alpha')^2} \int_{X_6} H_3 \wedge F_3 = \frac{i}{(4\pi^2\alpha')^2} \int_{X_6} \frac{G_3 \wedge \overline{G}_3}{2\mathrm{Im}\tau} \tag{244}$$

where $\tau = a + i/g_2$ is the IIB complex dilaton, and we complexify the 3-form fluxes

$$G_3 = F_3 - \tau H_3 \tag{245}$$

for convenience. The kinetic term for G_3 is

$$V = \frac{1}{4\kappa_{10}^2 \mathrm{Im}\tau} \int_{X_6} d^6 y G_3 \wedge *_6 \overline{G}_3 \tag{246}$$

which induces a scalar potential. It can be written as:

$$V = \frac{1}{2\kappa_{10}^2 \mathrm{Im}\tau} \int_{X_6} d^6 y \; G_3^- \wedge *_6 \overline{G}_3^- - \frac{i}{4\kappa_{10}^2 \mathrm{Im}\tau} \int_{X_6} d^6 y \; G_3 \wedge \overline{G}_3 \tag{247}$$

Here $G_3^{\pm}$ is the imaginary self-dual/anti-self-dual (ISD/IASD) part of G_3, i.e.,

$$*_6 \, G_3^{\pm} = \pm i G_3^{\pm} \tag{248}$$

The second term in the potential is a topological term proportional to N_{flux}. They will be canceled by other sources of RR charges in a compact model. The first term is positive definite F-term potential which precisely vanishes if the flux is imaginary self dual. Thus, the equation of motion imposes self-duality of the 3-form flux.

It has been shown that this F-term potential V_F can derived from the Gukov-Vafa-Witten superpotential:

$$W = \int_{X_6} G_3 \wedge \Omega \tag{249}$$

which depends only on the complex structure (shape) moduli and the dilaton and vanishes if these moduli are chosen such that G_3 is ISD. Thus all such moduli are generically stabilized. We can decompose the 3-form flux G_3 in terms of the Hodge cohomology according to the complex structure of the Calabi-Yau. The ISD condition implies that G_3 consists of only $(2,1)$ and $(0,3)$ forms. The $(2,1)$ component of the flux preserves $\mathcal{N} = 1$ SUSY whereas the $(0,3)$ component breaks SUSY while preserving the no-scale structure. We can see this from the F-term equation for the Kahler modulus ρ

$$0 = D_\rho W \sim W = \int G_3 \wedge \Omega \Rightarrow G = G^{(2,1)} \tag{250}$$

Indeed, $G^{(0,3)}$ induces a gravitino mass[16]of the order:

$$m_{3/2}^2 \sim \frac{|G_3 \wedge \Omega|^2}{Im\tau Vol(M_6)^2} \tag{251}$$

[16]The factors in the denominator come from $e^{\mathcal{K}}$ where $\mathcal{K}$ is the Kahler potential.

Although our discussion here is in the context of Type IIB string theory, there should be an alternative description in Type IIA string theory where intersecting D6-branes can be introduced. However, under duality, the three-form fluxes we consider here become metric fluxes on the Type IIA side and the underlying geometry become complicated (more precisely, non-Kahler). The types of 3-cycles that the D6-branes can wrap around in such geometries are not well understood. Therefore, we will restrict ourselves to D-brane model building in Type IIB theory, i.e., branes at singularities and magnetized D-branes. We will construct an example of each kind.

7 Warped Throats

Besides stabilizing moduli, another appealing feature of flux compactification is that the background fluxes backreact on the metric leading to a non-trivial warp factor. If the fluxes are localized in the compact space, strongly warped regions or warped throats can be generated.

Warped extra dimensions have been studied extensively in the past few years as a candidate for physics beyond the Standard Model. A prototypical example is the Randall-Sundrum scenario where the spacetime geometry is a slice of AdS_5 with two boundaries known as the Planck brane and the TeV brane, which can be interpreted as the UV and IR cutoff respectively. Localization of the SM fields (in particular the Higgs) at the strongly warped end (i.e., the IR brane) lead to an exponential suppression of the 4d scale, thus providing an interesting approach to the hierarchy problem.

Other than the generating the hierarchy between the Planck scale and the electroweak scale, there are several phenomenological appeals of warped throats. Warped throats are heavily used in the construction of string inflationary models. They are also useful in generating small numbers for supersymmetry breaking, its mediation, and in sequestering. From a string theory point of view, warped throats are interesting because the relevant interactions are peaked in the highly warped region, and so warping enables us to study physics in a local region of the compactification. The advantage is that a lot is known about local properties of string theory backgrounds such as their metrics and types of cycles that the branes can wrap around. So one can effectively use these results in the warped region to do concrete computations.

There are several motivations to embed warped phenomenology within string theory. First of all, the hierarchy set by the warp factor on the IR brane has so far been imposed by hand. We need a mechanism to stabilize this hierarchy. Secondly, as recent works have shown, details of the warped geometry could have significant effects on precision cosmology [40] and collider data [41,42]. Therefore, it is important to understand what kind of warped geometries can arise in string theory. Finally, inspired by the AdS/CFT correspondence in string theory, results in RS phenomenology have been interpreted in purely 4d terms by replacing the warped throat by a strongly interacting 4d conformal field theory[17]. However, a lack of microscopic understanding of holography in the effective field theory approach prevents this picture to go beyond a qualitative rephrasing. Hence it is worthwhile to study the microscopic constructions of warped throats and their holographic description. To illustrate the point, let's consider an explicit realization of the Randall-Sundrum scenario in string theory, namely, the warped deformed conifold.

Calabi-Yau manifolds are generically non-singular, but at special values of the parameters, they can develop singularities. The most generic singular space is a conifold. Locally, it can be described as a submanifold of $\mathbb{C}^4$ defined by

$$w_1^2 + w_2^2 + w_3^2 + w_4^2 = 0 \tag{252}$$

This submanifold is singular at $(w_1, w_2, w_3, w_4) = 0$ because the normal space is ill defined.[18] We can picture the conifold singularity as a cone whose base has the topology of $S^3 \times S^2$. The fact that it is

[17]The couplings in the low energy effective action of the strongly coupled theory is given by the wavefunction overlap in the extra dimensions Such warped wave functions in a string theory setting have been derived in [43,44].

[18]In general, a variety defined by $f(w_i) = 0$ in $\mathbb{C}^4$ is singular at $f = df = 0$ since the normal space (associated with df) is ill defined.

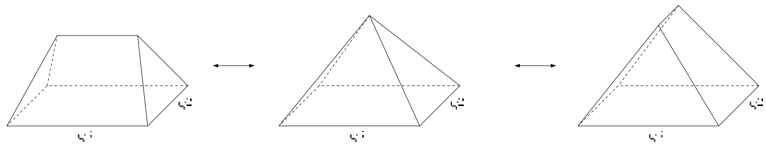

Figure 112: Conifold Transition

a cone is obvious because if w_i satisfy the above equation, so does λw_i for any complex constant λ. To see why it has the topology of $S^3 \times S^2$, let $w_i = x_i + iy_i$, and introducing a new coordinate ρ, the defining equation for a conifold can be recast as 3 real equations:

$$\vec{x} \cdot \vec{x} - \frac{1}{2}\rho^2 = 0 \qquad \vec{y} \cdot \vec{y} - \frac{1}{2}\rho^2 = 0 \qquad \vec{x} \cdot \vec{y} = 0 \tag{253}$$

The first equation describes and S^3 with radius $\rho/\sqrt{2}$. Then the last 2 equations can be interpreted as describing an S^2 fibered over S^3. At the singular point, both the S^3 and the S^2 shrink to zero size.

The conifold can be smoothed into a nonsingular CY manifold in two ways. In the small resolution of the conifold, the S^2 is expanded to a finitie size. In the deformed conifold, the S^3 is expanded to finite size. Since we will be turning on 3-form fluxes in the background, it is the deformed conifold that will be relevant to us. The deformation corresponds to replacing 0 by z which can be assumed to be real and non-negative after a rescaling of ccordinates:

$$w_1^2 + w_2^2 + w_3^2 + w_4^2 = z \tag{254}$$

To see that the S^3 has a finite size after the deformation, decompose w_i into real and imaginary parts as before yields

$$z = \vec{x} \cdot \vec{x} - \vec{y} \cdot \vec{y} \tag{255}$$

Using the definition

$$\rho^2 = \vec{x} \cdot \vec{x} + \vec{y} \cdot \vec{y} \tag{256}$$

we see that the size of the S^3 is finite:

$$z \leq \rho^2 < \infty \tag{257}$$

The singularity at the origin is avoided for $z > 0$. As ρ^2 gets close to z the S^2 disappears leaving just an S^3 with finite size.

We now introduce fluxes to this geometry in order to stabilize the (complex structure) modulus controlling the size of S^3. Dirac quantization implies that these fluxes integrated over all 3-cycles of the CY be integers. In the vicinity of the conifold, there are 2 relevant cycles: one of which (the A-cycle) is the S^3 on which all the w_i are real. In general compact examples, there also exists a dual B-cycle which intersects A exactly once (and can be constructed by taking $w_{1,2,3}$ to be imaginary and w_4 real and positive). The warped deformed conifold (sometimes known as the Klebanov-Strassler solution) corresponds to putting M units of RR 3-form flux F_3 on the A-cycle. The field equation requires that NSNS 3-form flux H_3 be supported on the dual cycle to F_3, so let there be $-K$ units on the B-cycle:

$$\frac{1}{2\pi\alpha'} \int_A F_3 = 2\pi M \qquad \frac{1}{2\pi\alpha'} \int_B H_3 = -2\pi K \tag{258}$$

The D3-charge is therefore $N = MK$. We can now evaluate the flux induced superpotential

$$W = \int_{\mathcal{M}} G_3 \wedge \Omega = \int_{\mathcal{M}} (F_3 - \tau H_3) \wedge \Omega = \int_A F_3 \int_B \Omega + \tau \int_B H_3 \int_A \Omega \tag{259}$$

where the sign flip in the last term is due to the ordering of A and B. The integrals appearing here are the *periods* defining the complex structure of the conifold. In particular, the complex coordinate for the collapsing A cycle is defined by

$$z = \int_A \Omega \tag{260}$$

The integral over the B-cycle can be determined from the monodromy around $z = 0$ where the A-cycle shrinks. The result is:

$$\int_B \Omega = \mathcal{G}(z) = \frac{z}{2\pi i} \ln z + \text{holomorphic} \tag{261}$$

Putting things together, the superpotential is then

$$W = (2\pi)^2 \alpha' \left(M\mathcal{G}(z) - K\tau z \right) \tag{262}$$

Consider the F-term equation

$$0 = D_z W \propto M\partial_z \mathcal{G} - K\tau + \partial_z \mathcal{K}(M\mathcal{G} - K\tau z) \tag{263}$$

where $\mathcal{K}$ is the Kahler potential. In order to obtain a large hierarchy, we will take K/g_s to be large: this result in z being exponentially small. In this regime,

$$D_z W \propto \frac{M}{2\pi i} \ln z - i\frac{K}{g_s} + \mathcal{O}(1) \tag{264}$$

It follows that for $K/Mg_s >> 1$, z is indeed exponentially small,

$$z \sim \exp(-2\pi K/Mg_s) \tag{265}$$

Thus, we obtain a hierarchy of scales if, for example, $M = 1$ and K/g_s is of order 5.

To determine the actual warp factor requires solving the supergravity equation of motion, but one can estimate it as follows. The warp metric for a D3-brane is:

$$ds^2 = \left(\frac{r}{R}\right)^2 ds_4^2 + \left(\frac{R}{r}\right)^2 \left(dr^2 + r^2 d\Omega_5^2\right) \qquad \text{where} \quad R^4 = 4\pi g_s N (\alpha')^2 \tag{266}$$

where r is the distance from the D3-branes located at $r = 0$. The deformation parameter sets a minimum for r and hence the warp factor $e^{A_{min}}$:

$$e^{A_{min}} \simeq r_{min} \simeq z^{1/3} \simeq \exp(-2\pi K/3Mg_s) \tag{267}$$

To summarize, the background fluxes generate and stabilize an exponent hierarchy. The role of the IR and UV branes in RS are played by the S^3 of the deformed conifold and the bulk geometry.

The holographic dual of the warped deformed conifold is an $\mathcal{N} = 1$ SUSY gauge theory with an $SU(N)\times SU(N+M)$ gauge group, chiral multiplets A_i, B_i, $i = 1, 2$ in the $(N, \overline{N+M})$ and $(\overline{N}, N+M)$ representations and a superpotential $W = \epsilon^{ij}\epsilon^{kl} tr A_i B_k A_j B_l$. Along the RG flow to the infrared, the theory undergoes a cascade of Seiberg dualities in which the effective N decreases in step of M. Eventually at an infrared scale after $K = N/M$ steps, the theory confines and the running stops. The size of the S^3 has the interpretation as the infrared confinement scale. The warp factor is associated to the ratio between the UV and IR scales generated by the RG flow.

Thus, AdS-like warped throats with exponentially small but finite warp factor at the tip provide a stringy realization of the RS scenario. In order to make this more precise, it is desirable to construct warped throats with rich enough geometry at their tip to allow for chiral configurations of D-branes.

7.1 Warped Throats and the Standard Model

Now, one might wonder if the singularity which support the chiral spectrum of the Standard Model discussed earlier in Section 4 can arise at the tip of some warped throats. Unfortunately, the KS throat is too simple to generate chiral physics in the infrared. On the gravity side, the geometry is smooth after the deformation, while on the field theory side, the light degrees of freedom are simply the glueballs of the confining theory. Hence the KS throat does not lead to the SM degrees of freedom by putting D3-branes at the tip.

The simplest possibility is to consider throats which contain a singularity at the tip, e.g., a $\mathbb{Z}_3$ orbifold singularity. The first thing one might try is to construct the quotient of the deformed conifold by a $\mathbb{Z}_3$ action with isolated fixed points. Unfortunately, the deformed conifold does not admit such symmetries. For instance, we can change variables and describe the conifold as

$$xy - uv = z \tag{268}$$

There is a $\mathbb{Z}_3$ symmetry: $(x, u) \to e^{2\pi i/3}(x, u)$ and $(y, v) \to e^{-2\pi i/3}(y, v)$, which unfortunately is freely-acting[19]. Other possible $\mathbb{Z}_3$, such as $x \to e^{2\pi i/3}x$, $y \to e^{-2\pi i/3}y$ while leaving u, v invariant, have a whole complex curve of fixed points [20] so locally the singularity is $\mathbb{C} \times \mathbb{C}^2/\mathbb{Z}_3$. This singularity leads to $\mathcal{N} = 2$ worldvolume theories which are non-chiral and thus not interesting.

Progress in understanding warped throats for other geometries, generalizing the conifold, as well as their interpretation in terms of duality cascades and infrared confinement provides useful techniques to implement these ideas. Skipping the details, it suffices for our purposes to consider a particular example. Consider the so called suspended pinch point (SPP) singularity, which can be described as a hypersurface in $\mathbb{C}^4$ given by

$$xy - zw^2 = 0 \tag{269}$$

This geometry admits a complex deformation to the smooth geometry

$$xy - zw^2 = \epsilon w \tag{270}$$

which contains a finite size[21] S^3.

Moreover, the deformed geometry is invariant under a $\mathbb{Z}_3$ acting as

$$x \to \alpha x \qquad y \to \alpha y \qquad z \to \alpha z \qquad w \to \alpha^2 w \tag{271}$$

with $\alpha = e^{2\pi i/3}$. Notice that the $\mathbb{Z}_3$ action leaves invariant the holomorphic 3-form $\Omega = \frac{dxdydz}{zw}$ of the SPP, guaranteeing that the quotient is a new CY singularity. Furthermore, the $\mathbb{Z}_3$ action has the origin as the unique fixed point, and hence there is a left-over $\mathbb{Z}_3$ singularity after the deformation.

On general grounds, it is expected that turning on M units of RR flux on the finite size 3-cycle (as well as a suitable NSNS flux on its dual (non-compact) 3-cycle) leads to a warped throat. At its bottom the throat is cutoff by the finite size 3-cycle, leaving behind a $\mathbb{C}^3/\mathbb{Z}_3$ singularity. A chiral gauge theory is obtained by introducing a small set of D3-branes at the singularity. The latter are probes, and do not modify the structure of the throat significantly.

In fact, one can embed the local D-brane model we just described within this throat. The D7-branes can wrap the 4-cycle defined by $w = 0$ which pass through the D3-branes located at $x = y = z = w = 0$.

To summarize, we have succeeded in finding a throat with a semi-realistic D-brane sector at its tip. The warped geometry also admits a tractable holographic dual. It would be interesting to construct an explicit metric[22] for these types of warped throats since they allow us to study properties of the strongly coupled field theory dual. For example, the KK spectrum in such warped throat background tells us about the glueball masses of the dual field theory.

---

[19] The fixed point $x = y = z = w = 0$ does not solve the deformed conifold equation.

[20] defined by $uv = z$

[21] To see this, it is most convenient to change coordinates: $\rho = x/w$. The deformed SPP can now be written as $\rho y - zw = \epsilon$.

[22] The SPP singularity arises as a particular case of a cone over the $L^{a,b,c}$ families of Einstein-Sasaki metrics constructed in recent years. The warped deformed versions of such metrics have not been worked out yet.

7.2 Flux Vacua with Magnetized D-branes

Finally, we construct another class of chiral D-brane models in warped compactifications Instead of branes at singularities, we consider magnetized D-branes. Given the materials on intersecting branes discussed earlier in Section 5, our strategy should be clear by now. Since we have developed already some useful results regarding intersecting branes in orientifold backgrounds, we will try to adopt these results here by T-dualizing the setup. The configuration of intersecting branes become sets of magnetized D-branes in the IIB theory. We can then combine these magnetized D-branes with 3-form fluxes directly within Type IIB string theory and look for vacuum solutions.

To be concrete, consider the $\mathbb{Z}_2 \times \mathbb{Z}_2$ orientifold that we discussed before. Under T-duality, the 4 types of O6-planes turn into O3-planes and 3 sets of O7-planes. The O3-planes are points in the Calabi-Yau whereas the O7-planes spans different compact dimensions. Let us focus on the O3-planes. The RR tadpole cancellation, in the covering space, reads:

$$N_{D3} + N_{O3} = 0 \qquad \Leftrightarrow \qquad N_{D3} = 32 \tag{272}$$

In the presence of fluxes, this tadpole condition is modified:

$$N_{D3} + N_{flux} = 32 \tag{273}$$

where the charges appear above are defined in the covering space T^6.

What can N_{flux} be for the orbifold we are considering? It depends on the 3-cycles on which the fluxes are quantized. In addition to the 3-cycles that are inherited from the torus, there are also collapsed 3-cycles at the orbifold singularities. Since these collapsed cycles are not in the large volume regime, we cannot trust the supergravity analysis for fluxes supported on these cycles. Therefore we consider only untwisted fluxes, namely flux choices which exist in the parent toroidal theory and are invariant under the $\mathbb{Z}_2 \times \mathbb{Z}_2$ symmetry. This requires that the 3-forms have one leg along each of the T^2. Furthermore, we will center on ISD fluxes, which have only $(2,1)$ and $(0,3)$ components. Hence, in complex notation, G_3 is a linear combination of the forms:

$$d\bar{z}_1 d\bar{z}_2 d\bar{z}_3 \;, \qquad dz_1 dz_2 d\bar{z}_3 \;, \qquad dz_1 d\bar{z}_2 dz_3 \;, \qquad d\bar{z}_1 dz_2 dz_3 \tag{274}$$

Of course, we have yet to impose the quantitization conditions of F_3 and H_3 in order for G_3 to be consistent. This fixes the dilaton and the complex structure moduli. In fact, the condition that flux quantization imposes on moduli is simply a rephrasing of the statement that a specific choice of the moduli minimizes the flux potential.

Now, in order for F_3 and H_3 to be properly quantized in the orbifold, they have to be quantized in multiples of N_{min} in the covering space where N_{min} is an integer depending on the order of the orbifold group. In the present case, N_{min} is 8 of which 4 comes from the order of the $\mathbb{Z}_2 \times \mathbb{Z}_2$ orbifold and a factor of 2 is due to the orientifold projection[23].

Back to the RR tadpoles. Due to the quantization we just discussed, N_{flux} is a multiple of 64. This seems to suggest that, no matter what kind of magnetized D-branes we use to embed the Standard Model, it is not possible to build consistent vacua without introducing some supersymmetry breaking anti D-branes.

However, this is not the case. It was realized that certain types of magnetized D9-branes may carry either anti D3-brane or anti D7-brane charge, while still preserving the $\mathcal{N} = 1$ supersymmetry of the orientifold background. This interesting fact was most apparent when we T-dualize the setup to Type IIA with intersecting branes, and in fact already implicit in one of the examples we discussed before. Consider a D6-brane wrapping the following 3-cycle:

$$[\pi] = (-2[a_1] + [b_1]) \circ (-3[a_2] + [b_2]) \circ (-4[a_3] + [b_3]) \tag{275}$$

[23]To be precise, $N_{min} = 4$ or 8 depending on whether the cycle Σ in the covering space passes through an odd or even number of $O3^{(+,+)}$ planes. There are no such exotic $O3^{(+,+)}$ planes for the choice of discrete torsion (i.e., $(h^{1,1}, h^{2,1}) = (3, 51)$) we considered, and so $N_{min} = 8$.

It carries a D6 charge of the *same* sign as that of an orientifold plane along the $[a_1] \circ [a_2] \circ [a_3]$ direction but as usual the opposite sign from that of other orientifold planes. Yet, the 3-cycle is sLag if the complex structure moduli $\chi_i = (R_2/R_1)_i$ of the torus satisfy[24]:

$$\arctan(\chi_1/2) + \arctan(\chi_2/3) + \arctan(\chi_3/4) = \pi \tag{276}$$

T-dualizing this exotic D6-brane to the IIB picture, we have D9-branes with magnetic fluxes given by

$$\frac{m_a^i}{2\pi} \int_{T^2} F_a^i = n_a^i \tag{277}$$

The orientifold action ΩR [25] which defines the O3-planes map $m_a^i \to -m_a^i$ and hence a D9-brane to an anti-D9 brane. The brane-antibrane system usually break supersymmetry but with suitable choices of gauge bundles on their worldvolumes, they can preserve the same supersymmetry as the orientifold background and carry the $\overline{D3}$ brane charge that we need. The condition for the $D9 - \overline{D9}$ system to preserve SUSY is:

$$\arctan(\mathcal{A}_1/2) + \arctan(\mathcal{A}_2/3) + \arctan(\mathcal{A}_3/4) = \pi \tag{278}$$

where $\mathcal{A}_i$ is the area of $(T^2)_i$ in string units, which is nothing but the T-dual version of Eq. (276). Note that a $D9 - \overline{D9}$ pair breaks SUSY in the non-compact limit as expected, but can nevertheless preserves SUSY when the Kahler moduli take on some specific finite values.

Other than the D3-branes, there are also RR tadpoles for the D7-branes:

$$\begin{aligned}
N_{D3} + N_{flux} = Q_{O3} \quad &\Leftrightarrow \quad 2\sum_a N_a n_a^1 n_a^2 n_a^3 + N_{flux} = 32 \\
N_{D7_1} = Q_{O7_1} \quad &\Leftrightarrow \quad 2\sum_a N_a m_a^1 m_a^2 n_a^3 = -32 \\
N_{D7_2} = Q_{O7_2} \quad &\Leftrightarrow \quad 2\sum_a N_a m_a^1 n_a^2 m_a^3 = -32 \\
N_{D7_3} = Q_{O7_3} \quad &\Leftrightarrow \quad 2\sum_a N_a n_a^1 m_a^2 m_a^3 = -32
\end{aligned} \tag{279}$$

There is, however, a subtlety regarding the cancellation of RR tadpoles. In the presence of orientifold planes, D-branes may carry discrete $\mathbb{Z}_2$ charges, known as K-theory charges, which are invisible from one-loop divergences of the open string diagrams and from the cubic anomalies in the low energy spectrum so the above tadpole constraints do not guarantee the absence of these discrete charges. Just like the ordinary RR charges, however, these $\mathbb{Z}_2$ charges need to cancel globally in a consistent model. The uncanceled $\mathbb{Z}_2$ charges could give rise to the so called $SU(2)$ Witten anomalies – although $SU(2)$ is free of cubic anomalies, it suffers from a global gauge anomaly if there is an odd number of fermions charged in the fundamental representation. We can detect these global $SU(2)$ anomalies by introducing probe D-branes on top of the orientifold planes since this gives rise to a $USp(2)$ and hence $SU(2)$ gauge group on the probes. By demanding that the number of fundamental representations charged under each probe $SU(2)$ group to be even, we found some additional $\mathbb{Z}_2$ constraints:

$$\begin{aligned}
&\sum_a N_a m_a^1 m_a^2 m_a^3 \in 4\mathbb{Z} \\
&\sum_a N_a n_a^1 n_a^2 m_a^3 \in 4\mathbb{Z} \\
&\sum_a N_a n_a^1 m_a^2 n_a^3 \in 4\mathbb{Z} \\
&\sum_a N_a m_a^1 n_a^2 n_a^3 \in 4\mathbb{Z}
\end{aligned} \tag{280}$$

[24] The RHS is π because the angles θ_i are bigger than π for $n_a^i \leq 0$.

[25] where $R : z_i \to -z_i$

These constraints tell us that the number of $D9 - \overline{D9}$ and $D5_i - \overline{D5}_i$ pairs must be even.

Collecting our results, an example satisfying these constraints is given as follows:

N_α	(n_α^1, m_α^1)	(n_α^2, m_α^2)	(n_α^3, m_α^3)
$N_a = 6$	$(1, 0)$	$(g, 1)$	$(g, -1)$
$N_b = 2$	$(0, 1)$	$(1, 0)$	$(0, -1)$
$N_c = 2$	$(0, 1)$	$(0, -1)$	$(1, 0)$
$N_d = 2$	$(1, 0)$	$(g, 1)$	$(g, -1)$
$N_{h1} = 2$	$(-2, 1)$	$(-3, 1)$	$(-4, 1)$
$N_{h2} = 2$	$(-2, 1)$	$(-4, 1)$	$(-3, 1)$
$8N_f$	$(1, 0)$	$(1, 0)$	$(1, 0)$

The brane configuration looks familiar. In fact, the part in blue is one of the MSSM modules introduced earlier. h_1 and h_2 label the exotic D9-branes which carry negative D3-charges. In order for the D-brane configuration to preserve SUSY, the Kahler moduli need to satisfy:

$$\begin{aligned} \mathcal{A}_2 &= \mathcal{A}_3 \\ \arctan(\mathcal{A}_1/2) + \arctan(\mathcal{A}_2/3) + \arctan(\mathcal{A}_3/4) &= \pi \end{aligned} \tag{281}$$

which have non-trivial solutions. It is worth noting that, although the open string sector in the presence of fluxes is not exactly solvable, the massless chiral sector is topological and hence protected so we can compute the chiral spectrum by the same index method before. On the other hand, non-chiral sectors can in general acquire mass terms induced by the fluxes and may disappear from the massless spectrum.

Given the brane configuration, the RR tadpole conditions become:

$$g^2 + N_f + 4n = 14 \tag{282}$$

where $N_{flux} = 64n$ with $n \in \mathbb{Z}$. There are several solutions, among them we find:

1. $n = 0$, $g = 3$, $N_f = 5$
2. $n = 1$, $g = 3$, $N_f = 1$
3. $n = 2$, $g = 2$, $N_f = 2$
4. $n = 3$, $g = 1$, $N_f = 1$

Let's look at these solutions in more detail. The first solution correspond to the 3-family model without the 3-form flux studied before. The last of these solutions is also interesting for another reason. The quantum of flux $N_{flux} = 3 \cdot 64$ can be achieved by considering the 3-form flux:

$$G_3 = \frac{8}{\sqrt{3}} e^{-\frac{\pi i}{6}} \left(d\bar{z}_1 dz_2 dz_3 + dz_1 d\bar{z}_2 dz_3 + dz_1 dz_2 d\bar{z}_3 \right) \tag{283}$$

which is well quantized at the particular value $\tau_1 = \tau_2 = \tau_3 = \tau = e^{\frac{2\pi i}{3}}$ for the untwisted complex structure moduli and the dilaton. These are indeed the values where those fields get fixed after the scalar potential generated by G_3 is minimized. Notice that the flux is a combination of $(2, 1)$ forms, and hence the closed string background as a whole preserves $\mathcal{N} = 1$ supersymmetry. Thus we find that it is actually possible to find chiral $\mathcal{N} = 1$ string theory vacua involving 3-form fluxes and magnetized D-branes. Since this model has only one Standard Model family, it shold be regarded as a toy model illustrating that it possible to get chirality and supersymmetry in explicit flux compactifications. Model building in general Calabi-Yau manifolds allows for more freedom to obtain realistic gauge sectors.

Exercise: Show that the above 3-form flux in Eq. (283) stabilizes the complex structure moduli and the dilaton to $\tau_1 = \tau_2 = \tau_3 = \tau = e^{\frac{2\pi i}{3}}$.

If we relax the requirement that the fluxes preserve supersymmetry, more possibilties open up. Indeed the second solution gives rise to a 3-family MSSM-like spectrum. This is achieved by a 3-form flux with $N_{flux} = 64$:

$$G_3 = 2(d\overline{z}_1 dz_2 dz_3 + dz_1 d\overline{z}_2 dz_3 + dz_1 dz_2 d\overline{z}_3 + d\overline{z}_1 d\overline{z}_2 d\overline{z}_3) \tag{284}$$

which contains a $(0, 3)$ component and hence breaks supersymmetry (although with vanishing cosmological constant at leading order due to the no-scale structure). A particular value of the moduli where such flux is well quantized is given by $\tau_1 = \tau_2 = \tau_3 = \tau = i$. Notice that this gives us $g_s = 1$ and the string perturbation theory may seem no longer realiable. It turns out that the scalar potential derived from the above flux has several flat directions. In particular, it vanishes when one imposes the complex structure moduli and the dilaton to be purely imaginary

$$\begin{aligned} \tau_i &= it_i \ , t_i \in \mathbb{R} \\ \tau &= i/g_s \end{aligned} \tag{285}$$

and to satisfy the constraint

$$g_s t_1 t_2 t_3 = 1 \tag{286}$$

Exercise: Prove the above constraint by minimizing the scalar potential induced by G_3 in Eq. (284) explicitly.

So, in principle, one can find solutions at weak coupling. Of course, α' corrections may lift the flat directions left by Eq. (286), dynamically fixing g_s. Such an analysis is beyond our current scope.

There are several further interesting features about these models such as the Higgs sector, anomalous $U(1)$'s and perturbative global symmetries, the effects of background fluxes on the open string sector including flux induced SUSY breaking, D-brane moduli stabilization, Freed-Witten anomalies, and etc. I don't have time to discuss these interesting topics, but I refer the readers to [31, 32] for a more detailed discussion.

Finally, let me emphasize that the purpose of presenting these explicit models is not that the models are fully realistic but that we want to illustrate the many subtle issues involved when one tries to construct the Standard Model from string theory. The consistency constraints on string theory models are highly intertwined. Contrary to what the landscape might naively suggest, not everything goes. Hopefully, these explicit constructions could point to more general lessons about physics beyond the Standard Model.

8 Loose Ends and Final Thoughts

I hope these lectures have given you some flavor of string phenomenology, with an emphasis on D-brane models of particle physics. Our discussions hopefully equip the readers for further studies of the recent developments in this field, which i did not have time to present during the school. For example, the techniques of D-brane model building have been geometrized in F-theory, see [45–49] for some recent reviews. The intersecting brane setup discussed in Section 5 has been adopted to constructing interesting dark matter scenarios in string theory [50–52], and in motivating novel signatures at the LHC [53]. The introduction to warped compactifications presented in Sections 6 and 7 would also prepare the readers for understanding an interesting way of communicating supersymmetry breaking, known as holographic gauge mediation [54–56]. There are certainly many more new physics scenarios to be explored.

As you have seen, many interesting issues arise when one tries to embed the Standard Model within string theory. Hopefully, the general lessons we have learned will take us one step closer to understanding what lies beyond the Standard Model.

Acknowledgments

I would like to thank Beatriz Gay Ducatti, Laszlo Jenkovszky, Dmitry Melnikov, Fernando Navarra, and Christophe Royon for organizing this wonderful workshop and school, and for their hospitality. This work has been supported in part by the DOE grant DE-FG-02-95ER40896.

References

1. M. B. Green, J. H. Schwarz and E. Witten, *Superstring Theory*, vol. 1 and 2, Cambridge Univ. Pr. (1987) [Cambridge Monogr. Math. Phys.].
2. J. Polchinski, *String theory,* vol. 1 and 2, Cambridge Univ. Pr. (1998).
3. C. V. Johnson, *D-Branes,* Cambridge Univ. Pr. (2003).
4. K. Becker, M. Becker and J. H. Schwarz, *String theory and M-theory: A modern introduction,* Cambridge Univ. Pr. (2007).
5. E. Kiritsis, *String theory in a nutshell,* Princeton Univ. Pr. (2007).
6. S. Weinberg, "Implications Of Dynamical Symmetry Breaking," Phys. Rev. D **13**, 974 (1976).
7. L. Susskind, Phys. Rev. D **20**, 2619 (1979).
8. J. M. Maldacena, Adv. Theor. Math. Phys. **2**, 231 (1998) [Int. J. Theor. Phys. **38**, 1113 (1999)] [hep-th/9711200 [hep-th]].
9. S. S. Gubser, I. R. Klebanov and A. M. Polyakov, Phys. Lett. B **428**, 105 (1998) [hep-th/9802109 [hep-th]].
10. E. Witten, Adv. Theor. Math. Phys. **2**, 253 (1998) [hep-th/9802150 [hep-th]].
11. O. Aharony, S. S. Gubser, J. M. Maldacena, H. Ooguri and Y. Oz, Phys. Rept. **323**, 183 (2000) [hep-th/9905111 [hep-th]].
12. L. Randall and R. Sundrum, Phys. Rev. Lett. **83**, 3370 (1999) [hep-ph/9905221 [hep-ph]].
13. L. Randall and R. Sundrum, Phys. Rev. Lett. **83**, 4690 (1999) [hep-th/9906064 [hep-th]].
14. R. Blumenhagen, M. Cvetic, P. Langacker and G. Shiu, Ann. Rev. Nucl. Part. Sci. **55**, 71 (2005) [hep-th/0502005 [hep-th]].
15. G. Shiu, *Strings for particle physicists,* in TASI 2008 Summer School Proceedings (2008).
16. A. Uranga, *String Compactifications and Model Building,* in TASI 2008 Summer School Proceedings (2005).
17. F. Quevedo, *Phenomenology Aspects of D-branes,* in ICTP Spring School on Superstrings and Related Matters, Trieste (2002).
18. L. J. Dixon, V. Kaplunovsky and C. Vafa, Nucl. Phys. B **294**, 43 (1987).
19. G. Shiu and S. H. H. Tye, Phys. Rev. D **58**, 106007 (1998) [hep-th/9805157 [hep-th]].
20. N. Arkani-Hamed, S. Dimopoulos and G. R. Dvali, Phys. Lett. B **429**, 263 (1998) [hep-ph/9803315 [hep-ph]].
21. I. Antoniadis, N. Arkani-Hamed, S. Dimopoulos and G. R. Dvali, Phys. Lett. B **436**, 257 (1998) [hep-ph/9804398 [hep-ph]].
22. N. Arkani-Hamed, S. Dimopoulos and G. R. Dvali, Phys. Rev. D **59**, 086004 (1999) [hep-ph/9807344 [hep-ph]].
23. L. J. Dixon, J. A. Harvey, C. Vafa and E. Witten, Nucl. Phys. B **261**, 678 (1985).
24. L. J. Dixon, J. A. Harvey, C. Vafa and E. Witten, Nucl. Phys. B **274**, 285 (1986).
25. M. R. Douglas and G. W. Moore, [hep-th/9603167 [hep-th].
26. M. E. Peskin, *Introduction to String and Superstring Theory,* in TASI 2008 Summer School Proceedings (1986).

27. G. Aldazabal, L. E. Ibanez, F. Quevedo and A. M. Uranga, JHEP **0008**, 002 (2000) [hep-th/0005067 [hep-th]].
28. D. Berenstein, V. Jejjala and R. G. Leigh, Phys. Rev. Lett. **88**, 071602 (2002) [hep-ph/0105042 [hep-ph]].
29. M. Grana, Phys. Rev. D **67**, 066006 (2003) [hep-th/0209200 [hep-th]].
30. M. Berkooz, M. R. Douglas and R. G. Leigh, Nucl. Phys. B **480**, 265 (1996) [hep-th/9606139 [hep-th]].
31. F. Marchesano and G. Shiu, Phys. Rev. D **71**, 011701 (2005) [hep-th/0408059 [hep-th]].
32. F. Marchesano and G. Shiu, JHEP **0411**, 041 (2004) [hep-th/0409132 [hep-th]].
33. K. Dasgupta, G. Rajesh and S. Sethi, JHEP **9908**, 023 (1999) [hep-th/9908088 [hep-th]].
34. B. R. Greene, K. Schalm and G. Shiu, Nucl. Phys. B **584**, 480 (2000) [hep-th/0004103 [hep-th]].
35. K. Becker and M. Becker, JHEP **0011**, 029 (2000) [hep-th/0010282 [hep-th]]; K. Becker and M. Becker, Nucl. Phys. B **477**, 155 (1996) [hep-th/9605053 [hep-th]].
36. S. B. Giddings, S. Kachru and J. Polchinski, Phys. Rev. D **66**, 106006 (2002) [hep-th/0105097 [hep-th]].
37. S. Kachru, R. Kallosh, A. Linde and S. P. Trivedi, Phys. Rev. D **68**, 046005 (2003) [hep-th/0301240 [hep-th]].
38. M. R. Douglas and S. Kachru, Rev. Mod. Phys. **79**, 733 (2007) [hep-th/0610102 [hep-th]].
39. R. Blumenhagen, B. Kors, D. Lust and S. Stieberger, Fluxes," Phys. Rept. **445**, 1 (2007) [hep-th/0610327 [hep-th]].
40. G. Shiu and B. Underwood, Phys. Rev. Lett. **98**, 051301 (2007) [hep-th/0610151 [hep-th]].
41. G. Shiu, B. Underwood, K. M. Zurek and D. G. E. Walker, Phys. Rev. Lett. **100**, 031601 (2008) [arXiv:0705.4097 [hep-ph]].
42. P. McGuirk, G. Shiu and K. M. Zurek, JHEP **0803**, 012 (2008) [arXiv:0712.2264 [hep-ph]].
43. F. Marchesano, P. McGuirk and G. Shiu, JHEP **0904**, 095 (2009) [arXiv:0812.2247 [hep-th]].
44. F. Marchesano, P. McGuirk and G. Shiu, JHEP **1105**, 090 (2011) [arXiv:1012.2759 [hep-th]].
45. J. J. Heckman, Ann. Rev. Nucl. Part. Sci. **60**, 237 (2010) [arXiv:1001.0577 [hep-th]].
46. T. Weigand, Class. Quant. Grav. **27**, 214004 (2010) [arXiv:1009.3497 [hep-th]].
47. M. Wijnholt, Proc. Symp. Pure Math. **85**, 275 (2012) [arXiv:1201.2520 [math.AG]].
48. G. K. Leontaris, PoS CORFU **2011**, 095 (2011) [arXiv:1203.6277 [hep-th]].
49. A. Maharana and E. Palti, Int. J. Mod. Phys. A **28**, 1330005 (2013) [arXiv:1212.0555 [hep-th]].
50. G. Shiu, P. Soler and F. Ye, Phys. Rev. Lett. **110**, no. 24, 241304 (2013) [arXiv:1302.5471 [hep-th]].
51. W. Z. Feng, G. Shiu, P. Soler and F. Ye, Phys. Rev. Lett. **113**, 061802 (2014) [arXiv:1401.5880 [hep-ph]].
52. W. Z. Feng, G. Shiu, P. Soler and F. Ye, JHEP **1405**, 065 (2014) [arXiv:1401.5890 [hep-ph]].
53. Z. Dong, T. Han, M. x. Huang and G. Shiu, JHEP **1009**, 048 (2010) [arXiv:1004.5441 [hep-ph]].
54. F. Benini, A. Dymarsky, S. Franco, S. Kachru, D. Simic and H. Verlinde, JHEP **0912**, 031 (2009) [arXiv:0903.0619 [hep-th]].
55. P. McGuirk, G. Shiu and Y. Sumitomo, Nucl. Phys. B **842**, 383 (2011) [arXiv:0910.4581 [hep-th]].
56. P. McGuirk, G. Shiu and Y. Sumitomo, Phys. Rev. D **81**, 026005 (2010) [arXiv:0911.0019 [hep-th]].

Short Contributions

Victor Fadin

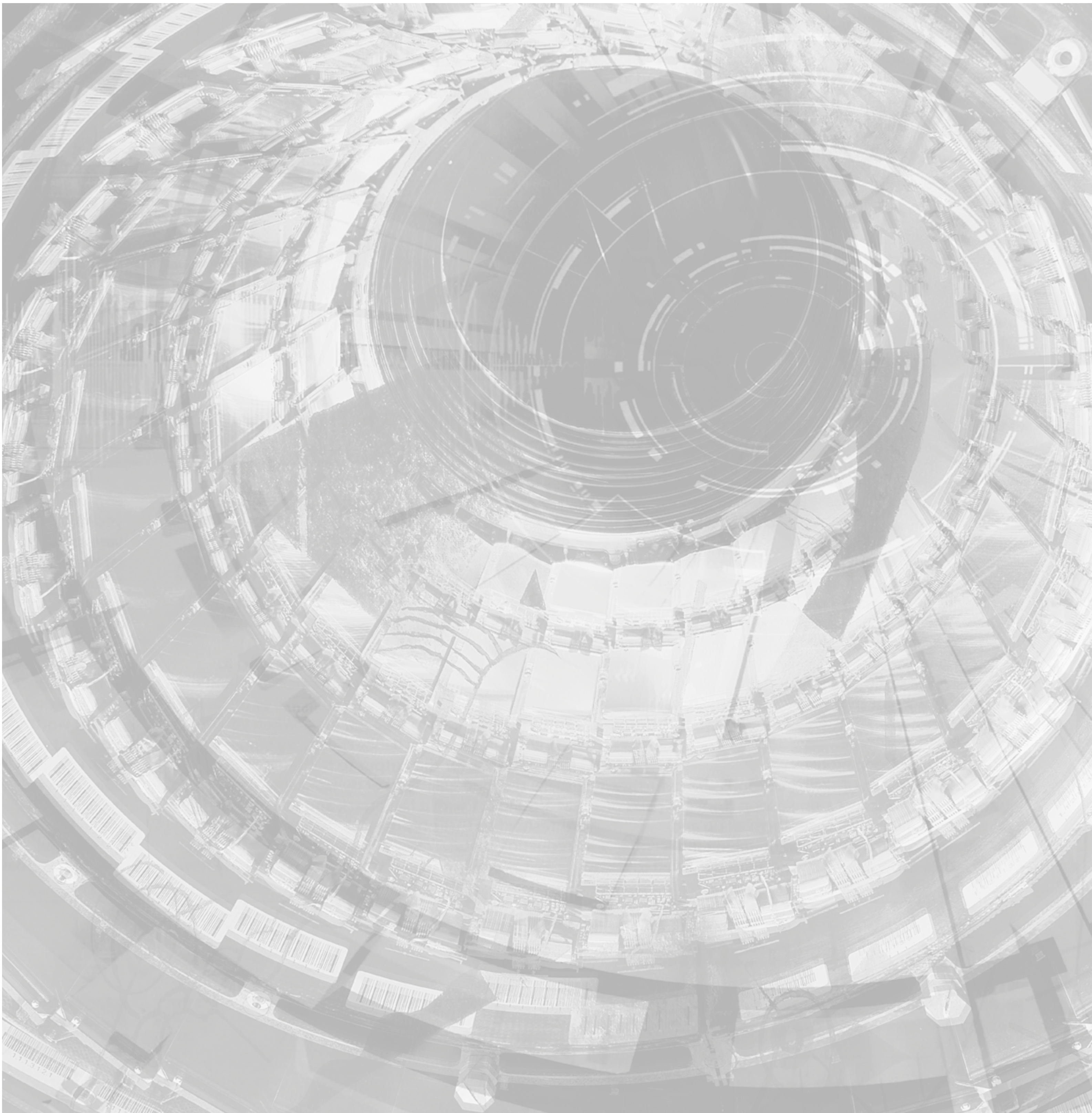

Impact Factors for Reggeon-Gluon Transitions

Victor S. Fadin [l, m]

[l]Budker Institute of Nuclear Physics of SD RAS, Novosibirsk, Russia

[m]Novosibirsk State University, Novosibirsk, Russia

Abstract

General expressions for the impact factors up to terms vanishing at the space-time dimension $D \to 4$ are presented. Their infrared behaviour is analysed and calculation of exact in $D \to 4$ asymptotics at small momenta of Reggeized gluons is discussed.

1 Introduction

Reggeon-gluon impact factors are natural generalization of particle-particle ones. In the BFKL approach [1]- [4], discontinuities of elastic amplitudes are given by the convolutions of the Green functions of two interacting Reggeized gluons with the impact factors of colliding particles describing scattering of these particles due to interaction with the Reggeized gluons. Similarly, discontinuities of many-gluon amplitudes in the multi-Regge kinematics (MRK) contain the Reggeon-gluon impact factors, which describe transitions of Reggeons (Reggeized gluons) into particles (ordinary gluons) due to interaction with the Reggeized gluons. These impact factors appeared firstly [5] in the derivation of the bootstrap conditions for the gluon Reggeization (more precisely, for the multi-Regge form of the many-gluon amplitudes). The idea of this form is the basis of the BFKL approach. It can be proved using the s-channel unitarity. Compatibility of the unitarity with the multi-Regge form leads to the bootstrap relations connecting discontinuities of the amplitudes with products of their real parts and gluon trajectories [6]. It turns out that fulfilment of an infinite set of these relations guarantees the multi–Regge form of scattering amplitudes. On the other hand, all bootstrap relations are fulfilled if several conditions imposed on the Reggeon vertices and the trajectory (bootstrap conditions) hold true [6]. Now fulfilment of all bootstrap conditions is proved. The most complicated condition, which includes the impact factors for Reggeon-gluon transition, was proved recently, both in QCD [7]- [9] and in supersymmetric Yang-Mills theories [10].

Discontinuities of n-gluon amplitudes in the MRK at $n \geq 6$ can be used [11] for a simple demonstration of violation of the ABDK-BDS (Anastasiou-Bern-Dixon-Kosower — Bern-Dixon-Smirnov) ansatz [12, 13] for amplitudes with maximal helicity violation (MHV) in Yang-Mills theories with maximal supersymmetry (N=4 SYM) in the planar limit and for the calculations of the remainder functions to this ansatz. There are two hypothesis about the remainder functions: the hypothesis of the dual conformal invariance [14]- [20], which asserts that the MHV amplitudes are given by the products of the BDS amplitudes and the remainder functions depending only on the anharmonic ratios of kinematic invariants, and the hypothesis of scattering amplitude/Wilson loop correspondence [18, 19], [21]- [24], according to which the remainder functions are given by the expectation values of the Wilson loops. Both these hypothesis are not proved. They can be tested by comparison of the BFKL discontinuities with the discontinuities calculated with their use [25]- [28].

The discontinuities of many-particle amplitudes are interesting also because they are necessary for further development of the BFKL approach. They do not need for derivation of the BFKL equation in the next-to-leading logarithmic approximation (NLLA), because they are suppressed by one power of some of large logarithms in comparison with the real parts of the amplitudes and therefore in the NLLA they don't contribute in the unitarity relations. But their account in the next-to-next-to-leading logarithmic approximation (NNLLA) is indispensable.

All this makes calculation of discontinuities of the MRK amplitudes to be very important. Since the discontinuities contain the Reggeon-gluon impact factors, the calculation requires knowledge of these impact factors and investigation of their properties very important. Here I discuss the current situation with the Reggeon-gluon impact factors.

2 Reggeon-gluon impact factors in the bootstrap scheme

As it is known, in the next-to-leading order (NLO) impact factors are scheme dependent. In the Yang-Mills theories of general form they contain contributions of gauge bosons (gluons), fermions and scalars. In the scheme adapted for verification of the bootstrap conditions (bootstrap scheme) these contributions were calculated in [8], [7] and [10] respectively. Using these results, one can obtain in these scheme the NLO Reggeon-gluon impact factors in the Yang-Mills theories with fermions and scalars in any representations of the colour group.

Here, the notation of Refs. [7]- [10] are used, in particular, the momentum expansion $p = p^+ n_1 + p^- n_2 + p_\perp$, where $n_{1,2}$ are the light-cone vectors, $(n_1, n_2) = 1$, and $\perp$ means transverse to the n_1, n_2 plane components. For amplitudes with the negative signature, the impact factor of the transition of the Reggeon R into the gluon G in the interaction with the Reggeized gluons $\mathcal{G}_1$ and $\mathcal{G}_2$ is antisymmetric with respect to the $\mathcal{G}_1 \leftrightarrow \mathcal{G}_2$ exchange. It can be written as the difference of the s and u parts

$$\langle GR_1| = \langle GR_1|_s - \langle GR_1|_u\ , \quad \langle GR|\mathcal{G}_1\mathcal{G}_2\rangle_u = \langle GR|\mathcal{G}_2\mathcal{G}_1\rangle_s\ . \tag{287}$$

In the NLO each of the parts contains two colour structures. In the light-cone gauge $(e(k), n_2) = 0$,

$$e = e_\perp - \frac{(e_\perp k_\perp)}{k^+} n_2 \tag{288}$$

for the gluon G with the momentum k and the polarization vector $(e(k)$, the s -part has the form

$$\langle GR_1|\mathcal{G}_1\mathcal{G}_2\rangle_s = g^2\delta(\vec{q}_1 - \vec{k} - \vec{r}_1 - \vec{r}_2)\vec{e}^{\,*}\left[\left(T^aT^b\right)_{c_1c_2}\left(2\vec{C}_1 + \bar{g}^2\vec{\Phi}_1(\vec{q}_1, \vec{k}; \vec{r}_1, \vec{r}_2)\right)\right.$$
$$\left. + \frac{1}{N_c}\,\mathrm{Tr}\left(T^{c_2}T^aT^{c_1}T^b\right)\,\bar{g}^2\vec{\Phi}_2(\vec{q}_1, \vec{k}; \vec{r}_1, \vec{r}_2)\right]\ . \tag{289}$$

Here g is the bare coupling constant, $\bar{g}^2 = g^2\Gamma(1-\epsilon)/(4\pi)^{2+\epsilon}$, $\Gamma(x)$ is the Euler gamma-function, $\epsilon = (D-4)/2$, D is the space-time dimension, T^i are the colour group generators in the adjoint representation, q_1, k, r_1, r_2 and a, b c_1, c_2 are the momenta and colour indices of the Reggeon R_1, the gluon G and the Reggeized gluons $\mathcal{G}_1$ and $\mathcal{G}_2$ respectively, the vector sign is used for transverse components of vectors,

$$\vec{C}_1 \;=\; \vec{q}_1 - (\vec{q}_1 - \vec{r}_1)\frac{\vec{q}_1^{\,2}}{(\vec{q}_1 - \vec{r}_1)^2}.$$

In the bootstrap scheme with the dimensional regularization

$$\vec{\Phi}_1(\vec{q}_1, \vec{k}; \vec{r}_1, \vec{r}_2)_* = \vec{C}_1\left(\ln\left(\frac{(\vec{q}_1 - \vec{r}_1)^2}{\vec{k}^{\,2}}\right)\ln\left(\frac{\vec{r}_2^{\,2}}{\vec{k}^{\,2}}\right) + \ln\left(\frac{(\vec{q}_1 - \vec{r}_1)^2\vec{q}_1^{\,2}}{\vec{k}^{\,4}}\right)\ln\left(\frac{\vec{r}_1^{\,2}}{\vec{q}_1^{\,2}}\right)\right.$$
$$\left. -4\frac{(\vec{k}^{\,2})^\epsilon}{\epsilon^2} + 6\zeta(2)\right) + \vec{C}_2\left(\ln\left(\frac{\vec{k}^{\,2}}{\vec{r}_2^{\,2}}\right)\ln\left(\frac{(\vec{q}_1 - \vec{r}_1)^2}{\vec{r}_2^{\,2}}\right) + \ln\left(\frac{\vec{q}_2^{\,2}}{\vec{q}_1^{\,2}}\right)\ln\left(\frac{\vec{k}^{\,2}}{\vec{q}_2^{\,2}}\right)\right)$$
$$+2\Big[\vec{C}_1 \times \big[\vec{q}_1 \times \vec{r}_1\big]\Big]I_{\vec{q}_1,-\vec{r}_1} + 2\Big[\vec{C}_2 \times \big[\vec{q}_1 \times \vec{k}\big]\Big]I_{\vec{q}_1,-\vec{k}} - 2\Big[\left(\vec{C}_1 - \vec{C}_2\right) \times \big[\vec{k} \times \vec{r}_2\big]\Big]I_{\vec{k},\vec{r}_2}\ .$$

$$+\frac{\beta_0}{N_c}\Big[\vec{C}_2\ln\big(\frac{\vec{q}_2^{\,2}(\vec{q}_1-\vec{r}_1)^2}{\vec{q}_1^{\,2}\vec{r}_2^{\,2}}\big)-\vec{C}_1\Big(\frac{1}{\epsilon}+\ln\big(\frac{(\vec{q}_1-\vec{r}_1)^2\vec{r}_1^{\,2}}{\vec{q}_1^{\,2}}\big)\Big)\Big]+\vec{C}_1\Big(\frac{67}{9}-\frac{10a_f}{9}-\frac{4a_s}{9}\Big)$$

$$+\Bigg[\frac{\beta_0}{N_c}\Big(\vec{C}_2\frac{\vec{q}_1^{\,2}+\vec{q}_2^{\,2}}{\vec{q}_1^{\,2}-\vec{q}_2^{\,2}}+\frac{\vec{k}}{\vec{k}^{\,2}}\frac{2\vec{q}_1^{\,2}\vec{q}_2^{\,2}}{\vec{q}_1^{\,2}-\vec{q}_2^{\,2}}\Big)\ln\big(\frac{\vec{q}_1^{\,2}}{\vec{q}_2^{\,2}}\big)+\frac{\tilde{\beta}_0}{N_c}\left(\left(\vec{C}_2\frac{2\vec{k}^{\,2}}{(\vec{q}_1^{\,2}-\vec{q}_2^{\,2})^2}-\frac{\vec{k}(2\vec{k}^{\,2}-\vec{q}_1^{\,2}-\vec{q}_2^{\,2})}{(\vec{q}_1^{\,2}-\vec{q}_2^{\,2})^2}\right)\right.$$

$$\left.\times\left(\vec{q}_1^{\,2}+\vec{q}_2^{\,2}-\frac{2\vec{q}_1^{\,2}\vec{q}_2^{\,2}}{\vec{q}_1^{\,2}-\vec{q}_2^{\,2}}\ln\big(\frac{\vec{q}_1^{\,2}}{\vec{q}_2^{\,2}}\big)\right)+\frac{\vec{k}}{\vec{q}_1^{\,2}}\right)-(\vec{q}_1\to\vec{q}_1-\vec{r}_1,\ \vec{q}_2\to\vec{r}_2,\ \vec{k}\to\vec{k})\Bigg]\,. \tag{290}$$

Here the subscript $*$ denotes the bootstrap scheme, $\zeta(n)$ is the Riemann zeta-function ($\zeta(2)=\pi^2/6$),

$$\vec{C}_2\;=\;\vec{q}_1-\vec{k}\frac{\vec{q}_1^{\,2}}{\vec{k}^{\,2}}, \tag{291}$$

$\big[\vec{a}\times c\big[\vec{b}\times\vec{c}\big]\big]$ is a double vector product,

$$I_{\vec{p},\vec{q}}=\int_0^1\frac{dx}{(\vec{p}+x\vec{q})^2}\ln\left(\frac{\vec{p}^{\,2}}{x^2\vec{q}^{\,2}}\right)\ ,\ \ I_{\vec{p},\vec{q}}=I_{-\vec{p},-\vec{q}}=I_{\vec{q},\vec{p}}=I_{\vec{p},-\vec{p}-\vec{q}}\ ,$$

$$\beta_0=\frac{11}{3}N_c-\frac{2}{3}a_f-\frac{1}{6}a_s\ ,\tilde{\beta}_0=\frac{1}{3}N_c-\frac{1}{3}a_f+\frac{1}{6}a_s\ ,$$

$a_f=2\kappa_f n_f T_f,\ \ a_s=2\kappa_s n_s T_s$, T_f and T_s are defined by the relations

$$\mathrm{Tr}\left(T_f^aT_f^b\right)=T_f\delta^{ab},\quad \mathrm{Tr}\left(T_s^aT_s^b\right)=T_s\delta^{ab}, \tag{292}$$

where T_f^a and T_s^a are the colour group generators for fermions and scalars, respectively, and κ_f (κ_s) is equal to $1/2$ for Majorana fermions (neutral scalars) in self-conjugated representations and 1 otherwise. In the case of n_M Majorana fermions and n_s scalars in the adjoint representation $a_f=n_MN_c,\ \ a_s=n_sN_c$. For N-extended SYM $n_M=N,\ \ n_s=2(N-1)$. Remind that the result (290) is obtained in the dimensional regularization, which differs from the dimensional reduction used in supersymmetric theories. For $N=4$ SYM in the dimensional reduction one has to take $n_s=6-2\epsilon$. In this case the terms with $\beta_0,\ \tilde{\beta}_0$ and $\left(\frac{67}{9}-\frac{10a_f}{9}-\frac{4a_s}{9}\right)$ in (290) disappear. Note that the expression (290) is obtained with the accuracy up to terms vanishing at $\epsilon\to 0$. With the same accuracy

$$\vec{\Phi}_2(\vec{q}_1,\vec{k};\vec{r}_1,\vec{r}_2)_*=\vec{q}_1^{\,2}\int_0^1dx_1\Bigg\{\frac{(\vec{q}_1-\vec{r}_1)}{(\vec{q}_1-\vec{r}_1)^2}\Bigg[\frac{(\vec{k}^{\,2})^\epsilon}{x_1^{1-2\epsilon}}-\zeta_2+\frac{(\vec{r}_2^{\,2}-x_1\vec{k}^{\,2})}{(\vec{r}_2+x_1\vec{k})^2}$$

$$\times\ln\Big(\frac{(\vec{r}_1+x_2\vec{k})^2(\vec{q}_1-\vec{r}_1)^2}{\vec{q}_1^{\,2}\vec{k}^{\,2}x_2^2}\Big)-\frac{1}{x_1}\ln\Big(\frac{(\vec{r}_1+x_1\vec{k})^2(\vec{r}_2+x_1\vec{k})^2(\vec{r}_2+x_2\vec{k})^2}{x_2^2\vec{r}_1^{\,2}\vec{r}_2^{\,2}(\vec{k}+\vec{r}_2)^2}\Big)\Bigg]$$

$$+\frac{\vec{k}}{\vec{k}^{\,2}}\Bigg[\frac{1}{x_1}\ln\Big(\frac{(\vec{r}_1+x_1\vec{k})^2}{\vec{r}_1^{\,2}}\Big)+\frac{x_1\vec{k}^{\,2}}{(\vec{r}_2+x_1\vec{k})^2}\ln\Big(\frac{(\vec{r}_1+x_2\vec{k})^2(\vec{q}_1-\vec{r}_1)^2}{\vec{q}_1^{\,2}\vec{k}^{\,2}x_2^2}\Big)\Bigg]$$

$$-\frac{\vec{q}_1}{\vec{q}_1^{\,2}}\frac{1}{x_1}\ln\Big(\frac{(\vec{r}_1+x_2\vec{k})^2(\vec{r}_1+x_1\vec{k})^2}{(\vec{r}_1+\vec{k})^2\vec{r}_1^{\,2}}\Big)\Bigg\}\,. \tag{293}$$

Eqs. (290), (293) give the impact factors in the bootstrap scheme. Transition to the standard scheme and to the scheme in which the BFKL kernel in $N=4$ SYM and the energy evolution parameter are invariant under Möbius transformations in the momentum space is discussed in [29].

3 Colour decomposition

To calculate discontinuities one needs to decompose the colour structures into irreducible representations of the colour group in the channel with two Reggeized gluons. The decomposition looks as follows

$$\left(T^aT^b\right)_{c_1c_2} = N_c\sum_R c_R\langle ab|\hat{\mathcal{P}}_R|c_1c_2\rangle,$$

$$\mathrm{Tr}\left(T^{c_2}T^aT^{c_1}T^b\right) = N_c\sum_R c_R(c_R-\frac{1}{2})\langle ab|\hat{\mathcal{P}}_R|c_1c_2\rangle, \tag{294}$$

where $\hat{\mathcal{P}}_R$ are the projections operators of the two-Reggeon colour states on the irreducible representations R. Explicit form of these operators and the values of the coefficients c_R can be found in [30]. In the limit of large N_c the term in (289) with the colour structure $\mathrm{Tr}\left(T^{c_2}T^aT^{c_1}T^b\right)$ disappears and with the account of (287) the impact factors take the form

$$\langle GR_1|\mathcal{G}_1\mathcal{G}_2\rangle = g^2\delta(\vec{q}_1-\vec{k}-\vec{r}_1-\vec{r}_2)\vec{e}^{\,*}\Bigg[f^{abc}f^{cc_1c_2}\Bigg(2\vec{q}_1-(\vec{q}_1-\vec{r}_1)\frac{\vec{q}_1^{\,2}}{(\vec{q}_1-\vec{r}_1)^2}$$
$$-(\vec{q}_1-\vec{r}_2)\frac{\vec{q}_1^{\,2}}{(\vec{q}_1-\vec{r}_2)^2}+\frac{\bar{g}^2}{2}\left(\vec{\Phi}_1(\vec{q}_1,\vec{k};\vec{r}_1,\vec{r}_2)+\vec{\Phi}_1(\vec{q}_1,\vec{k};\vec{r}_2,\vec{r}_1)\right)\Bigg)+d^{abc}d^{cc_1c_2}$$
$$\times\left[\frac{\vec{q}_1^{\,2}(\vec{q}_1-\vec{r}_2)}{(\vec{q}_1-\vec{r}_2)^2}-\frac{\vec{q}_1^{\,2}(\vec{q}_1-\vec{r}_1)}{(\vec{q}_1-\vec{r}_1)^2}+\frac{\bar{g}^2}{2}\left(\vec{\Phi}_1(\vec{q}_1,\vec{k};\vec{r}_1,\vec{r}_2)-\vec{\Phi}_1(\vec{q}_1,\vec{k};\vec{r}_2,\vec{r}_1)\right)\right)\Bigg]. \tag{295}$$

4 Infrared behaviour of the impact factors

As is clear from the foregoing, Eq. (295) gives the impact factor up to terms vanishing in the limit $\epsilon\to 0$. Unfortunately, using (295) for calculation of discontinuities does not provide such accuracy for them. The reason is the integration measure $d^{2+2\epsilon}r_{1\perp}d^{2+2\epsilon}r_{1\perp}/(r_{1\perp}^2r_{2\perp}^2)\delta(q_{2\perp}-r_{1\perp}-r_{2\perp})$ which is singular at $\epsilon\to 0$. To keep in the discontinuities all terms nonvanishing in the limit $\epsilon\to 0$ one has to calculate $\vec{\Phi}_1(\vec{q}_1,\vec{k};\vec{r}_1,\vec{r}_2)$ more accurately.

In fact, greater accuracy is required only in the region of small $|\vec{r}_2|$, because in the limit $|\vec{r}_1|\to 0$ $\vec{\Phi}_1(\vec{q}_1,\vec{k};\vec{r}_1,\vec{r}_2)$ turns to be zero, which is seen from (290). In contrast, in the limit $|\vec{r}_2|\to 0$ $\vec{\Phi}_1(\vec{q}_1,\vec{k};\vec{r}_1,\vec{r}_2)$ not only does not vanish but have logarithmic singularities. To keep in the discontinuities all terms nonvanishing in the limit $\epsilon\to 0$ one has to know in the region of small $|\vec{r}_2|$ terms of order ϵ in $\vec{\Phi}_1(\vec{q}_1,\vec{k};\vec{r}_1,\vec{r}_2)$ and must not expand $(\vec{r}_2^{\,2})^\epsilon$ in powers of ϵ.

In the NLO, the impact factor contains contributions of two types: virtual ones, which are obtained from the one-loop corrections to the Reggeon vertices and the gluon trajectory, and real contributions arising from production of two real particles. In the bootstrap scheme, the real contribution to $\vec{\Phi}_1(\vec{q}_1,\vec{k};\vec{r}_1,\vec{r}_2)$ can be calculated at small $|\vec{r}_2|$ exactly in ϵ using intermediate results of Refs. [7]- [10]. It is proportional to $(\vec{r}_2^{\,2})^\epsilon$ and has the form [31]

$$\vec{\Phi}_1(\vec{q}_1,\vec{k};\vec{r}_1,\vec{r}_2)_*^{real} = 4(\vec{r}_2^{\,2})^\epsilon\frac{\Gamma^2(1+\epsilon)}{\Gamma(1+2\epsilon)}\Bigg[\vec{C}_2\Big(\frac{1}{2\epsilon^2}+\frac{(\psi(1)-\psi(1+2\epsilon))}{\epsilon}$$
$$-\frac{\Gamma(1+2\epsilon)}{\Gamma(4+2\epsilon)}\Big(\frac{a_1(1+\epsilon)}{\epsilon}+a_2\Big)+\frac{2\Gamma(1+2\epsilon)}{\Gamma(4+2\epsilon)}\frac{\vec{r}_2(\vec{r}_2\vec{C}_2)}{\vec{r}_2^{\,2}}a_2\Bigg], \tag{296}$$

where

$$a_1 = 11+7\epsilon-2(1+\epsilon)a_f-\frac{a_s}{2},\quad a_2 = 1+\epsilon-a_f+\frac{a_s}{2}\ . \tag{297}$$

For $N = 4$ SYM, the coefficients a_1 and a_2 vanish in the dimensional reduction.

The virtual contribution to $\vec{\Phi}_1(\vec{q}_1, \vec{k}; \vec{r}_1, \vec{r}_2)$ in the limit of small $|\vec{r}_2|$ can be obtained with the required accuracy using its representation [8] in terms of the Reggeon vertices and the gluon trajectory and exact in ϵ expressions for the trajectory, the gluon-gluon-Reggeon vertex and fermion and scalar contributions to the Reggeon-Reggeon-gluon vertex which can be found in Refs. [32], [33] and [10, 34] respectively and the gluon production vertex in $N = 4$ SYM computed through to $\mathcal{O}(\epsilon^2)$ in [35]. Full expressions for the Reggeon-gluon impact factors in the region of small $|\vec{r}_2|$ in the bootstrap and the standard schemes will be given in [31].

5 Summary

The impact factors for Reggeon-gluon transitions are an integral part of the BFKL approach. They enter the expressions for the discontinuities of many-particle amplitudes and the bootstrap conditions for the gluon Reggeization, and enable to demonstrate in a simple way violation of the ABDK-BDS ansatz for MHV amplitudes in N=4 SYM in the planar limit and to check the hypotheses about the remainder functions to this ansatz. Their knowledge is necessary for further development of the BFKL approach.

Here the impact factors in Yang-Mills theories with fermions and scalars in any representations of the gauge group are presented up to terms vanishing at $\epsilon \to 0$. Their colour decomposition is performed and infrared behaviour is discussed.

Acknowledgments The work is supported by the Ministry of Education and Science of the Russian Federation and by the RFBR grant 13-02-01023.

References

1. V. S. Fadin, E. A. Kuraev and L. N. Lipatov, Phys. Lett. B **60**, 50 (1975).
2. . A. Kuraev, L. N. Lipatov and V. S. Fadin, Sov. Phys. JETP **44**, 443 (1976) [Zh. Eksp. Teor. Fiz. **71**, 840 (1976)].
3. E. A. Kuraev, L. N. Lipatov and V. S. Fadin, Sov. Phys. JETP **45**, 199 (1977) [Zh. Eksp. Teor. Fiz. **72**, 377 (1977)].
4. I. I. Balitsky and L. N. Lipatov, Sov. J. Nucl. Phys. **28**, 822 (1978) [Yad. Fiz. **28**, 1597 (1978)].
5. J. Bartels, V. S. Fadin and R. Fiore, Nucl. Phys. B **672**, 329 (2003) [hep-ph/0307076 [hep-ph]].
6. V. S. Fadin, R. Fiore, M. G. Kozlov and A. V. Reznichenko, Phys. Lett. B **639**, 74 (2006) [hep-ph/0602006 [hep-ph]].
7. M. G. Kozlov, A. V. Reznichenko and V. S. Fadin, Phys. Atom. Nucl. **74**, 758 (2011) [Yad. Fiz. **74** (2011) 784].
8. M. G. Kozlov, A. V. Reznichenko and V. S. Fadin, Phys. Atom. Nucl. **75**, 850 (2012).
9. M. G. Kozlov, A. V. Reznichenko and V. S. Fadin, Phys. Atom. Nucl. **75**, 493 (2012).
10. M. G. Kozlov, A. V. Reznichenko and V. S. Fadin, Phys. Atom. Nucl. **77**, 251 (2014). Yad. Fiz. **77** (2014) 273.
11. V. S. Fadin, AIP Conf. Proc. **1654**, 070006 (2015) [arXiv:1412.3253 [hep-th]].
12. C. Anastasiou, Z. Bern, L. J. Dixon and D. A. Kosower, Phys. Rev. Lett. **91**, 251602 (2003) [hep-th/0309040 [hep-th]].
13. Z. Bern, L. J. Dixon and V. A. Smirnov, Phys.Rev. D **72**, 085001 (2005) [hep-th/0505205 [hep-th]].
14. Z. Bern, M. Czakon, L. J. Dixon, D. A. Kosower and V. A. Smirnov, Phys. Rev. D **75**, 085010 (2007) [hep-th/0610248 [hep-th]].
15. J. M. Drummond, J. Henn, V. A. Smirnov and E. Sokatchev, JHEP **0701**, 064 (2007) [hep-th/0607160 [hep-th]].
16. Z. Bern, J. J. M. Carrasco, H. Johansson and D. A. Kosower, Phys. Rev. D **76**, 125020 (2007) [arXiv:0705.1864 [hep-th]].

17. L. F. Alday and J. M. Maldacena, JHEP **0706**, 064 (2007) [arXiv:0705.0303 [hep-th]].
18. J. M. Drummond, G. P. Korchemsky and E. Sokatchev, Nucl. Phys. B **795**, 385 (2008) [arXiv:0707.0243 [hep-th]].
19. J. M. Drummond, J. Henn, G. P. Korchemsky and E. Sokatchev, Nucl. Phys. B **795**, 52 (2008) [arXiv:0709.2368 [hep-th]].
20. D. Nguyen, M. Spradlin and A. Volovich, Phys. Rev. D **77**, 025018 (2008) [arXiv:0709.4665 [hep-th]].
21. A. Brandhuber, P. Heslop and G. Travaglini, Nucl. Phys. B **794** 231 (2008) [arXiv:0707.1153 [hep-th]].
22. J. M. Drummond, J. Henn, G. P. Korchemsky and E. Sokatchev, Nucl. Phys. B **826**, 337 (2010) [arXiv:0712.1223 [hep-th]].
23. J. M. Drummond, J. Henn, G. P. Korchemsky and E. Sokatchev, Phys. Lett. B **662**, 456 (2008) [arXiv:0712.4138 [hep-th]].
24. J. M. Drummond, J. Henn, G. P. Korchemsky and E. Sokatchev, Nucl. Phys. B **815**, 142 (2009) [arXiv:0803.1466 [hep-th]].
25. L.N. Lipatov and A. Prygarin, Phys. Rev. D **83**, 045020 (2011) [arXiv:1008.1016 [hep-th]].
26. L. N. Lipatov and A. Prygarin, Phys. Rev. D **83**, 125001 (2011) [arXiv:1011.2673 [hep-th]].
27. J. Bartels, L.N. Lipatov and A. Prygarin, Phys. Lett. B **705**, 507 (2011) [arXiv:1012.3178 [hep-th]].
28. V.S. Fadin and L.N. Lipatov, Phys. Lett. B **706**, 470 (2012) [arXiv:1111.0782 [hep-th]].
29. V. S. Fadin and R. Fiore, Phys. Lett. B **734**, 86 (2014) [arXiv:1402.5260 [hep-th]].
30. B. L. Ioffe, V. S. Fadin and L. N. Lipatov, *Quantum Chromodynamics. Perturbative and Nonperturbative Aspects*, Cambridge Monogr. Part. Phys. Nucl. Phys. and Cosmology **30** (2014).
31. V. S. Fadin and R. Fiore, to be published.
32. J. Bartels, V. S. Fadin, L. N. Lipatov and G. P. Vacca, Nucl. Phys. B **867**, 827 (2013) [arXiv:1210.0797 [hep-ph]].
33. V. S. Fadin, M. I. Kotsky and R. Fiore, Phys. Lett. B **359**, 181 (1995).
34. V. S. Fadin, R. Fiore and A. Quartarolo, Phys. Rev. D **50**, 5893 (1994) hep-th/9405127 [hep-th]].
35. V. Del Duca, C. Duhr and E. W. Nigel Glover, JHEP **0912**, 023 (2009) [arXiv:0905.0100 [hep-th]].

Pedro Costa
Márcio Ferreira
Constança Providência

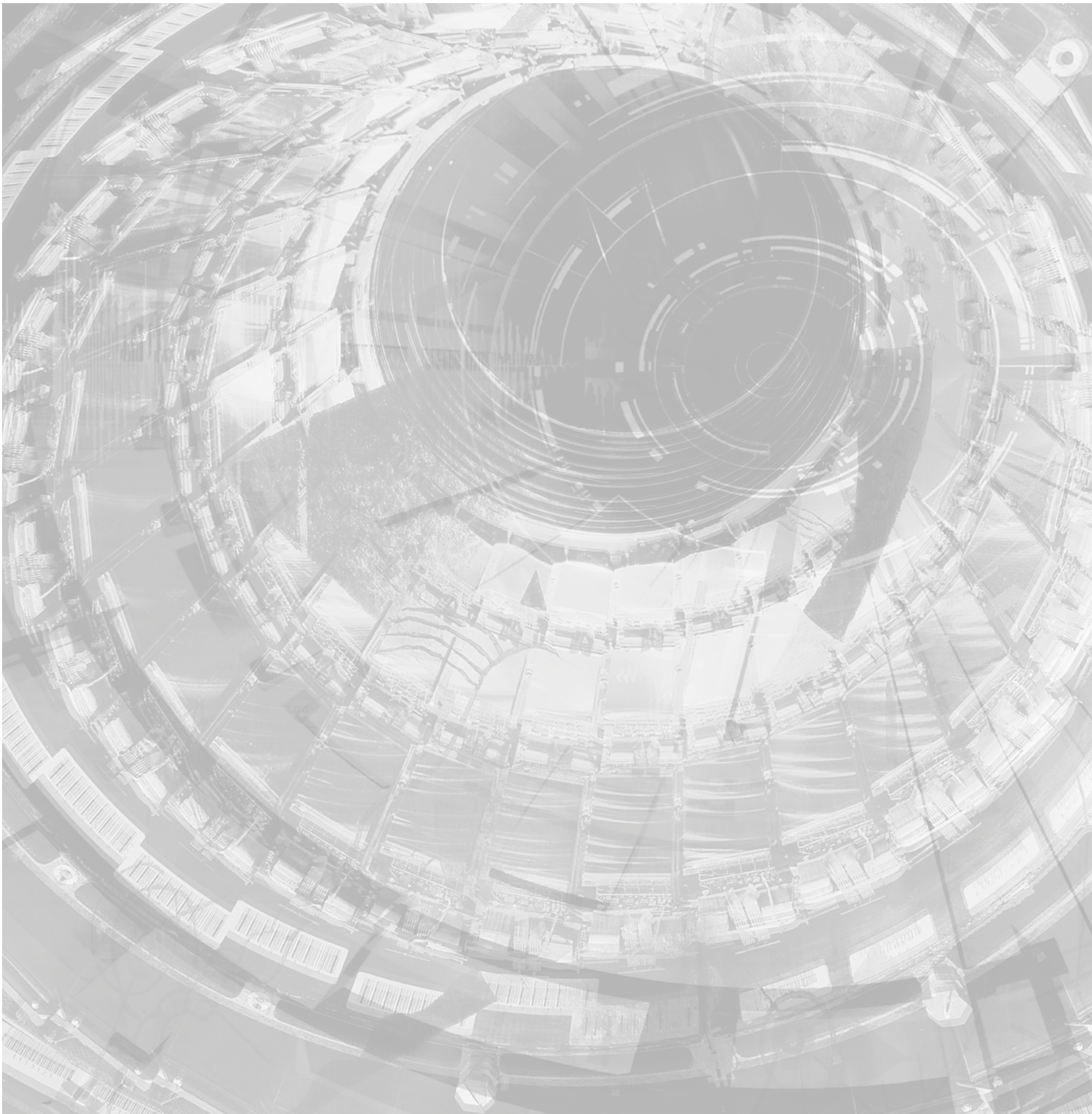

The QCD phase diagram in the presence of an external magnetic field: the role of the inverse magnetic catalysis

Pedro Costa, Márcio Ferreira[26], Constança Providência [n]

[n]Centro de Física Computacional, Department of Physics, University of Coimbra, Coimbra, Portugal

Abstract

The effect of an external magnetic field in QCD phase diagram, namely, in the the location of the critical end point (CEP) is investigated. Using the 2+1 flavor Nambu–Jona-Lasinio model with Polyakov loop, it is shown that when an external magnetic field is applied its effect on the CEP depends on the strength of the coupling. If the coupling depends on the magnetic field, allowing for inverse magnetic catalysis, the CEP moves to lower chemical potentials eventually disappearing, and the chiral restoration phase transition is always of first order.

1 Inverse magnetic catalysis in the PNJL model

The influence of strong external magnetic fields on the structure of the QCD phase diagram is a very important field of research due to its consequences on several physical phenomena: the measurements in heavy ion collisions at very high energies, the behavior of the first stages of the Universe and the understanding of compact astrophysical objects like magnetars.

The inclusion of a magnetic field in the Lagrangian density of the Nambu–Jona-Lasinio (NJL) model and of the Polyakov–Nambu–Jona-Lasinio (PNJL) model gives rise to the Magnetic Catalysis (MC) effect, i.e., the enhancement of the quark condensate due to the magnetic field [1–3], but fails to account for the Inverse Magnetic Catalysis (IMC) found in LQCD calculations [4–6] where the suppression of the quark condensate takes place due to the strong screening effect of the gluon interactions. In order to overcome this discrepancy, it was proposed, by using the SU(2) NJL model [7] and the SU(3) NJL/PNJL models [8], that the model coupling, G_s, can be seen as proportional to the running coupling, α_s, and consequently, a decreasing function of the magnetic field strength allowing to include the impact of $\alpha_s(eB)$ in both models. Indeed, the strong screening effect of the gluon interactions in the region of low momenta weakens the interaction which is reflected into a decrease of the scalar coupling with the intensity of the magnetic field [9].

Since there is no LQCD data available for $\alpha_s(eB)$, by using the NJL model we can fit $G_s(eB)$ in order to reproduce the pseudocritical chiral transition temperatures, $T_c^{\chi}(eB)$, obtained in LQCD calculations [4]. The resulting fit function that reproduces the $T_c^{\chi}(eB)$ is

$$G_s(\zeta) = G_s^0 \left(\frac{1 + a\,\zeta^2 + b\,\zeta^3}{1 + c\,\zeta^2 + d\,\zeta^4}\right) \tag{298}$$

with $a = 0.0108805$, $b = -1.0133 \times 10^{-4}$, $c = 0.02228$, and $d = 1.84558 \times 10^{-4}$ and where $\zeta = eB/\Lambda_{QCD}^2$. We also have used $\Lambda_{QCD} = 300$ MeV.

In the NJL model, the renormalized pseudocritical chiral transition temperatures, $T_c^{\chi}/T_c^{\chi}(eB=0)$, are plotted in left panel of Fig. 113 as a function of eB: with the magnetic field dependent coupling $G_s(eB)$ (green line), given by Eq. (298); with LQCD results (red dots); and the usual constant coupling $G_s = G_s^0$ (black dashed dot line), that shows magnetic catalyzes with increasing $T_c^{\chi}/T_c^{\chi}(eB=0)$ for all range of magnetic fields.

[26]Corresponding author. See Table 2 for the complete list of talks given at the workshop.

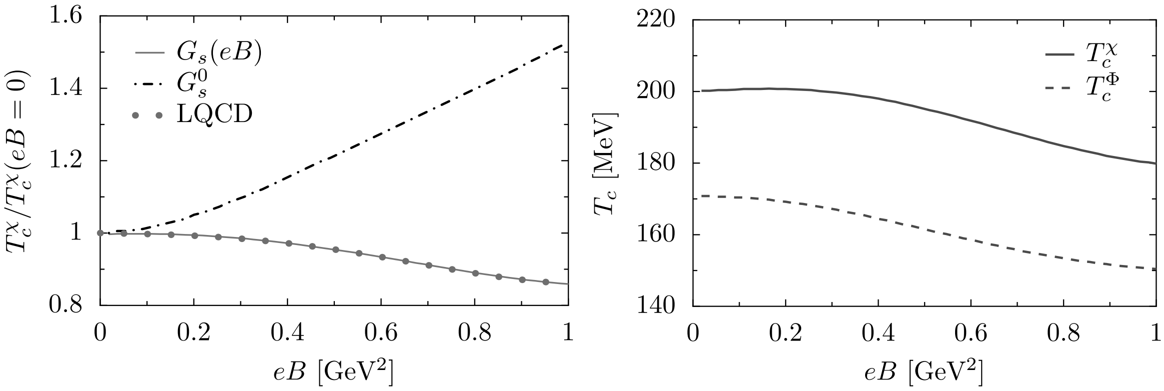

Figure 113: (Left panel) The renormalized critical temperatures of the chiral transition ($T_c^\chi(eB=0) =$ 178 MeV) as a function of eB in the NJL model with a magnetic field dependent coupling $G_s(eB)$ and a constant coupling G_s^0, and the lattice results [4]. (Right panel) The chiral (T_c^χ) and deconfinement (T_c^Φ) transitions temperatures as a function of eB in the PNJL, using $G_s(eB)$ given by Eq. (298).

Now, using $G_s(eB)$ given in Eq. (298), we calculate the chiral and deconfinement transitions temperatures as a function of eB in the PNJL model. The results are shown in the right panel of Fig. 113: due to the existing coupling between the Polyakov loop field and quarks within the PNJL model, the $G_s(eB)$ does not only affect the chiral transition but also the deconfinement transition. Consequently, both temperatures transitions decrease with increasing magnetic filed strength.

2 The influence of the inverse magnetic catalysis in the location of the critical end point

The nature of the phase transition and the existence of the critical end point (CEP) are open issues for theoretical studies about the QCD phase diagram [10]. From the experimental point of view the existence/location of the CEP is also a very timely topic. This renders important to know the conditions that can change the position of the CEP in the phase diagram, namely the presence of strong magnetic fields.

In the following, we will study two scenarios for the effect of a static external magnetic field on the location of the CEP when symmetric matter ($\mu_u = \mu_d = \mu_s$) is considered:
Case I − where we take the usual $G_s = G_s^0$ and no IMC effects are included;
Case II − where we will use $G_s(eB)$ given by Eq. (298) which will allow us to consider the IMC effects on the QCD phase diagram.

The results for Case I are plotted in the left panel of Fig. 114 and reproduce qualitatively the results previously obtained within the NJL model in [11]: as the intensity of the magnetic field increases, the transition temperature increases and the baryonic chemical potential decreases until the critical value $eB \sim 0.4$ GeV^2. For stronger magnetic fields both T and μ_B increase. In the right panel of Fig. 114 the CEP is given in a T versus baryonic density plot. It is seen that when eB increases from 0 to 1 GeV^2 the baryonic density at the CEP increases from $2\rho_0$ to $\sim 14\rho_0$ [12].

With respect to Case II the results for the CEP are presented in Fig. 115, red points. We clearly observe a different behavior when compared with Case I (black points): at $B = 0$ both CEP's coincide but, already for small values of B, the CEP is moved to lower temperatures and chemical potentials. Nevertheless, until $eB \sim 0.3$ GeV^2 the pattern is similar for both Cases. However, for stronger magnetic fields the position of the CEP in Case II oscillates between $T \approx 169$ and $T \approx 177$ MeV while the chemical potential takes increasingly smaller values: a completely different behavior when compared with Case I, where both values of T and μ_B for the CEP increase.

The reason of this behavior lies in fact that the restoration of chiral symmetry is stressed by the

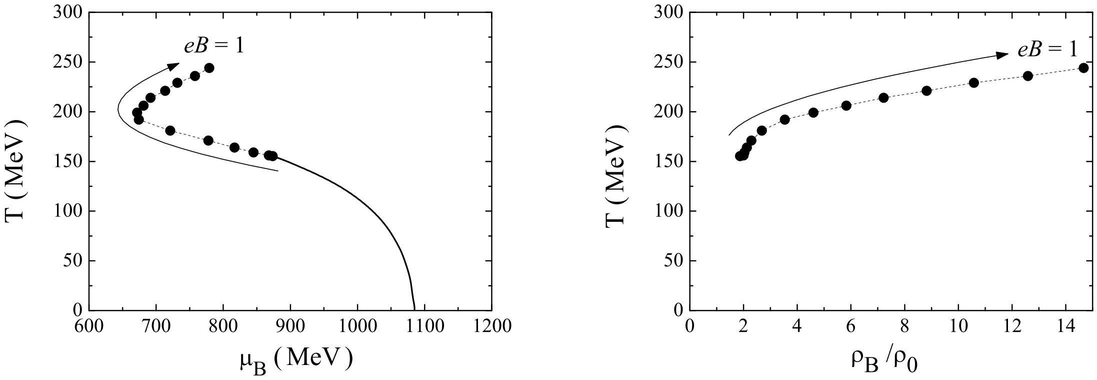

Figure 114: Location of the CEP on temperature vs baryonic chemical potential μ_B (left) and temperature vs baryonic density ρ_B (right) diagrams, for Case I. The baryonic density ρ_B is in units of nuclear saturation density, $\rho_0 = 0.16$ fm^{-3}.

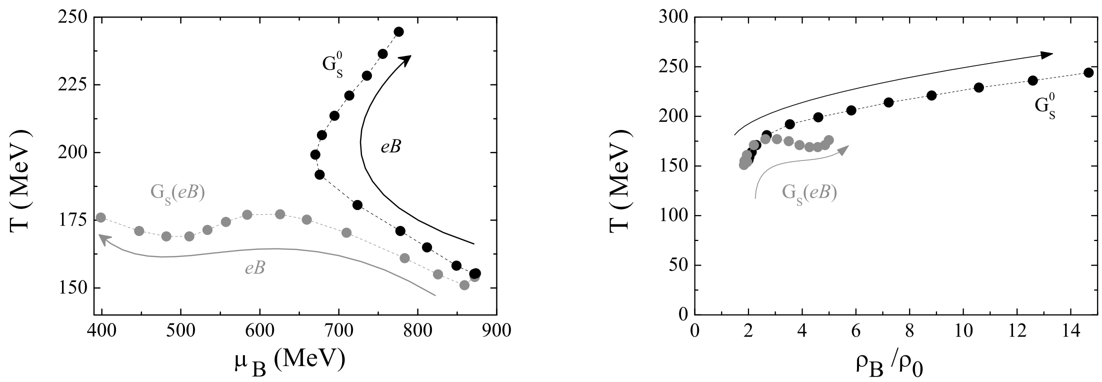

Figure 115: Location of the CEP on temperature vs baryonic chemical potential μ_B (left) and temperature vs baryonic density ρ_B (right) diagrams, for both cases. The baryonic density ρ_B is in units of nuclear saturation density, $\rho_0 = 0.16$ fm^{-3}.

decreasing of the coupling $G_s(eB)$. The increasing of the magnetic filed is not sufficient to counteract this effect as can be seen if Fig. 116, where we plot the quarks masses (M_u-black line; M_d-red line; M_s-blue line) as function of μ_B for the respective temperature where the CEP occurs (T^{CEP}) at $eB = 0.1$ and $eB = 0.5$ GeV^2. At $eB = 0.1$ GeV^2 (left panel) G_s is barely affected by the magnetic field, the values of the quark masses are very close to each other for both cases, and the CEP occurs at smaller temperatures and at close, but smaller, chemical potentials. When $eB = 0.5$ GeV^2, the quark masses in Case I are increased with respect to the $B = 0$ case (due to MC effect), being the restoration of chiral symmetry more difficult to achieve. However, when $G_s(eB)$, Case II, the masses of the quarks are already smaller than the $B = 0$ case (due to IMC effect) leading to an faster restoration of chiral symmetry at small temperatures and chemical potentials. Eventually, with the increase of B, the CEP would disappear in the temperature axis and the transition to the chiral restored phase is always of first order.

Acknowledgement

This work was partially supported by Project No. PEst-OE/FIS/UI0405 /2014 developed under the initiative QREN financed by the UE/FEDER through the program COMPETE – “Programa Operacional Factores de Competitividade”, and by Grant No. SFRH/BD/51717/2011 from FCT.

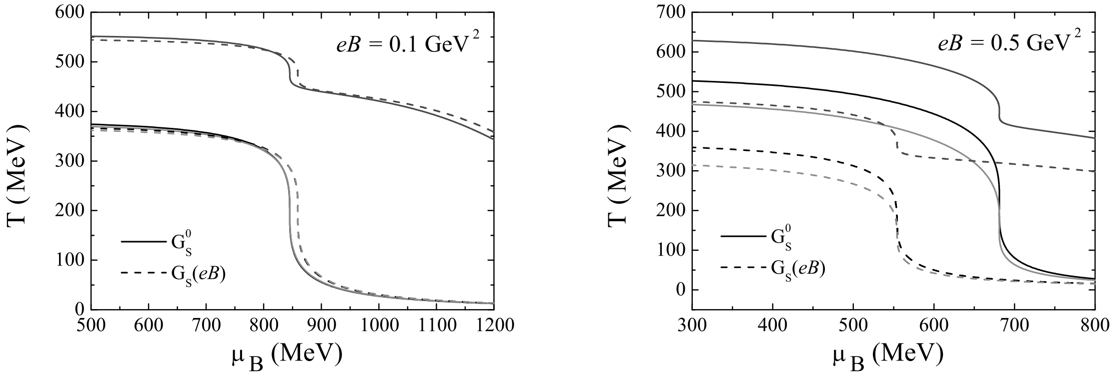

Figure 116: Masses of the quarks as function of μ_B for the respective T^{CEP} for both Cases.

References

1. M. Ferreira, P. Costa, D. P. Menezes, C. Providência and N.N. Scoccola, Phys. Rev. D **89**, 016002 (2014) [arXiv:1305.4751 [hep-ph]].
2. M. Ferreira, P. Costa and C. Providência, Phys. Rev. D **89**, 036006 (2014) [arXiv:1312.6733 [hep-ph]].
3. M. Ferreira, P. Costa and C. Providência, Phys. Rev. D **90**, 016012 (2014) [arXiv:1406.3608 [hep-ph]].
4. G. S. Bali, F. Bruckmann, G. Endrodi, Z. Fodor, S. D. Katz, S. Krieg, A. Schafer and K. K. Szabo, JHEP **1202**, 044 (2012) [arXiv:1111.4956 [hep-lat]].
5. G. S. Bali, F. Bruckmann, G. Endrödi, Z. Fodor, S. D. Katz, and A. Schäfer, Phys. Rev. D **86**, 071502 (2012) [arXiv:1206.4205 [hep-lat]].
6. F. Bruckmann, G. Endrodi and T. G. Kovacs, JHEP **1304**, 112 (2013) [arXiv:1303.3972 [hep-lat]].
7. R. L. S. Farias, K. P. Gomes, G. I. Krein and M. B. Pinto, Phys. Rev. C **90**, 025203 (2014) [arXiv:1404.3931 [hep-ph]].
8. M. Ferreira, P. Costa, O. Lourenço, T. Frederico and C. Providência, Phys. Rev. D **89**, 116011 (2014) [arXiv:1404.5577 [hep-ph]].
9. V. A. Miransky and I. A. Shovkovy, Phys. Rev. D **66**, 045006 (2002) [hep-ph/0205348 [hep-ph]].
10. P. Costa, M. Ferreira, D. P. Menezes, J. Moreira and C. Providência, Phys. Rev. D **92**, 036012 (2015) [arXiv:1508.07870 [hep-ph]].
11. S. S. Avancini, D. P. Menezes, M. B. Pinto and C. Providência, Phys. Rev. D **85**, 091901 (2012) [arXiv:1202.5641 [hep-ph]].
12. P. Costa, M. Ferreira, H. Hansen, D. P. Menezes and C. Providência, Phys. Rev. D **89**, 056013 (2014) [arXiv:1307.7894 [hep-ph]].

Sylvain Fichet

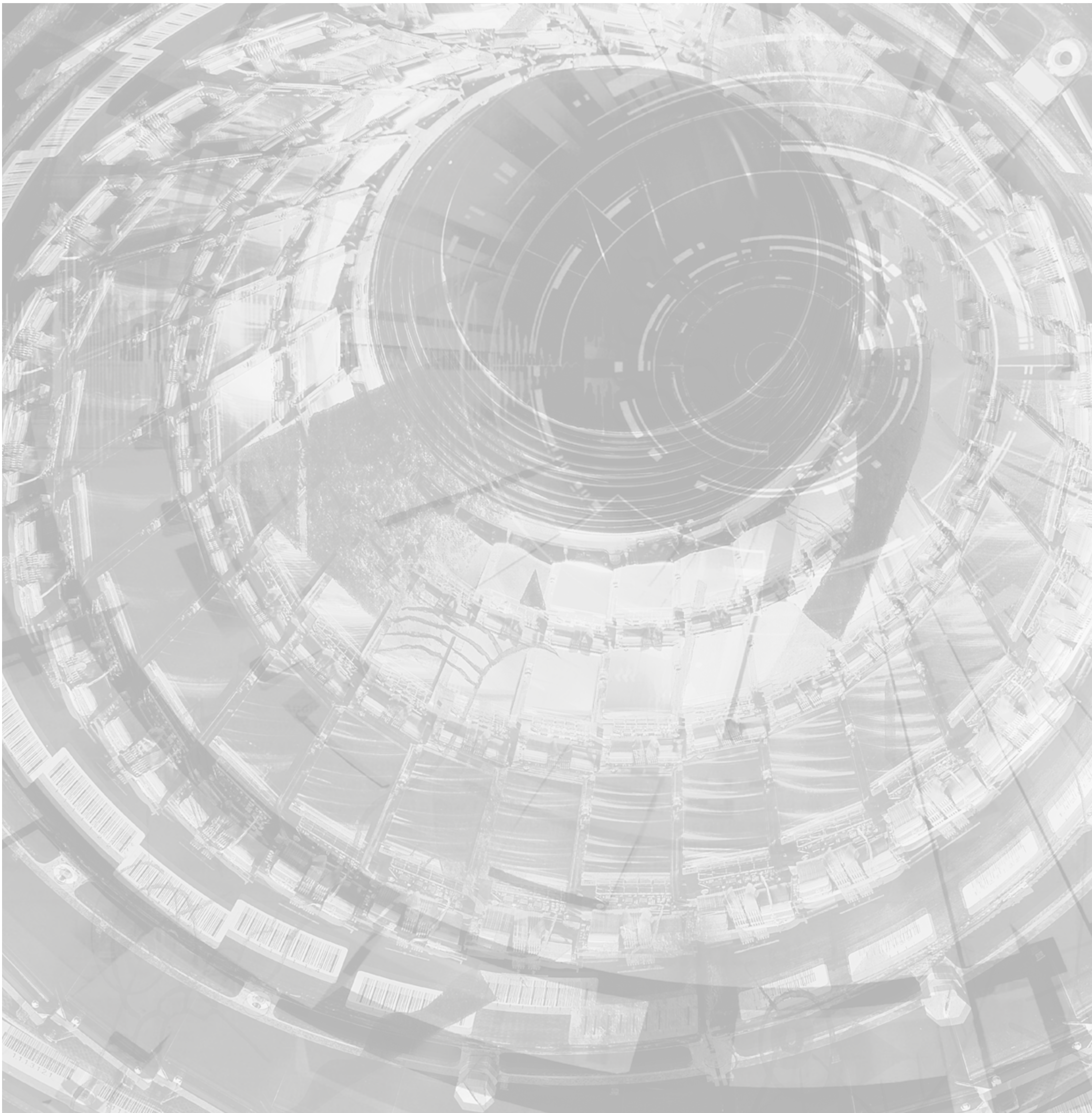

Anomalous light-by-light scattering at the LHC: recent developments and future perspectives

Sylvain Fichet [c, o]

[c]The International Institute of Physics, UFRN, Natal, Brazil

[o]ICTP South American Institute for Fundamental Research, Instituto de Física Teorica, Sao Paulo State University, Brazil

Abstract

The installation of forward proton detectors at the LHC will provide the possibility to perform high-precision measurements, opening a novel window on physics beyond the Standard Model. We review recent simulations and theoretical developments about the measurement of anomalous light-by-light scattering. The search for this process will provide bounds on a wide range of new particles. Future perspectives for precision QED at the LHC are also briefly discussed.

1 Effective Lagrangian and precision physics

Several major facts like the gauge-hierarchy problem or the observation of dark matter suggest that a new physics beyond the Standard Model of particles (SM) should emerge at a mass scale close from the electroweak scale. However, after the first LHC run, a certain amount of popular models has been ruled out or they are cornered in fine-tuned regions of their parameter space. While the next LHC run is coming, it is more than ever important to be prepared to search for any kind of new physics in the most possible robust ways.

In a scenario of new physics out of reach from direct observation at the LHC, one may expect that the first manifestations show up in precision measurements of the SM properties. Assuming that the new physics scale Λ is higher than the typical LHC energy reach $E_{\rm LHC}$, the correlation functions of the SM fields can be expanded with respect to $E_{\rm LHC}/\Lambda$. At the Lagrangian level, this generates a series of local operators of higher dimension, which describe all the manifestations of new physics observable at low-energy. This low-energy effective Lagrangian reads

$$\mathcal{L}_{\rm eff} = \mathcal{L}_{\rm SM} + \sum_{i,n} \frac{\alpha_i^{(n)}}{\Lambda^n}\,. \tag{299}$$

The coefficients $\alpha_i^{(n)}$ are roughly $O(1)$ if generated at tree-level or $O(1/16\pi^2)$ if generated at one-loop level.

The effective Lagrangian is somehow the natural companion of precision physics. In all generality, the goal of SM precision physics is to get information on the coefficients $\alpha_i^{(n)}$ and the new physics scale Λ. For a given set of data, bounds on $\alpha_i^{(n)}$ can be obtained if one fixes Λ. However, it is also obviously interesting to draw bounds on Λ itself. In order to get meaningful bounds on Λ, a statistical subtlety has to be taken into account (see [1]), that conceptually boils down to require new physics to be testable.

Among the various sectors of the SM that can be probed at the LHC, the pure Yang-Mills sector describes triple and quartic gauge boson interactions, that are all fixed by gauge symmetry. Among these interactions, the self-interactions of neutral gauge bosons are particularly appealing. Indeed, these interactions are generated only at loop-level in the SM, such that the SM irreducible background is small. Neutral gauge-bosons self-interactions should be thus considered as smoking-gun observables for new physics.

For $\Lambda > E_{\mathrm{LHC}}$, neutral gauge-boson interactions beyond the SM are described by dimension-8 operators with two kinds of structure, $(DH)(DH)^{\dagger}VV\,/\Lambda^4$ and $VVVV\,/\Lambda^4$. Schematically, the former is expected to dominate for energies lower than the electroweak scale, while the later is expected to dominate for energies higher than the EW scale. The second kind, *i.e. pure-gauge* operators, are thus fully relevant for the LHC, and should be the dominant ones at a future collider with higher energy reach.

Four-photon interactions are described by two pure-gauge operators,

$$\mathcal{L}_{4\gamma} = \zeta_1 F_{\mu\nu}F^{\mu\nu}F_{\rho\sigma}F^{\rho\sigma} + \zeta_2 F_{\mu\nu}F^{\nu\rho}F_{\rho\lambda}F^{\lambda\mu}\,. \tag{300}$$

The effect of any object beyond the SM can be parametrized in terms of the ζ_1, ζ_2 parameters, as well as any experimental search results.

2 Precision physics with intact protons

New possibilities for precision measurements will be opened with the installation of the new forward detectors, which is scheduled at both ATLAS (ATLAS Forward Proton detector [2]) and CMS (CT-PPS detector [3]). The purpose of these detectors is to measure intact protons arising from diffractive processes at small angle. They will be built at $\sim$ 200 m on both sides of CMS and ATLAS. The detectors should host tracking stations, as well as timing detectors (see Fig. 117). The proton taggers are expected to determine the fractional proton momentum loss ξ in the range $0.015 < \xi < 0.15$ with a relative resolution of 2%. In addition, the time-of-flight of the protons can be measured within 10 ps, which translates into $\sim$ 2 mm resolution on the determination of the interaction point along the beam axis z.

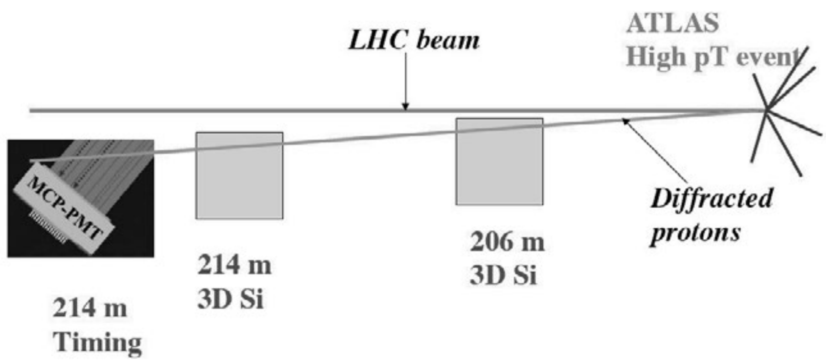

Figure 117: Scheme of the AFP detector. Roman pot hosting Si and timing detectors will be installed on both sides of ATLAS at 206 and 214 m from the ATLAS nominal interaction point. The CMS-TOTEM collaborations will have similar detectors.

The crucial feature of the forward detectors is that they provide the complete kinematics of the event, which in turn can be used to drastically reduce the backgrounds. This setup constitutes an excellent method to look for the effective operators describing physics beyond the SM. Proton scattering processes with intermediate photons are the mostly studied ones, because the equivalent photon approximation is well understood. In principle, at the LHC energies, intermediate W, Z bosons could also happen, however a precise estimation of the fluxes is needed.

Forward proton detectors open thus a new window on physics beyond the SM. They provide a clean environment to search for the effective operators describing physics beyond the SM. For example,

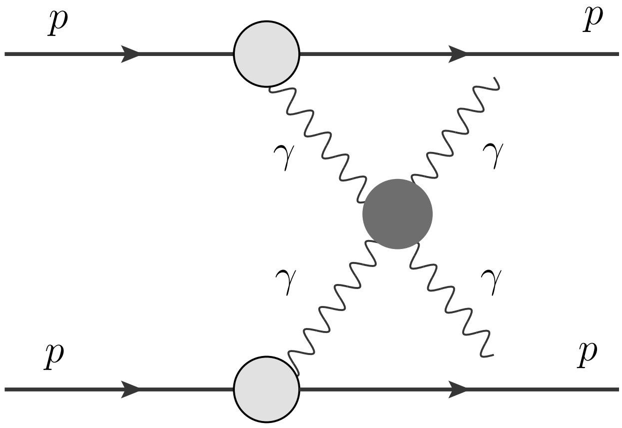

Figure 118: Light-by-light scattering with intact protons.

operators like $|H|^2 V_{\mu\nu} V^{\mu\nu}/\Lambda^2$ induce anomalous single or double Higgs production (for the MSSM case, see [4, 5]). The flavour-changing dipole operators like $\bar{q}\sigma_{\mu\nu} t V^{\mu\nu}/\Lambda^2$ induce single top plus one jet production (see [6]). Finally, the four-photon operators of Eq. 300 induce light-by-light scattering. This last process is pictured in Fig. 118. Studies using proton-tagging at the LHC for new physics searches can be found in [7–20].

3 Light-by-light scattering at the LHC

Given the promising possibilities of forward detectors, a realistic simulation of the search for anomalous $\gamma\gamma \to \gamma\gamma$ at the 14 TeV LHC has been carried out in [20]. The search for light-by-light scattering at the LHC without proton tagging has been first thoroughly analyzed in [21]. Let us review the setup, the backgrounds, the event selection, and the sensitivity to the $\zeta_{1,2}$ anomalous couplings expected at the 14 TeV LHC.

The Forward Physics Monte Carlo generator (FPMC, [22]) is designed to produce within a same framework the double pomeron exchange (DPE), single diffractive, exclusive diffractive and photon-induced processes. The emission of photons by protons is correctly described by the Budnev flux [23, 24], which takes into account the proton electromagnetic structure. The SM $\gamma\gamma \to \gamma\gamma$ process induced by loops of SM fermions and W, the exact contributions from new particles with arbitrary charge and mass, and the anomalous vertices described by the effective operators Eq. (300) have been implemented into FPMC.

The backgrounds are divided into three classes. Exclusive processes with two intact photons and a pair of photon candidates include the SM light-by-light scattering, $\gamma\gamma \to e^+e^-$ and the central-exclusive production of two photons via two-gluon exchange, simulated using ExHume [25]. Processes involving DPE can result in protons accompanied by two jets, two photons and a Higgs boson that decay into two photons. Finally, one can have gluon or quark-initiated production of two photons, two jets or two electrons (Drell-Yan) with intact protons arising from pile-up interactions.

The knowledge of the full event kinematics is a powerful constraint to reject the background from pile-up. The crucial cuts consist in matching the missing momentum (rapidity difference) of the di-proton system with the invariant mass (rapidity difference) of the di-photon system, which is measured in the central detector. Extra cuts rely on the event topology, using the fact that the photons are emitted back-to-back with similar p_T. Further background reduction could even possible by measuring the protons time-of-flight, which provides a complete reconstruction of the primary vertex with a typical precision of 1mm.

The estimation of the LHC sensitivities to effective four-photon couplings ζ_i provided by measuring light-by-light scattering with proton tagging is performed in [14, 20]. These sensitivities are given in Table 23 for different scenarios corresponding to the medium luminosity at the LHC (300 fb^{-1}) and the high luminosity (3000 fb^{-1} in ATLAS). The 5σ discovery potential as well as the 95% CL limits with a pile-up of 50 are given.

It turns out that the selection efficiency is sufficiently good so that the background amplitudes are negligible with respect to the anomalous $\gamma\gamma \to \gamma\gamma$ signal. A handful of events is therefore enough to reach a high significance. In that regime, the signal-background interference can be neglected, and the unpolarized differential cross-section in presence of effective operators takes a simple form

$$\frac{d\sigma}{d\Omega} = \frac{1}{16\pi^2 s}(s^2 + t^2 + st)^2 \left[48(\zeta_1)^2 + 40\zeta_1\zeta_2 + 11(\zeta_2)^2\right] \tag{301}$$

where s, t are the usual Mandelstam variables.

The obvious inconvenience of the EFT approach is that it is valid only in the high mass region, $m \gg E$. In order to use the EFT result down to $m \sim E$, it is common to introduce ad-hoc form factors which mimics the behaviour of the – unknown – amplitudes near the threshold. Clearly, this method introduces arbitrariness into the results. Not only do the results depend on the functional form of the form factor, but also on the energy scale at which they are introduced.

Luminosity	300 fb^{-1}	300 fb^{-1}	3000 fb^{-1}
pile-up (μ)	50	50	200
coupling (GeV^{-4})	5 σ	95% CL	95% CL
ζ_1	$1.5 \cdot 10^{-14}$	$9 \cdot 10^{-15}$	$7 \cdot 10^{-15}$
ζ_2	$3 \cdot 10^{-14}$	$2 \cdot 10^{-14}$	$1.5 \cdot 10^{-14}$

Table 23: $5\,\sigma$ discovery and 95% CL exclusion limits on ζ_1 and ζ_2 couplings in GeV^{-4} (see Eq. 300). All sensitivities are given for 300 fb^{-1} and $\mu = 50$ pile-up events (medium luminosity LHC) except for the numbers of the last column which are given for 3000 fb^{-1} and $\mu = 200$ pile-up events (high luminosity LHC).

4 Sensitivity to generic charged particles

What about actual new physics candidates ? The perturbative contributions to anomalous gauge couplings appear at one-loop and can be parametrized in terms of the mass and quantum numbers of the new particle [13]. In the case of four-photon interactions, only electric charge matters. New particles with exotic electric charges can for example appear in composite Higgs model [26] or in warped extra-dimension models with custodial symmetry [27]. The new particles have in general a multiplicity with respect to electromagnetism. For instance, the multiplicity is three if the particles are colored. It is convenient to take into account this multiplicity by defining

$$Q^4_{\text{eff}} = \operatorname{tr} Q^4 \tag{302}$$

where the trace goes over all particles with the same approximate mass. In the case of new electrically charged particles with arbitrary spin S, the coefficients read

$$\zeta_i = \frac{\alpha^2_{\text{em}} Q^4_{\text{eff}}}{m^4}\, c_{i,S}\,, \tag{303}$$

where

$$c_{1,S} = \begin{cases} \frac{1}{288} & S=0 \\ -\frac{1}{36} & S=\frac{1}{2} \\ -\frac{5}{32} & S=1 \end{cases}, \quad c_{2,S} = \begin{cases} \frac{1}{360} & S=0 \\ \frac{7}{90} & S=\frac{1}{2} \\ \frac{27}{40} & S=1 \end{cases} . \tag{304}$$

The contributions from the scalar are smaller by one order of magnitude with respect to the fermion and vector. It can easily be checked that in the case of fermions $\mathcal{L}_{4\gamma}$ reduces to the famous Euler-Heisenberg Lagrangian [28]. [27].

The effective field theory analysis has the advantage of being very simple. However it is only valid as long as the center-of-mass energy is small with respect to the threshold of pair-production of real particles, $s \ll 4m^2$. Since the maximum proton missing mass (corresponding to the di-photon invariant mass in our case) is of the order of ~ 2 TeV at the 14 TeV LHC, for particles lighter than ~ 1 TeV the effective field theory computation needs to be corrected. This can be done by using ad-hoc form factors, as often done in the literature. The more correct approach is to take into account the full momentum dependence of the four-photon amplitudes. The SM loops have been computed in Refs. [31–33] and are collected in Ref. [20]. At LHC energies, the W loop dominates over all fermion loops including the top because it grows logarithmically.

The results of the simulation with full amplitudes are given in Tab. 24 and Fig. 119 where are displayed the 5σ discovery, 3σ evidence and 95% C.L. limit for fermions and vectors for a luminosity of 300 fb^{-1} and a pile-up of 50. It is found that a vector (fermion) with $Q_{\rm eff} = 4$, can be discovered up to mass $m = 700$ GeV (370 GeV). At high mass, the exclusion bounds follow isolines $Q \propto m$, as dictated by the EFT couplings Eq. 303. Extrapolating the same analysis to a higher luminosity of 3000 fb^{-1}for a pile-up of 200 leads to a slighlty improved sensitivity of $m = 740$ GeV (410 GeV) for vectors (fermions).

One may notice that some searches for vector-like quarks, as motivated from e.g. Composite Higgs models, already lead to stronger bounds than the ones projected here. For instance, vector-like top partners arising from the $(2,2)$ (corresponding to $Q_{\rm eff} \approx 2.2$) of mass $m = 500$ GeV would be excluded from present LHC data, while they would be out of reach using light-by-light scattering. On the other hand, the light-by-light scattering results are completely model-independent. They apply just as well to different effective charges, are independent of the amount of mixing with the SM quarks, and even apply to vector-like leptons!

Four-photon amplitudes also contribute to the magnetic dipole moment of the muon a_μ via two and three-loop diagrams. An estimating of these loop contributions shows that with an experimental bound on $a_\mu \sim 6 \cdot 10^{-10}$, the sensitivity of this measurement is $m/Q_{\rm eff} \sim 5$ GeV. Comparing this estimate to the projections from Fig. 119, it appears that, despite its impressive accuracy, the $g-2$ measurement is not competitive with the light-by-light scattering measurement.

Mass (GeV)	300	600	900	1200	1500
$Q_{\rm eff}$ (vector)	2.2	3.4	4.9	7.2	8.9
$Q_{\rm eff}$ (fermion)	3.6	5.7	8.6	-	-

Table 24: $5\,\sigma$ discovery limits on the effective charge of new generic charged fermions and vectors for various masses scenarios and full integrated luminosity at the medium-luminosity LHC (300 fb^{-1}, $\mu = 50$).

[27]These results also match early computations [29, 30]

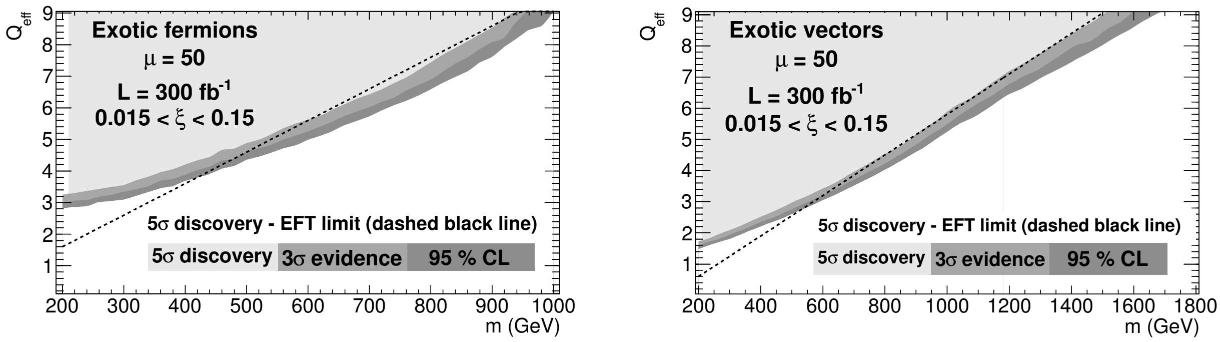

Figure 119: Exclusion plane in terms of mass and effective charge of generic fermions and vectors with full integrated luminosity at the medium-luminosity LHC (300 fb^{-1}, $\mu = 50$).

5 Sensitivity to neutral particles

Beyond the perturbative contributions from charged particles, non-renormalizable interactions of neutral particles are also present in common extensions of the SM. Such theories can contain scalar, pseudo-scalar and spin-2 resonances, respectively denoted by φ, $\tilde{\varphi}$ and $h^{\mu\nu}$ [14]. Independently of the particular new physics model they originate from, their leading couplings to the photon are fixed completely by Lorentz and CP symmetry as

$$\begin{aligned}\mathcal{L}_{\gamma\gamma} =& f_{0^+}^{-1}\, \varphi\, (F_{\mu\nu})^2 + f_{0^-}^{-1}\, \tilde{\varphi}\, F_{\mu\nu} F_{\rho\lambda}\, \epsilon^{\mu\nu\rho\lambda} \\ &+ f_2^{-1}\, h^{\mu\nu}\, (-F_{\mu\rho} F_\nu{}^\rho + \eta_{\mu\nu} (F_{\rho\lambda})^2/4)\,,\end{aligned} \tag{305}$$

where the f_S have mass dimension 2. They then generate 4γ couplings by tree-level exchange as $\zeta_i = (f_S\, m)^{-2}\, d_{i,s}$, where

$$d_{1,s} = \begin{cases} \frac{1}{2} & s = 0^+ \\ -4 & s = 0^- \\ -\frac{1}{8} & s = 2 \end{cases}, \quad d_{2,s} = \begin{cases} 0 & s = 0^+ \\ 8 & s = 0^- \\ \frac{1}{2} & s = 2 \end{cases}. \tag{306}$$

The model independent sensitivities for these three cases are shown in Fig. 120.

It appears that the non-renormalizable contributions from neutral particles are sensibly larger than the charged particles contributions. Light-by-light scattering offers therefore a privileged window on strongly interacting phenomena. Considering actual models, two kind of candidates are known: the Kaluza-Klein (KK) gravitons and the strongly-interacting heavy dilaton (SIHD).

- *Kaluza-Klein gravitons:* The contribution of the entire tower of KK gravitons of warped extra dimensions is computed in [13]. The strength of warped gravity κ can be taken of order unity. For $\kappa = 2$, and using the $5\,\sigma$ and 95% CL sensitivities for the medium luminosity LHC (see Tab. 23), the effect of the KK resonances can be detected up to mass

$$m_{\rm KK} < 5670\,{\rm GeV}\,(5\,\sigma)\,, \quad m_{\rm KK} < 6450\,{\rm GeV}\ (95\%{\rm CL})\,. \tag{307}$$

  These sensitivities are competitive with respect to searches for direct production of KK resonances at the LHC.

- *Strongly-interacting dilaton* [20]: Extensions of the Standard Model sometimes feature a new strongly-interacting sector. Provided that this sector is conformal in the UV, it is most likely explicitly broken in the IR, at least by the appearance of electroweak scale and QCD confinement.

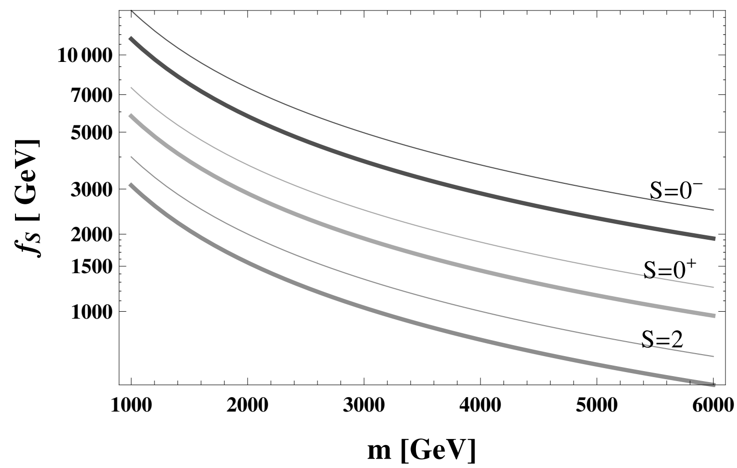

Figure 120: Sensitivities for the neutral simplified models in the (m, f_S) plane. Thick lines correspond to $5\,\sigma$, thin lines correspond to 95% CL limits. The limits are given for the medium luminosity LHC with all photons (no conversion required) and no form-factor (see Tab. 23).

As a result, the spectrum of the strong sector features a neutral scalar, the so-called dilaton, whose mass lies close to the scale of conformal breaking. In the absence of fine-tuning the dilaton's couplings are unsuppressed with respect to this scale. To distinguish it from the weakly coupled (fine-tuned) light dilaton often considered in the literature one refers to it as the Strongly-Interacting Heavy Dilaton. If the photon is at least partially composite, it also couples strongly to the dilaton. Using the $5\,\sigma$ and 95% CL sensitivities for the medium luminosity LHC, the effect of the SIHD can be detected up to mass

$$m_\varphi < 4260\,\mathrm{GeV}\,(5\,\sigma)\,, \quad m_\varphi < 4840\,\mathrm{GeV}\,(95\%\mathrm{CL})\,. \tag{308}$$

6 Summary and perspectives

The installation of forward proton detectors at the LHC will provide a – somewhat surprising – opportunity to measure the scattering of light by light, providing a new window on physics beyond the Standard Model. Recent simulations and theoretical developments show that such precision measurement gives access to a wide range of new particles, both electrically charged and neutral. A summary plot with the expected sensitivity at the 14 TeV LHC as well as new physics candidates is shown in Fig. 121.

These positive results on precision QED at the LHC open new perspectives, as well as new challenges, from both theoretical and experimental sides. Here is a non-exhaustive list of works in progress and future directions.

- Anomalous three-photon production. The 4γ operators contribute to anomalous $\bar{q}q \to \gamma\gamma\gamma$ production. Contrary to the light-by-light scattering case, one photon is virtual. It is interesting to evaluate the sensitivity provided by this potential measurement.

- Light-by-light scattering in heavy-ions collisions. The photon fluxes from heavy ions are coherent, and therefore enhanced by Z^2. On the other hand the typical center-of-mass energy of the diphoton system is smaller. It is interesting to evaluate the sensitivity provided by this potential measurement. For an earlier study, see [21].

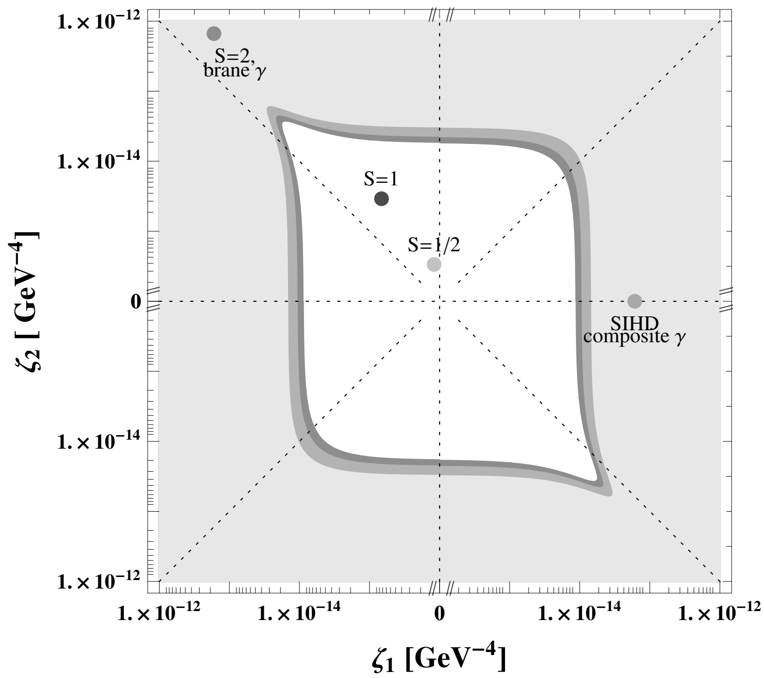

Figure 121: Experimental sensitivity and models in the (ζ_1, ζ_2) plane. Axes follow a logarithmic scale spanning $|\zeta_i| \in [10^{-12}, 10^{-16}]$. The yellow, grey, and red regions can be probed at $5\,\sigma$, $3\,\sigma$ and 95% CL using proton tagging at the LHC, while the white region remains inaccessible. The limits are given for the medium luminosity LHC with all photons (no conversion required) and no form-factor (see Tab. 23). Also shown are contributions from electric particles with spin 1/2 and 1, charge $Q_{\rm eff} = 3$, mass $m = 1$ TeV, the contribution from warped KK gravitons with mass $m_{\rm KK} = 3$ TeV, $\kappa = 2$ and brane-localized photon, and the contribution from a strongly-interacting heavy dilaton (SIHD) with mass $m_\varphi = 3$ TeV coupled to a composite photon.

- Experimentally disentangling between ζ_1 and ζ_2. Polarization-based observables could play this role. This would open the possibility of identifying the nature of the new particle producing light-by-light scattering.

- Modelling the W, Z fluxes. At high energy, gauge boson fluxes from electroweak charges inside the nucleons can be expected to be partly coherent. Having a model of these fluxes would certainly be useful to study electroweak ultrapheripheral collisions.

- Light-by-light scattering from higher-spin particles. Extended objects of higher spin do exist in many extensions of the SM. This is potentially the case with the composite states from any strongly coupled sector, and also with the excitations of low-energy strings. The tools necessary to handle quantum computations involving higher-spin particles are under development.

References

1. S. Fichet, Nucl. Phys. B **884**, 379 (2014) [arXiv:1307.0544 [hep-ph]].
2. ATLAS Collaboration, report CERN-LHCC-2011-012.
3. CMS and TOTEM Collaboration, report CERN-LHCC-2014-021.
4. S. Heinemeyer, V. A. Khoze, M. G. Ryskin, W. J. Stirling, M. Tasevsky and G. Weiglein, Eur. Phys. J. C **53**, 231 (2008), [arXiv:0708.3052 [hep-ph]].
5. M. Tasevsky, Int. J. Mod. Phys. A **29**, 1446012 (2014) [arXiv:1407.8332 [hep-ph]].
6. S. Fichet, B. Herrmann and Y. Stoll, JHEP **1505**, 091 (2015) [arXiv:1501.05307 [hep-ph]].

7. E. Chapon, C. Royon and O. Kepka, Phys. Rev. D **81**, 074003 (2010) [arXiv:0912.5161 [hep-ph]].
8. O. Kepka and C. Royon, Phys. Rev. D **78**, 073005 (2008) [arXiv:0808.0322 [hep-ph]].
9. İ. Şahin and S. C. İnan, JHEP **0909**, 069 (2009) [arXiv:0907.3290 [hep-ph]].
10. S. Atag, S. C. İnan and İ. Şahin, JHEP **1009**, 042 (2010) [arXiv:1005.4792 [hep-ph]].
11. R. S. Gupta, Phys. Rev. D **85**, 014006 (2012) [arXiv:1111.3354 [hep-ph]].
12. P. Lebiedowicz, R. Pasechnik and A. Szczurek, Nucl. Phys. B **881**, 288 (2014) [arXiv:1309.7300 [hep-ph]].
13. S. Fichet and G. von Gersdorff, JHEP **1403**, 102 (2014) [arXiv:1311.6815 [hep-ph]].
14. S. Fichet, G. von Gersdorff, O. Kepka, B. Lenzi, C. Royon and M. Saimpert, Phys. Rev. D **89**, 114004 (2014) [arXiv:1312.5153 [hep-ph]].
15. H. Sun, Nucl. Phys. B **886**, 691 (2014) [arXiv:1402.1817 [hep-ph]].
16. H. Sun, Eur. Phys. J. C **74**(8), 2977 (2014) [arXiv:1406.3897 [hep-ph]].
17. H. Sun, Phys. Rev. D **90**(3), 035018 (2014) [arXiv:1407.5356 [hep-ph]].
18. İ. Şahin, M. Köksal, S. C. İnan, A. A. Billur, B. Şahin, P. Tektaş, E. Alıcı and R. Yıldırım, Phys. Rev. D **91**, 035017 (2015) [arXiv:1409.1796 [hep-ph]].
19. S. C. İnan, Nucl. Phys. B **897**, 289 (2015) [arXiv:1410.3609 [hep-ph]].
20. S. Fichet, G. von Gersdorff, B. Lenzi, C. Royon and M. Saimpert, JHEP **1502**, 165 (2015) [arXiv:1411.6629 [hep-ph]].
21. D. d'Enterria and G. G. da Silveira, Phys. Rev. Lett. **111**, 080405 (2013) [Erratum: Phys. Rev. Lett. **116**(12), 129901 (2016)][arXiv:1305.7142 [hep-ph]].
22. M. Boonekamp, A. Dechambre, V. Juranek, O. Kepka, M. Rangel, C. Royon and R. Staszewski, arXiv:1102.2531 [hep-ph].
23. M. S. Chen, I. J. Muzinich, H. Terazawa and T. P. Cheng, Phys. Rev. D **7**, 3485 (1973).
24. V. M. Budnev, I. F. Ginzburg, G. V. Meledin and V. G. Serbo, Phys. Rept. **15**, 181 (1975).
25. J. Monk and A. Pilkington, Comput. Phys. Commun. **175**, 232 (2006) [hep-ph/0502077 [hep-ph]].
26. K. Agashe, R. Contino and A. Pomarol, Nucl. Phys. B **719**, 165 (2005) [hep-ph/0412089 [hep-ph]].
27. K. Agashe, A. Delgado, M. J. May and R. Sundrum, JHEP **0308**, 050 (2003) [hep-ph/0308036 [hep-ph]].
28. W. Heisenberg and H. Euler, Z. Phys. **98**, 714 (1936) [physics/0605038 [physics]].
29. F. Boudjema, Phys. Lett. B **187**, 362 (1987).
30. M. Baillargeon, F. Boudjema, E. Chopin and V. Lafage, Z. Phys. C **71**, 431 (1996) [hep-ph/9506396 [hep-ph]].
31. R. Karplus and M. Neuman, Phys. Rev. **80**, 380 (1950).
32. V. Costantini, B. De Tollis and G. Pistoni, Nuovo Cim. A **2**, 733 (1971).
33. G. Jikia and A. Tkabladze, Phys. Lett. B **323**, 453 (1994) [hep-ph/9312228 [hep-ph]].

Daniel A. Fagundes
László Jenkovszky
Eduardo Q. Miranda
Giulia Pancheri
Paulo V. R. G. Silva

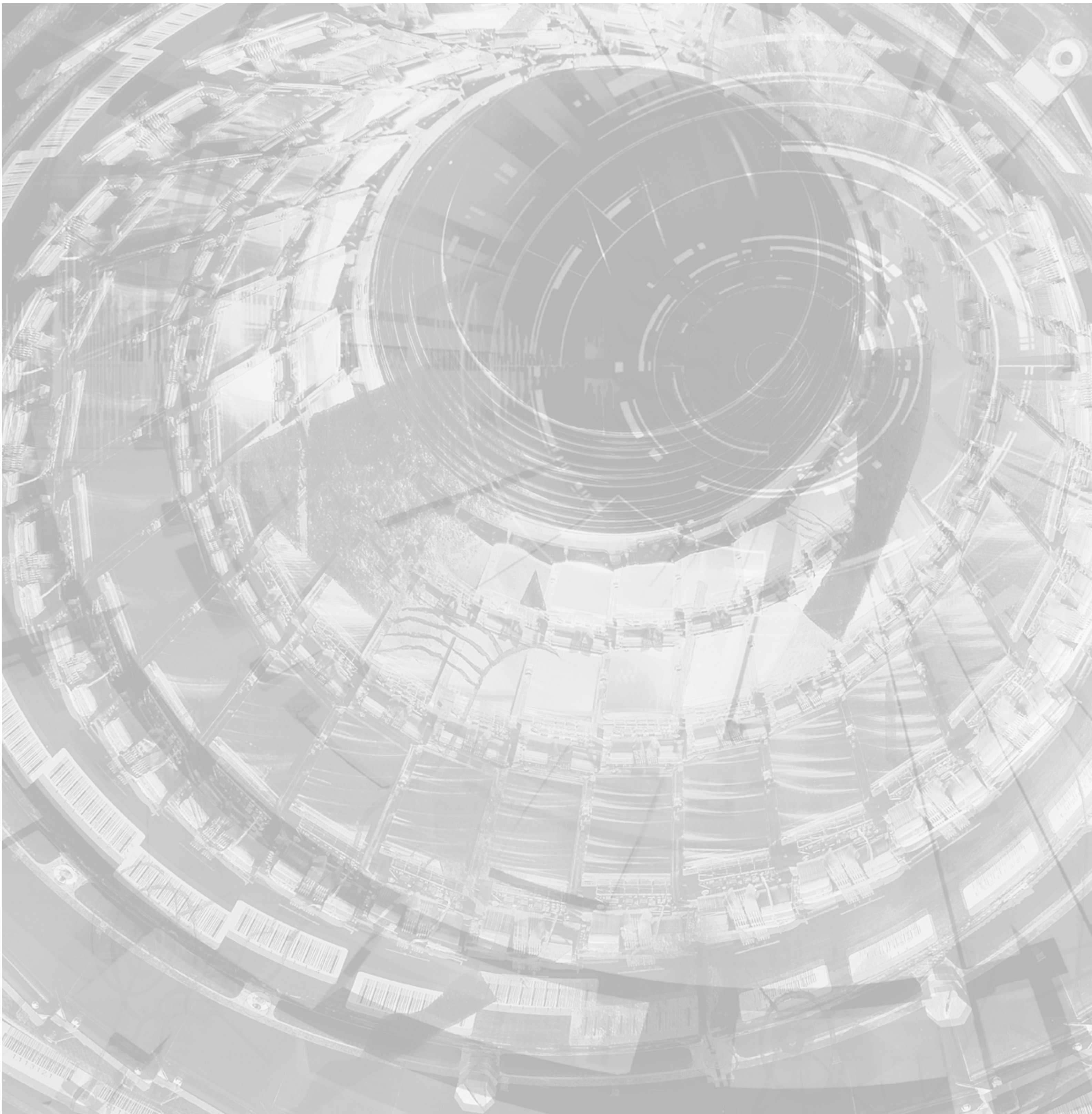

Unitarity and fine structure of the Pomeron

Daniel. A. Fagundes [p], László Jenkovszky [b28], Eduardo Q. Miranda [q], Giulia Pancheri [r], Paulo V. R. G. Silva [s]

[p]Universidade Federal de Santa Catarina, Blumenau, Brazil

[b]Bogolyubov Institute for Theoretical Physics, Kiev, Ukraine

[q]InSTEC, Quinta de los Marinos, La Habana, Cuba

[r]INFN Frascati National Laboratories, Frascati, Italy

[s]Instituto de Física Gleb Wataghin, Universidade Estadual de Campinas, Campinas, Brazil

Abstract

We argue that the low-$|t|$ structure in the elastic diffractive cone, recently reported by the TOTEM Collaboration at 8 TeV, is a consequence of the threshold singularity required by $t-$channel unitarity. By using simple Regge-pole models, we analyze the available data on *pp* elastic differential cross section in a wide range of c.m. energies, namely those from ISR to LHC and argue that the non-exponential behaviour observed at LHC at 8 TeV is a recurrence of the low-$|t|$ "break" observed in the seventies at the ISR.

1 Introduction

In early 70-ies a new phenomenon was observed at the CERN Intersectiong Storage Rings (ISR): the otherwise exponential diffraction cone of elastic proton-proton scattering showed a "break" near $t = -0.1$ GeV^2. In fact the "break "is a smooth curvature manivest in the increase of the exponential slope by about 2 units of GeV^{-2}, a large – nearly 20% effect in those high-precision measurements. The phenomenon found a theoretical explanation independently in Refs. [1] and [2].

Recent measurements by TOTEM at the LHC revealed [3] a similar effect at 8 TeV nearly in the same t interval. In this contribution [29] we argue that both phenomena - seen at the ISR and the LHC - are of the same nature, manifesting the effect of t channel unitarity, see also [4, 5].

A model based on the Phillips and Barger (PB) model-independent description [6], has recently highlighted this relation [7]. Below we revisit the problem of modelling the elastic differential cross section also in model [7]. We test the PB model, appended by a threshold singularity [7], with the present LHC8 data [3].

It is well-known that unitarity constrains the analytic properties of the scattering amplitude. In particular, as shown in Refs. [8], Regge trajectories near the threshold behave as

$$\mathrm{Im}\,\alpha(t) \sim (t - t_0)^{\mathrm{Re}\,\alpha(t_0)+1/2}, \tag{309}$$

where t_0 is the lightest threshold, e.g. $t_0 = 4m_\pi^2$ for the f or Pomeron trajectory. A good approximation to the lightest threshold is by a square root [1]:

$$\alpha(t) \sim \alpha_1\sqrt{t_0 - t}, \tag{310}$$

[28]Corresponding author. See Table 2 for the complete list of talks given at the workshop.

[29]An extended version of this work will be publishced in the Proceedings of the V.N. Gribov Memorial Seminar, World Scientific, 2016

where α_1 is a free parameter, that in Refs. [9] was associated with the pion mass, $\alpha_1 = m_\pi/(1\ \mathrm{GeV}^2)$. While the low-mass $4m_\pi^2$ threshold is responsible for the low-$|t|$ structure (the so-called "break" near $t \approx -0.1$ GeV^2), the otherwise exponential shape of the forward cone is provided by the nearly linear behaviour of the Pomeron trajectory beyond the break (in fact, a smooth curvature) and untill $t \approx -1$ GeV^2. At large $|t|$ the trajectory tends to its logarithmic asymptotics, but this is beyond the scope of the present study (see, *e.g.* [4] and earlier references therein).

2 Double Pomeron Pole

In the framework of the so-called Dipole Pomeron Model (DPM), the Pomeron amplitude is regarded as a two-term amplitude being written as [4]:

$$A_P(s,t) = i\frac{a_P}{b_P}\frac{s}{s_0}[r_1^2(s)e^{r_1^2(s)[\alpha-1]} - \epsilon_P r_2^2(s)e^{r_2^2(s)[\alpha-1]}], \tag{311}$$

where

$$\alpha(t) = \alpha_0 + \alpha' t - \alpha_1\sqrt{t_0 - t} \tag{312}$$

represent the Pomeron ("effective") trajectory and

$$r_1^2(s) = b_P + L - i\pi/2, \tag{313}$$
$$r_2^2(s) = L - i\pi/2, \tag{314}$$

$L = \ln(s/s_0)$ and a_P, b_P, α_0 (adim.), α' (GeV^{-2}), α_1 (GeV^{-1}) and ϵ_P are free parameters. In this model, the energy-dependent functions $r_1(s)$ and $r_2(s)$, having logarithm growth in s reflect the unitarization of the Pomeron amplitude at high-energies. Here, $t_0 = 4m_\pi^2$ (GeV^2) and $s_0 = 1$ GeV^2 are fixed. Just like with Model 1, we considered here also two possible cases (variants), namely:

We calculate the elastic differential cross section from the amplitude in Eq. (311) using the following expression:

$$\frac{d\sigma_{el}}{dt} = \frac{\pi}{s^2}|A_P(s,t)|^2. \tag{315}$$

While the parameter ϵ_P in Eq. (311) - reflecting absorptive effects - plays a major role in the dip-bump region it can be approximately neglected on dealing with the physics we are interested in, namely the break at very small $-t$.

3 Data Analysis and Fits

In the following we shall briefly discuss our data analysis, presenting in the first place the datasets used in data reductions and then showing the main results achieved.

3.1 Datasets

The datates analyzed here are those of the elastic differential cross section for *pp* scattering [10] at ISR energies, namely in the interval 23.5 – 62.5 GeV as well as the recent ones at LHC7, measured by the TOTEM Collaboration [11]. In our first approach to data reductions, the LHC8 data [3] is not taken into account. However, as we explain along the text, it can be used when properly specified. In Table 25 we display the number of points in comprising each dataset used for data reductions. As we are analyzing the effect of deviations of exponential behaviour $\sim e^{-b|t|}$ at the diffraction cone, only the data in the interval $|t| : 0.01 - 0.35$ GeV^2 were considered on performing χ^2 goodness of fit analyses.

$\sqrt{s}$ (GeV)	23.5	30.7	44.7	52.8	62.5	7000	8000
N^o points	62	88	139	59	53	81	30

Table 25: Number of points in each energy in the range of momentum transfer range $|t| : 0.01 - 0.35$ GeV^2 used for data reductions.

3.2 Fitting to the data

In this section we present the results obtained with Model 2, namely the Dipole Pomeron Model. As explained in section 2, we consider here only fits with $\epsilon_P = 0$ fixed and, as in Model 1, we investigate the effect of the linear term in the trajectory by considering either $\alpha' = 0$ fixed or α' as a free parameter. For the first variant, the fits without and with LHC7-TOTEM data are shown in table 26. For the latter, the results are shown in table 27. For both cases, the comparison among data and curves are in figure 122.

	without TOTEM	with TOTEM
a_P	0.660 ± 0.046	1.270 ± 0.012
b_P	1.230 ± 0.097	5.258 ± 0.076
α_0	1.1483 ± 0.0013	1.15325 ± 0.00073
α'	0 (fixed)	0 (fixed)
α_1	0.6026 ± 0.0038	0.4304 ± 0.0023
ϵ_P	0 (fixed)	0 (fixed)
χ^2/DOF	14.43	19.07
DOF	397	478

Table 26: Fits using Model 2 with $\alpha' = 0$ fixed and $\epsilon_P = 0$ fixed without and with TOTEM data. Statistical informations are also shown.

	without TOTEM	with TOTEM
a_P	2.91 ± 0.10	1.598 ± 0.012
b_P	6.76 ± 0.31	8.03 ± 0.11
α_0	0.9625 ± 0.0028	1.0260 ± 0.0015
α'	0.6014 ± 0.0088	0.4453 ± 0.0058
α_1	-0.0549 ± 0.0088	-0.0096 ± 0.0049
ϵ_P	0 (fixed)	0 (fixed)
χ^2/DOF	1.99	5.93
DOF	396	477

Table 27: Fits using Model 2 with α' free and $\epsilon_P = 0$ fixed without and with TOTEM data. Statistical informations are also shown.

4 Fine Structure in the LHC8-TOTEM data

If one expects to extrapolate the results here presented to higher energies, specially to 13 TeV, it is of great importance to include the data obtained for the differential cross section in 8 TeV by TOTEM Collaborarion [3]. In this section, we present results of these updated fits.

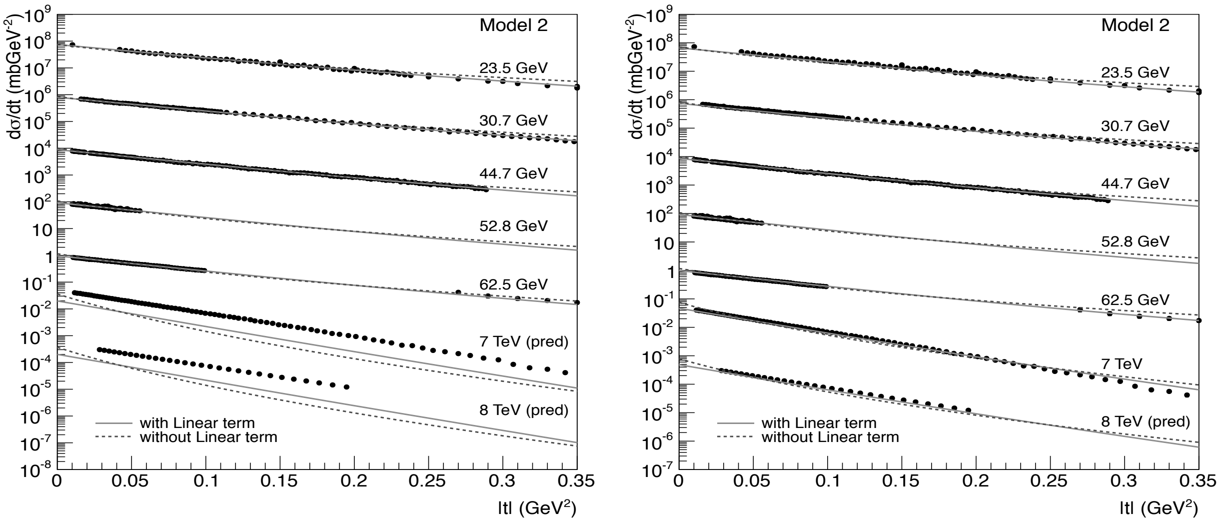

Figure 122: Fits of Model 2, with or without TOTEM data (*left*) in datasets. In the left panel we show this model prediction for the case where the LHC7 data is not added in the data sets. In the right panel we refit the data, now including the LHC7 data, as given in [11]. In both cases we investigate the effect of a linear term in Pomeron trajectory, finding a slightly better agreement with data for the model with a linear term. Curves and data are multiplied by $10^{\pm 2}$ factors to appear in the same canvas.

The results for Model 1 and 2 are showed in tables 28 and 29, respectively, and in figure 123 for both models. For all cases, we consider two variants: with linear term and without linear term in the trajectory.

	without Linear term	with Linear term
r	23.008 ± 0.058	22.307 ± 0.058
b	7.193 ± 0.034	6.130 ± 0.034
α_0	1.16548 ± 0.00030	1.09924 ± 0.00078
α'	0 (fixed)	0.3195 ± 0.0035
α_1	0.27321 ± 0.00081	0.0402 ± 0.0027
χ^2/DOF	21.4	4.51
DOF	508	507

Table 28: Fits using Model 1 including LHC8-TOTEM [3] data in two variants: without and with the linear term in the trajectory. Statistical informations are also shown.

To see in more details the deviation from a pure exponential form, we compare the data and curves to a reference function by means of the ratio:

$$R = \frac{d\sigma/dt - \mathrm{Ref}}{\mathrm{Ref}}, \tag{316}$$

where $\mathrm{Ref} = Ae^{Bt}$ with A and B determined from a fit to the experimental data. For 8 TeV, we have obtained $A = 518.87 \pm 0.40$ mbGeV^{-2} and $B = 19.3880 \pm 0.0088$ GeV^{-2}.

In figure 124 we compare the results obtained with and without the linear term for the two Models considered. Again, it is clear that the linear term is necessary to describe the data analyzed, particularly the deviation from a pure exponential behaviour presented by 8 TeV data.

	without Linear term	with Linear term
a_P	1.3450 ± 0.0024	1.4716 ± 0.0023
b_P	7.613 ± 0.045	8.604 ± 0.055
α_0	1.13539 ± 0.00012	1.02574 ± 0.00058
α'	0 (fixed)	0.4512 ± 0.0025
α_1	0.34239 ± 0.00063	-0.034 ± 0.0020
ϵ_P	0 (fixed)	0 (fixed)
χ^2/DOF	81.6	7.20
DOF	508	507

Table 29: Fits using Model 2 with $\epsilon_P = 0$ fixed including LHC8-TOTEM data [3] in two variants: without and with the linear term in the trajectory. Statistical informations are also shown.

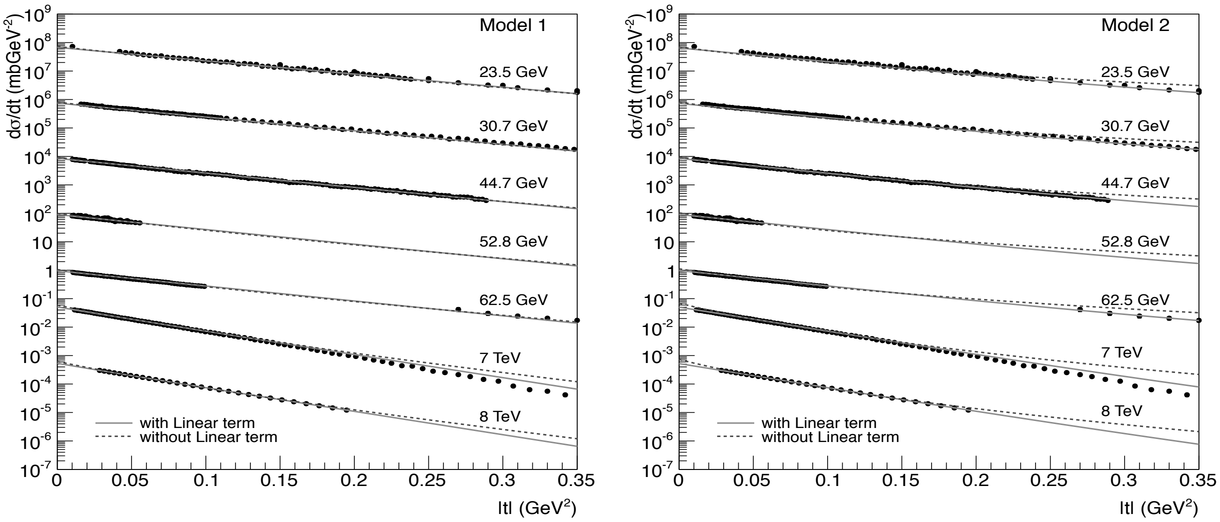

Figure 123: Fit of Model 1 (*left*) and Model 2 (*right*) with and without the linear term in the trajectory with LHC8-TOTEM data [3] in datasets. In both cases we investigate the effect of a linear term in the Pomeron trajectory, finding, again, a slightly better agreement with data for the model with a linear term. Curves and data are multiplied by $10^{\pm 2}$ factors to appear in the same canvas.

5 The Phillips-Barger model with the pion loop singularity added

Here we show the results from a model-independent parametrization which can describe both the small and the large $|t|$ region and which had been proposed in 1972 by Phillips and Barger (PB) [6]. This model was recently modified as [7]:

$$A_{el} = i\{F_p^2(t)\sqrt{A(s)}e^{B(s)t/2} + \sqrt{C(s)}e^{i\phi(s)}e^{D(s)t/2}\} \tag{317}$$

and three cases can be considered:

1. $F_p(t) = 1$ which corresponds to the original PB formulation [6];
2. $F_p^2(t) = e^{-\gamma(s)\sqrt{4m_\pi^2 - t}}$ which includes a parametrization of the pion loop singularity, labelled as MBP1;
3. $F_p(t) = 1/[1 + |t|/t_0]^2$ which modifies the very small $-t$ behaviour with a form factor type behaviour, labelled as MBP2.

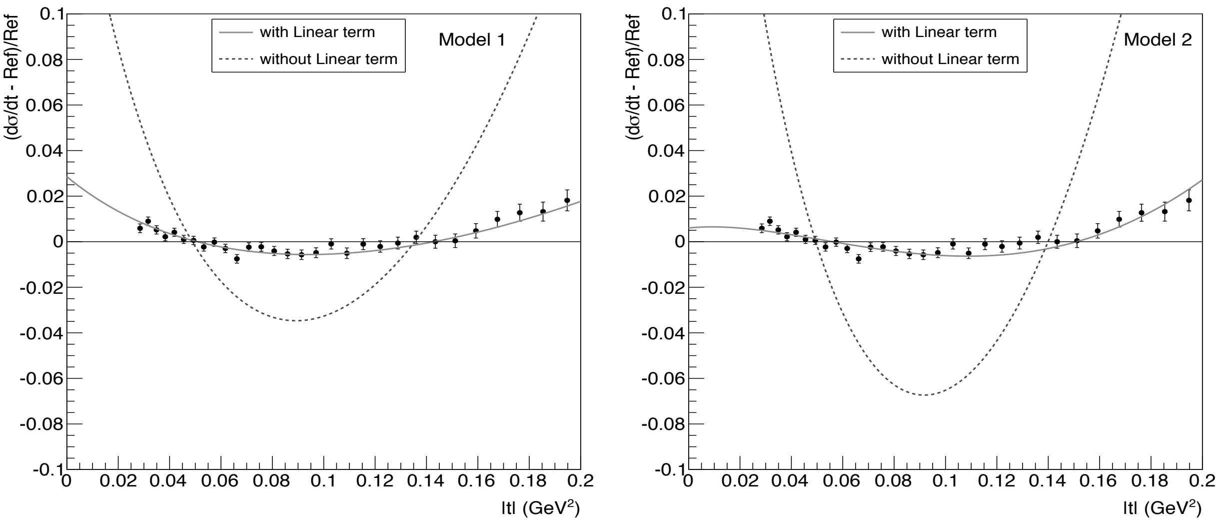

Figure 124: Ratio R (eq.(316)) calculated for 8 TeV comparing data and fits with and without linear term for Model 1 (*left*) and Model 2 (*right*).

Of interest to the present discussion is the second case, a square root singularity. To argue how this model results can be compared with the TOTEM 8 TeV data, we show a fit of the data using the model MBP1, and the comparison with the REF model (one exponential) in Fig. 125. We find that

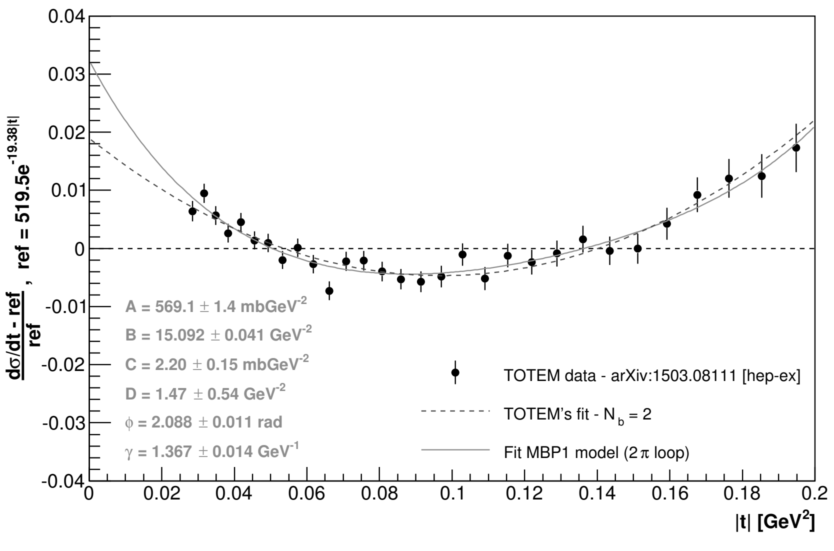

Figure 125: Fit to TOTEM data with the empirical model of [7] using the pion loop singularity modification of the PB model, MBP1.

an independent fit, such as the one indicated by the red curve, can give a very good description of the data, confirming, in this model independent description, the agreement with the presence of the pion loop singularity at very small $-t$-values. The parameter values indicated in the figure correspond to option n.2 in Eq. (317) and to a $\chi^2/dof = 1.03$.

6 Conclusions

We have shown the role of the two-pion loop in determining the fine structure of the diffraction cone, namely in affecting the local slope $B(s,t)$ at the small momentum transfer. Despite the fact that other sources - such as a form factor, eikonal rescatterings and diffractive dissociation [12] - can change the behaviour of $B(s,t)$ at small $-t$, our strategy here was to separately investigate the insertion of a two-pion loop in the Pomeron trajectory. Therefore, we have tried to interpolate/extrapolate our fit results for diffraction cone from ISR to LHC. While the interpolation is very good, the extrapolaton is only qualitatively satisfactory and shall be investigated in much more detail in a future publication. The small mismatch may be attributed mainly to the simplified treatment of multiple Regge-pole exchanges replaced by a single "effective" Regge trajectory. While at the LHC the contribution from secondary trajectories in the nearly forward direction is negligible [4] this is not true at the ISR, where the f trajectory may contribute by half of the total. Two ways how to cure this sufficiency can be envisaged. One is by including all allowed/required Regge exchanges, namely ω, f and the Odderon, apart from the Pomeron. The other one is to account for these by introducing energy-dependent parameters in a single "effective" exchange.

The fine structure of the cone can be better seen on the local slope $B(s,t) = \frac{d}{dt}\ln\frac{d\sigma}{dt}$. It should be, however, remembered that the result depends on the t interval in which the slope is calculated. The relevant bins can be wide or narrow, overlapping or not. This point was recently discussed in Ref. [13]. We also notice that simple and elegant formulae extrapolating the forward slope in energy was derived in Ref. [14]. They read

$$B(s,t) = k\alpha'(t)\sigma_{tot}(s), \quad B(s_2,t)/B(s_1,t) = \sigma_{tot}(s_2)/\sigma_{tot}(s_1), \tag{318}$$

where the coefficient k is determined explicitly in [14]. The virtue of this formula, following [14] from $s-$ channel unitarity is that it is model-independent in the sense that for the total cross section in its r.h.s. on can use either model extrapolations or experimentally measured values of the cross section. The problem with the trajectory is the same as discussed above: in Eq. (318) a single trajectory appears, providing exact predictions when the reaction is dominated by a single Reggeon exchange, as is the case beyond 1 TeV (LHC), dominated by a single Pomeron. Otherwise, an effective trajectory should be used, as discussed above.

The parametrization of trajectories is a key issue in the Regge-pole theory. Linear trajectories are popular for their simplicity, however they contradict unitarity and the analytic properties required by the S-matrix theory and the asymptotic constraints, particularly those imposed by the quark model and perturbative quantum chromodynamics (QCD). For practical purposes one chooses a parametrization relevant to the given kinematical region. As shown in the present paper, the economic, parameter-free single square root parametrization, Eq. (310), used e.g. in Ref. [9] produces too strong curvature in the cone, incompatible with the data, as seen in Figs. 122 and 123. The inclusion of a linear term balances this distortion providing good fits to the data.

Finally we note that the reason of non-observation of any fine structure in the cone at the Tevatron or RHIC may be attributed to poor statistics in relevant experiments. As already mentioned, that is one the reasons we did not perform fits using $\bar{p}p$ datsets. It is also possible that for the same reason it was not observed in diffraction dissociation either. Future experiments may reveal similar effects at the very small $-t$ domain of high-energy diffractive scattering process, either in elastic or inelastic processes. Investigations on this subject are currently in progress.

Acknowledgements

P.V.R.G.S., E.M. and L.J. thank the International Institute of Physics (IIP) at Natal, Brazil, where this work started, for its hospitality and support during the *School and Workshop on New Trends in High-Energy Physics* in October-November, 2014. Research supported by FAPESP, Contract 2013/27060-3 (P.V.R.G.S.) is acknowledged. L.J. was supported also by DOMUS of the Hungarian Academy of Sciences.

References

1. G. Cohen-Tannoudji, V. V. Ilyin and L. L. Jenkovszky, Lett. Nuovo Cim. **5**(2), 957 (1972) [Lett. Nuovo Cim. **5**, 957 (1972)].
2. A. A. Anselm and V. N. Gribov, Phys. Lett. B **40**, 487 (1972).
3. G. Antchev *et al.* [TOTEM Collaboration], Nucl. Phys. B **899**, 527 (2015) [arXiv:1503.08111 [hep-ex]].
4. L. L. Jenkovszky, A. I. Lengyel and D. I. Lontkovskyi, Int. J. Mod. Phys. A **26**, 4755 (2011) [arXiv:1105.1202 [hep-ph]].
5. R. Fiore, L. L. Jenkovszky, R. Orava, E. Predazzi, A. Prokudin and O. Selyugin, Int. J. Mod. Phys. A **24**, 2551 (2009) [arXiv:0810.2902 [hep-ph]].
6. R. J. N. Phillips and V. D. Barger, Phys. Lett. **46B**, 412 (1973).
7. D. A. Fagundes, A. Grau, S. Pacetti, G. Pancheri and Y. N. Srivastava, Phys. Rev. D **88**(9), 094019 (2013) [arXiv:1306.0452 [hep-ph]].
8. A. O. Barut and D. E. Zwanziger, Phys. Rev. **127**, 974 (1962); V. N. Gribov and I. Y. Pomeranchuk, Sov. Phys. JETP **16** 220 (1963) [Zh. Eksp. Teor. Fiz. **43**, 308 (1962)] [Nucl. Phys. **38**, 516 (1962)]; R. Oehme, in *Strong interactions and high energy physics*, Scottish Summer School 1963, edited by R. G. Moorhouse et al., 129, Edinburgh (1964).
9. R. Fiore, L. L. Jenkovszky, F. Paccanoni and A. Prokudin, Phys. Rev. D **68**, 014005 (2003) [hep-ph/0302195 [hep-ph]].
10. http://www.theo.phys.ulg.ac.be/alldata-v2.zip.
11. G. Antchev *et al.* [TOTEM Collaboration], Europhys. Lett. **101**, 21002 (2013).
12. V. A. Khoze, A. D. Martin and M. G. Ryskin, J. Phys. G **42**(2), 025003 (2015) [arXiv:1410.0508 [hep-ph]].
13. L. Jenkovszky and A. Lengyel, Acta Phys. Polon. B **46**, 863 (2015) [arXiv:1410.4106 [hep-ph]].
14. L. L. Jenkovszky and B. V. Struminsky, Yad. Fiz. **39**, 1252 (1984).

Errol Gotsman
Eugene Levin
Uri Maor

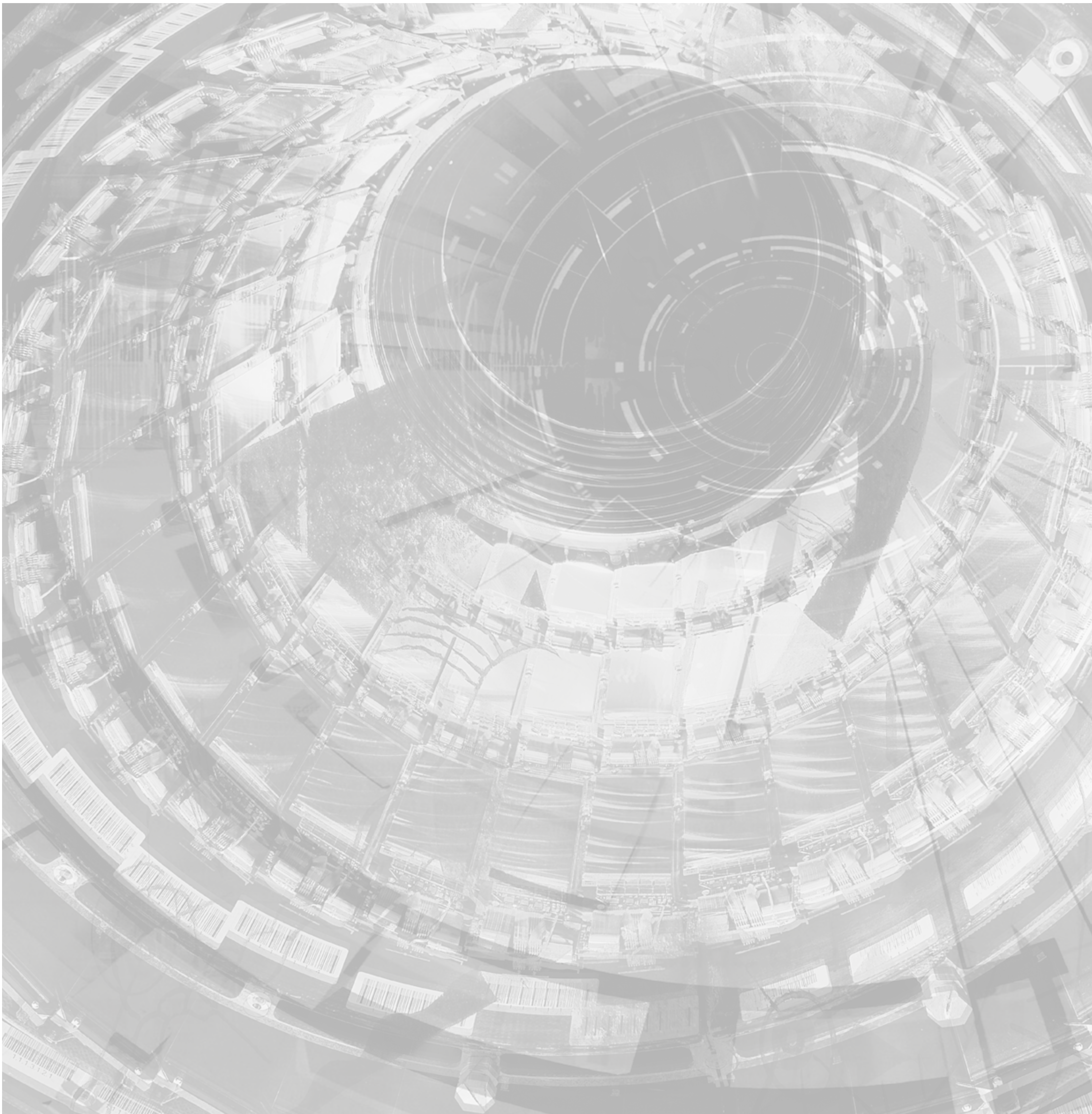

Diffraction as a Fundamental Ingredient in Soft Scattering

Uri Maor[30], Errol Gotsman and Eugene Levin [t]

[t]Raymond and Beverly Sackler Faculty of Exact Science, Tel Aviv University, Tel Aviv, Israel

1 Historic Introduction

The s-channel unitarity screenings date back to the ISR, providing a simple way out of paradoxical traps.

1. Given that non screened σ_{tot} grows with energy, σ_{el} grows faster (optical theorem). With no screening, σ_{el} will, eventually, be larger than σ_{tot}.
2. Even though elastic and diffractive scatterings are dynamically similar, the energy dependences of the two channels are different.
3. The elastic amplitude is central in impact parameter, peaking at $b = 0$. The peripheral diffractive amplitudes peak at large b, which gets larger with energy.
4. 40 years post ISR, estimates of soft scattering channels at the TeV-scale require a unified analysis of elastic and diffractive scatterings, incorporating s and t unitarity screenings.

2 S-channel unitarity

The simplest s-channel unitarity bound on $a_{el}(s, b)$ is obtained from a diagonal re-scattering matrix, where repeated elastic scatterings secure s-channel unitarity,

$$2Im a_{el}(s, b) = |a_{el}(s, b)|^2 + G^{in}(s, b) \tag{319}$$

i.e. At a given (s, b), $\sigma_{tot} = \sigma_{el} + \sigma_{inel}$. Its general solution is:

$$a_{el}(s, b) = i\left(1 - e^{-\Omega(s,b))/2}\right), \qquad G^{in}(s, b) = 1 - e^{-\Omega(s,b)}. \tag{320}$$

Ω is model dependent. The output s-unitarity bound is $|\ a_{el}(s, b)\ | \leq 2$, leading to very large total and elastic LHC cross sections, which are not supported by the recent TOTEM data.

In a Glauber/Gribov eikonal approximation, the input opacity $\Omega(s, b)$ is real. It equals to the imaginary part of the input model Born term, a Pomeron exchange in our context. The output amplitude, $a_{el}(s, b)$, is imaginary. The consequent black disc bound is $|\ a_{el}(s, b)\ | \leq 1$. In a single channel eikonal model, the screened cross sections are:

$$\sigma_{tot} = 2\int d^2b \left(1 - e^{-\Omega(s,b)/2}\right), \tag{321}$$

$$\sigma_{el} = \int d^2b \left(1 - e^{-\Omega(s,b)/2}\right)^2, \tag{322}$$

$$\sigma_{inel} = \int d^2b \left(1 - e^{-\Omega(s,b)}\right). \tag{323}$$

[30]Corresponding author. See Table 2 for the complete list of talks given at the workshop.

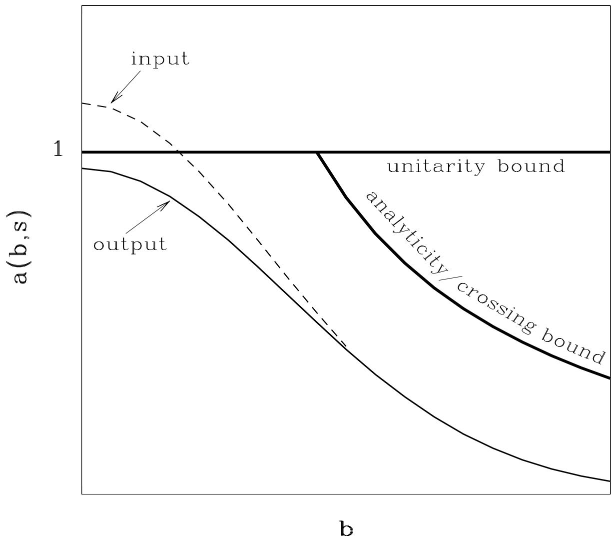

Figure 126: s-channel unitarity bound and the analyticity/crossing bound.

Figure 126 shows the s-channel unitarity black bound, and the analyticity/crossing bound implied by the $\ln^2(s)$ expanding amplitude radius. The consequent Froissart-Martin bound is:

$$\sigma_{tot} \le C\,\ln^2(s/s_0), \qquad s_0 = 1\,\mathrm{GeV}^2, \qquad C \propto 1/2m_\pi^2 \simeq 30\,\mathrm{mb}. \tag{324}$$

C is far too large to be relevant at the TeV-scale. s-unitarity implies:

$$\sigma_{el} \le \frac{1}{2}\sigma_{tot} \qquad \text{and} \qquad \sigma_{inel} \ge \frac{1}{2}\sigma_{tot}. \tag{325}$$

At saturation: $\sigma_{el} = \sigma_{inel} = \frac{1}{2}\sigma_{tot}$.

Introducing diffraction significantly changes the features of s-unitarity. However, the saturation signatures remain valid.

3 Good-Walker decomposition

Consider a system of two orthonormal states, a hadron Ψ_h and a diffractive state Ψ_D. Ψ_D replaces the continuous diffractive Fock states. Good-Walker (GW) noted that Ψ_h and Ψ_D do not diagonalize the 2×2 interaction matrix $\mathbf{T}$. Let Ψ_1 and Ψ_2 be eigen states of $\mathbf{T}$:

$$\Psi_h = \alpha\Psi_1 + \beta\Psi_2, \tag{326}$$
$$\Psi_D = -\beta\Psi_1 + \alpha\Psi_2, \tag{327}$$

where $\alpha^2+\beta^2 = 1$. The eigen states initiate 4 $A_{i,k}$ elastic GW amplitudes ($\psi_i + \psi_k \to \psi_i + \psi_k$), where $i,k = 1,2$. For initial $p(\bar{p}) - p$ we have $A_{1,2} = A_{2,1}$.

I shall follow GLM, where the diffractive mass distribution is not defined and requires a specification. The elastic, SD and DD amplitudes in a 2 channel screened GW model are:

$$A_{i,k}(s,b) = \left(1 - e^{\frac{1}{2}\Omega_{i,k}(s,b)}\right) \le 1. \tag{328}$$
$$a_{el}(s,b) = i\{\alpha^4 A_{1,1} + 2\alpha^2\beta^2 A_{1,2} + \beta^4 A_{2,2}\}, \tag{329}$$
$$a_{sd}(s,b) = i\alpha\beta\{-\alpha^2 A_{1,1} + (\alpha^2-\beta^2)A_{1,2} + \beta^2 A_{2,2}\}, \tag{330}$$
$$a_{dd}(s,b) = i\alpha^2\beta^2\{A_{1,1} - 2A_{1,2} + A_{2,2}\}, \tag{331}$$

Introducing t-channel screening results in a distinction between GW and non-GW diffraction. In the GW sector:

- We obtain the Pumplin bound:
$$\sigma_{el} + \sigma_{diff}^{GW} \leq \frac{1}{2}\sigma_{tot}. \tag{332}$$
σ_{diff}^{GW} sums of the GW soft diffractive cross sections.

- Below saturation,
$$\sigma_{el} \leq \frac{1}{2}\sigma_{tot} - \sigma_{diff}^{GW}, \qquad \text{and} \qquad \sigma_{inel} \geq \frac{1}{2}\sigma_{tot} + \sigma_{diff}^{GW}. \tag{333}$$

- $a_{el}(s,b) = 1$, when and only when $A_{1,1}(s,b) = A_{1,2}(s,b) = A_{2,2}(s,b) = 1$.

- When $a_{el}(s,b) = 1$, all diffractive amplitudes at the same (s,b) vanish.

- The saturation signature, $\sigma_{el} = \sigma_{inel} = \frac{1}{2}\sigma_{tot}$, in a multi channel calculation is coupled to $\sigma_{diff} = 0$. Consequently, prior to saturation the diffractive cross sections stop growing and start to decrease with energy.

- The above holds only in a multi channel analysis. It does not hold in a single channel model.

- GW saturation signatures are valid also in the non-GW sector.

4 Crossed Channeled Unitarity

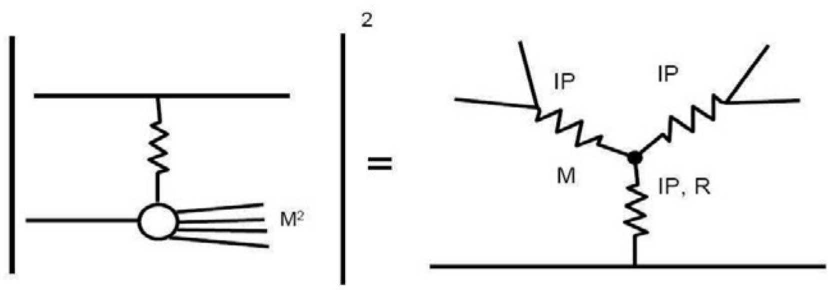

Figure 127: Crossed channeled unitarity.

Translating the concepts presented into a viable phenomenology requires a specification of $\Omega(s,b)$, for which Regge Pomeron ($\mathbb{P}$) theory is a powerful tool. Mueller (1971) applied 3 body unitarity to equate the cross section of: $a + b \to M_{sd}^2 + b$ to the triple Regge diagram $a + b + \bar{b} \to a + b + \bar{b}$ (figure 127), with a leading $3\mathbb{P}$ vertex term. The $3\mathbb{P}$ approximation is valid when:

$$\frac{m_p^2}{M_{sd}^2} << 1 \qquad \text{and} \qquad \frac{M_{sd}^2}{s} << 1. \tag{334}$$

The leading energy/mass dependences are:

$$\frac{d\sigma^{3\mathbb{P}}}{dt\, dM_{sd}^2} \propto s^{2\Delta_{\mathbb{P}}} \qquad \text{and} \qquad \left(\frac{1}{M_{sd}^2}\right)^{1+\Delta_{\mathbb{P}}}. \tag{335}$$

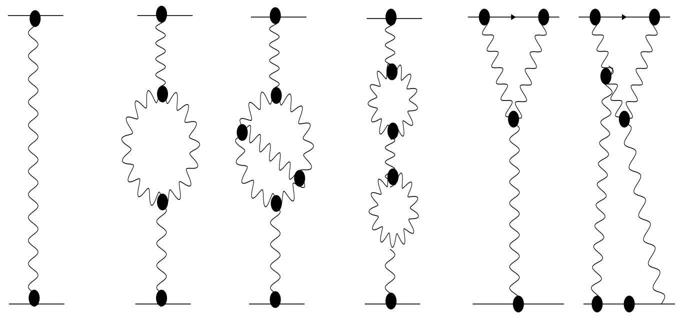

Figure 128: $\mathbb{P}$ Green function.

Mueller's 3$\mathbb{P}$ approximation for non GW diffraction is the lowest order of t-channel multi $\mathbb{P}$ interactions, compatible with t-channel unitarity. Recall that unitarity screening of GW ("low mass") diffraction is carried out explicitly by eikonalization, while the screening of non GW ("high mass") diffraction is carried out by the survival probability. Figure 128 shows the $\mathbb{P}$ Green function. Multi $\mathbb{P}$ interactions induce large mass diffraction. Note the analogy with QED:

a) Enhanced diagrams induce the propagator renormalization.

b) Semi enhanced diagrams, present the p$\mathbb{P}$p vertex renormalization.

5 Incorporating Good-Walker and Mueller diffraction

Both the experimental and theoretical studies of soft diffraction are hindered by conflicting definitions of signatures and bounds. In our context, I wish to discuss the relationship between GW and non GW diffraction versus Mueller's low and high diffractive mass.

Kaidalov, at the time, equated (with no proof) Mueller's low diffractive mass with GW diffraction, and high diffractive mass with non GW diffraction. The problem is how do we define the bounds of these diffractive mass domains. Following Kaidalov, GW low mass upper bound and Mueller's high mass lower bound, which is 4-5 GeV, coincide, *i.e.* there is no overlap of low and high mass diffraction. This point of view is shared by KMR, Ostapchenko and Poghosyan.

I find this assumption problematic, as it offers no procedure which secures a smooth behaviour of the diffractive mass through this transition. In GLM model GW diffractive mass is not defined. We presume (also without a proof) that GW and non GW (high mass diffraction) have the same upper bound, commonly taken to be 0.05s. Recall that, the main difference between the two diffractive modes is that GW is suppressed by eikonal screenings, while non GW is suppressed by the survival probability which has an s-chanel eikonal component initiated by the re-scattering of the initial projectiles, and a t-channel screening induced by the multi $\mathbb{P}$ interactions. In GLM most of the diffraction is GW, while in KMR it is non GW high mass.

Originally, GLM did not define a diffractive mass distribution. This has been amended in one of GLM recent papers, where we consider the Pomeron as a partonic probe. In this model $\mathbb{P}$-q interactions contribute to GW mass $\mathbb{P}$-g interactions contribute to non GW, high mass.

6 The partonic Pomeron

Current $\mathbb{P}$ models differ in details, but have in common a relatively large adjusted $\Delta_{\mathbb{P}}$ input, and a diminishing $\alpha'_{\mathbb{P}}$. Recall that, traditionally, $\Delta_{\mathbb{P}}$ determines the energy dependence of the total, elastic and diffractive cross sections, while $\alpha'_{\mathbb{P}}$ determines the forward slopes.

This picture is modified in updated $\mathbb{P}$ models in which s and t unitarity screenings induce a smaller $\mathbb{P}$ intercept at $t = 0$, which gets smaller with energy. The exceedingly small fitted $\alpha'_{\mathbb{P}}$ implies a partonic description of the IP which leads to a pQCD interpretation. Gribov's partonic Regge theory provides the microscopic sub structure of the IP, where the slope of the IP trajectory is related to the mean transverse momentum of the partonic dipoles constructing the Pomeron.

$$\alpha'_{\mathbb{P}} \propto 1/<p_t>^2, \qquad \text{accordingly:} \qquad \alpha_S \propto \pi/ln\left(<p_t^2>/\Lambda^2_{QCD}\right) << 1.$$

We obtain a IP with hardness changing continuesly from hard (BFKL like) to soft (Regge like). This is a non-trivial relation as the soft IP is a moving pole in J-plane, while, the BFKL hard IP is a branch cut, approximated, sometimes, as a simple pole with $\Delta_{\mathbb{P}} = 0.2 - 0.3$, $\alpha'_{\mathbb{P}} \simeq 0$.

GLM and KMR models are rooted in Gribov's partonic IP theory with a hard pQCD IP input. It is softened by unitarity screening (GLM), or the dependence of its partons' transverse momenta on their rapidity (KMR). The two definitions are correlated. GLM and KMR have a bound of validity, at 60(GLM) and 100(KMR) TeV, implied by their approximations. Consequently, as attractive as updated Pomeron models are, we can not utilize them above 100 TeV at the most. To this end, the only relevant models are single channeled, most of which have a logarithmic parametrization input such as $Aln(s) + Bln^2(s)$.

7 DIS: from SQFT to hard

The single IP picture, suggested by GLM and KMR models, implies a smooth transition from the input hard IP to a soft IP. In a different context, such a transition is supported by HERA dependence of $\lambda = \Delta_{\mathbb{P}}$ on Q^2 shown on figure 129.Note, though, that a smooth transition from a soft to hard IP can be reproduced also by a 2 IPs (soft and hard) model, such as Ostapchenko's.

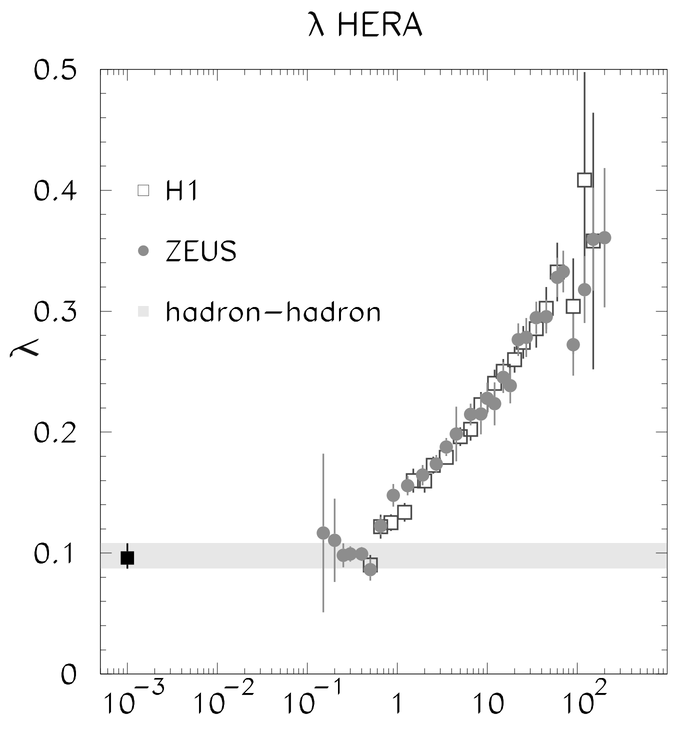

Figure 129: HERA dependence of $\lambda = \Delta_{\mathbb{P}}$ on Q^2.

8 Unitarity saturation

Unitarity saturation is coupled to 4 experimental signatures:

$$\frac{\sigma_{inel}}{\sigma_{tot}} = \frac{\sigma_{el}}{\sigma_{tot}} = 0.5, \ \frac{\sigma_{tot}}{B_{el}} = 9\pi, \qquad \text{and } \sigma_{diff}{=}0 \text{ in a multi-channel model.} \tag{336}$$

Following are p-p TeV-scale data, relevant to the assessment of saturation:

- CDF(1.8 TeV):

$$\sigma_{tot} = 80.03 \pm 2.24\,\text{mb}, \tag{337}$$
$$\sigma_{el} = 19.70 \pm 0.85\,\text{mb}, \tag{338}$$
$$B_{el} = 16.98 \pm 0.25\,\text{GeV}^{-2}. \tag{339}$$

- TOTEM(7 TeV):

$$\sigma_{tot} = 98.3 \pm 0.2(\text{stat}) \pm 2.8(\text{sys})\,\text{mb}, \tag{340}$$
$$\sigma_{el} = 24.8 \pm 0.2(\text{stat}) \pm 2.8(\text{sys})\,\text{mb}, \tag{341}$$
$$B_{el} = 20.1 \pm 0.2(\text{stat}) \pm 0.3(\text{sys})\,\text{GeV}^{-2}. \tag{342}$$

- ATLAS(7 TeV):

$$\sigma_{tot} = 95.4 \pm 1.4\,\text{mb}, \tag{343}$$
$$\sigma_{el} = 24.0 \pm 0.6\,\text{mb}. \tag{344}$$

- AUGER(57 TeV):

$$\sigma_{tot} = 133 \pm 13(\text{stat}) \pm^{17}_{20}(\text{sys}) \pm 16(\text{Glauber})\,\text{mb}, \tag{345}$$
$$\sigma_{inel} = 92 \pm 7(\text{stat}) \pm^{9}_{11}(\text{sys}) \pm 16(\text{Glauber})\,\text{mb}. \tag{346}$$

We get:

$$\frac{\sigma_{inel}}{\sigma_{tot}} = 0.754(\text{CDF}), \quad 0.748(\text{TOTEM}), \quad 0.748(\text{ATLAS}), \quad 0.692(\text{AUGER}). \tag{347}$$

The numbers above suggest a very slow approach toward saturation, well above the TeV-scale. Consequently, the study of *pp* saturation depends on information above the TeV-scale.

There are 2 sources from which we may obtain the desired information:

- Cosmic Rays data. Recall that $p - p$ cross sections obtained from p-Air data have relatively large margin of error. AUGER $p - p$ cross sections are a good example.
- Since updated $I\!P$ models are confined to the TeV-scale, $p - p$ cross sections at higher energies can be calculated only in single channeled models, the deficiencies of which have been stated before.

Out of a few single channeled nodels, I shall quote Block and Halzen (BH), which reproduce well the inelastic and total cross sections at the TeV-scale. The BH model can be applied at exceedingly high energies. BH prediction at the Planck-scale ($1.22{\cdot}10^{16}$ TeV) is:

$$\frac{\sigma_{inel}}{\sigma_{tot}} = \frac{1131\,\text{mb}}{2067\,\text{mb}} = 0.547. \tag{348}$$

It indicates that saturation will be attained, if at all, at non-realistic energies.

The predicted multi channel vanishing of the diffractive cross sections at saturation implies that σ_{sd}, which up to the TEVATRON grows slowly with energy, will eventually start to reduce. This may serve as an early signature that saturation is being approached. Specifically, the preliminary TOTEM measurement of:

$$\sigma_{sd} = 6.5 \pm 1.3\text{mb}, \qquad 3.4 < M_{sd} < 1100\,\text{GeV}, \qquad 2.4 \cdot 10^{-7} < \xi < 0.025 \tag{349}$$

suggests a radical change in the energy dependence of $\sigma_{sd}/\sigma_{inel}$ which is considerably smaller than its value at CDF.

$$\frac{\sigma_{sd}}{\sigma_{inel}} \;=\; 0.151(\text{CDF}), \quad 0.088(\text{TOTEM}). \tag{350}$$

This feature, if correct, is, presently, particular to diffraction. It suggests a much faster approach toward unitarity saturation than suggested by $\frac{\sigma_{inel}}{\sigma_{tot}}$. TOTEM diffractive data is preliminary, as the upper diffractive mass bound of 0.025s is half of the commonly used bound of 0.05s (including GLM). The GLM SD cross sections (in mb) are:

$$\sigma_{sd}(W) \;=\; \sigma_{sd}^{GW} \;+\; \sigma_{sd}^{nonGW} \;=\; 9.2 + 1.95(1.8),\, 10.7 + 4.18(7),\, 11.5 + 5.81(14). \tag{351}$$

ALICE 7 TeV diffractive cross sections: $\sigma_{sd} = 14.9 + 3.4 - 5.9\,\text{mb}$ and $\sigma_{dd} = 9.0 \pm 2.6\,\text{mb}$ are significantly different from TOTEM data.They are compatible with GLM based on 0.05s diffractive mass bound! Recall that, EL, SD and DD cross section values are obtained from a b^2 integration of the corresponding amplitude square.

The growth of σ_{sd}, as a function of W, is mainly a consequence of $a_{sd}(s,b)$ moving slowly toward higher b values. The net result is a continuation of SD moderate increase with energy. Consequently, I do not expect a suppression of σ_{sd} at an energy of 7 TeV. An explanation of an early reduction of the diffractive channels at relatively low energies, will require, thus, a fundamental change in our understanding of soft scattering at the TeV-scale.

Cristiano B. Mariotto
Victor Gonçalves

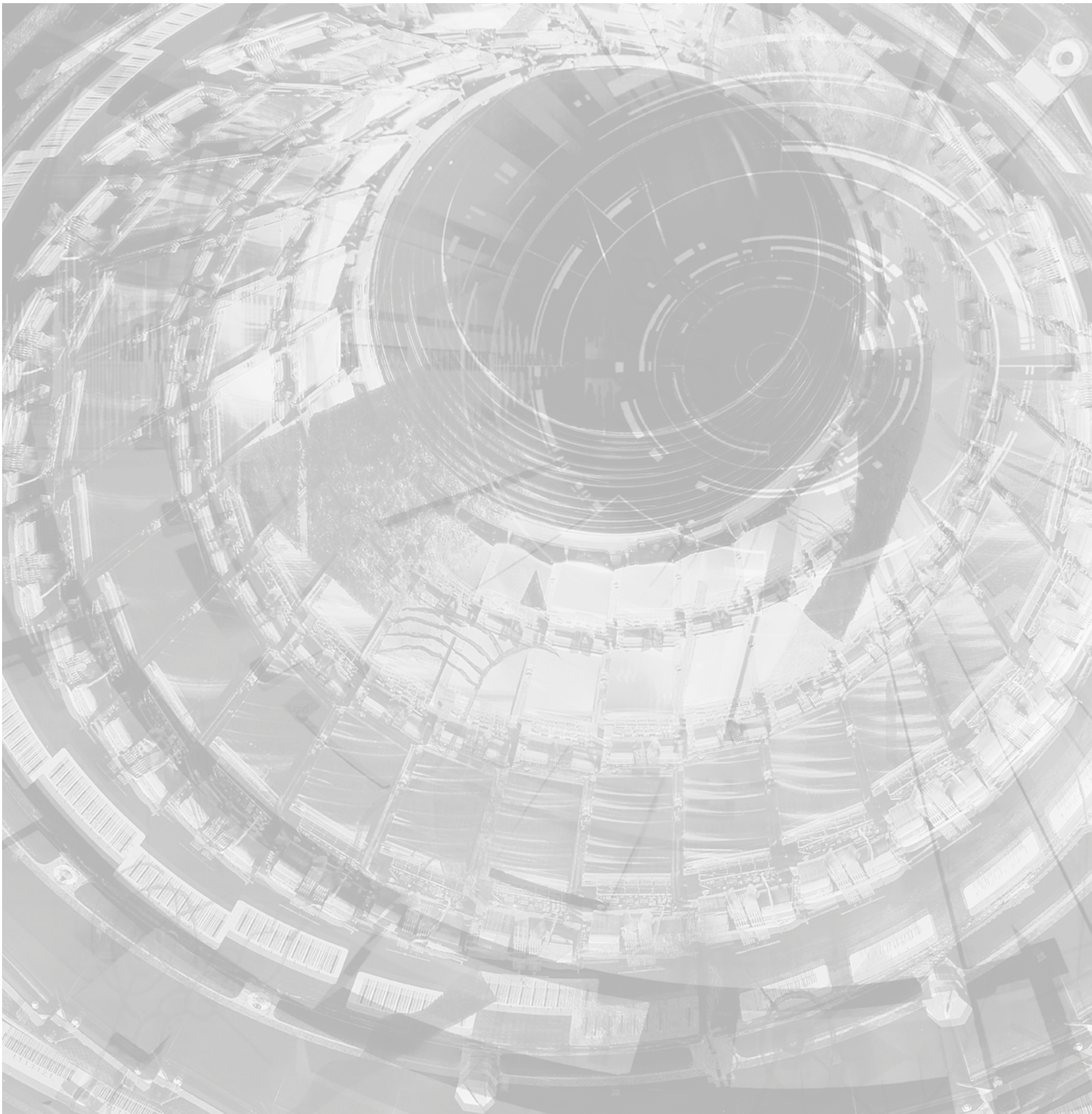

Double J/ψ production in diffractive processes at the LHC

C. Brenner Mariotto [u][31], V. P. Goncalves [v]

[u]Instituto de Matemática, Estatística e Física, Universidade Federal do Rio Grande, Rio Grande, Brazil

[v]High and Medium Energy Group, Instituto de Física e Matemática, Universidade Federal de Pelotas, Pelotas, Brazil

Abstract

In this work we calculate, using the Pomeron resolved model, the diffractive double J/ψ production in pp collisions at the LHC, considering double Pomeron exchange processes. Since the quarkonium production is dominated by gluon-gluon initiated subprocesses, this channel might be usefull to test the validity of this model for diffractive interactions. We obtain the rapidity and transverse momentum distributions and estimate the total cross section for the kinematic regions of the LHC experiments.

Quarkonium production at high energies probes the proton's gluon distribution due to dominance of subprocesses with two gluons in the initial state. On the other hand, diffractive processes involve the exchange of a Pomeron, an object with the vacuum quantum numbers, and lead to events with rapidity gaps in the hadronic final state. The nature of the Pomeron is a subject of intense debate in the literature. In the Resolved Pomeron Model [1] one assumes the validity of the diffractive factorization formalism and that the Pomeron has a partonic structure. In this contribution we study the central diffractive double J/ψ production as a complementary test of diffractive processes and the Pomeron structure [2].

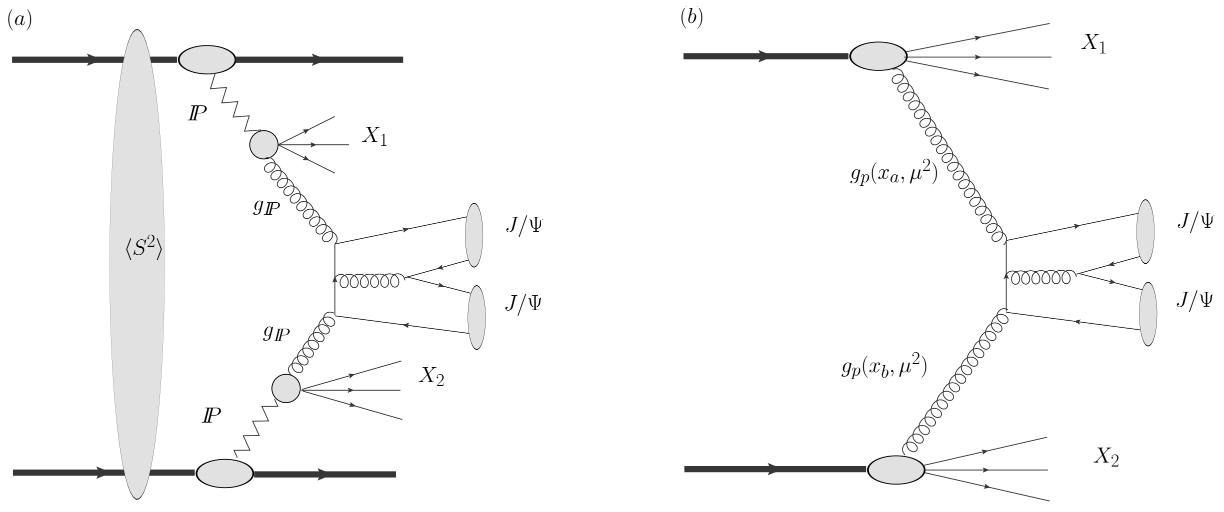

Figure 130: Typical diagrams for the double J/ψ production in (a) central diffractive and (b) inclusive processes.

[31]Corresponding author. See Table 2 for the complete list of talks given at the workshop.

At high energies the double quarkonium production is dominated by gluon-gluon interactions. In the central diffractive case, the hard process takes place in $I\!PI\!P$ interactions, and the contributing diagrams are the same as in the inclusive case, as ilustrated in Fig. 130. The differential cross section for double J/ψ production in central diffractive processes can be written as

$$\frac{d\sigma}{dydp_T^2} = \int_{x_{a\,min}} dx_a g^D(x_a,\mu^2) g^D(x_b,\mu^2) \frac{x_a x_b}{2x_a - \bar{x}_T e^y} \sum_{i=1,8} \frac{d\hat{\sigma}^{gg\to 2c\bar{c}_i(^3S_1)}}{d\hat{t}} \cdot \langle \mathcal{O}_i^{J/\psi}(^3S_1)\rangle^2 \cdot \langle S^2\rangle \,, \quad (352)$$

where $x_{a\,min} = \frac{\bar{x}_T e^y}{2-\bar{x}_T e^{-y}}$, $x_b = \frac{x_a \bar{x}_T e^{-y}}{2x_a - \bar{x}_T e^y}$, $\bar{x}_T = \frac{2m_T}{\sqrt{s}}$ and $m_T = \sqrt{M^2+p_T^2}$. Here M is the J/ψ mass, p_T its transverse momentum, y its rapidity, and $\mu = m_T$ is the hard scale. Also, $\frac{d\hat{\sigma}}{d\hat{t}}$ in Eq. (352) are the hard scattering differential cross sections, given by leading order (LO) α_s^4 expressions. The contributing diagrams include those associated to the nonfragmentation contribution, with the leading contribution being the color singlet $(c\bar{c})_1(^3S_1) + (c\bar{c})_1(^3S_1)$ channel, and diagrams associated to the gluon fragmentation contribution, associated to the color octet $(c\bar{c})_8(^3S_1) + (c\bar{c})_8(^3S_1)$ channel. For the gluon-initiated color singlet contributions, one has [3]

$$\frac{d\hat{\sigma}^{gg\to 2c\bar{c}_1(^3S_1)}}{d\hat{t}} \langle O_1^{J/\psi}(^3S_1)\rangle^2 = \frac{16\pi\alpha_s^4 |R(0)|^4}{81 M^2 s^8 (M^2-t)^4 (M^2-u)^4} \sum_{jkl} a_{jkl} M^j t^k u^l \quad (353)$$

where, as in the Ref. [3], $|R(0)|^2 = 0.8$ GeV^3 is the squared radial function at the origin, s, t, u are the usual Mandelstam variables, $M = 2m_c$, and $m_c = 1.5$ GeV (see Ref. [3] for the detailed expressions for the a_{jkl} coefficients). For the color octet contributions, the differential cross section for the gluon initiated partonic subprocesses can be written as [4]

$$\frac{d\hat{\sigma}^{gg\to 2c\bar{c}_8(^3S_1)}}{d\hat{t}} = \frac{\pi\alpha_s^4}{972 M^6 s^8 (M^2-t)^4 (M^2-u)^4} \sum_{j=0}^{14} a_j M^{2j} \,, \quad (354)$$

where the a_j coefficients can be found in Ref. [4], and $\langle O_8^{J/\psi}(^3S_1)\rangle = 3.9\times 10^{-3} GeV^3$ is the only relevant NRQCD matrix element, taken from [5].

Also, $g^D(x_i,\mu^2)$ are the diffractive gluon distribution functions from the two colliding protons. In the present work, they are taken from the Resolved Pomeron Model [1], being defined as a convolution of the Pomeron flux emitted by the proton, $f_{I\!P}(x_{I\!P})$, and the gluon distribution in the Pomeron, $g_{I\!P}(\beta,\mu^2)$, where β is the momentum fraction carried by the partons inside the Pomeron. The Pomeron flux is given by $f_{I\!P}(x_{I\!P}) = \int_{t_{min}}^{t_{max}} dt f_{I\!P/p}(x_{I\!P},t)$, where $f_{I\!P/p}(x_{I\!P},t) = A_{I\!P}\cdot \frac{e^{B_{I\!P}t}}{x_{I\!P}^{2\alpha_{I\!P}(t)-1}}$ and t_{min}, t_{max} are kinematic boundaries. The Pomeron flux factor is motivated by Regge theory, where the Pomeron trajectory is assumed to be linear, $\alpha_{I\!P}(t) = \alpha_{I\!P}(0) + \alpha'_{I\!P} t$, and the parameters $B_{I\!P}$, $\alpha'_{I\!P}$ and their uncertainties are obtained from fits to H1 data [6]. The diffractive gluon distribution is then given by $g^D(x,\mu^2) = \int_x^1 \frac{dx_{I\!P}}{x_{I\!P}} f_{I\!P}(x_{I\!P}) g_{I\!P}\left(\frac{x}{x_{I\!P}},\mu^2\right)$. In our analysis we use the diffractive gluon distribution obtained by the H1 Collaboration at DESY-HERA [6]. Finally, one important ingredient to obtain realistic predictions for the double J/Ψ production in central diffractive processes is the gap survival probability, $\langle \mathcal{S}^2\rangle$, which accounts for the probability that secondaries produced by soft rescatterings do not populate the rapidity gaps. Here we assume that $\langle \mathcal{S}^2\rangle = 2\,\%$ for proton-proton collisions at LHC energies [7]. However, the magnitude of $\langle \mathcal{S}^2\rangle$ is still a theme of intense debate (See, e.g., Ref. [8]).

In Fig. 131 we present our results for the transverse momentum distribution for double J/Ψ production at midrapidities ($|y| \leq 2.5$) in central diffractive processes for LHC energies. For the sake of comparison, we also show the results for the inclusive case, obtained using the CTEQ6L parametrization [9] for the gluon distribution in the proton, which agree with the predictions presented in Ref. [4].

The central diffractive predictions at small p_T are a factor $\approx 10^3$ smaller than in the inclusive one. We obtain that the p_T distributions in the low p_T region are dominated by the color singlet contributions. Moreover, as in the inclusive case [4], the distribution vanishes at $p_T = 0$ and increases rapidly until it reaches a maximum at $p_T \approx 1.5$ GeV. Then it decreases monotonically as p_T increases. We obtain that the color singlet contributions are dominant except at large p_T. The cross-over, beyond that the color octet contributions start to be dominant, occurs at $p_T \approx 15$ GeV. Furthermore, in the dominant low-p_T peak, the color octet contribution is four orders of magnitude less important than the color singlet one.

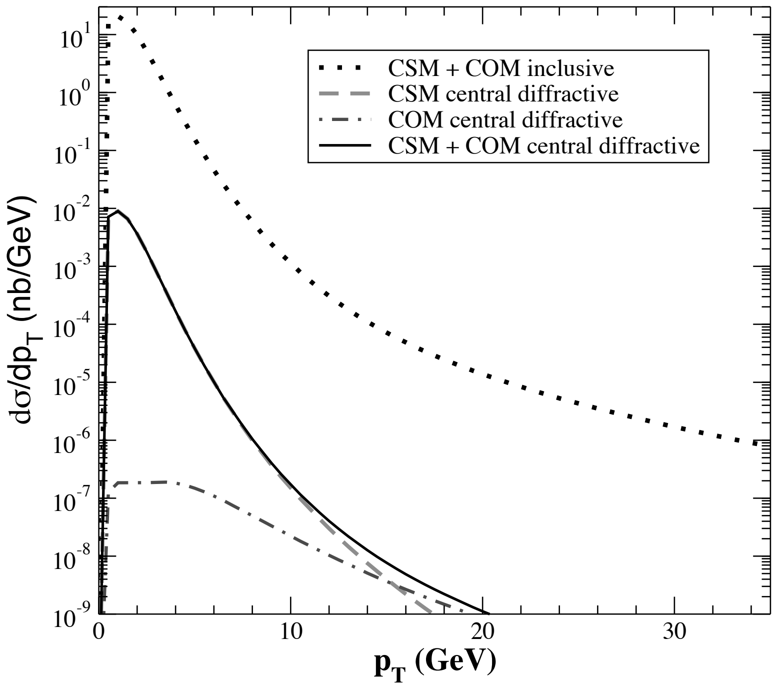

Figure 131: Transverse momentum distributions for double J/ψ production in central diffractive processes at 14 TeV. The prediction for the inclusive production is presented for comparison.

In Fig. 132 we present our results for the rapidity distribution for double J/ψ production in central diffractive processes at $\sqrt{s} = 8$ and 14 TeV. The inclusive predictions are also presented for comparison. We have verified that the color singlet contributions dominate all regions for the p_T-integrated spectra, and the color octet one are negligible in all rapidity regions. Moreover, we have a reduction of four orders of magnitude when going from the inclusive to the central diffractive case. In Table 30 we present our predictions for the total cross section considering the production at midrapidities ($|y| \leq 2.5$), which can be analyzed by CMS, ATLAS and ALICE Collaborations, and for the kinematical range probed by the LHCb Collaboration ($2 \leq y \leq 4.5$). For comparison we show the predictions for the inclusive production and for the double J/Ψ production in central exclusive processes (CEP) obtained in Ref. [10] using the CTEQ6L parton distribution functions. We obtain that our predictions for the central diffractive production are similar to those for the central exclusive production obtained in Ref. [10]. Of course, the topology of the final state of these two processes is different. While in central exclusive processes one has only the leading hadrons, two J/ψ's and nothing else, in the central diffractive case one expect to have some extra particles coming from the Pomeron remnants. However, it is not obvious that the double diffractive and the central exclusive mechanisms could be differentiated experimentally at the LHC.

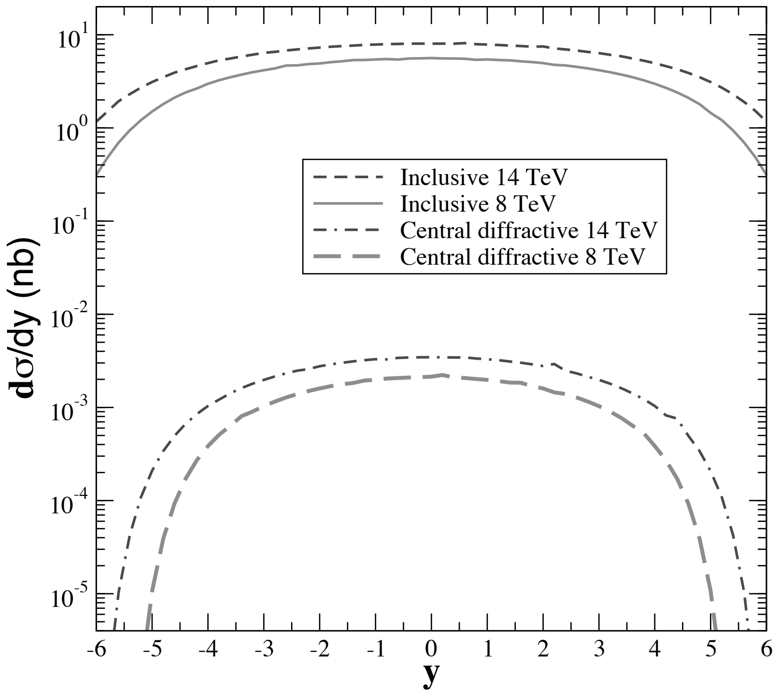

Figure 132: Rapidity distributions for double J/ψ production in inclusive and central diffractive processes in pp collisions at $\sqrt{s} = 8$ and 14 TeV.

CM energy	Rapidity range	Inclusive	Central Diffractive	CEP
8 TeV	$\|y\| < 2.5$	27203 pb	9.51 pb	10 pb
8 TeV	$2 < y < 4.5$	9709 pb	2.16 pb	2.5 pb
14 TeV	$\|y\| < 2.5$	39690 pb	16.02 pb	17 pb
14 TeV	$2 < y < 4.5$	15220 pb	4.43 pb	4.7 pb

Table 30: Total cross sections for double J/ψ production for different energies and rapidity cuts. Also shown the predictions from Ref. [10] for the central exclusive production (CEP).

References

1. G. Ingelman and P. E. Schlein, Phys. Lett. B **152**, 256 (1985).
2. C. Brenner Mariotto and V. P. Goncalves, Phys. Rev. D **91**(11), 114002 (2015) [arXiv:1502.02612 [hep-ph]].
3. C. F. Qiao, Phys. Rev. D **66**, 057504 (2002) [hep-ph/0206093 [hep-ph]].
4. P. Ko, C. Yu and J. Lee, JHEP **1101**, 070 (2011) [arXiv:1007.3095 [hep-ph]].
5. E. Braaten, B. A. Kniehl and J. Lee, Phys. Rev. D **62**, 094005 (2000) [hep-ph/9911436 [hep-ph]].
6. A. Aktas *et al.* [H1 Collaboration], Eur. Phys. J. C **48**, 715 (2006) [hep-ex/0606004 [hep-ex]].
7. V. A. Khoze, A. D. Martin and M. G. Ryskin, Eur. Phys. J. C **18**, 167 (2000) [hep-ph/0007359 [hep-ph]].
8. E. Gotsman, E. Levin and U. Maor, Eur. Phys. J. C **71**, 1685 (2011) [arXiv:1101.5816 [hep-ph]].
9. J. Pumplin, D. R. Stump, J. Huston, H. L. Lai, P. M. Nadolsky and W. K. Tung, JHEP **0207**, 012 (2002) [hep-ph/0201195 [hep-ph]].
10. L. A. Harland-Lang, V. A. Khoze and M. G. Ryskin, J. Phys. G **42**(5), 055001 (2015)

[arXiv:1409.4785 [hep-ph]].

Gilberto Ramalho

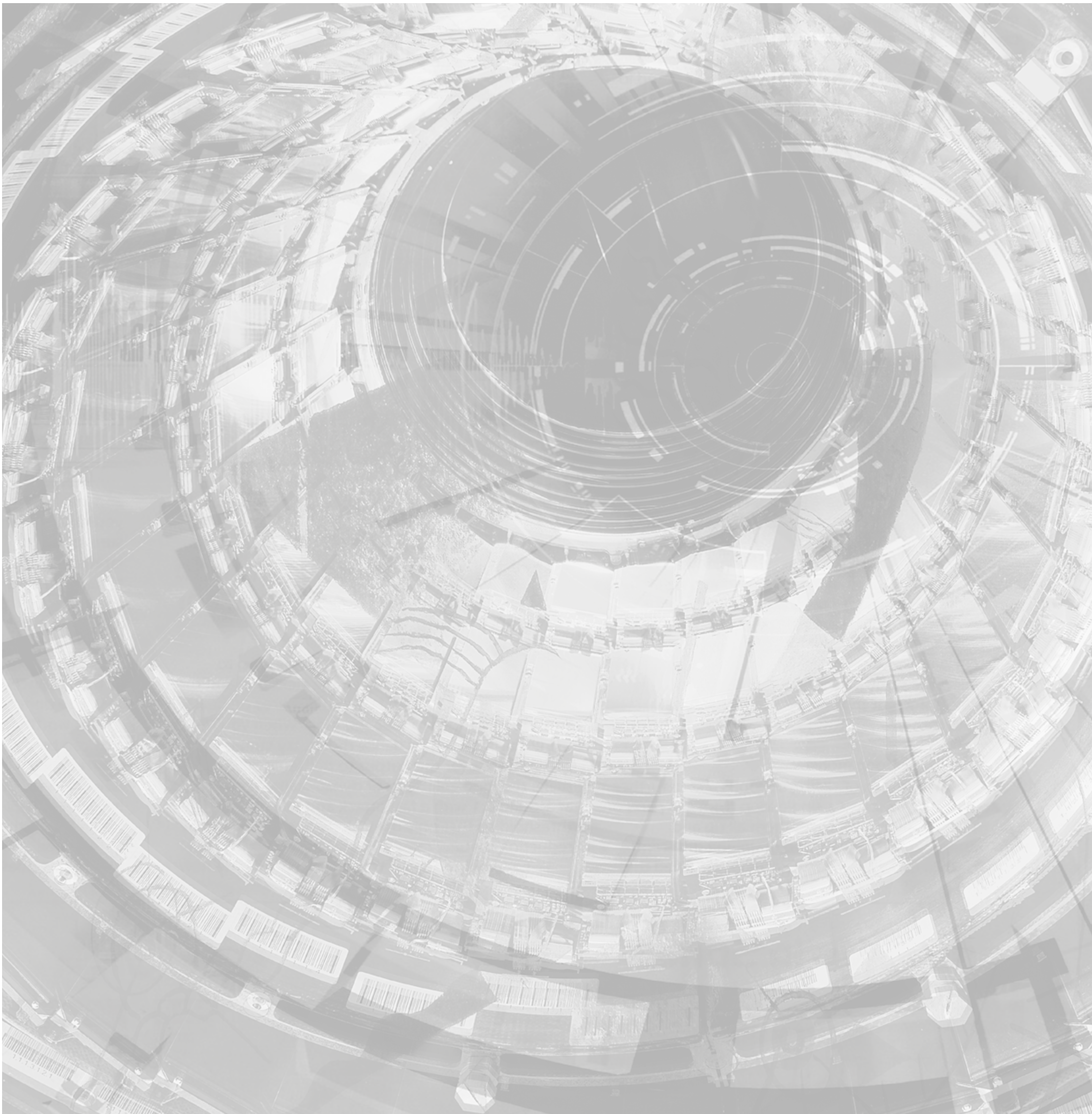

A covariant model for the nucleon spin structure

G. Ramalho [c]

[c]The International Institute of Physics, UFRN, Natal, Brazil

Abstract

We present the results of the covariant spectator quark model applied to the nucleon structure function $f(x)$ measured in unpolarized deep inelastic scattering, and the structure functions $g_1(x)$ and $g_2(x)$ measured in deep inelastic scattering using polarized beams and targets (x is the Bjorken scaling variable). The nucleon is modeled by a valence quark-diquark structure with S, P and D components. The shape of the wave functions and the relative strength of each component are fixed by making fits to the deep inelastic scattering data for the structure functions $f(x)$ and $g_1(x)$. The model is then used to make predictions on the function $g_2(x)$ for the proton and neutron.

The covariant spectator quark model (CSQM) is a model in which the electromagnetic structure of the constituent quark is parametrized by Dirac (f_{1q}) and Pauli (f_{2q}) form factors for the quarks ($q = u, d$) [1, 2]. The quark electromagnetic form factors f_{1q}, f_{2q} simulate the effects associated with the gluons and the quark-antiquark pairs. The CSQM was developed within the covariant spectator theory [3] and was first applied to the nucleon using a S-state approximation to the quark-diquark system [1]. The quark form factors and the radial wave functions are fitted to the nucleon electromagnetic form factor data. It was concluded that the falloff of the ratio between the magnetic and electric observed for the first time at Jefferson Lab can be explained by a model based on quarks with no orbital momentum, if the quarks have an internal structure [1]. The model was later extended to several nucleon resonances and other baryons [2, 4–8].

The next step on this, it is to check if CSQM can be extended to the deep inelastic scattering (DIS) regime, and if a qualitative description of the DIS phenomenology can be achieved. In the deep inelastic scattering the photon transfer momentum squared, Q^2, and the photon energy in the lab frame, ν, are both very large but the ratio $x = \frac{Q^2}{2M\nu}$ is kept finite (M is the nucleon mass). If the CSQM is in fact compatible with DIS, the DIS data can be used to discriminate the individual contributions of the orbital angular momentum states in the nucleon wave function and also used to estimate the shape of those components.

The nucleon structure in DIS is parametrized in terms of the unpolarized structure functions $f_q(x) = q(x)$ and the polarized structure functions $g_1^q(x) = \Delta q(x)$ and $g_2^q(x)$. The unpolarized structure functions determine the quark contributions to the nucleon momentum, but explain only about 50% of the total amount ($\int dx(2xf_u + xf_d) \approx 0.5$). The remaining 50% are due to the gluons. The functions Δq measures the contributions to the quark orbital momentum for the proton spin. It is known since the 80s, from the EMC experiments at CERN [9], that the contribution of the orbital momentum of the quarks to the proton spin is only about 30% [9, 10]. That conclusion was obtained from the result of the first moment of the function $g_1(x)$ for the proton [11, 12]

$$\Gamma_1^p = \int_0^1 dx\, g_{1p}^{\exp}(x) = 0.128 \pm 0.013. \tag{355}$$

Theoretical calculations based on the naive assumption that the nucleon is made of quarks with no orbital angular momentum (pure relative S-state) give larger values. In our S-state model for the nucleon, $\Gamma_1^p = 0.278$ [13].

Since a nucleon wave function (Ψ_N) dominated by the S-state [1, 12] overestimates the quark contributions to the proton spin, we now consider a wave function that include also P and D-states [13]

$$\Psi_N = n_S \Psi_S + n_P \Psi_P + n_D \Psi_D, \tag{356}$$

where n_S, n_P and n_D are the coefficients of the states ($n_S^2 + n_P^2 + n_D^2 = 1$). All the components of the wave function are represented in terms of an off-shell quark and two on-shell quarks (quark pair). We can integrate in the internal degrees of freedom of the quark pair and represent the wave function in terms of the a quark and a diquark structure dependent on the nucleon (P) and the diquark (k) momenta [13]. Since in the DIS limit the quarks are pointlike the adjustable part of the model is restricted to the radial wave functions of the states S, P and D. To increase the flexibility of the model we also consider different distributions (radial wave functions ψ_q^S) for the quarks u and d. This asymmetry is supported by the data [12, 13].

From the calculation of the hadronic tensor, in which we integrate on the quark and diquark on-shell momenta, we derive the expressions for the DIS structure functions. In particular the expression for the unpolarized structure function associated with the S-state can be written as

$$f_q^S(x) = \frac{M^2}{16\pi^2} \int_\xi^{+\infty} d\chi |\psi_q^S(\chi)|^2, \qquad \frac{df_q^S}{dx} = -\frac{x(2-x)}{(1-x)^2} \frac{M^2}{16\pi^2} |\psi_q^S(\chi)|^2, \tag{357}$$

where $\xi = \frac{x^2}{1-x}$ is a function of the Bjorken variable x, and χ is a covariant variable of the nucleon and diquark momenta. Similar expressions can be written for the P and D components.

Equations (357) can be used to conclude that the radial wave functions ($L = S, P, D$) can be represented in the form

$$\psi_q^L(\chi) \propto \frac{\alpha + \beta}{\chi^{n_0} (\beta + \chi)^{n_1 - n_0}}, \tag{358}$$

where α is a constant, β is a dimensionless parameter and n_0, n_1 are indices that can be related to the values a_q, b_q from the parametrizations $x f_q(x) \propto x^{a_q} (1-x)^{b_q}$.

To confirm if the CSQM is consistent with the DIS regime, we try to adjust the parameters of our model to the DIS phenomenology. Since the experimental data is in some cases obtained for very small Q^2 (while in the DIS limit Q^2 is very large) we choose to fit our model to the well known parametrizations of the data: Martin, Roberts, Stirling and Thorn (2002) – **MRST(02)** (unpolarized structure functions) [14] and Leader, Siderov and Stamenov (2010)– **LSS(10)** (polarized structure functions) [15]. We consider the parametrizations for the scale $Q^2 = 1$ GeV^2. We divide the fitting process into 3 steps:

- first we estimate the parameters of the radial wave functions ψ_q^L by a fit to the unpolarized data, f_u and f_d, assuming that all components S, P, D have the same shape [see Eq. (358)],
- based on the first estimate of the radial wave functions we calculate the mixture coefficients n_P and n_D by making a fit to the first moment of the function g_1^q: $\Gamma_1^u = 0.333 \pm 0.039$, and $\Gamma_1^d = -0.335 \pm 0.080$ [12, 14],
- finally the parameters of the radial wave functions: α, β are adjusted independently to the polarized data for Δu and Δd.

The results of the fit for the functions q and Δq are presented in the Fig. 133, and are compared with the parametrizations MRST(02) and LSS(10).

Once all the parameters are fixed by the q and Δq data, we use the model to predict the function $g_2(x)$ for the proton and the neutron. The results are presented in Fig. 134 by the solid line.

From the previous study we conclude that CSQM be used in the nucleon DIS regime, in addition to the electromagnetic excitations of the baryons. The results presented here are derived under the assumption that the valence quarks are the relevant degrees of freedom in DIS and that the gluon and meson cloud (sea quarks) effects can be neglected in a first approximation.

In our study the nucleon has contributions of several angular momentum states ($L = S, P, D$) and the DIS data are used to probe the shape of the components of the nucleon wave function.

The results of our best model are consistent with the experimental data obtained for the unpolarized $f_q(x)$ and polarized $g_1^q(x)$ structure functions, which are also compatible with a zero contribution of the gluons for the proton spin ($J_g = 0$).

Finally we present predictions for the spin dependent structure function $g_2(x)$ of the nucleon. The predictions are consistent with the available data (see Fig. 134) and can be tested in future by more accurate data.

Since the gluon degrees of freedom are not included explicitly, although some effects are effectively considered in the structure of the radial wave functions, we cannot make direct predictions for very large Q^2. We can however use the QCD evolution equations (DGLAP) [16] to extrapolate the results to very large Q^2, dominated by the gluon effects, using the results of our model for the valence quark structure at $Q^2 = 1$ GeV^2.

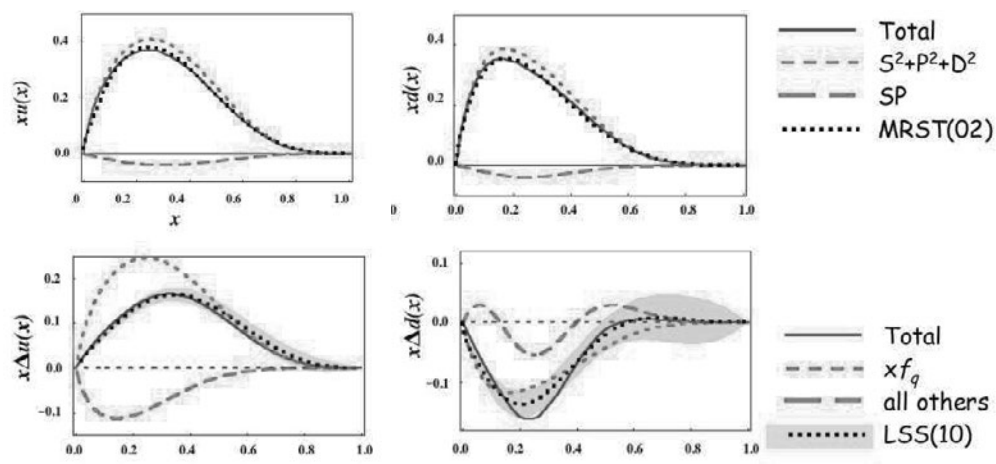

Figure 133: Results for the unpolarized $q(x)$ and polarized $\Delta q(x)$ structure functions (Total) compared with theparametrizations MRST(02) and LSS(10) [14, 15]. The P- and D- state mixtures are respectively 1% and 35% [12].

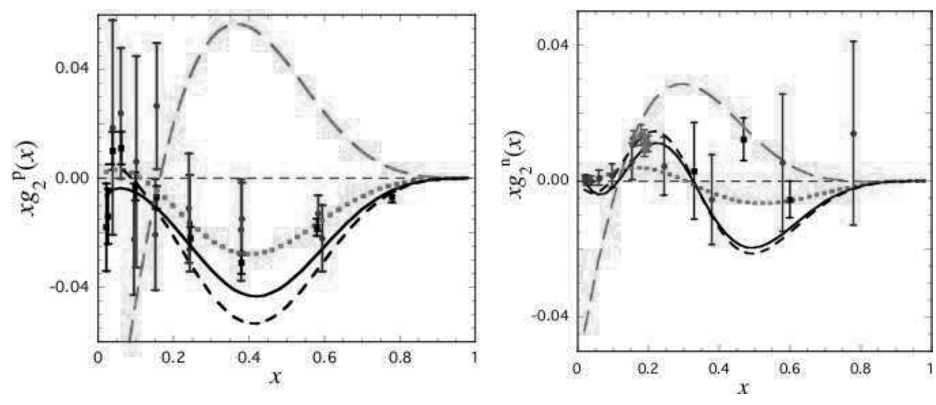

Figure 134: Predictions of the function $g_2(x)$ for the proton and neutron (solid line) [12].

The author's research was supported by the Brazilian Ministry of Science, Technology and Innovation (MCTI-Brazil).

References

1. F. Gross, G. Ramalho and M. T. Peña, Phys. Rev. C **77**, 015202 (2008) [nucl-th/0606029 [nucl-th]].
2. G. Ramalho, K. Tsushima and F. Gross, Phys. Rev. D **80**, 033004 (2009) [arXiv:0907.1060 [hep-ph]].
3. F. Gross, Phys. Rev. **186**, 1448 (1969).
4. I. G. Aznauryan *et al.*, Int. J. Mod. Phys. E **22**, 1330015 (2013) [arXiv:1212.4891 [nucl-th]].
5. G. Ramalho, Phys. Rev. D **90**, 033010 (2014) [arXiv:1407.0649 [hep-ph]].
6. G. Ramalho, M. T. Peña and F. Gross, Phys. Rev. D **78**, 114017 (2008) [arXiv:0810.4126 [hep-ph]];
7. G. Ramalho and K. Tsushima, Phys. Rev. D **81**, 074020 (2010) [arXiv:1002.3386 [hep-ph]]; G. Ramalho and K. Tsushima, Phys. Rev. D **84**, 051301 (2011) [arXiv:1105.2484 [hep-ph]].
8. G. Ramalho and K. Tsushima, Phys. Rev. D **84**, 054014 (2011) [arXiv:1107.1791 [hep-ph]].
9. J. Ashman *et al.* [European Muon Collaboration], Phys. Lett. **B206**, 364 (1988).
10. A. Airapetian *et al.* [HERMES Collaboration], Phys. Rev. D **75**, 012007 (2007) [hep-ex/0609039 [hep-ex]].
11. S. E. Kuhn, J.-P. Chen and E. Leader, Prog. Part. Nucl. Phys. **63**, 1 (2009) [arXiv:0812.3535 [hep-ph]].
12. F. Gross, G. Ramalho and M. T. Peña, Phys. Rev. D **85**, 093006 (2012) [arXiv:1201.6337 [hep-ph]].
13. F. Gross, G. Ramalho and M. T. Peña, Phys. Rev. D **85**, 093005 (2012) [arXiv:1201.6336 [hep-ph]].
14. A. D. Martin, R. G. Roberts, W. J. Stirling and R. S. Thorne, Phys. Lett. B **531**, 216 (2002) [hep-ph/0201127 [hep-ph]].
15. E. Leader, A. V. Sidorov and D. B. Stamenov, Phys. Rev. D **82**, 114018 (2010) [arXiv:1010.0574 [hep-ph]].
16. G. Altarelli and G. Parisi, Nucl. Phys. B **126**, 298 (1977); Y. L. Dokshitzer, Sov. Phys. JETP **46**, 641 (1977) [Zh. Eksp. Teor. Fiz. **73**, 1216 (1977)]. V. N. Gribov and L. N. Lipatov, Sov. J. Nucl. Phys. **15**, 438 (1972) [Yad. Fiz. **15**, 781 (1972)].

Murilo Rangel

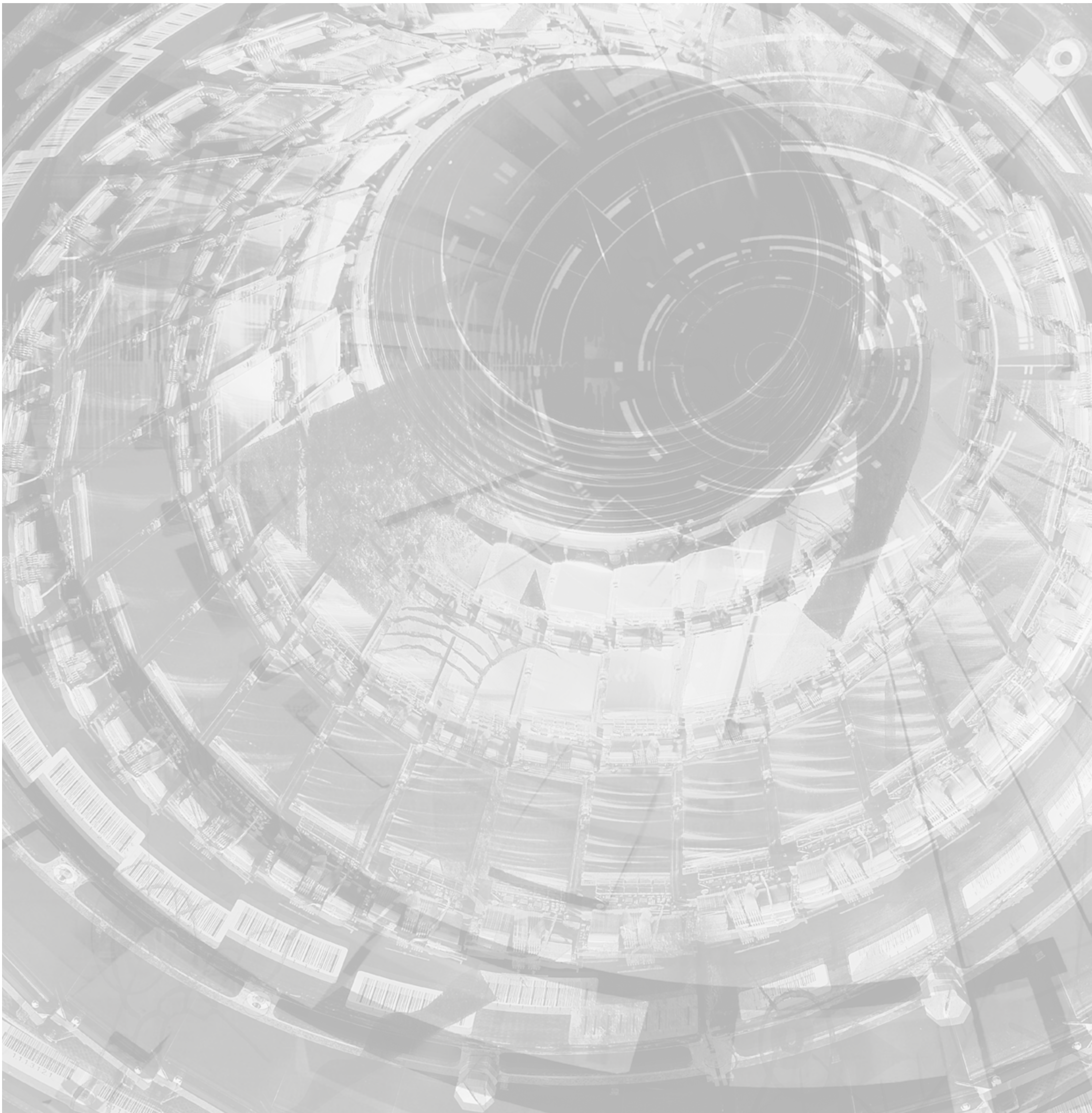

Experimental aspects of jet physics at LHC

Murilo Rangel [w]

[w]Universidade Federal do Rio de Janeiro, Rio de Janeiro, Brazil

Abstract

Jet physics provides a powerful tool to investigate interaction properties of quarks and gluons. These studies have been possible at an energy never investigated before at LHC. In this proceedings we review the main characteristics of experimental methods to measure jets in proton–proton collisions at center-of-mass energies of 7 and 8 TeV. Novel methods are expected to play an important role for searching new physics at center-of-mass energy of 13 TeV.

1 Introduction

Jets are the signatures of quarks and gluons produced in high-energy collisions such as the proton-proton interactions at the Large Hadron Collider (LHC). The understanding of the jet properties are key ingredients of several physics measurements and for New Physics searches. The study of jets have been used to test perturbative QCD (pQCD), to probe proton structure and to search for New Physics.

This paper is a summary of two lectures given in the school *New Trends in High-Energy Physics and QCD*. The slides can be found in this link. Deliberately no figure is used here and the focus will be on the main ingredients of performing jet phyics at LHC and novel techniques introduced in RunI.

This paper is organized as follows. The general aspects of experimental inputs for jet reconstruction are described in Sec. 2. Section 3 introduces the jet reconstruction. Jet energy measurement is discussed in section 4. Novel jet physics methods studied at LHC RunI are presented in section 5. A summary is found in section 6.

2 Particles from detector

The first step of any jet analysis is the particles to be used in the jet reconstruction algorithm. Two main approaches are used by LHC experiments: calorimeter measurements and particle flow candidates. Calorimeter (CALO) jets are reconstructed from energy deposits in the calorimeter clusters while particle flow (PF) jets are reconstructed from from particles identified from different sub-detectors. The main differences from these approaches will be discussed below.

The four main detectors at LHC are capable of measuring energy and hits of emerging particles of the high-energy collision with proper time bigger than 10^{-8} s. Detailed information of the ALICE, ATLAS, CMS and LHCb detectors can be found elsewhere [1–4]. From these measurements, particle momentum and identification can be inferred with good precision. With a certain level of generalisation, we can say five types of particles are identified: photons, electrons, muons, charged hadrons and neutral hadrons. In the PF algorithm, particle identification is the main feature to provide information of the jet characteristics.

Muons are the easiest particles to identify in high-energy physics detectors. Since they are heavy and do not interact via quantum chromodynamics, they traverse all the sub-detectors and produce hits in the so-called muon stations.

Photons are identified as clustes in the eletromagnetic calorimeter with void of hits in the track sub-detectors. The electrons produce similar showers in the eletromagnetic calorimeter, but a reconstructed track is used as main discrimination from photon showers. To reduce interaction of hadrons in the eletromagnetic calorimeter, low density with high-Z material is used as absorber. In more complex algorithms, photon convertion in the track sub-detectors is also considered.

Neutral and charged hadrons are reconstructed in the hadronic calorimeter where low nuclear interaction length is used as absorber. When a track extrapolated to the hadronic calorimeter matches with a cluster, the track is taken as charged hadron. Energy in the hadron calorimeter that is matched with a track is not used since the track momentum resolution is better than calorimeter energy resolution. In more detailed algorithms, V0's decays are identified from displaced vertices and $\pi^0 \to \gamma\,\gamma$ are selected using the eletromagnetic calorimeter.

Jets reconstructed from PF-particles have usually better energy resolution and smaller calibration factors, but they have properties harder to model due to the heterogeneity of the inputs. CALO-jets have in general well understood modeling and their energy resolution and scale are improved with indirect information from other sub-detectors, e.g., calorimeter is calibrated using tracks.

Reconstruction of jets using stable particles produced by a given event generator is used to calibrate jets reconstructed from detector inputs. Jet physics observables can only have a meaning if detector-level jets are calibrated. Discussion on jet calibration is presented in section 4.

3 Jet reconstruction

LHC experiments use in general reconstruction algorithms implemented in the FastJet package [5]. The most widely used algorithms are the anti-k_T [6], k_T [7–9] and the Cambridge-Aachen (C/A) algorithm [10, 11]. The k_T and C/A algorithms provides spatial and kinematic information about the substructure of jets, since they carry the clustering history. The anti-k_T algorithm define jets using successive recombinations providing almost no information about the $p_T$ordering of the shower. Therefore, the k_T and C/A algorithms are usually used for jet substructure studies, while anti-k_T is used to study single-parton jet physics.

The jet algorithms do not reject jets originating from detector noise, pile-up particles, high-$p_T$leptons, hadronic τ decays and cosmic rays. Criteria to reject fake and noise jets are used called jet identification (JetID). Background jets rate are reduced to $\mathcal{O}(1\,\%)$ by using jet properties, e.g., charged energy fraction (see studies performed by CMS as example [12]).

Many interesting physics processes at LHC have bottom or charm quark production, e.g., Higgs and top quark decays. Therefore, identifying jets originating from bottom or charm quarks becomes a very important task. Fragmentation of bottom and charm quarks produces hadrons with relatively large masses, long lifetimes and high-$p_T$charged particles. Besides good track momentum resolution, the detector needs to have precise reconstruction of the secondary vertex of $\mathcal{O}$ (30 μm). These aspects are explored in various algorithms that have about 50 % tagging efficiency for 1 % fake rate. ALICE, ATLAS, CMS and LHCb have documented their studies of bottom and charm quark jet identification in ref. [13–16].

Discrimination between light quark- and gluon-initiated jets can be very helpful when searching for new processes with many light quarks [17, 18]. Since the color factor of the gluon is 3 and for light quarks (u, d and s) is 4/3, it is expected that the number of particles produced in gluon-initiated jets is 9/4 times than in light quark initiated jets. The width of gluon-initiated jets are also expected to be larger than light quark-initiated jets. In general, these jet characteristics are explored in multivariate discriminant that provide 60 % efficiency for a fake rate of 30 %.

4 Jet energy measurement

The jet energy clustered from the reconstructed particles differs from the corresponding true jet energy clustered from the stable particles before interacting with the detector. Huge part of effort of understanding jets is the jet energy calibration, i.e., correct the detector-level jet to the particle-level jet. In other words, the jet energy measurement becomes independent of the detector. Since jets are a collection of particles or calorimeter clusters, jet energy calibration is a very difficult task (see ref. [19, 20]).

In general, the calibration is factorized in different factors: offset, relative and absolute. In some cases, the jet direction is also corrected for which can be up $\mathcal{O}(1\,\%)$ correction. Dedicated jet energy calibration (JEC) can also be derived for different parton where the jet originates from.

The offset correction is usually derived in data-driven studies and treated as a linear correction with the number of vertices reconstructed in the event. This assumption works well for CALO-jets, but PF-jets need to use more sophisticated methods, e.g., jet area [21]. The main goal of this factor is to subtract the energy not associated with the high-p_{T}scattering. Most of the energy excess originates from pile-up or out-of-time events. This factor becomes extreme important at high luminosity conditions.

The relative factor explores the best region of the detector for jet reconstruction. The goal is to calibrate regions of the detector with poor resolution with respect to the best understood region. One of the main advantages of this procedure is that no simulation is needed. The most used technique is the dijet p_{T}-balance. Due the high cross-section and the two jet well balanced in p_{T}, the dijet production provides an unique sample to measure the relative response of jet energy measurement.

The absolute correction factor aims the calibration of the jet energy to the true jet, i.e., the energy that would have been measured by a perfect detector. This factor is in general derived in simulation and residual corrections are estimated with data. Two event samples are usually used to compare data with simulation: γ +jets and Z +jets. The method is based on the correlation between the jet $p_{\mathrm{T}}$and the γ or Z p_{T}. While the γ +jets sample provides much more statistics, the size of backgrounds is also larger. Besides the background contamination and event sample size differences, γ and Z have also different energy resolutions. Compromise of background, size sample and resolution of the reference object needs to be studied.

Dedicated calibration for jets originating from bottom quarks can also be derived using Z +b-jets, top quark or $Z \to b\bar{b}$ decays (for example, see ref. [22]). Differences between different parton-initiated jets can be up to 2 %. Most of experiments include this effect in the JEC error.

After calibrating the jet energy, precise knowledge of its resolution is crucial for jet physics. In differential cross-section measurements, the jet energy measurement needs to be unfolded to the true jet energy, and the main impact of the unfolding procedure is the jet energy resolution (JER). Other analyses need good understanding of the differences between data and simulation, e.g., Higgs decaying to $b\bar{b}$. JER can studied with dijet, γ +jets and Z +jets samples (see refs. [19, 23]). In the case of dijet events, the impact of the final state radiation in the dijet p_{T}asymmetry must be done by using different p_{T}thresholds for the third jet. The extrapolation to zero p_{T}threshold provides the true jet energy resolution.

W/Z and top quark masses are known with relatively high precision, therefore, hadronic decays of these particles can be used to certify jet energy measurements.

5 Novel methods using jets

It is crucial to develop novel methods to improve the impact of experimental results using the available data. LHC RunII data will provide great opportunity to apply novel jet methods. Many ideas are already successfully tested with RunI data and we shall summarize them below.

Various theoretical ideas has been developed by using large are jets or fat jets [24–26]. When an unstable particle is produced at p_{T}greater than twice its mass, their decay products are produced collimated with respect to the beam axis. The LHC data probes kinematic regimes with the production of SM particles with significant Lorentz boosts, or even new massive particles that decay to highly boosted SM particles. For example, when sufficiently boosted, the decay products of W bosons, top quarks, and Higgs bosons can become collimated to the point that standard jet reconstruction techniques fail. In other words, when the separation of the quarks in these boosted topologies is smaller than the radius parameter of the jet reconstruction, individually resolved jets can not be identified. At RunI, many studies provided promising results for the use of these techniques at RunII.

Boosted W production was studied by CMS [27] using the C/A algorithm with distance parameter $R = 0.8$ and jets with $p_T$greater than 200 GeV. The W boson is selected to be a decay product of a top quark and another leptonically decaying W boson in the event is selected. The W-jet is then submitted to various tests that ensure it has substructure. The typical efficiency of this method to tag a boosted W is 65 % with a background rejection of 96 %.

ATLAS collaboration also published studies with boosted top quarks, W and Z bosons [28]. In general, the C/A algorithm provides better framework to tag boosted objects, but $\mathrm{k_T}$ and anti-$\mathrm{k_T}$ are also used to in specific cases. The main challenge is to suppress parton-initiated jets while keeping the signal mass peak unaffected. Techniques as the grooming algorithms show great performance on this task.

Searches for new physics using RunI data and boosted objects were performed by both CMS and ATLAS experiments [29, 30]. Heavy particles ranging with masses up to 2000 GeVcan be probed in these analyses. Jet substructure simulation studies at very high luminosity collisions show promising prospects for the future results with RunII data.

ALICE experiment measured the ratio of the inclusive differential jet cross sections for $R = 0.2$ and $R = 0.4$ [31]. This ratio allows a more stringent comparison of data and calculations than the individual inclusive cross sections [32], since many systematic uncertainties are common or highly correlated. The pQCD calculation considers the ratio directly, rather than each distribution separately, making the calculated ratio effectively one perturbative order higher than the individual cross sections [32]. This is nice example novel methos in jet physics can help to test precisely the SM.

6 Summary

This letter highlighted the main ingredients to build jets and the novel ideas explored in RunI. Jet physics played a major role at LHC RunI. Precise tests of the SM and possible discoveries with RunII data will certainly depend on the jet tools.

Acknowledgements

We acknowledge support from the brazilian agencies CAPES, CNPq and FAPERJ.

References

1. K. Aamodt *et al.* [ALICE Collaboration], JINST **3**, S08002 (2008).
2. G. Aad *et al.* [ATLAS Collaboration], JINST **3**, S08003 (2008).
3. S. Chatrchyan *et al.* [CMS Collaboration], JINST **3**, S08004 (2008).
4. A. A. Alves, Jr. *et al.* [LHCb Collaboration], JINST **3**, S08005 (2008).
5. M. Cacciari, G.P. Salam, and G. Soyez. FastJet user manual. 2011.
6. M. Cacciari, G. P. Salam and G. Soyez, Eur. Phys. J. C **72**, 1896 (2012) [arXiv:1111.6097 [hep-ph]].
7. S. Catani, Y. L. Dokshitzer, M. Olsson, G. Turnock and B. R. Webber, Phys. Lett. B **269** 432 (1991).
8. S. D. Ellis and D. E. Soper, Phys. Rev. D **48** 3160 (1993) [hep-ph/9305266 [hep-ph]].
9. S. Catani, Y. L. Dokshitzer, M. H. Seymour and B. R. Webber, Nucl. Phys. B **406**, 187 (1993).
10. Y. L. Dokshitzer, G. D. Leder, S. Moretti and B. R. Webber, JHEP **9708**, 001 (1997) [hep-ph/9707323 [hep-ph]].

11. M. Wobisch and T. Wengler, in Hamburg 1998/1999, *Monte Carlo generators for HERA physics*, 270 (1999) [hep-ph/9907280 [hep-ph]].
12. CMS Collaboration, report CMS-PAS-JME-09-008.
13. ATLAS Collaboration, report ATLAS-CONF-2012-043.
14. S. Chatrchyan *et al.* [CMS Collaboration], JINST **8**, P04013 (2013) [arXiv:1211.4462 [hep-ex]].
15. R. Aaij *et al.* [LHCb Collaboration], JINST **10**(6), P06013 (2015) [arXiv:1504.07670 [hep-ex]].
16. L. Feldkamp [ALICE Collaboration], J. Phys. Conf. Ser. **509**, 012061 (2014) [arXiv:1310.2817 [hep-ex]].
17. G. Aad *et al.* [ATLAS Collaboration], Eur. Phys. J. C **74**(8), 3023 (2014) [arXiv:1405.6583 [hep-ex]].
18. CMS Collaboration, report CMS-PAS-JME-13-002.
19. S. Chatrchyan *et al.* [CMS Collaboration], JINST **6**, P11002 (2011) [arXiv:1107.4277 [physics.ins-det]].
20. G. Aad *et al.* [ATLAS Collaboration], Eur. Phys. J. C **75**, 17 (2015) [arXiv:1406.0076 [hep-ex]].
21. M. Cacciari and G. P. Salam, Phys. Lett. B **659**, 119 (2008) [arXiv:0707.1378 [hep-ph]].
22. CMS Collaboration, *Determination of b-jet energy corrections using Z+b events* [report CMS-PAS-JME-13-001].
23. G. Aad *et al.* [ATLAS Collaboration], Eur. Phys. J. C **73**(3), 2306 (2013) [arXiv:1210.6210 [hep-ex]].
24. T. Plehn, G. P. Salam and M. Spannowsky, Phys. Rev. Lett. **104** 111801 (2010) [arXiv:0910.5472 [hep-ph]].
25. S. Schätzel and M. Spannowsky, Phys. Rev. D **89**(1), 014007 (2014) [arXiv:1308.0540 [hep-ph]].
26. A. J. Larkoski, I. Moult and D. Neill, Phys. Rev. D **91**(3), 034035 (2015) [arXiv:1411.0665 [hep-ph]].
27. V. Khachatryan *et al.* [CMS Collaboration], JHEP **1412**, 017 (2014) [arXiv:1410.4227 [hep-ex]].
28. G. Aad *et al.* [ATLAS Collaboration], JHEP **1309**, 076 (2013) [arXiv:1306.4945 [hep-ex]].
29. G. Aad *et al.* [ATLAS Collaboration], Phys. Rev. D **87**(11), 112006 (2013) [arXiv:1305.0125 [hep-ex]].
30. V. Khachatryan *et al.* [CMS Collaboration], JHEP **1408**, 174 (2014) [arXiv:1405.3447 [hep-ex]].
31. B. Abelev *et al.* [ALICE Collaboration], Phys. Lett. B **722**, 262 (2013) [arXiv:1301.3475 [nucl-ex]].
32. G. Soyez, Phys. Lett. B **698**, 59 (2011) [arXiv:1101.2665 [hep-ph]].

Christophe Royon

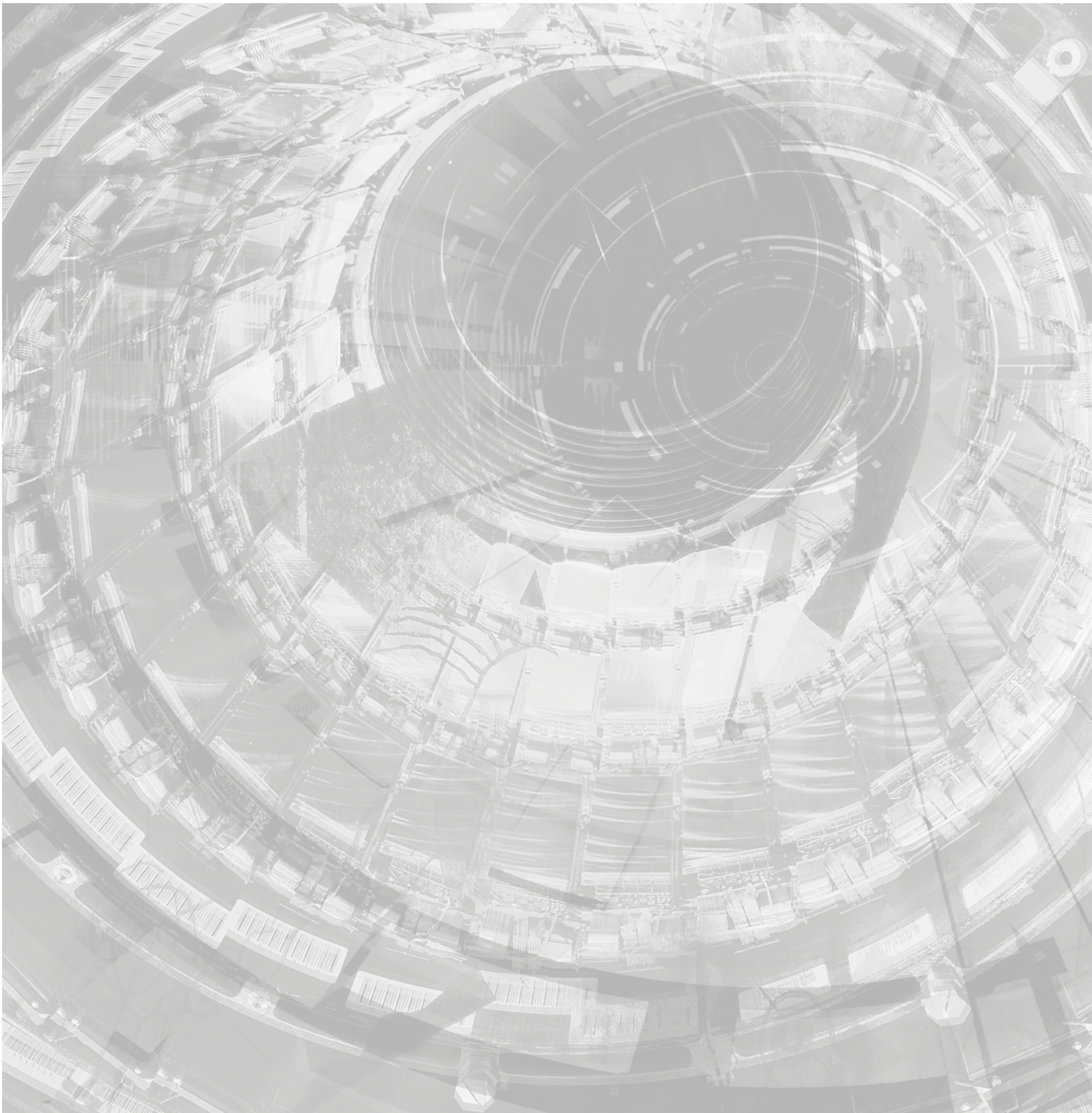

Probing BFKL resummation at hadronic colliders

Christophe Royon [e, i, j]

[e]The University of Kansas, Lawrence, USA

[i]Institute of Physics, Academy of Science of the Czech Republic, Prague, Czech Republic

[j]Institute of Nuclear Physics, Polish Academy of Sciences, Krakow, Poland

Abstract

We describe two different possible measurements sensitive to BFKL resummation effects to be performed at the LHC, namely the Mueller Navelet jets and the jet gap jet cross sections. We perform a NLL calculation of these processes and compare it to recent Tevatron measurements, and give predictions at LHC energies. We also discuss the possibility of measuring jet gap jet events in diffraction at the LHC.

1 Mueller Navelet jets at the LHC

In this section, we give the BFKL NLL cross section calculation for Mueller Navelet processes at the Tevatron and the LHC. Since the starting point of this study was the description of forward jet production at HERA, we start by describing briefly these processes.

1.1 Forward jets at HERA

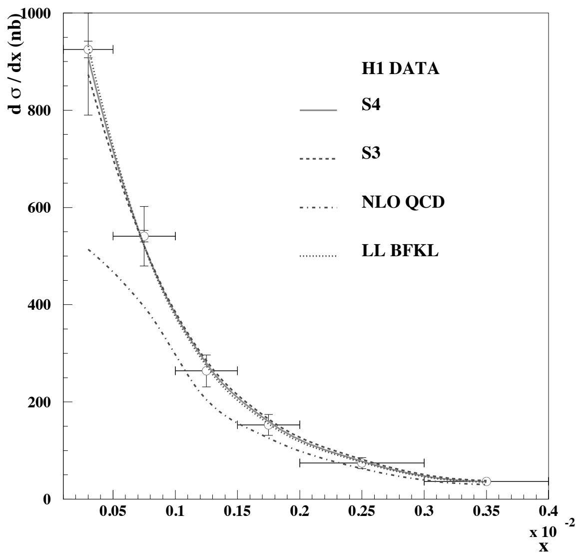

Figure 135: Comparison between the H1 $d\sigma/dx$ measurement with predictions for BFKL-LL, BFKL-NLL (S3 and S4 schemes) and DGLAP NLO calculations (see text). S4, S3 and LL BFKL cannot be distinguished on that figure.

Following the successful BFKL [1] parametrisation of the forward-jet cross-section $d\sigma/dx$ at Leading Order (LO) at HERA [2,3], it is possible to perform a similar study using Next-to-leading (NLL) resummed BFKL kernels. Forward jets at HERA are an ideal observable to look for BFKL resummation effects. The interval in rapidity between the scattered lepton and the jet in the forward region is large, and when the photon virtuality Q is close to the transverse jet momentum k_T, the DGLAP cross section is small because of the k_T ordering of the emitted gluons. In this short report, we will only discuss the phenomelogical aspects and all detailed calculations can be found in Ref. [4] for forward jets at HERA and in Ref. [5] for Mueller Navelet jets at the Tevatron and the LHC.

1.2 BFKL NLL formalism

The BFKL NLL [6] longitudinal transverse cross section reads:

$$\frac{d\sigma_{T,L}^{\gamma*p\to JX}}{dx_J dk_T^2} = \frac{\alpha_s(k_T^2)\alpha_s(Q^2)}{k_T^2 Q^2} \; f_{eff}(x_J, k_T^2) \int d\gamma \left(\frac{Q^2}{k_T^2}\right)^{\gamma} \phi_{T,L}^{\gamma}(\gamma) \; e^{\bar{\alpha}\chi_{eff}Y} \tag{359}$$

where x_J is the proton momentum fraction carried by the forward jet, χ_{eff} is the effective BFKL NLL kernel and the ϕs are the transverse and longitunal impact factors taken at LL. The effective kernel $\chi_{eff}(\gamma, \bar{\alpha})$ is defined from the NLL kernel $\chi_{NLL}(\gamma, \omega)$ by solving the implicit equation numerically

$$\chi_{eff}(\gamma, \bar{\alpha}) = \chi_{NLL}\left[\gamma, \bar{\alpha}\; \chi_{eff}(\gamma, \bar{\alpha})\right] \; . \tag{360}$$

The integration over γ in Eq. 359 is performed numerically. It is possible to fit directly $d\sigma/dx$ measured by the H1 collaboration using this formalism with one single parameter, the normalisation. The values of χ_{NLL} are taken at NLL [6] using different resummation schemes to remove spurious singularities defined as S3 and S4 [7]. Contrary to LL BFKL, it is worth noticing that the coupling constant α_S is taken using the renormalisation group equations, the only free parameter in the fit being the normalisation.

To compute $d\sigma/dx$ in the experimental bins, we need to integrate the differential cross section on the bin size in Q^2, x_J (the momentum fraction of the proton carried by the forward jet), k_T , while taking into account the experimental cuts. To simplify the numerical calculation, we perform the integration on the bin using the variables where the cross section does not change rapidly, namely k_T^2/Q^2, $\log 1/x_J$, and $1/Q^2$. Experimental cuts are treated directly at the integral level (the cut on $0.5 < k_T^2/Q^2 < 5$ for instance) or using a toy Monte Carlo. More detail can be found about the fitting procedure in Appendix A of Ref. [3].

The NLL fits [4] can nicely describe the H1 data [8] for the S4 and S3 schemes [2–4] ($\chi^2 = 0.48/5$ and $\chi^2 = 1.15/5$ respectively per degree of freedom with statistical and systematic errors added in quadrature). The curve using a LL fit is indistinguishable in Fig. 135 from the result of the BFKL-NLL fit. The DGLAP NLO calculation fails to describe the H1 data at lowest x (see Fig. 135). We also checked the effect of changing the scale in the exponential of Eq. 359 from $k_T Q$ to $2k_T Q$ or $k_T Q/2$ which leads to a difference of 20% on the cross section while changing the scale to k_T^2 or Q^2 modifies the result by less than 5% which is due to the cut on $0.5 < k_T^2/Q^2 < 5$. Implementing the higher-order corrections in the impact factor due to exact gluon dynamics in the $\gamma^* \to q\bar{q}$ transition [9] changes the result by less than 3%.

The H1 collaboration also measured the forward jet triple differential cross section [8] and the results are given in Fig. 136. We keep the same normalisation coming from the fit to $d\sigma/dx$ to predict the triple differential cross section. The BFKL LL formalism leads to a good description of the data when $r = k_T^2/Q^2$ is close to 1 and deviates from the data when r is further away from 1. This effect is expected since DGLAP radiation effects are supposed to occur when the ratio between the jet k_T and the virtual photon Q^2 are further away from 1. The BFKL NLL calculation including the Q^2 evolution via the renormalisation group equation leads to a good description of the H1 data on the full range. We note that the higher order corrections are small when $r \sim 1$, when the BFKL effects are supposed to dominate. By contrast, they are significant as expected when r is different from one, ie when DGLAP evolution becomes relevant. We notice that the DGLAP NLO calculation fails to describe the data when $r \sim 1$, or in the region where BFKL resummation effects are expected to appear.

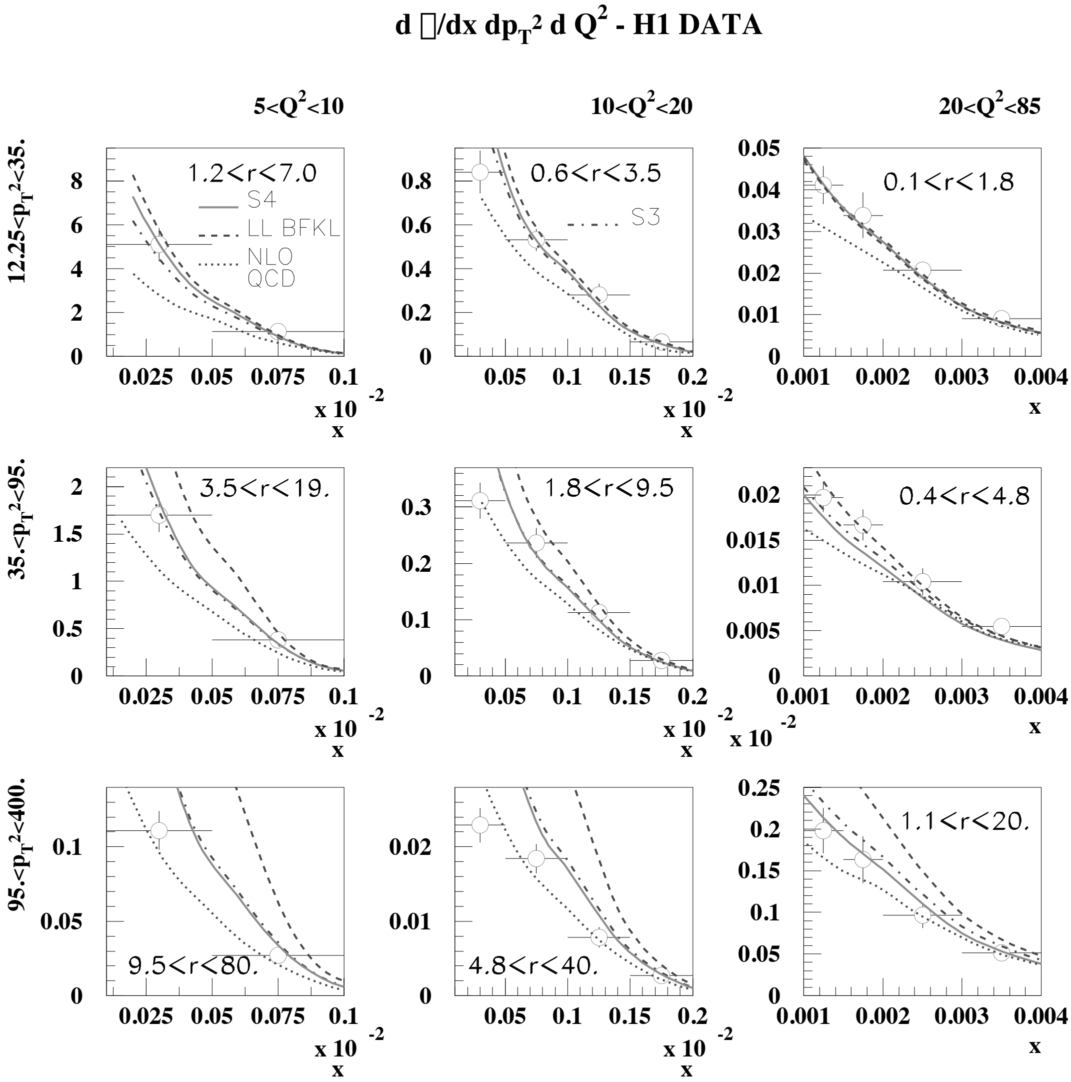

Figure 136: Comparison between the H1 measurement of the triple differential cross section with predictions for BFKL-LL, BFKL-NLL and DGLAP NLO calculations (see text).

In addition, we checked the dependence of our results on the scale taken in the exponential of Eq. 359. The effect is a change of the cross section of about 20% at low p_T increasing to 70% at highest p_T. Taking the correct gluon kinematics in the impact factor lead as expected to a better description of the data at high p_T [4].

1.3 Mueller Navelet jets at the Tevatron and the LHC

Mueller Navelet jets are ideal processes to study BFKL resummation effects [5]. Two jets with a large interval in rapidity and with similar tranverse momenta are considered. A typical observable to look for BFKL effects is the measurement of the azimuthal correlations between both jets. The DGLAP prediction is that this distribution should peak towards π - ie jets are back-to-back- whereas multi-gluon emission via the BFKL mechanism leads to a smoother distribution. The relevant variables to

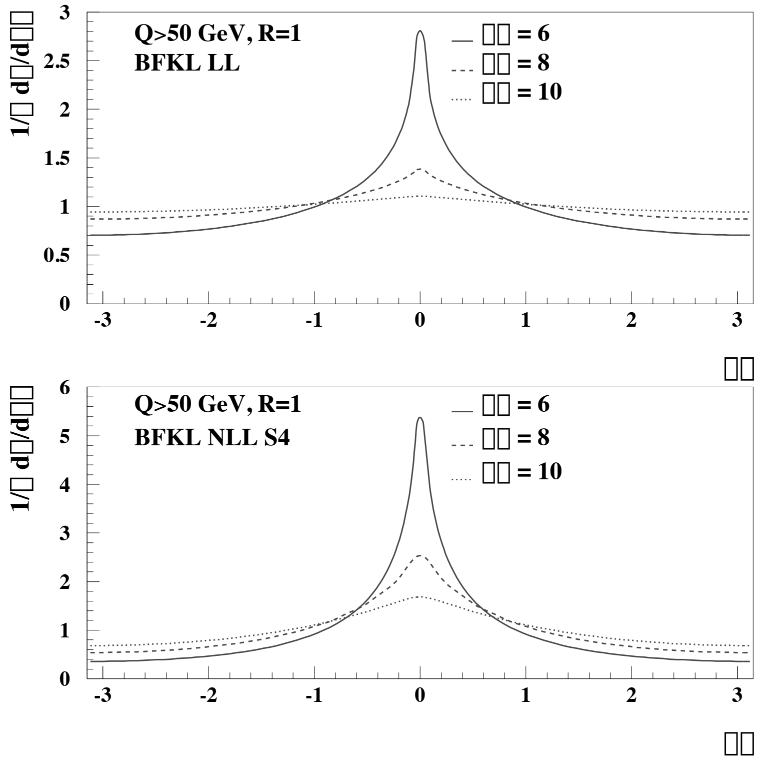

Figure 137: The Mueller-Navelet jet $\Delta\Phi$ distribution for LHC kinematics in the BFKL framework at LL (upper plots) and NLL-S4 (lower plots) accuracy for $\Delta\eta = 6,\ 8,\ 10$.

look for azimuthal correlations are the following:

$$\begin{aligned}
\Delta\eta &= y_1 - y_2 \\
y &= (y_1 + y_2)/2 \\
Q &= \sqrt{k_1 k_2} \\
R &= k_2/k_1
\end{aligned}$$

where $y_{1,2}$ and $k_{1,2}$ are respectively the jet rapidities and transverse momenta. The azimuthal correlation for BFKL reads:

$$2\pi \, \frac{d\sigma}{d\Delta\eta dR d\Delta\Phi} \bigg/ \frac{d\sigma}{d\Delta\eta dR} = 1 + \frac{2}{\sigma_0(\Delta\eta, R)} \sum_{p=1}^{\infty} \sigma_p(\Delta\eta, R) \cos(p\Delta\Phi)$$

where in the NLL BFKL framework,

$$\begin{aligned}
\sigma_p &= \int_{E_T}^{\infty} \frac{dQ}{Q^3} \alpha_s(Q^2/R) \alpha_s(Q^2 R) \left(\int_{y_<}^{y_>} dy x_1 f_{eff}(x_1, Q^2/R) x_2 f_{eff}(x_2, Q^2 R) \right) \\
& \int_{1/2-\infty}^{1/2+\infty} \frac{d\gamma}{2i\pi} R^{-2\gamma} \, e^{\bar{\alpha}(Q^2)\chi_{eff}(p,\gamma,\bar{\alpha})\Delta\eta}
\end{aligned}$$

and χ_{eff} is the effective resummed kernel. Computing the different σ_p at NLL for the resummation schemes S3 and S4 allowed us to compute the azimuthal correlations at NLL. As expected, the $\Delta\Phi$ dependence is less flat than for BFKL LL and is closer to the DGLAP behaviour [5]. In Fig. 137, we display the observable $1/\sigma d\sigma/d\Delta\Phi$ as a function of $\Delta\Phi$, for LHC kinematics. The results are displayed for different values of $\Delta\eta$ and at both LL and NLL accuracy using the S4 resummation scheme. In general, the $\Delta\Phi$ spectra are peaked around $\Delta\Phi = 0$, which is indicative of jet emissions occuring back-to-back. In addition the $\Delta\Phi$ distribution flattens with increasing $\Delta\eta = y_1 - y_2$. Note the change of scale on the vertical axis which indicates the magnitude of the NLL corrections with respect to the LL-BFKL results. The NLL corrections slow down the azimuthal angle decorrelations for both increasing $\Delta\eta$ and R deviating from 1. We also studied the R dependence of our prediction which is quite weak [5] and the scale dependence of our results by modifying the scale Q^2 to either $Q^2/2$ or $2Q^2$ and the effect on the azimuthal distribution is of the order of 20%. The effect of the energy conservation in the BFKL equation [5] is large when R goes away from 1. The effect is to reduce the effective value of $\Delta\eta$ between the jets and thus the decorrelation effect. However, it is worth noticing that this effect is negligible when R is close to 1 where this measurement will be performed. Recent calculations include in addition NLL impact factors [5].

A measurement of the cross-section $d\sigma^{hh\to JXJ}/d\Delta\eta dR d\Delta\Phi$ at the LHC will allow for a detailed study of the BFKL QCD dynamics since the DGLAP evolution leads to much less jet angular decorrelation (jets are back-to-back when R is close to 1). In particular, measurements with values of $\Delta\eta$ reaching 8 or 10 using the CASTOR calorimeter of the CMS collaboration for instance will be of great interest, as these could allow to distinguish between BFKL and DGLAP resummation effects and would provide important tests for the relevance of the BFKL formalism.

2 Jet veto measurements in ATLAS

The ATLAS collaboration measured the so-called jet veto cross section [10], namely the events with two high p_T jets, well separated in rapidity and with a veto on jet activity with p_T greater than a given threshold Q_0 between the two jets. The ATLAS collaboration measured the jet veto fraction with respect to the standard dijet cross section, and it was advocated that it might be sensitive to BFKL dynamics. In Ref. [11], we computed the gluon emission at large angles (which are not considered in usual MC) using the Banfi-Marchesini-Smye equation, and we showed that the measurement can be effectively described by the gluon resummation and is thus not related to BFKL dynamics as shown in Fig. 138. The sensivity to the BFKL resummation effects appears when one looks for gaps between jets as described in the following section.

3 Jet gap jets at the Tevatron and the LHC

In this section, we describe another possible measurement which can probe BFKL resummation effects and we compare our predictions with existing D0 and CDF measurements [12].

3.1 BFKL NLL formalism

The production cross section of two jets with a gap in rapidity between them reads

$$\frac{d\sigma^{pp\to XJJY}}{dx_1 dx_2 dE_T^2} = \mathcal{S} f_{eff}(x_1, E_T^2) f_{eff}(x_2, E_T^2) \frac{d\sigma^{gg\to gg}}{dE_T^2}, \tag{361}$$

where $\sqrt{s}$ is the total energy of the collision, E_T the transverse momentum of the two jets, x_1 and x_2 their longitudinal fraction of momentum with respect to the incident hadrons, S the survival probability, and f the effective parton density functions [12]. The rapidity gap between the two jets is $\Delta\eta = \ln(x_1 x_2 s/p_T^2)$.

The cross section is given by

$$\frac{d\sigma^{gg\to gg}}{dE_T^2} = \frac{1}{16\pi} \left|A(\Delta\eta, E_T^2)\right|^2 \tag{362}$$

in terms of the $gg \to gg$ scattering amplitude $A(\Delta\eta, p_T^2)$.

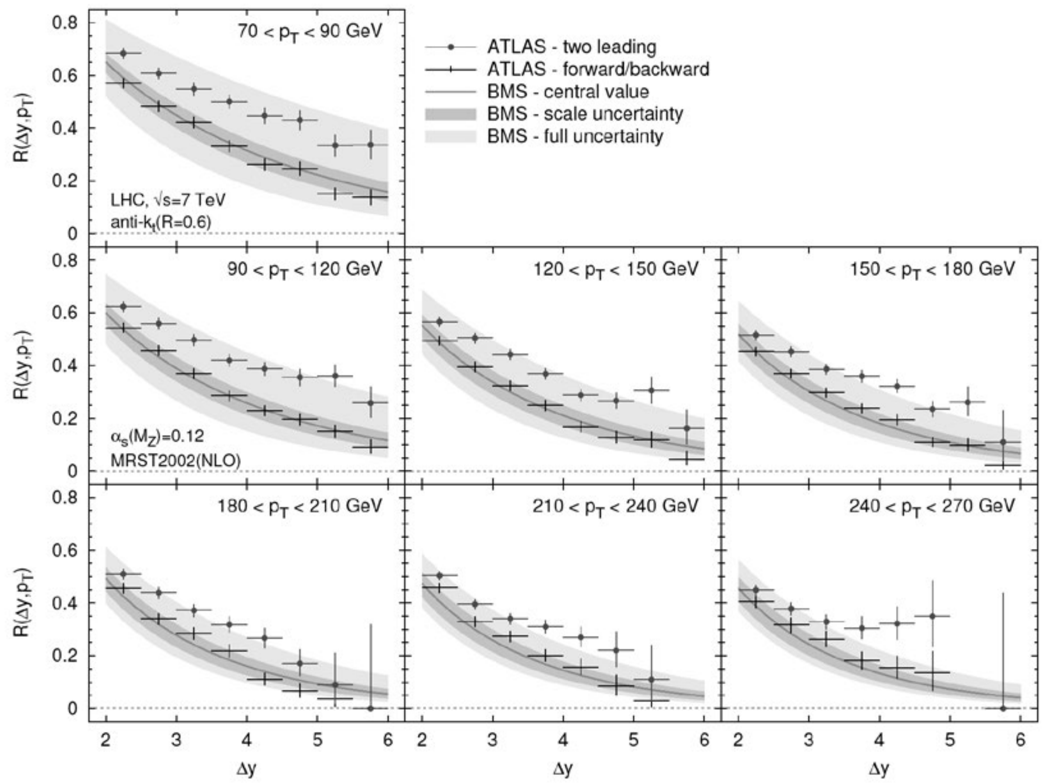

Figure 138: Comparison of the resummed veto fraction with the ATLAS measurement, for a fixed veto energy of $E_{out} = 20$ GeV, in different bins of p_T . The inner (green) uncertainty band is obtained taking into account only the renormalization and factorization scale uncertainties, while the outer (yellow) band also includes the subleading logarithmic uncertainty. For the ATLAS data, circles represent the case where the two leading jets are selected while the one where the most forward and backward jets are selected are represented by crosses.

In the following, we consider the high energy limit in which the rapidity gap $\Delta\eta$ is assumed to be very large. The BFKL framework allows to compute the $gg \to gg$ amplitude in this regime, and the result is known up to NLL accuracy

$$\begin{aligned} A(\Delta\eta, E_T^2) &= \frac{16 N_c \pi \alpha_s^2}{C_F E_T^2} \sum_{p=-\infty}^{\infty} \int \frac{d\gamma}{2i\pi} \frac{[p^2 - (\gamma - 1/2)^2]}{[(\gamma - 1/2)^2 - (p - 1/2)^2]} \\ & \quad \frac{\exp\left\{\bar{\alpha}(E_T^2)\chi_{eff}[2p, \gamma, \bar{\alpha}(E_T^2)]\Delta\eta\right\}}{[(\gamma - 1/2)^2 - (p + 1/2)^2]} \end{aligned} \tag{363}$$

with the complex integral running along the imaginary axis from $1/2 - i\infty$ to $1/2 + i\infty$, and with only even conformal spins contributing to the sum, and $\bar{\alpha} = \alpha_S N_C / \pi$ the running coupling.

As for the Mueller-Navelet jets, the NLL-BFKL effects are phenomenologically taken into account by the effective kernels $\chi_{eff}(p, \gamma, \bar{\alpha})$. The NLL kernels obey a *consistency condition* which allows to reformulate the problem in terms of $\chi_{eff}(\gamma, \bar{\alpha})$.

In this study, we performed a parametrised distribution of $d\sigma^{gg \to gg}/dE_T^2$ so that it can be easily implemented in the Herwig Monte Carlo [13] since performing the integral over γ in particular would be too much time consuming in a Monte Carlo. The implementation of the BFKL cross section in a Monte Carlo is absolutely necessary to make a direct comparison with data. Namely, the measurements are sensitive to the jet size (for instance, experimentally the gap size is different from the rapidity interval between the jets which is not the case by definition in the analytic calculation).

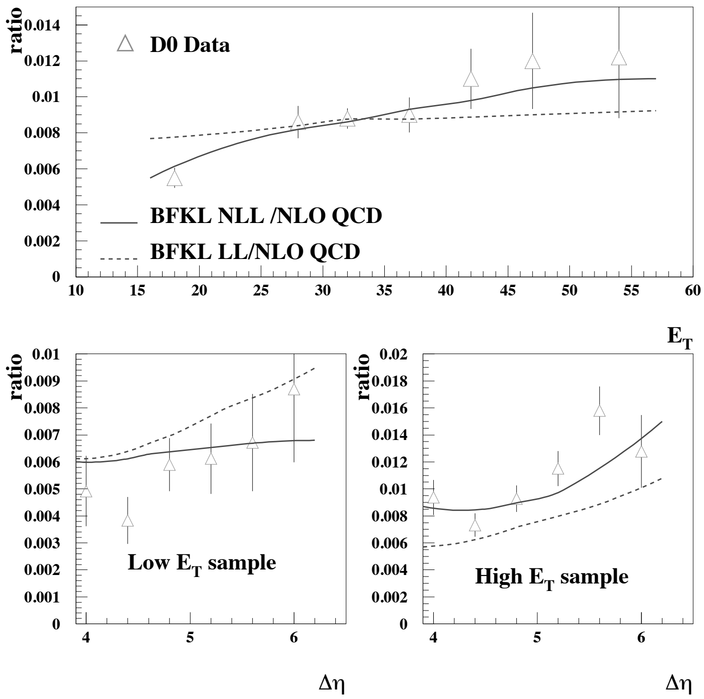

Figure 139: Comparisons between the D0 measurements of the jet-gap-jet event ratio with the NLL- and LL-BFKL calculations. The NLL calculation is in fair agreement with the data. The LL calculation leads to a worse description of the data.

3.2 Comparison with D0 and CDF measurements

Let us first notice that the sum over all conformal spins is absolutely necessary. Considering only $p = 0$ in the sum of Equation 363 leads to a wrong normalisation and a wrong jet E_T dependence, and the effect is more pronounced as $\Delta\eta$ diminishes.

The D0 collaboration measured the jet gap jet cross section ratio with respect to the total dijet cross section, requesting for a gap between -1 and 1 in rapidity, as a function of the second leading jet E_T, and $\Delta\eta$ between the two leading jets for two different low and high E_T samples (15< E_T <20 GeV and E_T >30 GeV). To compare with theory, we compute the following quantity

$$Ratio = \frac{BFKL\ NLL\ HERWIG}{Dijet\ Herwig} \times \frac{LO\ QCD}{NLO\ QCD} \tag{364}$$

in order to take into account the NLO corrections on the dijet cross sections, where $BFKL\ NLL\ HERWIG$ and $Dijet\ Herwig$ denote the BFKL NLL and the dijet cross section implemented in HERWIG. The NLO QCD cross section was computed using the NLOJet++ program [14].

The comparison with D0 data [15] is shown in Fig. 139. We find a good agreement between the data and the BFKL calculation. It is worth noticing that the BFKL NLL calculation leads to a better result than the BFKL LL one (note that most studies in the literature considered only the $p = 0$ component which is not a valid assumption).

The comparison with the CDF data [15] as a function of the average jet E_T and the difference in rapidity between the two jets is shown in Fig. 140, and the conclusion remains the same: the BFKL NLL formalism leads to a better description than the BFKL LL one.

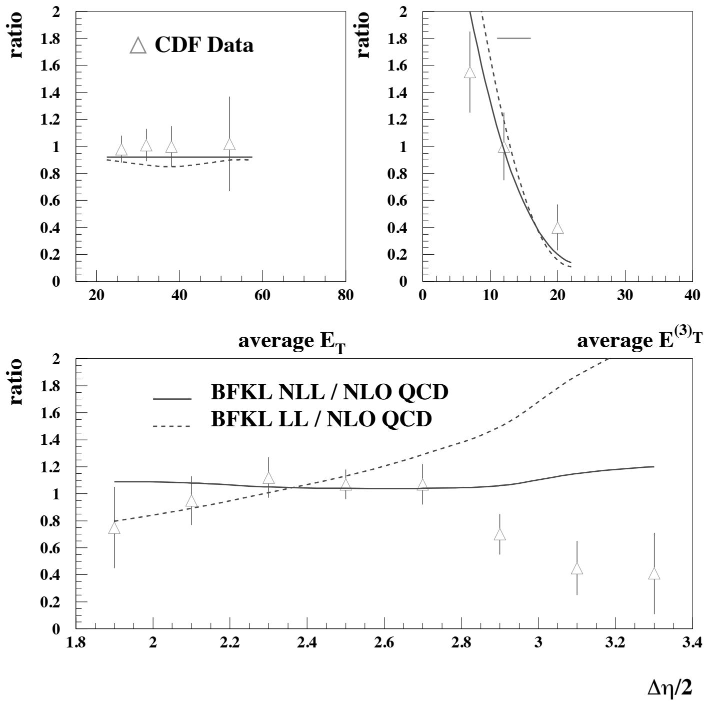

Figure 140: Comparisons between the CDF measurements of the jet-gap-jet event ratio with the NLL- and LL-BFKL calculations. The NLL calculation is in fair agreement with the data. The LL calculation leads to a worse description of the data.

3.3 Predictions for the LHC

Using the same formalism, and assuming a survival probability of 0.03 at the LHC, it is possible to predict the jet gap jet cross section at the LHC. While both LL and NLL BFKL formalisms lead to a weak jet E_T or $\Delta\eta$ dependence, the normalisation is found to be quite different (see Fig. 141) leading to lower cross section for the BFKL NLL formalism.

4 Jet gap jet events in diffraction at the LHC

A new process of detecting jet-gap-jet events in diffractive double pomeron exchange processes was introduced recently [16]. The idea is to tag the intact protons inside the ATLAS Forward Physics (AFP) detectors [17] located at about 210 m from the ATLAS interaction point on both sides. The advantage of such processes is that they are quite clean since they are not “polluted” by proton remnants and it is possible to go to larger jet separation than for usual jet-gap-jet events. The normalisation for these processes come from the fit to the D0 discussed in the previous section. The ratio between jet-gap-jet to inclusive jet events is shown in Fig. 142 requesting protons to be tagged in AFP for both samples. The ratio shows a weak dependence as a function of jet p_T (and also as a function of the difference in rapidity between the two jets). It is worth noticing that the ratio is about 20-30% showing that the jet-gap-jet events are much more present in the diffractive sample than in the inclusive one as expected.

It is worth noticing that there are many measurements that can be performed in diffraction in addition to the search for BFKL dymamics in jet gap jet events [18]

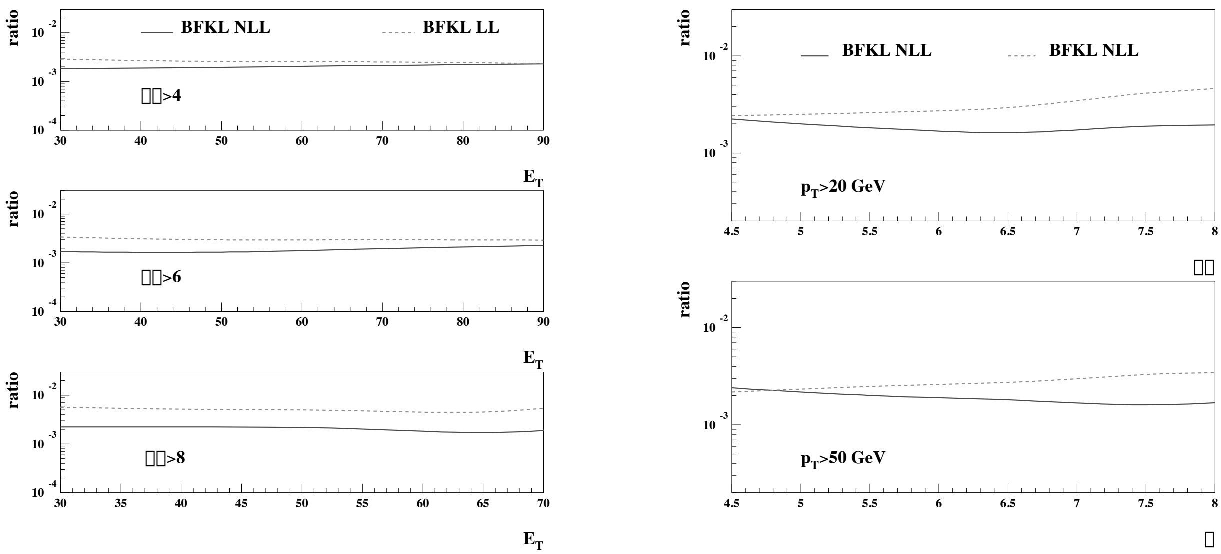

Figure 141: Ratio of the jet gap jet to the inclusive jet cross sections at the LHC as a function of jet p_T and $\Delta\eta$.

5 Conclusion

In this short paper, we presented different observables sensitive to BFKL dynamics that can be looked at especially at the LHC, namely the Mueller Navelet jets and the gap between jets in standard or diffractive events. Some mew measurements are expected soon and might lead to a clear signature.

References

1. L. N. Lipatov, Sov. J. Nucl. Phys. **23**, 338 (1976) [Yad. Fiz. **23**, 642 (1976)]; E. A. Kuraev, L. N. Lipatov and V. S. Fadin, Sov. Phys. JETP **45**, 199 (1977) [Zh. Eksp. Teor. Fiz. **72**, 377 (1977)]; I. I. Balitsky and L. N. Lipatov, Sov. J. Nucl. Phys. **28**, 822 (1978) [Yad. Fiz. **28**, 1597 (1978)].
2. J. G. Contreras, R. B. Peschanski and C. Royon, Phys. Rev. D **62**, 034006 (2000) [hep-ph/0002057 [hep-ph]]; C. Marquet, R. B. Peschanski and C. Royon, Phys. Lett. B **599**, 236 (2004) [hep-ph/0407011 [hep-ph]].
3. C. Marquet and C. Royon, Nucl. Phys. B **739**, 131 (2006) [hep-ph/0510266 [hep-ph]].
4. O. Kepka, C. Royon, C. Marquet and R. B. Peschanski, Phys. Lett. B **655**, 236 (2007) [hep-ph/0609299 [hep-ph]]; O. Kepka, C. Royon, C. Marquet and R. B. Peschanski, Eur. Phys. J. C **55**, 259 (2008) [hep-ph/0612261 [hep-ph]]; C. Marquet and C. Royon, Phys. Rev. D **79**, 034028 (2009) [arXiv:0704.3409 [hep-ph]]; A. Sabio Vera and F. Schwennsen, Nucl. Phys. B **776**, 170 (2007) [hep-ph/0702158 [hep-ph]].
5. A. H. Mueller and H. Navelet, Nucl. Phys. B **282**, 727 (1987); C. Marquet and C. Royon, Phys. Rev. D **79**, 034028 (2009) [arXiv:0704.3409 [hep-ph]]; A. Sabio Vera and F. Schwennsen, Nucl. Phys. B **776**, 170 (2007) [hep-ph/0702158 [hep-ph]]; B. Ducloué, L. Szymanowski and S. Wallon, Phys. Rev. Lett. **112**, 082003 (2014) [arXiv:1309.3229 [hep-ph]].
6. V. S. Fadin and L. N. Lipatov, Phys. Lett. B **429**, 127 (1998) [hep-ph/9802290 [hep-ph]]; M. Ciafaloni, Phys. Lett. B **429**, 363 (1998) [hep-ph/9801322 [hep-ph]]; M. Ciafaloni and G. Camici, Phys. Lett. B **430**, 349 (1998) [hep-ph/9803389 [hep-ph]].
7. G. P. Salam, JHEP **9807**, 019 (1998) [hep-ph/9806482 [hep-ph]].

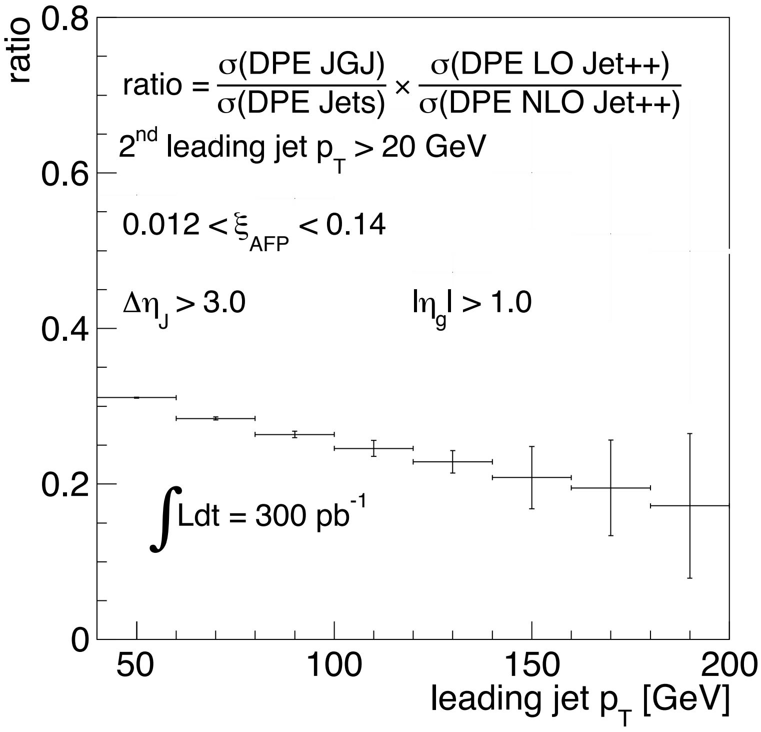

Figure 142: Ratio of the jet gap jet to the inclusive jet cross sections at the LHC as a function of jet p_T in double pomeron exchange events where the protons are detected in AFP.

8. A. Aktas *et al.* [H1 Collaboration], Eur. Phys. J. C **46**, 27 (2006) [hep-ex/0508055 [hep-ex]].
9. C. D. White, R. B. Peschanski and R. S. Thorne, Phys. Lett. B **639**, 652 (2006) [hep-ph/0606169 [hep-ph]].
10. G. Aad *et al.* [ATLAS Collaboration], JHEP **1109**, 053 (2011) [arXiv:1107.1641 [hep-ex]].
11. Y. Hatta, C. Marquet, C. Royon, G. Soyez, T. Ueda and D. Werder, Phys. Rev. D **87**(5), 054016 (2013) [arXiv:1301.1910 [hep-ph]].
12. O. Kepka, C. Marquet and C. Royon, Phys. Rev. D **83**, 034036 (2011) [arXiv:1012.3849 [hep-ph]]; F. Chevallier, O. Kepka, C. Marquet and C. Royon, Phys. Rev. D **79**, 094019 (2009) [arXiv:0903.4598 [hep-ph]].
13. G. Marchesini, B. R. Webber, G. Abbiendi, I. G. Knowles, M. H. Seymour and L. Stanco, Comput. Phys. Commun. **67**, 465 (1992).
14. Z. Nagy and Z. Trocsanyi, Phys. Rev. Lett. **87**, 082001 (2001) [hep-ph/0104315 [hep-ph]].
15. B. Abbott *et al.* [D0 Collaboration], Phys. Lett. B **440**, 189 (1998) [hep-ex/9809016 [hep-ex]]; F. Abe *et al.* [CDF Collaboration], Phys. Rev. Lett. **80**, 1156 (1998).
16. . Marquet, C. Royon, M. Trzebiński and R. Žlebčík, Phys. Rev. D **87**(3), 034010 (2013) [arXiv:1212.2059 [hep-ph]].
17. ATLAS Collaboration, report CERN-LHCC-2011-012.
18. C. Marquet, C. Royon, M. Saimpert and D. Werder, Phys. Rev. D **88**(7), 074029 (2013) [arXiv:1306.4901 [hep-ph]]; S. Fichet, G. von Gersdorff, O. Kepka, B. Lenzi, C. Royon and M. Saimpert, Phys. Rev. D **89**, 114004 (2014) [arXiv:1312.5153 [hep-ph]]; E. Chapon, C. Royon and O. Kepka, Phys. Rev. D **81**, 074003 (2010) [arXiv:0912.5161 [hep-ph]]; O. Kepka and C. Royon, Phys. Rev. D **78**, 073005 (2008) [arXiv:0808.0322 [hep-ph]]; S. Fichet, G. von Gersdorff, B. Lenzi, C. Royon and M. Saimpert, JHEP **1502**, 165 (2015) [arXiv:1411.6629 [hep-ph]].

Victor Gonçalves
Werner Sauter

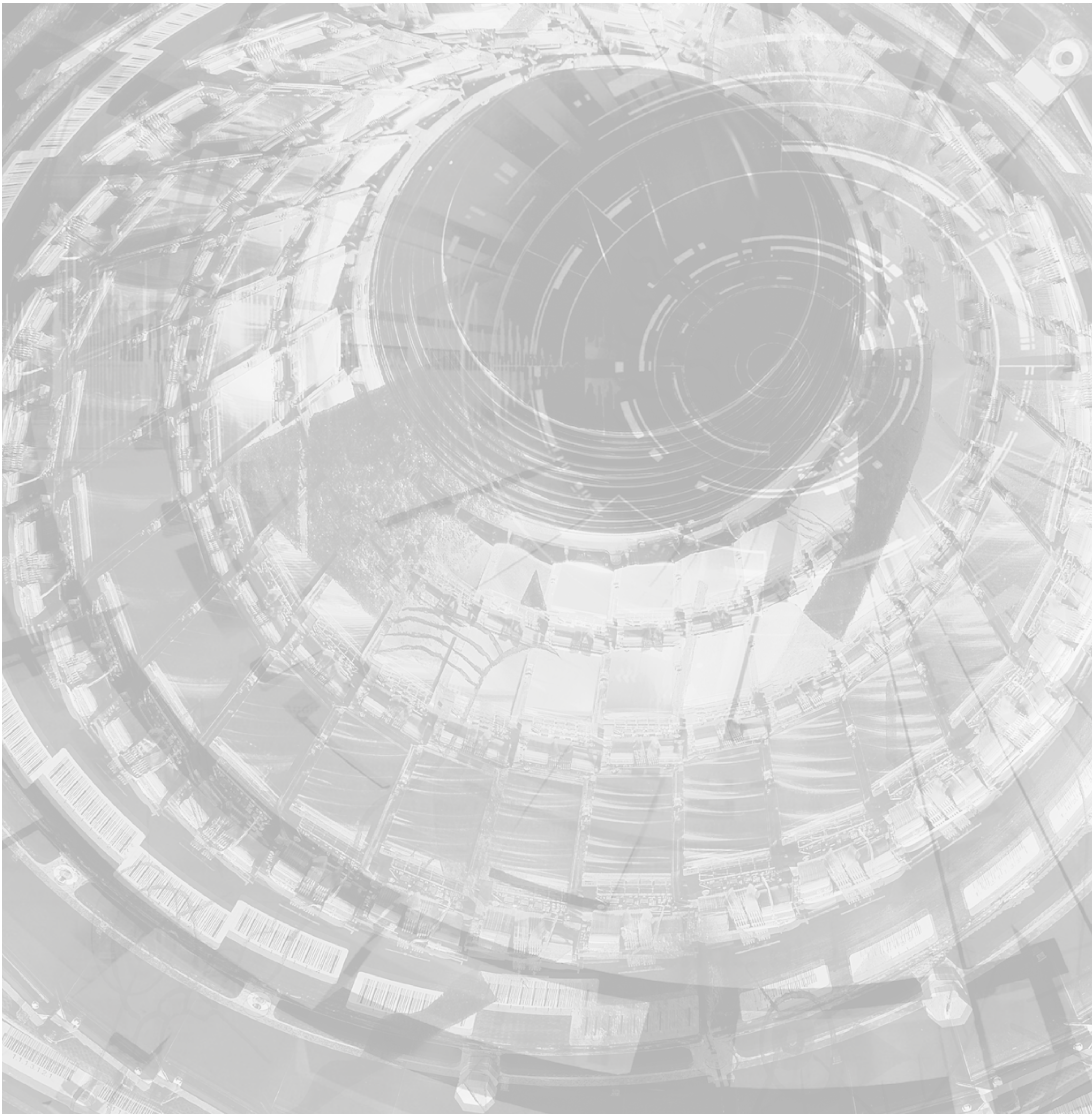

Production of particles at large momentum transfer

Victor P. B. Gonçalves, Werner K. Sauter [v32]

[v]High and Medium Energy Group, Instituto de Física e Matemática,
Universidade Federal de Pelotas, Pelotas, Brazil

Abstract

The diffractive particle production in coherent hadron-hadron interactions at LHC energies is studied assuming that the color singlet t channel exchange carries large momentum transfer. We consider the LO and NLO non-forward solutions of the BFKL equation at high energy and large momentum transfer and estimate the rapidity distribution and total cross section for different final states. In this work, the vector meson and photon production are analysed in ep and hadronic collisions. In the meson case, we predict large rates, which implies that the experimental identification can be feasible at the LHC and in the photon case, we obtain a reasonable agreement with the DESY HERA data.

1 Introduction

The description of exclusive diffractive processes has been proposed as a probe of the Quantum Chromodynamics (QCD) dynamics in the high energy limit (For a recent reviews see, e.g. Ref. [1]). It is expected that the study of these processes provide insight into the parton dynamics of the diffractive exchange when a hard scale is present. In particular, the diffractive vector meson and photon production at large momentum transfer is expected to probe the QCD Pomeron, which is described by the Balitsky, Fadin, Kuraev, and Lipatov (BFKL) equation [2–5]. In this contribution, we present a brief summary of the results obtained in Refs. [6–8], where the vector meson and photon production at large momentum transfer were studied considering the non-forward solution of the BFKL equation at leading order (LO) and next-to-leading order (NLO). In particular, we have estimated the cross sections for the ρ, J/Ψ and γ production at large-t in ep collisions at HERA energy which can represented by the diagram presented in Fig. 143 (left panel). Moreover, we have studied the vector meson production at large-t in coherent pp interactions as represented in Fig. 143 (right panel), which is an alternative way to study the QCD dynamics at high energies.

This contribution is organized as follows. In the next section we summarize the formalism used in the calculation. Our results are presented in Section 3 and the main conclusions are discussed in Section 4.

2 Formalism

The differential and total cross sections for the diffractive particle photoproduction at large momentum transfer reads

$$\frac{d\sigma_{\gamma h\to YX}}{dt} = \int_{x_{\min}}^{1} dx_j \, \frac{d\sigma}{dtdx_j}, \quad \sigma_{\text{tot}} = \int_{t_{\min}}^{t_{\max}} dt \, \frac{d\sigma_{\gamma h\to YX}}{dt} \tag{365}$$

where h denote a hadron, Y the produced particle ($J/\psi, \Upsilon, \rho$ and γ), X the hadron fragments and

$$\frac{d\sigma}{dtdx_j} = \left[\frac{81}{16}G(x_j,|t|) + \sum_j (q_j(x_j,|t|) + \bar{q}_j(x_j,|t|))\right]\frac{d\hat{\sigma}}{dt}. \tag{366}$$

[32]Corresponding author. See Table 2 for the complete list of talks given at the workshop.

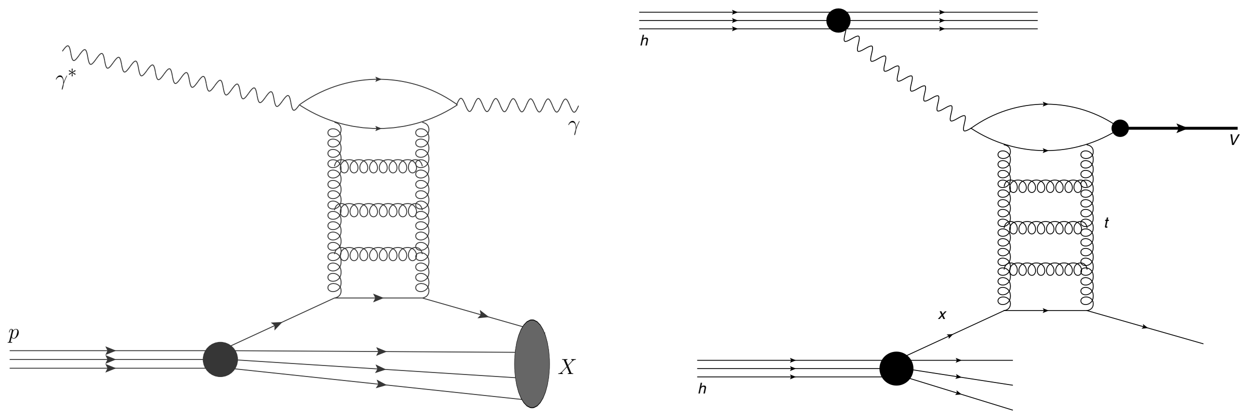

Figure 143: The exclusive photon and vector meson production at large-t in ep collisions (left panel) and coherent pp interactions (right panel).

Moreover, G, q and $\bar{q}$ are parton distribution functions (we are using CTEQ6L parametrization). The partonic cross section for vector meson production is given by

$$\frac{d\hat{\sigma}}{dt}(\gamma q \to V q) = \frac{1}{16\pi}|\mathcal{A}_V(s,t)|^2. \tag{367}$$

and for photon production,

$$\frac{d\hat{\sigma}}{dt}(\gamma^* q \to \gamma q) = \frac{1}{16\pi}\left\{|\mathcal{A}_{(+,+)}(s,t)|^2 + |\mathcal{A}_{(+,-)}(s,t)|^2\right\}. \tag{368}$$

The amplitudes, in both cases, have a general expression (for details, see [7, 8]),

$$\mathcal{A} \propto \int d\nu \; G_{V,\gamma}(\nu)\left(\frac{s}{\Lambda^2}\right)^{\omega(\nu)} I_{\gamma/V,\gamma}(\nu) I_{q,q}(\nu) \tag{369}$$

where G depends on the produced particle, $\omega(\nu) = \bar{\alpha}_s \chi(1/2 + i\nu)$ is the BFKL characteristic function and I are related with the impact factors for the transitions $\gamma \to (V, \gamma)$ and $q \to q$.

At leading order the BFKL function $\chi(\gamma)$ is given by

$$\chi^{\mathrm{LO}}(\gamma) = 2\psi(1) - \psi(\gamma) - \psi(1-\gamma) \tag{370}$$

where $\psi(z)$ is the digamma function. In what follows this expression is used in our calculations of the vector meson production at large-t. Several shortcomings are present in a leading order calculation: the energy scale Λ is arbitrary; α_s is not running at LO BFKL and the power growth with energy violates s-channel unitarity at large rapidities. Some of these shortcomings are reduced if we consider the NLO corrections for the BFKL kernel obtained originally in Refs. [9, 10]. In this case, one have that

$$\chi(\gamma) = \chi^{\mathrm{LO}}(\gamma) + \overline{\alpha}_s \chi^{\mathrm{NLO}}(\gamma), \quad \bar{\alpha}_s = N_c \alpha_s/\pi, \tag{371}$$

with the χ^{NLO} function found in [9, 10]. However, there are several problems associated with these corrections (See, e.g. [11]). Among of them, exist problems associated to the choice of energy scale, the renormalization scheme and related ambiguities.

An alternative is to use the ω-expansion, developed to resum collinear effects at all orders in a systematic way. This approach was revisited in Ref. [12] obtaining an expression for the collinearly improved BFKL kernel characteristic function, denoted All-poles hereafter, which full expression can be found in [12].

Another alternative to solve the problems present in the original NLO kernel was proposed in Ref. [13]. To solve the energy scale ambiguity, the Brodsky-Lepage-Mackenzie (BLM) optimal scale setting [14] and the momentum space subtraction (MOM) scheme of renormalization were used to obtain the another BFKL characteristic function (see the complete expression in [13]).

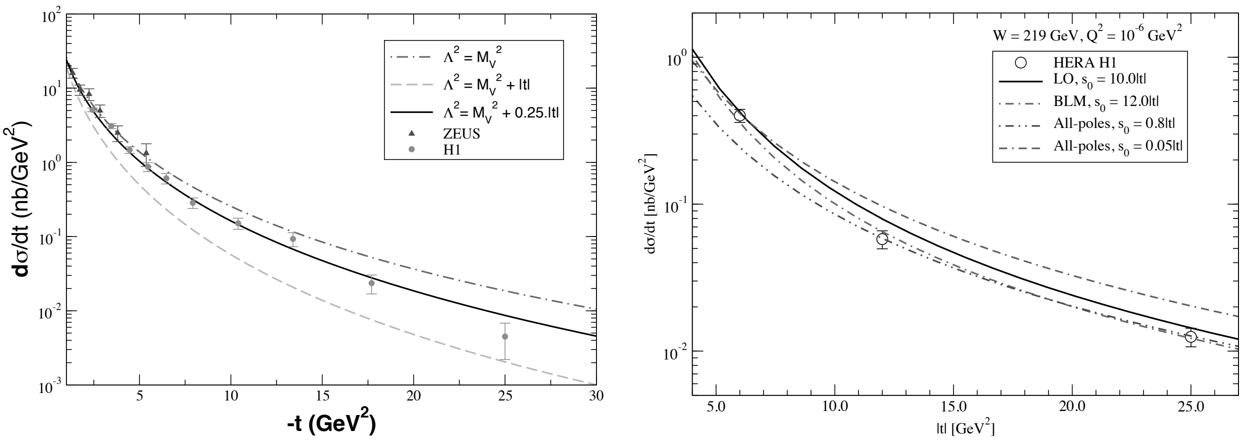

Figure 144: Cross section for the exclusive particle production at large-t in ep collisions. Left: J/ψ production. Right: γ production. Data from HERA [16–19].

3 Results

The results strongly depend on the coupling constant and the choice of the energy scale Λ. In Refs. [6,7] we have performed an detailed study of these choices in the predictions. We assumed a fixed coupling constant ($\alpha_s = 0.21$) and that the energy scale for vector mesons can be expressed by $\Lambda^2 = \beta M_V^2 + \gamma|t|$, following [15], where β and γ are free parameters to be fixed by the data. In the case of the photon production at large-t, we assumed that the scale can be expressed by $\Lambda^2 = \gamma'|t|$, with γ' depending on the BFKL function (see [8]).

Our results for the differential cross section are presented in Fig. 144, where we demonstrated that BFKL formalism is able to describe the HERA data. In the photon case, we analyze the effects of change the BFKL dynamics, using distinct analytically forms for the NLO BFKL kernel as well as the LO one. We have obtained that a reasonable agreement with the HERA experimental data. This results must be taken as an educated estimate, due the fact that we have used the impact factors of the transition $\gamma^* \to \gamma$ at leading order.

Lets now consider the vector meson production at large-t in coherent pp collisions. The cross section in a coherent hadron-hadron collision is given by

$$\frac{d\sigma\ [h_1 + h_2 \to h_1 \otimes Y \otimes X]}{dy} = \int_{t_{\min}}^{t_{\max}} dt\ \omega \frac{dN_\gamma(\omega)}{d\omega}\,\frac{d\sigma_{\gamma h \to YX}}{dt}\,(\omega) \tag{372}$$

where $dN_\gamma(\omega)/d\omega$ is the equivalent photon flux as a function of photon energy ω. In our calculations we have used the photon flux proposed in Ref. [20] for the proton. Our predictions for the rapidity distributions for the ρ and J/Ψ production are shown in Fig. 145 considering different t-ranges. In Ref. [7] we also have calculated the Υ production. In [6, 7], we present our predictions for the event rates at LHC energy. Our results indicate that the experimental identification of these processes can be feasible at the LHC.

4 Conclusions and perspectives

The description of the high energy limit of the Quantum Chromodynamics (QCD) is an important open question in the Standard Model. During the last decades several approaches were developed in order to improve our understanding from a fundamental perspective. In particular, after a huge theoretical effort, now we have available the NLO corrections for the BFKL characteristic function, which allow us to improve the analysis of the exclusive vector meson and photon production at large-t

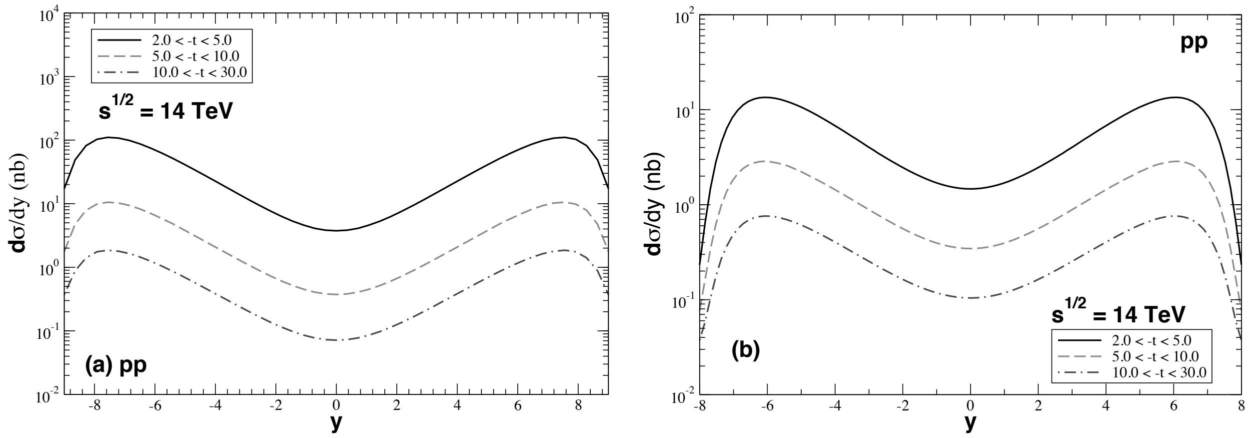

Figure 145: Rapidity distribution for the ρ (left panel) and J/Ψ (right panel) production in coherent pp interactions at LHC energy.

which are expected to probe the underlying QCD dynamics. Our results for vector meson and photon production in ep collisions at HERA demonstrated that the BFKL formalism is able to describe the current experimental data. Moreover, our estimates for the vector meson production in coherent pp interactions at LHC demonstrated that the study of this process can be able to constrain the QCD dynamics. It is important to emphasize that our results are complementary to the recent theoretical and phenomenological studies that use NLO BFKL Pomeron [21–24]. Presently, we are performing a more accurate analysis on the choice of the energies scales in exclusive production using the principle of maximum conformality in NLO BFKL Pomeron [25].

Acknowledgments

This work is supported by FAPERGS, CNPq and CAPES.

References

1. L. Schoeffel, Prog. Part. Nucl. Phys. **65**, 9 (2010) [arXiv:0908.3287 [hep-ph]].
2. L. N. Lipatov, Sov. J. Nucl. Phys. **23**, 338 (1976) [Yad. Fiz. **23**, 642 (1976)].
3. E. A. Kuraev, L. N. Lipatov and V. S. Fadin, Sov. Phys. JETP **44**, 443 (1976) [Zh. Eksp. Teor. Fiz. **71**, 840 (1976)].
4. E. A. Kuraev, L. N. Lipatov and V. S. Fadin, Sov. Phys. JETP **45**, 199 (1977) [Zh. Eksp. Teor. Fiz. **72**, 377 (1977)].
5. I. I. Balitsky and L. N. Lipatov, Sov. J. Nucl. Phys. **28**, 822 (1978) [Yad. Fiz. **28**, 1597 (1978)].
6. V. P. Goncalves and W. K. Sauter, Phys. Rev. D **81**, 074028 (2010) [arXiv:0911.5638 [hep-ph]].
7. V. P. Goncalves and W. K. Sauter, Eur. Phys. J. A **47**, 117 (2011) [arXiv:1004.1952 [hep-ph]].
8. V. P. Goncalves and W. K. Sauter, Phys. Rev. D **87**, 054035 (2013) [arXiv:1302.2058 [hep-ph]].
9. V. S. Fadin and L. N. Lipatov, Phys. Lett. B **429**, 127 (1998) [hep-ph/9802290 [hep-ph]].
10. M. Ciafaloni and G. Camici, Phys. Lett. B **430**, 349 (1998) [hep-ph/9803389 [hep-ph]].
11. D. A. Ross, Phys. Lett. B **431**, 161 (1998) [hep-ph/9804332 [hep-ph]].
12. A. Sabio Vera, Nucl. Phys. B **722**, 65 (2005) [hep-ph/0505128 [hep-ph]].
13. S. J. Brodsky, V. S. Fadin, V. T. Kim, L. N. Lipatov and G. B. Pivovarov, JETP Lett. **70**, 155 (1999) [hep-ph/9901229 [hep-ph]].
14. S. J. Brodsky, G. P. Lepage and P. B. Mackenzie, Phys. Rev. D **28**, 228 (1983).
15. J. R. Forshaw and G. Poludniowski, Eur. Phys. J. C **26**, 411 (2003) [hep-ph/0107068 [hep-ph]].

16. S. Chekanov *et al.* [ZEUS Collaboration], Eur. Phys. J. C **26**, 389 (2003) [hep-ex/0205081 [hep-ex]].
17. A. Aktas *et al.* [H1 Collaboration], Phys. Lett. B **568**, 205 (2003).
18. S. Chekanov *et al.* [ZEUS Collaboration], Eur. Phys. J. C **26**, 389 (2003) [hep-ex/0306013 [hep-ex]].
19. F. D. Aaron *et al.* [H1 Collaboration], Phys. Lett. **B672**, 219 (2009) [arXiv:0810.3096 [hep-ex]].
20. M. Drees and D. Zeppenfeld, Phys. Rev. D **39**, 2536 (1989).
21. M. Hentschinski, A. S. Vera and C. Salas, Phys. Rev. Lett. **110**, 041601 (2013) [arXiv:1209.1353 [hep-ph]].
22. M. Hentschinski, A. Sabio Vera and C. Salas, Phys. Rev. D **87**, 076005 (2013) [arXiv:1301.5283 [hep-ph]].
23. D. Colferai, F. Schwennsen, L. Szymanowski and S. Wallon, JHEP **1012**, 026 (2010) [arXiv:1002.1365 [hep-ph]].
24. B. Ducloué, L. Szymanowski and S. Wallon, Phys. Rev. Lett. **112**, 082003 (2014) [arXiv:1309.3229 [hep-ph]].
25. X. C. Zheng, X. G. Wu, S. Q. Wang, J. M. Shen and Q. L. Zhang, JHEP **1310**, 117 (2013) [arXiv:1308.2381 [hep-ph]].

Tiago C. Adorno
Caio V. Costa
Dmitri Gitman
Anatoly Shabad

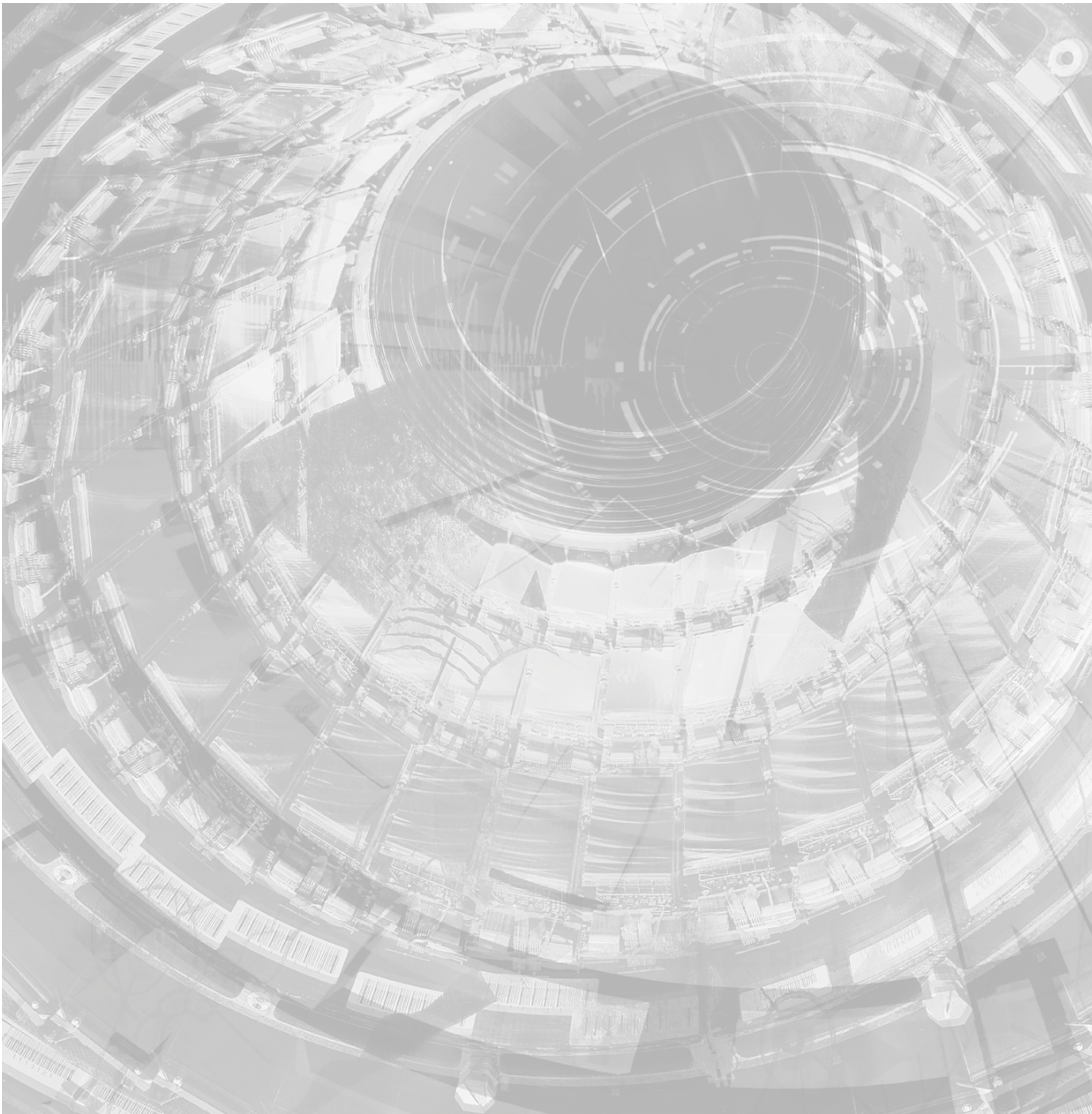

Static field configurations in truncated QED

Tiago C. Adorno [d], Caio. V. Costa [d], Dmitri M. Gitman [d, x, y], Anatoly E. Shabad [x, y33]

[d] The Institute of Physics, University of Sao Paulo, Sao Paulo, Brazil

[x] P. N. Lebedev Physics Institute, Moscow, Russia

[y] Tomsk State University, Tomsk, Russia

Abstract

Due to the nonlinearity of QED, a static charge becomes a magnetic dipole if placed in a magnetic field, and a magnetic monopole if the background is a combination of constant electric and magnetic fields. Already without external field, the cubic Maxwell equation for the field of a point charge has a soliton solution with a finite field energy. Equations are given for self-coupling dipole moments. Any theoretically found value for a multipole moment of a baryon or a meson should be subjected to nonlinear renormalization.

1 Introduction

In this talk we give an overview of the results presented in Refs. [1]– [4] and [5]. Yet unpublished results are reported in Subsection 2.2.

The static nonlinear Maxwell equations produced by the Euler-Heisenberg Lagrangian $\mathcal{L}$ truncated at the fourth power of its Taylor expansion in the fields have the form [1]

$$(\boldsymbol{\nabla}\cdot\mathbf{E}(\mathbf{x})) = j_0^{\mathrm{lin}} + j_0^{\mathrm{nl}}, \quad [\boldsymbol{\nabla}\times\mathbf{B}(\mathbf{x})] = \mathbf{j}^{\mathrm{lin}} + \mathbf{j}^{\mathrm{nl}}. \tag{373}$$

Here $j_0^{\mathrm{lin}}$and $\mathbf{j}^{\mathrm{lin}}$ are external current components, while the nonlinear current j_μ^{nl} is the one induced by the electric, $\mathbf{E}$, and magnetic, $\mathbf{B}$, fields themselves:

$$j_0^{\mathrm{nl}} = \mathcal{L}_{\mathfrak{F}\mathfrak{F}}\left(\boldsymbol{\nabla}\cdot\mathfrak{F}(\mathbf{x})\mathbf{E}(\mathbf{x})\right) - \mathcal{L}_{\mathfrak{G}\mathfrak{G}}\left(\boldsymbol{\nabla}\cdot\mathbf{B}(\mathbf{x})\right)\mathfrak{G}(\mathbf{x}), \tag{374}$$

$$\mathbf{j}^{\mathrm{nl}} = \mathcal{L}_{\mathfrak{F}\mathfrak{F}}\left[\boldsymbol{\nabla}\times\mathbf{B}(\mathbf{x})\right]\mathfrak{F}(\mathbf{x}) + \mathcal{L}_{\mathfrak{G}\mathfrak{G}}\left[\boldsymbol{\nabla}\times\mathbf{E}(\mathbf{x})\right]\mathfrak{G}(\mathbf{x}). \tag{375}$$

Here $\mathcal{L}_{\mathfrak{F}\mathfrak{F}}$ and $\mathcal{L}_{\mathfrak{G}\mathfrak{G}}$ are the second derivatives of $\mathcal{L}$ with respect to the field invariants $=\frac{B^2-E^2}{2}$, $\mathfrak{G} = (\mathbf{E}\cdot\mathbf{B})$, taken at constant values of the fields that make up the background above which the expansion of the Lagrangian has been done. In QED $\mathcal{L}_{\mathfrak{F}\mathfrak{F}}$ and $\mathcal{L}_{\mathfrak{G}\mathfrak{G}}$ are at least quadratic with respect to the fine-structure constant α. Unlike the cited works, we have disregarded here the third derivative $\mathcal{L}_{\mathfrak{F}\mathfrak{F}\mathfrak{G}}$, since it is smaller with respect to α. The differentiaton operators ∇ in (374), (375) act on everything to the right of them.

Equations (373) should be completed with the "first pair" of static Maxwell equations $[\boldsymbol{\nabla}\times\mathbf{E}(\mathbf{x})] = (\boldsymbol{\nabla}\cdot\mathbf{B}(\mathbf{x})) = 0$.

2 Spheric charge in a static and homogeneous background

In this section the Maxwell equations (373) will be treated perturbatively, with their right-hand sides linearized near an external field. The nonlinear current $\mathbf{j}^{\mathrm{nl}}$, its constituents $\mathcal{L}_{\mathfrak{F}\mathfrak{F}}$ and $\mathcal{L}_{\mathfrak{G}\mathfrak{G}}$ included,

[33] Corresponding author. See Table 2 for the complete list of talks given at the workshop.

will be taken at $\mathfrak{G} = \overline{\mathfrak{G}} \equiv \overline{\mathbf{B}}{\cdot}\overline{\mathbf{E}} = const,$ $2\mathfrak{F} = 2\overline{\mathfrak{F}} \equiv \overline{B}^2 - \overline{E}^2 = const.$ It depends only on the background time- and space-independent electric, $\overline{\mathbf{E}}$, and magnetic fields $B = |\overline{\mathbf{B}}|$. These constant fields identically satisfy the Maxwell equations (373) without external currents needed to support them: this is a manifestation of the gauge invariance. The electric field will be that produced by a spherically-symmetric charge $j_0^{\rm lin} \neq 0$. Its self-interaction $j_0^{\rm nl}$ is neglected. The magnetic field will be due only to the electric charge, its external source $\mathbf{j}^{\rm lin}$ will be kept equal to zero throughout this section.

2.1 Magnetic dipole solution produced by electric charge in a magnetic background [2], [3], [4].

In this subsection the constant electric field is not included, $\overline{\mathbf{E}}= \mathbf{0}$. The electric field $\mathbf{E}$ is only that of an non-selfinteracting external spherical charge distribution.Then the nonlinear current (374), (375) is: $j_0^{\rm nl}(\mathbf{x}) = 0\,,\;\; j_k^{\rm nl}(\mathbf{x}) = \epsilon_{ijk}\nabla_i\mathfrak{h}_k$, where

$$\mathfrak{h}_i(\mathbf{x}) = -\frac{\overline{B}_i}{2}\mathcal{L}_{\mathfrak{F}\mathfrak{F}}E^2 + E_i\left(\overline{\mathbf{B}}{\cdot}\mathbf{E}\right)\mathcal{L}_{\mathfrak{G}\mathfrak{G}} \tag{376}$$

is an auxiliary magnetic field. From this current, the part containing the magnetic field $\delta\mathbf{B} = \mathbf{B} - \overline{\mathbf{B}}$ produced by the electric field is omitted as containing higher-order corrections with respect to α. The magnetic excitation of the background results from equations (373) and from equation $(\boldsymbol{\nabla}\cdot\mathbf{B}(\mathbf{x})) = 0$ to be:

$$\delta B_i(\mathbf{x}) = \left(\delta_{ik} - \frac{\nabla_i\nabla_k}{\nabla^2}\right)\mathfrak{h}_k(\mathbf{x}) = \mathfrak{h}_i(\mathbf{x}) + \frac{\partial_i\partial_k}{4\pi}\int d^3y\frac{\mathfrak{h}_k(\mathbf{y})}{|\mathbf{x}-\mathbf{y}|}\,. \tag{377}$$

Let us take the electric field $\mathbf{E}$ as the one produced – disregarding the higher-order effect of the linear electrization in the magnetic field – by the charge distributed with the constant density $j_0^{\rm lin}(\mathbf{x}) = \rho(r) = \left(\frac{3}{4\pi}\frac{q}{R^3}\right)\theta(R-r)$ inside a sphere with the radius R. The long-range asymptotic behavior of (377) proves to be that of a magnetic dipole:

$$\delta B_i^{\rm LR}(\mathbf{x}) = \frac{3\,(\mathbf{x}\cdot\mathbf{M})\,x_i}{r^5} - \frac{M_i}{r^3}\,, \tag{378}$$

with $\mathbf{M}$ being an equivalent magnetic dipole moment. It cannot be otherwise, because Eq. (378) is the only axial-symmetric magnetic field satisfying the free Maxwell equations $[\boldsymbol{\nabla}\times\mathbf{B}(\mathbf{x})] = (\boldsymbol{\nabla}\cdot\mathbf{B}(\mathbf{x})) = 0$, bearing in mind that the electric field contribution into (375) decreases at large distances as r^{-5}, while the deviation from zero of any axial-symmetric field other than (378) would produce a larger extra addition to the current of the order of r^{-4}. The value of the magnetic moment was calculated in ([3], [4]) to be

$$M_i = \left(\frac{q}{4\pi}\right)^2\frac{1}{5R}\left(3\mathcal{L}_{\mathfrak{F}\mathfrak{F}} - 2\mathcal{L}_{\mathfrak{G}\mathfrak{G}}\right)\overline{B}_i\,. \tag{379}$$

The extension beyond the spherical symmetry of the electric field is also available [4].

2.2 Magnetic monopole solution produced by electric charge in a magnetic plus electric background

All is the same as in the previous item, except that now both electric and magnetic fields in the constant background are different from zero. They are taken to be parallel to each other in the Lorentz frame, where the electric charge is at rest, $\overline{\mathbf{B}} \parallel \overline{\mathbf{E}}$. Their common direction is presented by a unit vector μ, $\mu = 1$. We are going to consider the deviations of the electric $\delta\mathbf{E}(\mathbf{x}) = \overline{\mathbf{E}} - \mathbf{E}(\mathbf{x})$ and magnetic $\delta\mathbf{B}(\mathbf{x}) = \overline{\mathbf{B}} - \mathbf{B}(\mathbf{x})$ fields to be small as compared to their constant parts $\delta\mathbf{E} << \overline{\mathbf{E}}$, $\delta\mathbf{B} << \overline{\mathbf{B}}$. Omitting the deviations squared and also neglecting $\mathcal{L}_{\mathfrak{F}\mathfrak{F}}\mathfrak{F}$ and $-\mathcal{L}_{\mathfrak{F}\mathfrak{F}}\overline{B}^2 + \overline{E}^2\mathcal{L}_{\mathfrak{G}\mathfrak{G}}$ as compared to unity[34] (this reduces to omitting from the current (375) the contribution of $\delta\mathbf{B}$, analogous to what has been done in the previous subsection, when passing to Eq. (376)) equation (373) becomes

$$[\boldsymbol{\nabla}\times\delta\mathbf{B}(\mathbf{x})]-\mathcal{L}_{\mathfrak{FF}}\left[\overline{\mathbf{B}}\times\boldsymbol{\nabla}\right](\overline{\mathbf{E}}\cdot\delta\mathbf{E}))+\mathcal{L}_{\mathfrak{GG}}\left[\overline{\mathbf{E}}\times\nabla\right]\left(\delta\mathbf{E}\cdot\overline{\mathbf{B}}\right)=0 \tag{380}$$

For the special case of the Coulomb field $\delta\mathbf{E}=\frac{q\mathbf{x}}{4\pi r^3}$ (outside the charge) this equation is compatable with the ansatz $\delta\mathbf{B}=\mathbf{x}\frac{1}{r^3}f(\frac{z}{r})$, where $z=(\mu\cdot\mathbf{x})=r\cos\theta$ is the coordinate component along the common direction of the constant fields, $r\equiv|\mathbf{x}|$. This ansatz formally obeys the other Maxwell equation not included into (373) $(\boldsymbol{\nabla}\cdot\delta\mathbf{B})=0$ outside the charge, which may be violated only inside the charge or in the point $r=0$, where the charge is located, when the charge is pointlike. Equation (380) reduces to a linear first-order differential equation for the function $f(\frac{z}{r})$, ready to solve. In this way the magnetic field is found

$$\delta\mathbf{B}=-\frac{q}{8\pi}(\mathcal{L}_{\mathfrak{FF}}+\mathcal{L}_{\mathfrak{GG}})\overline{\mathfrak{G}}\frac{\mathbf{x}}{r^5}z^2=-\frac{q}{8\pi}(\mathcal{L}_{\mathfrak{FF}}+\mathcal{L}_{\mathfrak{GG}})\overline{\mathfrak{G}}\frac{\mathbf{x}\cos^2\theta}{r^3},$$

whose lines of force are directed along the radius-vector $\mathbf{x}$. Note that in the limit $\overline{\mathbf{E}}=0$ this solution disappears not to turn into the solution of the previous subsection, which is of completely different character. To determine the magnetic charge q_M it is necessary to integrate $\delta\mathbf{B}$ over the surface of a sphere with arbitrary radius r

$$q_M=\int(\delta\mathbf{B}\cdot\mathrm{d}\mathbf{S})=-\frac{q}{6}(\mathcal{L}_{\mathfrak{FF}}+\mathcal{L}_{\mathfrak{GG}})\overline{\mathfrak{G}}$$

Hence, for the pointlike electric charge, its magnetic charge density in the constant background is

$$(\nabla\cdot\delta\mathbf{B})=q_M\delta^3(\mathbf{x})\,.$$

3 Cubic self-interaction of electro- and magneto-static fields in blank vacuum

In this section no background field will be present. Unlike the previous section, now the nonlinearity in the Maxwell equation will not be taken as small, but will be treated seriously. In the two subsections below we include only the cases, where either only electric, E, or only magnetic, B, field is present, and not the both fields simultaneously. Then the nonlinear current (374, 375) is

$$j_0^{\mathrm{nl}}(x)=\frac{1}{2}\mathcal{L}_{\mathfrak{FF}}\partial_i\left[\left(B^2-E^2\right)E_i\right],\qquad j_i^{\mathrm{nl}}(x)=-\frac{1}{2}\mathcal{L}_{\mathfrak{FF}}\partial_j\left[\left(B^2-E^2\right)B_k\right]\epsilon_{ijk}. \tag{381}$$

In the present section the derivative $\mathcal{L}_{\mathfrak{FF}}\equiv\gamma$ is understood as taken at $\mathfrak{F}=\mathfrak{G}=0$.

3.1 Self-coupling of a charge. Finiteness of the point-charge electrostatic field-energy

Let there be a point charge e placed at the origin $r=0$. We are looking for a spherically symmetric solution of the Maxwell equation (373) with $B=0$, which, given the nonlinear current (381), takes the form

$$\nabla\left[\left(1+\frac{\gamma}{2}E^2\right)\mathbf{E}\right]=0, \tag{382}$$

valid everywhere outside the origin $\mathbf{x}=0$, since $j_0=0$ there. At large r the standard Coulomb field of the point charge e

$$\frac{e}{4\pi r^2}\frac{\mathbf{x}}{r}, \tag{383}$$

[34]This disregard is not necessary. Solutions can be found without referring to it within the same ansatz (see below). These are, however, a bit more complicated.

should be implied as the boundary condition. Then with the spherically symmetric Ansatz $E(r)\frac{\mathbf{x}}{r} = \mathbf{E}\,(\mathbf{x})$ equation (382) is solved as

$$\left(1 + \frac{\gamma}{2}E^2(r)\right)E\,(r) = \frac{e}{4\pi r^2}. \tag{384}$$

This cubic equation is readily solved by the Cardano formula (see [5] for the explicit representation), but the most important thing about its solution is clear without solving it: at short distances $r \to \infty$ the field E also infinitely grows, hence one can neglect the unity in (384) to immediately obtain $E\,(r) \sim \left(\frac{e}{2\pi\gamma}\right)^{\frac{1}{3}}\left(\frac{1}{r}\right)^{\frac{2}{3}}$. This behavior of the electrostatic field , produced by the point charge e via the nonlinear field equations, is essentially less singular in the vicinity of the charge than the standard Coulomb field $\frac{e}{4\pi r^2}$. This is an extension of elecrodynamics to the domain of short distances compatable with the traditional theory of electromagnetism surely established for larger distances.

Let us see that this suppression of the singularity is enough to provide convergence of the integrals giving the energy of the field configuration that solves equation (382). To this end note that on the subclass of electromagnetic field we are considering here, the equations of motion (382) are generated by the quartic Lagrangian

$$-\,F\,(x) + \mathcal{L} = -F\,(x) + \frac{\gamma}{2}\,(F(x))^2\,. \tag{385}$$

With this Lagrangian, the energy density calculated on spherically-symmetric electric field configuration following the Noether theorem is

$$\Theta^{00} = \frac{E^2}{2} + \frac{3\gamma E^4}{8}. \tag{386}$$

The behaviour $E\,(r) \sim \left(\frac{1}{r}\right)^{\frac{2}{3}}$ obtained provides the ultraviolet, near $|\mathbf{x}| = 0$, convergence of the electrostatic field energy $\int \Theta^{00}d^3x$ of the point charge. As for the convergence of this integral at $|\mathbf{x}| \to \infty$, it is provided by the standard long-range Coulomb behaviour (383) of the solution to equation (382) obtained by neglecting the second term inside the bracket as compared to the unity in the far-off region.

The explicit use of the Cardano formula in (386) allows to calculate the integral for the field energy. If the value $\mathcal{L}_{\mathfrak{FF}} = \frac{e^4}{45\pi^2 m^4}$,where e and m are the electron charge and mass, is accepted – referring to the Euler-Heisenberg effective Lagrangian – for γ, the result for the "rest mass of the electron," understood as a point charge, is about twice the true electron mass: $\int \Theta^{00}d^3x = 2.09m$.

The conclusion about finiteness of the electrostatic field energy of a point charge can be extended [6] to any nonlinear electrodynamics with the effective Lagrangian growing faster than $\mathfrak{F}^{3/2}$, any-power polynomial of the field invariants included, thereby also to QED truncated at any finite term of its Taylor expansion in powers of the field in place of (373).

3.2 Self-coupling of magnetic and electric dipoles

Consider first a magnetic dipole. This means that only B is kept in the nonlinear current (381), hence $j_0^{\mathrm{n}l} = 0$. As for the nonlinear 3-current, it is expressed as

$$j_i{}^{\mathrm{nl}}\,(\,\mathbf{x}) = \epsilon_{ijk}\nabla_j\eta_k\,(\mathbf{x})\,, \qquad \eta_i\,(\mathbf{x}) = -\frac{1}{2}\mathcal{L}_{\mathfrak{FF}}B_i\,(\mathbf{x})\,B^2\,(\mathbf{x}) \tag{387}$$

in terms of the auxiliary magnetic field $\mathfrak{h}$ analogous to (376). Eq. (377) is again valid for the magnetic field induced by the nonlinear current, this time without the reservations made in the previous section about the disregard of the linear magnetization. This field is to be added to the initial magnetic field $\mathbf{h}^{\mathrm{nl}}$ (linearly produced by the current $\mathbf{j}$) to make the total resulting magnetic field $\mathbf{h}^{\mathrm{tot}} = \mathbf{h}^{\mathrm{nl}} + \mathbf{h}$.

Let there be a sphere with the radius R, and a time-independent current $\mathbf{j}(\mathbf{x})$ concentrated on its surface:

$$\mathbf{j}(\mathbf{x}) = \frac{[\mathbf{M}^{(0)} \times \mathbf{x}]}{r^4}\delta(r - R). \tag{388}$$

Here $\mathbf{M}^{(0)}$ is a constant vector directed, say, along the axis 3. The current density (388) obeys the continuity condition $\nabla\mathbf{j} = 0$, its flow lines are circular in the planes parallel to the plane (1,2). The magnetic field produced by this current via the Maxwell equation $\nabla \times \mathbf{h}^{\text{lin}}(\mathbf{x}) = \mathbf{j}(\mathbf{x})$ is

$$\mathbf{h}^{\text{lin}}(\mathbf{x}) = \theta\left(R - r\right)\frac{2\mathbf{M}^{(0)}}{R^3} + \theta\left(r - R\right)\left(-\frac{\mathbf{M}^{(0)}}{r^3} + 3\frac{(\mathbf{x}\cdot\mathbf{M}^{(0)})}{r^5}\mathbf{x}\right). \tag{389}$$

Outside the sphere this is the magnetic dipole field with the constant vector density $\mathbf{M}^{(\mathbf{0})}$ playing the role of its magnetic moment. Using this expressioin in the r.-h. side of Eq. (377), after a lengthy calculation the nonlinear correction h to the field (389) of the magnetic dipole (388) was obtained in [1] both inside and outside the sphere. At large distances the resulting field reproduces the original magnetic dipole behaviour:

$$\mathbf{h}^{tot}\left(\mathbf{x}\right)\Big|_{r>>R} = \mathbf{h}^{\text{lin}}\left(\mathbf{x}\right)\left(1 - \frac{7}{5}\mathcal{L}_{\mathfrak{F}\mathfrak{F}}\frac{M^{(0)2}}{R^6}\right). \tag{390}$$

Once we want to treat the nonlinearity seriously, and not just as a perturbation, we should for self-consistency demand that the magnetic field forming the nonlinear current (387) be not (389), but its final result, which is again the magnetic dipole field, but with the bare magnetic moment $\mathbf{M}^{(\mathbf{0})}$ replaced by the final magnetic moment to be denoted as $\mathbf{M}$. Then in the long range for the total field we obtain

$$-\frac{\mathbf{M}}{r^3} + 3\frac{\mathbf{x}\cdot\mathbf{M}}{r^5}\mathbf{x} = -\frac{\mathbf{M}^{(0)}}{r^3} + 3\frac{\mathbf{x}\cdot\mathbf{M}^{(0)}}{r^5}\mathbf{x} - \left(\frac{\mathbf{M}}{r^3} + 3\frac{\mathbf{x}\cdot\mathbf{M}}{r^5}\mathbf{x}\right)\left(\frac{7}{5}\mathcal{L}_{\mathfrak{F}\mathfrak{F}}\frac{M^2}{R^6}\right). \tag{391}$$

From this the equation for self-coupling of the magnetic moment follows to be:

$$\mathbf{M}\left(1 + \frac{7}{5}\mathcal{L}_{\mathfrak{F}\mathfrak{F}}\frac{M^2}{R^6}\right) = \mathbf{M}^{(0)} \tag{392}$$

Analogous equation for the electric moment is

$$\mathbf{p}\left(1 + \frac{1}{10}\mathcal{L}_{\mathfrak{F}\mathfrak{F}}\frac{p^2}{R^6}\right) = \mathbf{p}^{(0)}. \tag{393}$$

Acknowledgments

Supported by FAPESP under grants 2013/00840-9, 2013/16592-4 and 2014/08970-1, by RFBR under Project 14-02-01171, and by the TSU Competitiveness Improvement Program, by a grant from "The Tomsk State University D. I. Mendeleev Fund Program". D.G. also thanks CNPq and FAPESP for permanent support.

References

1. C. V. Costa, D. M. Gitman and A. E. Shabad, Phys. Rev. D **88**, 085026 (2013) [arXiv:1307.1802 [hep-th]].
2. D. M. Gitman and A. E. Shabad, Phys. Rev. D **86**, 125028 (2012) [arXiv:1209.6287 [hep-th]].
3. T. C. Adorno, D. M. Gitman and A. E. Shabad, Eur. Phys. J. C **74**, 2838 (2014) [arXiv:1311.4081 [hep-th]].
4. T. C. Adorno, D. M. Gitman and A. E. Shabad, Phys. Rev. D **89**(4), 047504 (2014) [arXiv:1402.3848 [hep-th]].
5. C. V. Costa, D. M. Gitman and A. E. Shabad, Phys. Scripta **90**(7), 074012 (2015) [arXiv:1312.0447 [hep-th]].
6. C. V. Costa, D. M. Gitman and A. E. Shabad, to be published.

Author Index

Ministério da Ciência, Tecnologia e Inovação

ISBN: 978-85-42506976